## SYNTHESIS AND MODIFICATION IN 2D NANOMATERIALS BASED COMPOSITES FOR CANCER DIAGNOSTIC APPLICATIONS

**Thesis Submitted** 

in Partial Fulfillment of the Requirements for the

Degree of

**Doctor of Philosophy** 

in

**Applied Physics** 

by

Kanika Sharma

(2K18/Ph.D./AP/16)

Under the Supervision and Co-Supervision of

Prof. Nitin K. Puri and Dr. Bharti Singh

**Department of Applied Physics** 



#### **DELHI TECHNOLOGICAL UNIVERSITY**

(Formerly Delhi College of Engineering)
Shahbad Daulatpur, Main Bawana Road
Delhi-110042, India
August 2025

©Delhi Technological University-2025 All rights reserved.



#### DELHI TECHNOLOGICAL UNIVERSITY

### (Govt. of National Capital Territory of Delhi) Shahbad Daulatpur, Bawana Road, Delhi-110042

#### CANDIDATE'S DECLARATION

I, Ms. Kanika Sharma, hereby certify that the thesis titled "Synthesis and Modification in 2D Nanomaterials based Composites for Cancer Diagnostic Applications" submitted in the fulfilment of the requirements for the award of the **Degree of Doctor of Philosophy** in the discipline of **Physics**, submitted in the Department of Applied Physics, Delhi Technological University (Formerly Delhi College of Engineering), Delhi is an authentic record of my own work carried out during the period from July 2018 to August 2025 under the Supervision of **Prof. Nitin K. Puri** and Co-Supervision of **Dr. Bharti Singh**. The matter presented in the thesis has not been submitted by me for the award of any other degree of this or any other Institute.

Kanika Sharma (2K18/Ph.D./AP/16) **Department of Applied Physics Delhi Technological University Delhi – 110042, India** 

This is to certify that the candidate has incorporated all the corrections suggested by the examiner in the thesis and the statement made by the candidate is correct to the best of our knowledge

> Prof. Nitin K. Puri **Supervisor Delhi Technological University** Delhi-110042, India

Dr. Bharti Singh Co-Supervisor **Delhi Technological University** Delhi-110042, India

Signature of Examiners



#### **CERTIFICATE**

This is to certify that the thesis entitled "Synthesis and Modification in 2D Nanomaterials based Composites for Cancer Diagnostic Applications" submitted by Ms. Kanika Sharma (2K18/Ph.D./AP/16) for the award of Doctor of Philosophy from Department of Applied Physics, Delhi Technological University, Delhi, under my supervision. The thesis embodies results of original work, and studies are carried out by the candidate herself in the Nanomaterials Research Laboratory (NRL), Department of Applied Physics, Delhi Technological University (DTU), Delhi, India and the contents of the thesis do not form the basis for the award of any other degree to the candidate or to anybody else from this or any other University/Institution.

Prof. Nitin K. Puri Supervisor **Department of Applied Physics Delhi Technological University** Delhi-110042, India

Dr. Bharti Singh Co-Supervisor **Delhi Technological University** Delhi-110042, India

**Prof. Vinod Singh Head of the Department** Department of Applied Physics 
Department of Applied Physics **Delhi Technological University** Delhi-110042, India

### **Acknowledgements**

With utmost reverence and humility, I express my heartfelt and sincere gratitude to the Almighty God, whose blessings, grace, and infinite strength have made me capable of reaching this level of academic pursuit. Every step of this journey has been possible only through His divine guidance, which has filled me with courage, perseverance, and determination to overcome challenges and move forward with faith. I extend my heartfelt reverence to my spiritual Guru, whose enlightening words and timeless wisdom have instilled in me the power of positive thinking and clarity of vision. Their guidance has been a beacon of light during moments of difficulty, enabling me to face challenges with calmness, hope, and resilience. The timely help and divine interventions I have received at crucial junctures have further strengthened my faith and inspired me to approach even the most testing situations with renewed energy and optimism. This spiritual support has been a constant force in shaping not only my academic journey but also my personal growth.

First and the foremost, I express my earnest and deepest gratitude to my research supervisor, Prof. Nitin K. Puri, Professor, Department of Applied Physics, Delhi Technological University, whose invaluable guidance, encouragement, and steadfast support have been the very foundation of this research work. His depth of knowledge, pedagogical wisdom, and understanding nature have been a constant source of inspiration, motivating me to persevere through challenges and evolve as a dedicated researcher. It has been a privilege to work under his mentorship, and I shall always cherish this invaluable association while aspiring to maintain a lifelong bond with him and with Delhi Technological University. I extend my wholehearted gratitude to my research co-supervisor, Dr. Bharti Singh, Assistant Professor, Department of Applied Physics, for her unwavering support, meticulous mentoring, and consistent encouragement throughout my doctoral research. Her keen observations, constructive feedback, and patient guidance have strengthened my research work in every possible way and have inspired me to constantly strive for excellence.

I owe deep appreciation and sincere thanks to Prof. Bansi D. Malhotra, Department of Biotechnology, DTU, and Dr. Saurabh Srivastava, Assistant Professor, Rajkiya Engineering College, Ambedkar Nagar (U.P.), whose valuable insights, scholarly advice, and genuine encouragement have been instrumental in shaping the course of my research. Their mentorship not only enriched my academic endeavors but also helped me nurture qualities of discipline, patience, and self-confidence as an individual.

With deep respect, I acknowledge the contributions of the Honorable Vice Chancellors, Prof. Yogesh Singh (former), Prof. Jai Prakash Saini (former), and Prof. Prateek Sharma (current); along with Prof. Rinku Sharma (Academic Dean–PG), Prof. A.S. Rao (former HOD), and Prof. Vinod Singh (current HOD), Department of Applied Physics, DTU. Their leadership, vision, and timely support through infrastructural and

academic facilities have been fundamental in enabling the successful completion of my research work. My heartfelt recognitions go to Prof. S.C. Sharma, former DRC Chairperson, Department of Applied Physics, DTU, and my esteemed SRC & DRC committee members, for their valuable guidance, constructive feedback, and encouragement. Their support has provided me with clarity and direction at crucial stages of my work.

I also extend my warm thanks to the members of the Department of Biotechnology, DTU, particularly Dr. Shine Augustine and Dr. Niharika Gupta, whose consistent support and creation of a collegial and pleasant environment enriched my working experience. I remain deeply grateful to my friends and colleagues at the Nanomaterial Research Laboratory (NRL) – Dr. Deepika Sandil, Dr. Kamal Arora, Dr. Ritika Khatri, Anurag Bhandari, Abhishek Tanwar, and Sunil – for their constant encouragement, helpful discussions, and companionship during my research journey. A special word of gratitude goes to Dr. Lakshana Mahajan Puri and Dr. Mukesh Kumari for her generous guidance and timely assistance, which proved invaluable on many occasions. My appreciation also extends to my colleagues and batchmates – Dr. Km. Komal, Ms. Shilpa Rana, Dr. Deepali Chauhan, Dr. Komal Verma, Dr. Anchali Jain, Mr. Gagan Sharma, Dr. Deepali Alhuwalia, Dr. Ritika Kubba, Dr. Majot Kaur, Mr. Jewel Agarwal, Mr. Kunal Madaan, Ms. Parisha Diwan, Mr. Himanshu Nath, Mr. Arun Saji, Ms. Tripti Gupta, Ms. Archana, and Ms. Devanshika Jha – whose camaraderie, encouragement, and presence made this journey enriching and memorable. I equally acknowledge all research scholars of the Department of Applied Physics, DTU, for their goodwill, support, and valuable advice. I extend my heartfelt appreciation to the dedicated staff of the Department of Applied Physics and the Central Research Facilities, for their technical support and cooperation during the course of this work. I also wish to acknowledge the invaluable help of the laboratories in the Departments of Applied Physics, Chemistry, and Biotechnology for providing essential characterization facilities and for their readiness to assist whenever required. Their combined expertise, professionalism, genuine commitment, and timely support have greatly contributed to the quality and reliability of this research.

No words can fully capture my indebtedness to my family, whose unconditional love and blessings gave me the strength to begin, sustain, and accomplish this research. With deep respect, I bow before my grandfathers, Sh. Triloki Nath Sharma and Late Sh. Banwari Lal Joshi, and grandmothers, Smt. Sushma Sharma and Smt. Krishna Devi, whose blessings have always been my guiding light. I owe heartfelt gratitude to my parents, Sh. Pankaj Raj Sharma and Smt. Renu Sharma, for their sacrifices, encouragement, and unwavering faith in me. I remain forever thankful to my younger brother, Mr. Kunal Sharma, and my cousins, Vandana Sharma and Deepika Sharma, whose support and affection have been constant pillars of strength and guiding force in this journey. I feel truly blessed to acknowledge my dear friend, Ms. Shivani Chahal,

Ms. Parul Jadaun and Ms. Sheetal Joshi, who stood beside me like a pillar, inspiring me to maintain positivity, resilience, and balance throughout the ups and downs of this research journey.

I gratefully acknowledge the assistance and cooperation of the DTU staff from the Administration, Accounts, Store & Purchase, Central Library, and Computer Centre for their timely professional support, cooperation, and assistance throughout this work with their dedicated and valuable services. I sincerely acknowledge Delhi Technological University for extending essential facilities and for the financial assistance provided through the SERB-DST sponsored project, under which I was honoured to serve as a Junior Research Fellow during my Ph.D. program. This support was instrumental in facilitating my research goals.

Lastly, I humbly extend my thanks to each and every individual whose timely interventions, words of encouragement, or acts of kindness made this journey smoother, more pleasant, and profoundly meaningful.

Kanika Sharma

#### **Abstract**

This thesis has undertaken a systematic and in-depth exploration into the synthesis, characterization, and electrochemical applications of hexagonal boron nitride nanosheets (hBNNS) and their nano-hybrid composites with the overarching goal of developing ultrasensitive biosensors for the detection of carcinoembryonic antigen (CEA), a critical biomarker associated with several malignancies. The investigation addressed both the fundamental material challenges associated with pristine hBNNS and the engineering of innovative hybrid architectures capable of overcoming these intrinsic limitations to deliver enhanced electrochemical biosensing performance.

Hexagonal boron nitride nanosheets, due to their atomically thin morphology, large specific surface area, superior physicochemical stability, and dielectric properties, have attracted significant attention as a next-generation nanomaterial platform. Their layered structure provides smooth, chemically robust surfaces that are highly desirable for biomolecule immobilization and interface engineering. However, unlike conductive counterparts such as graphene, pristine hBNNS possess inherent chemical inertness and poor charge-transfer capability, severely restricting their direct applicability in electrochemical devices. This limitation forms the central bottleneck in translating the theoretical advantages of hBNNS into practical biosensing platforms.

To address these fundamental shortcomings, the present work systematically designed and fabricated hBNNS-based nano-hybrid composites through strategic integration with conductive, catalytically active, and structurally complementary materials. The rationale was to leverage synergistic effects wherein the weaknesses of pristine hBNNS are counterbalanced by the strengths of co-integrated nanostructures. Three representative material classes were employed: (i) reduced graphene oxide (rGO), a two-dimensional conductor with excellent electron mobility; (ii) copper/copper oxide (Cu/CuxO), a three-dimensional hierarchical material providing abundant catalytic and redox-active sites; and (iii) titanium dioxide (TiO<sub>2</sub>), a one-dimensional nanostructure renowned for its high surface area, photocatalytic activity, and electrochemical stability.

Each of these hybrid interfaces was engineered under optimized synthesis conditions to ensure controlled morphology, strong interfacial bonding, and homogeneous dispersion on the hBNNS surface. For instance, the incorporation of rGO introduced highly conductive networks that drastically improved electron transport and minimized interfacial resistance. The Cu/Cu<sub>X</sub>O component, synthesized into nanoflower and composite morphologies, imparted abundant catalytic sites and enhanced redox reactivity, thereby increasing charge transfer kinetics at the electrode interface. Similarly, TiO<sub>2</sub> nanostructures provided chemically stable scaffolds with enriched surface area that supported efficient immobilization of bio-recognition elements, while also acting as electron mediators. Collectively, these integrations transformed inert hBNNS into multifunctional hybrid architectures possessing conductivity, catalytic activity, and structural robustness.

Comprehensive physicochemical characterizations confirmed the successful formation of these hybrid systems. X-ray diffraction (XRD), Raman spectroscopy, FTIR, and UV–Visible spectroscopy validated structural integrity, phase purity, and bonding interactions. Microscopy analyses, including SEM and TEM, revealed the unique morphologies, ranging from layered nanosheets and hierarchical nanoflowers to well-distributed heterointerfaces, confirming the intended hybridization strategies. These

characterizations provided the structural and morphological foundation upon which electrochemical evaluations were subsequently built.

Electrochemical studies offered clear evidence of the enhanced performance delivered by hBNNS nano-hybrids. Cyclic voltammetry (CV) and differential pulse voltammetry (DPV) confirmed that hybrid electrodes demonstrated significantly improved electron transfer rates, lower charge-transfer resistance, and amplified current responses in comparison to pristine hBNNS. Furthermore, the reproducibility, selectivity, and stability studies highlighted the reliability of the fabricated immunoelectrodes. For instance, incorporation of rGO ensured superior conductivity and sensitivity, Cu/Cu<sub>x</sub>O contributed strong catalytic activity and favorable redox reactions, while TiO<sub>2</sub> offered chemical stability that enhanced long-term electrode performance. These synergistic effects collectively established hBNNS hybrids as versatile and high-performance electrochemical platforms.

The practical utility of these hybrid materials was demonstrated through their application in CEA biosensing. CEA is a clinically relevant biomarker whose sensitive detection is crucial for the early diagnosis and monitoring of cancers, including colorectal, pancreatic, and lung cancers. The fabricated immunoelectrodes exhibited ultrasensitive detection capability with low detection limits, wide linear ranges, and robust selectivity against common interferents. Blocking agents such as BSA ensured suppression of nonspecific binding, further improving selectivity. Real-sample analysis in spiked serum confirmed the applicability of the developed biosensors in clinically relevant conditions, thereby bridging the gap between laboratory synthesis and practical diagnostic implementation.

Importantly, the insights gained in this work extend beyond the development of CEA biosensors. The systematic demonstration of hybridization strategies provides a generalized framework for tailoring the properties of otherwise inert materials like hBNNS to suit diverse electrochemical applications. The ability to tune conductivity, generate defect-mediated active sites, and enhance biomolecule immobilization through rational material engineering opens new opportunities in multiple domains, including enzymatic and non-enzymatic biosensing, energy storage, catalysis, and environmental monitoring. Thus, this thesis establishes hBNNS-based nano-hybrids not merely as specialized materials for CEA detection but as a broader materials platform with multifunctional utility.

From a scientific perspective, this work makes three key contributions. First, it provides a comprehensive understanding of how intrinsic limitations of pristine hBNNS can be systematically overcome through strategic hybridization with conductive, catalytic, and stable nanostructures. Second, it validates the importance of defect generation, interface engineering, and synergistic interactions in dictating the electrochemical behavior of hybrid nanomaterials. Third, it demonstrates the successful translation of these materials into practical biosensing devices with clinical relevance, thereby bridging the gap between fundamental material science and biomedical application.

Looking forward, the findings of this thesis pave the way for future investigations in several directions. One promising avenue is the integration of hBNNS hybrids with emerging materials such as MXenes, metal—organic frameworks (MOFs), and covalent organic frameworks (COFs), which could further enrich electrochemical performance. Another potential direction involves exploring flexible and wearable biosensor architectures utilizing hBNNS hybrids, thereby advancing toward real-time, point-of-

care diagnostics. Additionally, coupling the developed biosensors with microfluidic platforms and smartphone-based readouts may provide cost-effective and accessible diagnostic technologies, particularly beneficial in resource-limited settings.

In conclusion, this thesis has successfully established hBNNS nano-hybrid composites as a new class of multifunctional materials with exceptional promise for advanced biosensing applications. Through a combination of careful material design, detailed structural and electrochemical characterization, and practical demonstration in CEA biosensing, the work not only addressed the inherent limitations of pristine hBNNS but also advanced the broader field of hybrid nanomaterials in biomedical sensing.

#### **List of Publications in Journals:**

- 1. Kanika Sharma, and Nitin K. Puri. "Enhanced electrochemical performance of hydrothermally exfoliated hexagonal boron nitride nanosheets for applications in electrochemistry." *Journal of The Electrochemical Society, Volume* 168, issue no.-5, (2021); Pages:056512-056522. DOI: 10.1149/1945-7111/abfe41.
- 2. Kanika Sharma, Nitin K. Puri, and Bharti Singh. "Fabrication of rGO-decorated hBNNS hybrid nanocomposite via organic-inorganic interfacial chemistry for enhanced electrocatalytic detection of carcinoembryonic antigen." *Analytical and Bioanalytical Chemistry, Volume 416*, (2024); Pages:4789-4805. DOI: https://doi.org/10.1007/s00216-024-05379-6
- 3. Kanika Sharma, Nitin K. Puri, and Bharti Singh. "An efficient electrochemical nano-biosensor based on hydrothermally engineered ultrathin nanostructures of hexagonal boron nitride nanosheets for label-free detection of carcinoembryonic antigen." *Applied Nanoscience, Volume* 14, issue no.-1, (2024); Pages:217-230. DOI: <a href="https://doi.org/10.1007/s13204-023-02971-7">https://doi.org/10.1007/s13204-023-02971-7</a>
- 4. Kanika Sharma, Nitin K. Puri, and Bharti Singh. "Self-assembled nano-hybrid composite based on Cu/CuxO nanoflower decorated onto hBNNS for high-performance and ultra-sensitive electrochemical detection of CEA biomarker". *Bioelectrochemistry Journal, Volume* 14, issue no.-165, (2025); Pages:108993. DOI: 10.1016/j.bioelechem.2025.108993

#### Papers communicated and to be communicated in journal:

Integration of 1D-2D hierarchical nanostructures based on Mixed-phase TiO<sub>2</sub> nanowires decorated onto hBNNS for ultra-sensitive and high-performance electrochemical sensing of Carcinoembryonic antigen. (To be Communicated).

#### **List of conferences attended:**

- 1. Attended and Presented Poster entitled, "Synthesis and Characterization of 2D Nanosheets of Hexagonal Boron Nitride (h-BN) for Electrochemical Sensing Application" at International Conference on Advanced Materials, (ICAM) held at Jamia Millia Islamia, New Delhi, India from 06<sup>th</sup>-07<sup>th</sup>, March, 2019.
- 2. Attended and Presented Poster entitled, "Facile Chemical Exfoliation and Characterization of Functionalized Boron Nitride Nanosheets for Electrochemical

**Study**" at International Conference on Atomic, Molecular, Optical and Nano Physics with Application (CAMNP-2019) held at Delhi Technological University from 18<sup>th</sup> - 20<sup>th</sup> December, 2019.

- 3. Attended and Presented Poster entitled, "Investigating the Electrochemical Sensing potential of Hydrothermally Engineered Nanocomposite based on Copper Nanoparticles decorated Boron Nitride Nanosheets for NSCLC Detection" at International Conference on Atomic, Molecular, Material, Nano, and Optical Physics with Applications (ICAMNOP-2023) held at Delhi Technological University from 20<sup>th</sup>-22<sup>nd</sup>, December, 2023.
- 4. Attended and Presented Poster entitled, "Tailoring the Electrochemical Properties of Hexagonal Boron Nitride Nanosheets via APTES Surface Modification for Enhanced Electrochemical Sensing Applications" at 3rd International Conference on Advances in Nanomaterials and Devices for Energy and Environment (CANDEE-2024), held at Atal Bihari Vajpayee Indian Institute of Information Technology and Management (ABV-IIITM), Gwalior from 3-5 December 2024.

#### **Chapters contributed in books:**

1. Kanika Sharma, Nitin K. Puri, and Bharti Singh "Hexagonal Boron Nitride in Sensing and Biosensing Applications." In *Hexagonal Boron Nitride*, pp. 511-552. Elsevier, 2024.

#### **Publications Other than Thesis Work**

- 1. Deepika Sandil, Saurabh Srivastava, Ritika Khatri, Kanika Sharma, and Nitin K. Puri. "Synthesis and fabrication of 2D tungsten trioxide nanosheets based platform for Impedimetric sensing of cardiac biomarker" *Sensing and Bio-Sensing Research, Volume* 32, (2021); Pages:100423. DOI: 10.1016/j.sbsr.2021.100423
- 2. Parisha Diwan, Kanika Sharma, and Nitin K. Puri, "Green route synthesis and characterization of zinc oxide nanorods and its composite with PVA", *Materials Today Proceedings*, *Volume* 62, Part 6 (2022); Pages:3832-3836. DOI: 10.1016/j.matpr.2022.04.491

## **Table of Contents**

Chapter 1: Literature Insights into Emerging 2D Nanomaterials and the Fabrication Strategies of Nanohybrid Composites for High-Performance Nano-Biosensing Technologies in Clinical Diagnostics and Healthcare		
	Global Surge in Cancer Statistics and Associated Healthcare Challenges	
	Pivotal Role of Nano-Biosensors in Bridging Gaps in Conventional Diag	
1.3 N	ches and Early Disease Detection	)-
	Hexagonal Boron Nitride: A Key Inorganic Layered Material Driving	
	ements in High-Performance Nano-Biosensors	12
1.5 S	Strategic Role of Nano-Hybrid Composites in Improving hBNNS hemical Efficiency	15
Reference	Ces	13 18
rereren		10
Chap	oter 2: Systematic Overview of Advanced Material and Electroche Characterization Techniques and Synthesis Methodologies	emical
2.1 I	Introduction	
2.1.1		
•	d Composites	22
	1.1 Bottom-Up Synthesis Approach:	22
	1.2 Top-Down Synthesis Approach:	
2.2 N 2.2.1	Material Characterization Techniques:X-ray Diffraction Spectroscopy (XRD):	
2.2.1	Scanning Electron Microscopy (SEM) and Energy-Dispersive X-ray Anal	
	X):	.ysis 28
2.2.3		
2.2.4	UV-Visible Spectroscopy:	33
	ing and Principle:	34
	cations:	34
2.2.5	Raman Spectroscopy:	35
2.2.6	Fourier Transform Infrared (FT-IR) Spectroscopy:	37
	ing Principle:	38
2.2.7	Atomic Force Microscopy (AFM):	
2.2.8	Thermogravimetric Analysis (TGA)	40
2.2.9	Cytotoxicity Test:	
	Electrochemical Characterization Techniques:	
2.3.1 2.3.2	Cyclic Voltammetry (CV): Differential Pulse Voltammetry (DPV):	
2.3.1	Electrochemical Impedance Spectroscopy (EIS):	
Reference		
_	er 3: Strategic Tailoring of Hydrothermal Parameters to Optimizensional Architecture of Hexagonal Boron Nitride (h-BN) for Imp Electrochemical Performance	roved
		50
3.1.1	Bottom-Up Approach for Synthesis of Two-Dimensional (2D) Hexagonal	l Boron

Nitride Nanosheets (h-BNNS)	3.2 Experi	shoots (h. DNNC)	
3.2.1 Chemical, Reagents and Instrumentation: 3.2.2 Tailored Hydrothermal Approach for Optimizing Two-dimensional (2D) Hexagonal Boron Nitride Nanosheets Morphology: 3.2.3 Fabrication of h-BN-Coated ITO Electrodes via Controlled Electrophoretic Deposition: 58 3.3 Experimental Results & Analysis: 60 3.3.1 Analytical Nanomaterial Characterizations: 60 3.3.1.1 Crystallographic Evaluation of Hydrothermally Synthesized h-BN Nanostructures: 60 3.3.1.2 Nano-Scale Morphological Investigation using various High-Resolution Electron Microscopy Techniques (SEM, TEM, and AFM): 63 3.3.1.3 Investigation of Optical Bandgap Transitions in Hydrothermally Engineered 63 3.3.1.4 Raman Spectroscopy Investigating Phonon-Electronic Interactions in 64 3.3.1.5 Investigating Molecular Vibrational Dynamics in Hydrothermally Tailored h-BN Nanostructures through Fourier Transform Infrared (FT-IR) Spectroscopy 63 3.3.2 Electrochemical Profiling and Analysis: 63 3.3.2.1 Assessment of Interfacial Electron Kinetics in Hydrothermally Engineered h-BN Nanostructures via Cyclic Voltammetry 63 3.3.2.2 Electrochemical impedance spectroscopy (EIS) 63 63 63 64 64 64 64 64 64 64 64 64 64 64 64 64			
3.2.2 Tailored Hydrothermal Approach for Optimizing Two-dimensional (2D) Hexagonal Boron Nitride Nanoshects Morphology:  573.2.3 Fabrication of h-BN-Coated ITO Electrodes via Controlled Electrophoretic Deposition:  583.3 Experimental Results & Analysis:  583.3 Experimental Results & Analysis:  583.3.1.1 Crystallographic Evaluation of Hydrothermally Synthesized h-BN Nanostructures:  583.3.1.2 Nano-Scale Morphological Investigation using various High-Resolution Electron Microscopy Techniques (SEM, TEM, and AFM):  3.3.1.2 Nano-Scale Morphological Investigation using various High-Resolution Electron Microscopy Techniques (SEM, TEM, and AFM):  3.3.1.3 Investigation of Optical Bandgap Transitions in Hydrothermally Engineered h-BN Nanostructures:  683.3.1.4 Raman Spectroscopy Investigating Phonon-Electronic Interactions in Hydrothermally Engineered h-BN Nanostructures:  683.3.1.5 Investigating Molecular Vibrational Dynamics in Hydrothermally Tailored h-BN Nanostructures through Fourier Transform Infrared (FT-IR) Spectroscopy 693.3.2 Electrochemical Profiling and Analysis:  703.3.2.1 Assessment of Interfacial Electron Kinetics in Hydrothermally Engineered h-BN Nanostructures via Cyclic Voltammetry  3.3.2.2 Electrochemical impedance spectroscopy (EIS)  3.3.2.3 Differential pulse voltammetry (DPV)  713.3.2.2 Electrochemical impedance spectroscopy (EIS)  723.3.2.3 Differential pulse voltammetry (DPV)  734.3.2.4 Chemical, Reagents and Instrumentation:  4.1 Introduction  4.2 Experimental Section:  4.2.1 Chemical, Reagents and Instrumentation:  4.2.2 In-Situ Hydrothermal Approach for Simultaneous Exfoliation and Functionalization of Few-Layered h-BN Nanosheets  4.3 In-Situ Hydrothermal Approach for Simultaneous Exfoliation and Functionalization of Few-Layered h-BN Nanosheets  4.3.1 Analytical Nanomaterial Characterizations:  4.3.1 Analytical Nanomaterial Characterizations:  4.3.1 Analytical Nanomaterial Characterizations:  4.3.1 Analytical Nanomaterial Characterizations:  4.3.1 Advanced Electron Microscopy-Based Nanostructur			
Hexagonal Boron Nitride Nanosheets Morphology:  3.2.3 Fabrication of h-BN-Coated ITO Electrodes via Controlled Electrophoretic Deposition:  53.3 Experimental Results & Analysis:  3.3.1 Analytical Nanomaterial Characterizations:  3.3.1.1 Crystallographic Evaluation of Hydrothermally Synthesized h-BN Nanostructures:  60.3.3.1.2 Nano-Scale Morphological Investigation using various High-Resolution Electron Microscopy Techniques (SEM, TEM, and AFM):  61.3.3.1.3 Investigation of Optical Bandgap Transitions in Hydrothermally Engineered h-BN Samples through UV-Visible Spectroscopy  62.3.3.1.4 Raman Spectroscopy Investigating Phonon-Electronic Interactions in Hydrothermally Engineered h-BN Nanostructures  63.3.1.5 Investigating Molecular Vibrational Dynamics in Hydrothermally Tailored h-BN Nanostructures through Fourier Transform Infrared (FT-IR) Spectroscopy  63.3.2.2 Electrochemical Profiling and Analysis:  70.3.3.2.1 Assessment of Interfacial Electron Kinetics in Hydrothermally Engineered h-BN Nanostructures via Cyclic Voltammetry  71.3.3.2.2 Electrochemical Impedance spectroscopy (EIS)  72.3.3.2.3 Differential pulse voltammetry (DPV)  73.3.2.2 Electrochemical Impedance spectroscopy (EIS)  74.3.3.2.3 Differential pulse voltammetry (DPV)  75.4 Conclusions  76.4 Regents and Instrumentation:  67.4 Lexperimental Section:  68.6 Lexperimental Section:  69.6 Lexperimental Section:  69.6 Lexperimental Section:  60.7 Lexperimental Section:  60.8 Lexperimental Section:  60.8 Lexperiment			56
3.2.3 Fabrication of h-BN-Coated ITO Electrodes via Controlled Electrophoretic Deposition:			
Deposition:	Hexagonal B	oron Nitride Nanosheets Morphology:	57
Deposition:	3.2.3 Fabr	ication of h-BN-Coated ITO Electrodes via Controlled Electrophoretic	
3.3.1.1 Analytical Nanomaterial Characterizations: 3.3.1.1 Crystallographic Evaluation of Hydrothermally Synthesized h-BN Nanostructures: 60 3.3.1.2 Nano-Scale Morphological Investigation using various High-Resolution Electron Microscopy Techniques (SEM, TEM, and AFM): 61 3.3.1.3 Investigation of Optical Bandgap Transitions in Hydrothermally Engineered h-BN Samples through UV-Visible Spectroscopy. 62 3.3.1.4 Raman Spectroscopy Investigating Phonon-Electronic Interactions in Hydrothermally Engineered h-BN Nanostructures. 63 3.3.1.5 Investigating Molecular Vibrational Dynamics in Hydrothermally Tailored h-BN Nanostructures through Fourier Transform Infrared (FT-IR) Spectroscopy. 63 3.2.1 Electrochemical Profiling and Analysis: 63 3.3.2.1 Assessment of Interfacial Electron Kinetics in Hydrothermally Engineered h-BN Nanostructures via Cyclic Voltammetry. 71 3.3.2.2 Electrochemical impedance spectroscopy (EIS). 75 3.3.2.3 Differential pulse voltammetry (DPV). 77 Conclusions. 80 References. 80  Chapter 4: Development of an Electrochemical Nano-Biosensing Interface based on Hydrothermally Engineered Ultrathin h-BN Nanosheets for High-Performance, Label-Free Detection of Carcinoembryonic Antigen 4.2 Experimental Section: 4.2.1 Chemical, Reagents and Instrumentation: 4.2.2 In-Situ Hydrothermal Approach for Simultaneous Exfoliation and Functionalization of Few-Layered h-BN Nanosheets 4.3 Experimental Results & Analysis: 91 4.3.1 Analytical Nanomaterial Characterizations: 94 4.3.1 Analytical Nanomaterial Characterizations: 94 4.3.1.1 Quantitative Structural Analysis of Hydrothermally Exfoliated Ultrathin h-BN Nanosheets Derived from Bulk h-BN utilizing X-ray diffraction (XRD): 94 4.3.1.2 Advanced Electron Microscopy-Based Nanostructure Profiling of Hydrothermally Exfoliated h-BNNS 1-1-1-1-1-1-1-1-1-1-1-1-1-1-1-1-1-1-1-	Deposition: -		
3.3.1.1 Crystallographic Evaluation of Hydrothermally Synthesized h-BN Nanostructures:  3.3.1.2 Nano-Scale Morphological Investigation using various High-Resolution Electron Microscopy Techniques (SEM, TEM, and AFM):  3.3.1.3 Investigation of Optical Bandgap Transitions in Hydrothermally Engineered h-BN Samples through UV-Visible Spectroscopy  3.3.1.4 Raman Spectroscopy Investigating Phonon-Electronic Interactions in Hydrothermally Engineered h-BN Nanostructures  3.3.1.5 Investigating Molecular Vibrational Dynamics in Hydrothermally Tailored h-BN Nanostructures through Fourier Transform Infrared (FT-IR) Spectroscopy  68  3.3.2 Electrochemical Profiling and Analysis:  70  3.3.2.1 Assessment of Interfacial Electron Kinetics in Hydrothermally Engineered h-BN Nanostructures via Cyclic Voltammetry  3.3.2.2 Electrochemical impedance spectroscopy (EIS)  73  3.3.2.3 Differential pulse voltammetry (DPV)  78  Conclusions  References  80  Chapter 4: Development of an Electrochemical Nano-Biosensing Interface based on Hydrothermally Engineered Ultrathin h-BN Nanosheets for High-Performance, Label-Free Detection of Carcinoembryonic Antigen  4.1 Introduction  4.2 Experimental Section:  4.2.1 Chemical, Reagents and Instrumentation:  4.2.2 In-Situ Hydrothermal Approach for Simultaneous Exfoliation and Functionalization of Few-Layered h-BN Nanosheets  4.2.3 Electrophoretic Deposition-Assisted Fabrication of Functionalized h-BNNS Films nonto ITO Electrodes for High-Performance Interfaces  4.3.1 Analytical Nanomaterial Characterizations:  4.3.1 Analytical Nanomaterial Characterizations:  4.3.1 Avanosheets Derived from Bulk h-BN utilizing X-ray diffraction (XRD):  4.3.1.2 Advanced Electron Microscopy-Based Nanostructure Profiling of Hydrothermally Exfoliated h-BNNS  4.3.1.3 UV-Visible Spectroscopy-Based Band Structure Analysis and Optical Transition Analysis of Bulk and Exfoliated h-BN Nanostructures  95  4.3.1.4 Raman Spectroscopic Evaluation of Molecular Vibrations and Sequential	3.3 Experi	mental Results & Analysis:	60
3.3.1.1 Crystallographic Evaluation of Hydrothermally Synthesized h-BN Nanostructures:  3.3.1.2 Nano-Scale Morphological Investigation using various High-Resolution Electron Microscopy Techniques (SEM, TEM, and AFM):  3.3.1.3 Investigation of Optical Bandgap Transitions in Hydrothermally Engineered h-BN Samples through UV-Visible Spectroscopy  3.3.1.4 Raman Spectroscopy Investigating Phonon-Electronic Interactions in Hydrothermally Engineered h-BN Nanostructures  3.3.1.5 Investigating Molecular Vibrational Dynamics in Hydrothermally Tailored h-BN Nanostructures through Fourier Transform Infrared (FT-IR) Spectroscopy  68  3.3.2 Electrochemical Profiling and Analysis:  70  3.3.2.1 Assessment of Interfacial Electron Kinetics in Hydrothermally Engineered h-BN Nanostructures via Cyclic Voltammetry  3.3.2.2 Electrochemical impedance spectroscopy (EIS)  73  3.3.2.3 Differential pulse voltammetry (DPV)  78  Conclusions  References  80  Chapter 4: Development of an Electrochemical Nano-Biosensing Interface based on Hydrothermally Engineered Ultrathin h-BN Nanosheets for High-Performance, Label-Free Detection of Carcinoembryonic Antigen  4.1 Introduction  4.2 Experimental Section:  4.2.1 Chemical, Reagents and Instrumentation:  4.2.2 In-Situ Hydrothermal Approach for Simultaneous Exfoliation and Functionalization of Few-Layered h-BN Nanosheets  4.2.3 Electrophoretic Deposition-Assisted Fabrication of Functionalized h-BNNS Films nonto ITO Electrodes for High-Performance Interfaces  4.3.1 Analytical Nanomaterial Characterizations:  4.3.1 Analytical Nanomaterial Characterizations:  4.3.1 Avanosheets Derived from Bulk h-BN utilizing X-ray diffraction (XRD):  4.3.1.2 Advanced Electron Microscopy-Based Nanostructure Profiling of Hydrothermally Exfoliated h-BNNS  4.3.1.3 UV-Visible Spectroscopy-Based Band Structure Analysis and Optical Transition Analysis of Bulk and Exfoliated h-BN Nanostructures  95  4.3.1.4 Raman Spectroscopic Evaluation of Molecular Vibrations and Sequential	3.3.1 Anal	ytical Nanomaterial Characterizations:	60
Nanostructures:  3.3.1.2 Nano-Scale Morphological Investigation using various High-Resolution Electron Microscopy Techniques (SEM, TEM, and AFM):  3.3.1.3 Investigation of Optical Bandgap Transitions in Hydrothermally Engineered h-BN Samples through UV-Visible Spectroscopy  66.  3.3.1.4 Raman Spectroscopy Investigating Phonon-Electronic Interactions in Hydrothermally Engineered h-BN Nanostructures  68.  3.3.1.5 Investigating Molecular Vibrational Dynamics in Hydrothermally Tailored h-BN Nanostructures through Fourier Transform Infrared (FT-IR) Spectroscopy  69.  3.2.2 Electrochemical Profiling and Analysis:  70.  3.3.2.1 Assessment of Interfacial Electron Kinetics in Hydrothermally Engineered h-BN Nanostructures via Cyclic Voltammetry  71.  3.3.2.2 Electrochemical impedance spectroscopy (EIS)  75.  3.3.2.3 Differential pulse voltammetry (DPV)  77.  Conclusions  80.  References  80.  Chapter 4: Development of an Electrochemical Nano-Biosensing Interface based on Hydrothermally Engineered Ultrathin h-BN Nanosheets for High-Performance, Label-Free Detection of Carcinoembryonic Antigen  4.1 Introduction  4.2.1 Chemical, Reagents and Instrumentation:  4.2.2 In-Situ Hydrothermal Approach for Simultaneous Exfoliation and Functionalization of Few-Layered h-BN Nanosheets  4.2.3 Electrophoretic Deposition-Assisted Fabrication of Functionalized h-BNNS Films onto ITO Electrodes for High-Performance Interfaces  4.3.1 Analytical Nanomaterial Characterizations:  4.3.1 Analytical Nanomaterial Characterizations:  4.3.1.1 Quantitative Structural Analysis of Hydrothermally Exfoliated Ultrathin h-BN Nanosheets Derived from Bulk h-BN utilizing X-ray diffraction (XRD):  4.3.1.2 Advanced Electron Microscopy-Based Nanostructure Profiling of Hydrothermally Exfoliated h-BNNS  4.3.1.3 UV-Visible Spectroscopy-Based Band Structure Analysis and Optical Transition Analysis of Bulk and Exfoliated h-BN Nanostructures  95.  4.3.1.5 FT-IR Spectroscopic Evaluation of Molecular Vibrations and Sequential		Crystallographic Evaluation of Hydrothermally Synthesized h-BN	
Electron Microscopy Techniques (SEM, TEM, and AFM): ————————————————————————————————————		tures:	60
Electron Microscopy Techniques (SEM, TEM, and AFM): ————————————————————————————————————	3.3.1.2	Nano-Scale Morphological Investigation using various High-Resolution	
3.3.1.3 Investigation of Optical Bandgap Transitions in Hydrothermally Engineered h-BN Samples through UV-Visible Spectroscopy ————————————————————————————————————			63
h-BN Samples through UV-Visible Spectroscopy  3.3.1.4 Raman Spectroscopy Investigating Phonon-Electronic Interactions in Hydrothermally Engineered h-BN Nanostructures  6.3.3.1.5 Investigating Molecular Vibrational Dynamics in Hydrothermally Tailored h-BN Nanostructures through Fourier Transform Infrared (FT-IR) Spectroscopy			
3.3.1.4 Raman Spectroscopy Investigating Phonon-Electronic Interactions in Hydrothermally Engineered h-BN Nanostructures			
Hydrothermally Engineered h-BN Nanostructures 3.3.1.5 Investigating Molecular Vibrational Dynamics in Hydrothermally Tailored h-BN Nanostructures through Fourier Transform Infrared (FT-IR) Spectroscopy ————————————————————————————————————			
3.3.1.5 Investigating Molecular Vibrational Dynamics in Hydrothermally Tailored h-BN Nanostructures through Fourier Transform Infrared (FT-IR) Spectroscopy ————————————————————————————————————			68
BN Nanostructures through Fourier Transform Infrared (FT-IR) Spectroscopy ———69 3.3.2 Electrochemical Profiling and Analysis: ———70 3.3.2.1 Assessment of Interfacial Electron Kinetics in Hydrothermally Engineered h-BN Nanostructures via Cyclic Voltammetry ————71 3.3.2.2 Electrochemical impedance spectroscopy (EIS) ————75 3.3.2.3 Differential pulse voltammetry (DPV) ————78  Conclusions ————————————————————————————————————	•		
3.3.2 Electrochemical Profiling and Analysis:  3.3.2.1 Assessment of Interfacial Electron Kinetics in Hydrothermally Engineered h-BN Nanostructures via Cyclic Voltammetry  3.3.2.2 Electrochemical impedance spectroscopy (EIS)  3.3.2.3 Differential pulse voltammetry (DPV)  75  Conclusions  References  80  Chapter 4: Development of an Electrochemical Nano-Biosensing Interface based on Hydrothermally Engineered Ultrathin h-BN Nanosheets for High-Performance, Label-Free Detection of Carcinoembryonic Antigen  4.1 Introduction  4.2 Experimental Section:  90  4.2.1 Chemical, Reagents and Instrumentation:  90  4.2.2 In-Situ Hydrothermal Approach for Simultaneous Exfoliation and Functionalization of Few-Layered h-BN Nanosheets  91  4.2.3 Electrophoretic Deposition-Assisted Fabrication of Functionalized h-BNNS Films onto ITO Electrodes for High-Performance Interfaces  91  4.3.1 Analytical Nanomaterial Characterizations:  94  4.3.1.1 Quantitative Structural Analysis of Hydrothermally Exfoliated Ultrathin h-BN Nanosheets Derived from Bulk h-BN utilizing X-ray diffraction (XRD):  94  4.3.1.2 Advanced Electron Microscopy-Based Nanostructure Profiling of Hydrothermally Exfoliated h-BNNS  1.3 UV-Visible Spectroscopy-Based Band Structure Analysis and Optical Transition Analysis of Bulk and Exfoliated h-BN Nanostructures  97  4.3.1.4 Raman Spectroscopy-Based Band Structure Analysis and Optical Transition Analysis of Bulk and Exfoliated h-BN Nanostructures  99  4.3.1.5 FT-IR Spectroscopic Elucidation of Molecular Vibrations and Sequential			
3.3.2.1 Assessment of Interfacial Electron Kinetics in Hydrothermally Engineered h-BN Nanostructures via Cyclic Voltammetry			
BN Nanostructures via Cyclic Voltammetry  3.3.2.2 Electrochemical impedance spectroscopy (EIS)  3.3.2.3 Differential pulse voltammetry (DPV)  78  Conclusions  References  80  Chapter 4: Development of an Electrochemical Nano-Biosensing Interface based on Hydrothermally Engineered Ultrathin h-BN Nanosheets for High-Performance, Label-Free Detection of Carcinoembryonic Antigen  4.1 Introduction  4.2 Experimental Section:  90  4.2.1 Chemical, Reagents and Instrumentation:  90  4.2.2 In-Situ Hydrothermal Approach for Simultaneous Exfoliation and Functionalization of Few-Layered h-BN Nanosheets  91  4.2.3 Electrophoretic Deposition-Assisted Fabrication of Functionalized h-BNNS Films onto ITO Electrodes for High-Performance Interfaces  91  4.3.1 Analytical Nanomaterial Characterizations:  94  4.3.1.1 Quantitative Structural Analysis of Hydrothermally Exfoliated Ultrathin h-BN Nanosheets Derived from Bulk h-BN utilizing X-ray diffraction (XRD):  94  4.3.1.2 Advanced Electron Microscopy-Based Nanostructure Profiling of Hydrothermally Exfoliated h-BNNS  96  4.3.1.3 UV-Visible Spectroscopy-Based Band Structure Analysis and Optical Transition Analysis of Bulk and Exfoliated h-BN Nanostructures  97  4.3.1.4 Raman Spectroscopy-Based Band Structure Analysis and Optical Transition Analysis of Bulk and Exfoliated h-BN Nanostructures  97  4.3.1.4 Raman Spectroscopic Elucidation of Phonon Behaviour and Electronic Coupling in Bulk and Exfoliated h-BN Nanostructures  99  4.3.1.5 FT-IR Spectroscopic Evaluation of Molecular Vibrations and Sequential		· · · · · · · · · · · · · · · · · · ·	
3.3.2.2 Electrochemical impedance spectroscopy (EIS)————————————————————————————————————			
Conclusions———————————————————————————————————	3 3 2 2	Electrochemical impedance spectroscopy (FIS)	75
Conclusions———————————————————————————————————	2 2 2 2	Differential pulse voltammetry (DDV)	79 79
Chapter 4: Development of an Electrochemical Nano-Biosensing Interface based on Hydrothermally Engineered Ultrathin h-BN Nanosheets for High-Performance, Label-Free Detection of Carcinoembryonic Antigen  4.1 Introduction ————————————————————————————————————	3.3.2.3	Differential pulse voltaminetry (DF v)	· / C
Chapter 4: Development of an Electrochemical Nano-Biosensing Interface based on Hydrothermally Engineered Ultrathin h-BN Nanosheets for High-Performance, Label-Free Detection of Carcinoembryonic Antigen  4.1 Introduction ————————————————————————————————————	Canalusians		
on Hydrothermally Engineered Ultrathin h-BN Nanosheets for High-Performance, Label-Free Detection of Carcinoembryonic Antigen  4.1 Introduction ————————————————————————————————————			
4.2.1 Chemical, Reagents and Instrumentation:————————————————————————————————————	References		80
4.2.1 Chemical, Reagents and Instrumentation:————————————————————————————————————	Chapter 4: D on Hyd Perfo	evelopment of an Electrochemical Nano-Biosensing Interface barothermally Engineered Ultrathin h-BN Nanosheets for High- rmance, Label-Free Detection of Carcinoembryonic Antigen	80 ised
4.2.2 In-Situ Hydrothermal Approach for Simultaneous Exfoliation and Functionalization of Few-Layered h-BN Nanosheets	Chapter 4: D on Hyd Perfor  4.1 Introde	evelopment of an Electrochemical Nano-Biosensing Interface barothermally Engineered Ultrathin h-BN Nanosheets for High- rmance, Label-Free Detection of Carcinoembryonic Antigen	80 ised 84
Functionalization of Few-Layered h-BN Nanosheets	Chapter 4: D on Hyd Perform 4.1 Introde 4.2 Experi	evelopment of an Electrochemical Nano-Biosensing Interface barothermally Engineered Ultrathin h-BN Nanosheets for High- rmance, Label-Free Detection of Carcinoembryonic Antigen action	80 ised 84
4.2.3 Electrophoretic Deposition-Assisted Fabrication of Functionalized h-BNNS Films onto ITO Electrodes for High-Performance Interfaces	Chapter 4: D on Hyd Perfor  4.1 Introd 4.2 Experi 4.2.1 Cher	evelopment of an Electrochemical Nano-Biosensing Interface barothermally Engineered Ultrathin h-BN Nanosheets for High-rmance, Label-Free Detection of Carcinoembryonic Antigen uction	80 ised 84
onto ITO Electrodes for High-Performance Interfaces	Chapter 4: D   on Hyd   Perform	evelopment of an Electrochemical Nano-Biosensing Interface barothermally Engineered Ultrathin h-BN Nanosheets for High-rmance, Label-Free Detection of Carcinoembryonic Antigen uction	<b>8</b> 0 <b>8</b> 4 <b>9</b> 0
4.3.1 Analytical Nanomaterial Characterizations: ————————————————————————————————————	Chapter 4: D on Hyd Perfor  4.1 Introde 4.2 Experi 4.2.1 Cher 4.2.2 In-Si Functionaliza	evelopment of an Electrochemical Nano-Biosensing Interface barothermally Engineered Ultrathin h-BN Nanosheets for High-rmance, Label-Free Detection of Carcinoembryonic Antigen uction	<b>80 84 90</b> 90
4.3.1 Analytical Nanomaterial Characterizations:	Chapter 4: D on Hyd Perfor  4.1 Introde 4.2 Experi 4.2.1 Cher 4.2.2 In-Si Functionalize 4.2.3 Elect	evelopment of an Electrochemical Nano-Biosensing Interface barothermally Engineered Ultrathin h-BN Nanosheets for High-rmance, Label-Free Detection of Carcinoembryonic Antigen uction	<b>80 84 90</b> 90 91 lms
4.3.1.1 Quantitative Structural Analysis of Hydrothermally Exfoliated Ultrathin h-BN Nanosheets Derived from Bulk h-BN utilizing X-ray diffraction (XRD):94 4.3.1.2 Advanced Electron Microscopy-Based Nanostructure Profiling of Hydrothermally Exfoliated h-BNNS	Chapter 4: D on Hyd Perfor  4.1 Introde 4.2 Experi 4.2.1 Cher 4.2.2 In-Si Functionalize 4.2.3 Elector onto ITO Elector  A series of the series	evelopment of an Electrochemical Nano-Biosensing Interface barothermally Engineered Ultrathin h-BN Nanosheets for High-rmance, Label-Free Detection of Carcinoembryonic Antigen action	<b>80 84 90</b> 91 lms
BN Nanosheets Derived from Bulk h-BN utilizing X-ray diffraction (XRD):94 4.3.1.2 Advanced Electron Microscopy-Based Nanostructure Profiling of Hydrothermally Exfoliated h-BNNS	Chapter 4: D on Hyd Perfor  4.1 Introde 4.2 Experi 4.2.1 Cher 4.2.2 In-Si Functionaliz 4.2.3 Elect onto ITO Elect 4.3 Experi	evelopment of an Electrochemical Nano-Biosensing Interface barothermally Engineered Ultrathin h-BN Nanosheets for High-rmance, Label-Free Detection of Carcinoembryonic Antigen uction	80 84 90 91 llms 91
4.3.1.2 Advanced Electron Microscopy-Based Nanostructure Profiling of Hydrothermally Exfoliated h-BNNS96 4.3.1.3 UV-Visible Spectroscopy-Based Band Structure Analysis and Optical Transition Analysis of Bulk and Exfoliated h-BN Nanostructures97 4.3.1.4 Raman Spectroscopic Elucidation of Phonon Behaviour and Electronic Coupling in Bulk and Exfoliated h-BN Nanostructures99 4.3.1.5 FT-IR Spectroscopic Evaluation of Molecular Vibrations and Sequential	Chapter 4: D on Hyd Perfor  4.1 Introde 4.2 Experi 4.2.1 Cher 4.2.2 In-Si Functionaliz 4.2.3 Elect onto ITO Elect 4.3 Experi	evelopment of an Electrochemical Nano-Biosensing Interface barothermally Engineered Ultrathin h-BN Nanosheets for High-rmance, Label-Free Detection of Carcinoembryonic Antigen uction	80 84 90 91 llms 91
Hydrothermally Exfoliated h-BNNS	Chapter 4: D on Hyd Perfor  4.1 Introde 4.2 Experi 4.2.1 Cher 4.2.2 In-Si Functionalize 4.2.3 Elector onto ITO Elector 4.3 Experi 4.3.1 Anal	evelopment of an Electrochemical Nano-Biosensing Interface barothermally Engineered Ultrathin h-BN Nanosheets for High-rmance, Label-Free Detection of Carcinoembryonic Antigen uction	80 ased 84 909091 lms94
4.3.1.3 UV-Visible Spectroscopy-Based Band Structure Analysis and Optical Transition Analysis of Bulk and Exfoliated h-BN Nanostructures97 4.3.1.4 Raman Spectroscopic Elucidation of Phonon Behaviour and Electronic Coupling in Bulk and Exfoliated h-BN Nanostructures99 4.3.1.5 FT-IR Spectroscopic Evaluation of Molecular Vibrations and Sequential	Chapter 4: D on Hyd Perfor  4.1 Introde 4.2 Experi 4.2.1 Cher 4.2.2 In-Si Functionalize 4.2.3 Electoric onto ITO Electoric 4.3 Experi 4.3.1 Anal 4.3.1.1	evelopment of an Electrochemical Nano-Biosensing Interface barothermally Engineered Ultrathin h-BN Nanosheets for High-rmance, Label-Free Detection of Carcinoembryonic Antigen action	80 84 90 91 91 94 94
4.3.1.3 UV-Visible Spectroscopy-Based Band Structure Analysis and Optical Transition Analysis of Bulk and Exfoliated h-BN Nanostructures97 4.3.1.4 Raman Spectroscopic Elucidation of Phonon Behaviour and Electronic Coupling in Bulk and Exfoliated h-BN Nanostructures99 4.3.1.5 FT-IR Spectroscopic Evaluation of Molecular Vibrations and Sequential	Chapter 4: D on Hyd Perfor  4.1 Introde 4.2 Experi 4.2.1 Cher 4.2.2 In-Si Functionalize 4.2.3 Electonto ITO Electo	evelopment of an Electrochemical Nano-Biosensing Interface barothermally Engineered Ultrathin h-BN Nanosheets for High-rmance, Label-Free Detection of Carcinoembryonic Antigen action	80 84 90 91 91 94 94
Transition Analysis of Bulk and Exfoliated h-BN Nanostructures97 4.3.1.4 Raman Spectroscopic Elucidation of Phonon Behaviour and Electronic Coupling in Bulk and Exfoliated h-BN Nanostructures99 4.3.1.5 FT-IR Spectroscopic Evaluation of Molecular Vibrations and Sequential	Chapter 4: D on Hyd Perfor  4.1 Introde 4.2 Experi 4.2.1 Cher 4.2.2 In-Si Functionalize 4.2.3 Elect onto ITO Elect 4.3 Experi 4.3.1 Anal 4.3.1.1 BN Nanos 4.3.1.2	evelopment of an Electrochemical Nano-Biosensing Interface barothermally Engineered Ultrathin h-BN Nanosheets for High-rmance, Label-Free Detection of Carcinoembryonic Antigen uction ————————————————————————————————————	<b>80 84 90</b> 91 lms 94 h 94
<ul> <li>4.3.1.4 Raman Spectroscopic Elucidation of Phonon Behaviour and Electronic</li> <li>Coupling in Bulk and Exfoliated h-BN Nanostructures99</li> <li>4.3.1.5 FT-IR Spectroscopic Evaluation of Molecular Vibrations and Sequential</li> </ul>	Chapter 4: D on Hyd Perfo  4.1 Introde 4.2 Experi 4.2.1 Cher 4.2.2 In-Si Functionalize 4.2.3 Electoric ITO Elector	evelopment of an Electrochemical Nano-Biosensing Interface barothermally Engineered Ultrathin h-BN Nanosheets for High-rmance, Label-Free Detection of Carcinoembryonic Antigen uction ————————————————————————————————————	<b>80 84 90</b> 91 lms 94 h 94
Coupling in Bulk and Exfoliated h-BN Nanostructures99 4.3.1.5 FT-IR Spectroscopic Evaluation of Molecular Vibrations and Sequential	References On Hyd Perfor  4.1 Introde 4.2 Experi 4.2.1 Cher 4.2.2 In-Si Functionalize 4.2.3 Electoric ITO Ele	evelopment of an Electrochemical Nano-Biosensing Interface barothermally Engineered Ultrathin h-BN Nanosheets for High-rmance, Label-Free Detection of Carcinoembryonic Antigen action	80 84 90 91 94 94 94
4.3.1.5 FT-IR Spectroscopic Evaluation of Molecular Vibrations and Sequential	Chapter 4: D on Hyd Perfor  4.1 Introde 4.2 Experi 4.2.1 Cher 4.2.2 In-Si Functionalize 4.2.3 Electonto ITO Electo	evelopment of an Electrochemical Nano-Biosensing Interface barothermally Engineered Ultrathin h-BN Nanosheets for High- rmance, Label-Free Detection of Carcinoembryonic Antigen uction	80 84 90 91 94 94 94
	Chapter 4: D on Hyd Perfor  4.1 Introde 4.2 Experi 4.2.1 Cher 4.2.2 In-Si Functionalize 4.2.3 Electonto ITO Electo	evelopment of an Electrochemical Nano-Biosensing Interface barothermally Engineered Ultrathin h-BN Nanosheets for High-rmance, Label-Free Detection of Carcinoembryonic Antigen action ————————————————————————————————————	<b>80 84 90</b> 91 lms 94 h 94
11000m minioomizwion in 11, wie thomashy Enterwood in E1 (1 twineshood)	Chapter 4: D on Hyd Perfor  4.1 Introde 4.2 Experi 4.2.1 Cher 4.2.2 In-Si Functionalize 4.2.3 Elect onto ITO Ele 4.3 Experi 4.3.1 Anal 4.3.1.1 BN Nanos 4.3.1.2 Hydrother 4.3.1.3 Transition 4.3.1.4 Coupling	evelopment of an Electrochemical Nano-Biosensing Interface barothermally Engineered Ultrathin h-BN Nanosheets for High- rmance, Label-Free Detection of Carcinoembryonic Antigen uction	<b>80 84 90</b> 91 lms 94 94 97

4.3.1.3 In Vitro Cytotoxicity Assessment of Engineered h-BN Nanosheets	
Synthesized via Hydrothermal Exfoliation	
4.3.2 Electrochemical Profiling and Analysis:	104
4.3.2.1 Investigating the Interfacial Electrochemical Kinetics of Ultrathin h-	
BNNS/ITO Electrodes and Successive Protein Immobilization	104
4.3.2.2 Evaluating Electron Transfer Dynamics of h-BNNS/ITO-based Nano	<b>)-</b>
biosensing Interfaces via Scan Rate-Dependent Cyclic Voltammetry	
4.3.2.3 Calibrating CEA Concentrations through stepwise Electroanalytical	
Response Analysis of Functionalized h-BNNS/ITO Nano-biosensing Interface -	
4.3.2.4 Comprehensive Performance Evaluation of Optimal Working pH, Se	
Operational Reproducibility, Long-Term Stability, and Real-Sample Applicabil	
h-BNNS/ITO-Based Nano-biosensor	
Conclusion	
References	
Chapter 5: Construction of Engineered 2D-2D Hybrid Nanocomposite rGO-integrated hBNNS through Strategic Organic—Inorganic Interfa Chemistry for High-Performance Electrocatalytic Detection of Carcinoembryonic Antigen.	
5.1 Introduction	
5.2 Experimental Section:	
5.2.1 Chemical, Reagents and Instrumentation:	
5.2.2 Sustainable and Efficient Synthesis of Graphene Oxide Using Modified H	ummer's
Approach	129
5.2.3 Facile One-Pot Hydrothermal Route for Producing rGO-hBNNS Hybrid	
Nanocomposites with Enhanced Interfacial Integration	
5.2.3 Fabrication of Functionalized rGO-hBNNS/ITO Immunoelectrodes via Co	ontrolled
Electrophoretic Deposition (EPD) and Nano-interface Engineering enabled Covale	ent
Antibody Immobilization	
5.3 Experimental Results & Analysis:	
5.3.1 Analytical Nanomaterial Characterizations:	134
5.3.1.1 Comprehensive Crystallographic Characterization of rGO-hBNNS H	Iybrid
Nanocomposite Using X -Ray Diffraction (XRD) Analysis:	134
5.3.1.2 Integrated High-Resolution Electron Microscopy and EDAX-Based	
Elemental Investigation for Detailed Morphological and Compositional Analysi	is of
Elemental Investigation for Detailed Morphological and Compositional Analysi rGO-hBNNS Hybrid Nanocomposite	136
5.3.1.3 Spectroscopic Band Structure and Optical Transition Investigation of	f rGO–
hBNNS Hybrid Nanocomposite Using UV-Visible Absorption Analysis	138
5.3.1.4 Raman Spectroscopy Elucidating Phonon Dynamics, Vibrational Mo	odes, and
Electronic Interactions in the rGO-hBNNS Hybrid Nanocomposite	139
5.3.1.5 FT-IR Spectroscopy—Driven Investigation of Molecular Bond Dynar	nics and
Sequential Protein Immobilization Mechanisms in rGO-hBNNS Hybrid	
Nanocomposites	142
5.3.2 Electrochemical Profiling and Analysis:	146
5.3.2.1 Interfacial Electrochemical Kinetics of rGO–hBNNS/ITO Electrodes	
Sequential Protein Immobilization	
5.3.2.2 Assessment of Scan Rate-Dependent Interfacial Electron Transfer Be	
in rGO-hBNNS/ITO-Based Nano-Biosensors Using Cyclic Voltammetry Meas	
5.3.2.3 Electrochemical Calibration Strategy for CEA Detection on Function	nalized
rGO-hBNNS/ITO Nano-Biosensors	

Figure 5.17: Linear calibration graph correlating peak DPV current as a function of Cl	EΑ
concentration, validating the performance and quantitative detection capability of the	rGO-
hBNNS-based immunosensor	
Table 5.5: Evaluation and comparison of rGO-hBNNS-based nano-biosensor me	trics
with conventional immunosensors.	155
5.3.2.4 Detailed Systematic Investigation of Electroanalytical Performance of ro	GO-
hBNNS/ITO Nano-Biosensor	156
Conclusion	163
References	163
Chapter 6: Fabrication of a Self-assembled 3D-2D Nano-Hybrid Composi	te
combining hBNNS and Cu/Cu <sub>X</sub> O nanoflowers for High-Performance	
Electrochemical detection of the CEA Biomarker	
6.1 Introduction	168
6.2 Experimental Section:	170
6.2.1 Chemical, Reagents and Instrumentation:	170
6.2.2 Facile One-Step Polyol-Mediated Synthesis of Dandelion-Like Cu <sub>X</sub> O	
Nanoflowers:	171
6.2.2 Stepwise In-situ Hydrothermal Approach for the Synthesis of Cu/Cu <sub>X</sub> O-hBN	NS
Nano-hybrid Composite	173
6.2.3 Electrophoretic deposition (EPD) of Cu/Cu <sub>x</sub> O-hBNNS film onto ITO substrate	tes:
176	
6.2.4 Fabrication of Cu/Cu <sub>x</sub> O-hBNNS based immunosensor:	178
6.3 Experimental Results & Analysis:	
6.3.1 Analytical Nanomaterial Characterizations:	
6.3.1.1 In-depth Structural and Crystallographic Insights into Cu/Cu <sub>X</sub> O-hBNNS	
Hybrid Nanocomposite Using Advanced XRD Analysis	179
6.3.1.2 Morphological Assessment and Microstructural Insights into Cu <sub>X</sub> O, hBN	√NS,
and Cu/Cu <sub>x</sub> O-hBNNS Using High-Resolution SEM and TEM Techniques	184
6.3.1.3 Investigation of Electronic Band Structure, Optical Transition Mechanis	ms,
and Urbach Energy in Cu/Cu <sub>X</sub> O-hBNNS Hybrid Nanocomposite Using UV-Vis	
Spectroscopy	185
6.3.1.4 Raman Spectroscopic Analysis of Phonon Dynamics, Vibrational Signat	ures,
and Electronic Interactions in Cu/Cu <sub>X</sub> O-hBNNS Nano-Hybrid Nanocomposites	188
6.3.1.5 FT-IR Spectroscopy elucidating Molecular Bond Dynamics and Protein	
Immobilization Mechanisms in Cu/Cu <sub>X</sub> O-hBNNS Hybrid Nanocomposites	
Table 6.2:	
6.3.2 Electrochemical Profiling and Analysis:	195
6.3.2.1 Electrochemical Behaviour and Interfacial Kinetics of Sequential Protein	
Immobilization in Cu/Cu <sub>X</sub> O-hBNNS Electrodes	195
6.3.2.2 Quantitative Evaluation of Scan Rate-Controlled Interfacial Electron	
Transport in Cu/Cu <sub>X</sub> O-hBNNS/ITO-Based Nano-Biosensors	197
6.3.2.3 Assessment of the Sensing Performance and Electrochemical Response	
Dynamics of Cu/Cu <sub>X</sub> O-hBNNS-Based Immunoelectrodes	199
6.3.2.4 Comprehensive Evaluation of the Electroanalytical Performance of	
Cu/Cu <sub>X</sub> O-hBNNS/ITO-Based Nano-Biosensors	203
Conclusion:	
References:	

Chapter 7: Integration of hierarchical nanostructures featuring 2D-hBNN	
decorated with mixed-phase 1D-TiO <sub>2</sub> nanowires for ultra-sensitive, High	-
Performance Electrochemical Sensing of Carcinoembryonic Antigen.	
7.1 Introduction	
7.2 Experimental Section:	
7.2.1 Chemical, Reagents and Instrumentation:	221
7.2.2 Energy-Efficient Solvothermal Approach for the Controlled Growth of One-	
Dimensional High-Aspect-Ratio TiO <sub>2</sub> Nanowires	- 222
7.2.3 An In-Situ Strategic Hydrothermal Synthesis of TiO <sub>2</sub> -hBNNS Nano-Hybrid	
Composite	- 224
7.2.4 Preparation of TiO <sub>2</sub> -hBNNS Functional Films on ITO Surfaces through	
Electrophoretic Deposition	
7.2.5 Preparation of TiO <sub>2</sub> -hBNNS Integrated Immunosensing Electrode	
7.3 Experimental Results & Analysis:	228
7.3.1 Analytical Nanomaterial Characterizations:	- 228
7.3.1.1 X-Ray Diffraction Characterization Elucidating Structural Integrity and	
Phase Evolution in TiO <sub>2</sub> -hBNNS Hybrid Nanocomposite	
7.3.1.2 High-Resolution Electron Microscopy for Comprehensive Morphologica	ıl and
Microstructural Evaluation of TiO <sub>2</sub> -NW, hBNNS, and TiO <sub>2</sub> -hBNNS Hybrid	
Nanocomposite	
7.3.1.3 Detailed UV-Visible Spectroscopic Analysis of Electronic Band Structu	
Optical Transitions, and Urbach Energy in TiO2-hBNNS Hybrid Nanocomposite	
7.3.1.4 Comprehensive Raman Spectroscopic Investigation of Phonon Behaviou	
Vibrational Modes, and Electronic Coupling in TiO <sub>2</sub> –hBNNS Nano-Hybrid Compo	sites
7.3.1.5 Comprehensive FT-IR Spectroscopic Investigation of Molecular Bondin	g
Dynamics, Surface Functionalization, and Protein Immobilization Strategies in TiO	2-
hBNNS Hybrid Nanomaterials	
7.3.2 Electrochemical Profiling and Analysis:	- 247
7.3.2.1 Electrochemical Dynamics and Interfacial Kinetics Governing Sequentia	ıl
Protein Immobilization on TiO <sub>2</sub> –hBNNS Electrodes	- 247
7.3.2.2 Scan Rate-Dependent Analysis of Interfacial Electron Dynamics in TiO <sub>2</sub>	_
hBNNS/ITO Nano-Biosensors	
7.3.2.3 Electrochemical Response Kinetics and Analysis of Sensing Performance	e of
TiO <sub>2</sub> -hBNNS-Based Nano-Biosensing Interfaces	- 251
7.3.2.4 Systematic Assessment of Electroanalytical Efficiency and Functional	
Reliability in TiO <sub>2</sub> -hBNNS/ITO-Based Nano-Biosensors for Advanced Clinical	
Diagnostics	- 255
Conclusion	262
References	262
Chapter 8: Summary and Future Scope	
Summary	268
Conclusion	
Future Prospects	274

#### **List of Figures** Chapter 1 Figure 1.1: Cancer incidences in both sexes based on different Cancer sites 2 3 Figure 1.2: Cancer mortality in both sexes based in different Cancer sites Figure 1.3: Schematic depicting various applications of Nano-biosensor 5 7 Figure 1.4: Evolution of Sensing Technology Figure 1.5: Components of Nano-biosensor Figure 1.6: Different types of Biosensors based on Biorecognition Element 9 Figure 1.7: Classification of Nanomaterials Based on distinct Geometric Dimensions and potential functional behaviour in nanoscale systems. 10 Figure 1.8: Properties of Two-Dimensional Nanomaterials 11 Figure 1.9: Properties of Group III-Nitride Family 13 Figure 1.10: Challenges in Synthesizing of 2D hexagonal Boron Nitride (hBN) 14 Figure 1.11: Advantages of Nano-Hybrid Composite (NHC) 15 Figure 1.12: Different types of Nanomaterials based on Chemical Architecture 16 Chapter 2 Figure 2.1: Schematic representation of Botton-up and Top-Down Synthesis Approach of Nanomaterials, ------23 Figure 2.2: A Hydrothermal Autoclave Assembly ------24 Figure 2.3: Schematic depicting Electrophoretic Deposition Setup------25 Figure 2.4: Diagrammatic representation of X-ray Diffractometer (Left) and Fundamental transitions depicting generation of X-rays (Right)----- 26 Figure 2.5: Schematic description of Bragg's Law. ----- 27 Figure 2.6: Schematic illustration of working of Scanning Electron Microscopy (SEM) and Energy-dispersive X-ray Spectroscopy (EDAX). ----- 29 Figure 2.7: Diagram representing working of Transmission Electron Microscopy (TEM) Figure 2.8: Stepwise illustration of working of UV-Visible Spectrometer. ----- 34 Figure 2.9: Diagram illustrating working of Raman Spectroscopy------ 35 Figure 2.10: Schematic working of Fourier Transform Infrared Spectroscopy (FT-IR)37 Figure 2.11: Diagrammatic depiction of working of Atomic Force Microscope (AFM) 39 Figure 2.12: Working of Thermogravimetric Analysis (TGA) ------ 41 Figure 2.13: Electrochemical Autolab Setup------43 Chapter 3 Figure 3.1: Diagrammatic representation of systematic hydrothermal synthesis of enhanced Two-dimensional (2D) Hexagonal Boron Nitride Nanosheets (h-BNNS) architecture Figure 3.2: Schematic representation of the electrophoretic deposition (EPD) assembly employed for precise deposition of hydrothermally synthesized h-BN nanostructures onto pre-hydrolyzed ITO substrates. Figure 3.3: Image depicting the homogenous deposition of (a) h-BN 2 (hBNNS), (b) Bulk h-BN, (c) h-BN 1, (d) h-BN 3, (e) h-BN 4 coatings onto ITO glass substrates fabricated through effective electrophoretic deposition. Figure 3.4: X-ray diffractogram depicting Bulk h-BN (purple) and h-BN nanosheets exfoliated under tailored hydrothermal conditions as h-BN 1 (220 °C, 12 h-Red), h-BN 2 (220 °C, 18 h-Green), h-BN 3 (250 °C, 12 h-Blue), and h-BN 4 (250 °C, 18 h-Black), respectively. **60**

Figure 3.5: Graphical depiction of Williamson-Hall (W-H) plots representing linear relationship between  $\beta$  Cos $\theta$  versus 4 Sin $\theta$  for samples (a) Bulk h-BN, (b) h-BN\_1, (c) h-BN\_2, (d) h-BN\_3, and (e) h-BN\_4 to evaluate micro-strain and crystallite size. 62 Figure 3.6: SEM top-view micrographs depicting (a) pristine bulk h-BN and hydrothermally exfoliated variants: (b) h-BN\_1 at 220 °C for 12 h, (c) h-BN\_2 at 220 °C for 18 h, (d) h-BN\_3 at 250 °C for 12 h, and (e) h-BN\_4 at 250 °C for 18 h. 63 Figure 3.7: High-resolution TEM imaging depicting morphological evolution from (a) pristine bulk h-BN to hydrothermally treated samples: (b) h-BN\_1 (220 °C, 12 h), (c) h-BN\_2 (220 °C, 18 h), (d) h-BN\_3 (250 °C, 12 h), and (e) h-BN\_4 (250 °C, 18 h), highlighting nanosheet formation and degree of exfoliation as a function of temperature and duration.

Figure 3.8: AFM analysis images depicting surface roughness and topography of electrophoretically deposited h-BN films on ITO substrates mentioned as (a) Bulk h-BN, (b) h-BN\_1, (c) h-BN\_2, (d) h-BN\_3, and (e) h-BN\_4, respectively.

65
Figure 3.9: Absorbance versus wavelength relationship obtained from UV-Visible spectroscopy for (a) bulk h-BN and (b) h-BN\_1, (c) h-BN\_2, (d) h-BN\_3, (e) h-BN\_4, respectively, demonstrating optical response influenced by tuning hydrothermal synthesis

Figure 3.10: Energy bandgap determination through Tauc plots for (a) bulk h-BN and hydrothermally processed variants (b) h-BN\_1, (c) h-BN\_2, (d) h-BN\_3, and (e) h-BN\_4, depicting quantum confinement effects and optical tunability influenced by hydrothermal synthesis parameters.

conditions.

Figure 3.11: Raman analysis in the  $E_{2g}$  phonon region for (a) Bulk h-BN, (b) h-BN\_1, (c) h-BN\_2, (d) h-BN\_3, and (e) h-BN\_4, clearly demonstrating synthesis-dependent shifts in vibrational frequency.

Figure 3.12: Fourier Transform Infrared (FT-IR) Spectra highlighting dominant vibrational modes in (a) Bulk h-BN, (b) h-BN\_1, (c) h-BN\_2, (d) h-BN\_3, and (e) h-BN\_4 elucidating vibrational interactions in sp<sup>2</sup>-hybridized B-N bonding across the synthesized variants.

Figure 3.13: Cyclic voltametric response illustrating redox behaviour of (a) Bulk h-BN, (b) h-BN\_1, (c) h-BN\_2, (d) h-BN\_3, and (e) h-BN\_4 electrodes in PBS electrolyte with 5 mM  $[Fe(CN)_6]^{3-/4-}$  at a scan rate of 50 mV/s.

Figure 3.14: Representation of scan rate-dependent cyclic voltammograms for (a) bulk h-BN and its modified derivatives (b) h-BN\_1, (c) h-BN\_2, (d) h-BN\_3, and (e) h-BN\_4, obtained over the potential range -0.9 V to +1.2 V at scan rates from 30 to 120 mV s<sup>-1</sup>, along with (f) the linear fitting plots of Ipa and Ipc versus the square root of the scan rate, confirming diffusion-controlled redox behaviour.

Figure 3.15: Nyquist plots derived from Electrochemical Impedance Spectroscopy (EIS) reveal the interfacial resistance behaviour of (a) bulk h-BN and hydrothermally exfoliated samples (b) h-BN\_1, (c) h-BN\_2, (d) h-BN\_3, and (e) h-BN\_4, recorded across a frequency range of 0.1–10<sup>5</sup> Hz under a constant bias potential of 10 mV.

Figure 3.16: Electrical equivalent circuit models representing the fitted impedance parameters derived from EIS analysis for samples (a) bulk h-BN and hydrothermally exfoliated samples (b) h-BN\_1, (c) h-BN\_2, (d) h-BN\_3, and (e) h-BN\_4, effectively capture their interfacial charge transfer dynamics and diffusion behaviour.

Figure 3.17: Electrochemical investigations from Differential Pulse Voltammetry between -0.7 V and +1.2 V for (a) Bulk h-BN, and structurally modified counterparts (b) h-BN\_1, (c) h-BN\_2, (d) h-BN\_3, and (e) h-BN\_4, reveal the influence of nanoscale refinement on redox behaviour.

#### Chapter 4

Figure 4.1: (a) Schematic representation of electrophoretic deposition (EPD) of h-BNNS films on pre-hydrolyzed ITO substrate, (b) Pictorial depiction of electrophoretically deposited uniform h-BNNS films on ITO electrode, and (c) Sequential process detailing the fabrication of the h-BNNS-based immunoelectrode.

Figure 4.2: X-ray diffraction characterization conducted on bulk h-BN (Red) and hydrothermally exfoliated h-BNNS (Green) within the  $2\theta$  range between  $10^{\circ}$  to  $80^{\circ}$ , revealing characteristic diffraction peaks consistent with the standard JCPDS card No. 034-0421 (Blue) by retention of the hexagonal crystal structure post-exfoliation. 94 Figure 4.3: SEM micrographs distinctly reveal (a) bulk h-BN at  $20 \mu m$  scale, (b) exfoliated h-BN nanosheets (h-BNNS) at  $20 \mu m$ , and (c) a cross-sectional view of the electrophoretically deposited h-BNNS film on ITO substrate at  $10 \mu m$  scale (inset:  $2 \mu m$ ). High-resolution TEM imaging distinctly captures (d) hexagonal h-BNNS, (e) bulk h-BN, and (f) ultrathin nanosheets at  $500 \mu m$  resolution.

Figure 4.4: UV-visible absorption spectra of bulk h-BN (Red) and hydrothermally exfoliated h-BNNS (Green), with Tauc plots inset to accurately estimate their optical band gaps.

Figure 4.5: Raman spectroscopic analysis was performed on bulk h-BN (red) and hydrothermally exfoliated h-BNNS (green) over the 1250–1500 cm<sup>-1</sup> wavenumber range to assess their vibrational characteristics.

Figure 4.6: The FT-IR spectra recorded between 400 and 4000 cm<sup>-1</sup> powerfully capture and confirm the molecular fingerprints of h-BNNS and successive bio-conjugation steps, including Anti-CEA/h-BNNS, BSA/Anti-CEA/h-BNNS, and CEA/BSA/Anti-CEA/h-BNNS, affirming successful functionalization and immobilization at each stage. 101 Figure 4.7: Comprehensive cell viability analysis after 24 (red), 36 (green), and 72 (blue) hours of incubation with different h-BNNS concentrations, reflecting consistent and reliable cellular responses. 104

Figure 4.8: Cyclic voltammetry (CV) analysis, performed within a -0.9 to 1.2 V potential range, clearly demonstrates the successful modification of the h-BNNS/ITO electrode with protein biomolecules.

Figure 4.9: Electrode study on stepwise protein biomolecule modification of the h-BNNS/ITO electrode is confirmed by Differential pulse voltammetry (DPV) analysis conducted in the -0.2 to 1.2 V potential range.

Figure 4.10: Scan rate study conducted using cyclic voltammetry on the BSA/Anti-CEA/h-BNNS/ITO electrode across scan rates from 10 to 150 mV/s, elucidating the charge transfer kinetics and diffusion-controlled behaviour.

Figure 4.11: A linear correlation is observed in the scan rate analysis of the BSA/Anti-CEA/h-BNNS/ITO electrode between (i) anodic and cathodic peak potentials and (ii) peak currents plotted versus the square root of the scan rate (mV/s).

Figure 4.12: Differential pulse voltammetry (DPV) analysis of the CEA/BSA/Anti-CEA/h-BNNS/ITO immunoelectrode was performed over 0–50 ng/mL CEA concentrations. (b) The corresponding calibration curve shows a robust linear relationship between DPV current and CEA concentration, supported by inset linear regression.

Figure 4.13: The influence of pH within the 6.0 to 8.0 range on the electrochemical peak current of the Anti-CEA/h-BNNS/ITO immunoelectrode was conducted to optimize antibody-antigen interaction efficiency.

Figure 4.14: Bar graph depicting the selectivity study conducted using DPV measurements to investigate the effect of various interferents relevant to NSCLC patients on the electrochemical performance of the BSA/Anti-CEA/h-BNNS/ITO immunosensor.

114

Figure 4.15: Reproducibility was evaluated using four independently fabricated BSA/Anti-CEA/h-BNNS/ITO immunoelectrodes prepared under identical protocols. 115

immunoelectrode, monitored over six weeks with regular weekly intervals.
Figure 4.17: Evaluation of the CEA/BSA/Anti-CEA/h-BNNS/ITO immunoelectrode using
spiked serum sample analysis, to comprehensively test the sensitivity and accuracy of as-
fabricated immunoelectrodes' applicability for real sample analysis.
Chapter 5
Figure 5.1: Diagram illustrating the eco-friendly modified Hummer's route for the
synthesis of graphene oxide (GO) from natural graphite powder 130
Figure 5.2: Sequential fabrication steps of rGO-hBNNS hybrid nanocomposite via one-
pot hydrothermal synthesis route. and Schematic representation interfacial chemistry
driving rGO-hBNNS Nanocomposite formation 131
Figure 5.3: Diagrammatic representation of (a) electrophoretic fabrication of rGO-
hBNNS-coated ITO electrode, and (b) stepwise biointerface engineering using Anti-CEA
immobilization, BSA passivation, and CEA conjugation to produce the nano-biosensing
interface.
Figure 5.4: Depiction of molecular interactions involving amide bond formation: (a) L-
glutamic acid with amine-functional hBNNS, (b) L-lysine with epoxide-functional rGO,
and (c) L-lysine with carboxyl-functional rGO.
Figure 5.5: Powder X-ray diffraction patterns of (I) hBNNS, (II) GO, and (III) rGO-
hBNNS nanocomposite obtained across the 20 range of 5°-80°, demonstrating key
crystallographic attributes. 134
Figure 5.6: Morphological and elemental characterization conducted using (a) Scanning
electron microscopy (SEM) images at 2 µm resolution capturing surface topography, (b)
transmission electron microscopy (TEM) images at 200 nm resolution detailing nanoscale
morphology, and (c) energy-dispersive X-ray analysis (EDAX) spectra highlighting
elemental composition, presented for (I) hBNNS, (II) GO, and (III) rGO-hBNNS
nanocomposite 137
Figure 5.7: Detailed UV-visible absorption spectra and associated Tauc plots for (I)
hBNNS (Pink), (II) GO (Cyan), and (III) rGO-hBNNS (Green), to estimate the optical
band gap energies by analyzing their electronic transitions.
Figure 5.8: Raman spectroscopic analysis conducted on (I) hBNNS (Pink), (II) GO (Cyan),
and (III) rGO-hBNNS (Green) across the 900-3000 cm <sup>-1</sup> wavenumber range to evaluate
their distinct vibrational modes.
Figure 5.9: FT-IR spectra obtained from 400 to 4000 cm <sup>-1</sup> distinctly demonstrate the
characteristic molecular features of h-BNNS, GO, and rGO-hBNNS, confirming successful synthesis and hybridization at the molecular level.
Figure 5.10: FT-IR Spectroscopic Analysis for Time-Dependent Optimization of Anti-
CEA Immobilization on rGO-hBNNS Hybrid Nanocomposite 144
Figure 5.11: Distinct FT-IR analysis over 400–4000 cm <sup>-1</sup> depicting the characteristic
vibrational fingerprints of rGO-hBNNS and progressive bio-conjugation process,
confirming the stepwise achievement of antibody coupling, protein blocking, and antigen
binding with high precision. 145
Figure 5. 12: Cyclic voltammetry (CV) analysis, conducted over a potential range of -0.9
to 1.2 V, provides clear and detailed evidence of successful stepwise modification of the
rGO-hBNNS/ITO electrode with protein biomolecules, highlighting the progressive
formation of an efficient bio-interface.
Figure 5.13: Differential Pulse Voltammetry (DPV) performed within the -0.2 to 1.2 V
potential window reveals the progressive biofunctionalization of rGO-hBNNS/ITO

Figure 4.16: Differential pulse voltammetry (DPV) investigation to systematically

stability of the CEA/BSA/Anti-CEA/h-BNNS/ITO

shelf-life

electrodes, enabling precise monitoring of electron transfer dynamics ar	ıd successful
protein modification at each fabrication step.	148
Figure 5.14: Influence of Scan Rate on the Cyclic Voltammetric Response	of BSA/Anti-
CEA/rGO-hBNNS/ITO Immunoelectrode in Presence of [Fe(CN) <sub>6</sub> ] <sup>3-/4-</sup> el	ectrolyte for

CEA/rGO-hBNNS/ITO Immunoelectrode in Presence of  $[Fe(CN)_6]^{3-/4-}$  electrolyte for scan rate ranging from 10-150 mV/s

Figure 5.15: Quantitative Linear Relationship derived between Peak Currents and Potentials response with the Square Root of Scan Rate for BSA/Anti-CEA/rGO-hBNNS/ITO Immunoelectrode in the Presence of [Fe(CN)<sub>6</sub>]<sup>3-/4-</sup>electrolyte.

Figure 5.16: Differential pulse voltammetry (DPV) response upon successive addition of CEA in the range 0–50 ng/mL onto BSA/Anti-CEA/rGO-hBNNS/ITO immunoelectrode 151

Figure 5. 17: Linear calibration graph correlating peak DPV current as a function of CEA concentration, validating the performance and quantitative detection capability of the rGO-hBNNS-based immunosensor.

Figure 5.18:Influence of buffer pH on peak DPV current of the Anti-CEA/rGO-hBNNS/ITO immunosensor, demonstrating sensitivity and stability across physiologically relevant pH ranges for optimal electrochemical performance.

Figure 5.19: Bar graph illustrating the control experiment on rGO-hBNNS/ITO electrodes depicting the negligible electrochemical response upon addition of different CEA concentrations.

Figure 5.20: Bar graph illustrating the reproducibility of DPV current responses across multiple independently fabricated BSA/Anti-CEA/rGO-hBNNS/ITO immunoelectrodes.

Figure 5. 21: Quantitative bar representation of Sequential selectivity evaluation of the BSA/Anti-CEA/rGO-hBNNS/ITO immunoelectrode with stepwise addition of target CEA and potential interferents: (A) BSA/Anti-CEA/rGO-hBNNS/ITO, (B) + CEA (2 ng/mL), (C) + cTnI (0.5 ng/mL), (D) + CRP (100 ng/mL), (E) + NSE (10 ng/mL), (F) + ET-1 (1 ng/mL), (G) + Glucose (7 ng/mL), and (H) + NaCl (20 mM).

159 Figure 5.22: Bar graph illustrating the weekly operational stability of the as-fabricated BSA/Anti-CEA/rGO-hBNNS/ITO immunosensor, confirming sustained sensor activity.

Figure 5.23: Real-sample validation of the CEA/BSA/Anti-CEA/rGO-hBNNS/ITO immunoelectrode through controlled spiked serum experiments to quantify its sensitivity, reproducibility, and reliability for clinical applications.

161

#### Chapter 6

Figure 6.1: Schematic illustration of the sequential steps followed in the polyol-assisted synthesis of dandelion-shaped Cu<sub>x</sub>O nanoflowers.

Figure 6.2: Stepwise schematic representation of the hydrothermal synthesis route employed for the fabrication of  $Cu/Cu_XO$ -hBNNS nano-hybrid composite. 174 Figure 6.3: (I) Pictorial illustration of  $Cu/Cu_XO$ -hBNNS film deposition via electrophoretic deposition (EPD); (II) Schematic representation of sequential steps involved in the fabrication of the  $Cu/Cu_XO$ -hBNNS-based nano-biosensor; (III) Optical images of  $Cu/Cu_XO$ -hBNNS/ITO micro-electrodes (a) prior to and (b) following electrochemical characterization; (IV) Proposed mechanistic pathway for amide bond formation: (a) between L-glutamic acid and amine-functionalized hBNNS, (b) between cysteine and zero-valent copper, (c) between cysteine and cuprous oxide, and (d) between histidine and cupric oxide.

Figure 6.4: X-ray diffraction (XRD) analysis was performed on (I)  $Cu_XO$  Nanoflowers, (II) hBNNS, and (III)  $Cu/Cu_XO$ -hBNNS nano-hybrid composite, recording diffraction patterns within the  $2\theta$  range of  $10^\circ$ - $80^\circ$ .

Figure 6.5: (I) Scanning electron microscopy (SEM), (II) transmission electron microscopy (TEM), and (III) particle size distribution curves corresponding to (a) $Cu_XO$ , (b) hBNNS, and (c) $Cu/Cu_XO$ -hBNNS nanohybrid composite (NHC); (d) SEM micrograph depicting the surface morphology of the as-fabricated $Cu/Cu_XO$ -hBNNS/ITO electrode.
Figure 6.6: UV-Vis spectroscopic absorption data with corresponding Tauc plots, highlighting the electronic transition and bandgap estimation in Cu <sub>X</sub> O (Blue), hBNNS (Red), Cu/Cu <sub>X</sub> O/hBNNS (Purple) 186 Figure 6.7: Urbach Energy evaluation for Cu/Cu <sub>X</sub> O-hBNNS Nano-hybrid Composite 187
Figure 6.8: Raman spectroscopic response for Cu <sub>x</sub> O (Blue), hBNNS (Red), and Cu/Cu <sub>x</sub> O-hBNNS (Purple)  189  Figure 6.9: FTIR spectra of Cu <sub>x</sub> O (Blue), hBNNS (Red), and Cu/Cu <sub>x</sub> O-hBNNS (Purple)  191
Figure 6.10: Immobilization of Anti-CEA antibodies on Cu/Cu <sub>x</sub> O-hBNNS/ITO electrodes monitored by FTIR spectroscopy at 12 hours (Orange) and 24 hours (Cyan), demonstrating stepwise enhancement of biomolecular attachment.
Figure 6.11: Stepwise fabrication of the Cu/Cu <sub>X</sub> O-hBNNS based immunoelectrode evaluated using FTIR spectroscopy  Figure 6.12: The progressive preparation of the Cu/Cu <sub>X</sub> O-hBNNS based immunoelectrode was validated using cyclic voltammetry (CV) analysis  195
Figure 6.13: Monitoring of $Cu/Cu_XO$ -hBNNS based immunoelectrode construction was performed through DPV response analysis. 196 Figure 6.14: Scan rate-dependent cyclic voltammetric investigation of BSA/Anti-
CEA/Cu/Cu <sub>x</sub> O-hBNNS/ITO immunoelectrodes, measured across 10–200 mV/s; inset demonstrates the linear relationship between $\Delta$ Vp and $\sqrt{s}$ can rate. 197 Figure 6.15: Linear correlation established between (i) applied potential and (ii) current response with respect to the square root of scan rate for BSA/Anti-CEA/Cu/Cu <sub>x</sub> O-
hBNNS/ITO immunoelectrode.  198 Figure 6.16: (a) Differential Pulse Voltammetry (DPV) responses recorded for varying CEA concentrations (0–50 ng/mL) on the BSA/Anti-CEA/Cu/Cu <sub>x</sub> O-hBNNS/ITO
immunoelectrode; (b) Corresponding calibration curve illustrating the linear correlation between DPV current signals and CEA concentration.  199 Figure 6.17: Bar graph representation of the DPV responses of the Anti-CEA/Cu/Cu <sub>X</sub> O-PNNS/JTO improve allocated a corresponding buffer pH values (6.0, 8.0), highlighting the
hBNNS/ITO immunoelectrode across varying buffer pH values (6.0–8.0), highlighting the influence of pH on electrochemical performance.  203 Figure 6.18: Control study illustrated through a bar graph, depicting the DPV current variations of the Cu/Cu <sub>x</sub> O-hBNNS/ITO electrode in response to CEA concentrations of
0.01, 4, 8, and 15 ng/mL. 204 Figure 6.19: Evaluation of the reproducibility of electrochemical current response in the as-prepared CEA/BSA/Anti-CEA/Cu/Cu <sub>x</sub> O-hBNNS/ITO immunoelectrode. 205
Figure 6.20: Selectivity analysis illustrated by bar chart, demonstrating the electrochemical response of the BSA/Anti-CEA/Cu/Cu <sub>x</sub> O-hBNNS/ITO immunoelectrode in the presence of CEA and potential interfering biomolecules: (A) electrode baseline, (B) + CEA (2 ng/mL), (C) + CRP (100 ng/mL), (D) + cTnI (0.5 ng/mL), (E) + ET-1 (1 ng/mL), (F) + NSE (10 ng/mL), (G) + Glucose (7 ng/mL), and (H) + NaCl (20 mM). 206 Figure 6.21: Current stability analysis of the CEA/BSA/Anti-CEA/Cu/Cu <sub>x</sub> O-hBNNS/ITO
immunoelectrode, evaluated over a period of 10 days at regular time intervals. 207 Figure 6.22: Bar chart representation of differential DPV responses obtained from blank control, pure serum, and CEA-spiked serum samples, confirming the detection capability of the as-fabricated immunoelectrode. 208

Chapter 7
Figure 7.1: Stepwise schematic Illustration for the synthesis of TiO <sub>2</sub> nanowires through
the solvothermal method.
Figure 7.2: Schematic illustration of the engineered solvothermal mechanism facilitating
TiO <sub>2</sub> nanowire decoration on hBNNS nano-hybrid composite. 225
Figure 7.3: (a) Schematic diagram showcasing TiO <sub>2</sub> -hBNNS film deposition through
electrophoretic deposition (EPD) technique, (b) Systematic illustration demonstrating
sequential steps involved in fabricating TiO <sub>2</sub> -hBNNS-based nano-biosensor. 226
Figure 7.4: X-ray diffraction studies were conducted to investigate the crystalline
structure of (I) TiO <sub>2</sub> -NW, (II) hBNNS, and (III) TiO <sub>2</sub> -hBNNS, with diffraction patterns
obtained over the 2θ interval spanning 10°–80°.
Figure 7.5: Morphological characterization of (I) TiO2-NW (green), (II) hBNNS (pink),
(III) TiO <sub>2</sub> -hBNNS (blue), and (IV) TiO <sub>2</sub> -hBNNS/ITO electrode: (a) SEM images at 2 μm
scale, (b) TEM images at 500 nm scale, (c) TEM images at 100 nm scale, and (d) statistical
evaluation of TiO2 nanowire mean diameter before and after nanohybrid composite
formation. 233
Figure 7.6: Optical characterization depicting (a) UV-Visible absorption spectra (Inset:
Tauc plot for bandgap estimation), and (b) Urbach energy estimation for (I) TiO2, (II)
hBNNS, and (III) TiO <sub>2</sub> -hBNNS samples. 235
Figure 7.7: Raman spectra of (I) TiO2-NW, (II) hBNNS, and (III) TiO2-hBNNS was
carried out in the 1250-1500 cm <sup>-1</sup> range, providing detailed insights into their vibrational
modes and structural interactions.
Figure 7.8: FTIR spectra of (I) TiO <sub>2</sub> nanowires (TiO <sub>2</sub> -NW), (II) hexagonal boron nitride
nanosheets (hBNNS), and (III) TiO2-hBNNS composite were recorded in the 400-4000
cm <sup>-1</sup> wavenumber region to examine their functional group vibrations and bonding
characteristics. 241
Figure 7.9: FTIR spectra analyzing Anti-CEA antibody immobilization on the TiO2-
hBNNS/ITO electrode at 12 and 24 hours.
Figure 7.10: Immunoelectrode preparation on immobilization of Anti-CEA, BSA, and
CEA onto TiO2-hBNNS/ITO electrode analyzed through FTIR spectroscopy 246
Figure 7.11: Cyclic voltammetry (CV) measurements performed within the potential
window of -0.9 to 1.2 V demonstrate the sequential modification of the TiO2-hBNNS/ITO
electrode with protein biomolecules, thereby confirming the progressive assembly of a
stable and efficient bio-interface. 247
Figure 7.12: Stepwise biofunctionalization of TiO2-hBNNS/ITO electrodes is confirmed

Figure 7.12: Stepwise biofunctionalization of TiO2-hBNNS/ITO electrodes is confirmed through DPV analysis conducted over the -0.2 to 1.2 V range, demonstrating precise control of protein immobilization and associated changes in electron transfer efficiency.

248

Figure 7.13: (a)Influence of scan rate on the cyclic voltammetric behavior of the BSA/Anti-CEA/TiO2O-hBNNS/ITO immunoelectrode recorded in  $[Fe(CN)_6]^{3-/4-}$  electrolyte, evaluated over a scan rate range of 10-160 mV/s., (b) Linear correlation between peak current response and the square root of scan rate for the BSA/Anti-CEA/TiO2-hBNNS/ITO immunoelectrode in  $[Fe(CN)_6]^{3-/4-}$  electrolyte, confirming diffusion-controlled electron transfer kinetics.

Figure 7. 14: (a) Differential pulse voltammetry (DPV) response illustrating the electrochemical interaction of CEA concentrations (0–50 ng/mL) with the BSA/Anti-CEA/TiO<sub>2</sub>-hBNNS/ITO immunoelectrode, and (b) calibration curve depicting the linear correlation between DPV signal on elevating CEA concentration.

Figure 7.15: Bar plot representing the buffer pH dependence of peak DPV current for the Anti-CEA/TiO2-hBNNS/ITO immunosensor, establishing the optimal electrochemical environment for enhanced biosensor sensitivity and stability.

Figure 7.16: Quantitative bar plot illustrating the control experiment on TiO2-hBNNS/ITO electrodes, confirming the absence of significant electrochemical activity upon exposure to different CEA concentrations.

Figure 7.17: A reproducibility study was performed by preparing four individual BSA/anti-CEA/TiO<sub>2</sub>—hBNNS/ITO immunoelectrodes under consistent fabrication conditions and analyzing their electrochemical responses.

Figure 7.18: Quantitative bar chart depicting the sequential selectivity analysis of the BSA/Anti-CEA/TiO<sub>2</sub>-hBNNS/ITO immunoelectrode, examined through stepwise introduction of the target CEA (2 ng/mL) and potential interfering biomolecules: (A) BSA/Anti-CEA/TiO<sub>2</sub>-hBNNS/ITO, (B) + CEA, (C) + cTnI (0.5 ng/mL), (D) + NSE (10 ng/mL), (E) + CRP (100 ng/mL), (F) + ET-1 (1 ng/mL), (G) + NaCl (20 mM), and (H) + Glucose (7 ng/mL).

Figure 7.19: The shelf-life stability of the CEA/BSA/anti-CEA/TiO<sub>2</sub>-hBNNS/ITO immunoelectrode was assessed through differential pulse voltammetry (DPV), with electrochemical responses recorded at regular weekly intervals across a 10-day monitoring period.

Figure 7.20: (a) Assessment of current reproducibility in the as-fabricated CEA/BSA/Anti-CEA/TiO<sub>2</sub>-hBNNS/ITO immunoelectrode. (b) Bar chart illustrating the selectivity study upon sequential addition of various interferents to CEA, defined as: A = BSA/Anti-CEA/rGO-hBNNS/ITO, B = A + CEA (2 ng/mL), C = B + CRP (100 ng/mL), D = C + cTnI (0.5 ng/mL), E = D + ET-1 (1 ng/mL), E = D + ET-1 (1 ng/mL), E = D + ET-1 (1 ng/mL), E = D + ET-1 (20 mM). (c) Stability evaluation of the CEA/BSA/Anti-CEA/TiO<sub>2</sub>-hBNNS/ITO immunoelectrode over 10-day intervals. (d) Bar graph presenting DPV response variations for spiked serum samples compared to actual CEA concentrations, validating sensor performance.

### **List of Tables**

Chapter 3
Table 3.1: Comparative Assessment of Crystallite Size (d) and induced lattice strain (ε) of
different Hydrothermally Synthesized h-BN Samples evaluated from Williamson-Hall
(W–H) plot fitting with relative error estimation.
Table 3.2: A comparison table depicting lattice parameter values derived using X-powder
analysis to evaluate the impact of nano-confinement-induced compression on
crystallographic structure of h-BN samples synthesized at different hydrothermal
conditions. 62
Table 3.3: Distinct transmittance peak assignments in the fingerprint region affirm the
structural integrity of hydrothermally synthesized h-BN.
Table 3.4: Quantitative evaluation of the Electrochemical performance given by peak
anodic and cathodic currents (Ipa, Ipc), Ipa/Ipc ratio, and calculated electroactive surface
area fabricated via electrophoretic deposition. 73
Table 3.5: Electrochemical impedance spectroscopy (EIS)-derived values tabulating key
parameters, including charge transfer resistance (Rct), Warburg admittance (Zw.Yo),
and CPE admittance (CPE.Yo) for h-BN nanosheet electrochemical analysis.
Chapter 4
Table 4.1: Comprehensive tabular presentation of wavenumbers assigned to the
vibrational bands characteristic of the protein structure associated with the Amide bands
of IgG antibody.  Error! Bookmark not defined.
Table 4.2: Determination of the diffusion coefficients of the modified electrode accurately
calculated using the Randles-Sevcik equation.  Error! Bookmark not defined.
Table 4.3: A comprehensive comparison table summarizing the analytical performance,
including linear range and limit of detection, of different immunosensors designed for
CEA monitoring in clinical diagnostics.
Table 4.4: Quantitative determination of relative standard deviation (RSD%) and
recovery rates for CEA in spiked serum, with reference to actual CEA concentration
values.
Chapter 5
Table 5.1: Intense diffraction peaks, corresponding <i>hkl</i> planes, peak positions, full width
at half maximum (FWHM), calculated crystallite sizes, and interplanar spacings for
hBNNS, GO, and rGO-hBNNS nanocomposite samples.
Table 5.2: Elemental analysis presenting atomic and weight percentages, as well as B/N
and C/O ratios, for (I) hBNNS, (II) GO, and (III) the synthesized rGO-hBNNS hybrid
nanocomposite.
Table 5.3: Assigned FT-IR vibrational peaks validating the successful synthesis of (I)
hBNNS, (II) GO, and (III) rGO-hBNNS hybrid nanocomposite, confirming the
preservation of key functional groups and the emergence of composite-specific features.
143
Table 5.4: Evaluation of interfacial electron transfer from peak anodic current (CV),
diffusion coefficient, and DPV current monitored throughout sequential fabrication of the
immunoelectrode. 147
Table 5.5: Evaluation and comparison of rGO-hBNNS-based nano-biosensor metrics with
conventional immunosensors. 155
Table 5. 6: Differential pulse voltammetry (DPV) response and corresponding relative
standard deviation (RSD%) upon sequential addition of various interfering analytes to
evaluate the selectivity of the fabricated rGO-hBNNS/ITO nano-biosensor. 160
evaluate the selectivity of the fabilicated 100-hbm/110 hand-bloschsof.

Table 5.7: Quantitative evaluation of recovery currents and RSD (%) for spiked CEA concentrations in human serum with actual concentrations, illustrating the capability of the BSA/Anti-CEA/rGO-hBNNS/ITO immunoelectrode to achieve consistent, precise, and clinically relevant measurements.

#### Chapter 6

enapter v	
Table 6.1: Evalution of microstrain and dislocation density in as-synthesized (I)	Cu <sub>x</sub> O,
(II) hBNNS, (III) Cu/Cu <sub>X</sub> O-hBNNS samples respectively.	183
Table 6.2: FT-IR band assigned to (I) CuxO, (II) hBNNS, and (III) Cu/CuXO-I	ıBNNS
samples respectively.	192
Table 6.3: Comparison of sensing characteristics of Cu/CuxO-hBNNS based	nano-
biosensor with existing metal- and semiconductor-based immunosensors.	202
Table 6.4: Tabular representation of stepwise fabrication of Cu/CuxO-hBNNS	based
Nano-biosensor examined by Anodic Peak Current, Diffusion Coefficient, and	d DPV
Current respectively.	207
Table 6.5: Evaluation of recovery current and relative standard deviation (RSD,	<b>%)</b> for
detecting spiked CEA concentrations in human serum samples, relative to the actual	al CEA
concentration and estimation of bare serum concentration using DPV and	ELISA

#### Chapter 7

techniques respectively.

Table 7.1: Wavenumber Assigned to FTIR peaks of (I) TiO<sub>2</sub>-NW, (II) hBNNS, and (III) TiO<sub>2</sub>-hBNNS respectively. 241

209

Table 7.2: Comparison of sensing characteristics of TiO2-hBNNS based nano-biosensor with existing metal-, metal oxides- and semiconductor-based immunosensors. 254

#### DMEM: Dulbecco's Modified Eagle Medium **List of Abbreviations** DMSO: Dimethyl Sulfoxide · 101 DNA: Deoxyribonucleic Acid · 4 DPV: Differential Pulse Voltammetry · 19 |Z|: Magnitude of Impedance · 41 DSSCs: Dye-Sensitized Solar Cells · 202 DTG: Derivative Thermogravimetric · 36 **DUV: Deep Ultra-Violet · 13** 0D: Zero Dimensional · 10 $\overline{E}$ E: Photon Energy · 69 **EBSD: Electron Back-Scattered Diffraction** 1D: One Dimensional · 10 EDAX: Energy Dispersive X-ray Analysis · 19 2D: Two Dimensional · 1 EDC: 1-(3-(Dimethylamino)-propyl)-3-Ethylcarbodiimide Hydrochloride · 92 EDS/EDX: **Energy-Dispersive** Spectroscopy · 26 3D: Three Dimensional · 10 EDTA: Ethylenediaminetetraacetic Acid · Eg: Optical Bandgap · 69 EG: Ethylene Glycol · 162 AC: Alternating Current · 40 Electrochemical **Impedance AFM: Atomic Force Microscopy · 19** Spectroscopy · 19 Ag/AgCl: Silver/Silver Chloride · 60 **ELISA: Enzyme-linked Immunosorbent** AlN: Aluminium Nitride · 11 Assay · 242 Anti-CEA: CEA Antigen · 103 **Epa: Anodic Potential · 73 Epc: Cathodic Potential · 73** R **EPD: Electrophoretic Deposition · 22** B: Boron · 54 ET-1: Endothelin-1 · 111 BN: Boron Nitride · 12 BSA: Bovine Serum Albumin · 92 F FBS: Fetal Bovine Serum · 101 $\boldsymbol{C}$ Fc: Fragment Crystallizable · 159 Fourier C: Carbon · 54 **Transform** Infrared Spectroscopy · 19 CA: Chronoamperometry · 38 FWHM: Full Width at Half Maximum · 98 Cdl: Double-Layer Capacitance · 40 **CEA:** Carcinoembryonic Antigen · 4 **COFs: Covalent-Organic Frameworks · 54** G **CP:** Chronopotentiometry · 38 GaN: Gallium Nitride · 11 **CPE: Constant Phase Element · 40** GCD: Galvanostatic Charge–Discharge · 38 CRP: C-reactive Protein · 111 GLOBOCAN: Global Cancer Observatory · CT: Computed Tomography · 4 cTnI: Cardiac Troponin-I · 111 GO: Graphene Oxide · 124 CuxO: Copper/Copper Oxide Nanoflowers · CV: Cyclic Voltammetry · 19 Н

DC: Direct Current · 23

**DFT: Density Functional Theory · 186** 

CVD: Chemical Vapour Deposition · 20

DI: Deionized · 68

hBNNS:

Nanosheets · 1

hBN: Hexagonal Boron Nitride · 12

Hexagonal

HEK: Human Embryonic Kidney Cells · 83

HLB: Hydrophilic-Lipophilic Balance · 162

HSP: Hansen solubility parameters · 57

Nitride

**Boron** 

Pt: Platinum · 90 IARC: International Agency for Research on Cancer · 2 R InN: Indium Nitride · 11 Rct: Charge-Transfer Resistance · 40 Ipa: Peak Anodic Current · 73 rGO: Reduced Graphene Oxide · 119 IPA: Isopropyl Alcohol · 165 RNA: Ribonucleic Acid · 4 Ipc: Peak Cathodic Current · 73 Rs: Solution Resistance · 40 ITO: Indium Tin Oxide · 60 RSD: Relative Standard Deviation · 112 IUPAC: International Union of Pure and Applied Chemistry · 6 S SAED: Selected Area Electron Diffraction · JCPDS: Joint Committee Powder SARS-CoV-2: Severe Acute Respiratory Diffraction Standards · 63 Syndrome Coronavirus 2 · 3 **SEM: Scanning Electron Microscopy · 19 SERS: Surface-Enhanced** Raman Spectroscopy · 32 KCl: Potassium Chloride · 60 SNR: Signal-to-Noise Ratio · 55 SPR: Surface Plasmon Resonance · 220 L STM: Scanning Tunnelling Microscopy · 35 LDH: Lactate Dehydrogenase · 37 LDHs: Layered Double Hydroxides · 54 T LEDs: Light Emitting Diodes · 29 TEM: Transmission Electron Microscopy · **LOD:** Limit of Detection · 83 LPE: Liquid-Phase Exfoliation · 57 TG: Thermogravimetric · 36 TGA: Thermogravimetric Analysis · 19 M TiO<sub>2</sub>: Titanium Dioxide · 200 **MOFs: Metal-Organic Frameworks · 54** TMDs: Transition Metal Dichalcogenides · MRI: Magnetic Resonance Imaging · 4 MTT: 3- (4,5-Dimethylthiazol-2-yl)-2,5-Diphenyltetrazolium Bromide · 37 **UV: Ultra-Violet · 19** N: Nitrogen · 54 NaCl: Sodium Chloride · 111 NCDs: Non-Communicable Diseases · 2 vdW: van der Waals · 120 NFs: Nanoflowers · 164 NHC: Nano-Hybrid Composite · 14 NHCs: Nano-Hybrid Composites · 158 W-H: Williamson-Hall · 80 NHS: N-hydroxysuccinimide · 92 WHO: World Health Organization · 3 NSCLC: Non-Small Cell Lung Cancer · 3 WST: Water-Soluble Tetrazolium · 37 NSE: Neuron-Specific Enolase · 111 NWs: Nanowires · 200 XRD: X-ray Diffraction · 19 0 **OIHNs:** Organic-Inorganic Hybrid Nanocomposites · 119 Zimag: Imaginary part of Impedance · 40 Zreal: Real part of Impedance · 40 PBS: Phosphate Buffer Saline · 92

PET: Positron Emission Tomography · 4 PLD: Pulsed Laser Deposition · 56

POC: Point-of-Care · 6

# Chapter 1

#### Literature Insights into Emerging 2D Nanomaterials and the Fabrication Strategies of Nanohybrid Composites for High-Performance Nano-Biosensing Technologies in Clinical Diagnostics and Healthcare

This chapter commences by addressing the pressing global issue of cancer, emphasizing the prevalence of lung cancer and the critical need for innovative solutions for early detection, facilitated by convenient analytical tools such as biosensors. It proceeds to detail the fundamental aspects of nano-biosensors, elaborating on their key components—bio-recognition elements, nano-interface matrices immobilization platforms, transducers and their classifications, as well as display mechanisms. Attention is given to the transformative impact of nanoscience and nanotechnology in engineering detection platforms that prioritize sensitivity, specificity, and operational stability. Furthermore, the chapter systematically provides a focused literature review that categorizes nanomaterials by dimensionality, with an in-depth focus on 2D nanomaterials due to their promising and unique attributes conducive to nano-biosensor development. Particularly, the chapter focuses on hexagonal Boron Nitride Nanosheets (hBNNS) as a promising nano-interface material, underscoring their versatile physicochemical properties and potential for advancing biosensor technology. This work addresses the potential difficulties and inherent challenges confronted in fabrication of stable, scalable, economical nano-interface matrix that limits robust electroanalytical performance for clinical applications. The motivation of this chapter is driven to effectively present the imperative rationale for development of nano-hybrid composites to augment the electroanalytical performance of hBNNS-based nano-biosensors for clinical applications.

## 1.1 Global Surge in Cancer Statistics and Associated Healthcare Challenges

Cancer has emerged as a leading cause of death worldwide, posing a significant obstacle to increasing life expectancy in every nation. Its growing prominence is partly attributed to declining mortality rates from stroke and coronary heart disease, indicating substantially high cancer incidences and deaths thereby making it a dominant health threat. The global burden of cancer continues to rise rapidly, driven by aging populations, population growth, and shifts in the prevalence of major risk factors, many of which are tied to socioeconomic development. As a result, cancer now accounts for nearly one in six deaths globally (16.8%) and almost one in four deaths from noncommunicable diseases (22.8%). Alarmingly, it contributes to three in ten premature deaths from Non-Communicable Disease (NCDs - 30.3% among those aged 30-69 years) and ranks among the top three causes of death in 177 of 183 countries. Beyond its health impact, cancer imposes enormous social and economic costs, varying across regions, cancer types, and genders. The most recent GLOBOCAN 2022 estimates from the International Agency for Research on Cancer (IARC) highlights the scale of the global cancer burden and its far-reaching implications for public health and society [1].

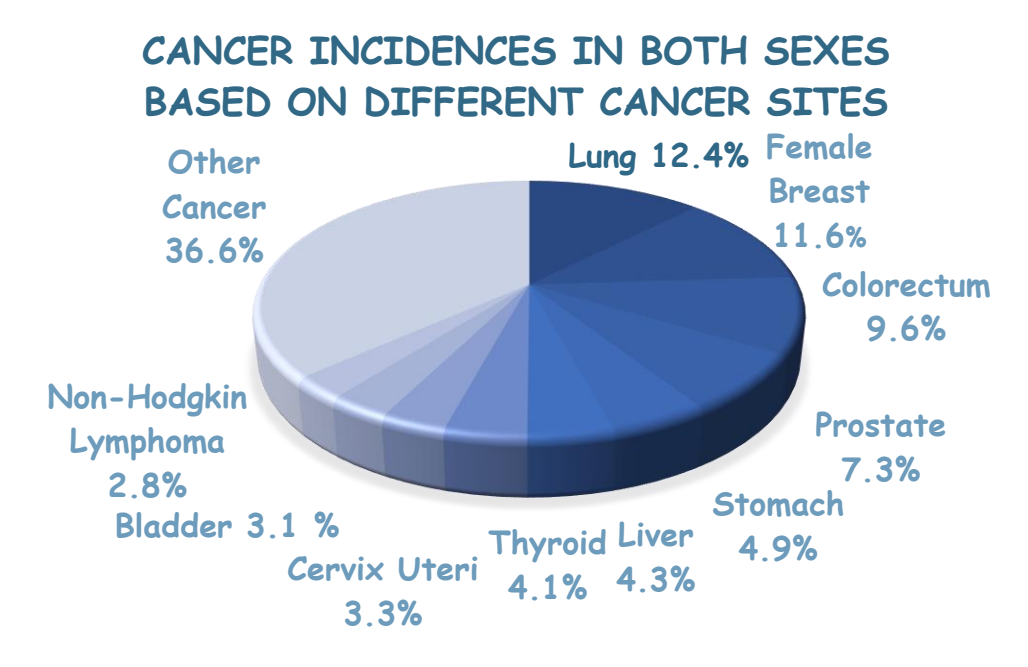


Figure 1.1: Cancer incidences in both sexes based on different Cancer sites Lung cancer remains the most frequently diagnosed cancer across the globe in the year 2022, accounting for 12.4% of all reported cases. It is followed in prevalence by breast cancer in women (11.6%), colorectal cancer (9.6%), prostate cancer (7.3%), and stomach cancer (4.9%) (Fig. 1.1). Importantly, lung cancer is also the foremost contributor to cancer-related mortality, responsible for 18.7% of total deaths, underscoring its highly aggressive and lethal nature. Colorectal cancer ranks second in mortality (9.3%), followed by liver cancer (7.8%), breast cancer in women (6.9%), and stomach cancer (6.8%) (Fig. 1.2). The cancer burden, however, varies distinctly between genders. Among women, breast cancer is the most frequently diagnosed

malignancy and the primary cause of cancer deaths, reflecting both high incidence and significant mortality. Gender-specific statistics highlight critical differences: breast cancer is the most common and deadliest cancer in women, followed closely by lung and colorectal cancers [1]. In men, however, lung cancer is both the most diagnosed and the leading cause of cancer death, with prostate and colorectal cancers ranking high in incidence and liver and colorectal cancers emerging as key contributors to mortality. In men, lung cancer is the most prevalent and fatal cancer, with prostate and colorectal cancer contributing most to new cases, while liver and colorectal cancers are the primary causes of cancer deaths after lung cancer, highlighting the growing global impact of lifestyle and environmental risk factors impacting male cancer mortality. These statistics highlight the prominence of lung cancer and the distinct gender-specific patterns in cancer incidence and mortality, which demand tailored approaches for prevention, screening, and treatment.

# CANCER MORTALITY IN BOTH SEXES BASED ON DIFFERENT CANCER SITES

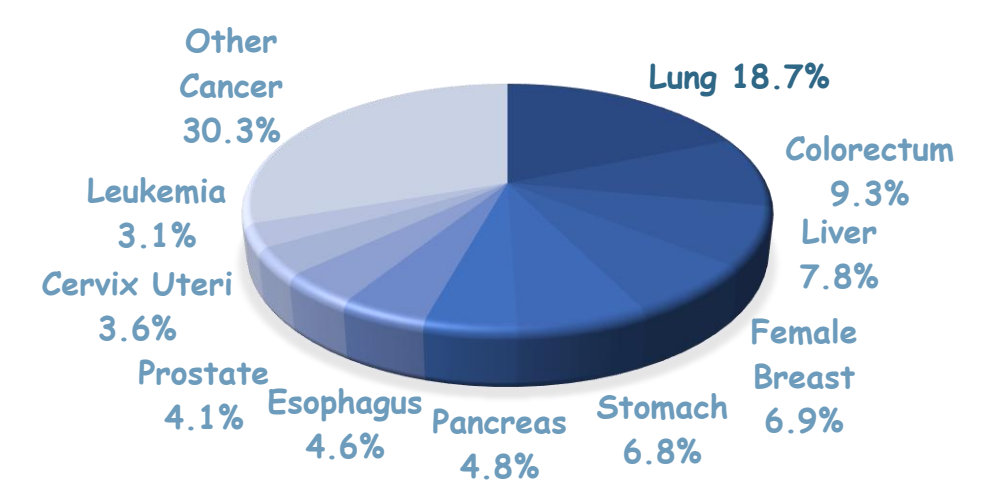


Figure 1.2: Cancer mortality in both sexes based in different Cancer sites

With cancer emerging as the global health burden with leading cause of premature mortality in 134 of 183 countries, WHO estimates predict a sharp increase in global cases—from 18.1 million in 2018 to 29.4 million by 2040[2]. Lung cancer dominates the burden, representing the most common malignancy worldwide, with non-small cell lung cancer (NSCLC) comprising 80–85% of cases in both men and women [3]. While countries with higher human development indices demonstrate better prevention of premature lung cancer deaths, the global challenge demands stronger strategies. Central to these strategies is the advancement of analytical technologies designed for fast, comprehensive, and practical detection of malignant cell growth, ensuring timely intervention and improved survival outcomes [3].

Non-small cell lung cancer (NSCLC) is the predominant histological subtype of lung cancer, representing approximately 85% of total cases [4]. It is characterized by a biologically complex and heterogeneous profile, with major risk factors including smoking, pulmonary fibrosis, chronic obstructive pulmonary disease, prolonged

exposure to air pollutants, metal and mineral dust, and radioactive gases [4]. Recent findings further suggest that NSCLC patients are highly vulnerable to severe complications from SARS-CoV-2 infection [5]. Clinically, patients often present with vague symptoms such as persistent cough, chest pain, shortness of breath, unintentional weight loss, and loss of appetite, which are commonly misdiagnosed as pulmonary tuberculosis during early disease stages. This misdiagnosis leads to delayed detection, allowing the cancer to remain unnoticed until it progresses into advanced and often incurable stages. Conventional diagnostic approaches—such as X-rays, computed tomography (CT), magnetic resonance imaging (MRI), and positron emission tomography (PET)—although routinely employed, are costly, time-intensive, and inadequate in identifying sub-micrometer tumors [6]. As a result, delayed diagnosis accelerates tumor spread to secondary organs, complicating treatment and contributing significantly to the high fatality rates associated with NSCLC.

Monitoring tumor-associated proteins offers a promising solution to overcome the limitations of conventional diagnostic approaches, as it provides a simplified, reliable, and cost-effective method for early cancer detection. Such biomarker-based strategies reduce dependency on complex and expensive imaging tools while ensuring timeefficient outcomes, thereby making diagnostics more accessible and patient-friendly [7]. Biomarkers are measurable biological molecules present in blood, body fluids, and tissues that serve as critical indicators of both normal physiological functions and abnormal pathological conditions [8]. They play a central role in understanding disease onset, progression, and treatment outcomes. In the context of cancer, biomarkers provide essential insights into how the body responds to therapeutic interventions, thereby assisting clinicians in tailoring treatment strategies and monitoring patient recovery. These biomarkers can take various molecular forms, including RNA, proteins such as antibodies, hormones, and oncogenes, as well as DNA alterations involving amplification, mutation, and translocation. Each of these categories offers valuable information about the molecular mechanisms underlying cancer and other diseases. For instance, protein biomarkers can help identify immune responses or hormonal imbalances, while genetic biomarkers can reveal mutations driving tumor growth and metastasis.

The importance of biomarkers lies in their wide-ranging applications across diagnostics, prognosis, and personalized medicine [9]. In diagnostics, they enable early and accurate detection of diseases, often before clinical symptoms appear, improving chances of successful intervention. Prognostically, biomarkers provide information about disease aggressiveness and likely outcomes, helping clinicians determine the intensity of treatment required. In therapeutic monitoring, biomarkers track treatment efficacy in real time, allowing adjustments to therapies and minimizing unnecessary side effects. Furthermore, in the era of precision medicine, biomarkers are indispensable for stratifying patients, guiding targeted therapies, and predicting responses to immunotherapy and chemotherapy. Thus, biomarkers are not just passive indicators of health or disease; they are active tools that bridge molecular biology and clinical decision-making. Their growing importance in research and clinical practice underscores their potential to transform healthcare by enabling earlier detection, more accurate diagnoses, effective treatment monitoring, and ultimately improved patient survival and quality of life. With the rapid advancement of proteomics, the

identification and validation of specific serum tumor biomarkers have become a cornerstone in oncology research. These biomarkers enable the clear differentiation between healthy and malignant states, allowing for the early detection of cancer and, consequently, improved survival outcomes. Among various oncofetal biomarkers, carcinoembryonic antigen (CEA) has gained particular attention due to its consistent overexpression in approximately 70% of non-small cell lung cancer (NSCLC) cases [10]. CEA is a glycoprotein with a molecular mass of around 200 kDa and is normally found in the blood at very low concentrations [11]. Clinically, a threshold concentration of 5 ng/mL is widely accepted as the cutoff, above which CEA levels indicate a pathological state. This makes CEA not only an important diagnostic biomarker but also a valuable tool for monitoring tumor progression, evaluating treatment response, and predicting recurrence, thereby playing a crucial role in reducing lung cancer-related mortality.

## 1.2 Pivotal Role of Nano-Biosensors in Bridging Gaps in Conventional Diagnostic Approaches and Early Disease Detection



Figure 1.3: Schematic depicting various applications of Nano-biosensor

Nano-biosensing has emerged as a transformative alternative to conventional diagnostic methods, offering nanotechnology-driven tools for the early detection of cancer, one of the most fatal and widespread diseases globally. A nano-biosensor is an advanced analytical device that integrates engineered nanostructures with a biosensitive layer, enabling the detection and transduction of subtle biochemical signals generated during bio-recognition events [12]. The exponential growth of nano-biosensing research is driven by the global need for diagnostic technologies that combine sensitivity, selectivity, robustness, stability, and cost-effectiveness with the

added advantage of being biocompatible. In this regard, two-dimensional (2D) nanomaterials, particularly nanosheets, have emerged as highly effective candidates for constructing nano-bio interfaces [13]. Their ultrathin structures, expansive lateral surfaces, tunable morphologies, and nanoscale features create a superior sensing matrix. These materials provide immense sensitivity to detect trace-level analytes, abundant active sites for biomolecule immobilization, and interconnected porous channels that facilitate rapid electron transfer, thereby boosting detection efficiency. Additionally, their interlayer mechanical strength ensures stability, while their scalable synthesis methods make them practical for widespread clinical adoption. Altogether, the integration of 2D nanostructures into nano-biosensors not only enhances detection kinetics but also positions these devices as vital tools for revolutionizing cancer oncofetal biomarker detection, bridging the gap between advanced nanotechnology and clinical healthcare diagnostics [14, 15].

The last two decades have witnessed a remarkable surge in the development of biosensors, propelling them to the forefront of modern diagnostic and analytical technologies. Biosensors are widely recognized as powerful tools due to their ability to integrate biological recognition components with advanced physicochemical transducers, resulting in devices that can deliver highly sensitive, specific, and realtime analytical information [16] Their applications extend beyond healthcare into agriculture, food safety, and environmental protection, underscoring their universal importance (Fig. 1.3). The International Union of Pure and Applied Chemistry (IUPAC) defines a biosensor as an integrated receptor-transducer device that provides quantitative or semi-quantitative information through biological recognition of a target analyte. In practice, this means that when an analyte interacts with the biological element of the device, the response is converted into a measurable signal, typically electrical or optical, by the transducer. Biosensors offer distinct advantages over conventional detection methods. Traditional approaches are often expensive, laborious, and time-consuming, requiring specialized facilities. In contrast, biosensors provide immediate, accurate, and cost-effective detection with enhanced selectivity and specificity [17]. Their reusability, portability, and robustness make them ideal for fieldbased applications and Point-of-Care (POC) testing, where rapid decision-making is critical. The applications of biosensors are wide-ranging and extend far beyond their medical origins. In human healthcare, they play a crucial role in early disease diagnosis, therapeutic monitoring, and personalized medicine. In agriculture, biosensors are applied to detect pathogens, monitor soil quality, and ensure sustainable farming practices. Within food security, they safeguard against contamination and spoilage, while in homeland security they serve as rapid-response tools for detecting biological or chemical threats. Environmental applications include monitoring pollutants, toxins, and water quality, whereas industrial uses span bioprocess monitoring and quality control. These diverse applications underscore the transformative impact of biosensors, making them essential analytical tools that continue to redefine diagnostics, monitoring, and safety across multiple sectors. In essence, biosensors provide a robust, userfriendly, and scalable platform that bridges molecular recognition with real-time analysis. Their evolution reflects advancements in nanotechnology and bioengineering and demonstrates their indispensable role in shaping the future of diagnostics, where speed, accuracy, and accessibility are important.

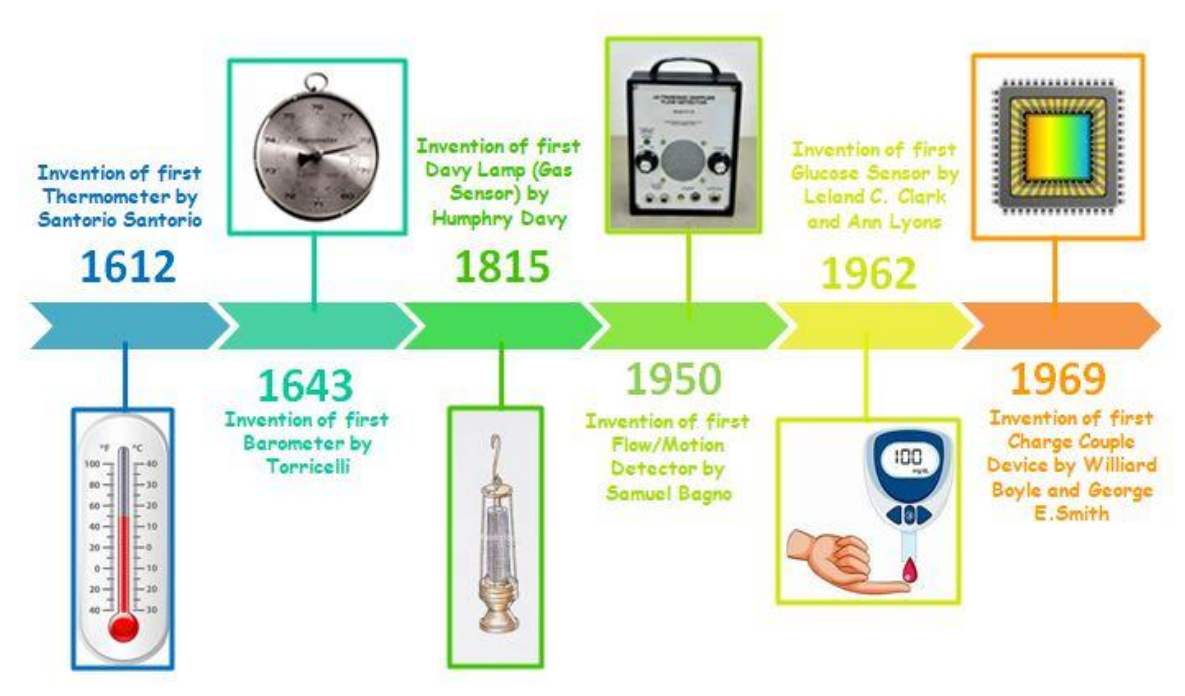


Figure 1.4: Evolution of Sensing Technology

Biosensor technology traces its origins back to the pioneering work of Clark and Lyons in the 1960s, when they designed an oxygen electrode capable of measuring blood oxygen levels during open-heart surgery, as illustrated in **Fig. 1.4** [27]. This innovation demonstrated the groundbreaking ability of biosensors to detect and interpret biological signals, marking the beginning of a transformative field. Since then, biosensors have advanced considerably, and modern designs now include wearable and implantable systems that allow continuous health monitoring and real-time disease detection [28]. A biosensor is a highly integrated analytical device that fundamentally comprises four major components working in synergy to deliver precise detection and interpretation of biological signals, as shown in **Fig. 1.5** [18].

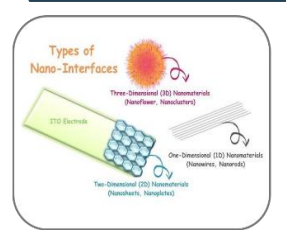
- 1. Biorecognition Element- It serves as the selective interface responsible for specifically identifying and binding the target analyte. This recognition element may consist of enzymes, antibodies, nucleic acids, aptamers, or whole cells, depending on the application, and its role is crucial in ensuring high selectivity and sensitivity toward the biological signal of interest.
- 2. Nano-interface- It bridges the gap between the biological recognition system and the transducer. This layer, often composed of engineered nanomaterials such as nanoparticles, nanowires, nanosheets, and nanoflowers, significantly enhances the performance of biosensors by amplifying the interaction signal, increasing surface area for biomolecule immobilization, and ensuring faster electron or ion transfer. The nanointerface is vital for improving sensitivity, stability, and biocompatibility, making it a key component in modern Nano-biosensing technology.
- **3. Transducer** It plays the key role of converting the biological recognition event into a measurable physicochemical signal. Depending on the biosensor type, this signal may be electrical, optical, thermal, or piezoelectric in nature. The efficiency and accuracy of the transducer determine the reliability of the biosensor, as it effectively translate the biological interaction into a quantifiable output without distortion.

4. Signal processor or display unit- It amplifies, filters, processes, and interprets the converted signal, presenting the results in a user-friendly, human-readable format. This component ensures that the complex biological interactions occurring at the recognition level are translated into clear, readable information, whether displayed on a digital screen, transmitted wirelessly to a monitoring device, or integrated into healthcare systems for clinical decision-making.

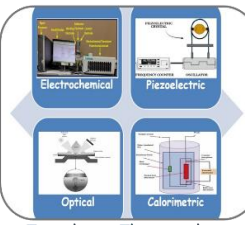
# Components of Nano-Biosensors



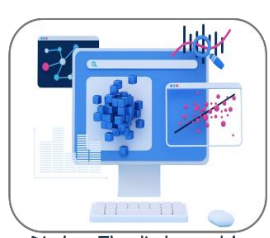
Biorecognition Element: It ensures the selective identification of the target analyte. These elements can be broadly classified into biological, biomimetic, and synthetic recognition



Nano-Interface: It serves as a bridge between the biorecognition element and the transducer. It enhances the sensor's sensitivity, signal-to-noise ratio, and detection limit through nanoscale properties.



Transducer: The transducer converts the biological interaction between the biorecognition element and the target analyte into a measurable signal. They are broadly categorized based on the type of signal they generate.



Display: The display module processes and presents the data generated by the transducer in an interpretable format for the user. Enhances the applicability of the biosensor in remote or point-of-care settings.

### Figure 1.5: Components of Nano-biosensor

Together, these four integrated components make biosensors versatile and powerful tools in diagnostics, environmental monitoring, agriculture, food safety, and industrial bioprocessing. The synergy of precise biorecognition, nanoscale enhancement, efficient signal transduction, and accessible data presentation allows biosensors to provide real-time, sensitive, selective, and user-friendly analytical solutions, firmly establishing them as indispensable devices in point-of-care diagnostics and healthcare. The classification of sensors is primarily based on the unique characteristics and functional mechanisms of their recognition elements, which serve as the critical component for detecting analytes (**Fig. 1.6**). Recognition elements govern the selectivity of the sensor, ensuring that it responds only to the target of interest while minimizing interference from other substances. Accordingly, sensors are categorized into two distinct types [19].

**Bio-Catalytic Sensors:** It is a fundamental class of biosensors in which biocatalysts such as enzymes, tissues, oligonucleotides, or whole cells are immobilized at the active sensing sites to act as recognition elements. These biocatalysts accelerate the rate of biochemical reactions with high specificity toward the target analyte, yet remain unaltered by the reaction itself. Importantly, they enhance the kinetics of the detection process without altering the equilibrium constant, ensuring both efficiency and stability. Due to their inherent catalytic properties, bio-catalytic sensors can be designed with relatively simple instrumentation and straightforward electrode configurations, making them cost-effective and practical. Historically, the concept was pioneered in 1962 by Clark and Lyons, who developed the first bio-catalytic sensor for glucose detection using the enzyme glucose oxidase. The working mechanism of these sensors is well-explained by the Michaelis-Menten kinetic model of enzyme-catalyzed reactions, represented as **Eq. [1.1]**:

$$E + S \stackrel{K_1 \& K_{-1}}{\longleftrightarrow} ES \stackrel{K_2}{\longleftrightarrow} E + P$$
 [1.1]

Here, E refers to the enzyme, S denotes the substrate, ES represents the enzyme-substrate complex, and P is the final product. The rate constants  $K_1$ ,  $K_{-1}$ , and  $K_2$  define the dynamics of complex formation and breakdown. This model serves as the foundation for bio-catalytic sensor design, guiding their use in clinical diagnostics, biotechnology, food quality control, and metabolic monitoring. By combining simplicity with high specificity, bio-catalytic sensors continue to play a pivotal role in the advancement of biosensing technologies.

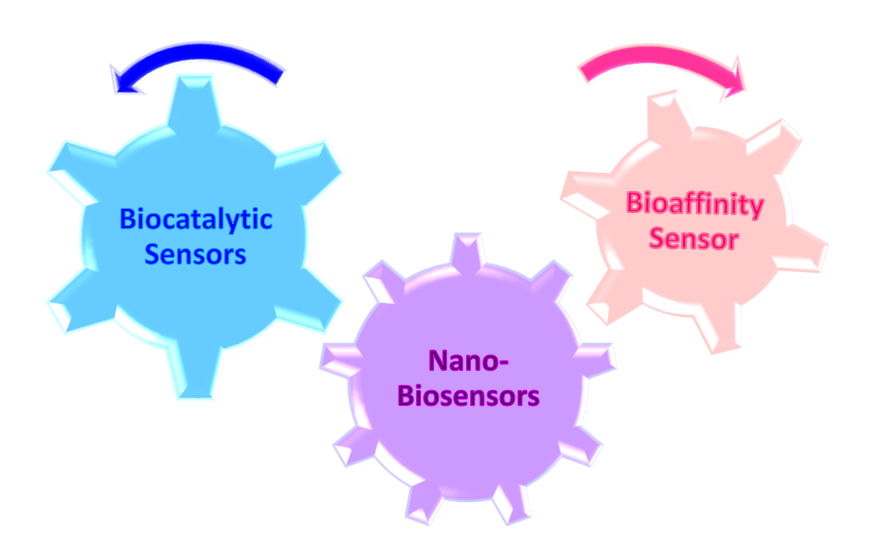


Figure 1.6: Different types of Biosensors based on Biorecognition Element **Bio-Affinity Sensors:** Bio-affinity sensors represent a vital class of biosensing devices specifically designed for applications that demand an exceptionally selective response to distinguish between healthy and diseased states. These sensors rely on the principle of molecular recognition, in which biomolecules such as nucleic acids (DNA, RNA), receptor proteins, antibodies, or even biomimetic materials act as bio-affinity compounds. These molecules exhibit precise binding interactions with target analytes, enabling accurate identification and discrimination even at very low concentrations. To ensure stability and functionality, the bio-affinity molecules are immobilized onto the sensing matrix through chemisorption mechanisms. Chemisorption provides covalent binding of the biomolecules to the sensor surface, creating durable active sites. These active sites serve as highly specific recognition zones that allow only the desired analyte to interact, minimizing cross-reactivity and false signals. Following analyte recognition and binding, the induced biochemical response is seamlessly transmitted to a transducer, which converts it into a measurable signal. Depending on the design of the biosensor, this conversion can occur through various transduction mechanisms such as electrochemical detection (measuring current, potential, or impedance), optical systems (fluorescence, surface plasmon resonance, absorbance), piezoelectric approaches (measuring mass changes), spectroscopic techniques, or calorimetric detection (measuring heat changes). Each of these transduction methods enhances the precision and sensitivity of the device. The integration of selective recognition with advanced signal conversion enables bio-affinity sensors to provide rapid, robust, and reliable measurements. As a result, they have emerged as powerful diagnostic tools for early disease detection, monitoring therapeutic responses, ensuring food and water safety, and advancing research in biotechnology and molecular medicine. Their high

specificity and adaptability underscore their transformative role in the future of biosensor technology.

# 1.3 Nanotechnology-Driven Engineering of Nano-Interfaces: A Key to Nano-Biosensors Architecture

Over time, technological progress has ushered in a revolutionary transformation in science and engineering, with nanoscience and nanotechnology standing at the core of this advancement [20]. To fully understand their impact, it is essential to distinguish them. Nanoscience is primarily concerned with studying atoms and molecules at the nanoscale, investigating their arrangements, interactions, and intrinsic properties. Nanotechnology, on the other hand, translates this scientific understanding into practice by manipulating matter at the atomic and molecular level to design and fabricate new nanomaterials with tailored functionalities. This distinction highlights how nanoscience provides the fundamental knowledge, while nanotechnology transforms it into tangible innovations.

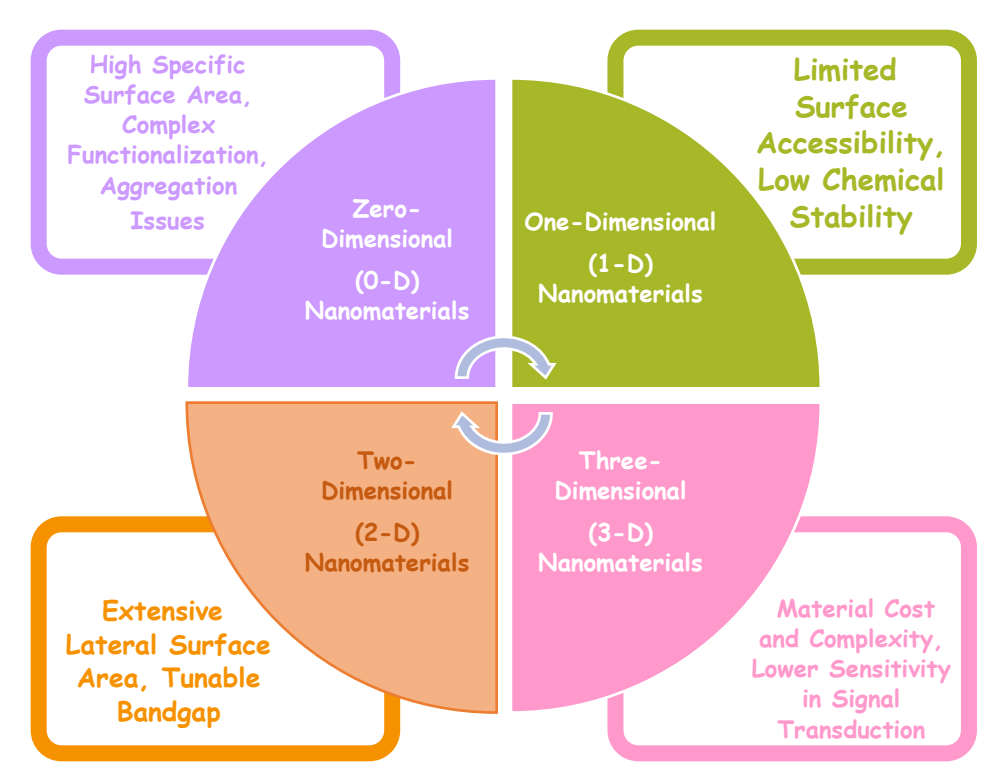


Figure 1.7: Classification of Nanomaterials Based on distinct Geometric Dimensions and potential functional behaviour in nanoscale systems.

As a multidisciplinary domain, nanotechnology draws from physics, chemistry, biology, materials science, and diverse engineering fields to achieve precision manipulation of matter at the nanoscale. Its ability to control parameters such as size, geometry, and surface chemistry has enabled the development of materials with unique properties—superior strength, catalytic efficiency, enhanced electronic conductivity, advanced optical responses, and remarkable biomedical compatibility. This nanoscale precision has been particularly critical in the fabrication of nano-interfaces for nano-biosensors. Nano-biointerfaces form the vital communication bridge between the

biological recognition elements (such as enzymes, antibodies, or nucleic acids) and the transducer [21]. By optimizing surface morphology, increasing surface-to-volume ratios, and providing tunable chemical functionalities, nanotechnology ensures that bio-analytes can be captured more efficiently and selectively. The engineered nano-interfaces not only enhance sensitivity and selectivity but also reduce detection limits to trace levels, thereby making biosensors far more reliable and effective. The importance of nanotechnology in nano-biosensor development extends beyond basic performance improvements. It enables integration of multiple detection platforms on a single chip, supports miniaturization for point-of-care diagnostics, and allows real-time monitoring of biological processes with unprecedented precision. Consequently, nanotechnology is not only advancing the general frontiers of science and technology but also establishing itself as the cornerstone of modern biosensor engineering. Its role in shaping nano-interfaces directly defines the sensitivity, reliability, and future capabilities of nano-biosensors, positioning it as the driving force of innovation in healthcare, environmental monitoring, food safety, and personalized medicine.

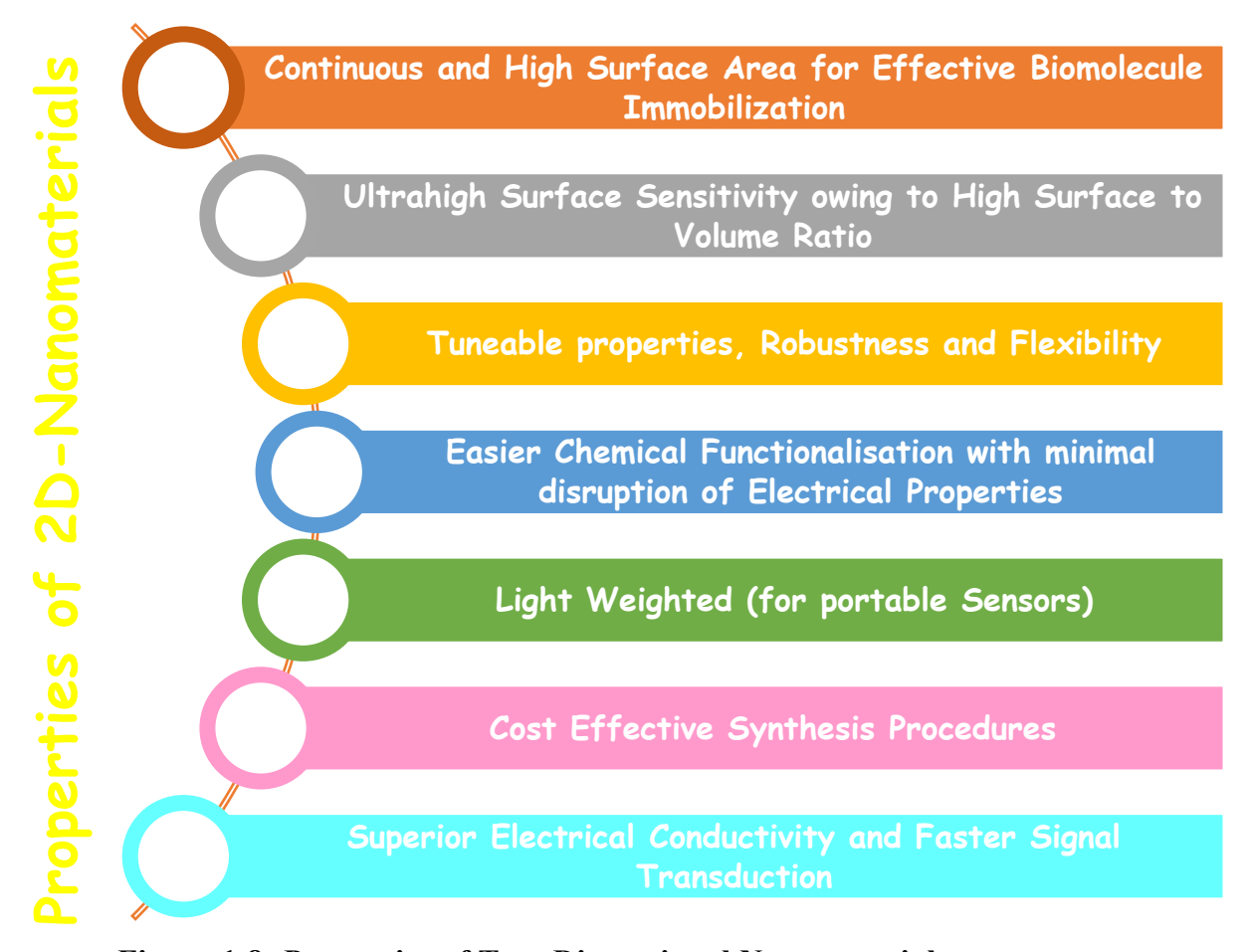


Figure 1.8: Properties of Two-Dimensional Nanomaterials

Nanomaterials, or low-dimensional materials, are uniquely defined by the confinement of charge carriers within nanoscale limits (1–100 nm), where their geometric dimensions approach the de Broglie wavelength. Unlike their bulk counterparts, nanostructured materials exhibit size- and shape-dependent properties governed by the quantum confinement effect. As electrons and holes are restricted to discrete energy

levels near the exciton Bohr radius, they transition from continuous to quantized density states, leading to tuneable optical, electrical, and chemical behaviours. This principle forms the foundation for categorizing nanomaterials into four distinct classes (**Fig. 1.7**): 0D (Quantum dots, Nanoparticles), 1D (Nanowires, Nanotubes), 2D (Nanosheets, Nanoplates), and 3D (Nanoflowers, Hierarchical frameworks), each offering unique physicochemical attributes [22].

Low-dimensional materials are systematically classified into four categories: 0D, 1D, 2D, and 3D, depending on the degrees of freedom available for electron movement. The importance of these low-dimensional materials becomes particularly evident in the field of nano-biosensing, where sensitivity, selectivity, and rapid response are critical. Each nano-dimension contributes differently to biosensing innovation: 0D offers sharp optical features, 1D delivers efficient electron transport, and 3D provides large scaffolds for biomolecule anchoring. However, among the four categories of lowdimensional materials, 2D nanomaterials distinguish themselves as the most promising for advanced nano-biosensing applications. Their atomically thin layers maximize the lateral surface exposure, creating abundant active sites for biomolecule immobilization, while their superior electrical conductivity ensures rapid and precise signal transduction. Moreover, their tuneable chemical functionalities make them highly adaptable to various recognition elements, including enzymes, antibodies, and nucleic acids. Furthermore, 2D nanomaterials exhibit highly sensitive modulation of electronic properties upon molecular adsorption, enabling real-time, label-free detection of biomolecules at ultra-low concentrations (Fig. 1.8). They also provide superior integration capabilities with microfluidic platforms, flexible electronics, and wearable devices, making them highly adaptable for point-of-care diagnostics [23].

# 1.4 Hexagonal Boron Nitride: A Key Inorganic Layered Material Driving Advancements in High-Performance Nano-Biosensors

The advent of graphene in 2004 revolutionized materials science, particularly in nanotechnology and sensing applications, prompting the exploration of structurally similar two-dimensional systems owing to their low-dimensional structures which endowed peculiar properties, distinctly superior to those of their bulk or higherdimensional counterparts. In the realm of two-dimensional nanomaterials, Group III-Nitride nanostructures have emerged as a promising layered inorganic material owing to their superior physical and chemical attributes, which lend themselves to multidisciplinary applications spanning electronics, optoelectronics, and energy technologies. The nanoscale architecture of these materials imparts distinct advantages, including continuous crystalline domains, exceptional crystal quality, and strong interatomic forces, all of which enable outstanding thermal stability even under extreme conditions. Such properties distinguish them as highly favorable candidates for nextgeneration devices. Within this family, nearly all compounds such as GaN, InN, and AlN, are well recognized for their semiconducting behavior, forming the backbone of many modern electronic innovations. Boron nitride (BN), however, represents a unique anomaly, unlike its semiconducting counterparts in group III-Nitride family by demonstrating insulating characteristics, which historically limited its perceived utility in electronics and consequently overshadowed its importance in research [24]. Ferrari and collaborators presented a compelling statistical survey comparing global research

outputs on BN against graphene, covering the period from 2000 to 2020 [25]. Their findings clearly illustrated a disparity, with graphene receiving far greater focus. Nonetheless, boron nitride is gradually gaining recognition for its indispensable role as a complementary material in nano-device fabrication, particularly as a dielectric, protective, and structural component, thereby redefining its place within the broader Group III-Nitride family (**Fig. 1.9**).

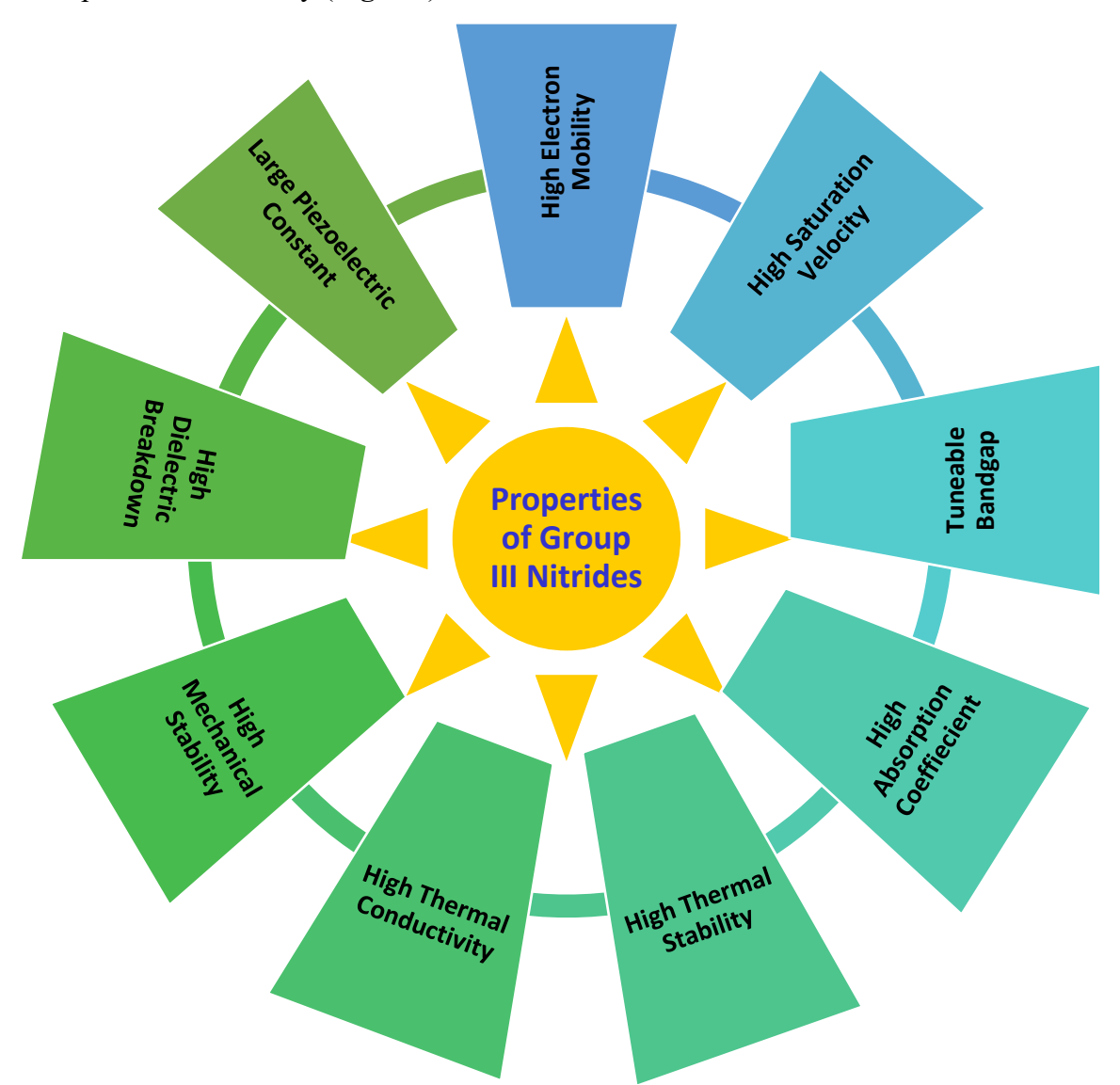


Figure 1.9: Properties of Group III-Nitride Family

Hexagonal boron nitride (hBN), widely referred as "White Graphene," has gained remarkable attention, despite being an electrical insulator [26]. Interestingly, hBN possesses unique physical, chemical and electrochemical characteristics, including ultra-flat surface, remarkable thermal and chemical stability, sustainable redox activity, and excellent structural robustness [24]. Over the years, hBN has emerged as a material of choice for applications ranging from advanced optoelectronic devices to electrochemical sensor platforms. The material consists of alternating boron and nitrogen atoms covalently bonded in a hexagonal lattice, which endows it with structural stability and a wide electronic band gap of approximately 5.1–5.9 eV.

Nanostructure engineering is a powerful tool that aids tuning of electronic bandgap of hBN from insulating to semiconducting by tailoring the surface chemistry through strategies such as doping, substitution, functionalization, and hybridization. Furthermore, hBN plays a critical role as an interface material for other 2D semiconductors, including graphene, MoS<sub>2</sub>, and black phosphorus, where it enhances carrier mobility by minimizing Coulomb scattering and simultaneously protects the active layers from contamination, oxidation, and thermal or electrical degradation. Owing to its vast technological promise, single- and few-layer hBN nanosheets have been extensively synthesized and investigated, demonstrating exceptional potential in advanced applications including deep-ultraviolet (DUV) photonics, dielectric tunneling, high-power electronics,7 electronic packaging, fuel cell technology, and biomedicine [27]. Nevertheless, intact or pristine h-BN alone is insufficient for sensor functionality because effective signal generation demands adequate conductivity within active sensing layers. Therefore, the advancement of this material hinges on wellregulated fabrication processes coupled with controlled functionalization of its surface and edges, enabling tailored conductivity and chemical reactivity [28]. These modifications expand hBN's potential beyond its insulating nature, opening pathways for its incorporation into next-generation sensing devices and multifunctional nanotechnology platforms.

Challenges in
Doping and
Surface
Functionalization

Limited
Tunability of
Wide Bandgap
affects electron
transfer kinetics

Aggregation
Issues in
Nanosheets
Assembly

Exfoliation
Challenges to
Synthesize
Ultrathin
Nanosheet

Figure 1.10: Challenges in Synthesizing of 2D hexagonal Boron Nitride (hBN)

The integration of two-dimensional hBN nanosheets into electrochemical sensors has recently emerged as a promising development in nanomaterials research. Their inherently large surface-to-volume ratio, reactive edge states, biocompatibility, and catalytic capability position them as versatile candidates for high-performance sensing applications. A key advantage of h-BN is its adaptability; when combined with other nanomaterials, particularly noble or transition metal nanoparticles. It can deliver enhanced sensing responses by providing synergistic pathways for charge transfer and analyte recognition. To further optimize their electrochemical functionality, postsynthetic treatments are applied, with three major strategies dominating: edge and surface functionalization, nanoparticle deposition on the basal planes, and defect engineering within the crystal lattice. Each of these modifications enables precise control of hBN's electronic and surface properties. For instance, introducing hydroxyl groups to nanosheet edges significantly narrows the band gap to around 3.5 eV, while other functionalization techniques such as amination, fluorination, or oxygen and carbon doping have been successfully utilized to adjust conductivity and catalytic behaviour. These modifications, whether incorporated during synthesis or achieved through targeted surface engineering, provide chemically active sites on the otherwise inert h-BN framework. As a result, functionalized h-BN nanosheets can interact with analytes selectively and with improved efficiency, making them an increasingly valuable component in the design of advanced electrochemical sensing devices.

In the development of high-performance nano-biosensors, the choice of interface material plays a decisive role in determining sensitivity, selectivity, and long-term operational stability. Hexagonal boron nitride (hBN) has emerged as a promising material in the design of next-generation nano-biosensing platforms due to its exceptional structural integrity, wide bandgap, strong dielectric behaviour, atomically smooth surface, and chemical inertness, which together provide long-term stability and biocompatibility under diverse operating environments. However, this very chemical inertness that makes hBN stable also presents one of its most significant challenges, its inability to support the covalent immobilization of biomolecules. Covalent immobilization is a cornerstone in biosensor engineering, as it enables the creation of highly specific binding sites, facilitates efficient electron transfer pathways between the target analyte and sensing surface, and ensures reproducibility and selectivity in detection. Without such functional binding, pristine hBN surfaces suffer from poor interfacial charge-transfer kinetics, reduced sensitivity, and limited practical applicability in ultrasensitive detection tasks. To address this limitation, advanced modification techniques such as surface oxidation, heteroatom doping, plasma treatment, and hybrid integration with other nanomaterials are increasingly employed. These strategies introduce chemically active sites or functional groups onto the hBN lattice, enabling stable covalent binding of biomolecules and significantly improving sensor performance. Consequently, while pristine hBN's inert nature may restrict its direct use, targeted engineering of its surface chemistry transforms it into a highly versatile and powerful platform for high-performance nano-biosensing technologies (Fig. 1.10).

# 1.5 Strategic Role of Nano-Hybrid Composites in Improving hBNNS Electrochemical Efficiency

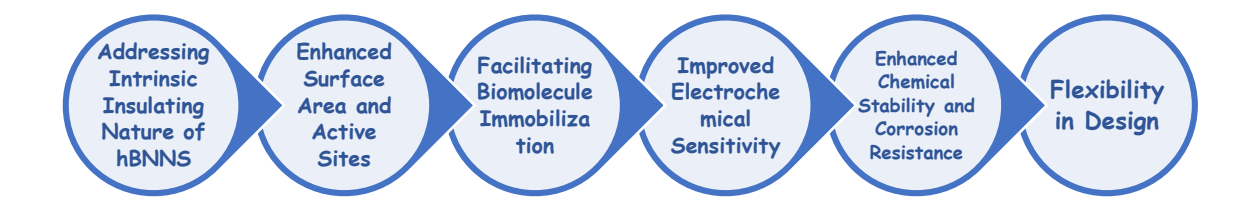


Figure 1.11: Advantages of Nano-Hybrid Composite (NHC)

The field of nano-engineering has witnessed remarkable progress in the development of bio-analytical platforms, primarily through innovative approaches such as defect induction, chemical functionalization, modulation of nanoscale structural and morphological features, and the construction of hybrid composites [13]. These engineering strategies are designed to tune the intrinsic physicochemical properties of nanomaterials, enabling improved signal transduction, heightened sensitivity, and enhanced analytical precision. However, despite their potential, each of these techniques presents inherent limitations that constrain their applicability in real-world conditions. Defect engineering, while capable of introducing highly active surface states, often results in instability and unpredictable degradation over time. Structural and morphological modulation, though effective at tailoring surface area and catalytic

activity, involves complex synthesis routes that are difficult to reproduce consistently. Furthermore, issues such as compromised chemical resistance, reduced biological compatibility, and limited durability in ambient environments pose additional barriers to large-scale deployment of such nanostructures in biosensing applications.

Nano-hybrid composites have emerged as transformative materials in the advancement of electrochemical devices due to their ability to synergistically merge the complementary properties of their constituent phases (Fig. 1.11). By integrating organic, inorganic, or metallic nanostructures into hybrid matrices, these composites effectively overcome limitations posed by individual materials such as poor stability, limited active surface area, or sluggish charge-transfer kinetics. The formation of biphasic host-guest systems provide a unique framework where structural stability, conductivity, and reactivity can be simultaneously optimized. Defect engineering, surface functionalization, and morphological tailoring within nano-hybrid composites significantly increase the density of electroactive sites and facilitate rapid electron and ion transport across the electrode-electrolyte interface. This results in enhanced sensitivity, selectivity, and durability in electrochemical biosensing applications. Furthermore, the chemical tunability of hybrid systems ensures improved biomolecule immobilization, minimizes fouling, and promotes biocompatibility, all of which are crucial for long-term reliability in real-world biosensing environments. Consequently, nano-hybrid composites act not only as performance enhancers but also as enabling platforms for the development of next-generation electrochemical biosensors with ultrasensitive and stable detection capabilities.

Material science represents a vast and multidisciplinary domain that encompasses an extraordinary diversity of materials, each defined by its internal structure and chemical architecture. The term chemical architecture refers to the unique arrangement and composition of atoms that collectively give rise to the physical identity of a material. These constituent atoms, by virtue of their distinct electronic configurations and bonding characteristics, impart unique physical, chemical, mechanical, and functional properties that set one material apart from another.



Figure 1.12: Different types of Nanomaterials based on Chemical Architecture

In view of chemical architecture, materials can be broadly classified into two principal categories: Layered Materials and Non-Layered Materials (**Fig. 1.12**) [29]. This classification is based on the spatial arrangement of atoms and the way they interact with each other within the crystal lattice. Layered materials exhibit strong in-plane bonding within individual layers but weak van der Waals interactions between layers, allowing them to be exfoliated into thin sheets with nanoscale thickness. Such materials often display anisotropic behaviour, high surface area, and tuneable electronic properties, making them particularly significant in emerging technologies like energy

storage, catalysis, and biosensing. Distinct layered materials, including graphene, hexagonal boron nitride (hBN), transition metal dichalcogenides (TMDs), and other 2D architectures, have gained prominence due to their tuneable band structures, high surface-to-volume ratios, and potential for miniaturized device fabrication. Their layered nature facilitates exfoliation into nanosheets. In contrast, non-layered materials possess uniform bonding throughout the lattice, resulting in isotropic physical and chemical characteristics. Non-layered material includes bulk crystalline metals, metal oxides, metal nitrides, ceramics, and polymers. These materials often demonstrate robustness, high mechanical strength, and structural stability, lending themselves to diverse industrial and technological applications.

In the present work, a systematic and comprehensive investigation is undertaken to elucidate the pivotal role of both layered and non-layered materials in advancing the electrochemical performance of hexagonal boron nitride nanosheets (hBNNS) through the strategic formation of nano-hybrid composites. Hexagonal boron nitride, despite its outstanding properties such as chemical inertness, high thermal conductivity, wide bandgap, and mechanical robustness, is intrinsically limited in its electrochemical activity due to the lack of readily available active sites on its pristine surface. This limitation hampers efficient charge transfer and restricts its direct applicability in electrochemical sensing and energy-related domains. To overcome these inherent shortcomings, the integration of layered and non-layered nanomaterials into hybrid composites provides a rational design strategy, enabling the tailoring of interfacial properties, surface reactivity, and synergistic functionalities.

Layered materials, such as reduced graphene oxide, bring unique advantages by offering high surface area, tunable band structures, and facile electron transport pathways. When combined with hBNNS, these layered materials contribute to enhanced charge carrier dynamics, improved adsorption of analytes, and a modulation of the electronic environment at the interface. Their two-dimensional nature ensures intimate contact with hBN nanosheets, thereby amplifying conductivity and promoting faster redox reactions. On the other hand, non-layered materials, including metal oxides, are equally indispensable in this hybridization approach. These materials are renowned for their abundant catalytic sites, structural stability, and superior electrochemical activity. Their incorporation introduces abundant electroactive centers, reduces electron-transfer resistance, and augments sensitivity, thereby addressing the limitations of pristine hBN.

The synergy achieved by coupling layered and non-layered materials with hBNNS lies in the creation of unique physicochemical environments at the nano-interface. Host—guest interactions, defect engineering, and interfacial charge redistribution facilitate a cooperative mechanism where the dielectric stability of hBN is retained, while the electrochemical performance is substantially enhanced by its hybrid partners. Such nano-hybrid composites not only ensure improved charge-transfer kinetics but also provide superior durability, reproducibility, and selectivity under electrochemical conditions. This integration effectively transforms hBNNS from an electrically insulating material into a multifunctional platform for advanced electrochemical applications.

The present study, therefore, highlights the transformative potential of nano-hybrid composites in redefining the functionality of hBNNS. By systematically combining layered and non-layered materials, this work establishes a robust framework for engineering hybrid interfaces that harness the complementary strengths of diverse material classes. The findings are expected to accelerate the development of next-generation electrochemical devices, including nano-biosensors, supercapacitors, and energy conversion systems, where high sensitivity, stability, and selectivity are of paramount importance. Ultimately, this comprehensive study positions hBNNS-based nano-hybrid composites as a powerful and versatile platform in the rapidly advancing field of nanotechnology-driven electrochemistry.

### References

- [1] F. Bray, M. Laversanne, H. Sung, J. Ferlay, R.L. Siegel, I. Soerjomataram, A. Jemal, Global cancer statistics 2022: GLOBOCAN estimates of incidence and mortality worldwide for 36 cancers in 185 countries, CA: a cancer journal for clinicians, 74 (2024) 229-263.
- [2] W.H. Organization, WHO report on cancer: setting priorities, investing wisely and providing care for all, World Health Organization, 2020.
- [3] D.S. Ettinger, W. Akerley, G. Bepler, M.G. Blum, A. Chang, R.T. Cheney, L.R. Chirieac, T.A. D'Amico, T.L. Demmy, A.K.P. Ganti, Non–small cell lung cancer, Journal of the national comprehensive cancer network, 8 (2010) 740-801.
- [4] C. Jiang, M. Zhao, S. Hou, X. Hu, J. Huang, H. Wang, C. Ren, X. Pan, T. Zhang, S. Wu, The Indicative Value of Serum Tumor Markers for Metastasis and Stage of Non-Small Cell Lung Cancer, Cancers, 14 (2022) 5064.
- [5] L. Calabrò, S. Peters, J.-C. Soria, A.M. Di Giacomo, F. Barlesi, A. Covre, M. Altomonte, V. Vegni, C. Gridelli, M. Reck, Challenges in lung cancer therapy during the COVID-19 pandemic, The Lancet Respiratory Medicine, 8 (2020) 542-544.
- [6] A.K. Ganti, J.L. Mulshine, Lung cancer screening, The oncologist, 11 (2006) 481-487.
- [7] X. Li, T. Asmitananda, L. Gao, D. Gai, Z. Song, Y. Zhang, H. Ren, T. Yang, T. Chen, M. Chen, Biomarkers in the lung cancer diagnosis: a clinical perspective, Neoplasma, 59 (2012) 500-507.
- [8] I. Horvath, Z. Lazar, N. Gyulai, M. Kollai, G. Losonczy, Exhaled biomarkers in lung cancer, European Respiratory Journal, 34 (2009) 261-275.
- [9] S.B. Nimse, M.D. Sonawane, K.-S. Song, T. Kim, Biomarker detection technologies and future directions, Analyst, 141 (2016) 740-755.
- [10] M. Grunnet, J. Sorensen, Carcinoembryonic antigen (CEA) as tumor marker in lung cancer, Lung cancer, 76 (2012) 138-143.
- [11] S. Hammarström, The carcinoembryonic antigen (CEA) family: structures, suggested functions and expression in normal and malignant tissues, in: Seminars in cancer biology, Elsevier, 1999, pp. 67-81.
- [12] K. Sharma, N.K. Puri, B. Singh, An efficient electrochemical nano-biosensor based on hydrothermally engineered ultrathin nanostructures of hexagonal boron nitride nanosheets for label-free detection of carcinoembryonic antigen, Applied Nanoscience, (2023) 1-14.
- [13] R. Batool, A. Rhouati, M.H. Nawaz, A. Hayat, J.L. Marty, A review of the construction of nano-hybrids for electrochemical biosensing of glucose, Biosensors, 9 (2019) 46.
- [14] S. Roy, X. Zhang, A.B. Puthirath, A. Meiyazhagan, S. Bhattacharyya, M.M. Rahman, G. Babu, S. Susarla, S.K. Saju, M.K. Tran, Structure, properties and applications of two-dimensional hexagonal boron nitride, Advanced Materials, 33 (2021) 2101589.
- [15] J.N. Coleman, M. Lotya, A. O'Neill, S.D. Bergin, P.J. King, U. Khan, K. Young, A. Gaucher, S. De, R.J. Smith, Two-dimensional nanosheets produced by liquid exfoliation of layered materials, Science, 331 (2011) 568-571.

- [16] A. Haleem, M. Javaid, R.P. Singh, R. Suman, S. Rab, Biosensors applications in medical field: A brief review, Sensors International, 2 (2021) 100100.
- [17] V. Naresh, N. Lee, A review on biosensors and recent development of nanostructured materials-enabled biosensors, Sensors, 21 (2021) 1109.
- [18] M.B. Kulkarni, N.H. Ayachit, T.M. Aminabhavi, Recent advancements in nanobiosensors: current trends, challenges, applications, and future scope, Biosensors, 12 (2022) 892.
- [19] C. Ziegler, W. Göpel, Biosensor development, Current opinion in chemical biology, 2 (1998) 585-591.
- [20] Z.-c. Zhang, B. Xu, X. Wang, Engineering nanointerfaces for nanocatalysis, Chemical Society Reviews, 43 (2014) 7870-7886.
- [21] D. Singh, Nano-Bio Interfaces: Pioneering Targeted Approaches for Disease Treatment and Prevention, Journal of Macromolecular Science, Part B, (2024) 1-18.
- [22] B. Mekuye, B. Abera, Nanomaterials: An overview of synthesis, classification, characterization, and applications, Nano select, 4 (2023) 486-501.
- [23] W. Wen, Y. Song, X. Yan, C. Zhu, D. Du, S. Wang, A.M. Asiri, Y. Lin, Recent advances in emerging 2D nanomaterials for biosensing and bioimaging applications, Materials Today, 21 (2018) 164-177.
- [24] S. Angizi, M. Khalaj, S.A.A. Alem, A. Pakdel, M. Willander, A. Hatamie, A. Simchi, Towards the two-dimensional hexagonal boron nitride (2D h-BN) electrochemical sensing platforms, Journal of The Electrochemical Society, 167 (2020) 126513.
- [25] A. García-Miranda Ferrari, S.J. Rowley-Neale, C.E. Banks, Recent advances in 2D hexagonal boron nitride (2D-hBN) applied as the basis of electrochemical sensing platforms, Analytical and Bioanalytical Chemistry, 413 (2021) 663-672.
- [26] K. Zhang, Y. Feng, F. Wang, Z. Yang, J. Wang, Two dimensional hexagonal boron nitride (2D-hBN): synthesis, properties and applications, Journal of Materials Chemistry C, 5 (2017) 11992-12022.
- [27] M. Llenas, L. Cuenca, C. Santos, I. Bdikin, G. Gonçalves, G. Tobías-Rossell, Sustainable Synthesis of Highly Biocompatible 2D Boron Nitride Nanosheets, Biomedicines, 10 (2022) 3238.
- [28] Y. Lin, J.W. Connell, Advances in 2D boron nitride nanostructures: nanosheets, nanoribbons, nanomeshes, and hybrids with graphene, Nanoscale, 4 (2012) 6908-6939.
- [29] H. Ma, Y. Xing, B. Cui, J. Han, B. Wang, Z. Zeng, Recent advances in two-dimensional layered and non-layered materials hybrid heterostructures, Chinese Physics B, 31 (2022) 108502.

# Chapter 2

# Systematic Overview of Advanced Material and Electrochemical Characterization Techniques and Synthesis Methodologies

The literature in Chapter 2 reviews potential synthesis strategies for development of various nano-dimensional morphology of inorganic as well as organic layered nanomaterials, broadly classified as bottom-up and top-down techniques. Considering the requirement for highly scalable, facile, cost-effective, and high-quality production of two-dimensional hexagonal boron nitride nanosheets (hBNNS) at relatively lowtemperature, this chapter discusses in-depth significance and application of hydrothermal technique in yielding 2D nanomaterials with controlled morphologies and fabricating nano-hybrid composites. Furthermore, this chapter explores promising synthesis techniques including polyol method, chemical exfoliation, and sol-gel synthesis capable of tailoring nanostructure morphologies. The successful synthesis of 2D nanomaterials and their nano-hybrid composites, as well as the fabrication of immunoelectrode, is validated through various characterization techniques, including X-ray diffraction (XRD), Raman spectroscopy, scanning electron microscopy (SEM), thermogravimetric analysis (TGA), Fourier-transform infrared spectroscopy (FTIR), transmission electron microscopy (TEM), atomic force microscopy (AFM), energydispersive X-ray analysis (EDAX), UV-Visible spectroscopy, and biocompatibility testing. The importance of these advanced characterization techniques is briefly discussed, as they ensure the structural, morphological, chemical, and spectroscopic integrity of the materials, optimizing their functionality for biosensor applications. Furthermore, literature focusing on electrochemical analysis techniques, including cyclic voltammetry (CV), differential pulse voltammetry (DPV), and electrochemical impedance spectroscopy (EIS), is reviewed to evaluate the practical impact of the developed innovative nano-biosensors. This discussion emphasizes their significance in addressing the critical need for effective healthcare diagnostics. This chapter give insight of various methodologies for preparation of sensing electrodes and the detailed elaboration on stepwise fabrication of nano-interface matrix onto indium tin oxide electrodes utilising electrophoretic deposition technique. Furthermore, it provides a detailed description of the stepwise fabrication of the nano-interface matrix and immunoelectrode, highlighting the significance of each step in achieving a robust and optimized biosensor platform for clinical applications.

#### 2.1 Introduction

The synthesis and processing methodologies exert a profound influence on the structure, crystallinity, and intrinsic properties of two-dimensional hexagonal boron nitride (2D-hBN) nanosheets, which in turn directly determine their functional performance in device applications [1]. Achieving nanosheets with well-defined crystallographic order, controlled thickness, and minimal structural defects remains a formidable challenge, particularly when tailoring materials for application-specific requirements. The pursuit of high-quality 2D-hBN demands precise optimization of processing parameters such as reaction conditions, exfoliation strategies, and posttreatment techniques, each of which governs not only the lateral size and morphology but also the degree of disorder and functional group incorporation [2]. Consequently, researchers have introduced a diverse range of synthesis approaches, including mechanical exfoliation, liquid-phase exfoliation, chemical vapor deposition (CVD), and hydrothermal methods each offering distinct advantages and limitations in balancing scalability, yield, and structural integrity. These strategies are especially targeted toward producing both monolayer and few-layer hBN nanosheets with uniform size distribution, large lateral dimensions, and enhanced structural homogeneity. Such progress is critical for unlocking the full technological potential of 2D-hBN in areas spanning nanoelectronics, photonics, catalysis, and biomedical engineering, where the interplay between structural perfection and functional behaviour dictates overall device efficiency and stability.

# 2.1.1 Synthesis Methodologies from Engineering Inorganic Layered Materials to Nano-Hybrid Composites

Two principal strategies have been established for large-scale synthesis of BNNS: bottom-up and top-down approaches [3]. The bottom-up approach involves building BNNS atom-by-atom or molecule-by-molecule using techniques such as chemical vapor deposition (CVD) [4]and segregation methods [5]. While this pathway enables the formation of high-quality, single-layer BNNS with precise structural control, it requires extreme temperature and pressure, rendering it impractical for mass production. Conversely, the top-down approach focuses on breaking down bulk h-BN crystals into thinner nanosheets by means of exfoliation, employing mechanical cleavage [6] or ultrasonic sonication [7]. This methodology, which mirrors the techniques successfully applied to graphene, allows for scalable production of BNNS. However, unlike graphene, where C–C covalent bonding permits easier delamination, h-BN's partially ionic B–N bonds and strong interlayer "lip-lip" interactions complicate layer separation, presenting a fundamental obstacle in top-down exfoliation (**Fig. 2.1**).

#### 2.1.1.1 Bottom-Up Synthesis Approach:

The bottom-up strategy for nanomaterial development focuses on constructing nanoscale structures directly from atomic or molecular precursors [8]. Instead of breaking down larger bulk materials, this approach capitalizes on natural self-assembly processes driven by short-range interactions such as van der Waals forces, dipole—dipole interactions, ionic bonding, and hydrogen bonding. These forces encourage atoms and molecules to organize themselves into stable, well-defined nanoparticles. Compared to top-down techniques, bottom-up synthesis provides a higher degree of precision and control, allowing scientists to design nanomaterials with uniform sizes, controlled shapes, and consistent surface properties. An additional benefit is its capacity

to produce nanoparticles with highly tuneable characteristics simply by adjusting synthesis conditions like pH, temperature, precursor concentration, and surfactant type. Furthermore, the bottom-up strategy enables precise control over particle properties by fine-tuning the synthesis parameters, such as reaction temperature, solvent environment, concentration of precursors, and reaction time. This makes it especially attractive not only for laboratory-scale research but also for industrial production, where scalability, cost-effectiveness, and reproducibility are essential. The adaptability of this approach has led to its wide use in the fabrication of nanostructured metals, oxides, semiconductors, and hybrid materials. Ultimately, bottom-up synthesis provides a pathway to engineer highly functional nanomaterials with desirable physical, chemical, and electronic characteristics that would be difficult to achieve through conventional bulk methods.

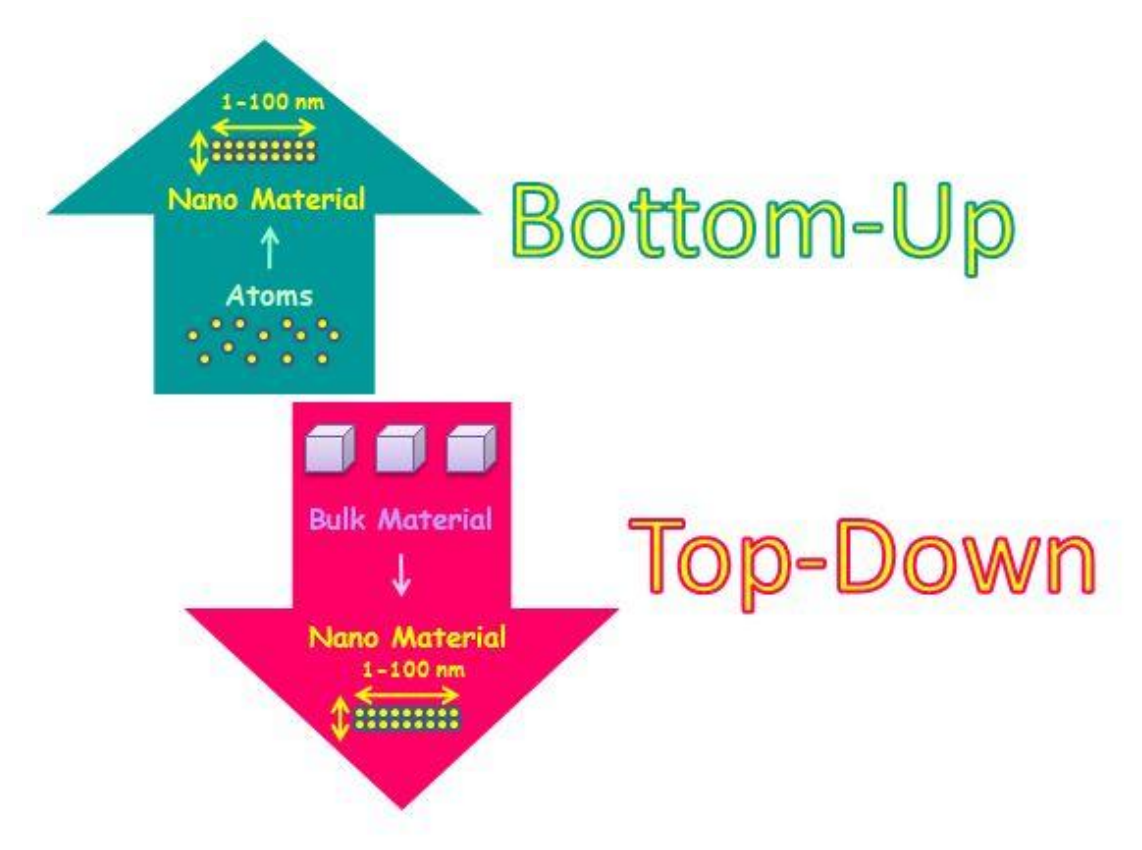


Figure 2.1: Schematic representation of Botton-up and Top-Down Synthesis Approach of Nanomaterials.

### 2.1.1.2 Top-Down Synthesis Approach:

The top-down strategy for nanomaterial synthesis is based on breaking down larger bulk materials into smaller fragments until nanoscale structures are obtained [8]. This method primarily employs physical and mechanical techniques such as mechanical milling, lithographic patterning, chemical etching, and sputtering. Most significant advantage of top-down approach is the ability to produce nanostructured materials in large quantities, making it highly suitable for industrial applications where scalability is essential. In addition, top-down methods often require relatively straightforward processing steps and do not depend heavily on complex chemical environments or expensive precursors, which makes them more practical and cost-effective for bulk

fabrication. Another advantage is their compatibility with existing microfabrication and industrial technologies, allowing the integration of nanostructures into larger systems such as semiconductor devices, thin films, and coatings. Furthermore, these techniques are particularly beneficial for fabricating nanostructured bulk materials, composites, and patterned surfaces where precise control at the atomic or molecular level is not strictly required.

#### **Hydrothermal Synthesis Technique for Synthesis of Nanomaterials:**

The hydrothermal method has emerged as a highly effective and versatile route for the synthesis of nanomaterials, particularly because it combines low reaction temperatures with high autogenous pressures [9]. This controlled environment provided by hydrothermal autoclave promotes the formation of unique and well-defined nanostructures that are often difficult to achieve by conventional techniques (Fig. 2.2). Under supercritical hydrothermal conditions, substances that are otherwise sparingly soluble in water become highly reactive and can participate in chemical transformations at relatively high concentrations [10]. This phenomenon not only enhances the overall reaction kinetics but also contributes to achieving higher yields compared to traditional solid-state reactions conducted at elevated temperatures. Moreover, the hydrothermal method provides an energy-efficient alternative, as it reduces the need for extreme thermal input while still enabling complex crystal growth and tailored morphology. Despite these advantages, the detailed reaction pathways remain difficult to fully elucidate due to the closed, "dark-room" nature of the system, where direct observation of intermediates is challenging. Nonetheless, its ability to regulate particle size, control morphology, and enhance crystallinity has made the hydrothermal method a cornerstone in nanomaterial synthesis, widely applied in areas such as photocatalysis, energy storage, and biomedical engineering.



Figure 2.2: A Hydrothermal Autoclave Assembly

Under hydrothermal conditions, reactants that are usually insoluble under normal environments can dissolve effectively by forming complexes in the presence of mineralizers or solvents. This dissolution process facilitates chemical transport reactions, which is why hydrothermal synthesis is often regarded as a specific case of chemical transport phenomena. The unique physical properties of solvents under hydrothermal conditions—such as their exceptional solvation ability, high compressibility, and enhanced capacity for mass transport—make it possible to carry out a variety of chemical transformations that are otherwise difficult to achieve. These reactions include the synthesis of entirely new phases or the stabilization of otherwise

metastable complexes that could not be obtained by conventional high-temperature methods. Furthermore, the method enables controlled crystal growth of various inorganic compounds, producing crystals with defined orientation and structural quality. It also serves as a powerful technique for the preparation of finely divided materials and micro-crystallites, where particle size, uniformity, and morphology can be tuned to meet the demands of applications in catalysis, sensors, or energy storage. Beyond material synthesis, hydrothermal processes play a vital role in the extraction of metals through ore leaching, offering a pathway for selective separation and recovery of valuable elements. Additionally, these conditions support processes such as decomposition, alteration, corrosion, and surface etching, which are significant in both geological systems and material science research. Together, these capabilities highlight the versatility of hydrothermal methods, allowing scientists to design materials with enhanced structural and functional properties.

**Electrophoretic Deposition for Electrode Preparation** 

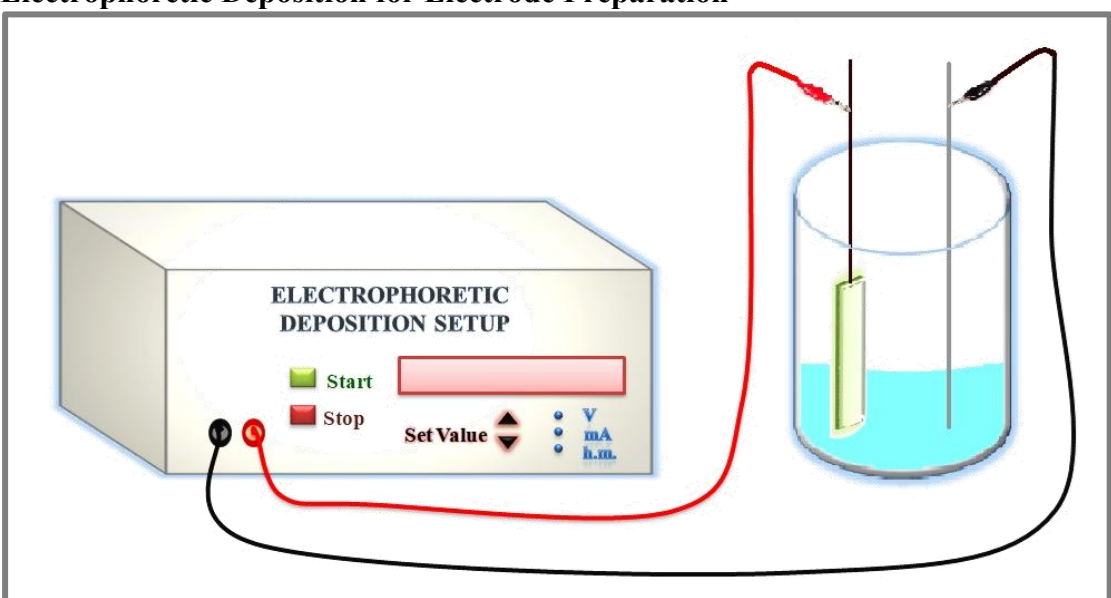


Figure 2.3: Schematic depicting Electrophoretic Deposition Setup

Electrophoretic deposition (EPD) is an advanced fabrication process that has become an important method in the production of ceramics and functional coatings [11]. It offers several unique advantages, such as rapid film formation, low-cost apparatus, adaptability to substrates of different shapes, and the elimination of additional steps like binder removal, since the films generally contain minimal organic materials. This makes EPD more convenient and cost-effective compared to traditional shaping techniques. Its versatility lies in the fact that only minor changes in electrode design are required to coat surfaces of different geometries, making it suitable for both simple and complex shapes. A major benefit of this method is its controllability; the thickness, density, and microstructure of the deposited layer can be precisely managed by altering deposition time, applied voltage, or suspension concentration. In practice, EPD works by dispersing charged ceramic or composite particles in a liquid suspension, which then move toward and deposit onto a conductive substrate with the opposite charge under the influence of an applied DC electric field (Fig. 2.3). This results in coatings with uniform thickness and good adhesion, which are particularly useful in applications such as protective barriers, fuel cells, and biomedical implants. While the term "electrodeposition" is sometimes used ambiguously, it usually refers to electroplating, a process that involves the electrochemical reduction of ions in solution. In contrast, EPD is based on the physical movement of colloidal particles, giving it a broader range of applications in modern materials science. The ability to create dense, uniform, and even multi-component layers makes EPD a powerful and adaptable tool in advanced ceramic processing and beyond.

# 2.2 Material Characterization Techniques:

### 2.2.1 X-ray Diffraction Spectroscopy (XRD):

Human vision is capable of observing the macroscopic world through scattering of visible light ( $\lambda_{\text{Visible light}} \sim 6000 \text{ Å}$ ), yet it lacks the resolving power to reveal the atomic arrangement within solids. While X-rays exhibiting angstrom-scale wavelength (0.5-2.5 Å) produces high energy electromagnetic waves residing between gamma and ultraviolet rays that demonstrates high penetrating power [12]. These high-energy Xrays penetrates and traverse through atomic-scale structures and yield a unique diffraction pattern from constructive interference of scattered X-rays on interacting with the internal three-dimensional arrangement of atoms. X-ray diffraction (XRD) technique became an indispensable tool for crystallographic analysis after historical foundation laid by Max von Laue in 1912, following Roentgen's initial discovery of Xrays in 1895. Max von Laue postulated that X-rays were electromagnetic waves with angstrom-scale wavelengths comparable to the interatomic distances in periodic crystal lattice that act as natural 3D diffraction gratings. This critical finding marked a vital transformation in material science discipline, making XRD a principle investigative tool for determining crystal structure, crystallinity, lattice parameters, interplanar spacing, lattice strain, crystal defects, dislocation density, and phase composition.

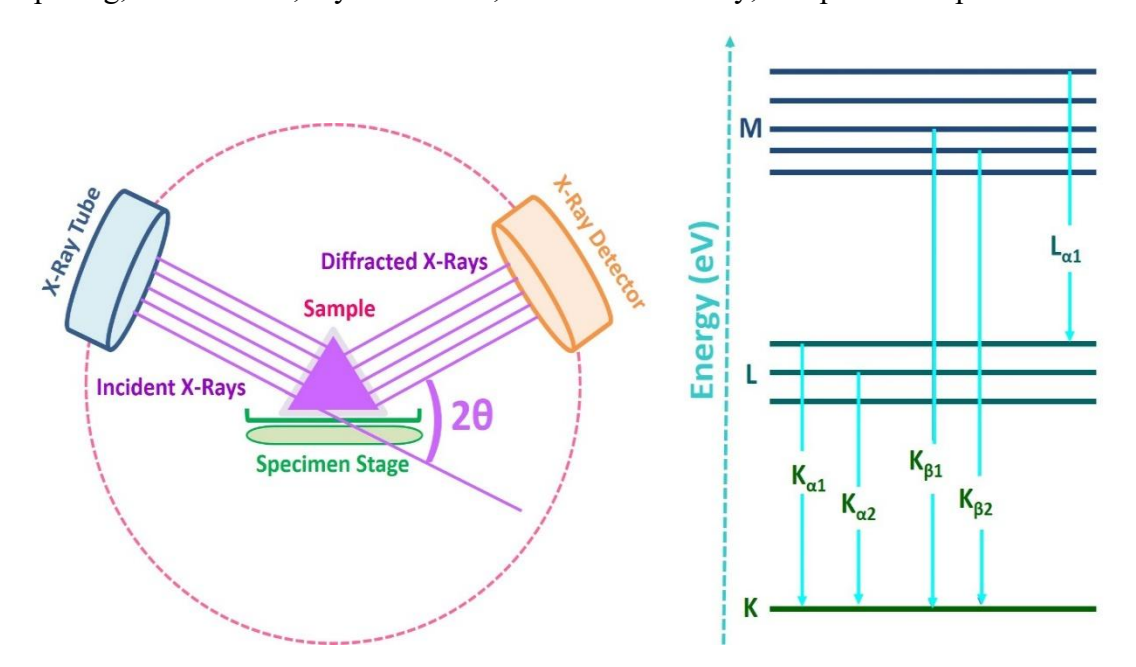


Figure 2.4: Diagrammatic representation of X-ray Diffractometer (Left) and Fundamental transitions depicting generation of X-rays (Right)

**Working:** Generation of X-rays is accomplished using sealed tubes, rotating anodes, or synchrotron sources. In laboratory instruments, sealed tubes and rotating anodes

operate on the same principle. A tungsten filament is heated in a vacuum, releasing electrons through thermionic emission. These electrons are then accelerated by a strong potential difference and directed onto a solid target, typically composed of a metal such as copper, molybdenum, or chromium. When the high-energy electrons strike the target, two distinct processes generate X-rays. Two mechanisms produce these X-rays:

- **1. Bremsstrahlung radiation or "braking radiation."** The high energy electrons are decelerated by the strong electric fields of the atomic nuclei in the target. In the process, electrons lost their kinetic energy which is emitted as photons with a wide and continuous range of wavelengths. This gives rise to a broad background spectrum.
- 2. Characteristic radiation When the incident electrons have sufficient energy, they can eject tightly bound electrons from the inner atomic shells of the target atoms. This creates a vacancy, and electrons from higher-energy shells fall into the lower-energy states to restore stability. The difference in binding energies between the shells is released as X-ray photons with discrete energies specific to the element. These emissions are referred to as characteristic radiation, with the strongest and most commonly used being the  $K\alpha$  line. The exact photon energy depends on the target material, since each element has a unique electronic structure.

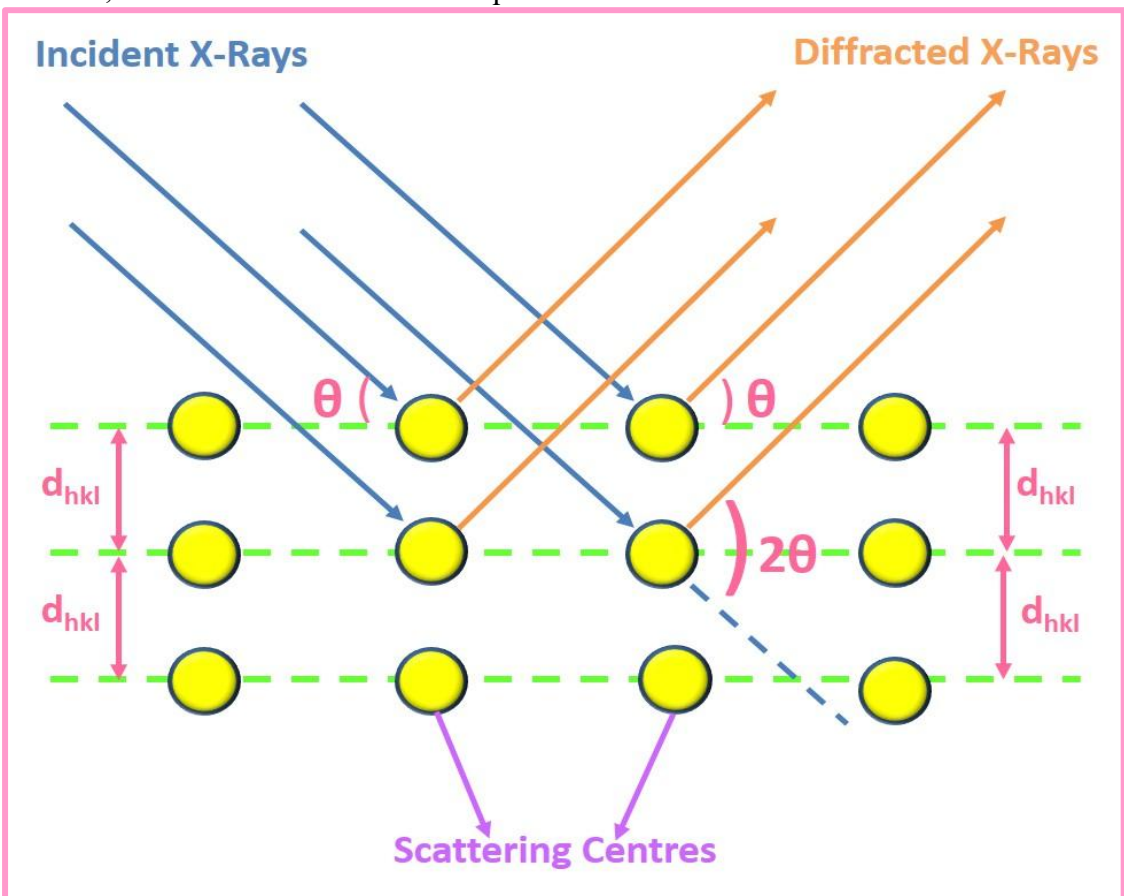


Figure 2.5: Schematic description of Bragg's Law.

The resulting radiation is a superposition of the continuous Bremsstrahlung spectrum and sharp characteristic peaks (**Fig. 2.4**). For X-ray diffraction (XRD), only the most intense characteristic line is  $K\alpha$  radiation, typically used for crystallographic investigations. Unwanted radiation, including Bremsstrahlung and  $K\beta$  lines, is removed

with filters or monochromators. To isolate this radiation, filters or monochromators are employed. Filtering relies on the nonlinear absorption properties of certain materials, which exhibit absorption edges at specific wavelengths. By choosing an appropriate filter, the unwanted continuous spectrum and the weaker  $K\beta$  line can be strongly absorbed, while most of the desired  $K\alpha$  radiation is transmitted. Each target material has a corresponding filter that optimally suppresses the undesired components.

**Principle:** When X-ray photons interact with matter, several scattering and absorption processes occur. Among these, elastic (coherent) scattering, also known as Rayleigh scattering, is of primary importance. In this interaction, photons interact with electrons bound to atomic nuclei without any loss of energy, preserving their phase relationship with the incident wave. As a result, all atoms in the irradiated volume scatter X-rays in various directions. In crystalline materials, the ordered periodic structure gives rise to constructive and destructive interferences, producing characteristic diffraction patterns. The scattering occurs in all directions, but in crystalline materials the periodic lattice ensures that constructive and destructive interferences emerge, forming distinctive diffraction phenomena, as illustrated in **Fig. 2.5**.

The fundamental concept behind X-ray diffraction (XRD) is the interaction of X-rays with these periodic atomic planes. X-ray diffraction (XRD) exploits this principle by analyzing the diffraction of X-rays by periodic atomic planes and detecting the resulting signals as a function of angle or energy. W.L. Bragg (1913) provided the geometrical explanation of these constructive interferences, which is formalized in Bragg's law **Eq.** [2.1]:

Bragg's law: 
$$2d \times Sin\theta = n\lambda$$
. [2.1]

Bragg's law relates the order of diffraction (n), the incident wavelength ( $\lambda$ ), the lattice spacing (d<sub>hkl</sub>), and the diffraction angle ( $\theta$ ). In polycrystalline materials with fine, randomly oriented grains, every lattice plane capable of satisfying Bragg's law contributes to diffraction. This produces diffraction cones that, when captured by a planar detector, manifest as Debye rings (or diffraction rings)

# 2.2.2 Scanning Electron Microscopy (SEM) and Energy-Dispersive X-ray Analysis (EDAX):

Scanning Electron Microscope (SEM) are advanced imaging instruments that provide nanoscale visualization with exceptional magnification, resolution, and depth of field, surpassing the inherent limitations of conventional optical microscopes [13]. Electron microscopy was pioneered in Germany in 1931 by Max Knoll and Ernst Ruska, marking a breakthrough that overcame the ~200 nm resolution limit of optical microscopes. Early contributions from M. Knoll and Manfred von Ardenne further propelled progress in this domain. JEOL later revolutionized accessibility to the technology by releasing its first commercial SEM in 1966, a move that positioned the company as the largest global manufacturer of SEMs.

Unlike compound or simple microscopes that rely on visible light and are constrained by its wavelength, SEMs utilize electrons to generate high-clarity images of surface structures. While optical microscopes enable observation of samples in natural colour, their magnification and depth of field remain restricted. In contrast, SEMs not only deliver superior topographical detail but also integrate spectroscopic capabilities for precise chemical analysis. This dual functionality makes SEM an indispensable research tool, capable of revealing intricate micro- and nanostructures where even a single greyscale image may suffice to achieve critical investigative objectives.

Energy-dispersive X-ray spectroscopy (EDS/EDX) is a powerful analytical tool for elemental analysis and chemical characterization of materials. The technique operates on the principle that each element possesses a distinct atomic structure, producing unique X-ray emission peaks as described by Moseley's law. By directing an electron or X-ray beam onto the specimen, inner-shell electrons can be ejected, creating vacancies that are filled by outer-shell electrons. This transition releases characteristic X-rays whose energies are directly related to the atomic structure of the element. Measurement of these emitted X-rays by an energy-dispersive detector enables precise determination of the elemental composition of the sample.

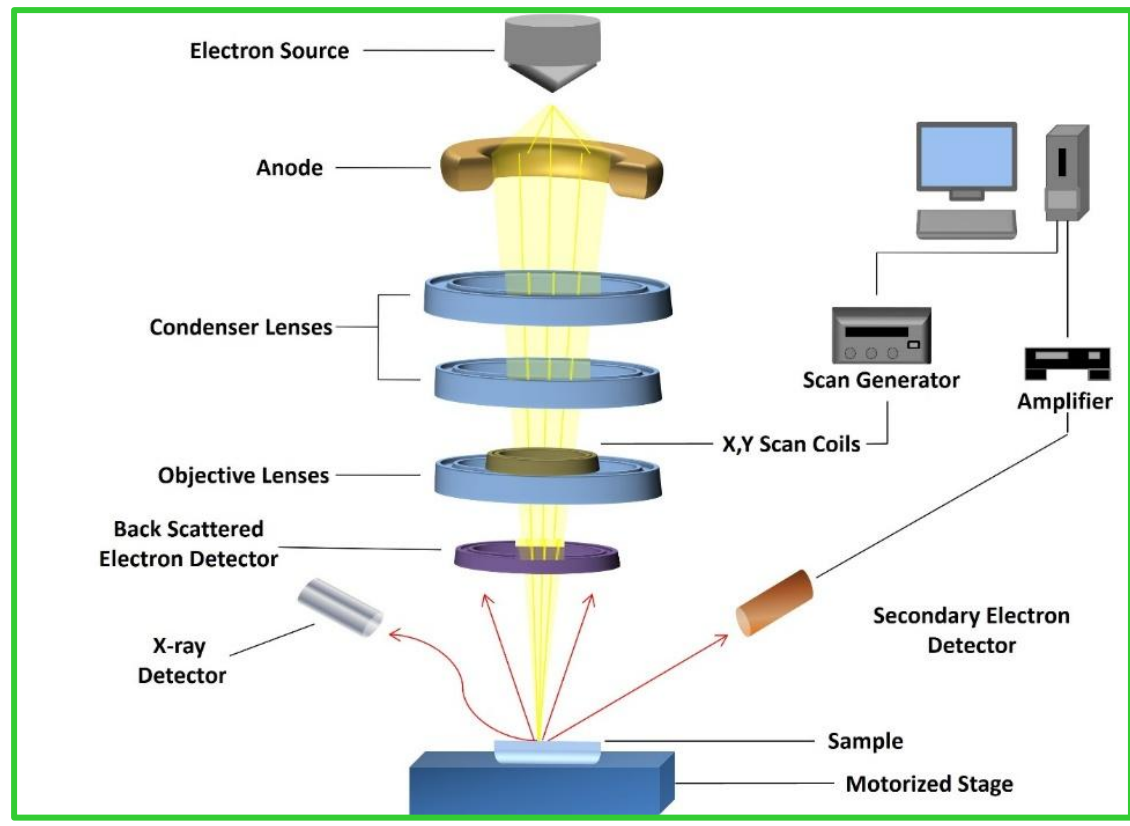


Figure 2.6: Schematic illustration of working of Scanning Electron Microscopy (SEM) and Energy-dispersive X-ray Spectroscopy (EDAX).

Working Principle: The working principle of the Scanning Electron Microscope (SEM) is based on the interaction between high-energy electrons and the specimen surface, producing signals including secondary electrons, backscattered electrons, and diffracted backscattered electrons, each offering unique analytical insights (Fig. 2.6). Secondary electrons, emitted from atoms located just a few nanometers below the surface, are particularly effective in rendering high-resolution images of morphology, edge sharpness, particle distribution, and surface irregularities. Backscattered electrons, which are elastically reflected primary electrons, carry information linked to the atomic number of constituent elements, thereby creating compositional contrast and facilitating material phase identification. Diffracted backscattered electrons form the foundation of

electron backscatter diffraction (EBSD), which provides quantitative crystallographic information such as grain orientation, texture, and strain distribution. Complementary signals such as X-rays, generated by inelastic scattering, enable elemental mapping through energy-dispersive X-ray spectroscopy (EDS), while photon emissions can reveal optical characteristics of luminescent materials. Collectively, these signal outputs allow SEM to serve as a multi-dimensional analytical platform, capable of simultaneously assessing structural, compositional, and crystallographic features of materials. This makes SEM particularly powerful in optimizing nanostructure synthesis, validating thin-film deposition, investigating catalytic surfaces, and probing biological interfaces. By integrating morphological imaging with elemental and crystallographic analysis, SEM ensures a comprehensive characterization framework that is indispensable for both fundamental research and industrial applications.

Energy-dispersive X-ray spectroscopy (EDS/EDX) is widely employed for identifying and quantifying elements within a material based on their characteristic X-ray emissions. When a focused electron or X-ray beam strikes the specimen, it displaces electrons from inner atomic shells, creating vacancies that are filled by higher-energy electrons. The resulting energy difference is released as X-ray photons, each with a signature energy unique to the element. By detecting and analyzing these emissions, EDS provides accurate elemental profiling and chemical characterization across diverse materials.

Electron Microscopy Applications: Scanning Electron Microscope (SEM) is an indispensable analytical tool for morphological characterization, offering highresolution, three-dimensional visualization of material surfaces at micro- and nanoscales. By directing a finely focused electron beam onto the specimen and detecting the emitted secondary electrons, SEM enables precise examination of critical surface attributes such as particle size, shape, surface roughness, exfoliation level, layer stacking, and degree of agglomeration. This powerful imaging capability allows direct correlation between synthesis parameters such as temperature, reaction time, and chemical environment and the resulting morphological evolution of the material. In the context of nanomaterials, SEM is particularly effective in revealing nanosheet exfoliation, nanoparticle dispersion, film homogeneity, and interfacial continuity, factors that directly govern performance in advanced applications including sensors, catalytic platforms, energy devices, and protective coatings. Moreover, SEM serves as a complementary technique to crystallographic tools like XRD and atomic-scale probes like TEM, by providing real-space morphological evidence essential for validating structural hypotheses and optimizing fabrication strategies. Its ability to ensure reproducibility and structural consistency makes SEM an essential component in the comprehensive evaluation and engineering of functional nanostructures.

Scanning Electron Microscopy (SEM) has extensive applicability across diverse fields. In material science, it is indispensable for surface characterization of metals, polymers, ceramics, and composites, fracture analysis to identify failure mechanisms, and evaluation of coatings and thin films. In the semiconductor industry, SEM ensures microchip integrity through integrated circuit inspection and supports failure analysis by detecting nanoscale defects. In biology and medicine, it provides high-resolution imaging of cells, tissues, viruses, and surface features of biological samples, supplementing histological studies with greater detail than light microscopy. In

nanotechnology, SEM is vital for characterizing nanomaterials such as nanoparticles and carbon nanotubes, as well as for monitoring the fabrication of nanoscale structures.

### 2.2.3 Transmission Electron Microscopy (TEM):

Transmission Electron Microscopy (TEM) plays a pivotal tool in nanoscale morphological studies owing to its ability to deliver high-resolution atomic-level imaging of a material's internal architecture [14]. In contrast to Scanning Electron Microscopy (SEM), which focuses primarily on surface topography, TEM directs an electron beam through an ultrathin specimen, unveiling structural details such as lattice arrangements, crystallinity, and internal defects. This makes TEM particularly indispensable for characterizing nanomaterials like hexagonal boron nitride (h-BN) nanosheets, where features such as layer thickness, stacking order, edge morphology, and imperfections govern their physical and chemical performance. Beyond morphology, TEM also provides selected area electron diffraction (SAED) data, which reveals crystallographic orientation and phase composition, adding a powerful dimension to structural analysis. By correlating these findings with synthesis parameters, TEM enables researchers to understand how preparation methods shape nanoscale features and, in turn, refine processing strategies for applications in electronics, catalysis, nanocomposites, and biomedical devices. Its unmatched resolution and ability to probe internal features position TEM as an indispensable cornerstone in advanced material characterization.

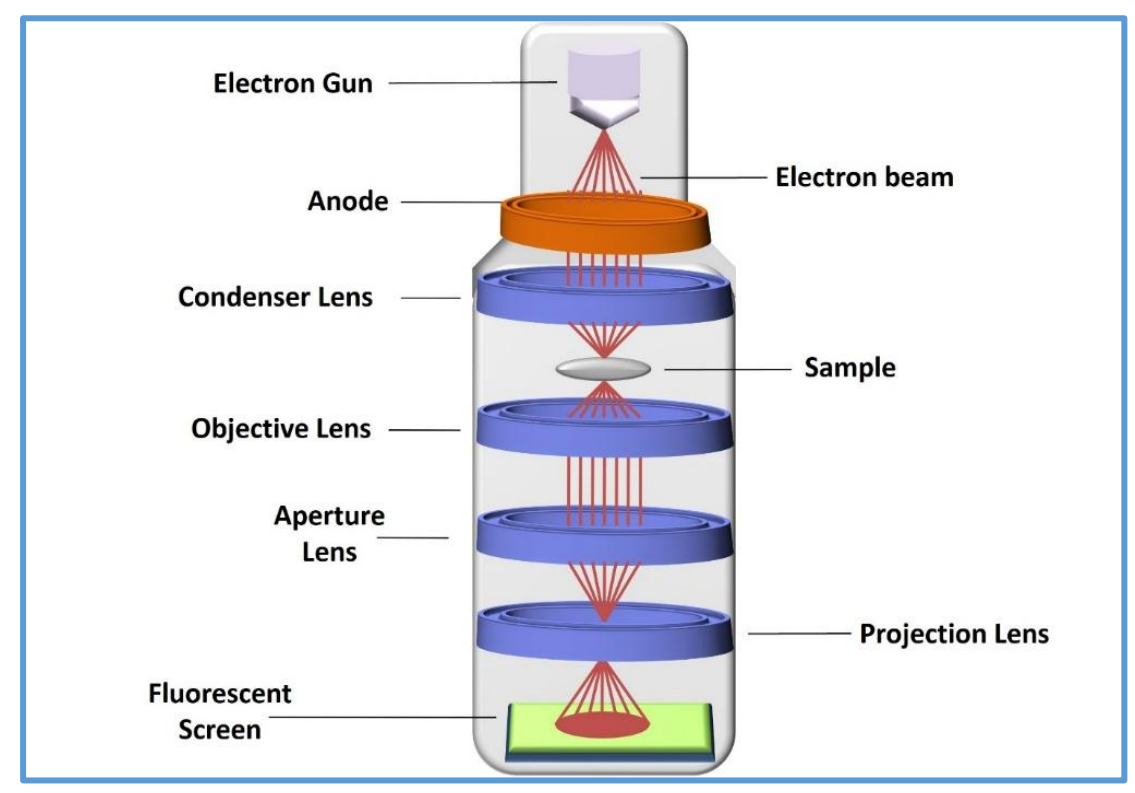


Figure 2.7: Diagram representing working of Transmission Electron Microscopy (TEM)

In the early 1920s, Louis de Broglie revolutionized scientific thought by proposing that particles such as electrons could exhibit wave-like behaviour. This groundbreaking idea

was confirmed through experiments with electron beams, which revealed their ability to generate wave motion. The concept of electron wave-particle duality opened new possibilities for imaging at resolutions far beyond the limits of visible light. To manipulate and direct these electron waves effectively, scientists employed magnetic fields as a means of focusing them, similar to how glass lenses bend light in optical microscopes. Building on this principle, Ernst Ruska, together with Max Knoll, successfully designed the first working electron microscope in 1931. Only two years later, Ruska advanced his work further by collaborating with the Siemens company, leading to the development of the first transmission electron microscope (TEM) in 1933. This instrument marked a technological milestone and transformed material science, biology, and physics by enabling the visualization of structures at the nanometer scale, far surpassing what was achievable with traditional light microscopy.

Working Principle: A Transmission Electron Microscope (TEM) differs fundamentally from a light microscope by employing electrons instead of photons, enabling it to visualize structures far beyond the diffraction limit of visible light (Fig. 2.7). The electron beam used in TEM has a wavelength of approximately 0.005 nm, which is drastically shorter than the wavelength of light, thereby offering resolution up to a thousand times greater than optical microscopes. When the accelerated electron beam strikes an ultrathin specimen, some electrons penetrate with little interaction while others are scattered by atomic nuclei and electron clouds. This variation in scattering intensity generates contrast, with denser or heavier atomic regions appearing darker in the final image. Electromagnetic lenses then focus the transmitted electrons to produce magnified images that can reach atomic resolution. Because of this, TEM is a vital tool for examining ultrastructural details of biological entities such as viruses and organelles, as well as material systems like nanoparticles, thin films, and crystalline lattices. Its ability to provide high-resolution insights into morphology, composition, and defects makes it essential in fields ranging from nanotechnology to biomedical research.

Applications: Transmission Electron Microscopy (TEM) is a transformative technique that enables atomic- and nanoscale imaging of internal structures, offering unmatched resolution for diverse fields. In materials science, it reveals defects, grain boundaries, and crystal structures critical for optimizing metals, ceramics, and polymers. In nanotechnology, TEM characterizes nanoparticles, nanotubes, and thin films with precision, supporting the development of nano-sensors, drug delivery systems, and electronic devices. Its role in biology and medicine is equally pivotal, as it unveils cellular ultrastructure and viral morphology, advancing disease research and therapeutic design. The semiconductor industry depends on TEM for atomic-scale inspection of microchips and transistors, ensuring reliability in next-generation electronics. Furthermore, TEM is instrumental in environmental science, where it characterizes pollutants and nanomaterials in air, water, and soil, guiding effective remediation strategies.

#### 2.2.4 UV-Visible Spectroscopy:

UV-Visible spectroscopy provides a direct and precise method to investigate electronic transitions in advanced materials, particularly semiconductors and nanostructured systems [15]. The technique measures wavelength-dependent absorption, which

corresponds to the excitation of electrons between energy states, enabling accurate determination of the optical bandgap. Since the bandgap governs a material's interaction with light and its electronic response, this information is central to optimizing functionality in optoelectronic applications. In nanostructures, the method reveals critical effects of quantum confinement, morphology, and defect states on energy levels, offering a clear picture of how nanoscale dimensions dictate optical properties. Its non-invasive nature, high sensitivity, and flexibility across diverse sample types make it an invaluable characterization tool. From photovoltaic cells to LEDs, photodetectors, and biosensors, UV-Visible spectroscopy provides the essential data required to engineer materials with enhanced efficiency, reliability, and performance.

UV-visible spectroscopy plays an essential role by providing insights into their electronic and optical properties through light absorption analysis. The method involves passing ultraviolet and visible light (200–800 nm) through a dispersed sample and recording how much light is absorbed at each wavelength. This generates absorption spectra that reveal electronic transitions within the material, including the energy required for electrons to move from the ground state to excited states. One of the most critical outcomes of this analysis is the determination of the optical bandgap, a parameter that governs how efficiently the material can interact with and respond to light. Since the bandgap strongly influences electrical conductivity and optical response, it directly determines the suitability of h-BN nanosheets for applications in optoelectronic systems such as photodetectors, lasers, and next-generation display technologies.

Beyond bandgap determination, UV-visible spectroscopy provides quantitative data on absorbance using the Beer-Lambert law ( $A = \varepsilon cl$ ), where absorbance is directly linked to concentration, molar absorptivity, and path length. This enables accurate calculation of the absorption coefficient, which reflects the degree of light attenuation in the sample. The technique can also shed light on the effects of synthesis methods, exfoliation processes, and morphological variations such as sheet thickness, layer stacking, and structural defects on the optical properties. Moreover, UV-visible spectroscopy is widely valued for being non-invasive, requiring minimal sample preparation, and offering high sensitivity, making it especially effective for analyzing delicate nanomaterials. Its non-destructive nature, rapid analysis capability, and high sensitivity make it ideal for repeated testing and optimization of nanomaterials without altering their intrinsic properties. Consequently, UV-visible spectroscopy remains a cornerstone in both fundamental research and practical optimization of nanomaterials for emerging technologies in electronics, photonics, and energy applications.

UV-visible spectroscopy (UV-Visible) is an analytical method that measures how molecules absorb light in the ultraviolet and visible range (200–800 nm). Originating in the early 20th century, it was developed as scientists explored how light interacts with matter. By recording absorption at specific wavelengths, the technique reveals information about molecular structure, concentration, and electronic transitions. Its applications expanded rapidly in the mid-20th century, particularly in chemistry, where it was used for compound identification, reaction monitoring, and quantitative analysis. With advancements in instrumentation—such as improved detectors, monochromators,

and light sources. UV-Visible spectroscopy has become an indispensable tool across pharmaceuticals, environmental monitoring, biochemistry, and clinical diagnostics.

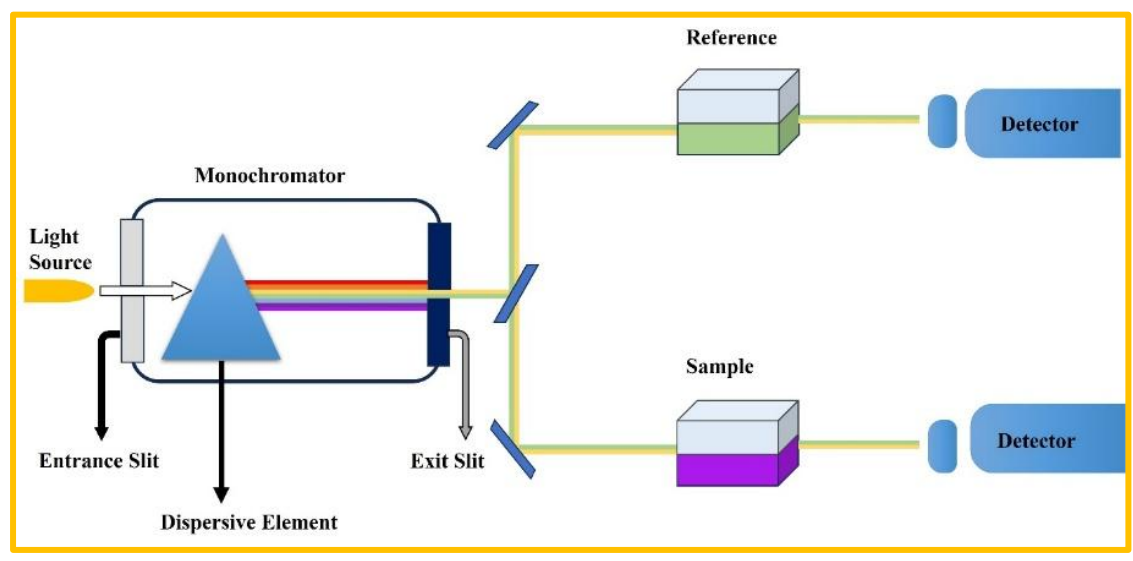


Figure 2.8: Stepwise illustration of working of UV-Visible Spectrometer.

Working and Principle: UV-visible spectroscopy operates on the principle that molecules absorb light within the ultraviolet or visible range (200-800 nm) at characteristic wavelengths corresponding to electronic transitions (Fig. 2.8). When light passes through a sample, certain wavelengths are absorbed as electrons are excited from lower to higher energy states, and the extent of absorption is directly proportional to the concentration of the absorbing species. Molecules with conjugated double bonds, aromatic rings, or metal-ligand complexes show distinctive absorption bands that reflect their electronic structure. A UV-Visible spectrophotometer typically consists of a light source (commonly a deuterium lamp for UV and a tungsten lamp for visible light), a monochromator to select the desired wavelength, a cuvette to hold the sample, and a detector to measure transmitted light intensity. The decrease in intensity after passing through the sample is expressed as absorbance, which is mathematically related to concentration through Beer's Law (A =  $\varepsilon$ cl), where  $\varepsilon$  is molar absorptivity, c is concentration, and I is the path length. This technique provides accurate quantitative analysis and is extensively applied in chemistry, biology, environmental monitoring, and pharmaceutical sciences for molecular identification and measurement.

Applications: UV-visible spectroscopy is a fundamental analytical tool used to quantify substances that absorb ultraviolet or visible light, making it essential for monitoring reaction kinetics and proposing mechanisms. In clinical chemistry, it is widely applied to study enzyme activity by tracking reaction rates, often serving as a diagnostic aid for organ damage when enzymes leak into the bloodstream. The pharmaceutical industry relies on it for dissolution testing to evaluate drug release profiles, ensuring consistency in formulation and manufacturing. In biochemistry and genetics, it enables precise measurement of DNA, proteins, and enzyme activity, as well as the study of DNA denaturation. Industrially, it is integral to quality control in the production of dyes, inks, and paints, while in environmental and agricultural sciences, it provides critical insights into water quality by detecting organic compounds and heavy metals.

### 2.2.5 Raman Spectroscopy:

Raman spectroscopy is a versatile, non-destructive analytical method that has become indispensable for exploring the molecular structure, composition, and dynamics of materials across numerous scientific and industrial domains [16]. The technique is based on the Raman effect, where incident light undergoes inelastic scattering, transferring energy to or from molecular vibrations, rotations, or other low-frequency modes. This process produces a Raman spectrum, a unique molecular fingerprint that enables direct identification of compounds and characterization of their structural features. Unlike techniques requiring significant sample preparation or destructive testing, Raman spectroscopy allows rapid, accurate analysis of solids, liquids, and gases with minimal preparation.

In chemistry, it provides vital information on bond vibrations, chemical environments, and reaction mechanisms, making it an excellent tool for monitoring chemical processes in real time. In materials science, it is extensively applied to investigate carbon-based systems such as graphene, graphite, and carbon nanotubes. Raman spectra can reveal layer thickness, defect density, crystallinity, and electronic interactions in these materials, knowledge that is essential for advancing electronic, optical, and energy storage technologies. For instance, the ability to distinguish between monolayer and multilayer graphene through characteristic Raman peaks is critical for applications in flexible electronics and nanodevices.

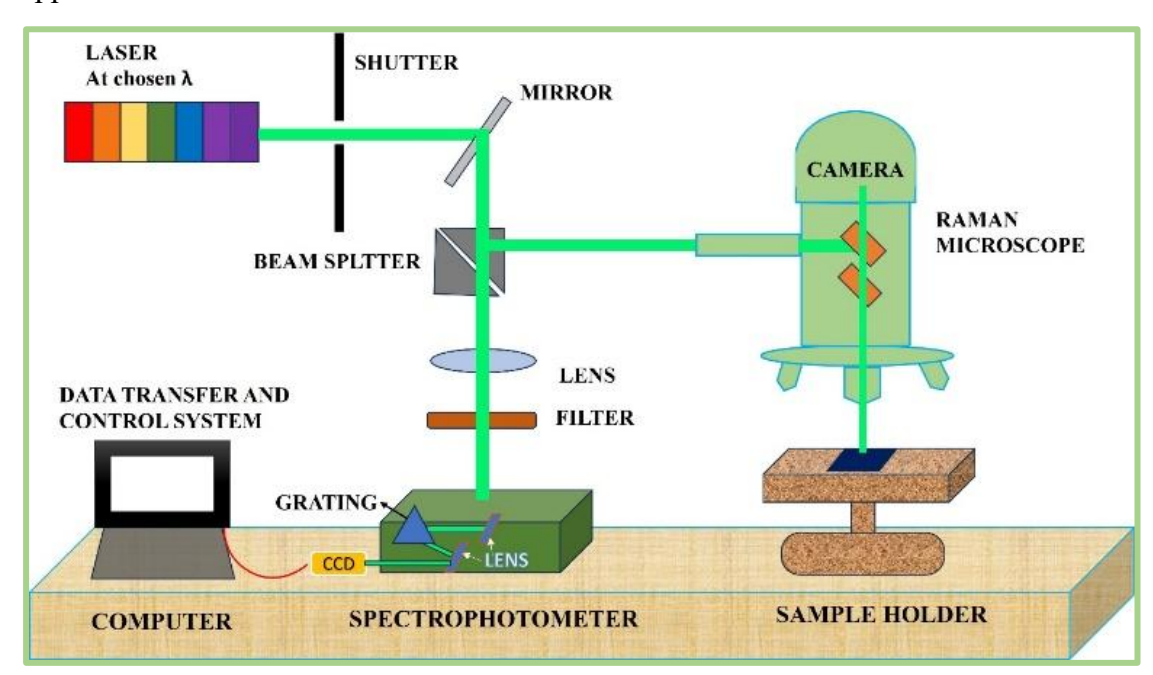


Figure 2.9: Diagram illustrating working of Raman Spectroscopy

The pharmaceutical industry also benefits greatly from Raman spectroscopy. It is routinely used for drug quality control, ensuring the correct identity and concentration of active pharmaceutical ingredients. Its ability to differentiate polymorphs distinct crystalline forms of the same compound—is especially significant, as polymorphism can alter drug solubility, stability, and therapeutic effectiveness. Raman mapping and imaging further allow visualization of drug distribution in tablets, supporting both formulation development and regulatory compliance. Beyond pharmaceuticals, Raman spectroscopy is increasingly applied in biology for studying proteins, lipids, and nucleic

acids, enabling label-free investigation of complex biological samples. Its expanding role across disciplines reflects its precision, versatility, and growing importance as a cornerstone of modern analytical science.

Working and Principle: In Raman spectroscopy, a non-ionizing laser serves as the excitation source, initiating interactions between photons and the molecules of the sample (Fig. 2.9). Photons may traverse the material unaltered, be absorbed if their energy matches molecular excitation levels, or scatter when they disturb the electron cloud. Absorption often results in fluorescence as the molecule releases energy upon returning to the ground state. Scattering phenomena dominate the process, with two main types observed in the visible and near-infrared ranges: Rayleigh and Raman scattering. Rayleigh scattering, the more common outcome, is elastic because there is no net energy transfer between the photon and the molecule. Raman scattering, however, is inelastic, as the photon either loses or gains energy while altering the molecule's vibrational state. Though inherently weak—occurring in only one out of every million to hundred million scattering events—Raman scattering delivers highly specific vibrational signatures, making it invaluable for molecular identification and structural analysis.

**Applications:** Raman spectroscopy is a highly versatile, non-destructive technique that provides molecular-level insights across a wide range of scientific, industrial, and cultural fields. In materials science, it is essential for investigating nanomaterials such as graphene, carbon nanotubes, and quantum dots, revealing structural defects and electronic properties. It also plays a critical role in analyzing polymers, composites, and thin films, ensuring structural integrity and performance in advanced applications, particularly in semiconductor manufacturing. In pharmaceuticals, Raman spectroscopy ensures drug quality through compound identification, quantification, and polymorph analysis, while also enabling real-time monitoring during production.

In environmental studies, Raman is widely employed to detect pollutants, pesticides, and heavy metals, as well as to analyze water quality for contaminants and pathogens. Biomedical applications include early disease diagnosis, tissue and cell imaging, and cancer detection through identification of molecular signatures. Forensic science relies on Raman for rapid, non-destructive identification of explosives, narcotics, and trace evidence. In cultural heritage, it aids in the authentication and preservation of artifacts by characterizing pigments, dyes, and degradation patterns. The food and agriculture sectors use Raman to detect adulterants, verify authenticity, assess pesticide residues, and monitor soil health.

The petrochemical and chemical industries apply Raman spectroscopy in oil and gas analysis, reaction monitoring, and process optimization. In nanotechnology, it is indispensable for nanoparticle characterization and, with surface-enhanced Raman spectroscopy (SERS), for detecting ultralow concentrations in biosensing and environmental monitoring. Finally, in catalysis and reaction engineering, Raman offers real-time monitoring of reaction pathways, catalyst stability, and molecular changes, guiding the development of efficient industrial processes. Its broad adaptability and sensitivity make Raman spectroscopy an essential tool for advancing research, technology, and conservation efforts worldwide.

### 2.2.6 Fourier Transform Infrared (FT-IR) Spectroscopy:

Fourier Transform Infrared (FTIR) spectroscopy is the versatile qualitative characterization technique that translate molecular vibrations into structural insights [17]. Historically, IR spectroscopy relied on dispersive instruments that separated light into individual frequencies using prisms or diffraction gratings. While effective, these instruments were relatively slow and less sensitive. FTIR revolutionized the process by replacing these dispersive components with an interferometer and Fourier transform algorithms, enabling rapid acquisition of high-resolution spectra. FTIR offers several advantages which included non-destructive measurements that requires no external calibration, and delivers higher sensitivity by averaging multiple scans to reduce noise. Additionally, it has high optical throughput, mechanical simplicity with only one moving mirror, and the capability of collecting data in seconds, making it far superior to earlier methods. Owing to these strengths, FTIR has become indispensable in diverse fields, including polymer analysis, pharmaceutical research, environmental monitoring, forensic science, and nanomaterials characterization. Its ability to analyze solids, liquids, thin films, and even gases broadens its application range. Modern software integration further enhances FTIR, allowing automated data processing, spectral libraries, and real-time quantitative measurements. Interpreting FTIR spectra involves identifying characteristic shapes and absorption bands, then correlating them with group frequency data, structural details, and supporting chemical or physical information about the sample.

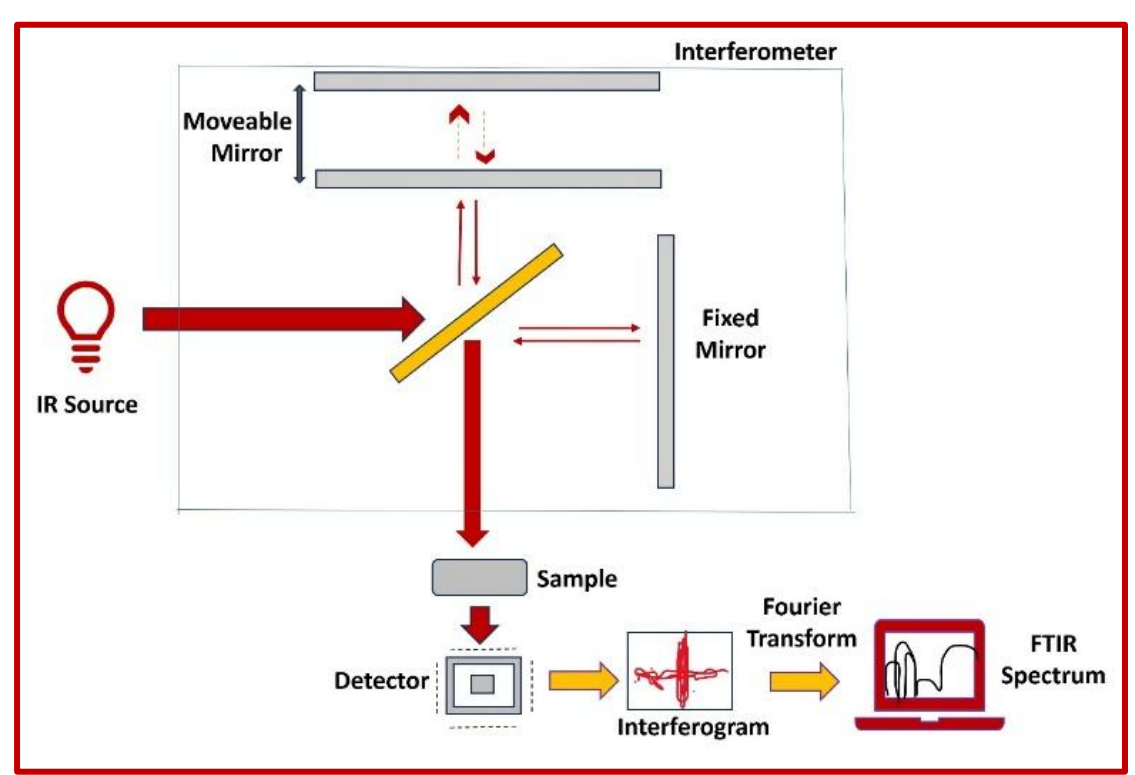


Figure 2.10: Schematic working of Fourier Transform Infrared Spectroscopy (FT-IR)

Working Principle: The working principle of Fourier Transform Infrared (FTIR) spectroscopy is centered on the Michelson interferometer (Fig. 2.10). This device is made up of a beam splitter, a fixed mirror, and a movable mirror. When infrared

radiation enters the system, the beam splitter divides the light into two paths—one directed toward the stationary mirror and the other toward the moving mirror. After reflection, the beams are recombined at the beam splitter. Because the moving mirror shifts back and forth, the optical path length changes continuously, which introduces a varying phase difference between the two beams. Their recombination produces an interference pattern, recorded as an interferogram. The horizontal axis of this interferogram corresponds to the optical path difference, while the vertical axis represents the recorded intensity of the light. To extract meaningful spectral information, the interferogram is mathematically converted using a Fourier transform, which produces the infrared absorption spectrum of the sample, displaying all frequencies simultaneously with high precision.

**Applications:** FTIR spectroscopy is an essential technique for analyzing the structure and composition of materials across a wide range of fields. In industrial applications, it is commonly used for quality control, where shifts in absorption band profiles signal compositional changes or contamination. Its versatility extends to monitoring and processing polymers, photoresists, and polyimides. In the biomedical domain, FTIR enables precise identification and quantification of biomolecules including proteins, lipids, and nucleic acids, and it contributes significantly to disease diagnostics. The method is also highly effective in the evaluation of biodiesel stability and the study of antioxidant interactions. In failure analysis, FTIR identifies material breakdown processes such as oxidation and incomplete curing of monomers. Its scope includes advanced applications like high-resolution spectral studies, trace analysis in raw materials and final products, ultrafast reaction monitoring, and combined analysis with chromatographic or thermogravimetric techniques. Furthermore, FTIR is invaluable in kinetic studies, reaction pathway analysis, and compound identification through spectral fingerprinting. By recognizing specific absorption bands, it also facilitates functional group identification in unknown compounds, making it useful for characterizing a wide variety of chemical classes including ketones, aldehydes, and carboxylic acids.

#### 2.2.7 Atomic Force Microscopy (AFM):

The Atomic Force Microscope (AFM) is a high-resolution scanning probe microscope designed to measure a wide range of surface properties, including height variations, magnetic interactions, and frictional forces, with precision at the nanometer scale [18]. Unlike conventional optical microscopes, which are constrained by the diffraction limit of light, AFM achieves atomic or near-atomic resolution by directly interacting with the sample surface. Its operation relies on a sharp probe mounted on a cantilever that physically touches or hovers near the surface, detecting forces between the probe tip and the sample. During scanning, the probe is rastered systematically across the sample, and localized data is collected to construct highly detailed three-dimensional images of surface topography and properties. The incorporation of piezoelectric elements into AFM systems is essential for its precision. These elements, when electrically stimulated, deform in controlled increments, allowing the probe to move with extraordinary accuracy. This precision enables the AFM to analyze materials ranging from hard crystals and semiconductors to delicate biomolecules like DNA and proteins, without significantly altering or damaging the sample. This adaptability has made AFM a cornerstone in fields such as nanotechnology, semiconductor research, materials

science, and biomedical engineering. Historically, the AFM was conceived in 1982 by Gerd Binnig, working at IBM, shortly after the invention of the Scanning Tunnelling Microscope (STM) in 1980 by Binnig and Heinrich Rohrer. While the STM could only analyze conductive materials, the AFM extended the technique to insulating surfaces, vastly broadening its applicability. The first experimental application of AFM took place in 1986, demonstrating its promise for nanoscale analysis. Just three years later, in 1989, the AFM entered commercial markets, rapidly gaining global adoption. Over time, AFM has been refined into multiple imaging modes—such as tapping, noncontact, and force modulation—each tailored to specific types of samples and measurements. Today, AFM is not only a tool for imaging but also for manipulating and modifying materials at the nanoscale, making it an indispensable technique in both fundamental research and advanced technological development.

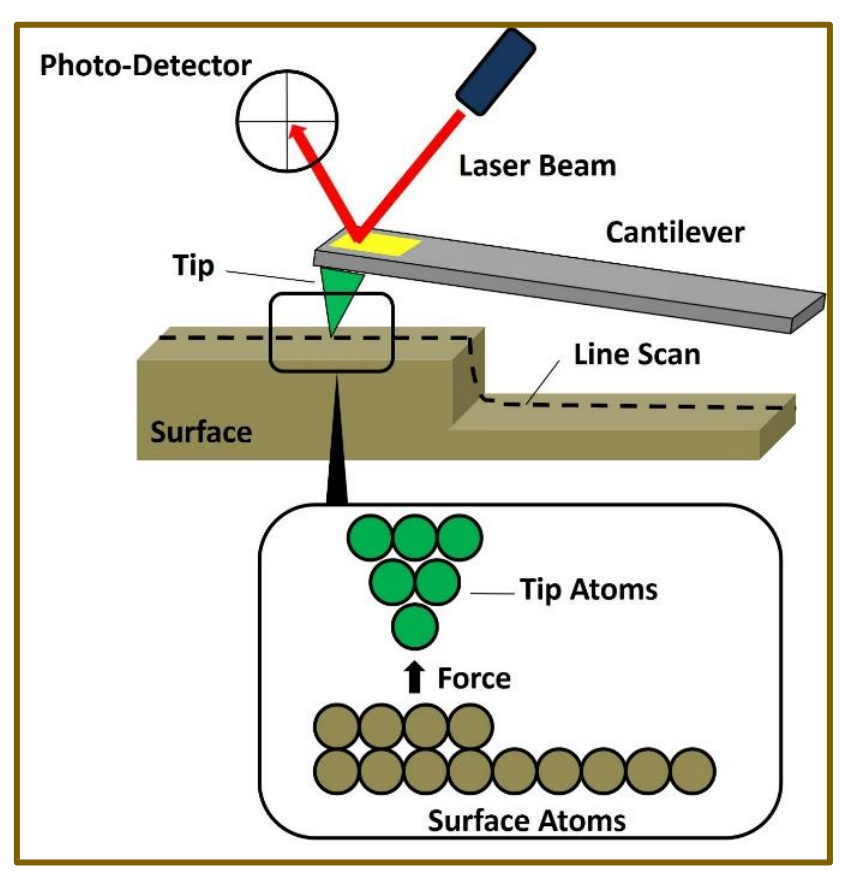


Figure 2.11: Diagrammatic depiction of working of Atomic Force Microscope (AFM)

Working Principle: The Atomic Force Microscope (AFM) operates on the principle of detecting intermolecular forces at the nanoscale, allowing scientists to visualize atoms and surface structures with remarkable precision (Fig. 2.11). Its core working mechanism relies on three interconnected principles: surface sensing, signal detection, and image construction. In the surface sensing stage, a cantilever—designed as a beam or plate fixed at one end—plays the central role. At its tip, a sharp probe approaches the sample's surface, where intermolecular forces act upon it. Attractive forces dominate when the tip is close, but as it moves into direct contact, repulsive forces push the cantilever away. This dynamic interaction enables precise measurement of surface variations. The detection system translates these movements into measurable data. A

laser beam is directed onto the back of the cantilever, and its reflection shifts with each cantilever deflection. A position-sensitive photodiode (PSPD), built on silicon PIN diode technology, tracks these changes with high accuracy, converting them into electrical signals. Imaging arises from scanning the cantilever across the specimen in a raster pattern. As the tip follows the nanoscale highs and lows of the surface, the resulting beam deflections are processed through a feedback loop. This system maintains the cantilever tip at a constant height, ensuring precision in mapping. The final output is a high-resolution three-dimensional image of the surface topography.

**Applications:** Atomic Force Microscopy (AFM) has established itself as a versatile tool in natural sciences, with applications including solid-state physics, semiconductor research, molecular engineering, polymer chemistry, surface chemistry, molecular biology, cell biology, medicine, and physics. One of its most valuable uses is in identifying and analyzing atoms from a wide range of materials, allowing scientists to investigate their structural and functional properties at the nanoscale. By evaluating the force interactions between atoms, AFM provides insight into atomic bonding strength, surface energy, and intermolecular interactions that govern material behaviour. This makes it particularly useful in studying how physical properties of atoms and molecules change under varying environmental or mechanical conditions.

In biology, AFM has been applied extensively to understand the architecture and dynamics of protein complexes and assemblies, such as microtubules, actin filaments, and other cytoskeletal structures. It allows researchers to investigate not only their structural integrity but also their mechanical properties, such as flexibility, stiffness, and resistance to force. In medical research, AFM contributes significantly to cancer diagnostics by enabling the differentiation between cancerous and healthy cells based on their surface morphology, elasticity, and cell wall rigidity. Moreover, it provides a means to evaluate neighbouring cells, their shapes, and the mechanical properties of their membranes, which is critical for understanding processes such as cell adhesion, migration, and tissue development. This broad applicability demonstrates AFM's importance in bridging fundamental research with real-world applications in materials science, biology, and medicine.

### 2.2.8 Thermogravimetric Analysis (TGA)

Thermogravimetric analysis (TGA) is an essential tool in thermal characterization, where the change in a sample's weight is measured relative to temperature or elapsed time [19]. This technique helps determine key properties of materials, such as their purity levels, chemical composition, degradation mechanisms, decomposition temperature thresholds, and absorbed moisture. It is particularly effective in studying the thermal behaviour of pharmaceuticals, polymers, elastomers, thermoset plastics, ceramics, and mineral-based materials. TGA techniques are generally divided into three major types. Static or isothermal thermogravimetry involves maintaining a constant temperature and recording mass variations over time. Quasistatic thermogravimetry measures changes in sample weight as the material is progressively heated until a constant mass is achieved. Dynamic thermogravimetry, which is most frequently employed in research and industry, records mass changes under continuous heating or cooling at a specified rate, most commonly in a linear progression. This dynamic method allows for detailed investigation of thermal stability and material transitions.

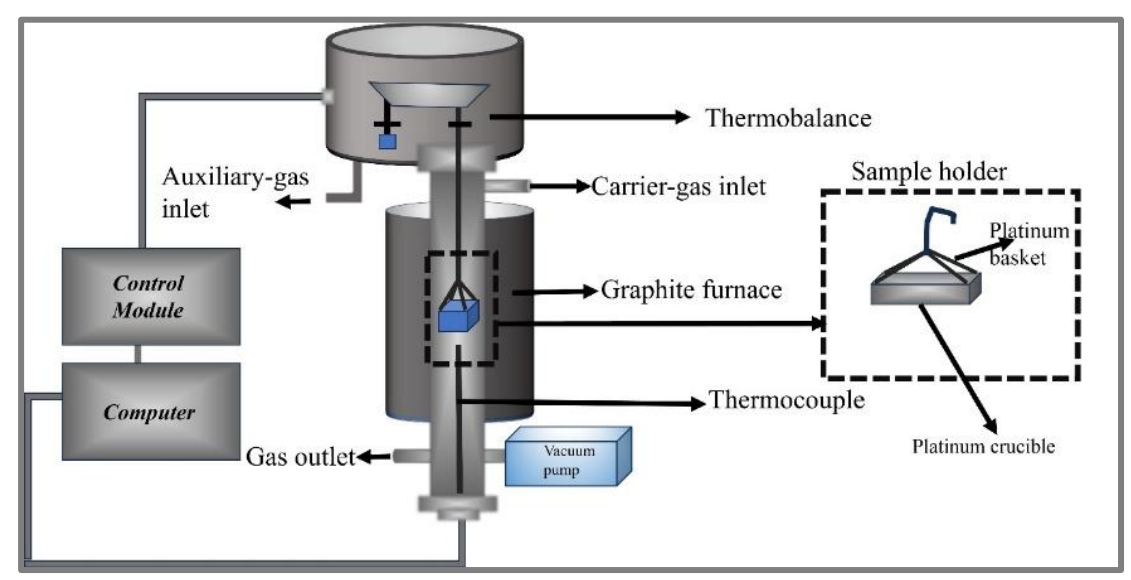


Figure 2.12: Working of Thermogravimetric Analysis (TGA)

Working Principle: The working principle of thermogravimetric analysis (TGA) is based on monitoring the weight changes of a material as it undergoes thermal transitions under controlled heating conditions (Fig. 2.12). A sample of known initial mass is subjected to a steadily increasing temperature, and its weight is continuously measured as a function of either time or temperature. The results are commonly represented in two forms: the thermogravimetric (TG) curve, which directly displays weight change versus temperature or time, and the derivative thermogravimetric (DTG) curve, which plots the rate of weight loss, serving as a pyrolysis profile. Each substance exhibits a distinctive TG pattern due to the sequential physical transitions and chemical reactions occurring at specific temperature intervals. The observed mass variations arise from processes such as evaporation, decomposition, oxidation, or bond rearrangements at elevated temperatures. TGA typically operates up to around 1200 °C, either in inert atmospheres like nitrogen or argon or in reactive atmospheres such as air or oxygen. The kinetics of these thermally induced processes are strongly influenced by the molecular structure of the material, making TGA a precise tool for understanding thermal stability and composition

**Applications:** Thermogravimetric analysis (TGA) finds wide application across multiple scientific and industrial fields due to its ability to measure weight changes under controlled thermal conditions. It is extensively used for the thermal characterization of polymers, providing insights into their decomposition behaviour and stability. In metallurgy, TGA helps determine the composition of alloys and complex mixtures. It is also an essential tool in assessing the purity and thermal stability of both primary and secondary reference standards. Beyond these, the technique is applied to evaluate the moisture content of organic and inorganic materials, industrial feedstocks, pharmaceuticals, and food products. TGA further aids in identifying the optimum drying temperatures and in validating the accuracy of gravimetric methods. Additionally, it plays a role in corrosion research, where mass variations reflect material degradation under high-temperature conditions. Importantly, TGA is also utilized for studying the kinetics of isothermal reactions, offering valuable information about reaction mechanisms and rates under constant temperature.

#### 2.2.9 Cytotoxicity Test:

Cytotoxicity assays are laboratory-based methods developed to measure the extent to which a chemical, drug, or environmental substance can harm living cells. The concept combines the study of cells ("cyto") with the study of harmful effects ("toxicity"), effectively describing substances that act as poisons to cells [20]. These assays involve controlled exposure of cells to the substance of interest, followed by detailed observation of changes in cell viability, growth, or function. Within pharmaceutical research, cytotoxicity assays are indispensable tools, particularly in cancer drug discovery, where they help identify agents that selectively destroy malignant cells while sparing normal tissues. They are equally important in toxicological testing, as they provide a reliable way to evaluate the safety of consumer products such as cosmetics, food ingredients, and industrial materials without resorting exclusively to animal models. In environmental studies, cytotoxicity assays are used to investigate the biological effects of pollutants, including industrial effluents, agricultural chemicals, and heavy metals. The insights gained from such studies not only help quantify ecological risks but also guide the establishment of policies and standards that protect both the environment and public health.

Working Principle: The working principle of cytotoxicity testing revolves around evaluating how cells respond to exposure from a particular chemical, drug, or environmental factor. One fundamental method involves examining cell membrane integrity. Healthy cells maintain intact membranes, but when they die, especially through necrosis, the membrane ruptures, releasing cellular contents into the surrounding environment. The Lactate Dehydrogenase (LDH) release assay is commonly used here, where detection of LDH in the culture medium serves as a measurable indicator of cell damage. Another widely applied strategy measures metabolic activity, which is a hallmark of living, functional cells. Tests such as the MTT and WST assays rely on dyes that are metabolized only by active cells into a colored product; the intensity of the color directly correlates with the number of viable cells present. Additionally, cytotoxicity can be assessed through the detection of apoptosis, a regulated and programmed form of cell death distinct from necrosis. Assays targeting apoptosis often identify biochemical events such as caspase activation or externalization of phosphatidylserine on the cell membrane. By differentiating between necrosis and apoptosis, cytotoxicity tests provide detailed insights into the mechanisms of cell death, supporting their use in pharmaceutical, toxicological, and biomedical studies.

Applications: Cytotoxicity testing plays a vital role in ensuring the safety and effectiveness of products across multiple sectors. In the pharmaceutical field, it serves as a key step in screening drug candidates, helping to identify compounds that selectively eliminate diseased cells while sparing healthy tissues. This process not only enhances therapeutic precision but also streamlines drug discovery by eliminating unsuitable candidates early. In the case of medical devices, cytotoxicity testing is a regulatory requirement for materials that will come into direct contact with the human body, including implants, dental applications, and contact lenses. Such testing safeguards patients by confirming that these devices do not leach harmful or toxic substances. Similarly, in the cosmetics and chemical industries, cytotoxicity assays are applied to evaluate the safety of ingredients in products such as creams, serums, and

skin-care formulations. These in vitro techniques provide a reliable and ethical alternative to traditional animal testing, ensuring consumer safety while supporting modern regulatory and ethical standards.

## 2.3 Electrochemical Characterization Techniques:

Electrochemical characterization are the most powerful and versatile methods for evaluating materials, particularly in the fields of energy storage, catalysis, and sensing. Its importance lies in its ability to probe fundamental processes such as charge transfer, electron movement, ionic transport through electrolytes, and mass transport at the electrode–electrolyte interface [21]. These processes directly influence the performance and durability of devices such as batteries, supercapacitors, electrochemical sensors, and fuel cells. To carry out such studies, an electrochemical workstation, also known as an electrochemical analyzer, is employed, as depicted in **Fig. 2.13**. This sophisticated unit integrates a variety of techniques, including cyclic voltammetry (CV), chronoamperometry (CA), differential pulse voltammetry (DPV), chronopotentiometry (CP), galvanostatic charge–discharge (GCD), and electrochemical impedance spectroscopy (EIS). Each method provides unique insights: for instance, CV is often used to understand redox mechanisms, GCD helps in determining energy and power densities in storage devices, and EIS reveals charge transfer resistance and ion diffusion pathways.

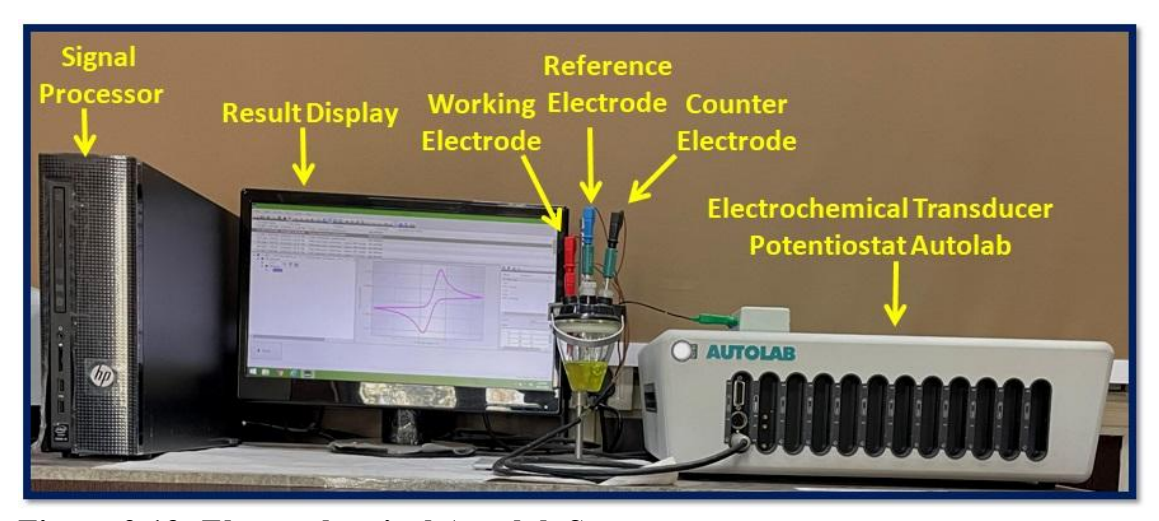


Figure 2.13: Electrochemical Autolab Setup

Electrochemical signals namely potential, current, and charge, form the foundation of these analytical methods. By carefully measuring these signals under controlled conditions, researchers can extract valuable information about an analyte's concentration, its chemical reactivity, and the kinetics of the reactions it undergoes. In addition, electrochemical characterization directly contributes to advancing analytical chemistry, a field dedicated to both qualitative and quantitative determination of matter. The integration of electrochemical techniques into analytical chemistry provides high sensitivity and selectivity, allowing researchers not only to study the composition of materials but also to explore their functional behaviors in real-world applications. As a result, electrochemical characterization continues to be indispensable in both fundamental research and applied sciences, offering detailed insights that shape the development of new technologies for sustainable energy, environmental monitoring, and biomedical diagnostics.

### 2.3.1 Cyclic Voltammetry (CV):

Cyclic Voltammetry (CV) is one of the most fundamental and widely applied electrochemical techniques for studying material behaviour. In this method, a potential is applied to the system in a cyclic manner, sweeping from positive to negative and then back again, while simultaneously recording the corresponding current response [22]. The output, known as a cyclic voltammogram, reveals distinct oxidation and reduction peaks, which provide key insights into the redox properties of the material. These peaks allow researchers to identify the potential at which a substance undergoes oxidation or reduction, while also highlighting capacitive characteristics of the electrode. The experiment operates by applying a ramp signal, where the forward scan is driven by a positive ramp (with a positive slope), followed by a negative ramp in the reverse direction, producing a mirror image of the voltammogram in the second half-cycle. As the system seeks equilibrium through redox processes, it follows a closed cyclic pattern. Analysis of CV curve to determine whether the reactions are reversible, irreversible, or quasi-reversible. The scan rate, which measures how fast the potential is swept (in volts per second), strongly influences the shape and characteristics of the voltammogram. Adjusting the scan rate, which can range from fractions of a millivolt per second to several hundred volts per second, helps uncover important details about the electrochemical kinetics of the electrode. For instance, if the faradaic current increases with higher scan rates, it indicates enhanced rate capability and superior pseudocapacitive behaviour of the material. At higher scan rates, the number of redox events also increases, due to the availability of electroactive species at the working electrode's surface.

The scan rate in cyclic voltammetry significantly influences both the sensitivity of detection and the reliability of data interpretation. At high scan rates, redox peaks are prominent due to limited time for secondary chemical reactions to occur. However, at slower scan rates, the extended time window allows intermediates produced during reduction or oxidation to react further. If these products lack electroactivity, they fail to contribute to the current signal, resulting in missing or diminished peaks in the voltammogram. This phenomenon makes accurate interpretation of the electrochemical process more challenging.

The Randles-Ševčík equation provides a mathematical framework for calculating peak current **Eq. [2.2]**:

$$I_p = (2.69 \times 10^5) n^{3/2} A C D^{1/2} \sqrt{\nu}$$
 [2.2]

Electrochemical investigations of the as-fabricated electrode is carried by the Randles—Sevcik equation, where Ip represents the peak current (anodic/cathodic), n the number of electrons exchanged, A the electroactive surface area, C the redox species concentration, D the diffusion coefficient, and v the scan rate. Together, these parameters link the measurable current response to the inherent electrochemical properties of the system, enabling both qualitative and quantitative assessments. Cyclic voltammetry is also highly valuable for studying kinetic and mechanistic aspects of reactions. It allows calculation of the electron transfer coefficient, rate constant, and identification of the rate-limiting step in the electrochemical process. The spacing between the anodic and cathodic peak potentials reveals diffusion effects and electron transfer kinetics. Additionally, the ratio of the anodic to cathodic peak currents provides

information about the reversibility of the system: a ratio of 1 indicates a fully reversible process, a ratio deviating from 1 indicates quasi-reversibility, and the absence of one peak altogether signals an irreversible reaction where the product does not revert to its original state. Importantly, CV experiments are generally carried out in an unstirred solution. Stirring disrupts the diffusion-controlled process, leading to the replacement of sharp peak currents with steady limiting currents. This fundamental principle is crucial for maintaining the integrity of CV data, particularly when investigating electrode materials, catalytic reactions, and redox-active molecules.

### 2.3.2 Differential Pulse Voltammetry (DPV):

Differential Pulse Voltammetry (DPV) is an advanced electroanalytical method where current is measured twice during each potential cycle, which consists of two pulses [23]. The difference between these two current measurements is plotted against the applied potential, producing a voltammogram that typically displays a peak-shaped response. This approach effectively minimizes capacitive or background currents, making the technique highly reliable for chemical analysis. One of the major advantages of DPV is its exceptional sensitivity, as the dual sampling method allows detection of analytes even at trace levels. Owing to its low detection and quantification limits, DPV is widely recognized as both a sensitive and selective technique. While DPV is primarily applied for precise quantitative analysis, cyclic voltammetry (CV), in comparison, is more suitable for qualitative studies, such as investigating redox mechanisms and reaction pathways.

### 2.3.1 Electrochemical Impedance Spectroscopy (EIS):

Electrochemical impedance spectroscopy (EIS) is a powerful diagnostic technique used to determine the impedance characteristics of an electrochemical cell [24]. The method involves applying a small-amplitude sinusoidal alternating current (AC) voltage to the electrode system under study. The resulting current response is measured in terms of both amplitude and phase angle relative to the applied signal. Using the relationship defined by Ohm's law, the impedance is then calculated. Since impedance is frequency-dependent, a complete impedance spectrum is generated by scanning across a broad frequency range.

EIS experiments are typically performed under controlled parameters, such as carefully selected AC voltage perturbation (expressed in millivolts, rms), frequency domain, and data acquisition rates, usually at room temperature. Electrochemical behaviour at the electrode–electrolyte interface, as well as redox activity, is frequently represented through an equivalent electrical circuit composed of resistors, capacitors, and inductors. This model allows a clear evaluation of the contributions from each component of the electrochemical system. In the widely used Randles equivalent circuit, the essential elements include the solution resistance (Rs), the double-layer capacitance (Cdl) at the electrode surface, the charge-transfer resistance (Rct), and the Warburg element (Zw), which accounts for diffusion effects at the interface. Since an ideal capacitor is rarely observed experimentally, a constant phase element (CPE) is often incorporated to capture the non-ideal capacitive behaviour caused by surface heterogeneity, roughness, or porosity of the electrode. Nyquist plots obtained from experimental data provide the primary reference for identifying and fitting these circuit elements, with the equivalent circuit constructed based on the specific shape of the curve. The appearance of the

Nyquist plot strongly depends on the electrode material and its electrochemical environment; for instance, it may show a single semicircle, multiple semicircles, or combinations such as half-semicircles, each corresponding to distinct electrochemical processes within the electrode or electrolyte.

In electrochemical impedance spectroscopy, the impedance response can be separated into two components: the real part (Zreal) and the imaginary part (Zimag). When these values are plotted with Zreal on the X-axis and Zimag on the Y-axis, the resulting graph is known as a Nyquist plot. Each point on this plot corresponds to the impedance measured at a particular frequency. Importantly, Zimag values are negative, which is why the curve is typically represented below the X-axis. In this representation, the right side of the X-axis corresponds to lower frequencies, while higher frequencies shift toward the left side of the plot. The impedance can also be visualized as a vector of magnitude |Z|, with the angle it makes with the X-axis defined as the phase angle, offering insights into resistive and capacitive contributions to the system. Alternatively, the Bode plot offers another way of presenting impedance results and is often preferred in engineering analysis. This approach separates the data into two distinct logarithmic plots: one showing the magnitude of impedance against frequency and the other illustrating the phase angle as a function of frequency. Together, these plots allow a comprehensive evaluation of frequency-dependent properties, making the Bode representation particularly useful for studying dynamic electrochemical processes.

Impedance phenomena can be classified into Faradaic and non-Faradaic responses. Faradaic impedance originates from charge transfer across the electrode surface during redox reactions, and the resulting Faradaic current provides a basis for quantitative analysis of electroactive species. On the other hand, non-Faradaic impedance arises without electron transfer, being governed instead by the charging and discharging of the double-layer capacitance at the electrode–electrolyte interface. Distinguishing between these two responses is crucial for understanding whether a system's behaviour is controlled by chemical reaction kinetics or purely capacitive processes.

### References

- [1] V. Vatanpour, S.A. Naziri Mehrabani, B. Keskin, N. Arabi, B. Zeytuncu, I. Koyuncu, A comprehensive review on the applications of boron nitride nanomaterials in membrane fabrication and modification, Industrial & Engineering Chemistry Research, 60 (2021) 13391-13424.
- [2] S. Goudarzi, Nano-engineered 2D hBN-Based Materials for Environmental and Healthcare Applications, in, Toronto Metropolitan University, 2022.
- [3] G. Darabdhara, P. Borthakur, P.K. Boruah, S. Sen, D.B. Pemmaraju, M.R. Das, Advancements in Two-Dimensional Boron Nitride Nanostructures: Properties, Preparation Methods, and their Biomedical Applications, Journal of Materials Chemistry B, (2025).
- [4] R. Singhal, Growth and Doping of Hexagonal Boron Nitride Films by Chemical Vapor Deposition, in, Oklahoma State University, 2022.
- [5] C. Maestre, B. Toury, P. Steyer, V. Garnier, C. Journet, Hexagonal boron nitride: a review on selfstanding crystals synthesis towards 2D nanosheets, Journal of Physics: Materials, 4 (2021) 044018.
- [6] J.J. Varughese, Predictive modelling of hexagonal boron nitride nanosheets yield through machine and deep learning: An ultrasonic exfoliation parametric evaluation, Results in Engineering, 25 (2025) 104127.

- [7] N. Vázquez-Canales, J. García-Serrano, Sonochemical amino-functionalization of hexagonal boron nitride nanosheets produced by liquid phase exfoliation, Journal of Molecular Liquids, 415 (2024) 126384.
- [8] N. Abid, A.M. Khan, S. Shujait, K. Chaudhary, M. Ikram, M. Imran, J. Haider, M. Khan, Q. Khan, M. Maqbool, Synthesis of nanomaterials using various top-down and bottom-up approaches, influencing factors, advantages, and disadvantages: A review, Advances in colloid and interface science, 300 (2022) 102597.
- [9] G. Yang, S.-J. Park, Conventional and Microwave Hydrothermal Synthesis and Application of Functional Materials: A Review, Materials, 12 (2019) 1177.
- [10] G. Yang, H. Wang, N. Wang, R. Sun, C.-P. Wong, Hydrothermal exfoliation for two-dimension boron nitride nanosheets, in: 2018 IEEE 68th Electronic Components and Technology Conference (ECTC), IEEE, 2018, pp. 1421-1426.
- [11] L. Besra, M. Liu, A review on fundamentals and applications of electrophoretic deposition (EPD), Progress in materials science, 52 (2007) 1-61.
- [12] A. Wilson, Elements of X-ray Diffraction by BD Cullity, in, International Union of Crystallography, 1957.
- [13] A. Mohammed, A. Abdullah, Scanning electron microscopy (SEM): A review, in: Proceedings of the 2018 international conference on hydraulics and pneumatics—HERVEX, Băile Govora, Romania, 2018, pp. 7-9.
- [14] Q. Yu, M. Legros, A. Minor, In situ TEM nanomechanics, Mrs Bulletin, 40 (2015) 62-70.
- [15] A. Mandru, J. Mane, R. Mandapati, A Review on UV-visible spectroscopy, Journal of Pharma Insights and Research, 1 (2023) 091-096.
- [16] A. Orlando, F. Franceschini, C. Muscas, S. Pidkova, M. Bartoli, M. Rovere, A. Tagliaferro, A comprehensive review on Raman spectroscopy applications, Chemosensors, 9 (2021) 262.
- [17] C. Berthomieu, R. Hienerwadel, Fourier transform infrared (FTIR) spectroscopy, Photosynthesis research, 101 (2009) 157-170.
- [18] F.J. Giessibl, Advances in atomic force microscopy, Reviews of modern physics, 75 (2003) 949.
- [19] R.B. Prime, H.E. Bair, S. Vyazovkin, P.K. Gallagher, A. Riga, Thermogravimetric analysis (TGA), Thermal analysis of polymers: Fundamentals and applications, (2009) 241-317.
- [20] M. Ghasemi, T. Turnbull, S. Sebastian, I. Kempson, The MTT assay: utility, limitations, pitfalls, and interpretation in bulk and single-cell analysis, International journal of molecular sciences, 22 (2021) 12827.
- [21] Y.S. Choudhary, L. Jothi, G. Nageswaran, Electrochemical characterization, in: Spectroscopic Methods for Nanomaterials Characterization, Elsevier, 2017, pp. 19-54.
- [22] N. Elgrishi, K.J. Rountree, B.D. McCarthy, E.S. Rountree, T.T. Eisenhart, J.L. Dempsey, A practical beginner's guide to cyclic voltammetry, Journal of Chemical Education, 95 (2018) 197-206.
- [23] A. Molina, J. González, Pulse voltammetry in physical electrochemistry and electrocanalysis, Monographs in electrochemistry, (2016).
- [24] O. Gharbi, M.T. Tran, B. Tribollet, M. Turmine, V. Vivier, Revisiting cyclic voltammetry and electrochemical impedance spectroscopy analysis for capacitance measurements, Electrochimica Acta, 343 (2020) 136109.

# Chapter 3

## Strategic Tailoring of Hydrothermal Parameters to Optimize Two-Dimensional Architecture of Hexagonal Boron Nitride (h-BN) for Improved Electrochemical Performance

This chapter focuses on addressing and overcoming the crucial challenges in achieving scalable exfoliation of few-layered hexagonal boron nitride nanosheets (hBNNS) attributable to the partial ionic nature together with intrinsic van der Waals bonding. Conventional exfoliation techniques established for fabricating hBNNS from bulk hBN are often time-consuming, labour-intensive, and operationally complex that poses potential obstacle for large-scale production. These strenuous synthesis techniques fail to harness optimum 2D architecture of hexagonal boron nitride (hBN, also known as white graphene) as promising inorganic layered matrix material for electroanalytical applications. Herein, Hydrothermal approach, leveraging the Lewis acid-base coordination chemistry was employed by synergistically adjusting the temperature-time variables to achieve an optimized two-dimensional morphology of hBN nanosheets. To assess structural integrity, vibrational dynamics, optical transitions, surface topography, and chemical bond interactions, a detailed investigation was conducted into using an array of techniques, including X-ray diffraction (XRD), Raman spectroscopy, UV-Visible spectroscopy, scanning electron microscopy (SEM), transmission electron microscopy (TEM), atomic force microscopy (AFM), and Fourier-transform infrared spectroscopy (FT-IR) respectively. To conduct electrochemical investigations, uniform hBNNS/ITO electrodes synthesized distinctly were fabricated using cost-effective and reproducible electrophoretic deposition (EPD) technique. Electrochemical characteristics were thoroughly analyzed by cyclic voltammetry (CV), differential pulse voltammetry (DPV), and electrochemical impedance spectroscopic performance. The cyclic voltammogram of effectively optimized h-BNNS demonstrated a 69.96% improvement in the redox peak current and a 71.04% increase in the electroactive surface area compared to bulk h-BN. The substantially optimized h-BNNS also exhibited reduced charge transfer resistance, and improved Warburg admittance, holding great promise for electroanalytical applications.

The research findings detailed in this chapter have been published in a scientific journal: "Enhanced Electrochemical Performance of Hydrothermally Exfoliated Hexagonal Boron Nitride Nanosheets for Applications in Electrochemistry"

Journal of The Electrochemical Society, 2021 (168) 056512

#### 3.1 Introduction:

Low-dimensional materials, widely known as Nanomaterials, are characterized by spatial confinement of charge carriers within limits of de Broglie wavelength (geometric dimensions: 1-100 nm), which distinguishes them from their bulk counterpart materials [1]. Nanostructured materials have been revolutionizing a plethora of disciplines and emerging technologies on account of their tuneable sizedependent attributes. Tailored physicochemical properties in low-dimensional materials emanate from the fundamental physics concept of nanoscale quantum confinement of charge carriers in discrete energy levels that approach the exciton Bohr radius, thereby transitioning to a quantized density of states from continuous states in their bulk counterpart [2]. The spatial architecture of nanostructured materials is fundamentally governed by the confinement of their geometric dimensions, which exhibits a remarkable influence on their electronic structure, functional behaviour, and physicochemical properties. This principle forms the basis for their primary classification into four distinct categories: zero-dimensional (0D), one-dimensional (1D), two-dimensional (2D), and three-dimensional (3D) nanomaterials, each characterized by the extent of electron mobility permitted within the nanoscale framework [3].

Ultrathin 2D nanomaterials have emerged as an indispensable class of materials, and their unmatched potential is now established in condensed matter physics, materials science, and electrochemistry applications [4]. They serve as prime base matrices for electrode systems that demand high electron mobility, surface reactivity, layerdependent properties, exceptional surface-to-volume ratios, and outstanding electrical conductivity, and design versatility. In contrast to the alternative counterparts of 2D nanomaterials, 2D materials offer a synergistic combination of high surface area, tuneable surface chemistry, lateral charge transport, and structural continuity, facilitating efficient biomolecule immobilization, while maintaining favourable electronic properties unlike 0D, 1D, and 3D systems that exhibits limited surface accessibility, lack planar continuity, complex functionalization, diffusion limitations and aggregation issues [5]. The transformative discovery of graphene stimulated an extensive interest of researchers and the scientific community towards the exploration of a wide and versatile class of 2D nanomaterials. The emerging and expansive diversity of 2D nanostructured systems spanning transition metals, transition metal oxides, transition metal dichalcogenides, group III-V compounds, mono elemental semiconductors, layered double hydroxides (LDHs), MXenes, 2D polymers, metalorganic frameworks (MOFs), covalent-organic frameworks (COFs), and perovskites, each class characterized by unique, unprecedented properties, that drives technological advancements to transform the future of research and innovation [5].

A fascinating discovery of graphene has compelled potential growth in its isostructural inorganic counterpart, hexagonal boron nitride (h-BN), extensively acquainted as "white graphene" [6]. Hexagonal boron nitride is a light-weight semiconductor that exhibits a peculiar wide bandgap of ~ 6 eV in contrast to materials of the group III-Nitride family. Alternate placement of boron (B) and nitrogen (N) atoms, substituting carbon (C) atoms in a honeycomb-like network, consisting of in-plane sp²-bonded trigonal geometry demonstrating covalent graphite-like sheets with out-of-plane relatively weak van der Waals interaction stimulated by partially ionic bonding between

B- and N- atoms [7]. Their astounding chemical and thermal stability, enduring temperature up to ~ 1100°C, establishes them as a durable and coherent protective scaffold with enduring catalytic performance [8]. Exceptional mechanical reinforcement exhibited by hBN ensures structural integrity, preventing nanoparticle agglomeration, deformation, or collapse under mechanical or thermal stress while maintaining uniform dispersion, enabling optimal performance [9, 10]. Intrinsic low dielectric constant of hexagonal boron nitride reduces capacitive coupling and lower dielectric polarization, which directly translates to minimal energy dissipation during signal transmission, leading to improved signal-to-noise ratio (SNR), leading to better sensitivity, reliability, and reproducibility of the detection system [11]. The robust barrier properties of hexagonal boron nitride nanosheets (hBNNS) due to its dense atomic packing, chemical inertness, and hydrophobic nature serve as a critical protective impermeable layer under ambient, high-humidity, or chemically reactive conditions. Moreover, the low toxicity profile of hBN enables its high suitability for biomedical applications that offer a large surface area and functionable edges, allowing for the efficient loading and targeted delivery of therapeutic agents into specific cells, enhancing treatment specificity while minimizing off-target effects [12]. Under ambient oxidative environments, h-BN does not form stable oxides or fluorides due to the lack of reactive intermediates in them, reflecting its superior chemical inertness, which enhances its thermal and oxidative stability.

However, the synthesis of ultrathin 2D hexagonal boron nitride nanosheets (hBNNS) is intrinsically constrained by strong interlayer van der Waals forces, reinforced by the partial ionic character of B–N bonds, which makes exfoliation more challenging than in graphene, resulting in low yield and poor thickness control [13]. Due to its intrinsic structural integrity, which depicts shorter interlayer spacing and stronger electrostatic interactions between partially ionic B–N bonds, the intercalation of foreign atoms, ions, or molecules into the layered structure of hBN is significantly hindered. While well-established synthesis strategies have been extensively explored for graphene production, the synthesis of hexagonal boron nitride nanosheets (h-BNNSs) remains in its early stages of development [14]. Nevertheless, h-BNNSs are now gaining traction, with current research focusing on both conventional top-down exfoliation and bottom-up growth mechanisms [15].

# 3.1.1 Bottom-Up Approach for Synthesis of Two-Dimensional (2D) Hexagonal Boron Nitride Nanosheets (h-BNNS)

Bottom-up approaches for synthesizing 2D h-BNNS directly entail the controlled chemical reaction of boron- and nitrogen-rich molecular precursors, such as melamine (C<sub>3</sub>H<sub>6</sub>N<sub>6</sub>), urea (CH<sub>4</sub>N<sub>2</sub>O), diboron trioxide (B<sub>2</sub>O<sub>3</sub>), boric acid (H<sub>3</sub>BO<sub>3</sub>), and ammonia gas (NH<sub>3</sub>) [16]. This route enables in situ formation, nucleation and controlled growth of h-BN at the atomic level through techniques like chemical vapor deposition (CVD), often allowing better control over crystallinity, thickness, morphology, and lateral size of the nanosheets. Compared to top-down exfoliation methods, bottom-up strategies offer greater control over thickness, crystallinity, lateral dimensions, and defect density of the resulting 2D sheets. However, these processes can be more complex, requiring specialized equipment and careful optimization of reaction parameters, making them less scalable compared to top-down methods.

Wet chemical synthesis incorporates a diverse solution-phase strategy for fabricating 2D h-BN nanosheets, including solvent evaporation and template-assisted processes [17]. Typical procedure comprises the reaction between boric acid (H<sub>3</sub>BO<sub>3</sub>) and urea (CH<sub>4</sub>N<sub>2</sub>O), which serve as boron- and nitrogen-rich precursors, respectively, at a molar mixture of 1:24 ratio. to ensure homogeneous dispersion and enhanced molecular interaction, it was first subjected to ultrasonication followed by drying and thermal treatment at 950 °C under a nitrogen (N2) atmosphere for 5 hours. This hightemperature pyrolysis initiates a series of decomposition and recombination reactions, ultimately fabricating 2D h-BN nanosheets. This sequence of reactions supports the bottom-up growth of 2D h-BN nanosheets through a gas-solid phase reaction route, where intermediate gases (B<sub>2</sub>O<sub>3</sub> and NH<sub>3</sub>) participate in the in-situ formation of BN layers. This approach not only enables the scalable synthesis of ultrathin h-BN but also provides control over phase purity, crystal orientation, and morphology. However, despite its advantages, this method exhibited several limitations, such as limited control over lateral size and thickness, high-temperature requirement, residual impurities, low crystallinity, and inconsistent reproducibility.

**Pulsed laser deposition (PLD)** employs high-energy laser beam often in the ultraviolet or infrared range for rapid, localized heating that generates a stoichiometrically accurate plasma plume from the target material, thereby addressing several limitations commonly associated with the conventional PVD method, including the inability to preserve complex stoichiometry in thin films due to the differential vapor pressures of constituent elements. In CO<sub>2</sub> laser PLD ( $\lambda \approx 10,600$  nm), Sajjad et al. deposited 2D h-BN nanosheets on a Si (100) wafer, cleaned and heated to 400°C, placed 3 cm from a pyrolytic h-BN target in a high vacuum chamber. Laser ablation generated a B<sup>+</sup> and N<sup>-</sup> plasma, forming nanosheets via surface bonding [18]. However, the method suffers from scalability constraints, high vacuum requirements, substrate heating, non-uniform films, and particulate-induced defects.

High-temperature solid-state reactions between boron- and nitrogen-rich precursors produce 2D hexagonal boron nitride (h-BN) sheets through chemical interactions without a liquid medium. At elevated temperatures, solid precursors transform into gaseous states, generating sufficient vapor pressure for efficient reactions that yield high-purity 2D h-BN nanosheets. However, high temperatures and flowing gases can introduce structural defects, which create mid-band states near HOMO or LUMO edges, enhancing electron transitions, electrochemical reactions, and sensing performance. Solid-state reaction carried out by Shen et al. to synthesize 2D hexagonal boron nitride (h-BN) exhibited one-step calcination using melamine borate (C3H6N6·xH3BO3) as a single precursor. Melamine borate was prepared by dissolving 4 g of melamine (C3H6N6) in 85 °C water, adding 1 g of boric acid (H3BO3), stirring for 1 hour, then filtering and drying the solution [19]. The precursor was heated to 900 °C for 4 hours in a reducing atmosphere, yielding defect-rich 2D h-BN nanosheets. Besides production of high-purity and crystalline nanostructures, this method possess various disadvantages for synthesis requiring extremely high temperatures (≥1600 °C) i.e. energy-intensive, limit compatibility with some substrates, defect generation, requires inert or reactive gas environments limited scalability and potential safety concerns.

Chemical Vapour Deposition (CVD) is a highly controlled thin-film fabrication technique that enables the growth of atomically precise hexagonal boron nitride (h-BN) layers by decomposing volatile precursors on a heated substrate [20]. This method is particularly advantageous for producing uniform, high-crystallinity h-BN sheets, often approaching the ideal monolayer or few-layer thickness, by meticulously regulating growth parameters such as temperature, pressure, and precursor flow rates. For instance, Song et al. successfully synthesized large-area h-BN films comprising 2-5 atomic layers, demonstrating the technique's capability for scalable and precise nanofabrication. The primary strength of CVD lies in its ability to fabricate defect-free, continuous h-BN films with excellent structural order, making it ideal for electronic and optoelectronic applications. However, the method exhibits several challenges as it typically demands extreme environmental conditions, including high temperatures, ultra-high vacuum systems, and costly catalytic or dielectric substrates, which can limit its cost-effectiveness and scalability. Despite these constraints, CVD remains a benchmark technique for the synthesis of high-quality h-BN nanosheets when purity and atomic precision are critical.

# 3.1.2 Top-Down Approach for Synthesis of Two-Dimensional (2D) Hexagonal Boron Nitride Nanosheets (h-BNNS)

In contrast, top-down approaches refer to exfoliation-based methods wherein bulk crystalline hexagonal boron nitride (h-BN) is mechanically or chemically broken down into few-layer or monolayer 2D h-BN nanosheets. These methods typically involve applying external physical forces, such as ultrasonication, shear mixing, or ball milling, or chemical intercalation processes that weaken and delaminate the stacked layers by overcoming the strong interlayer van der Waals interactions in bulk h-BN [21].

**Liquid-phase exfoliation (LPE)** refers to the exfoliation of bulk h-BN in the presence of a liquid medium, which not only acts as a dispersing agent but also facilitates energy transfer and minimizes sheet aggregation by disrupting the weak van der Waals forces that hold the adjacent atomic layers together. The liquid medium can be polar aprotic solvents such as N-methyl-2-pyrrolidone (NMP), dimethylformamide (DMF), isopropyl alcohol (IPA), ethylene glycol, ethanol, or even deionized water, each chosen based on their surface energy compatibility with h-BN to maximize exfoliation efficiency. To overcome the interlayer cohesive forces, various external driving mechanisms are applied, including ultrasonication, microwave irradiation, chemical assistance, or solvothermal treatment. These forces effectively delaminate the layers, resulting in the formation of well-dispersed, high-crystalline 2D hexagonal boron nitride (h-BN) nanosheets. Nevertheless, this technique suffers from very low concentrations of h-BN nanosheet after 10 hours of sonication in DMF, yielding approximately 0.5-1 mg from 1 g of bulk h-BN. Contrary to earlier assumptions considering the water insolubility of h-BN, recent studies confirm that h-BN can be effectively exfoliated in water through prolonged ultrasonication in aqueous environments [22].

**Ultrasonication-assisted exfoliation** involves the use of high-frequency ultrasonic waves in a liquid medium, either organic or aqueous, to break the weak van der Waals forces between adjacent layers. The fundamental driving force behind this technique is

the acoustic cavitation effect—the rapid formation, growth, and collapse of microscopic bubbles induced by pressure fluctuations within the solvent. This generates localized high-energy zones that initiate exfoliation. Additionally, solvent polarity effects and dipole-dipole interactions between solvent molecules and polarized h-BN surfaces further enhance the exfoliation efficiency. For polar solvents, nucleophilic interactions between electronegative atoms (e.g., oxygen in functional groups like carbonyl or ether) and partially positive boron atoms at the h-BN edges lower the surface energy, facilitating layer separation. Yola et al. demonstrated successful exfoliation of h-BN by dispersing 100 mg of bulk powder in 50 mL of IPA, heating the suspension at 50 °C with stirring for 24 h, followed by 20 h of ultrasonication. SEM images confirmed reduced thickness and lateral size, validating exfoliation [23, 24]. This technique remains a promising and adaptable strategy for large-scale nanosheet production with high-quality mesoporosity and high surface area, offering solvent tailoring possibilities via Hansen solubility parameters (HSP) and Coleman theory to minimize exfoliation energy. However, optimization of solvent systems and processing parameters is crucial to balance exfoliation efficiency, lateral dimension retention, and structural purity that can potentially limit their applicability.

Microwave-assisted exfoliation leverages high-energy dielectric heating in a liquid medium to transform bulk hexagonal boron nitride (h-BN) into 2D hexagonal boron nitride (h-BN) nanosheets. This process uses microwave radiation to drive solvent molecules, such as ethanol or water, into h-BN layers, acting as spacers to weaken van der Waals bonds and facilitate intercalation through solvent/h-BN interactions. Notably, the microwave absorption efficiency is highly dependent on the chemical composition—particularly the presence of oxygen-containing groups; although pristine h-BN lacks such groups, its excellent thermal conductivity compensates by enabling uniform heat distribution at the molecular level. A microwave-assisted synthesis strategy was reported in 2018, a mixture of h-BN (0.5 g), ethanol (100 ml), and 1 M NaOH was sonicated, then irradiated in an 800 W household microwave oven for 2 minutes, yielding high-quality, hydroxyl-functionalized 2D h-BN nanosheets with high surface area, as Na<sup>+</sup> and OH<sup>-</sup> ions enhanced layer separation [25]. The mechanism relies on h-BN's high thermal conductivity and lack of oxygen-containing groups, enabling efficient absorption and dissemination of microwave energy for swift exfoliation in minutes, unlike the time- and energy-intensive ultrasonication. The key advantages of this method include its speed, simplicity, cost-effectiveness, and green chemistry orientation, making it highly attractive for large-scale applications. However, a limitation lies in the dependency of material on microwave absorption capacity, potential defect introduction from rapid heating, and challenges in controlling nanosheet thickness and size, which may affect exfoliation uniformity. Additionally, while rapid heating aids in delamination, it may also impose the possibility of overheating or partial degradation if not properly controlled.

Chemical reaction-based exfoliation employs a facile, cost-effective sequential chemical-mediated reaction to break the weak van der Waals forces between layers, without requiring high temperatures or vacuum conditions to produce 2D hexagonal boron nitride (h-BN) nanosheets. The process occurs at room temperature in a wet chemical environment, where chemical compounds formed during reactions act as spacers to separate h-BN layers. A representative protocol, reported by Adeel et al.,

exfoliated h-BN by stirring 2 g of h-BN powder in 50 ml of H<sub>2</sub>SO<sub>4</sub> for 30 minutes, cooling the suspension in an ice bath, adding 1 g of KMnO<sub>4</sub> with 12 hours of stirring, and then introducing 10 ml of 30% H<sub>2</sub>O<sub>2</sub> for 5 hours [26]. The mechanism involves three steps: (1) intercalation of H<sup>+</sup> ions from sulfuric acid between the h-BN layers to expand interlayer spacing; (2) formation of MnO<sub>2</sub> nanoparticles through the redox reaction of KMnO<sub>4</sub> and H<sub>2</sub>SO<sub>4</sub>, which further expanding the lattice structure and preventing re-stacking; and (3) generation of O<sub>2</sub> gas from the reaction between H<sub>2</sub>O<sub>2</sub> and MnO<sub>2</sub>, which provided the substantial mechanical force for layer exfoliation. This process enabled the successful and scalable production of few-layered h-BN nanosheets owing to its simplicity, low energy demand. However, potential drawbacks include residual chemical contamination, the necessity for thorough post-synthesis purification, the use of hazardous chemicals like H<sub>2</sub>SO<sub>4</sub> and H<sub>2</sub>O<sub>2</sub>, potential defects from chemical interactions, challenges in controlling nanosheet thickness and size, and possible oxidative damage to the basal plane, which could alter intrinsic properties of h-BN.

Mechanochemical exfoliation, conducted either in the presence (wet milling) or absence (dry milling) of a liquid medium by mild shear forces generated during the milling process, effectively overcomes the weak van der Waals forces between h-BN layers. In this technique, exfoliation is driven by wet milling offers added advantages as the liquid medium acts as a lubricant, preventing particle re-welding and enhancing the exfoliation efficiency through solvent polarity effects and gravitational shear. Key operational parameters such as the size and type of milling balls, milling duration, and the physicochemical compatibility of the solvent with h-BN significantly influence the quality of exfoliation. For example, ethanol owing to its moderate polarity (4.3), low toxicity, high volatility, and compatible surface energy has been successfully used as a milling medium in a mechanochemical protocol to yield high-quality 2D h-BN sheets. While extended milling time beyond this point caused undesirable agglomeration. This approach synthesized hBNNS with high crystallinity, low defect formation, high yield, and size uniformity of exfoliated nanosheets. Yet, it exhibits certain limitations, including the need for careful control over milling time to prevent particle reagglomeration and the risk of mechanical damage to the crystal structure at prolonged durations.

Hydrothermal and solvothermal-assisted exfoliation process initiates at elevated temperatures and autogenous pressures within sealed Teflon-lined autoclaves, providing a highly controlled reaction environment. These conditions, when combined with ultrasonication, significantly enhance the exfoliation efficiency by weakening the strong interlayer interactions inherent in bulk h-BN. Herein, elevated temperature and pressure enable solvent molecules or ions from solvent self-dissociation to act as interlayer spacers, increasing interlayer distances and facilitating sheet separation. Under supercritical hydrothermal conditions, even materials with inherently low solubility can be effectively incorporated into reactions at relatively high concentrations, resulting in enhanced product yields compared to conventional high-temperature solid-state reactions. According to research literature, the selection of organic polar solvents based on the Hansen solubility parameter theory can effectively match the exfoliation energy of layered materials, enabling the successful delamination of 2D nanostructures. Intriguingly, isopropanol (IPA) has been reported to exfoliate hexagonal boron nitride nanosheets (hBNNS) under strong ultrasonication, achieving a

dispersion concentration of approximately 0.002 mg/mL. Furthermore, hydrazine hydrate (N<sub>2</sub>H<sub>4</sub>·H<sub>2</sub>O) has been reported to intercalate between the layers of such materials, thereby weakening interlayer interactions and facilitating exfoliation through molecular insertion [27].

Based on these research findings, the present study employs IPA as a polar organic solvent in conjunction with hydrazine hydrate (N<sub>2</sub>H<sub>4</sub>·H<sub>2</sub>O) under mild hydrothermal conditions to achieve effective exfoliation of bulk h-BN. The results demonstrate that IPA not only serves as an excellent solvent medium but also synergizes well with hydrazine hydrate, yielding high exfoliation efficiency with a remarkable yield. The partially polarized B-N bonds in hexagonal boron nitride (h-BN) exhibit a strong ionic and non-covalent character, rendering the material highly amenable to Lewis acid-base complexation chemistry. In this context, the electron-deficient boron atoms act as potent Lewis acids, making them highly susceptible to nucleophilic attack by Lewis base species, such as amines and phosphines. This inherent reactivity enables the formation of robust Lewis acid-base complexes, which are pivotal in facilitating exfoliation and chemical functionalization. Specifically, boron atoms readily form complexes with the amino groups of NH2-terminated hydrazine hydrate, disrupting the interlayer interactions in bulk h-BN. This targeted interaction weakens van der Waals forces between layers, enabling efficient delamination and promoting excellent dispersibility of BN nanosheets in both aqueous and organic media. This highlights the scalability and practicality of the N<sub>2</sub>H<sub>4</sub>·H<sub>2</sub>O-assisted hydrothermal exfoliation route using IPA, thereby offering a cost-effective and environment friendly pathway for the large-scale production of hBNNS with minimal structural damage. Unlike conventional harsh chemical treatments, this strategy ensures mild exfoliation, preserves crystallinity, and simultaneously introduces functional groups, which are critical for enhancing reactivity and interfacial compatibility. Such properties position the chemically modified h-BN nanosheets as a versatile and high-performance platform for applications in electrochemical sensing, catalysis, energy harvesting, and biointerfaces, where stability, dispersibility, and surface reactivity are crucial.

## 3.2 Experimental Section:

### 3.2.1 Chemical, Reagents and Instrumentation:

For optimized synthesis of Hexagonal Boron Nitride Nanosheets (hBNNS), we sourced high-purity h-BN powder (98%) from Sigma-Aldrich for structural integrity. Analytical-grade reagents such as isopropanol (IPA, (CH<sub>3</sub>)<sub>2</sub>CHOH) and hydrazine hydrate (Purity > 99%, N<sub>2</sub>H<sub>4</sub>·H<sub>2</sub>O<sub>3</sub>) were obtained from Fisher Scientific manufacturer to facilitate effective solution processing. High-quality analytical reagents from Merck, including acetonitrile (CH<sub>3</sub>CN), ethanol (C<sub>2</sub>H<sub>5</sub>OH), potassium ferrocyanide (K<sub>4</sub>[Fe(CN)<sub>6</sub>]·3H<sub>2</sub>O), sodium phosphate monobasic dihydrate (NaH<sub>2</sub>PO<sub>2</sub>·2H<sub>2</sub>O), potassium ferricyanide (K<sub>3</sub>[Fe(CN)<sub>6</sub>]), and sodium phosphate dibasic dihydrate (Na<sub>2</sub>HPO<sub>4</sub>·2H<sub>2</sub>O) were employed without further purification to maintain reproducibility. Electrochemical investigations were carried out in freshly prepared phosphate buffer saline (PBS) solutions and ultrapure Milli-Q water (18 MΩ·cm<sup>-1</sup>) was utilised for electrode washing and PBS preparation which were stored at 4°C.

Phase analysis of as-synthesized hBNNS powder was performed using a Bruker Advance D-8 X-ray Diffractometer (Cu-K $\alpha$ ,  $\lambda = 1.5418$  Å,  $10^{\circ}-80^{\circ}$  range) to confirm crystallinity. Morphology was examined via an EVO18 Zeiss scanning electron

microscope (SEM) and corroborated by WITec alpha 300 RA atomic force microscopy (AFM). Raman spectroscopy (WITec, 532 nm laser) identified vibrational modes, while PerkinElmer Spectrum Two instrument identified vibrational modes using Fourier transform infrared (FT-IR) spectroscopy (4000–400 cm<sup>-1</sup>) to verify chemical bonds and functional groups. UV-Visible spectroscopy (PerkinElmer 950) analyzed optical properties. Electrochemical experiments utilized a Metrohm Autolab Galvanostat/Potentiostat with a three-electrode setup: a platinum (Pt) rod employed as the counter electrode, indium tin oxide (ITO) glass (2.5 cm × 1 cm) functioning as the working electrode, and silver/silver chloride (Ag/AgCl) in 3M potassium chloride (KCl) acting as the reference electrode, ensuring precise electrochemical characterization.

3.2.2 Tailored Hydrothermal Approach for Optimizing Two-dimensional (2D) Hexagonal Boron Nitride Nanosheets Morphology:

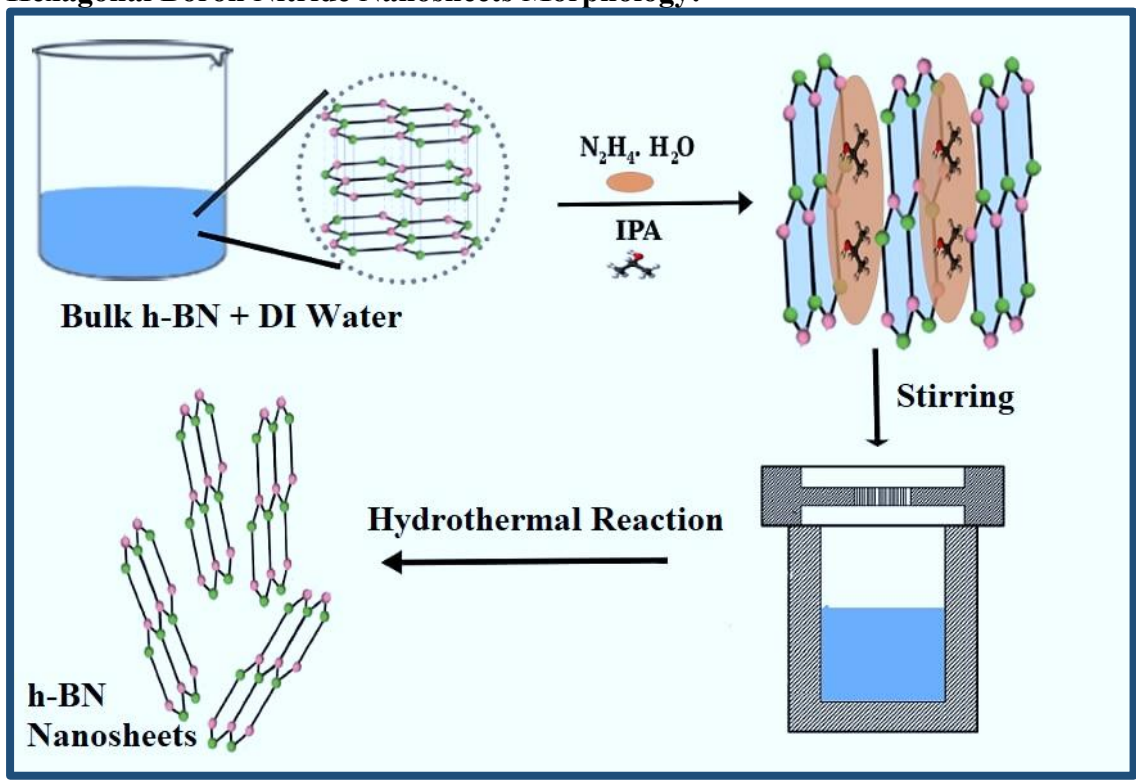


Figure 3.1: Diagrammatic representation of systematic hydrothermal synthesis of enhanced Two-dimensional (2D) Hexagonal Boron Nitride Nanosheets (h-BNNS) architecture

To achieve scalable exfoliation of high-purity, ultrathin nanosheets of hexagonal boron nitride (hBNNS), an in-situ hydrothermal technique under precisely controlled temperature-time conditions was employed (Fig. 3.1). A stable dispersion of 0.15 g of bulk h-BN was prepared comprising 10 mL isopropanol, 2 mL hydrazine hydrate, and 10 mL deionized water under constant magnetic stirring for 1 hour, initiating homogeneous particle distribution and strategically weakening interlayer van der Waals forces to promote effective chemical exfoliation. The homogeneous mixture was then transferred into a 50 mL Teflon-lined autoclave and subjected to hydrothermal treatment at 220°C for 12 h, leveraging autogenous pressure under controlled

temperature-time synergy ensuring efficient exfoliation of bulk hBN. Post-hydrothermal reaction, the autoclaved was allowed to cool to room temperature and resultant nanosheets underwent successive centrifugation (>6000 rpm) with Milli-Q DI water to ensure complete removal of residual solvents. The final product was dried at 90°C, yielding a stable, non-aggregated white powder stored under ambient conditions (25°C) in sealed eppendorf tubes. To refine the exfoliation protocol, additional three synthesis were carried out under varied temperature-time conditions: 220°C/12 h, 220°C/18 h, 250°C/12 h, and 250°C/18 h, labelled as h-BN\_1, h-BN\_2, h-BN\_3 to h-BN\_4, respectively, allowing a comprehensive assessment of temperature and duration impacts on yield, thickness, and structural properties of the nanosheets.

**Mechanism:** The hydrothermal exfoliation of hexagonal boron nitride nanosheets (hBNNS) from bulk h-BN crystals is established to achieve high yield through a synergistic combination of critical factors: isopropanol (IPA) as a well-matched organic polar solvent, hydrazine (N<sub>2</sub>H<sub>4</sub>·H<sub>2</sub>O) as an intercalant (insertion molecule), and high temperature-pressure in a controlled environment. This process, outlined in three key steps, efficiently produces exfoliated hBNNS.

- 1. Chemical Intercalation: Initially, hydrazine molecules intercalate between adjacent layers of bulk h-BN, loosening the structure by increasing interlayer spacing and priming it for exfoliation. This chemical insertion reduces the energy barrier for exfoliation by increasing interlayer spacing and weakening van der Waals forces.
- 2. Solvent-Assisted Energy Minimization: The polar solvent IPA, selected based on Hansen solubility parameter theory for its compatibility with h-BN's surface properties, further reduces the energy required for exfoliation by stabilizing the separated layers. Its excellent affinity for h-BN surfaces stabilizes the delaminated layers and supports efficient dispersion.
- **3. Hydrothermal Exfoliation under Controlled Environment:** The influence of elevated temperature and autogenous pressure, under hydrothermal conditions, drives the complete separation of hBNNS from the bulk material, yielding thin nanosheets. This environment facilitates the thermodynamic and kinetic driving forces necessary to achieve high-yield production of ultrathin hBNNS.

The overall exfoliation efficiency is governed by the synergistic interplay of each parameter, including hydrazine insertion, polar solvent compatibility, elevated temperature and pressure, and stirring intensity, which plays a pivotal role in enhancing exfoliation efficiency. However, variations in these parameters, such as hydrazine concentration, solvent polarity, temperature, pressure, or stirring speed, significantly influenced the yield, scalability, and high-quality exfoliation of hBNNS, with optimal conditions and precise control ensuring maximum efficiency and nanosheet integrity, while deviations reduced the optimum yield or caused sheet fragmentation.

# 3.2.3 Fabrication of h-BN-Coated ITO Electrodes via Controlled Electrophoretic Deposition:

Uniform deposition of reproducible h-BN film onto pre-hydrolyzed ITO-coated glass substrates was achieved using an eco-friendly, highly scalable, and economical electrophoretic deposition (EPD) technique (**Fig. 3.2**). Prior to film fabrication, hydrolysis of ITO substrates was carried out in a 1:1:5 mixture of liquid ammonia NH<sub>3</sub>, hydrogen peroxide H<sub>2</sub>O<sub>2</sub>, and DI water to pre-activate radical groups on the surface, enhancing its surface energy for improved nanoparticle adhesion. A well-dispersed

suspension of h-BN samples at a concentration of 0.25 mg mL<sup>-1</sup> in acetonitrile was obtained through 1-hour ultrasonication to ensure colloidal stability.

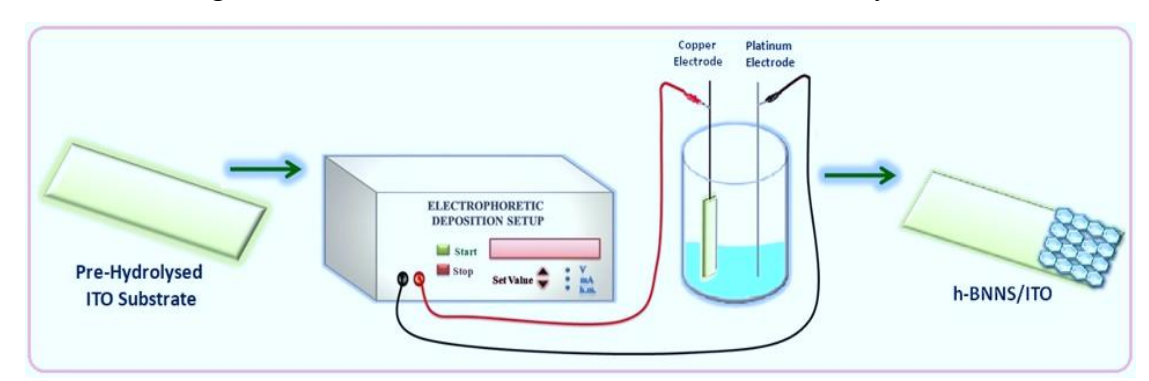


Figure 3.2: Schematic representation of the electrophoretic deposition (EPD) assembly employed for precise deposition of hydrothermally synthesized h-BN nanostructures onto pre-hydrolyzed ITO substrates.

Further, hBN-dispersed colloidal suspension was introduced with controlled addition of 10<sup>-5</sup>–10<sup>-4</sup> mol magnesium nitrate [Mg(NO<sub>3</sub>)<sub>2</sub>·6H<sub>2</sub>O] as an ionic additive, facilitating electrophoretic mobility to surface-charged hBN nanoparticles. The resulting colloidal suspension of charged h-BN particles was transferred to an EPD setup comprising a two-electrode configuration with pre-hydrolyzed ITO connected to a positively biased working electrode and a platinum wire connected to a negative counter electrode, respectively. Under a constant DC potential of 11 V, a sufficient electrophoretic force was generated, ensuring uniform directional migration of h-BN nanosheets onto the ITO electrode (**Fig. 3.3**). This DC voltage produced sufficient electric field strength to drive h-BN nanoparticles without causing dielectric breakdown or excessive Joule heating, allowing the formation of a homogeneous and electrochemically active matrix essential for sensing and interface engineering.

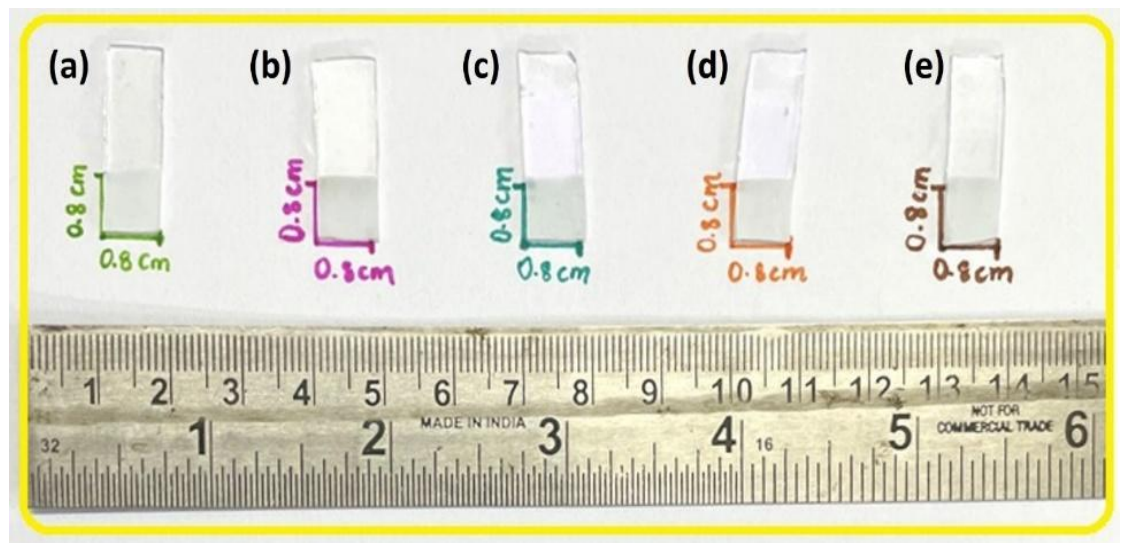


Figure 3.3: Image depicting the homogenous deposition of (a) h-BN\_2 (hBNNS), (b) Bulk h-BN, (c) h-BN\_1, (d) h-BN\_3, (e) h-BN\_4 coatings onto ITO glass substrates fabricated through effective electrophoretic deposition.

### 3.3 Experimental Results & Analysis:

### 3.3.1 Analytical Nanomaterial Characterizations:

# 3.3.1.1 Crystallographic Evaluation of Hydrothermally Synthesized h-BN Nanostructures:

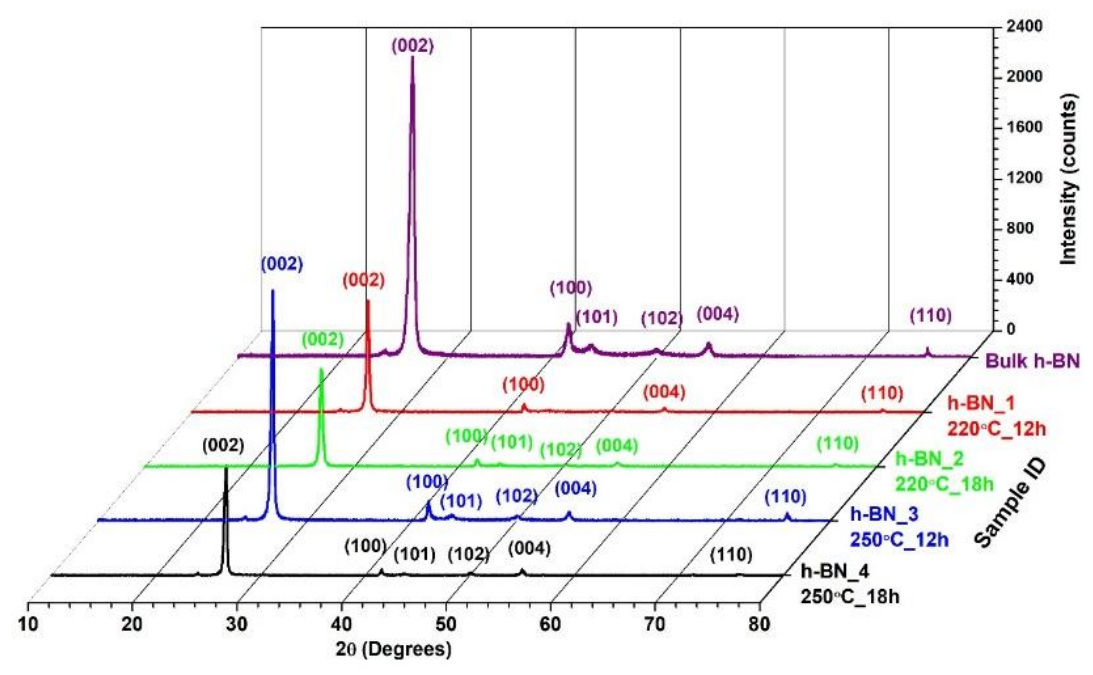


Figure 3.4: X-ray diffractogram depicting Bulk h-BN (purple) and h-BN nanosheets exfoliated under tailored hydrothermal conditions as h-BN\_1 (220 °C, 12 h-Red), h-BN\_2 (220 °C, 18 h-Green), h-BN\_3 (250 °C, 12 h-Blue), and h-BN\_4 (250 °C, 18 h-Black), respectively.

To investigate the impact of exfoliation-induced hydrothermal synergistically tailoring reaction temperature-time conditions, X-ray diffraction (XRD) analysis was conducted both prior to exfoliation (on bulk h-BN) and post-exfoliation (on as-synthesized variants of h-BNNS samples), as shown in Fig. 3.4. The diffraction spectra of both bulk hBN and exfoliated hBNNS samples exhibited prominent characteristic peaks at 26.85°, 41.8°, 44.01°, 50.5°, 55.23°, and 76.11°, attributed to (002), (100), (101), (102), (004), and (110) planes of hexagonal phase of boron nitride, respectively, consistent with the JCPDS Card No. 34-0421 [28, 29]. The absence of any extraneous diffraction peaks in as-exfoliated samples confirms the retention of high-purity hexagonal phase with excellent crystallinity. The marked decrease in diffraction peak intensities upon transitioning from bulk h-BN to h-BNNS variants demonstrates the efficacy of the exfoliation process in disrupting interlayer van der Waals interactions to form ultrathin layered structures. An intense (002) reflection plane indicates preferential stacking orientation of nanosheets along the basal plane and reduced structural disorder, essential for facilitating interfacial kinetics, electronic transport, and enhanced surface interactions. However, the relatively attenuated intensities for (101) and (102) peaks in h-BN 1 indicate limited crystallographic ordering along these directions due to insufficient nucleation time. Furthermore, quantitative measurement of microstructural parameters such as average crystallite size and lattice strain was estimated using the Williamson–Hall plots analysis, which utilizes

the linear relationship between  $\beta \cos \theta$  and  $4 \sin \theta$  to evaluate the intercept and slope (Eq. 3.1), thereby characterizing internal lattice distortions and nanodomain formation.

$$\beta \cos\theta = \frac{k\lambda}{D} + 4 \epsilon \sin\theta$$
 [3.1]

In the W-H equation,  $\beta$  refers to the full width at half maximum (FWHM) of the XRD peaks (in radians), while  $\theta$  represents the corresponding Bragg's diffraction angle (in radians). A standard shape factor (k=0.9) and Cu K $\alpha$  radiation wavelength ( $\lambda=1.54184$  Å) were utilized to construct a linear fit of  $\beta$  Cos $\theta$  versus 4 Sin $\theta$ , as depicted in Fig. 3.5. A linear regression graph obtained from the Williamson–Hall method was utilized to estimate the lattice micro-strain ( $\epsilon$ ) from the slope and crystallite size (d) from the y-intercept, which are essential parameters to assess the influence of synthesis-induced lattice strain on grain size evolution and lattice distortions. The derived values of crystallite size (d) and micro-strain ( $\epsilon$ ) parameters for a series of h-BN samples were summarized in **Table 3.1.** 

Table 3.1: Comparative Assessment of Crystallite Size (d) and induced lattice strain (ε) of different Hydrothermally Synthesized h-BN Samples evaluated from Williamson-Hall (W–H) plot fitting with relative error estimation.

Sample	Crystallite size (d, nm)	Micro-Strain (ε)
Bulk h-BN	$2.30 \pm (7.55 \times 10^{-4})$	$0.1956 \pm (1.16 \times 10^{-6})$
h-BN_1	$2.41 \pm (5.44 \times 10^{-3})$	$0.1952 \pm (7.36 \times 10^{-6})$
h-BN_2	$1.15 \pm (3.88 \times 10^{-4})$	$0.3867 \pm (2.39 \times 10^{-6})$
h-BN_3	$2.31 \pm (7.79 \times 10^{-4})$	$0.1956 \pm (1.19 \times 10^{-6})$
h-BN_4	$2.30 \pm (7.94 \times 10^{-4})$	$0.1957 \pm (1.22 \times 10^{-6})$

Estimation of microstructural parameters demonstrated that h-BN\_2 exhibited the highest compressive strain, which caused a significant reduction of 52.28% in crystallite size compared to h-BN\_1, which retained the most prominent crystallites. These pronounced microstructural differences between h-BN\_1 and h-BN\_2, despite identical synthesis temperatures (220 °C), arise from extended synthesis time of 18 h for h-BN\_2 relative to a lesser reaction time of 12 h provided for h-BN\_1. This prolonged thermal exposure in h-BN\_2 enhanced internal lattice stress, causing intensified compressive strain within the crystal lattice while facilitating the nucleation of finer grains, thereby tuning material stability and surface-driven performance. The significant correlation between time-dependent strain accumulation and structural refinement illustrates the critical role of thermal kinetics in engineering nanoscale material characteristics.

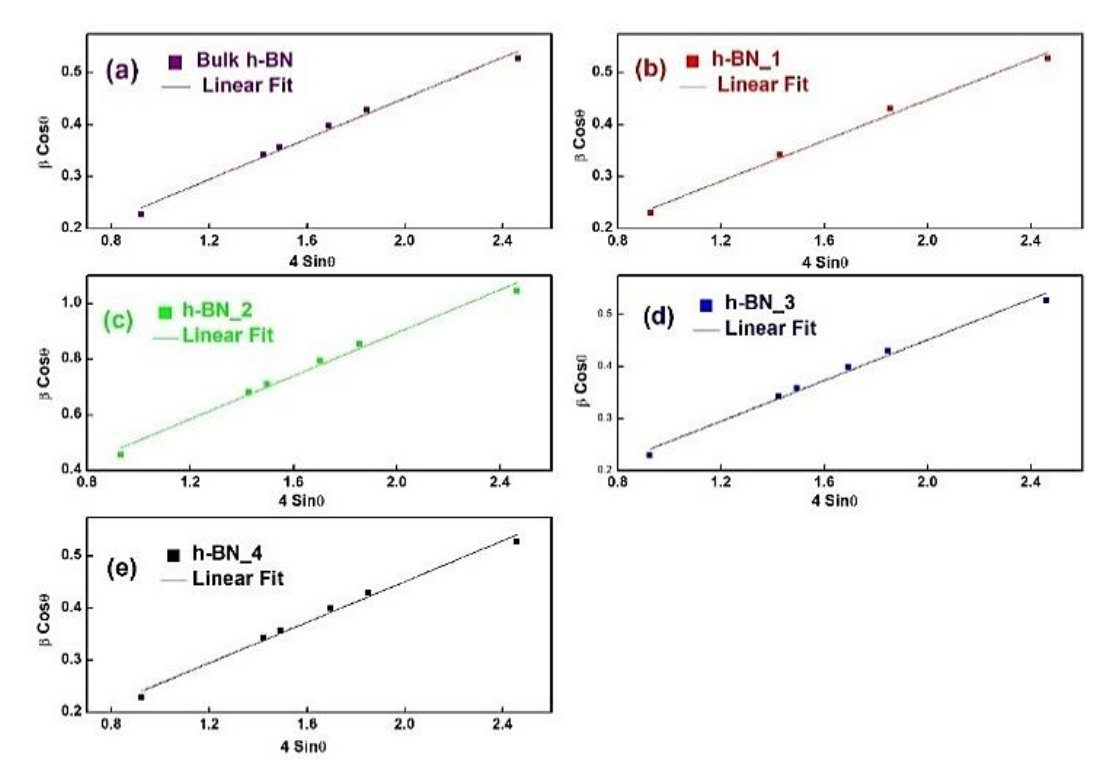


Figure 3.5: Graphical depiction of Williamson-Hall (W-H) plots representing linear relationship between  $\beta$  Cos $\theta$  versus 4 Sin $\theta$  for samples (a) Bulk h-BN, (b) h-BN\_1, (c) h-BN\_2, (d) h-BN\_3, and (e) h-BN\_4 to evaluate micro-strain and crystallite size.

As bulk h-BN transitions into its nanosheet morphology under controlled pressure-temperature-time environment provided by hydrothermal technique, the strain-induced stress redistributes the hexagonal packing of its layers to nano-confined dimensions to gain thermal stability. In accordance with fundamental physics, materials inherently strive to achieve thermal stability post-synthesis. During transition to nano-confinement, lattice strain emerges as a key agent in releasing residual lattice stress, which leads to measurable shifts in crystallographic parameters [30]. The resulting strain engineering facilitates lattice parameter modulations that reflect enhanced structural order and leads to the successful synthesis of durable, high-crystallinity h-BNNS, ideal for high-performance materials in thermally intense environments.

Table 3.2: A comparison table depicting lattice parameter values derived using X-powder analysis to evaluate the impact of nano-confinement-induced compression on crystallographic structure of h-BN samples synthesized at different hydrothermal conditions.

Sample	a (Å)	c (Å)	Volume of Unit Cell (ų)
h-BN_1	2.479	6.641	35.85
h-BN <sub>2</sub>	2.494	6.646	35.80
h-BN_3	2.502	6.661	36.11
h-BN 4	2.504	6.671	36.22

The detailed crystallographic analysis of XRD data, performed using X-powder software, facilitated the precise determination of lattice constants for the various hydrothermally synthesized h-BN samples, as presented in Table 3.2. A comparative evaluation of lattice parameter reveals that sample h-BN\_2 displays the lowest values for lattice constant as well as unit cell volume, indicating the influence of substantial compressive micro-strain induced by specific hydrothermal synthesis conditions. This crystallographic contraction highlights the impact of the time-temperature interplay on internal lattice stress accumulation. This lattice compression implies points to stress accumulation due to confined grain growth. Interestingly, on further increasing the reaction temperature and synthesis duration in hBN\_3 and hBN\_4 samples, the lattice experiences strain intensification, which leads to strain-induced lattice expansion, indicative of a structural reconfiguration under dynamic stress redistribution process during prolonged heat exposure.

# 3.3.1.2 Nano-Scale Morphological Investigation using various High-Resolution Electron Microscopy Techniques (SEM, TEM, and AFM):

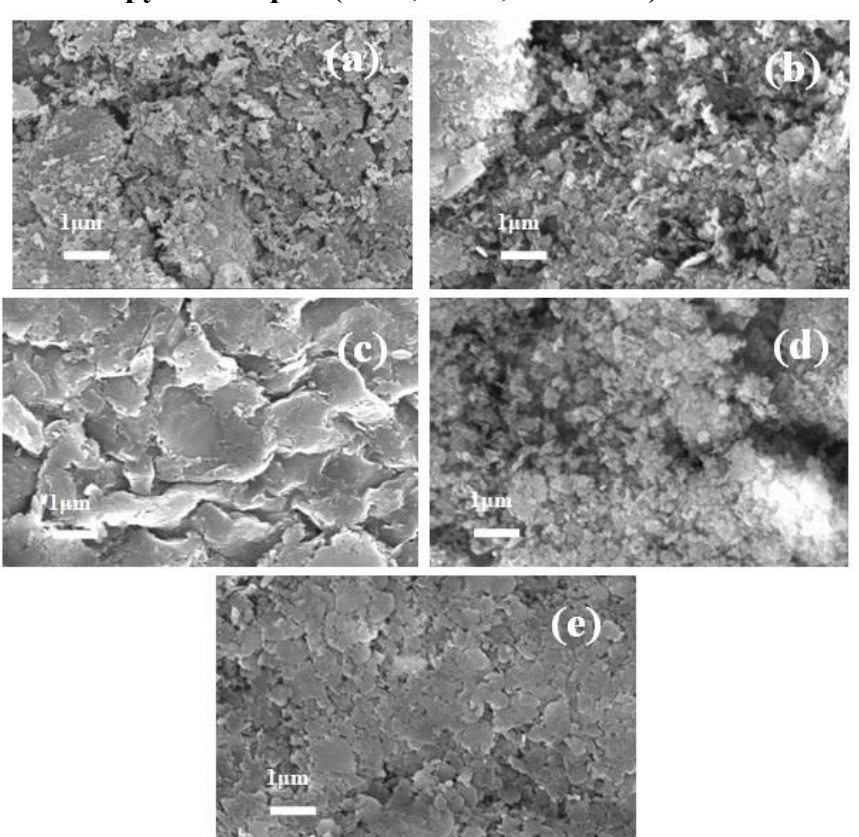


Figure 3.6: SEM top-view micrographs depicting (a) pristine bulk h-BN and hydrothermally exfoliated variants: (b) h-BN\_1 at 220 °C for 12 h, (c) h-BN\_2 at 220 °C for 18 h, (d) h-BN\_3 at 250 °C for 12 h, and (e) h-BN\_4 at 250 °C for 18 h.

Scanning Electron Microscopy (SEM) is a pivotal high-resolution surface imaging technique for characterizing the three-dimensional surface texture, morphological analysis, particle size, shape, layer distribution, and overall structural integrity of nanomaterials at the micro- to nanoscale. Herein, morphological transformation from

bulk hBN to h-BN nanosheets under varying reaction temperature-time conditions of hydrothermal synthesis was systematically examined by SEM investigation, as depicted in Fig. 3.6(a-e). Notably, the SEM image of h-BN 2 synthesized at 220°C for 18 h (Fig. 3.6c) exhibited well-dispersed, relatively broad lateral surface area, few-layered nanosheets, confirming highly efficient exfoliation and reduced interlayer cohesion owing to the effectiveness of prolonged moderate thermal processing. In contrast, h-BN 4 prepared at 250°C for 18 h (Fig. 3.6e) displayed hybrid nanostructures exhibiting nanosheets co-existence with agglomerated particles, suggesting that excessive thermal flux promotes localized nucleation and particle clustering. The absence of clear nanosheet topographies in h-BN 1 and h-BN 3 samples synthesized for shorter reaction durations of 12 hours at 220°C and 250°C (Fig. 3.6 b, d), failed to deliver substantial exfoliation, retaining bulk-agglomerated morphology of bulk hBN, affirming the role of insufficient reaction time or elevated temperature, respectively. Corroborative AFM data emphasize the impact of temperature-time calibration, directly influencing layer uniformity and lateral expansion at nanoscale level in optimally modulating sheet-like morphology.

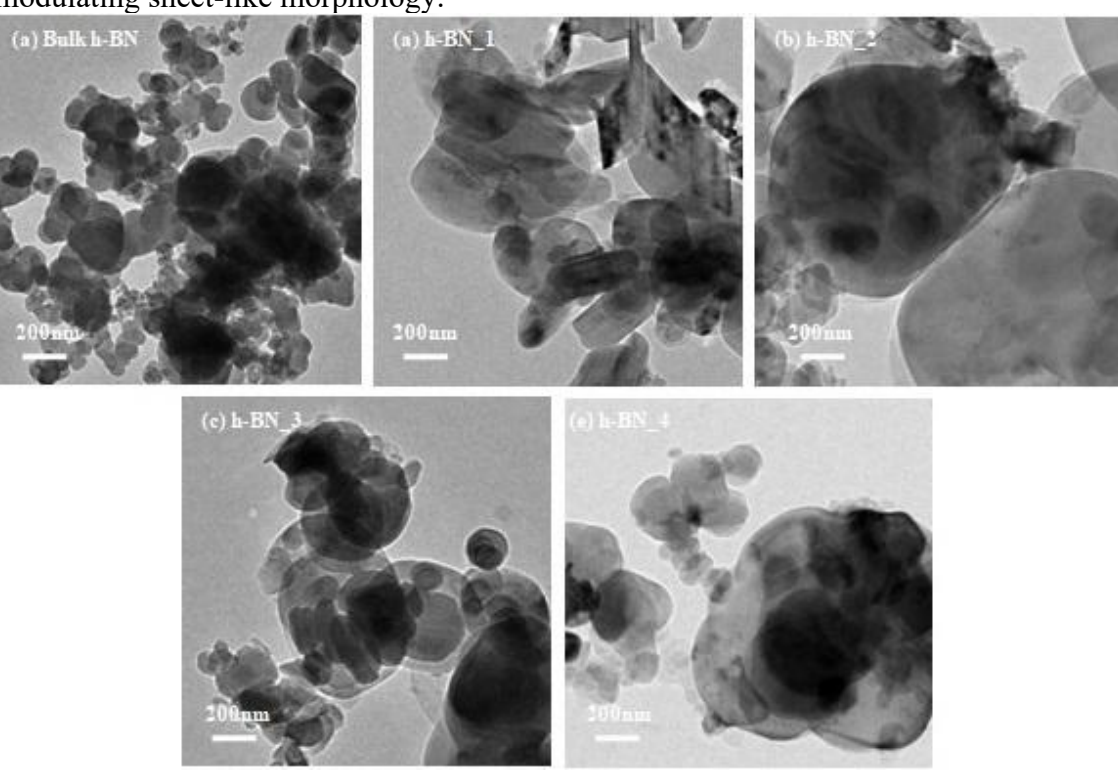


Figure 3.7: High-resolution TEM imaging depicting morphological evolution from (a) pristine bulk h-BN to hydrothermally treated samples: (b) h-BN\_1 (220  $^{\circ}$ C, 12 h), (c) h-BN\_2 (220  $^{\circ}$ C, 18 h), (d) h-BN\_3 (250  $^{\circ}$ C, 12 h), and (e) h-BN\_4 (250  $^{\circ}$ C, 18 h), highlighting nanosheet formation and degree of exfoliation as a function of temperature and duration.

High-resolution Transmission Electron Microscopy (TEM) is a powerful characterization tool crucial for visualizing atomic-level features, including layer thickness, edge structures, and defects, due to its ability to provide high-resolution, detailed imaging of a material's internal structure, arrangement, and uniformity at the nanoscale. **Fig. 3.7(a–e)** presents comparative transmission electron microscopy

(TEM) images to investigate the exfoliation behaviour of sequentially engineered h-BN nanosheets under controlled hydrothermal conditions from its bulk counterpart. In particular, the TEM micrograph of bulk h-BN (Fig. 3.7(a)) illustrated densely packed particles possessing substantial particle agglomeration, affirming poor dispersion and a stacked multilayered nature. In evident contrast, the h-BN\_2 sample synthesized at 220°C for 18 h achieved optimal exfoliation, thereby demonstrating ultrathin, highly transparent nanosheets with an improved lateral growth (~926.667 nm), signifying impactful layer delamination and exfoliation into few-layer domains. However, h-BN\_3 and h-BN\_4 samples were synthesized at elevated temperatures at 250°C, which depicted darker and denser nanosheets under TEM as shown in Fig. 3.7-(d), 3.7-(e), induced by thermally driven restacking, indicating characteristics of multiple stacked layers resulting in increased thickness and reduced exfoliation efficiency due to thermal-induced re-agglomeration

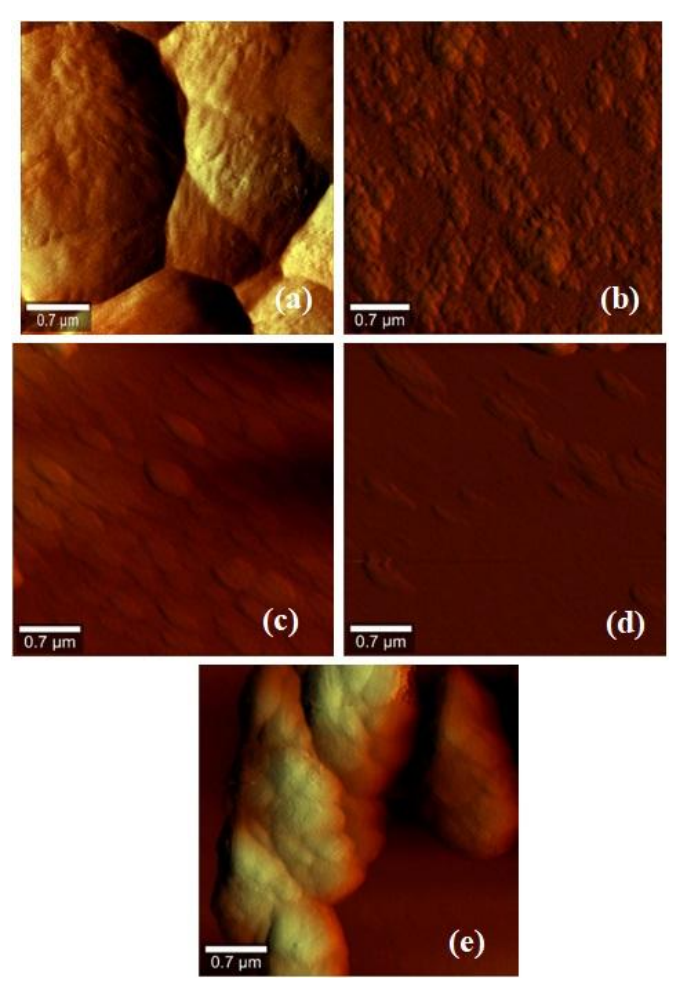


Figure 3.8: AFM analysis images depicting surface roughness and topography of electrophoretically deposited h-BN films on ITO substrates mentioned as (a) Bulk h-BN, (b) h-BN\_1, (c) h-BN\_2, (d) h-BN\_3, and (e) h-BN\_4, respectively.

Atomic Force Microscopy (AFM) is a highly sensitive and non-destructive surface imaging technique that provides high-resolution quantification of surface topography, including roughness, texture, height gradients, and particulate distribution at the

nanometer scale. AFM was employed to validate the surface topography and surface roughness characteristics of h-BN films fabricated using electrophoretic deposition (EPD) technique. As illustrated in Fig. 3.8(a-e), the surface topography of EPD films exhibited relatively smooth surfaces, with arithmetic average surface roughness (Ra) values quantified as 10.634 nm for h-BN\_1, 7.617 nm for h-BN\_2, 15.922 nm for h-BN\_3, and 28.503 nm for h-BN\_4, respectively. Sample h-BN\_2, comprising highly exfoliated and uniformly deposited 2D nanosheets, demonstrates exceptional surface smoothness with the lowest Ra value of 7.617 nm, making it highly suitable for applications requiring uniform interfacial interactions. The AFM topographical profiles corroborate well with the morphological features observed in SEM micrographs, ensuring reliable surface uniformity and dispersion quality of the as-synthesized h-BN films. Furthermore, the EPD technique ascertains fabrication of highly effective ultrathin, uniform h-BN film deposition characterized by minimal particle agglomeration, highlighting its potential for producing high-quality nanomaterial coatings.

# 3.3.1.3 Investigation of Optical Bandgap Transitions in Hydrothermally Engineered h-BN Samples through UV-Visible Spectroscopy

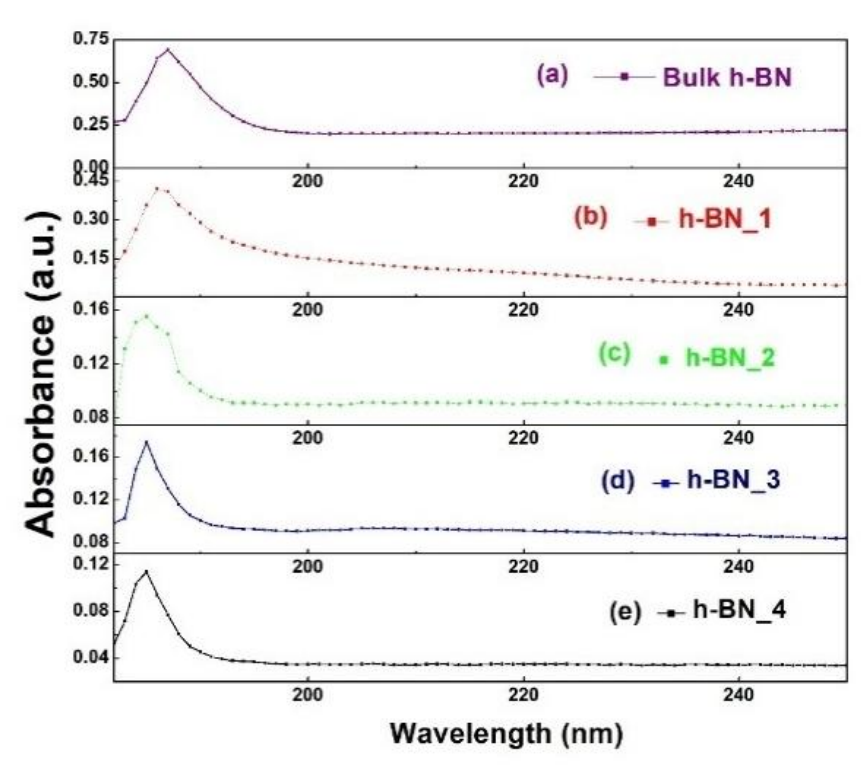


Figure 3.9: Absorbance versus wavelength relationship obtained from UV–Visible spectroscopy for (a) bulk h-BN and (b) h-BN\_1, (c) h-BN\_2, (d) h-BN\_3, (e) h-BN\_4, respectively, demonstrating optical response influenced by tuning hydrothermal synthesis conditions.

UV-Visible absorption spectroscopy is a fundamental tool that measures the interactions of ultraviolet and visible light with material non-destructively as a function of wavelength, enabling the determination of electronic transitions resulting from quantum confinement, which significantly influence energy states and size-dependent optical bandgap variations in materials. To elucidate the impact of strategic

hydrothermal fabrication on electronic characteristics of various h-BN nanosheet samples suspended in deionized (DI) water, UV-visible spectroscopy was employed to monitor the underlying energy shift and optical bandgap transition crucial for 2D morphology optimization. **Fig. 3.9** illustrates the absorbance-wavelength relationship, which highlights the direct influence of modulating synthesis parameters on nanosheet size and thickness upon photon interaction. The bandgap energy was accurately determined using **Eq. 3.2**, facilitating a detailed correlation between the influence of synthesis parameters and electronic transitions of tailored nanosheet morphologies. Furthermore, the absorption coefficient ( $\alpha$ ) was computed utilising the Beer-Lambert law to validate quantitative evaluation.

$$(\alpha E)^{1/n} = \beta \left( E - E_g \right)$$
 [3.2]

The Beer-Lambert equation entails the absorption coefficient ( $\alpha$ ) that characterizes how strongly a material absorbs UV-Visible light, whereas the photon energy (E=hv) was calculated using Planck's constant (h) and light frequency ( $\nu$ ), which is associated with the energy of incident photons. In this experiment,  $\beta$  characterizes the band tailing parameter, and for a wide bandgap material, hexagonal boron nitride (h-BN), n = 1/2 is employed owing to its direct allowed electronic transition [31].

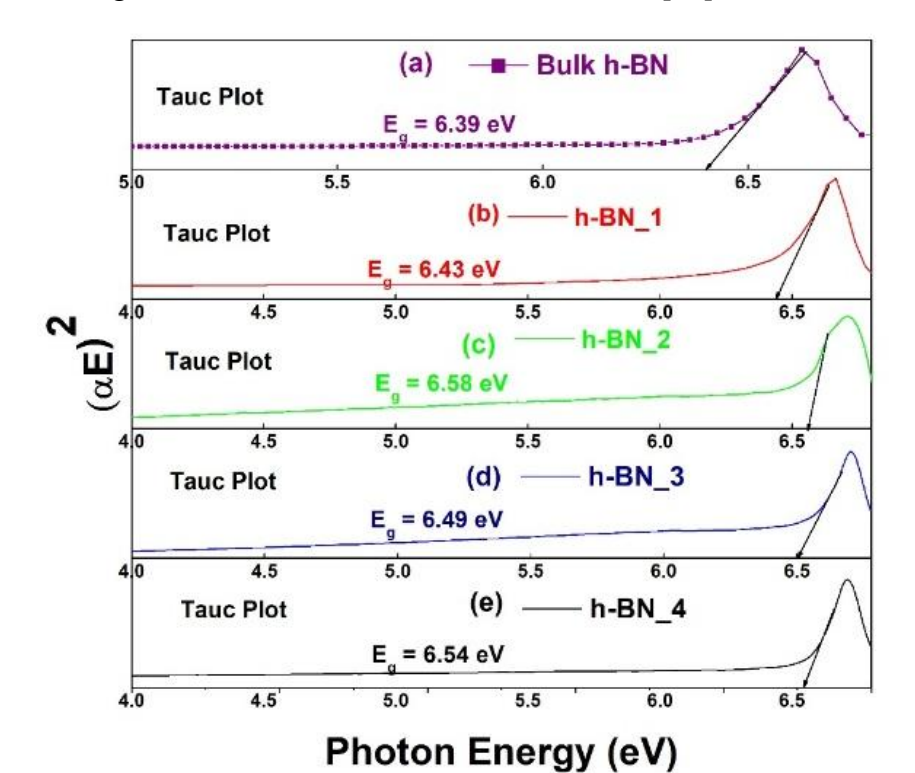


Figure 3.10: Energy bandgap determination through Tauc plots for (a) bulk h-BN and hydrothermally processed variants (b) h-BN\_1, (c) h-BN\_2, (d) h-BN\_3, and (e) h-BN\_4, depicting quantum confinement effects and optical tunability influenced by hydrothermal synthesis parameters.

Furthermore, Tauc plots associated with bulk hBN and each variant of hBN were obtained by plotting  $(\alpha hv)^2$  versus photon energy (E) to determine the optical bandgap (Eg) values by determination of x-axis intercepts, as depicted in **Fig. 3.10**. Evaluation of the optical bandgap (Eg) from x-axis intercepts yielded corresponding values of 6.39 eV (bulk h-BN), 6.43 eV (h-BN 1), 6.58 eV (h-BN 2), 6.49 eV (h-BN 3), and 6.54

eV (h-BN\_4) respectively. Interestingly, the highest optical bandgap was observed corresponding to h-BN\_2 sample (6.58 eV) in sharp contrast with bulk hBN, exhibiting the least Eg (6.39 eV), suggesting optimal exfoliation of nanosheets among other synthesized variants, a finding corroborated by XRD analysis. This result is attributed to enhanced quantum confinement, driven by effectively reduced crystallite domains, which reduces electron-hole overlap and increases transition bandgap energies [30, 32]. Furthermore, elevated synthesis temperatures and extended reaction times significantly contributed to smaller crystallite sizes, consequently enhancing the optical bandgap. Moreover, strain analysis obtained from Williamson-Hall plots in XRD study highlighted that h-sample hBN\_2 experienced the highest compressive strain, which further contributed to widening the bandgap [33]. This cohesive agreement between UV-Visible spectroscopy and XRD results validates the effectiveness of hydrothermal exfoliation in attaining structural refinement that directly tailors h-BN's optical and electronic properties.

# 3.3.1.4 Raman Spectroscopy Investigating Phonon-Electronic Interactions in Hydrothermally Engineered h-BN Nanostructures

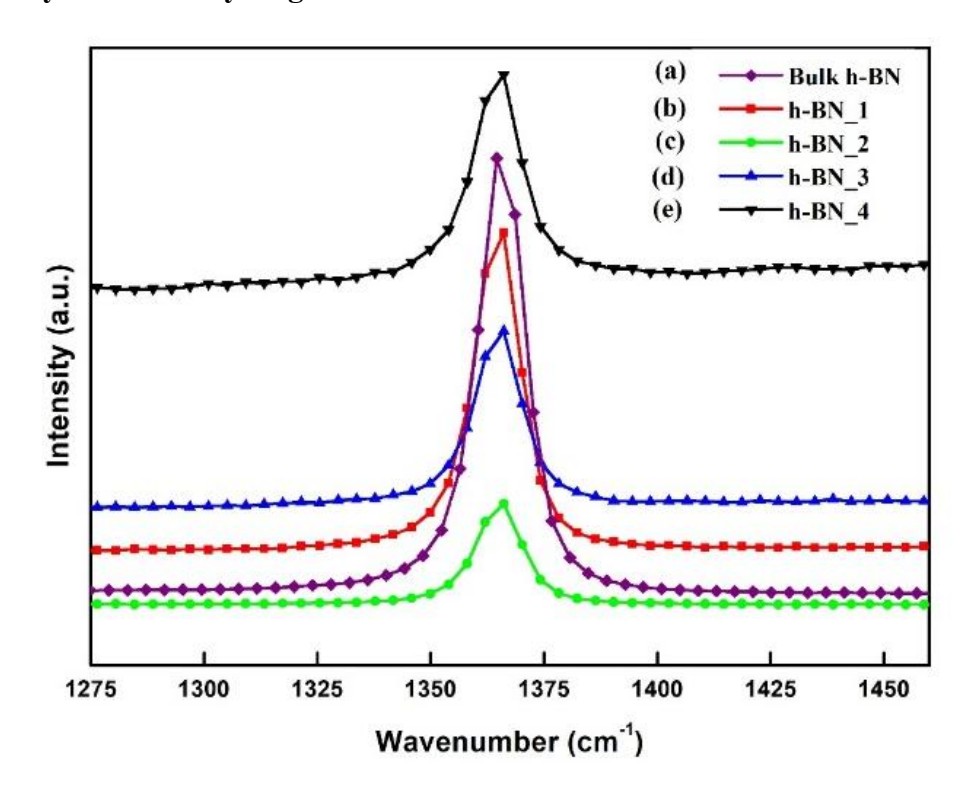


Figure 3.11: Raman analysis in the  $E_{2g}$  phonon region for (a) Bulk h-BN, (b) h-BN\_1, (c) h-BN\_2, (d) h-BN\_3, and (e) h-BN\_4, clearly demonstrating synthesis-dependent shifts in vibrational frequency.

Raman spectroscopy serves as a powerful, non-destructive technique by monitoring phonon–electron interactions and lattice dynamics, including vibrational, rotational, and electronic properties of materials at the molecular level, which enables indirect evaluation of strain, defects, doping, and layer thickness. Raman spectroscopy was employed to characterize the in-plane E<sub>2</sub>g vibrational phonon mode of h-BN nanosheets, offering valuable insights into the effects of exfoliation and synthesis

parameters on crystal structure. As illustrated in **Fig. 3.11**, the characteristic peak for bulk h-BN appears at 1364.56 cm<sup>-1</sup>, whereas subtle shifts to 1365.48 cm<sup>-1</sup> (h-BN\_1), 1366.09 cm<sup>-1</sup> (h-BN\_2), 1365.68 cm<sup>-1</sup> (h-BN\_3), and 1365.89 cm<sup>-1</sup> (h-BN\_4) reflect variations induced by hydrothermal treatment [34]. The blue shift of 1.53 cm<sup>-1</sup> in h-BN\_2 relative to bulk h-BN signifies the presence of compressive strain, a conclusion supported by complementary XRD strain analysis. Notably, the lowest Raman peak intensity observed for h-BN\_2 corresponds to few-layered nanosheets, affirming successful exfoliation [35]. In contrast, the elevated intensities in h-BN\_3 and h-BN\_4 suggest nanosheet stacking or particle agglomeration, which correlates well with SEM-based morphological observations. This investigation highlights the critical importance of optimizing hydrothermal parameters to achieve strain-engineered, high-quality, few-layered h-BN nanosheets.

# 3.3.1.5 Investigating Molecular Vibrational Dynamics in Hydrothermally Tailored h-BN Nanostructures through Fourier Transform Infrared (FT-IR) Spectroscopy

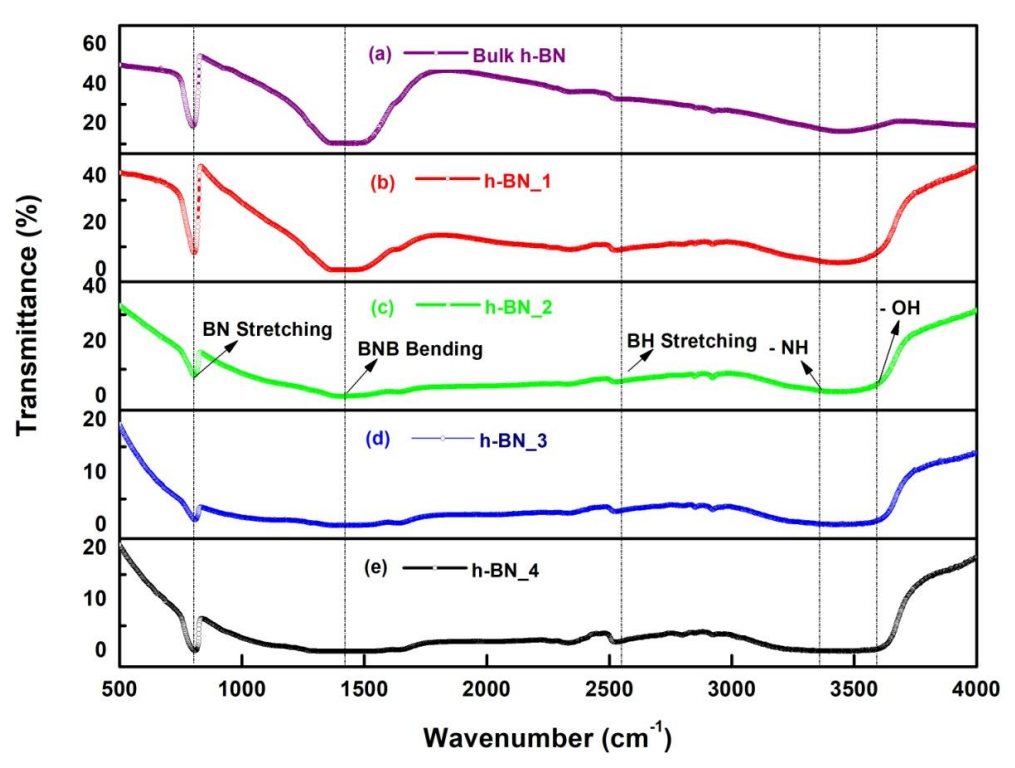


Figure 3.12: Fourier Transform Infrared (FT-IR) Spectra highlighting dominant vibrational modes in (a) Bulk h-BN, (b) h-BN\_1, (c) h-BN\_2, (d) h-BN\_3, and (e) h-BN\_4 elucidating vibrational interactions in sp²-hybridized B-N bonding across the synthesized variants.

Fourier Transform Infrared (FTIR) Spectroscopy is a critical analytical technique for investigating vibrational modes of chemical bonds in materials, enabling precise identification of functional groups, the chemical bonding in parent material, their interactions with impurities, or surface adsorbates, and molecular structure. To investigate the integrity of molecular structure in B-N bonding and identify functional groups vibrational modes induced during synthesis, FT-IR spectroscopy was conducted across the mid-infrared region (400–4000 cm<sup>-1</sup>). **Fig. 3.12** illustrates the intrinsic

infrared fingerprints of h-BN\_1 through h-BN\_4 and monitors the structural evolution from bulk to nanoscale. Characteristic transmittance bands were observed at 805 cm<sup>-1</sup> and 1413 cm<sup>-1</sup>, corresponding to B-N-B out-of-plane bending and B-N in-plane stretching vibrations, respectively [36]. Prominent absorption band at 805 cm<sup>-1</sup>, indicative of out-of-plane B-N-B deformation modes, and a key transmittance peak at 1413 cm<sup>-1</sup>, representative of in-plane B-N bond stretching, highlight the preserved sp<sup>2</sup> hybridization. The attenuation in spectral intensity across samples suggests a gradual transformation in thickness and bonding environment due to exfoliation. Specifically, h-BN\_2 exhibits the lowest peak intensities, indicating increased exfoliation, reduced layer stacking, and altered phonon dynamics, confirming the material's transformation at the nanoscale level. This spectral evolution directly correlates with observed morphological and crystallographic trends, validating successful exfoliation and reduction in crystallite size.

Table 3.3: Distinct transmittance peak assignments in the fingerprint region affirm the structural integrity of hydrothermally synthesized h-BN.

Sample	B-N-B Bending (cm <sup>-1</sup> )	B-N Stretching (cm <sup>-1</sup> )
Bulk h-BN	800	1420
h-BN_1	805.31	1413.50
h-BN_2	806.26	1395.52
h-BN 3	807.95	1432.50
h-BN 4	808.13	1426.00

The presence of a weak absorption band at approximately ~2500 cm<sup>-1</sup> is attributed to the weak B–H stretching vibrations, indicating potential hydrogen incorporation during the hydrothermal process. Progressive broadening of B–N stretching bands with elevated temperature and prolonged reaction time suggests increased disorder due to the formation of surface dangling bonds, directly tied to reduced particle dimensions. In the higher wavenumber region, a spectral overlap between –OH and –NH functional groups becomes increasingly evident, complicating their resolution yet confirming their coexistence. The emergence of a broad peak above 3500 cm<sup>-1</sup> is linked to O–H stretching from absorbed moisture, while distinct features between 3200–3500 cm<sup>-1</sup> further confirm residual N–H functionalities. These cumulative insights demonstrate the pivotal role of process tuning in enabling spontaneous and efficient surface modification of h-BN, bypassing the need for laborious chemical functionalization protocols.

#### 3.3.2 Electrochemical Profiling and Analysis:

The electrochemical evaluation aimed at understanding its electron transfer behavior and interfacial properties of hexagonal boron nitride (h-BN), synthesized under varying temperature and time conditions. Detailed electrochemical measurements were thoroughly investigated using advanced analytical techniques, including Cyclic Voltammetry (CV), Electrochemical Impedance Spectroscopy (EIS), and Differential Pulse Voltammetry (DPV) to provide a comprehensive understanding of redox dynamics, interface resistance, and faradaic responsiveness. All electrochemical measurements were performed in phosphate buffer saline (PBS, 50 mM, 0.9% NaCl, pH 7.0) containing 5 mM [Fe(CN)<sub>6</sub>]<sup>3-/4-</sup>, a standard redox couple that ensures reversible one-electron transfer (n = 1), thus serving as a reliable electrolyte for evaluating heterogeneous electron transfer kinetics.

CV was employed to explore the redox activity, and diffusion-controlled behaviour, with scan rate-dependent studies to study electron transfer kinetics at the h-BN electrode interface. By applying a linearly varying potential, CV enabled the measurement of current responses, revealing the material's ability to facilitate oxidation and reduction reactions. To investigate the influence of scan rate on electrochemical performance, CV experiments were conducted at scan rates ranging from 30 to 160 mV/s. This range allowed for the assessment of diffusion-controlled versus kinetically controlled processes, providing insights into the rate-limiting steps of electron transfer.

EIS experiments were utilized to understand the impedance characteristics of the h-BN electrode within a broad frequency range of 0.1 Hz to 100 kHz, applying a biasing potential of 10 mV. The Nyquist plot was generated, describing a polar representation with the real impedance (Z') on the abscissa and the imaginary impedance (Z") on the ordinate, illustrated the resistive and capacitive components of the system. The frequency-dependent impedance data were analyzed using an equivalent electrical circuit model, which helped deconvolute contributions from charge transfer resistance, double-layer capacitance, Warburg diffusion elements, and solution resistance.

DPV technique, also known as pulse-based differential cyclic voltammetry, was utilized to achieve highly sensitive and precise measurements of the faradaic current. The experiments were conducted at a scan rate of 10 mV/s, with the potential window of -0.7 V to 1.2 V. The DPV response is characterized by its ability to resolve small changes in current, where the abscissa represents the differential current between consecutive points on the voltammogram, and the ordinate corresponds to the applied potential. The differential nature of DPV renders effective identification of small current in faradaic transitions, which correspond to redox-active interfaces, making it indispensable for sensitive surface characterization and enhanced electrochemical signal transduction.

# 3.3.2.1 Assessment of Interfacial Electron Kinetics in Hydrothermally Engineered h-BN Nanostructures via Cyclic Voltammetry

Systematic investigation of the redox properties, electroactive surface area, scan rate dependencies, and interfacial charge kinetics of h-BN nanosheets, cyclic voltammetry (CV) was employed as a powerful electrochemical technique within a potential range of -0.9 V to +1.2 V at a scan rate of 50 mV/s. The CV experiments were performed in a 50 mM phosphate buffer saline (PBS) solution, adjusted to a neutral pH of 7.0 and containing 0.9% NaCl to ensure physiological relevance and electrolyte stability. The electrochemical setup was incorporated with a 5 mM ferro/ferricyanide ([Fe(CN)<sub>6</sub>]<sup>3-/4-</sup>) redox couple, providing a well-characterized, reversible one-electron transfer system that serves as a standard for evaluating electrode performance due to its fast kinetics and reproducibility. Fig 3.13 illustrates the CV responses to compare the electrochemical behaviour of bulk h-BN with four hydrothermally fabricated h-BN nanosheet samples (h-BN 1 to h-BN 4). Among all hydrothermally engineered samples, h-BN 2 denoted as h-BN nanosheets (h-BNNS), exhibited exceptional electrochemical performance, with a peak anodic current (Ipa) of 1.29 mA at an anodic potential (Epa) of 0.37201 V and a peak cathodic current (Ipc) of -1.23 mA at a cathodic potential (Epc) of -0.09613 V.

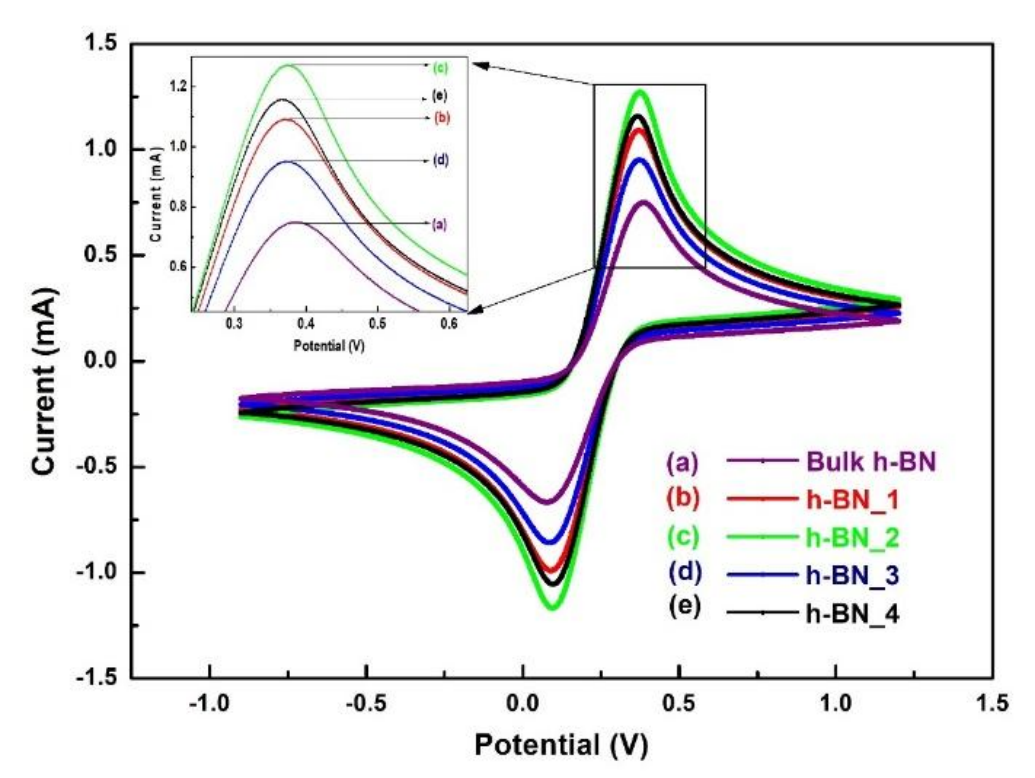


Figure 3.13: Cyclic voltametric response illustrating redox behaviour of (a) Bulk h-BN, (b) h-BN\_1, (c) h-BN\_2, (d) h-BN\_3, and (e) h-BN\_4 electrodes in PBS electrolyte with 5 mM  $[Fe(CN)_6]^{3-/4-}$  at a scan rate of 50 mV/s.

This markedly enhanced redox current in hBN\_2 demonstrates a significant 69.96% increase in current relative to bulk h-BN, highlighting the superior electrochemical activity of the nanosheet structure. The enhanced electrochemical response of h-BN\_2 is attributed to synthesis of ultrathin nanostructured morphology, characterized by a reduced number of layers and minimal particle agglomeration. These structural features decrease the diffusion path length for charge carriers and enhance electrode-electrolyte interaction, facilitating faster electron transfer and improving the overall conductivity of the material, which is critical for efficient electrochemical reactions. The elevated peak currents in h-BN\_2 indicate a high density of redox-active functional groups at the nanosheet surface, introduced during the hydrothermal exfoliation process. Fourier Transform Infrared (FT-IR) spectroscopy confirmed the presence of these redox moieties, which further contribute to the electroactive behaviour of h-BN\_2 to enhance their electrochemical reactivity. These characteristics collectively position h-BN\_2 as a highly efficient candidate for advanced applications, such as high-sensitivity electrochemical sensors, energy storage systems, and electrocatalytic devices.

Evaluation of the electroactive surface area of the as-fabricated h-BN-modified electrodes was quantitatively estimated using the Randles–Ševčík equation, a widely accepted analytical expression derived from cyclic voltammetry data for reversible redox systems. This relation correlates the peak current (Ip) observed in the voltammogram with fundamental parameters of the redox process, as shown in **Eq.** [3.3]. For a reversible one-electron transfer system such as [Fe(CN)<sub>6</sub>]<sup>3-/4-</sup>, the peak current (Ip) is given by [37, 38]:

$$I_p = 0.446 \, nFAC \, \left(\frac{nFvD_0}{RT}\right)^{1/2}$$
 [3.3]

Here, Ip represents the anodic or cathodic peak current (in mA), n is the number of electrons transferred (n = 1 for  $[Fe(CN)_6]^{3^-/4^-}$  redox couple), A is the electroactive surface area (cm²), C is the bulk concentration of the redox species (mol/cm³), D is the diffusion coefficient (cm²/s), v is the scan rate (V/s), F is Faraday's constant (96485 C/mol), R is the universal gas constant (8.314 J/K·mol), and T is the temperature (298 K or 25 °C). On substituting the constants: F = 96485 C/mol, R = 8.314 J/mol·K, and T = 298 K (25 °C), the **Eq. [3.4]** simplifies to:

$$I_p = (2.69 \times 10^5) n^{3/2} A C D^{1/2} \sqrt{\nu}$$
 [3.4]

Using experimentally determined peak current values (Ip) from cyclic voltammograms and substituting the constant values of known parameters, including n=1,  $D=0.667\times 10^{-5}$  cm²/s, C=5 mM, and v=50 mV/s, the electroactive surface area (A) was computed. Using these experimental parameters, the electroactive surface area (A), a critical parameter influencing electron transfer rates of the h-BN electrodes, was calculated as summarized in **Table 3.4**. The quantification of electroactive surface area provides a critical understanding of the charge-exchange at the interface of the electrodes, with higher surface areas indicating greater availability of surface-active sites for redox reactions. The effectiveness of the electroactive surface area is essential for optimizing h-BN electrodes to develop high-performance electrochemical interfaces, particularly for applications requiring high surface area, such as energy storage devices, electrochemical sensors and biosensors.

Table 3.4: Quantitative evaluation of the Electrochemical performance given by peak anodic and cathodic currents (Ipa, Ipc), Ipa/Ipc ratio, and calculated electroactive surface area fabricated via electrophoretic deposition.

Sample	I <sub>pa</sub> (In mA)	Ipc (In mA)	Ipa/Ipc	Surface Active Area (10 <sup>-3</sup> )
Bulk h-BN	0.759	-0.695	1.092	$4.894 \times 10^{-3}$
h-BN_1	1.11	-1.04	1.067	$7.176 \times 10^{-3}$
h-BN_2	1.29	-1.23	1.048	$8.371 \times 10^{-3}$
h-BN_3	0.96	-0.904	1.021	$6.232 \times 10^{-3}$
h-BN_4	1.18	-1.11	1.063	$7.633 \times 10^{-3}$

Cyclic voltammetry (CV) analysis demonstrated that h-BN\_2, referred to as h-BN nanosheets (h-BNNS), possesses the highest electroactive surface area among the tested samples, while h-BN\_3 exhibited the lowest. Quantitatively, h-BNNS offers a substantial enhancement of 34.3% in electroactive surface sites for h-BNNS compared to h-BN\_3, indicating a high density of electrochemically accessible redox active sites. Microstructural analysis conducted via Scanning Electron Microscopy (SEM) and Transmission Electron Microscopy (TEM) strongly supported that h-BN\_2 (h-BNNS) consists of well-separated nanosheets with a large surface area, maximizing the availability of electroactive sites. In contrast, h-BN\_3 depicted significant particle agglomeration, significantly reducing the effective surface area and potentially limiting electrochemical performance. This structural advantage of h-BNNS enables more efficient electron transfer kinetics that account for their higher peak anodic and cathodic currents.

Scan rate study illustrated in Fig. 3.14(a-f) demonstrates the increase in peak current (Ip, mA) with increasing scan rate (v, mV/s), with a linear correlation between peak

current and the square root of the scan rate( $\sqrt{v}$ ). This linear relationship, consistent with the Randles-Sevcik equation (Eq. 3.4), confirms that the electrochemical reaction is governed by diffusion-assisted electron transfer, where the reaction rate is limited by the diffusion of redox species to the electrode surface. With increasing scan rates, a positive shift in the oxidation (anodic) current peak and a negative shift in the reduction (cathodic) current peak were observed. These shifts indicate that higher scan rates increase the overpotential required for redox reactions, reflecting the kinetic limitations of the diffusion process. This behaviour is consistent with the characteristics of diffusion-controlled systems, where faster scan rates reduce the time available for redox species to diffuse to the electrode surface [39]. To properly assess the diffusiongoverned behaviour, the systematic shift in linear relationships between peak current and peak potentials with the square root of the scan rate was quantified through linear regression fitting equations, as represented by Eq. [3.5–3.14]. The high correlation coefficients (R<sup>2</sup>) of these equations indicate a strong linear fit, reinforcing the diffusioncontrolled nature of the electrochemical process. These equations provide a mathematical framework for predicting the electrochemical behaviour of h-BN electrodes under varying scan rates, aiding in the optimization of their performance for specific applications.

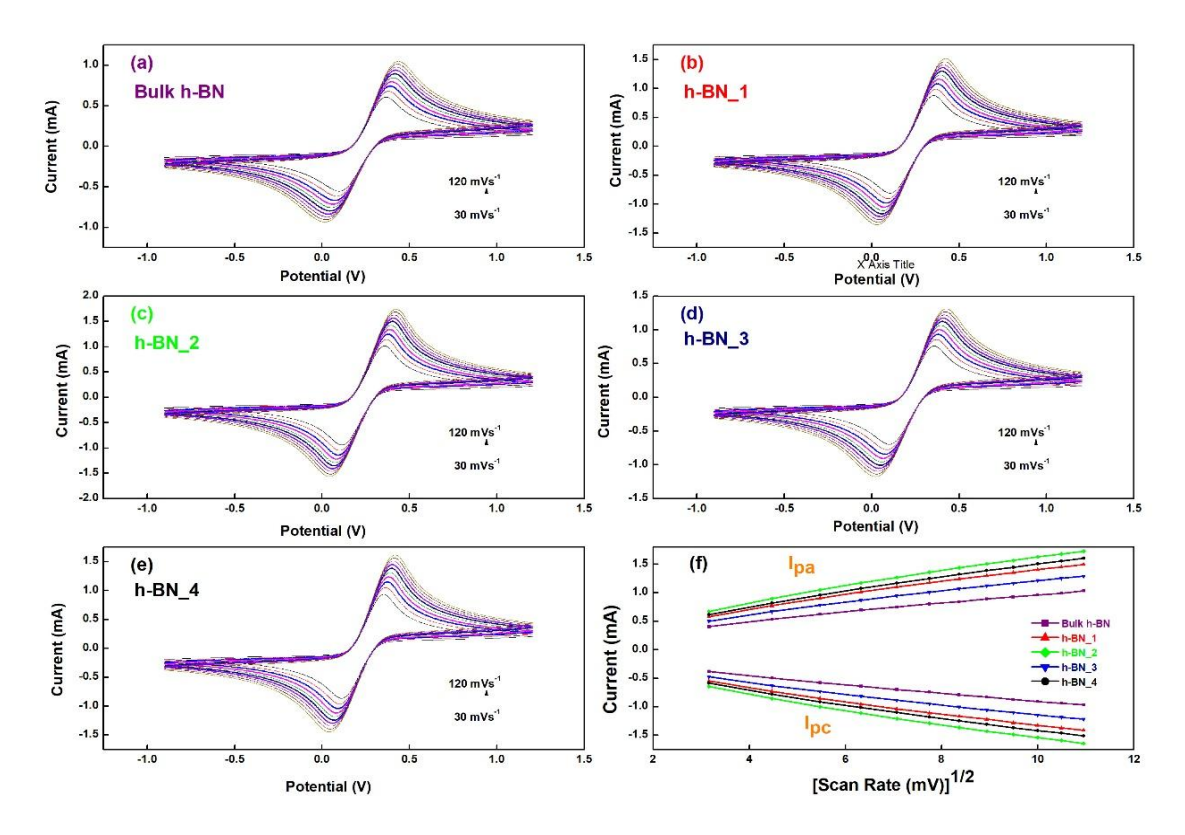


Figure 3.14: Representation of scan rate-dependent cyclic voltammograms for (a) bulk h-BN and its modified derivatives (b) h-BN\_1, (c) h-BN\_2, (d) h-BN\_3, and (e) h-BN\_4, obtained over the potential range -0.9 V to +1.2 V at scan rates from 30 to 120 mV s<sup>-1</sup>, along with (f) the linear fitting plots of Ipa and Ipc versus the square root of the scan rate, confirming diffusion-controlled redox behaviour.

$$I_{pa(Bulk\;h-BN)} = [1.84\times 10^{-4}\;mA + \; 0.782\times 10^{-4}\;mA \times \sqrt{s/mV} \times \sqrt{Scan\;Rate[mV/s]}] \eqno(3.5)$$
 
$$R^2 = \; 0.9956$$

$$I_{pc(Bulk\;h-BN)} = [-1.63\times 10^{-4}\;mA - 0.741\,\times 10^{-4}\;mA\,\times\,\sqrt{s/mV}\,\times \sqrt{Scan\;Rate[mV/s]}] \eqno(3.6)$$
 
$$R^2 = \ 0.9970$$

$$I_{pa(h-BN\_1)} = [3.7 \times 10^{-4} \text{ mA} + 1.01 \times 10^{-4} \text{ mA} \times \sqrt{s/mV} \times \sqrt{Scan \, Rate[mV/s]}]$$
 [3.7] 
$$R^2 = 0.9964$$

$$I_{pc(h-BN\_1)} = [-3.38 \times 10^{-4} \ mA - 0.97 \times 10^{-4} \ mA \times \sqrt{s/mV} \times \sqrt{Scan \, Rate[mV/s]}]$$
 [3.8] 
$$R^2 = 0.9974$$

$$I_{pa(h-BN\_2)} = [4.34 \times 10^{-4} \text{ mA} + 1.17 \times 10^{-4} \text{ mA} \times \sqrt{s/mV} \times \sqrt{Scan \, Rate[mV/s]}]$$
 
$$R^2 = 0.9966$$
 [3.9]

$$I_{pc(h-BN\_2)} = [-4.1 \times 10^{-4} \text{ mA} - 1.12 \times 10^{-4} \text{ mA} \times \sqrt{s/mV} \times \sqrt{Scan \, Rate[mV/s]}]$$
 [3.10] 
$$R^2 = 0.9973$$

$$I_{pa(h-BN\_3)} = [3.22 \times 10^{-4} \ mA + \ 0.87 \times 10^{-4} \ mA \times \ \sqrt{s/mV} \times \sqrt{Scan \, Rate[mV/s]}]$$
 
$$R^2 = \ 0.9971$$

$$I_{pc(h-BN\_3)} = [-2.7 \times 10^{-4} \ mA \ - 0.85 \times 10^{-4} \ mA \ \times \sqrt{s/mV} \times \sqrt{Scan \ Rate[mV/s]}]$$
 
$$R^2 = \ 0.9982$$
 [3.12]

$$I_{pa(h-BN\_4)} = [3.83 \times 10^{-4} \text{ mA} + \ 1.10 \times 10^{-4} \text{ mA} \times \sqrt{s/mV} \times \sqrt{Scan \, Rate[mV/s]}]$$
 [3.13] 
$$R^2 = 0.9967$$

$$I_{pc(h-BN\_4)} = [-3.58 \times 10^{-4} \ mA - 1.04 \times 10^{-4} \ mA \times \sqrt{s/mV} \times \sqrt{Scan \, Rate[mV/s]}]$$
 [3.14] 
$$R^2 = 0.9975$$

### 3.3.2.2 Electrochemical impedance spectroscopy (EIS)

Electrochemical Impedance Spectroscopy (EIS) measurements were performed across a frequency range of 0.1 Hz to 100 kHz using an AC perturbation of 10 mV to thoroughly investigate the intrinsic interfacial properties and charge transfer kinetics of hexagonal boron nitride (h-BN) nanosheet electrodes. This broad frequency range captures the interplay between charge transfer and diffusion processes, essential for understanding the electrode's performance in electrochemical systems. The Nyquist plot, presented in Fig. 3.15, visualizes the impedance response with real impedance (Z') on the x-axis and imaginary impedance (Z") on the y-axis. The plot exhibits a highfrequency semicircle, reflecting the charge transfer resistance (Rct) at the electrodeelectrolyte interface, and a low-frequency linear tail, indicative of diffusion-limited processes where mass transport of redox species dominates the electrochemical response. The impedance spectra were effectively deconvoluted using the equivalent electrical circuit, allowing precise quantification from fitting the modified Randles circuit model Rs(Q[RctZw]), where Solution Resistance (Rs) represents the resistance of the electrolyte and contributions from electrode geometry, Charge Transfer Resistance (Rct) denotes the electrode-electrolyte interfacial charge transfer resistance, Q is the constant phase element accounting for non-ideal capacitive behaviour, and Warburg Impedance Admittance (Zw, Yo) Accounts for diffusion processes at low frequencies.

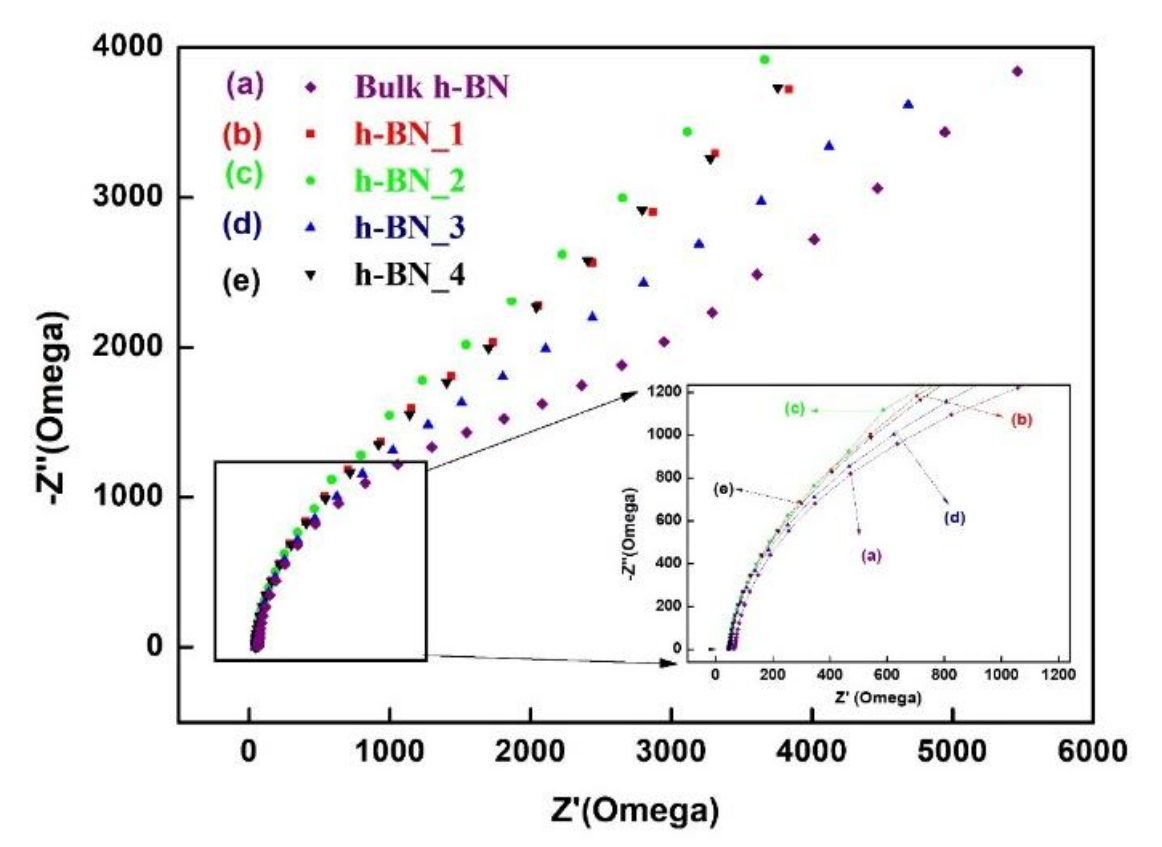


Figure 3.15 Nyquist plots derived from Electrochemical Impedance Spectroscopy (EIS) reveal the interfacial resistance behaviour of (a) bulk h-BN and hydrothermally exfoliated samples (b) h-BN 1, (c) h-BN 2, (d) h-BN 3, and (e) h-BN 4, recorded across a frequency range of 0.1–10<sup>5</sup> Hz under a constant bias potential of 10 mV.

The solution resistance (Rs) arises from the ionic conductivity of the electrolyte (50 mM phosphate buffer saline with 0.9% NaCl, pH 7.0) and the geometric configuration of the electrode setup. Rs remains relatively constant across measurements, as it is primarily determined by the electrolyte composition and electrode design, rather than dynamic interfacial processes, ensuring consistent baseline conditions for the EIS analysis. In an ideal electrochemical system, the double-layer capacitance at the electrode-electrolyte interface would produce a 90° phase shift in the AC response, indicative of purely capacitive behaviour [40]. However, due to surface inhomogeneities in h-BN nanosheet electrodes, such as variations in surface morphology or defects, a constant phase element (Q) is used instead of an ideal capacitor. The CPE accounts for the non-ideal capacitive behaviour, providing a more accurate representation of the electrode's interfacial properties and enhancing the understanding of h-BNNS electrochemical performance.

Electrochemical Impedance Spectroscopy (EIS) analysis elucidated the interfacial properties of h-BN nanosheet electrodes, with the constant phase element (CPE) admittance (Yo, in Mho) defined by Eq. [3.15],  $\mathbf{Z}_{\mathbf{w}} = \frac{1}{\mathbf{Y}_{\mathbf{0}}(j\omega)^{N}}$ 

$$Z_{W} = \frac{1}{Y_{0}(j\omega)^{N}}$$
 [3.15]

where  $\omega$  is circular frequency, j is the imaginary unit, and N (0 to 1) determines CPE behavior: N = 0 (pure resistor), N = 1 (pure capacitor), and N = 0.5 (Warburg element). The behaviour of the CPE is governed by the value of (N), which ranges between 0 and 1 and determines the electrochemical characteristics of the system. When (N=0), the CPE behaves as a pure resistor, exhibiting purely resistive impedance. When (N=1), it functions as a pure capacitor, displaying ideal capacitive behaviour with a 90° phase shift. At (N=0.5), the CPE corresponds to a Warburg element, indicative of diffusion-controlled processes where impedance is dominated by mass transport. This mathematical formulation captures the non-ideal impedance behaviour of electrochemical interfaces, accounting for surface heterogeneities in materials like hexagonal boron nitride (h-BN) nanosheets.

Table 3.5: Electrochemical impedance spectroscopy (EIS)-derived values tabulating key parameters, including charge transfer resistance (Rct), Warburg admittance (Zw.Yo), and CPE admittance (CPE.Yo) for h-BN nanosheet electrochemical analysis.

Sample	$R_{ct}(k\Omega)$	Zw.Yo (µMho)	CPE.Yo (µMho)
Bulk h-BN	2.12	180	12.2
h-BN_1	1.90	112	14.7
h-BN_2	1.61	101	15.7
h-BN_3	2.10	147	15.3
h-BN_4	1.71	110	14.0

The remarkably high CPE admittance observed in h-BN 2 reflects its outstanding pseudo-capacitive behaviour and charge storage capability. This outcome can be attributed to its few-layered architecture with minimal agglomeration enables better access to electroactive sites, optimizing its performance for rapid redox reactions and capacitive applications. Such performance marks h-BN 2 as a promising interface for high-sensitivity sensors and rapid electrochemical detection systems. The findings documented in Table III highlight the Electrochemical Impedance Spectroscopy (EIS) results, revealing that sample h-BN 2, synthesized at 220°C for 18 hours, exhibits the lowest charge transfer resistance (Rct). This low Rct signifies a minimal barrier owing to its reduced crystallite size and ultrathin morphology that facilitates an abundant electroactive site at the electrode-electrolyte interface for enhancing redox exchange efficiency of redox species, such as [Fe(CN)<sub>6</sub>]<sup>3-/4-</sup>, and lowering the energy barrier for electron transfer at the interface. Moreover, the remarkably low Warburg admittance value (Zw = 101 μMho) for h-BN 2 indicates highly efficient diffusion-controlled kinetics. This low Warburg admittance reflects the unhindered diffusion of electroactive species at the electrolyte-electrode interface, minimizing mass transport limitations and enhancing the overall electrochemical reaction rate. Such synergistic improvements at both electronic and ionic levels collectively translate into elevated peak currents and reduced electrochemical impedance, making h-BN 2 exceptionally well-suited for rapid and efficient redox processes.

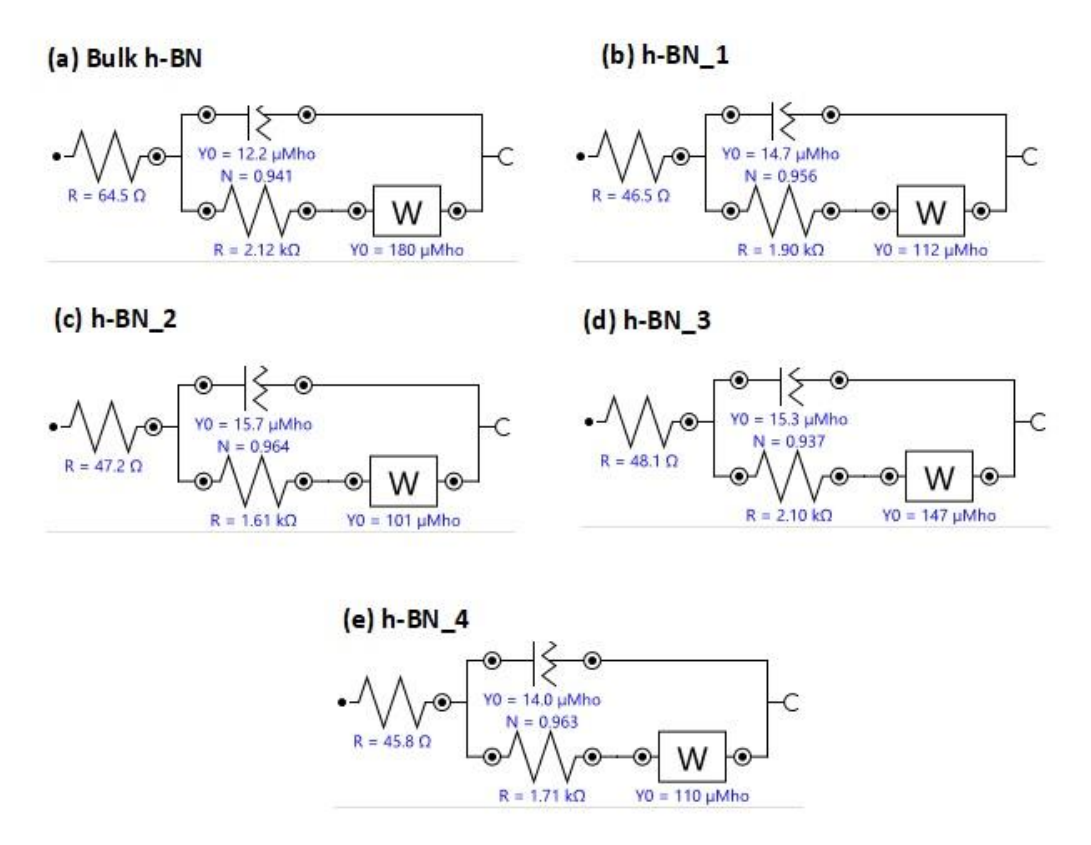


Figure 3.16: Electrical equivalent circuit models representing the fitted impedance parameters derived from EIS analysis for samples (a) bulk h-BN and hydrothermally exfoliated samples (b) h-BN\_1, (c) h-BN\_2, (d) h-BN\_3, and (e) h-BN\_4, effectively capture their interfacial charge transfer dynamics and diffusion behaviour.

### 3.3.2.3 Differential pulse voltammetry (DPV)

To evaluate the faradaic response characteristics of the synthesized h-BN electrodes, DPV measurements were performed at a controlled scan rate of 10 mV s<sup>-1</sup> over a wide potential range of -0.7 V to +1.2 V. This allowed for precise probing of electron transfer kinetics and redox activity. The DPV experiments aimed to quantify the faradaic current, which arises from the electron transfer reactions of the redox species ([Fe(CN)<sub>6</sub>]<sup>3-/4-</sup>) at the electrode-electrolyte interface (**Fig. 3.17**). By applying discrete potential pulses and measuring the resulting current differences, DPV enhances the resolution of redox peaks, making it ideal for evaluating the electrochemical performance of h-BN electrodes. The peak faradaic currents extracted from the voltammograms for Bulk h-BN, h-BN 1, h-BN 2, h-BN 3, and h-BN 4 were 0.16 mA, 0.28 mA, 0.32 mA, 0.23 mA, and 0.30 mA, respectively. Notably, h-BN 2 exhibited the most pronounced electrochemical response, clearly correlating with its tailored nanostructure marked by reduced crystallite size and increased surface reactivity—which collectively boost electrochemical interactions at the electrodeelectrolyte interface. The enhanced response establishes the strong correlation between nanoscale architecture and electrochemical efficiency by lowering charge transfer resistance and optimizing diffusion pathways. These DPV profiles, as depicted in Fig.

**3.17**, reveal the impact of structural tuning on the electrochemical activity of the materials.

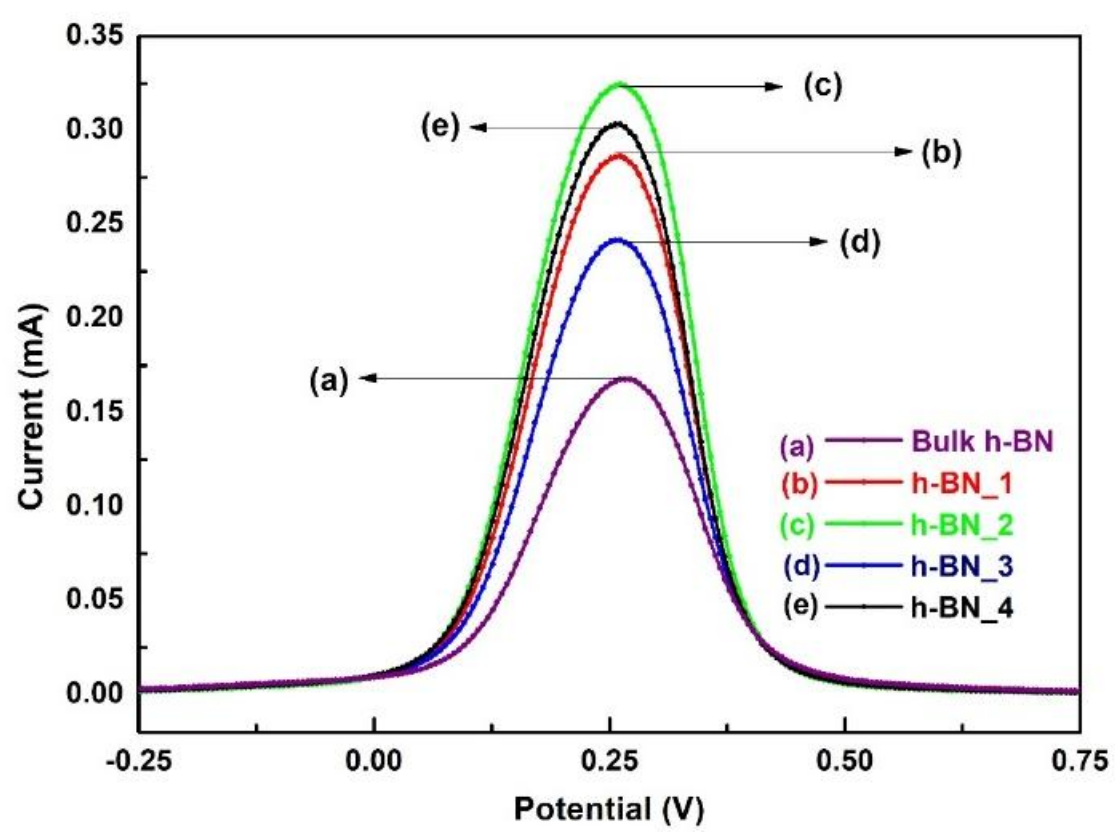


Figure 3.17: Electrochemical investigations from Differential Pulse Voltammetry between -0.7 V and +1.2 V for (a) Bulk h-BN, and structurally modified counterparts (b) h-BN\_1, (c) h-BN\_2, (d) h-BN\_3, and (e) h-BN\_4, reveal the influence of nanoscale refinement on redox behaviour.

Differential Pulse Voltammetry (DPV) offers superior sensitivity over Cyclic Voltammetry (CV) due to its refined peak resolution and sharper signal profile. This enhanced sensitivity stems from DPV's ability to precisely measure the differential increase in current (ΔI) as a function of small incremental changes in applied potential (ΔV), driven by the use of minimal pulse amplitude [41]. As a result, DPV effectively reduces background noise and accentuates faradaic current responses. Notably, the DPV response for the h-BN\_2 (exfoliated hBNNS) sample displayed a peak current magnitude twice that of bulk h-BN, highlighting its improved electrochemical activity and faster redox kinetics. This pronounced enhancement aligns well with the trends observed in CV, reaffirming the superior electron transfer dynamics of h-BN\_2. Additionally, when compared to h-BN\_3, the peak current of h-BN\_2 showed a marked increase of 39.13%, attributed to the optimized nanosheet structure that facilitates more efficient diffusion and exchange of redox species at the electrode interface.

#### **Conclusions**

A one-pot hydrothermal approach was successfully optimized to synthesize largelateral-size hexagonal boron nitride nanosheets (h-BNNS) with remarkable electrochemical performance. This work focused on investigating the synergy of hydrothermal synthesis parameters, including temperature and duration, that crucially influenced the exfoliation quality, lateral dimension, and structural integrity of the nanosheets that contributed towards enhancing charge transport. Moreover, our findings assert that the synergistic influence of hydrothermal temperature and treatment duration is instrumental in tailoring the morphological and functional properties of hBNNS. By optimizing these parameters, we have developed an environment-friendly, efficient, scalable, and industrially viable route for producing high-performance boron nitride-based nanomaterials. To correlate structure with function, we extended our material characterization through X-ray diffraction (XRD) using Williamson-Hall (W-H) analysis, UV-Visible spectroscopy, and Raman spectroscopy. These techniques provided strong evidence of quantum confinement effects and strain-induced modulation in optical and structural properties, confirming the nanoscale precision achieved through our method. Our study further investigated the interplay between micro-strain and morphological evolution, revealing that induced micro-strain not only influences nanosheet thickness and layer separation but also facilitates the formation of larger lateral-size nanosheets. These structural features directly contribute to enhanced electron diffusion dynamics, crucial for high-performance electrochemical applications. Unlike conventional approaches that require post-functionalization, our method enables direct functionalization during exfoliation, as confirmed by FT-IR spectroscopy, which revealed the generation of abundant redox-active functional groups. These functional moieties significantly enhance the material's electrochemical sensitivity by facilitating efficient electron transfer. Electrochemical analysis revealed an exceptionally high electroactive surface area of  $8.37 \times 10^{-3}$  cm<sup>2</sup>, underscoring the material's capacity to provide a dense network of electroactive sites. These sites are highly favourable for the adsorption and interaction with gas molecules and biomolecules, establishing hBNNS as a highly sensitive and responsive platform for electrochemical sensing applications. Moreover, the material demonstrated a notable charge storage capacity, with a CPE.Y<sub>0</sub> value of 15.7 μMho, indicating its strong potential for use in anticorrosion coatings, energy conversion devices, and supercapacitor or battery electrodes.

#### References

- [1] M.A. Kebede, T. Imae, Low-dimensional nanomaterials, in: Advanced Supramolecular Nanoarchitectonics, Elsevier, 2019, pp. 3-16.
- [2] W. Liu, R. Yin, X. Xu, L. Zhang, W. Shi, X. Cao, Structural engineering of low-dimensional metal—organic frameworks: synthesis, properties, and applications, Advanced science, 6 (2019) 1802373
- [3] Q. Xu, Y. Dai, Y. Peng, L. Hong, N. Yang, Z. Wang, Recent Development of Multifunctional Sensors Based on Low-Dimensional Materials, Sensors, 21 (2021) 7727.
- [4] C. Tan, X. Cao, X.-J. Wu, Q. He, J. Yang, X. Zhang, J. Chen, W. Zhao, S. Han, G.-H. Nam, Recent advances in ultrathin two-dimensional nanomaterials, Chemical reviews, 117 (2017) 6225-6331.
- [5] S. Hu, X. Wang, Ultrathin nanostructures: smaller size with new phenomena, Chemical Society Reviews, 42 (2013) 5577-5594.

- [6] Y. Sun, S. Gao, F. Lei, C. Xiao, Y. Xie, Ultrathin two-dimensional inorganic materials: new opportunities for solid state nanochemistry, Accounts of chemical research, 48 (2015) 3-12.
- [7] M.J. Molaei, M. Younas, M. Rezakazemi, A Comprehensive Review on Recent Advances in Two-Dimensional (2D) Hexagonal Boron Nitride, ACS Applied Electronic Materials, 3 (2021) 5165-5187.
- [8] Z. Liu, Y. Gong, W. Zhou, L. Ma, J. Yu, J.C. Idrobo, J. Jung, A.H. MacDonald, R. Vajtai, J. Lou, Ultrathin high-temperature oxidation-resistant coatings of hexagonal boron nitride, Nature communications, 4 (2013) 2541.
- [9] S.C. Yoo, J. Kim, W. Lee, J.Y. Hwang, H.J. Ryu, S.H. Hong, Enhanced mechanical properties of boron nitride nanosheet/copper nanocomposites via a molecular-level mixing process, Composites Part B: Engineering, 195 (2020) 108088.
- [10] W. Zhou, J. Zuo, X. Zhang, A. Zhou, Thermal, electrical, and mechanical properties of hexagonal boron nitride–reinforced epoxy composites, Journal of Composite Materials, 48 (2014) 2517-2526.
- [11] X. Yu, M. Xue, Z. Yin, Y. Luo, Z. Hong, C. Xie, Y. Yang, Z. Ren, Flexible boron nitride composite membranes with high thermal conductivity, low dielectric constant and facile mass production, Composites Science and Technology, 222 (2022) 109400.
- [12] S. Mateti, C.S. Wong, Z. Liu, W. Yang, Y. Li, L.H. Li, Y. Chen, Biocompatibility of boron nitride nanosheets, Nano Research, 11 (2018) 334-342.
- [13] A.K. Geim, I.V. Grigorieva, Van der Waals heterostructures, Nature, 499 (2013) 419-425.
- [14] G. Darabdhara, P. Borthakur, P.K. Boruah, S. Sen, D.B. Pemmaraju, M.R. Das, Advancements in Two-Dimensional Boron Nitride Nanostructures: Properties, Preparation Methods, and their Biomedical Applications, Journal of Materials Chemistry B, (2025).
- [15] S. Angizi, M. Khalaj, S.A.A. Alem, A. Pakdel, M. Willander, A. Hatamie, A. Simchi, Towards the two-dimensional hexagonal boron nitride (2D h-BN) electrochemical sensing platforms, Journal of The Electrochemical Society, 167 (2020) 126513.
- [16] Y. Lin, J.W. Connell, Advances in 2D boron nitride nanostructures: nanosheets, nanoribbons, nanomeshes, and hybrids with graphene, Nanoscale, 4 (2012) 6908-6939.
- [17] A. Nag, K. Raidongia, K.P. Hembram, R. Datta, U.V. Waghmare, C. Rao, Graphene analogues of BN: novel synthesis and properties, ACS nano, 4 (2010) 1539-1544.
- [18] M. Sajjad, P. Feng, Study the gas sensing properties of boron nitride nanosheets, Materials Research Bulletin, 49 (2014) 35-38.
- [19] W. Luo, T. Yang, L. Su, K.-C. Chou, X. Hou, Preparation of hexagonal BN whiskers synthesized at low temperature and their application in fabricating an electrochemical nitrite sensor, RSC Advances, 6 (2016) 27767-27774.
- [20] L. Song, L. Ci, H. Lu, P.B. Sorokin, C. Jin, J. Ni, A.G. Kvashnin, D.G. Kvashnin, J. Lou, B.I. Yakobson, P.M. Ajayan, Large Scale Growth and Characterization of Atomic Hexagonal Boron Nitride Layers, Nano Letters, 10 (2010) 3209-3215.
- [21] P. Dash, P.K. Panda, Top-Down Strategies Synthesis of 2D Nanomaterial, in: 2D Nanomaterials, 2024, pp. 1-16.
- [22] C. Zhi, Y. Bando, C. Tang, H. Kuwahara, D. Golberg, Large-Scale Fabrication of Boron Nitride Nanosheets and Their Utilization in Polymeric Composites with Improved Thermal and Mechanical Properties, Advanced Materials, 21 (2009) 2889-2893.
- [23] M.L. Yola, N. Atar, Gold Nanoparticles/Two-Dimensional (2D) Hexagonal Boron Nitride Nanosheets Including Diethylstilbestrol Imprinted Polymer: Electrochemical Detection in Urine Samples and Validation, Journal of The Electrochemical Society, 165 (2018) H897.
- [24] M.L. Yola, N. Atar, A novel detection approach for serotonin by graphene quantum dots/two-dimensional (2D) hexagonal boron nitride nanosheets with molecularly imprinted polymer, Applied Surface Science, 458 (2018) 648-655.
- [25] L. Fu, Z. Liu, Y. Huang, G. Lai, H. Zhang, W. Su, J. Yu, A. Wang, C.-T. Lin, A. Yu, Square wave voltammetric quantitative determination of flavonoid luteolin in peanut hulls and

- Perilla based on Au NPs loaded boron nitride nanosheets, Journal of Electroanalytical Chemistry, 817 (2018) 128-133.
- [26] M. Adeel, M.M. Rahman, J.-J. Lee, Label-free aptasensor for the detection of cardiac biomarker myoglobin based on gold nanoparticles decorated boron nitride nanosheets, Biosensors and Bioelectronics, 126 (2019) 143-150.
- [27] G. Yang, H. Wang, N. Wang, R. Sun, C.-P. Wong, Hydrothermal exfoliation for two-dimension boron nitride nanosheets, in: 2018 IEEE 68th Electronic Components and Technology Conference (ECTC), IEEE, 2018, pp. 1421-1426.
- [28] L. Hua Li, Y. Chen, B.-M. Cheng, M.-Y. Lin, S.-L. Chou, Y.-C. Peng, Photoluminescence of boron nitride nanosheets exfoliated by ball milling, Applied Physics Letters, 100 (2012).
- [29] L.H. Li, Y. Chen, G. Behan, H. Zhang, M. Petravic, A.M. Glushenkov, Large-scale mechanical peeling of boron nitride nanosheets by low-energy ball milling, Journal of Materials Chemistry, 21 (2011) 11862-11866.
- [30] T.A. Para, H.A. Reshi, S. Pillai, V. Shelke, Grain size disposed structural, optical and polarization tuning in ZnO, Applied Physics A, 122 (2016) 730.
- [31] K. Watanabe, T. Taniguchi, H. Kanda, Direct-bandgap properties and evidence for ultraviolet lasing of hexagonal boron nitride single crystal, Nature Materials, 3 (2004) 404-409. [32] F.K. Kessler, Y. Zheng, D. Schwarz, C. Merschjann, W. Schnick, X. Wang, M.J. Bojdys, Functional carbon nitride materials design strategies for electrochemical devices, Nature Reviews Materials, 2 (2017) 17030.
- [33] M.F. Malek, M.H. Mamat, M.Z. Musa, Z. Khusaimi, M.Z. Sahdan, A.B. Suriani, A. Ishak, I. Saurdi, S.A. Rahman, M. Rusop, Thermal annealing-induced formation of ZnO nanoparticles: Minimum strain and stress ameliorate preferred c-axis orientation and crystal-growth properties, Journal of Alloys and Compounds, 610 (2014) 575-588.
- [34] A. Falin, Q. Cai, E.J.G. Santos, D. Scullion, D. Qian, R. Zhang, Z. Yang, S. Huang, K. Watanabe, T. Taniguchi, M.R. Barnett, Y. Chen, R.S. Ruoff, L.H. Li, Mechanical properties of atomically thin boron nitride and the role of interlayer interactions, Nature Communications, 8 (2017) 15815.
- [35] R.V. Gorbachev, I. Riaz, R.R. Nair, R. Jalil, L. Britnell, B.D. Belle, E.W. Hill, K.S. Novoselov, K. Watanabe, T. Taniguchi, A.K. Geim, P. Blake, Hunting for Monolayer Boron Nitride: Optical and Raman Signatures, Small, 7 (2011) 465-468.
- [36] Z. Zhao, Z. Yang, Y. Wen, Y. Wang, Facile Synthesis and Characterization of Hexagonal Boron Nitride Nanoplates by Two-Step Route, Journal of the American Ceramic Society, 94 (2011) 4496-4501.
- [37] S. Augustine, P. Kumar, B.D. Malhotra, Amine-Functionalized MoO3@RGO Nanohybrid-Based Biosensor for Breast Cancer Detection, ACS Applied Bio Materials, 2 (2019) 5366-5378.
- [38] S.J. Konopka, B. McDuffie, Diffusion coefficients of ferri- and ferrocyanide ions in aqueous media, using twin-electrode thin-layer electrochemistry, Analytical Chemistry, 42 (1970) 1741-1746.
- [39] N. Kumar, A. Arora, A. Krishnan, Complementary AC Voltammetry—A Method for Simultaneous Measurement of Faradaic and Nonfaradaic Currents in an Electrochemically Reversible System, IEEE Sensors Journal, 20 (2020) 13196-13203.
- [40] R.-W. You, K.K. Lew, Y.-P. Fu, Effect of indium concentration on electrochemical properties of electrode-electrolyte interface of CuIn1-xGaxSe2 prepared by electrodeposition, Materials Research Bulletin, 96 (2017) 183-187.
- [41] A. Molina, C. Serna, Q. Li, E. Laborda, C. Batchelor-McAuley, R.G. Compton, Analytical Solutions for the Study of Multielectron Transfer Processes by Staircase, Cyclic, and Differential Voltammetries at Disc Microelectrodes, The Journal of Physical Chemistry C, 116 (2012) 11470-11479.

# Chapter 4

Development of an Electrochemical Nano-Biosensing Interface based on Hydrothermally Engineered Ultrathin h-BN Nanosheets for High-Performance, Label-Free Detection of Carcinoembryonic Antigen

Evolution in nanostructure engineering has enabled the development of ultrathin layered inorganic materials with controlled morphology, yielding ultrahigh surface area, enhanced mass transport, and abundant bio-affinity functional sites. These attributes make inorganic layered materials promising candidates for high-performance nano-biosensors. In this study, we developed engineered hexagonal boron nitride nanosheets (h-BNNS) as a robust electroanalytical platform for label-free detection of carcinoembryonic antigen (CEA), a critical biomarker for cancer diagnostics. The biocompatibility of the synthesized h-BNNS was rigorously validated using an MTT cytotoxicity assay on HEK 293 human cell lines, affirming their suitability for biological interfacing. The successful formation of few-layered, ultrathin, and highpurity hexagonal boron nitride nanosheets (h-BNNS) was confirmed through XRD, SEM, TEM, Raman, and UV-Visible analyses, which collectively validated structural integrity, exfoliation efficiency, and morphological uniformity. Electrophoretic deposition (EPD) was employed to fabricate uniform and stable h-BNNS microelectrodes on hydrolyzed indium tin oxide (ITO) glass substrates using a low DC potential of 20 V, offering a scalable and cost-effective method for nano-biosensor development. In-situ surface-functionalization with -OH, -NH, and -BH groups on hydrothermally exfoliated h-BNNS enabled effective covalent immobilization of Anti-CEA monoclonal antibodies via EDC-NHS coupling chemistry and BSA stabilization, as confirmed by FT-IR spectroscopy and diffusion studies. The developed nanobiosensor demonstrated an impressive analytical performance, with an exceptional sensitivity of 24.84 µA·mL/ng/cm<sup>2</sup> and a remarkable LOD of 22.5 pg/mL over a clinically relevant CEA concentration range (0-50 ng/mL), with excellent linear correlation ( $R^2 = 0.99988$ ). Moreover, the sensor displayed negligible cross-reactivity, long-term shelf stability, and excellent performance in human serum samples, underlining its clinical feasibility for early-stage cancer diagnostics. The findings of this work highlight the versatility and diagnostic potential of h-BNNS-based biosensing platforms together with an established new approach for cost-effective, label-free, and real-time detection of protein biomarkers in complex biological matrices.

The research findings detailed in this chapter have been published in a scientific journal:

"An efficient electrochemical nano-biosensor based on hydrothermally engineered ultrathin nanostructures of hexagonal boron nitride nanosheets for label-free detection of carcinoembryonic antigen" Applied Nanoscience, 2023

(14) 217-230

#### 4.1 Introduction

Over time, technological advancements have driven a remarkable and transformative evolution in science and engineering, with nanotechnology and nanoscience emerging as pivotal forces behind this progress [1]. Understanding the distinct difference between nanoscience and nanotechnology is required to distinguish their scope and purpose. Nanoscience focuses on the study of the arrangement of atoms and molecules at the nanoscale, along with their intrinsic properties. In contrast, nanotechnology applies this knowledge to manipulate matter at the atomic and molecular levels, enabling the synthesis of novel nanomaterials with tailored properties. As a multidisciplinary domain, nanotechnology integrates the principles of physics, chemistry, materials science, and multiple branches of engineering to manipulate matter at the atomic and molecular scales. Its unique ability to tailor size, shape, and surface characteristics at the nanoscale has unlocked unprecedented properties ranging from enhanced mechanical strength and catalytic efficiency to superior electronic, optical, and biomedical functionalities. Consequently, the applications of nanotechnology now permeate nearly every branch of science and technology, prompting breakthroughs in healthcare, energy systems, environmental remediation, electronics, photonics, and beyond. This pervasive influence firmly establishes nanotechnology not merely as a supportive discipline, but as the indispensable foundation and defining engine of modern innovation.

Back through time, the foundational innovation of the first glucose biosensor developed by Leland C. Clark in 1962, which pioneered the concept of integrating biological recognition elements with transducers for analytical detection [2]. These traditional biosensing platforms, while effective, are often limited by size, sensitivity, and operational speed constraints that can be critical in medical emergencies or environmental crises. While Clark's design marked the birth of biosensing, advances in nanotechnology address these challenges by introducing engineering of nanostructures with exceptionally high surface-to-volume ratios, superior electron transport properties, and tunable surface chemistry. Nanotechnology is poised to exert a transformative influence over biosensors to detect trace biomolecules, toxins, or pathogens within minutes, fulfilling the imperative need for rapid, reliable, and portable diagnostic systems in healthcare, agriculture, defense, and environmental protection. Thus, the scientific and technological research is focused on the evolution of modern biosensors, which leads to the emergence of nanotechnology-enabled nano-biosensors with exceptional detection capabilities.

Nano-biosensing has emerged as a highly promising and transformative diagnostic approach, harnessing the advancements of nanotechnology to develop sustainable point-of-care diagnostic tools capable of enabling the early detection of cancer, a disease that continues to be one of the most prevalent and life-threatening worldwide. Nano-biosensors are sophisticated analytical devices that integrate engineered nanostructures as bio-sensitive layers, designed to detect and transduce even the weakest biochemical signals generated during highly specific bio-recognition events [3]. The nanoscale architecture of these devices offers unique advantages, including an exceptionally high surface-to-volume ratio, tunable physicochemical properties, and enhanced interaction with target biomolecules, thereby significantly improving signal capture and transduction efficiency. By leveraging the unique physicochemical, optical,

and electrochemical properties of nano-engineered materials, these platforms achieve exceptional signal amplification and enhanced detection accuracy.

The surge in nano-biosensing interface development reflects the demand for nextgeneration platforms that offer exceptionally robust, reliable, resilient, sensitive, selective, precise, swift response, cost-effective, and biocompatible characteristics that establish the standard for effective and commercially operational nano-biosensing technologies. Two-dimensional (2D) nanosheets, engineered with ultrathin geometry, expansive lateral surface areas, controlled morphology, and embedded nano-sized particles, have emerged as substantially promising candidates for nano-biosensing interfaces due to their exceptional properties tailored to meet key technological requirements [4]. Quantum confinement in ultrathin, monolayer 2D materials drastically modifies their electronic band structure, resulting in unique, highly tunable properties like high carrier mobility, direct bandgaps, and strong many-body interactions. These features position single- or few-layered 2D nanomaterials as powerful platforms for advancing condensed matter physics and driving the development of high-performance electronic and optoelectronic devices. The coexistence of large lateral dimensions with atomic-scale thickness endows these nanosheets with an ultrahigh specific surface area, enabling exceptionally sensitive detection of minute analyte concentrations with high accuracy. This extensive surface area dramatically increases the availability of active sites, which is highly advantageous for surface-dependent applications such as heterogeneous catalysis, energy storage in supercapacitors, and sensing platforms.

Furthermore, the high surface-to-volume ratio promotes enhanced interaction with reactants or analytes with functionalized, extensive 2D architecture, thereby significantly improving the efficiency and sensitivity of the platform [5]. The robust inplane covalent bonding among atoms in these 2D materials provides exceptional mechanical strength and structural stability, despite their atomic-scale thickness. This intrinsic strength, combined with their inherent flexibility and optical transparency, renders them ideal for integration into flexible, lightweight, and transparent electronics. The high density of surface atoms exposed in these atomically thin layers facilitates facile and precise tuning of their physical and chemical properties through various surface engineering approaches. Surface modification and functionalization, controlled element doping, and the introduction of defects, strain, or phase transformations enable targeted manipulation of electronic, optical, and catalytic properties. This tunability allows for customized material behaviour, which is crucial for optimizing device performance and expanding the functional versatility of 2D nanomaterials. In addition, ultrathin 2D nanomaterials demonstrate exceptional solution processability, enabling uniform dispersion in solvents and fabrication of high-quality, free-standing thin films via scalable methods like vacuum filtration, electrophoretic deposition, spin coating, drop casting, spray coating, and inkjet printing. These facile, low-cost, and adaptable fabrication methods are vital for the practical deployment of 2D materials in large-area flexible electronics, energy devices like solar cells, sensors, and supercapacitors, bridging the gap between lab-scale research and industrial operations.

Research interest remarkably strengthened in two-dimensional (2D) nanostructured materials following the extraordinary exfoliation of graphene nanosheets, also known as a single atomic-scale sheet of graphite, by Geim and Novoselov in 2004 [6].

Graphene exhibits a unique ability to host relativistic charge carriers, highlighting its peculiar physical properties, including ultrahigh room-temperature carrier mobility, ballistic electron transport over micrometer scales, and quantum Hall effects observable even under ambient conditions. These phenomena arise from its strictly twodimensional atomic lattice and distinctive electronic band structure, where conduction and valence bands intersect at discrete Dirac points. In this regime, electrons behave as massless Dirac fermions, exhibiting a linear energy-momentum relationship characteristic of relativistic particles moving at a constant Fermi velocity. This unique electronic landscape not only advances fundamental condensed matter physics but also positions graphene as a platform for next-generation high-performance electronic, optoelectronic, and quantum devices. Yet, a fundamental limitation persists: the absence of an intrinsic bandgap. This zero-bandgap nature precludes the high ON/OFF current ratios essential for efficient, low-power digital logic applications [7]. Additionally, in harsh environments, graphene can undergo oxidation or fouling, affecting reproducibility and long-term stability, which can affect the consequential performance of the device.

While the physics of graphene is undeniably compelling, the very act of isolating a twodimensional (2D) crystal, especially from elements beyond carbon, has redefined the landscape of materials research. Following the extensive exploration of graphene, hexagonal boron nitride (h-BN) has emerged as a highly promising and strategically advantageous material as it retains several structural attributes of graphene while addressing some of its key limitations. Hexagonal boron nitride (h-BN), often mentioned as "white graphene," inherits unique structural architecture from graphene, featuring an atomically thin, honeycomb lattice with a two-dimensional layered architecture, strong in-plane covalent bonding, and van der Waals interlayer interactions. This structural configuration enables h-BN to be exfoliated into ultrathin nanosheets, significantly enhancing its specific surface area and preserving outstanding mechanical robustness [8]. These attributes are pivotal for constructing stable, durable, and highly sensitive electrochemical sensing platforms capable of enduring repeated operational cycles without structural constraints. In addition, the expansive surface area provides abundant surface-active sites for functionalization with catalytic or recognition elements that ensure efficient analyte interaction, thereby improving detection sensitivity, the limit of detection, and reproducibility.

In contrast to graphene, which is a zero-bandgap semimetal with high electrical conductivity, h-BN is an electrical insulator with a wide bandgap of approximately ~6 eV [9]. This intrinsic electronic characteristic fundamentally alters its functional behaviour by eliminating the excessive baseline conductivity that often contributes to background electrochemical noise, thereby improving the signal-to-noise ratio in sensing applications. Moreover, the wide bandgap endows h-BN with exceptional chemical inertness, preventing unwanted redox processes and non-specific adsorption that could otherwise interfere with accurate analyte detection. This insulating nature also enables h-BN to act as a high-performance dielectric barrier, contributing to overcoming key limitations of graphene by effectively preventing unwanted electron leakage and electrochemical cross-talk in multi-component or integrated sensor systems. Furthermore, h-BN demonstrates exceptional chemical stability and strong resistance to oxidation, corrosion, and harsh chemical environments, making it

particularly proficient for sensing in aggressive or biologically complex media where graphene may degrade or lose performance over time.

Beyond its electronic attributes, h-BN demonstrates exceptional chemical inertness, making it highly resistant to oxidation, corrosion, and chemical degradation, even under extreme pH conditions or in the presence of aggressive redox species. This stability is further complemented by its remarkable thermal endurance, maintaining structural integrity at temperatures exceeding 900 °C in oxidative environments, which ensures reliable performance in high-temperature or thermally fluctuating surroundings [10]. These properties collectively enable h-BN to address key limitations associated with graphene-based electrochemical sensors, particularly their vulnerability to non-specific surface reactions, environmental degradation, and background electrochemical noise. Hence, h-BN emerges as a robust and versatile platform material, well-suited for next-generation sensing technologies that demand long-term operational stability, high selectivity, and compatibility with complex or harsh environments.

Fabrication of efficient nano-biosensing platforms, the inherent chemical inertness of h-BN, while advantageous for exceptional stability, dielectric behaviour, and surface smoothness, presents a significant challenge for the covalent immobilization of biomolecules, a process critical for enhancing charge-transfer kinetics and achieving ultrasensitive analyte detection [11]. Covalent attachment of biomolecules enables the creation of specific binding sites, promotes efficient electron exchange between the sensing surface and target species, and improves selectivity, yet this is hindered in pristine h-BN due to its lack of chemically active sites.

To address this limitation, strategies have emerged that exploit the intrinsic physical and chemical characteristics of h-BNNS. Interestingly, one promising approach is to leverage the spatial confinement of electron—hole pairs through quantum confinement effects within ultrathin h-BN nanosheets (h-BNNS). This phenomenon, supported by reduction to a few atomic layers, spatial confinement of electron—hole pairs within narrow channels, stabilized by strong inter- and intra-layer covalent bonding, substantially enhances its surface adsorption capabilities. This was demonstrated in the work of Cai et al. [12], which provided both theoretical predictions and experimental validation showing that reduced dimensionality enriches surface reactivity and adsorption strength in h-BNNS, enabling better interaction with target molecules.

Another potential approach is surface functionalization, which involves deliberately tailoring the active sites on h-BNNS by introducing specific chemical functionalities that shift the surface energy from the bulk to the interface. This process increases surface reactivity, enabling selective binding of biomolecules or catalytic moieties, and allows fine control over the hydrophilicity, charge distribution, and catalytic properties of h-BNNS. Despite its promise, achieving effective functionalization is inherently challenging due to the strong in-plane covalent bonding and the absence of dangling bonds on pristine h-BN surfaces, which limit the availability of reaction sites. Effective surface functionalization can be attained through three principal routes: (1) covalent functionalization, which introduces chemical bonds directly to the h-BN lattice, (2) noncovalent functionalization, which utilizes  $\pi$ - $\pi$  stacking, van der Waals forces, or electrostatic interactions without disturbing the intrinsic lattice, and (3) Lewis acidbase chemistry, which exploits the partially ionic nature of the B-N bonds to form

strong donor-acceptor complexes. Among these, Lewis acid-base functionalization exhibits significant traction due to its efficiency and compatibility with h-BN's structural integrity [13]. Intriguingly, Lewis acid-base chemistry is particularly promising for h-BN modification because boron atoms in the lattice are electrondeficient and can readily form stable complexes with electron-rich Lewis bases. This interaction facilitates the intercalation of molecules between h-BN layers, creating opportunities for controlled nucleation and the synthesis of morphologically tailored nanostructures. Following intercalation, the strong van der Waals forces between h-BN layers must be overcome to achieve full exfoliation into nanosheets. This is often accomplished by employing hydrothermal techniques, where the synergistic effects of elevated temperature and vapor pressure provide the necessary energy to separate the layers efficiently without compromising their structural integrity [14]. Through these combined approaches, harnessing quantum confinement for enhanced adsorption, applying tailored functionalization strategies, and utilizing thermodynamically driven exfoliation, researchers have developed viable pathways to overcome the chemical inertness of h-BNNS, thereby revealing its complete potential as a stable, selective, and high-performance material for fabricating next-generation nano-biosensors.

Under uniform pressure and isothermal conditions, the hydrothermal environment promotes the formation of convection currents within the alkaline precursor solution, enabling the homogeneous distribution of reactants and the gradual formation of a saturated solution. This dynamic process ensures controlled nucleation and growth, favoring the development of well-defined ultrathin hexagonal h-BN structures. The alkaline medium not only facilitates dissolution and transport of precursor species but also stabilizes the growth fronts, allowing precise regulation of crystallinity and layer thickness. In the present work, a reduction-led hydrothermal synthesis route was strategically employed to harness these conditions. This method capitalizes on the combined effects of chemical reduction and hydrothermal confinement, yielding h-BN nanosheets (h-BNNS) with atomically thin geometry, large lateral dimensions, and a uniform hexagonal morphology that mirrors the intrinsic crystal symmetry of bulk h-BN. The hydrothermal process also plays a dual role—beyond structural control, it enables the in-situ generation of surface-active functional groups during synthesis. These functional moieties, introduced directly onto the h-BN basal planes and edges, significantly enhance the nanosheets' surface reactivity, creating active sites for subsequent covalent or noncovalent modification. By simultaneously achieving ultrathin geometry, expansive lateral surface area, high morphological integrity, and tailored surface chemistry, this approach not only overcomes the inherent chemical inertness of pristine h-BN but also positions the synthesized h-BNNS as an ideal platform for high-performance electrochemical and biosensing applications, where sensitivity, stability, and selective analyte interaction are paramount.

Cancer arises from abnormal and uncontrolled cell proliferation, with lung cancer ranking among the most prevalent and deadliest forms, accounting for an estimated 1.8 million deaths worldwide in 2020 [15, 16]. Non-small cell lung cancer (NSCLC) constitutes about 85% of lung cancer cases and is linked to risk factors such as smoking, chronic lung diseases, prolonged exposure to pollutants, and radioactive gases, and is further aggravated by susceptibility to SARS-CoV-2 infection [17-19]. Early symptoms—loss of appetite, cough, breathlessness, chest pain, and weight loss—are

often non-specific and may lead to misdiagnosis, delaying detection. Conventional imaging methods like X-ray, CT, MRI, and PET are costly, time-intensive, and inadequate for detecting sub-micrometer tumors, resulting in late-stage diagnosis and poor prognosis [20, 21]. Monitoring tumor-associated proteins offers a cost-effective, rapid, and reliable alternative [22, 23]. Proteomics has advanced early detection through specific serum biomarkers, notably carcinoembryonic antigen (CEA), which is overexpressed in about 70% of NSCLC cases. CEA, a 200 kDa glycoprotein, is clinically significant at concentrations above 5 ng/mL, serving as a clear indicator to distinguish cancerous from normal states [24, 25].

Engineered nanostructures of hexagonal boron nitride (h-BN) are regarded as highly promising in nano-biotechnology due to their exceptional biocompatible characteristics, which mitigate the conventional issue of biomolecule denaturation at nano-bio interfaces. This characteristic is considered critical for preserving the functional integrity of biological recognition elements during sensing processes. In a cytotoxicity study conducted by Singh et al. [26], the effects of boron nitride nanostructures on human embryonic kidney (HEK-293), Hela cervical cancer, and human breast adenocarcinoma (MCF-7) cells were evaluated, and outstanding biocompatibility at lower doses was reported. These findings have reinforced h-BN's potential for biomedical applications, particularly in biosensor development.

In this work, a biocompatible, label-free electrochemical nano-biosensor is developed using hydrothermally engineered hexagonal boron nitride nanosheets (h-BNNS) for the sensitive and selective detection of carcinoembryonic antigen (CEA), a key oncomarker widely recognized for its diagnostic and prognostic significance in non-small cell lung cancer (NSCLC). The sensing interface is constructed on indium tin oxide (ITO) substrates, selected for their superior electrochemical stability, broad potential window, low fabrication cost, scalability for large-scale production, and disposability, making them ideally suited for analytical and point-of-care applications [27].

The biosensor design incorporates a robust cross-linking chemistry to covalently immobilize monoclonal Anti-CEA antibodies onto the h-BNNS-modified ITO surface. This immobilization strategy ensures strong, stable, and oriented attachment of antibodies, preserving their biological activity and enabling efficient antigen recognition. By leveraging h-BNNS's unique properties—such as high mechanical chemical inertness, large specific surface area, and remarkable biocompatibility—the sensor offers an optimized platform for high-density antibody loading and enhanced electron transfer at the bio-electrode interface. The integrated system is engineered to detect CEA concentrations within the clinically relevant range of 0-50 ng/mL, providing a high signal-to-noise ratio, excellent reproducibility, and minimal non-specific binding. Such performance is particularly critical for early-stage cancer detection, where biomarker levels are often near the lower limit of detection for conventional methods. The synergy between the structural stability and surface functionality of h-BNNS and the precision of antibody immobilization establishes a reliable, durable, and highly sensitive biosensing platform capable of delivering rapid and accurate diagnostic data, thereby addressing an urgent need in early cancer screening and monitoring.

#### **4.2** Experimental Section:

#### 4.2.1 Chemical, Reagents and Instrumentation:

The successful hydrothermal synthesis of in-situ functionalized hexagonal boron nitride nanosheets (h-BNNS) for a highly sensitive nano-biosensor targeting carcinoembryonic antigen (CEA) demand the use of meticulously sourced, high-purity reagents to guarantee precision, reproducibility, and optimal electrochemical performance. Analytical-grade powdered hexagonal boron nitride (h-BN, 98% purity, 5 um particle size), 1-(3-(dimethylamino)-propyl)-3-ethylcarbodiimide hydrochloride (EDC), Nhydroxysuccinimide (NHS), bovine serum albumin (BSA), and monoclonal CEA antibodies and antigens, all procured from Sigma-Aldrich, ensure analytical-grade quality critical for effective biomolecule conjugation and selective CEA detection. High-purity reagents, including hydrazine hydrate (N<sub>2</sub>H<sub>4</sub>·H<sub>2</sub>O, >99%) and isopropanol ((CH<sub>3</sub>)<sub>2</sub>CHOH) from Fisher Scientific drive robust functionalization and solvent processes, while key electrochemical redox probes such as potassium ferricyanide (K<sub>3</sub>[Fe(CN)<sub>6</sub>]), potassium ferrocyanide (K<sub>4</sub>[Fe(CN)<sub>6</sub>]·3H<sub>2</sub>O), acetonitrile (CH<sub>3</sub>CN), sodium phosphate dibasic dihydrate (Na<sub>2</sub>HPO<sub>4</sub>·2H<sub>2</sub>O), sodium phosphate monobasic dihydrate (NaH2PO4·2H2O), and ethanol (C2H5OH) from Merck deliver unmatched purity, eliminating the need for further purification. Ultrapure Milli-Q water (18 MΩ·cm<sup>-1</sup>) ensures all washing and solution preparations, safeguarding experimental integrity. Freshly prepared phosphate buffer saline (PBS) solutions, made from NaH2PO4·2H2O and Na2HPO4·2H2O in Milli-Q water and stored at 4°C, maintain stability for electrochemical experiments, reinforcing the indispensable role of premium reagents in achieving a reliable, high-performance biosensor for CEA detection.

The structural and electrochemical properties of hexagonal boron nitride nanosheets (hBNNS) were thoroughly investigated using advanced characterization techniques to validate their quality and performance for electrochemical applications. Phase analysis conducted with a Bruker Advance D-8 X-ray Diffractometer confirmed the crystalline integrity and phase purity of the exfoliated hBNNS, ensuring their structural stability and the preservation of hexagonal stacking post-exfoliation. Morphological studies using scanning electron microscopy (SEM, EVO18 Zeiss) and transmission electron microscopy (TEM, TECNAI 200 kV) revealed an ultrathin, few-layered nanosheet structure with high aspect ratio, critical for enhanced surface area and reactivity. Fourier-transform infrared (FT-IR) spectroscopy, performed on a PerkinElmer Spectrum Two Spectrometer, verified the presence of functional groups introduced during in-situ hydrothermal treatment, enhancing the electroactive sites of the nanosheets to improve chemical activity. Further, Raman spectroscopy (WITec alpha300) confirmed the vibrational fingerprints and the retention of the E<sub>2</sub>g phonon mode, while UV-Visible spectroscopy (PerkinElmer Lambda 950) provided insights into optical bandgap modulation—indicative of quantum confinement and altered electronic transitions due to nanosheet thickness reduction and microstrain. For precise and uniform film fabrication on substrates, a Tarson Electrophoretic Deposition (EPD) setup was employed, enabling controlled deposition of h-BNNS onto conductive indium tin oxide (ITO) glass substrates (2.5 cm × 1 cm). Electrochemical performance was evaluated using a Metrohm Autolab Galvanostat/Potentiostat in a three-electrode configuration, featuring a platinum (Pt) rod as the counter electrode, indium tin oxide (ITO) glass (2.5 cm × 1 cm) as the working electrode, and silver/silver chloride

(Ag/AgCl) in 3 M potassium chloride (KCl) as the reference electrode, demonstrating the hBNNS's exceptional redox sensitivity. These comprehensive characterizations highlight the hBNNS's superior structural and electrochemical properties, positioning them as a high-performance material for sensing, energy storage, and related applications.

## 4.2.2 In-Situ Hydrothermal Approach for Simultaneous Exfoliation and Functionalization of Few-Layered h-BN Nanosheets

A strategically optimized hydrothermal synthesis protocol, incorporating potent intercalating and reducing agents, was employed to exfoliate few-layered hexagonal boron nitride nanosheets (h-BNNS) from bulk h-BN, as reported by Sharma and Puri (2021). Specifically, 0.15 g of bulk h-BN powder was dispersed in a solvent mixture comprising 2 mL of hydrazine hydrate, 10 mL of isopropanol (IPA), and 10 mL of deionized (DI) water. This dispersion was subjected to vigorous magnetic stirring for 12 hours to ensure homogeneous interaction among the constituents. The mixture was then transferred into a 50 mL Teflon-lined stainless-steel autoclave and thermally treated at 220 °C for 18 hours.

The synergistic action of IPA intercalation and hydrazine hydrate facilitated efficient exfoliation and functionalization. The amino (-NH<sub>2</sub>) groups of hydrazine and hydroxyl (-OH) groups of IPA participated in Lewis acid-base interactions with the electron-deficient boron sites in the partially ionic B–N bonds, promoting the formation of –NH, –OH, and –BH functionalities on the nanosheet surfaces. This process not only induced exfoliation into ultrathin layers but also preserved the characteristic hexagonal morphology of h-BN, thereby enhancing dispersion in both aqueous and organic media.

After synthesis, the resultant colloidal suspension was centrifuged at speeds exceeding 6000 rpm and washed multiple times with Milli-Q water to remove unreacted residues, with the pH of the final suspension adjusted to neutral (pH 7.0). The exfoliated material was subsequently dried at 90 °C to obtain a fine powder of ultrathin, large-area h-BNNS. These nanosheets, exhibiting surface functional groups and high crystallinity, are optimally tailored for high-performance nano-biosensing platforms due to their large electroactive surface area, excellent dispersibility, and chemical modifiability.

## 4.2.3 Electrophoretic Deposition-Assisted Fabrication of Functionalized h-BNNS Films onto ITO Electrodes for High-Performance Interfaces

A uniform nano-interface matrix for label-free detection of carcinoembryonic antigen (CEA) was fabricated through a meticulously optimized electrophoretic deposition (EPD) technique, enabling the uniform integration of hexagonal boron nitride nanosheets (h-BNNS) onto functionalized indium tin oxide (ITO) electrodes. The fabrication strategy began with surface activation of ITO substrates (dimensions: 0.8 cm × 2.5 cm) via hydrolysis in a 1:1:5 (v/v) mixture of ammonia (NH<sub>3</sub>), hydrogen peroxide (H<sub>2</sub>O<sub>2</sub>), and deionized (DI) water, a process known to generate hydroxyl and peroxide radicals on the ITO surface. This chemical pretreatment promotes surface hydroxylation and radical formation, thereby improving hydrophilicity and promoting strong adhesion of h-BNNS through electrostatic and hydrogen bonding interactions, promoting enhanced chemical affinity of the negatively charged h-BNNS during deposition (Fig. 4.1a).

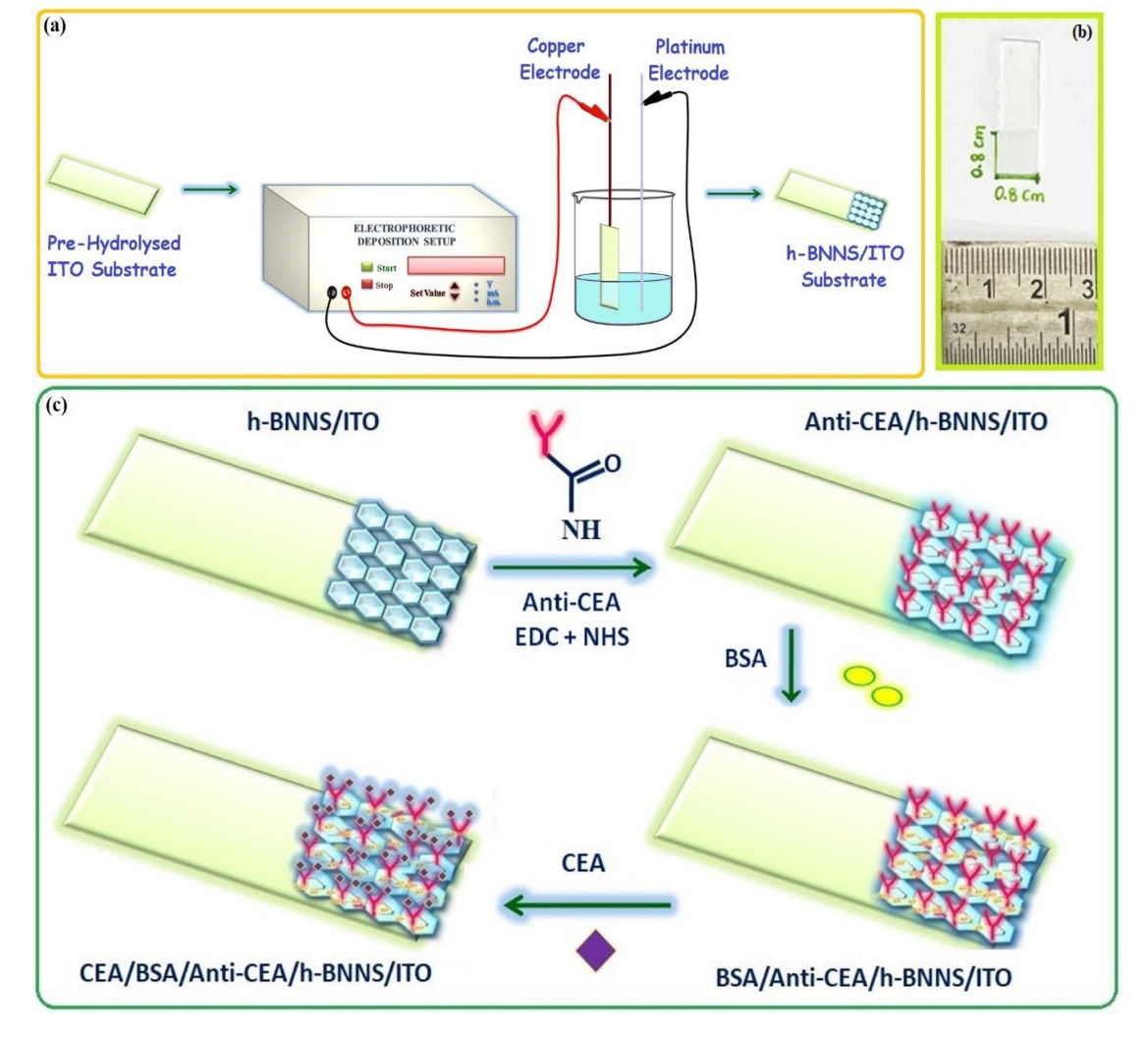


Figure 4.1: (a) Schematic representation of electrophoretic deposition (EPD) of h-BNNS films on pre-hydrolyzed ITO substrate, (b) Pictorial depiction of electrophoretically deposited uniform h-BNNS films on ITO electrode, and (c) Sequential process detailing the fabrication of the h-BNNS-based immunoelectrode.

A stable, homogeneous colloidal suspension of h-BNNS was prepared by dispersing the nanosheets at a concentration of 0.25 mg/mL in high-purity acetonitrile (CH<sub>3</sub>CN). The use of acetonitrile, an aprotic polar solvent, facilitated better particle dispersion due to its low viscosity and high dielectric constant. Ultrasonication for 1 hour ensured adequate exfoliation and delamination of nanosheets, promoting uniform particle dispersion. To further facilitate charge-based mobility during deposition and ensure uniform field-assisted alignment of the nanosheets, a controlled concentration (10<sup>-5</sup> to 10<sup>-4</sup> M) of magnesium nitrate [Mg(NO<sub>3</sub>)<sub>2</sub>] was introduced as a supporting electrolyte. This salt act as a supporting electrolyte to enhance the ionic conductivity of the medium and modulate the zeta potential, thereby enhancing particle mobility under an electric field, ensuring electrophoretic stability and promoting the formation of a homogeneous coating.

The deposition was carried out in a two-electrode configuration inside a glass vessel, with the pre-hydrolyzed ITO substrate acting as the positively biased working electrode and a platinum wire serving as the counter electrode. A direct current (DC) voltage of 20 V was applied for 1 minute, promoting electrophoretic migration and deposition of negatively charged h-BNNS onto the ITO surface. This process resulted in the formation of a uniform and adherent thin film confined to an active sensing area of 0.8 cm × 0.8 cm on the ITO substrate (**Fig.4.1b**). The resulting nanostructured film exhibited excellent uniformity and coverage, thereby offering a high surface area interface suitable for subsequent bio-recognition element immobilization and efficient electrochemical signal transduction. This deposition approach, characterized by simplicity, precision, and scalability, played a pivotal role in constructing a structurally stable and electrochemically active sensing platform. It laid the foundation for achieving high sensitivity and reproducibility in the subsequent detection of CEA, thereby reinforcing the efficacy of the EPD technique in developing advanced nanomaterial-modified interfaces for nano-biosensor architectures.

Following the successful electrophoretic deposition of h-BNNS onto ITO microelectrodes, stepwise protein biomolecule immobilization was conducted under controlled ambient conditions (25 °C) to fabricate a highly specific and stable hBNNS/ITO-based immunoelectrode for carcinoembryonic antigen (CEA) detection. All subsequent electrochemical characterizations were performed using the fully modified immunoelectrode to evaluate its sensing performance. Initially, a stock solution of monoclonal Anti-CEA antibodies (50 µg/mL) was prepared in phosphate buffer saline (PBS, pH 7.4) to maintain physiological compatibility. To activate the antibody carboxyl groups for covalent conjugation, 1-(3-(dimethylamino)-propyl)-3-ethylcarbodiimide hydrochloride (EDC, 0.2 M) and N-hydroxysuccinimide (NHS, 0.05 M) were added in a volumetric ratio of 2:1:1 (Anti-CEA:EDC:NHS). In this reaction scheme, EDC serves as a carbodiimide cross-linker activating the carboxyl groups, while NHS acts as a stabilizer, forming a semi-stable NHS ester intermediate to improve conjugation efficiency and prevent hydrolysis during the immobilization process [28].

A volume of  $20\,\mu\text{L}$  of the activated Anti-CEA antibody solution was then carefully drop-cast onto the uniformly coated h-BNNS/ITO electrode surface, allowing for targeted covalent immobilization onto the oxygen-containing functional groups on h-BNNS. After adequate incubation, the surface was treated with  $10\,\mu\text{L}$  of bovine serum albumin (BSA, 1% w/w in ultrapure Milli-Q water) to effectively block non-specific binding sites and prevent undesirable adsorption of free Anti-CEA antibodies or interfering species, thereby improving specificity by minimizing background noise. Subsequently,  $10\,\mu\text{L}$  of CEA antigen solution at varying concentrations was added to the BSA/Anti-CEA/h-BNNS/ITO-modified electrode and incubated for 30 minutes at room temperature to facilitate specific antibody—antigen interactions. This incubation step enables efficient formation of immune complexes that influence the interfacial electron transfer properties and thus serve as the basis for label-free electrochemical detection.

The fully fabricated BSA/Anti-CEA/h-BNNS/ITO immunoelectrode (**Fig.4.1c**) was stored at 4 °C when not in use to preserve the conformational stability and bioactivity of immobilized biomolecules. To ensure optimal performance and signal

reproducibility, systematic pH investigations were carried out using the fabricated immunoelectrode to determine the ideal buffer environment for antigen—antibody interactions and electrochemical signal transduction. These optimization studies were crucial to fine-tune the working conditions and enhance the sensitivity and specificity of the developed nano-biosensor for reliable clinical diagnostics.

#### 4.3 Experimental Results & Analysis:

#### 4.3.1 Analytical Nanomaterial Characterizations:

### 4.3.1.1 Quantitative Structural Analysis of Hydrothermally Exfoliated Ultrathin h-BN Nanosheets Derived from Bulk h-BN utilizing X-ray diffraction (XRD):

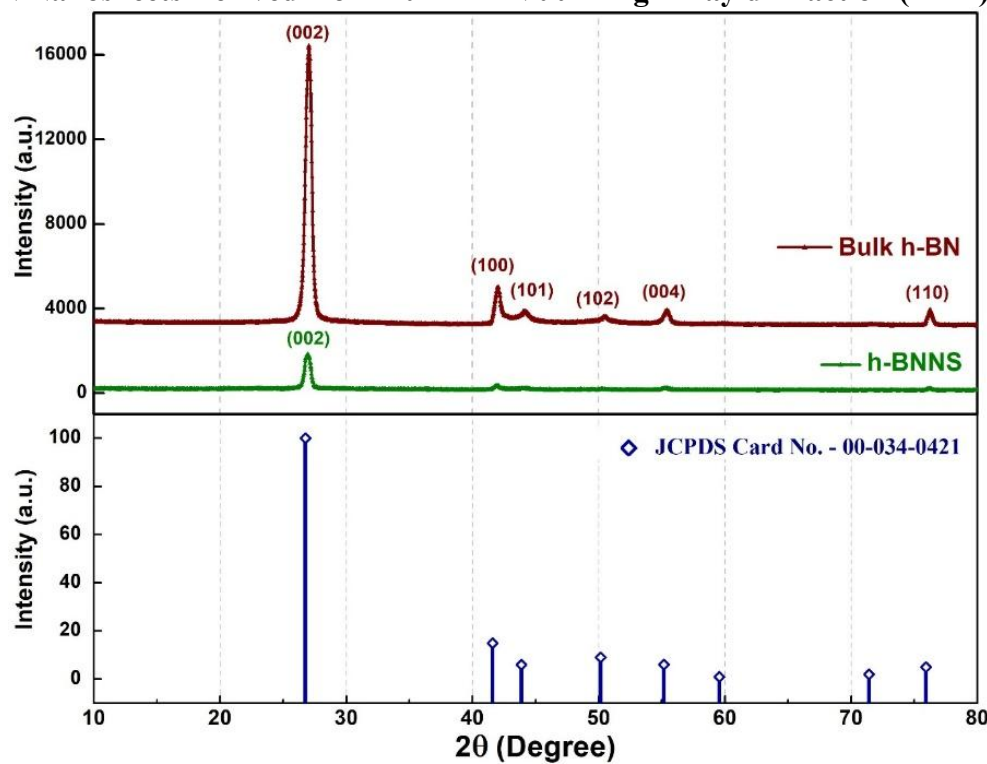


Figure 4.2: X-ray diffraction characterization conducted on bulk h-BN (Red) and hydrothermally exfoliated h-BNNS (Green) within the 20 range between 10° to 80°, revealing characteristic diffraction peaks consistent with the standard JCPDS card No. 034-0421 (Blue) by retention of the hexagonal crystal structure post-exfoliation.

X-ray diffraction (XRD) is a powerful, non-destructive analytical technique used to investigate the crystallographic structure, phase purity, and degree of crystallinity of materials. In the context of layered materials like hexagonal boron nitride (h-BN), XRD is particularly effective for evaluating exfoliation efficiency by revealing changes in interlayer stacking and peak intensity. To assess the extent of exfoliation of h-BN nanosheets (h-BNNS) from their bulk counterpart, XRD analysis was performed on both bulk h-BN and hydrothermally exfoliated h-BNNS, as shown in **Fig. 4.2**. The comparative XRD patterns clearly demonstrate the successful transformation of bulk h-BN into ultrathin nanosheets via hydrothermal synthesis.

The bulk h-BN exhibited sharp and well-defined diffraction peaks at  $2\theta$  values of  $26.65^{\circ}$ ,  $41.56^{\circ}$ ,  $43.86^{\circ}$ ,  $50.1^{\circ}$ , and  $55^{\circ}$ , corresponding to the (002), (100), (101), (102), and (004) crystallographic planes, respectively, in accordance with **JCPDS Card Number 00-034-0421 [29]**. These reflections confirm the presence of a highly ordered, multilayered hexagonal structure with strong interlayer stacking and long-range periodicity along both the basal plane and the c-axis.

In contrast, the XRD pattern of the hydrothermally synthesized h-BNNS displayed a complete disappearance of the (101), (102), and (004) reflections, accompanied by a substantial reduction in the intensity of the (002) peak. This suppression of higher-order and out-of-plane diffraction peaks directly correlates with the disruption of long-range stacking order along the c-axis, signifying a successful exfoliation process. The substantial weakening of the (002) peak in comparison to bulk hBN, which is characteristic of layered stacking in h-BN, further indicates a transition from multilayered bulk to few-layer or ultrathin nanosheet morphology.

A distinct and relatively intense peak corresponding to the (002) diffraction plane of h-BNNS (Green Colour) was observed in the X-ray diffraction pattern (**Fig. 4.2**), confirming the formation of highly ordered, crystalline layered structures stacked prominently in [002] direction. The pronounced intensity of this peak signifies successful exfoliation while retaining the in-plane crystallographic order of h-BN. To validate the crystallinity of the synthesized material, the degree of crystallinity was quantitatively evaluated using **Eq. [4.1]**:

Degree of Crystallinity (%) = 
$$\frac{A_c}{A_c + A_a} \times 100$$
 [4.1]

It represents the integrated areas under the crystalline and amorphous peaks, respectively. The calculated crystallinity was found to be remarkably high at 98.16%, indicating minimal amorphous content and excellent structural integrity of the exfoliated h-BNNS. Furthermore, to examine the structural refinement at the nanoscale, the crystallite size of both bulk and exfoliated h-BN was determined using Williamson-Hall (W–H) analysis, as given by Eq. [4.2]:

$$\beta \cos\theta = \frac{k\lambda}{d} + 4 \epsilon \sin\theta \qquad [4.2]$$

The W–H analysis revealed a crystallite size of  $2.30 \pm 7.55 \times 10^{-4}$  nm for bulk h-BN, while the hydrothermally exfoliated h-BN nanosheets exhibited a significantly reduced average crystallite size of  $1.15 \pm 3.88 \times 10^{-4}$  nm. This ~50% reduction in crystallite size strongly supports the successful exfoliation into few-layered nanosheets, consistent with quantum confinement effects and increased lattice strain typically associated with 2D morphology. Additionally, the disappearance of characteristic diffraction peaks observed in bulk h-BN, except for the (002) reflection, further confirms the exfoliation into few-layered structures. The absence of higher-order diffraction planes reflects the thinning down of the material along the c-axis and the reduction in interlayer interactions, substantiating the formation of few-layered or near-monolayer h-BN nanosheets. These observations collectively verify the successful synthesis of highly crystalline, few-layered h-BN nanosheets via hydrothermal exfoliation, with significant reduction in crystallite size and preserved in-plane hexagonal symmetry.

### 4.3.1.2 Advanced Electron Microscopy-Based Nanostructure Profiling of Hydrothermally Exfoliated h-BNNS

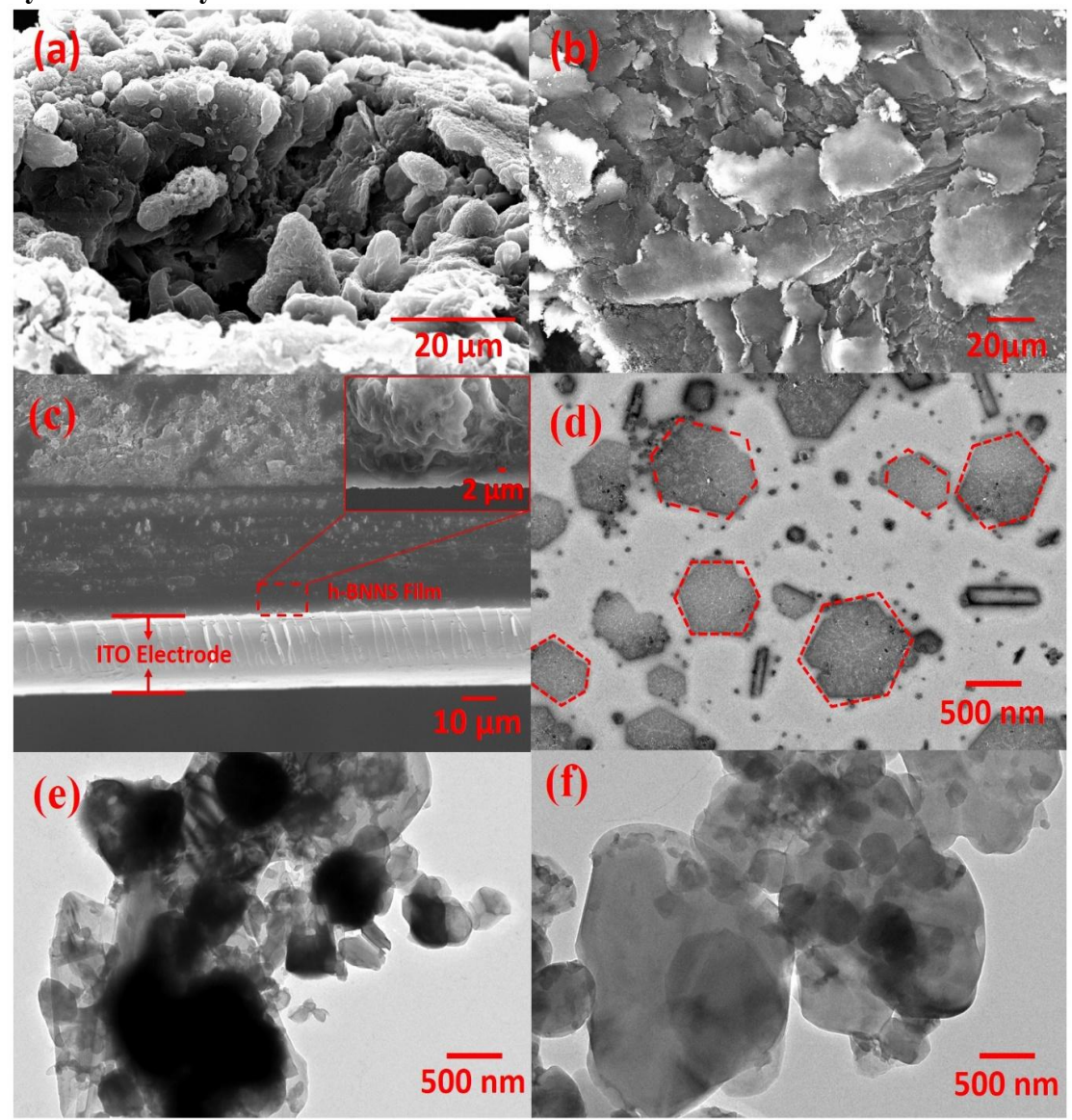


Figure 4.3: SEM micrographs distinctly reveal (a) bulk h-BN at 20  $\mu m$  scale, (b) exfoliated h-BN nanosheets (h-BNNS) at 20  $\mu m$ , and (c) a cross-sectional view of the electrophoretically deposited h-BNNS film on ITO substrate at 10  $\mu m$  scale (inset: 2  $\mu m$ ). High-resolution TEM imaging distinctly captures (d) hexagonal h-BNNS, (e) bulk h-BN, and (f) ultrathin nanosheets at 500 nm resolution.

Confirmation of the surface morphology at micro-and nano-scale upon successful exfoliation of hexagonal boron nitride nanosheets (h-BNNS) from bulk h-BN was thoroughly established through detailed imaging via Scanning Electron Microscopy (SEM) and Transmission Electron Microscopy (TEM), as depicted in **Fig. 4.3(a-f)**. These characterization techniques provided crucial insights into the nanoscale structural evolution and lateral dimensionality of the synthesized nanosheets, both of which are critical parameters influencing their functionality in surface-dominated

applications such as nano-biosensing. Key morphological attributes were thoroughly investigated through high-resolution electron microscopy analysis to assess structural refinement, size modulation, and surface uniformity.

SEM and TEM micrographs (**Fig. 4.3 (a, b)**) revealed that the hydrothermally exfoliated h-BNNS exhibit a predominantly well-dispersed disc-like morphology with lateral dimensions reaching up to  $\sim$ 4 µm. This large lateral surface area, achieved through the delamination of bulk layers, significantly enhances the material's surface-to-volume ratio, facilitating greater biomolecule immobilization and improved analyte accessibility in biosensor applications.

A cross-sectional SEM image (**Fig. 4.3(c)**) of the h-BNNS/ITO electrode—fabricated via electrophoretic deposition (EPD)—further supports the uniform deposition of the exfoliated nanosheets on the electrode surface. This conformal and well-adhered layer is essential for consistent electrochemical performance, as it ensures efficient matrix deposition, mechanical stability, and reproducibility across multiple sensing cycles.

The hexagonal morphology and few-layered structure of the exfoliated h-BNNS were clearly illustrated in the TEM micrograph (**Fig. 4.3(d)**), which captured transparent, ultrathin sheets with well-preserved crystallographic features. The successful exfoliation can be attributed to the synergistic interplay of several key factors during hydrothermal synthesis—namely, intercalation of solvent molecules, controlled nucleation, reduction reactions facilitated by a chemical reducing agent, and optimized temperature—pressure conditions. This combination of physical and chemical driving forces disrupts the van der Waals interactions between layers, enabling efficient exfoliation while retaining hexagonal structure in basal-plane order.

The contrast between bulk and exfoliated structures is strikingly evident in the comparative TEM images. In stark contrast, bulk h-BN appeared in TEM images, as shown in Fig. 4e, depicted dense, dark, and agglomerated clusters with indistinct morphology due to strong interlayer stacking and limited exfoliation. Fig. 4.3(f) displays the transformation of these bulky aggregates into thin, transparent, and well-dispersed nanosheets post-reduction-assisted hydrothermal treatment in breaking van der Waals interactions. This transition underscores the effectiveness of the employed synthesis strategy in producing high-quality, few-layered 2D h-BN nanosheets.

The morphological investigations conducted range from large lateral dimensions (up to  $2\text{--}4~\mu m$ ) to uniform electrode coating and preserved hexagonal sheet structure, which affirms the successful exfoliation and structural tailoring of h-BNNS. These attributes describe a significantly engineered hBNNS nanostructure that enhances electrochemical biosensing performance by promoting high surface reactivity, stable immobilization of bioreceptors, and improved electron transport properties.

## 4.3.1.3 UV-Visible Spectroscopy-Based Band Structure Analysis and Optical Transition Analysis of Bulk and Exfoliated h-BN Nanostructures

UV-Visible absorption spectroscopy serves as a vital, non-destructive analytical tool to probe the interaction of ultraviolet and visible light with matter across a range of wavelengths. This technique enables precise detection of electronic transitions within a material, which are often governed by nanoscale effects such as quantum confinement. In low-dimensional systems like hexagonal boron nitride nanosheets (h-BNNS), these

transitions strongly influence the electronic energy states, leading to distinct size-dependent variations in the optical bandgap—a key parameter for tuning optoelectronic and photonic properties.

In the present study, the optical bandgap (Eg) of hydrothermally exfoliated h-BNNS and bulk h-BN was quantitatively determined using Tauc's relation, represented in **Eq.** [4.3]:

$$(\alpha E)^{1/n} = \beta \left( E - E_g \right) \tag{4.3}$$

Here,  $\alpha$  denotes the absorption coefficient, E=hv represents the photon energy,  $\beta$  is the band tailing constant, and n is the power index that defines the nature of the electronic transition. For wide bandgap semiconductors like h-BN, which exhibit a direct allowed transition, the value of n=1/2 is employed. The absorption coefficient  $\alpha$  was calculated using the Beer–Lambert law, allowing a quantitative evaluation of light absorption based on material thickness and concentration. Photon energy (E), was computed from Planck's constant (h) and the frequency (v) of the incident light, capturing the energy content of each absorbed photon.

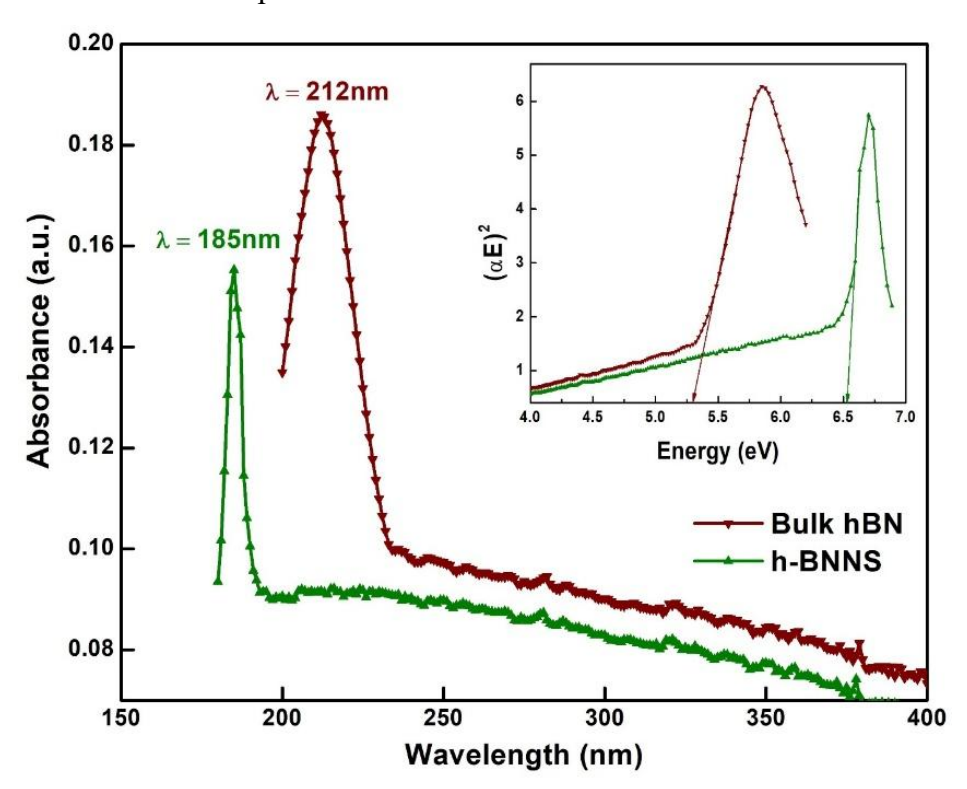


Figure 4.4: UV-visible absorption spectra of bulk h-BN (Red) and hydrothermally exfoliated h-BNNS (Green), with Tauc plots inset to accurately estimate their optical band gaps.

Using these parameters, Tauc plots were generated for bulk h-BN and various hydrothermally exfoliated h-BNNS samples by plotting  $(\alpha h \nu)^2$  versus photon energy (E). The optical bandgap values (Eg) were extracted by extrapolating the linear portion of each plot to the x-axis (photon energy axis), as shown in **Fig. 4.4**. These intercepts provide an accurate graphical representation of the onset of electronic transitions,

enabling a direct comparison of bandgap energies across samples with different layer thicknesses and morphological characteristics.

The UV-Visible absorption spectra of bulk h-BN and hydrothermally exfoliated h-BN nanosheets (h-BNNS) revealed distinct absorption peaks at 212 nm and 185 nm, respectively. This noticeable blue shift of 27 nm in the absorption edge for h-BNNS signifies a transition from multilayered bulk material to few-layer or atomically thin nanosheets. Such a shift is a hallmark of quantum confinement, wherein the reduction in dimensionality leads to an alteration in the electronic band structure, particularly the widening of the bandgap due to the spatial restriction of charge carriers [30]. Correspondingly, the optical bandgap energies, derived from Tauc plot analysis, demonstrated a significant increase from 5.29 eV for bulk h-BN to 6.53 eV for h-BNNS. This marked enhancement in bandgap (~1.24 eV) further confirms the successful exfoliation and thinning of h-BN layers, as bandgap expansion is directly linked to reduced interlayer interactions and increased quantum confinement in two-dimensional materials.

The observed bandgap widening in h-BNNS not only validates the formation of ultrathin nanosheets with minimal stacking but also highlights the tunability of electronic properties through morphological engineering. Thus, UV–Visible spectroscopy, in conjunction with Tauc analysis, effectively substantiates the influence of hydrothermal exfoliation on tailoring the optoelectronic behaviour of h-BN nanostructures. The ability to tune the bandgap through controlled exfoliation further enhances the versatility of h-BNNS, allowing tailored electronic and optical properties to meet specific application requirements. Such a tunable wide bandgap in the deep UV region renders h-BNNS highly promising for next-generation applications in UV photodetectors, insulating barriers in 2D electronics, and optoelectronic biosensing, where high bandgap materials are critical for device sensitivity and stability. These characteristics collectively position h-BNNS as a transformative material for high-performance, reliable, and sensitive devices in challenging technological and biomedical environments.

# 4.3.1.4 Raman Spectroscopic Elucidation of Phonon Behaviour and Electronic Coupling in Bulk and Exfoliated h-BN Nanostructures

Raman spectroscopy serves as a powerful, non-destructive technique for probing the phonon–electron interactions and lattice dynamics of materials by capturing vibrational, rotational, and low-frequency electronic transitions. This technique provides indirect yet highly sensitive evaluation of strain, crystallographic defects, impurity doping, and the number of atomic layers, all of which play pivotal roles in determining the physical and electronic behaviour of low-dimensional nanomaterials. In the present study, Raman spectroscopy was employed to analyze the characteristic in-plane E<sub>2</sub>g vibrational phonon mode of hexagonal boron nitride (h-BN) nanosheets [31]. This mode arises from the in-plane collective vibrations of boron and nitrogen atoms and serves as a reliable fingerprint for the evaluating structural integrity and dimensional confinement. Notably, shifts in the E<sub>2</sub>g peak position and variations in its full width at half maximum (FWHM) provide critical insights into interlayer van der Waals coupling, phonon confinement, and defect density, especially in exfoliated or few-layered systems.

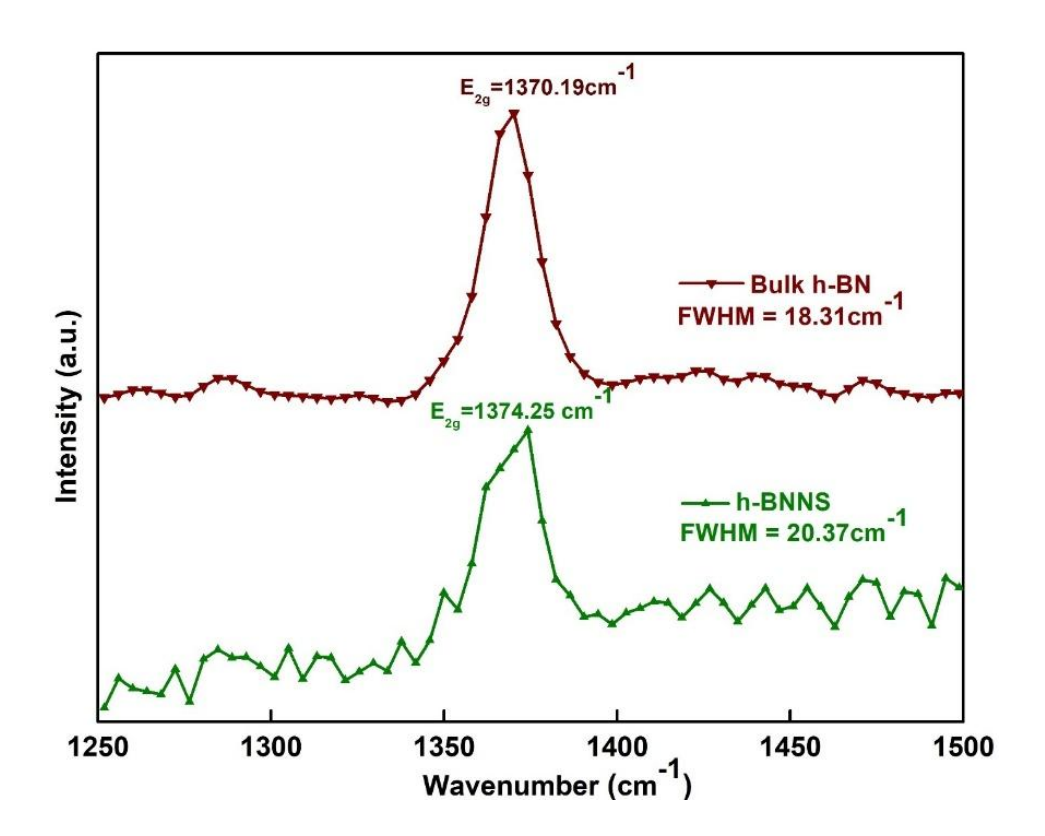


Figure 4.5: Raman spectroscopic analysis was performed on bulk h-BN (red) and hydrothermally exfoliated h-BNNS (green) over the 1250–1500 cm<sup>-1</sup> wavenumber range to assess their vibrational characteristics.

Raman spectroscopy analysis (Fig.4.5) revealed a distinct blue shift of 4.06 cm<sup>-1</sup> in the E<sub>2</sub>g in-plane vibrational mode of hydrothermally exfoliated h-BN nanosheets (h-BNNS), accompanied by a noticeable broadening of the full width at half maximum (FWHM). This spectral shift, when compared to bulk h-BN, provides compelling evidence of phonon confinement effects in the ultrathin layered structure of h-BNNS, as supported by prior studies (Li and Chen). The E2g vibrational mode, which is characteristic of the in-plane B-N bond stretching in h-BN, is highly sensitive to changes in layer thickness, interlayer coupling, and lattice strain. The observed blue shift signifies a reduction in interlayer van der Waals interactions, typically associated with the transition from multilayer to few-layer or monolayer nanosheets. Simultaneously, the FWHM broadening reflects increased lattice disorder or local strain induced during the exfoliation process, which alters the vibrational coherence of the lattice phonons. These features collectively point to the onset of quantum confinement, where the spatial restriction of phonon propagation due to reduced dimensionality alters the vibrational dynamics of the system. Additionally, the blueshifted and broadened Raman mode confirms the preservation of hexagonal symmetry while highlighting the subtle perturbations introduced during hydrothermal exfoliation such as edge defects, dangling bonds, or tensile/compressive strain. Thus, Raman spectroscopic data not only validate the successful exfoliation into few-layer h-BNNS but also provide crucial insights into phonon-electron coupling, structural refinement, and dimensional confinement, all of which play a vital role in modulating the optoelectronic and mechanical behaviour of h-BN-based nanostructures.

### 4.3.1.5 FT-IR Spectroscopic Evaluation of Molecular Vibrations and Sequential Protein Immobilization in Hydrothermally Exfoliated h-BN Nanosheets

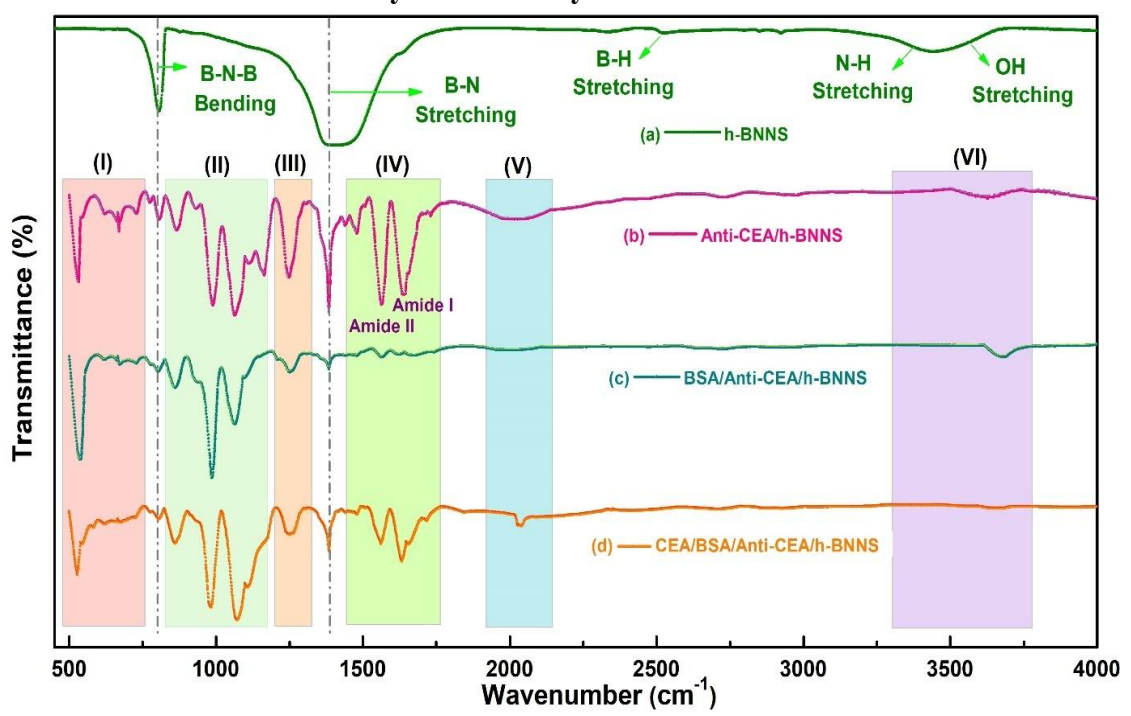


Figure 4.6: The FT-IR spectra recorded between 400 and 4000 cm<sup>-1</sup> powerfully capture and confirm the molecular fingerprints of h-BNNS and successive bio-conjugation steps, including Anti-CEA/h-BNNS, BSA/Anti-CEA/h-BNNS, and CEA/BSA/Anti-CEA/h-BNNS, affirming successful functionalization and immobilization at each stage.

Fourier Transform Infrared (FTIR) Spectroscopy is a powerful analytical technique that probes the vibrational modes of chemical bonds within materials, providing detailed insights into the molecular structure, functional group identification, chemical bonding in the parent material, interactions with impurities or surface adsorbates, and overall structural integrity. In this study, FTIR spectroscopy was employed in the mid-infrared region (400–4000 cm<sup>-1</sup>) to investigate the molecular structure and bonding characteristics of hexagonal boron nitride (h-BN) samples, specifically to assess the integrity of B-N bonding and to identify vibrational modes of functional groups introduced during synthesis.

Fourier-transform infrared (FT-IR) spectroscopy (400–4000 cm<sup>-1</sup>, **Fig. 4.6**) was employed to investigate the structural integrity and chemical functionalization of hydrothermally exfoliated hexagonal boron nitride nanosheets (h-BNNS) [32]. The presence of sharp and well-defined vibrational peaks at 804 cm<sup>-1</sup>, corresponding to out-of-plane B–N–B bending vibrations, and 1413 cm<sup>-1</sup>, assigned to in-plane B–N stretching, unequivocally confirmed the sp²-hybridized hexagonal lattice framework characteristic of crystalline h-BN. These vibrational modes serve as distinct molecular fingerprints of h-BN, reinforcing the preservation of its hexagonal structure post-exfoliation. In addition to the B–N signatures, weaker absorption features were observed at ~2500 cm<sup>-1</sup>, associated with –BH stretching, and broad bands spanning >3500 cm<sup>-1</sup> (–OH) and 3200–3500 cm<sup>-1</sup> (–NH), indicative of hydroxyl and amine

functionalities introduced during the hydrothermal exfoliation process. These broad and asymmetric transmittance regions are a direct consequence of the hydrothermal exfoliation and introduce reactive anchoring sites that facilitate subsequent covalent bioconjugation, while also enhancing the aqueous dispersibility and surface wettability of the nanosheets.

Upon covalent conjugation of monoclonal Anti-CEA antibodies, chemically activated using EDC (1-ethyl-3-(3-dimethylaminopropyl)carbodiimide) hydroxysuccinimide) crosslinkers, additional amide I and II bands emerged in the FT-IR spectrum of the Anti-CEA/h-BNNS nanoconjugate, signifying stable covalent immobilization via amide bond formation between carboxyl and amine functionalities, mentioned in **Table 4.1**. This immobilization was corroborated by the appearance of characteristic amide I and II bands, which serve as molecular markers for successful protein immobilization through peptide bond formation, thereby ensuring robust antibody orientation and bioactivity [33-35]. Subsequent blocking with bovine serum albumin (BSA) to passivate nonspecific adsorption sites led to a notable reduction in transmittance across vibrational regions III (~1500–1600 cm<sup>-1</sup>), IV (~1600–1700 cm<sup>-1</sup>), V (~2800–3000 cm<sup>-1</sup>), and VI (>3200 cm<sup>-1</sup>), suggesting successful steric hindrance and coverage of unbound sites. This attenuation is attributed to BSA's broad molecular coverage, which effectively minimizes background interference and enhances sensor selectivity by suppressing nonspecific adsorption. Upon specific introduction of carcinoembryonic antigen (CEA), the FT-IR spectra revealed increased intensity and slight shifts in transmittance peaks across these same regions, validating the antigenantibody interaction and bio-affinity-driven cross-linking [36]. These spectral changes are indicative of specific antibody-antigen binding events, leading to conformational rearrangements and hydrogen-bonding alterations at the immuno-interface.

Table 4.1: Comprehensive tabular presentation of wavenumbers assigned to the vibrational bands characteristic of the protein structure associated with the Amide bands of IgG antibody.

S.No.	Wavenumber (cm <sup>-1</sup> )	Assigned Bands	Description of Region
1.	537-606	Amide VI - Out of Plane Bending	I
2.	625-767	Amide IV- NH Bending	I
3.	640-800	Amide V - OCN Bending	I
4.	866	Protein Phosphorylation	II
5.	989	Symmetric Phosphate Stretching Vibration	II
6.	1066	Polysaccharides Stretching	II
7.	1113	Glycogen	II
8.	1164	Carbohydrates	II
9.	1229-1301	Amide III -NH Bending	III
10.	1480-1575	Amide II – CN Stretching	IV
11.	1600-1690	Amide I – C=O Stretching	IV
12.	1730	Lipids	IV
13.	2000- 2040	EDC-NHS Activation	V
14.	3100	Amide B – NH Stretching	VI
15.	3300	Amide A – NH Stretching	VI

These FT-IR findings substantiate the preservation of h-BN's crystal structure post-exfoliation but also confirm the stepwise functionalization and bioconjugation involved in constructing the immunosensing interface on h-BNNS, demonstrating its potential as a robust nano-interface for ultrasensitive and selective electrochemical detection of CEA, a critical biomarker for non-small cell lung cancer (NSCLC) diagnostics. These findings highlight the chemical integrity, biofunctional capability, and high molecular recognition efficiency of the h-BNNS-based platform, establishing its suitability for highly sensitive and selective electrochemical detection of CEA for advanced point-of-care diagnostics leveraging engineered 2D nanostructures with tailored surface chemistry.

# 4.3.1.3 In Vitro Cytotoxicity Assessment of Engineered h-BN Nanosheets Synthesized via Hydrothermal Exfoliation

Biocompatibility is considered essential for ensuring the clinical reliability of nano-biosensors, as it helps minimize false positives and supports safe interaction between the sensing material and biological components. To assess the cytotoxic effects of ultrathin hexagonal boron nitride nanosheets (h-BNNS), a non-radioactive colorimetric MTT assay was performed using human embryonic kidney (HEK-293T) cells, allowing the determination of an optimal concentration for fabricating biocompatible nanobiosensors for carcinoembryonic antigen [37].

HEK-293T cells were cultured in Dulbecco's Modified Eagle Medium/Nutrient Mixture F-12 (DMEM/F12) enriched with 10% fetal bovine serum (FBS) for optimal growth, and supplemented with 50 units/mL penicillin and 50 μg/mL streptomycin to prevent microbial contamination. Cells were maintained in a humidified incubator at 37°C with 5% CO<sub>2</sub> to mimic physiological conditions. Following standard subculturing protocols, cells were dissociated using trypsin-EDTA and seeded at a density of 37,977 cells/cm² (equivalent to 5000 cells/well) in 96-well plates, followed by overnight incubation to ensure proper adherence and recovery.

A range of h-BNNS concentrations, dispersed in 10% DMSO in DMEM/F12 to ensure uniform delivery, were applied to the adhered cells and incubated for 24, 36, and 48 hours, allowing time-resolved analysis of dose-dependent cytotoxic responses. After treatment, MTT reagent was introduced and allowed to react for 4 hours under 5% CO<sub>2</sub> at 37°C, facilitating mitochondrial reduction of MTT into insoluble purple formazan crystals—indicative of active metabolic activity. The formazan crystals were subsequently solubilized in 100  $\mu$ L of DMSO under constant agitation for 15 minutes, enabling accurate spectrophotometric quantification. Absorbance values were measured at 490 nm (reference: 690 nm) using a calibrated microplate reader. Cell viability (%) was calculated using the Eq. [4.4],

Cell Viability (%) = 
$$\frac{A_{Test}}{A_{Control}} \times 100 \%$$
 [4.4]

Where  $A_{Test}$  and  $A_{Control}$  represent the mean absorbance values measured for the h-BNNS-treated and untreated (control) cell groups, respectively. These absorbance values directly correlate with the number of metabolically active cells, thereby serving as a quantitative proxy for cell viability. To ensure the statistical robustness, reproducibility, and reliability of the cytotoxicity evaluation, all experimental

conditions were conducted in triplicate, and the resulting data were averaged to minimize random error and biological variability across replicates.

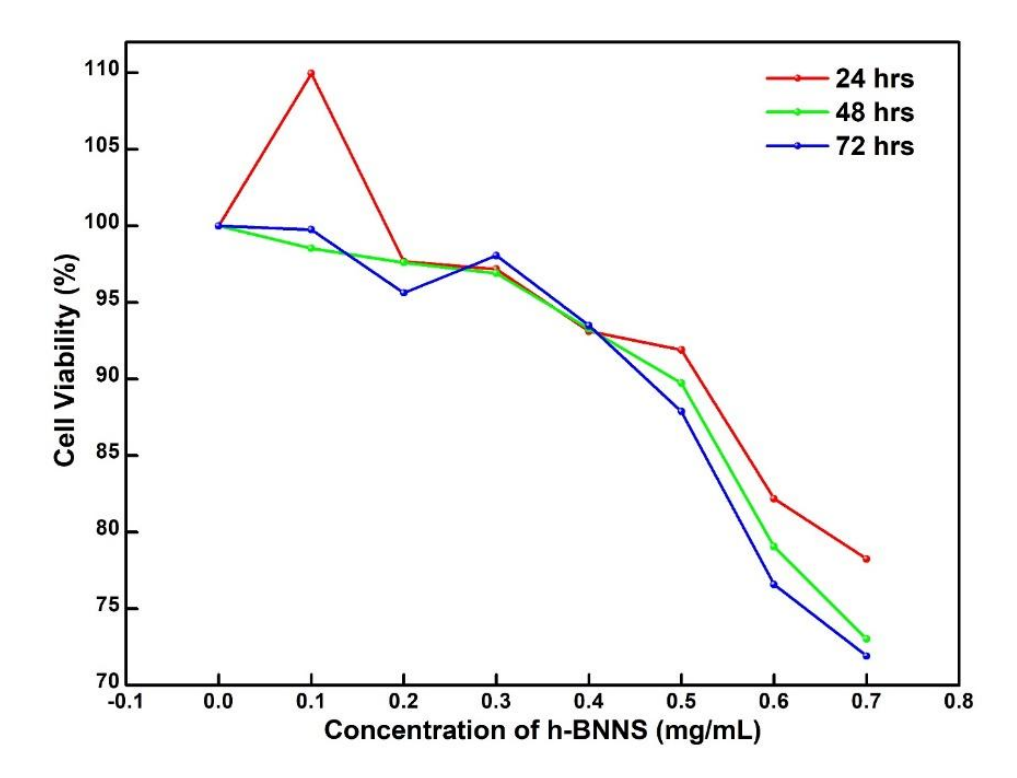


Figure 4.7: Comprehensive cell viability analysis after 24 (red), 36 (green), and 72 (blue) hours of incubation with different h-BNNS concentrations, reflecting consistent and reliable cellular responses.

The results revealed exceptional biocompatibility of h-BNNS at concentrations between 0.2–0.3 mg/mL, maintaining 80–95% cell viability across all incubation periods. Based on this, 0.25 mg/mL was selected as the optimal working concentration for nano-biosensor construction, maintaining a balance between nanomaterial efficacy and cellular tolerance. This concentration was found to be non-toxic and supportive of cellular function, thereby ensuring safe biointerface interaction and compatibility with protein immobilization strategies (**Fig. 4.7**). These findings conclusively validate the biosafety of hydrothermally exfoliated h-BNNS and establish a foundation for its reliable integration into non-invasive, highly sensitive carcinoembryonic antigen (CEA) detection platforms, particularly relevant for the early prognosis and clinical monitoring of non-small cell lung cancer (NSCLC).

#### 4.3.2 Electrochemical Profiling and Analysis:

## 4.3.2.1 Investigating the Interfacial Electrochemical Kinetics of Ultrathin h-BNNS/ITO Electrodes and Successive Protein Immobilization

Cyclic voltammetry (CV) was employed to monitor the sequential modifications of an electrode surface, as illustrated in **Fig. 4.8**, by analyzing the electrochemical behaviour at each modification step. The diffusion coefficients corresponding to each modification stage were quantitatively determined using the Randles–Sevcik **Eq. [4.5]**, as described by Elgrishi et al. [38], and are tabulated in **Table 4.2**. This approach enabled the quantitative assessment of the influence of surface engineering on redox

kinetics, confirming enhancements in electroactive surface area and charge transport behaviour following functionalization with ultrathin h-BNNS.

$$I_p = (2.69 \times 10^5) n^{\frac{3}{2}} A C D^{\frac{1}{2}} \sqrt{\nu}$$
 [4.5]

Where, Ip represents the peak current (anodic or cathodic) recorded from the cyclic voltammogram of the modified electrode, n is the number of electrons transferred during the redox reaction (in this case, n=1), A denotes the electroactive surface area of the electrode (experimentally determined to be 0.64 cm<sup>2</sup>), C is the molar concentration of the redox probe  $[Fe(CN)_6]^{3-/4-}$  (5 × 10<sup>-3</sup> M), D is the diffusion coefficient of the redox species, and v is the applied scan rate (50 mV/s).

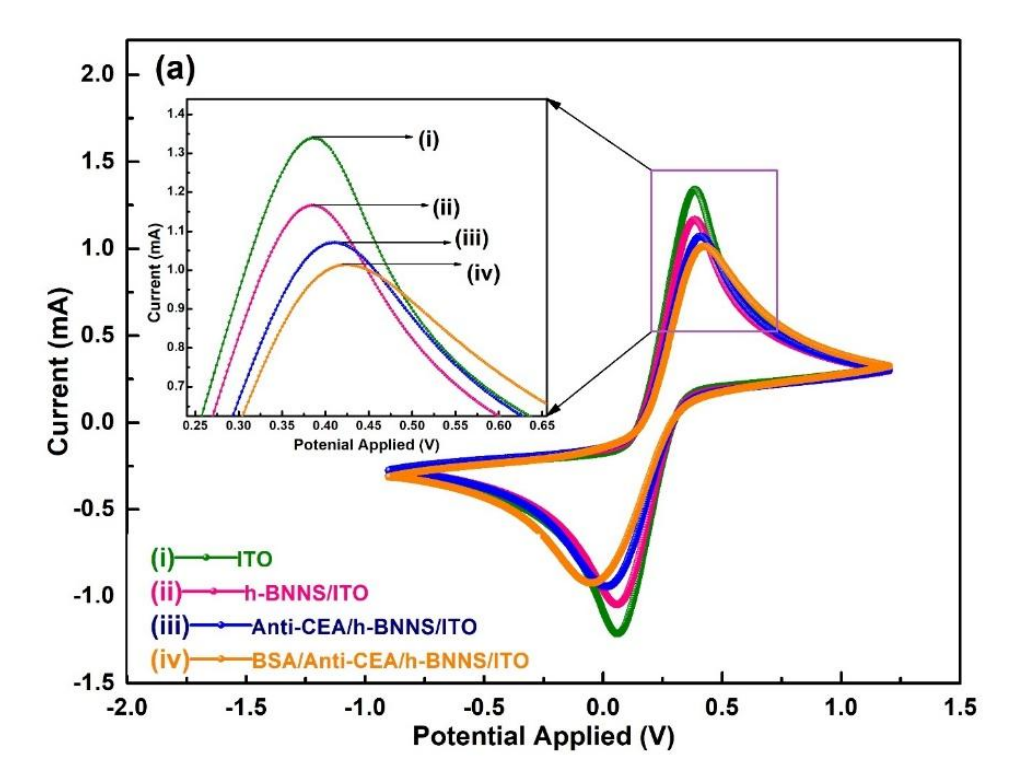


Figure 4.8: Cyclic voltammetry (CV) analysis, performed within a -0.9 to 1.2 V potential range, clearly demonstrates the successful modification of the h-BNNS/ITO electrode with protein biomolecules.

By substituting the experimentally obtained peak current values into the Randles—Sevcik Eq., the diffusion coefficients for each stage of electrode modification were quantitatively derived. These modifications involved the sequential addition of materials onto indium tin oxide (ITO) glass electrode, such as hexagonal boron nitride nanosheets (h-BNNS), anti-carcinoembryonic antigen (Anti-CEA) antibodies, or bovine serum albumin (BSA) for passivation, as part of fabricating a nano-biosensor for detecting carcinoembryonic antigen (CEA) in non-small cell lung cancer (NSCLC) diagnostics. These diffusion coefficients serve as direct electrochemical indicators of changes in the redox kinetics and confirm the successful functionalization of the electrode surface. The enhanced diffusion behaviour observed upon modification with ultrathin h-BNNS correlates well with the structural insights obtained from FT-IR spectroscopy, collectively affirming improved molecular accessibility, higher surface

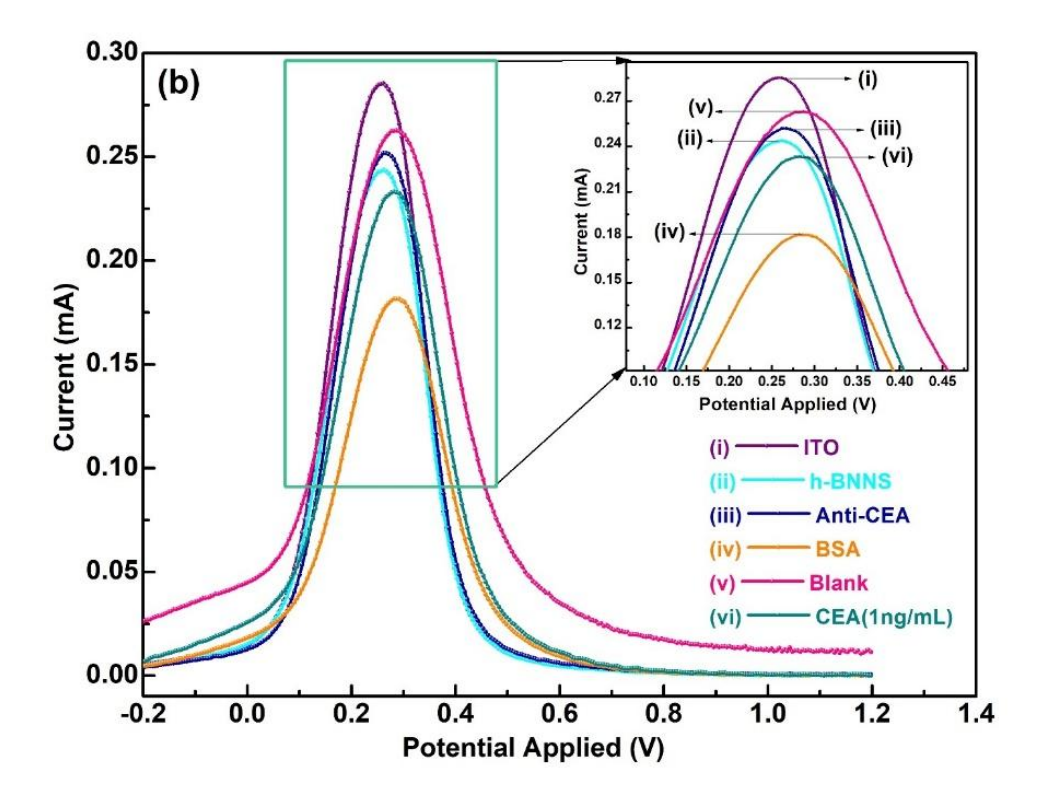
porosity, and strengthened electrode-analyte interaction, critical parameters for high-performance biosensing applications.

Table 4.2: Determination of the diffusion coefficients of the modified electrode accurately calculated using the Randles-Sevcik Eq..

Modification in Electrode	Diffusion Coefficient (cm <sup>2</sup> ·s <sup>-1</sup> )
ITO	$4.84 \times 10^{-11}$
h-BNNS/ITO	$3.67 \times 10^{-11}$
Anti-CEA/h-BNNS/ITO	$3.09 \times 10^{-11}$
BSA/Anti-CEA/h-BNNS/ITO	$2.77 \times 10^{-11}$

A meticulous assessment of the electron transfer kinetics during the stepwise surface modification of the h-BNNS/ITO electrode, Differential Pulse Voltammetry (DPV) was conducted at a scan rate of 10 mV s<sup>-1</sup> across an extended potential window ranging from -0.2 V to +1.2 V. This wide potential range was strategically selected to encompass both anodic and cathodic processes, ensuring the full capture of redox transitions and faradaic responses associated with the  $[Fe(CN)_6]^{3-/4-}$  redox couple. The primary objective of these DPV experiments was to systematically investigate and quantify the faradaic current, which originates from electron transfer reactions occurring at the modified electrode–electrolyte interface.

DPV, as a high-resolution electrochemical technique, applies a series of incremental voltage pulses superimposed on a linear potential ramp and measures the differential current responses. This technique significantly minimizes capacitive (non-faradaic) current contributions, thereby enhancing the sensitivity and resolution of redox peak currents. It is particularly advantageous for monitoring subtle changes in current due to surface modifications, such as biomolecular conjugation or nanomaterial deposition, which may not be distinctly resolved using traditional cyclic voltammetry.



# Figure 4.9: Electrode study on stepwise protein biomolecule modification of the h-BNNS/ITO electrode is confirmed by Differential pulse voltammetry (DPV) analysis conducted in the -0.2 to 1.2 V potential range.

The bare ITO substrate exhibited an anodic peak current of 0.285 mA, serving as a baseline for electron transfer activity and depicting unhindered electron exchange between the redox probe and the conductive substrate. Upon deposition of hexagonal boron nitride nanosheets (h-BNNS), the peak current dropped to 0.244 mA, which is attributed to the intrinsic insulating characteristics of h-BNNS combined with its large electroactive surface area. This morphological feature increased the surface roughness and electrochemical double-layer capacitance, thereby impeding direct electron transfer from the redox couple  $[Fe(CN)_6]^{3-/4-}$  to the ITO substrate. The subsequent immobilization of Anti-CEA antibodies onto the h-BNNS/ITO platform led to a modest increase in peak current to 0.252 mA, attributed to a conformational arrangement of the antibody that facilitated better charge transfer pathways. However, such immobilization can often result in random orientations and non-specific adsorption, thereby affecting antigen recognition efficiency. To overcome this, Bovine Serum Albumin (BSA) was introduced as a blocking agent to passivate unreacted sites and eliminate non-specific interactions. The incorporation of BSA resulted in a 26% reduction in peak current to 0.181 mA, which can be ascribed to the successful occupation of non-specific sites and disoriented antibody binding sites, imposing steric hindrance by the bulky BSA globular protein structure that further restricted electron diffusion across the electrode surface.

Following this, a blank measurement using 0 ng/mL CEA antigen was recorded, which caused a rise in current to 0.263 mA, clearly indicating ionic contributions from the PBS matrix (pH 7.4, 0.9% NaCl). This highlights the electrostatic interactions and background electrolyte conductivity influencing baseline current levels. This confirmed the system's sensitivity to ionic contributions from the electrolyte and reinforced the importance of precise control during blank calibration. Finally, the specific binding of 1 ng/mL CEA antigen to the Anti-CEA-modified electrode (after 30 min incubation) resulted in a notable drop in peak current to 0.233 mA. This decrease confirms successful antigen-antibody cross-linking, which introduces an additional barrier to electron transfer due to the formation of a stable immunocomplex. These electrochemical observations, further corroborated by FT-IR analysis, validate the stepwise construction of the biosensing interface and affirm the high specificity and sensitivity of the platform for CEA detection, underscoring its clinical potential for early-stage detection of onco-markers associated with non-small cell lung cancer (NSCLC).

#### 4.3.2.2 Evaluating Electron Transfer Dynamics of h-BNNS/ITO-based Nanobiosensing Interfaces via Scan Rate-Dependent Cyclic Voltammetry

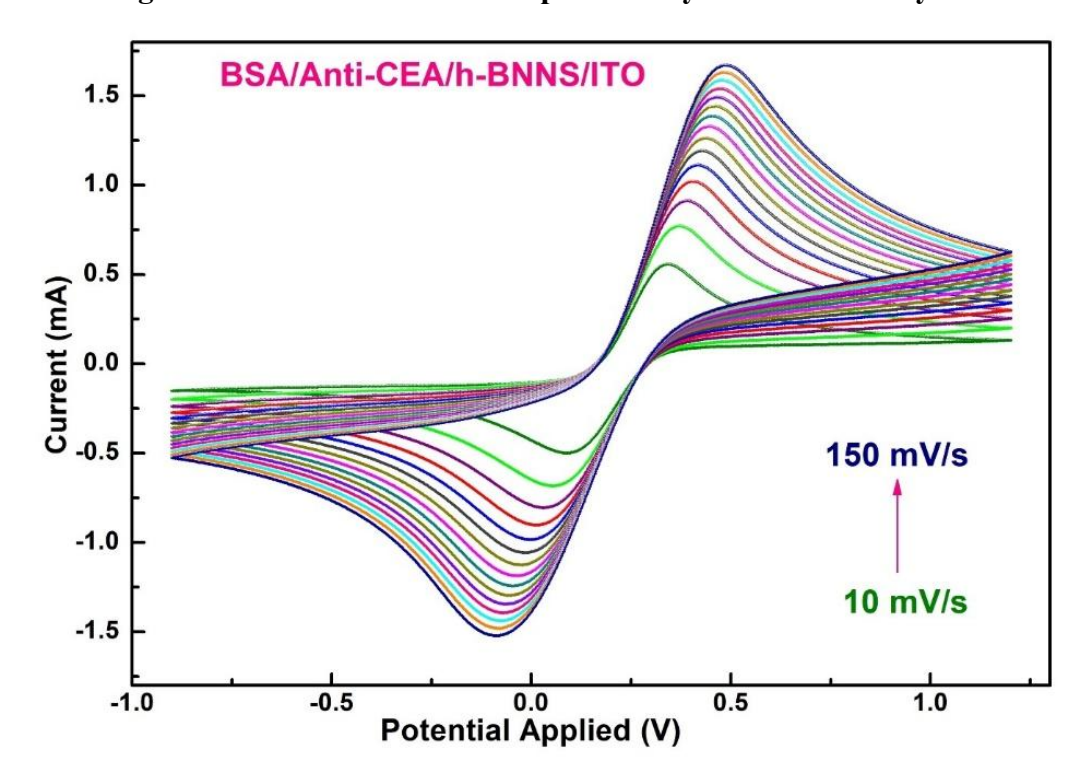


Figure 4.10: Scan rate study conducted using cyclic voltammetry on the BSA/Anti-CEA/h-BNNS/ITO electrode across scan rates from 10 to 150 mV/s, elucidating the charge transfer kinetics and diffusion-controlled behaviour.

The electron transfer kinetics of the BSA/Anti-CEA/h-BNNS/ITO immunoelectrode were systematically and rigorously evaluated using scan rate-dependent cyclic voltammetry (CV), to elucidate its electrochemical behaviour and analytical performance for carcinoembryonic antigen (CEA) detection (Fig. 6c). The CV experiments were performed in a conventional three-electrode system consisting of a 0.64 cm² h-BNNS/ITO working electrode, a platinum counter electrode, and an Ag/AgCl reference electrode, immersed in 50 mM phosphate-buffered saline (PBS, pH 7.4, 0.9% NaCl) containing a 5 mM equimolar redox couple of potassium ferro/ferricyanide ([Fe(CN)<sub>6</sub>]<sup>3-/4-</sup>).

A direct and linear correlation was established between both anodic (I\_pa) and cathodic (I\_pc) peak currents and the square root of the applied scan rate across a range of 10–150 mV/s (**Fig. 4.10**), in strong agreement with the Randles–Sevcik **Eq. [4.5]**. This linear correlation of peak currents on v<sup>1/2</sup> confirms that the electron transfer process at the immunoelectrode–analyte interface is governed by diffusion-controlled kinetics, as mentioned in **Eq. 4.6-4.9** [12, 13]. The selection of this scan rate window ensures accurate profiling of redox activity, as it preserves linearity while avoiding capacitive distortions, thereby providing consistent and reproducible electrochemical responses, making them optimal for studying the immunoelectrode's performance.

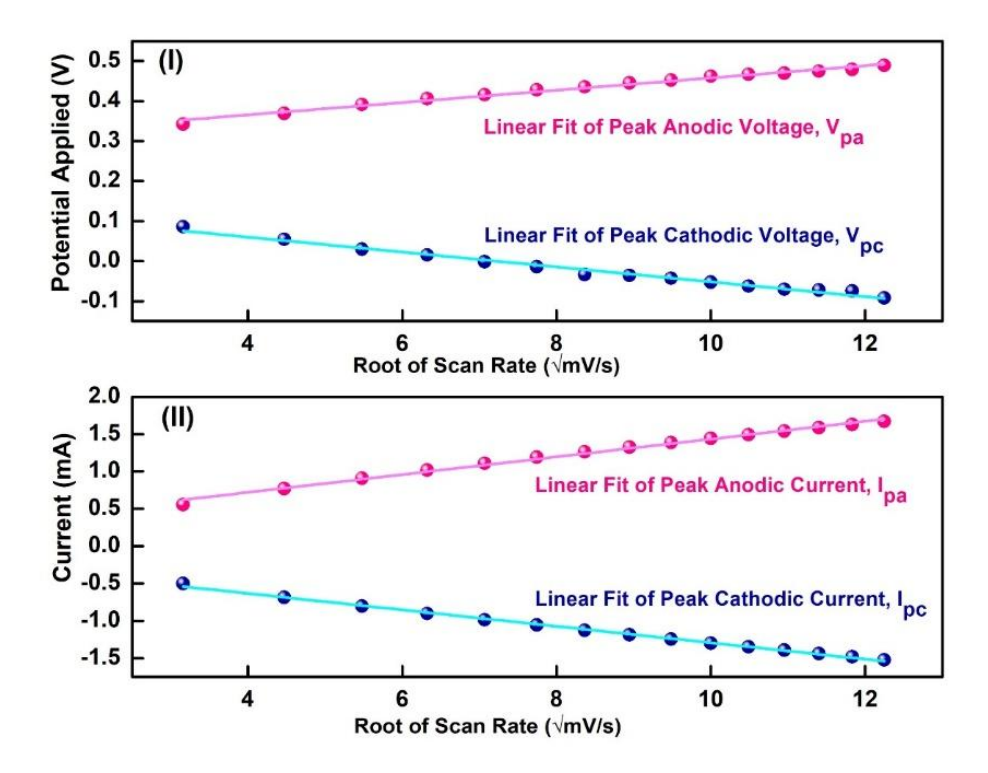


Figure 4.11: A linear correlation is observed in the scan rate analysis of the BSA/Anti-CEA/h-BNNS/ITO electrode between (i) anodic and cathodic peak potentials and (ii) peak currents plotted versus the square root of the scan rate (mV/s).

$$E_{pa} = [\ 3.04 \times 10^{-4}\ V +\ 1.53\ \times 10^{-5}\ V\sqrt{s/mV}\ \times \sqrt{Scan\ Rate[mV/s]}\ ];$$
 
$$R^2 = 0.98681 \qquad [4.6]$$
 
$$E_{pc} = [\ 1.35 \times 10^{-4}\ V - 1.86 \times 10^{-5}\ V\sqrt{s/mV} \times \sqrt{Scan\ Rate[mV/s]}\ ];$$
 
$$R^2 = 0.98624 \qquad [4.7]$$
 
$$I_{pa} = [\ 2.46 \times 10^{-4}\ A +\ 1.188 \times 10^{-4}\ A\sqrt{s/mV}\ \times \sqrt{Scan\ Rate[mV/s]}];$$
 
$$R^2 = 0.98363 \qquad [4.8]$$
 
$$I_{pc} = [\ -1.93 \times 10^{-4}\ A -\ 1.11 \times 10^{-4}\ A\sqrt{s/mV} \times \sqrt{Scan\ Rate[mV/s]}];$$
 
$$R^2 = 0.9973 \qquad [4.9]$$

Furthermore, the calculated peak-to-peak separation ( $\Delta Ep = Epc - Epa$ ) was 33.9 mV, which is well within the theoretical threshold ( $\Delta Ep \leq 57$  mV), indicative of an electrochemically reversible system [38]. This narrow  $\Delta Ep$  value demonstrates minimal resistance to electron transfer, reflecting rapid electron exchange between the redox probe and the modified electrode surface, attributed to the intrinsic conductivity and interfacial efficacy imparted by the hybrid nanoarchitecture of the immunoelectrode. Also, the specific binding of Anti-CEA antibodies onto extensive functionalized surface-active sites of h-BNNS ensures selective and efficient analyte interaction.

Altogether, these findings confirm that the BSA/Anti-CEA/h-BNNS/ITO immunoelectrode exhibits high electron transfer efficiency, strong reversibility, and robust faradaic response, key attributes that substantiate its potential as a highly sensitive and reliable electrochemical biosensing platform for non-small cell lung cancer (NSCLC) diagnostics through precise CEA biomarker detection, potentially improving patient outcomes through timely intervention. Its ability to facilitate fast, diffusion-governed electron transfer reactions with reproducible signal output positions it as a promising candidate for point-of-care diagnostic applications.

### 4.3.2.3 Calibrating CEA Concentrations through stepwise Electroanalytical Response Analysis of Functionalized h-BNNS/ITO Nano-biosensing Interface

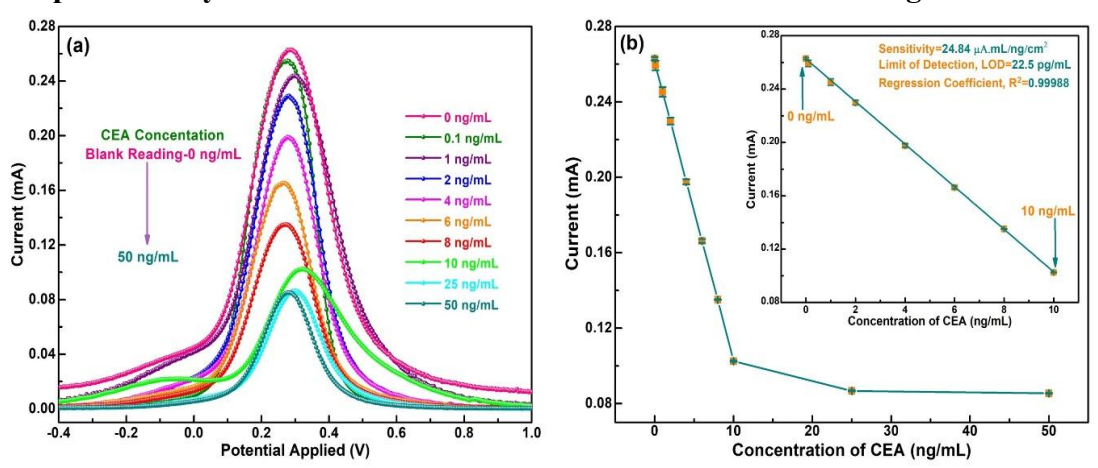


Figure 4.12: Differential pulse voltammetry (DPV) analysis of the CEA/BSA/Anti-CEA/h-BNNS/ITO immunoelectrode was performed over 0–50 ng/mL CEA concentrations. (b) The corresponding calibration curve shows a robust linear relationship between DPV current and CEA concentration, supported by inset linear regression.

Differential Pulse Voltammetry (DPV) was employed as a sensitive electroanalytical technique to evaluate the immunoelectrode's response to varying concentrations of Carcinoembryonic Antigen (CEA). The BSA/Anti-CEA/h-BNNS/ITO immunoelectrode was exposed to a physiologically relevant CEA concentration range (0–50 ng/mL), reflecting normal to elevated levels observed in clinical cases, particularly Non-Small Cell Lung Cancer (NSCLC), where serum CEA levels typically exceed 5 ng/mL [25]. For statistical reliability and reproducibility of the measurements, each concentration was tested in triplicate (n = 3) using fresh and independently fabricated immunoelectrodes.

The DPV peak current, which reflects the electron transfer efficiency between the electrode and the electrolyte, was observed to decrease as CEA concentration increased, as shown in Fig. 4.12. This inverse correlation is attributed to the formation of an insulating immune complex layer (antibody—antigen binding) on the electrode surface, which obstructs electron transport pathways between the electroactive matrix and the electrolyte. The accumulation of such complexes impedes charge transfer efficiency, thus leading to attenuated current signals. This behavior corroborates the principle of signal suppression commonly observed in label-free immunosensing platforms, where antibody—antigen complex restricts electron transfer between the electrode surface and

the electrolyte by creating a physical and electrical barrier, thereby reducing the availability of active sites for redox reactions. This electrochemical behavior demonstrates the immunoelectrode's high sensitivity and effective biorecognition capability, affirming its potential as a powerful analytical tool for the quantitative detection of CEA in clinical diagnostics, particularly for early-stage NSCLC prognosis.

The calibration curve obtained from Differential Pulse Voltammetry (DPV) measurements exhibits a linear decrease in peak current response with increasing CEA concentration within the detection range of 0–50 ng/mL, as shown in **Fig.4.12b**. This relationship is mathematically expressed by the following linear regression **Eq. [4.10]**:

$$I(mA) = [0.262 mA + 24.84 \mu AmL/ng/cm^2 \times (CEA Concentration)]$$
 [4.10]

This **Eq. [4.10]** indicates that the current response varies proportionally with the CEA concentration, particularly within the clinically significant range of 0–10 ng/mL, which was utilized to evaluate the analytical sensitivity of the fabricated immunosensor.

The sensitivity (m) of the immunoelectrode was calculated using the slope-to-surface area ratio, where the active surface area of the modified electrode was determined to be  $0.64~\text{cm}^2$ . Accordingly, the sensor demonstrated an exceptional linear sensitivity of  $24.84~\mu\text{A}\cdot\text{mL/ng}\cdot\text{cm}^2$  with an outstanding regression coefficient (R<sup>2</sup> = 0.99988), signifying excellent linearity and reproducibility in current response toward incremental CEA concentrations. Furthermore, the Limit of Detection (LOD), which defines the minimum analyte concentration that can be reliably detected by the sensor, was computed using the standard formula **Eq. [4.11]**:

Limit of Detection = 
$$3\sigma/m$$
 [4.11]

where σ represents the standard deviation of the y-intercept of the calibration curve, and m is the sensitivity of the biosensor as defined above. Based on this Eq., the LOD was calculated to be 22.5 pg/mL, signifying the immunosensor's high precision and ultrasensitive detection capability, particularly for trace-level concentrations of CEA. This ultra-low detection limit positions the BSA/Anti-CEA/h-BNNS/ITO immunoelectrode as a powerful diagnostic tool for the early detection of CEA-associated malignancies such as Non-Small Cell Lung Cancer (**Table 4.3**), even at subclinical biomarker levels, thereby demonstrating its strong potential for practical clinical applications.

Table 4.3: A comprehensive comparison table summarizing the analytical performance, including linear range and limit of detection, of different immunosensors designed for CEA monitoring in clinical diagnostics.

Sensing Platform	Sensing Matrix	Detection Technique	Linear Range (ng/mL)	Limit of Detection	Sensitivity	Ref.
Sandwich Immunoassay	AuNP/COFTFP-Thi based COF	CV, EIS	0.11 - 80	34 pg/mL		[39]
Immunosensor	Paper modified with SPGE	DPV	1 – 100	0.33 ng/mL	0.7184 μA·mL/ng	[40]
Sandwich Aptasensor	MCH-Apt/Gold	CV, DPV, EIS	5 – 40	3.4 ng/mL	0.436 μA·mL/ng	[41]
Immunoassay	rGO/GCE	CV, EIS	0.5 - 3	0.05 ng/mL		[42]
Immunosensor	SPGE modified with Fe <sub>2</sub> O <sub>3</sub> /PANI/AuNP	CV	0 – 10	0.25 ng/mL	0.3827 μ <b>A·m</b> L/ng	[43]
Immunosensor	Fe <sub>2</sub> O <sub>3</sub> /PEDOT:PSS modified Paper	Amperometry	4 – 25		10.2 μA·mL/ng/cm <sup>2</sup>	[44]
Immunosensor	Paper with PANI/Au	EIS	6 - 20	2.68 ng/mL	3.6 Ω·mL/ng	[45]
Immunosensor	Paper with PANI/Au	Amperometry	2 – 20	1.36 ng/mL	13.9 μA·mL/ng/cm <sup>2</sup>	[46]
Immunosensor	h-BNNS/ITO	DPV, CV	0 - 10	22.5 pg/mL	24.84 μA·mL/ng/cm <sup>2</sup>	Present Work

# 4.3.2.4 Comprehensive Performance Evaluation of Optimal Working pH, Selectivity, Operational Reproducibility, Long-Term Stability, and Real-Sample Applicability of the h-BNNS/ITO-Based Nano-biosensor

The influence of pH on immobilized antibody functionality was critically evaluated to establish optimal conditions for fabricating a robust and practical immunosensor. Selecting a buffer solution with an appropriate pH is essential to ensure maximum antibody receptivity, thereby achieving highly accurate and stable sensor responses. Differential pulse voltammetry (DPV) measurements were conducted on the Anti-CEA/h-BNNS/ITO electrode across a pH range of 6.0 to 8.0, with the corresponding responses detailed in **Fig. 4.13**.

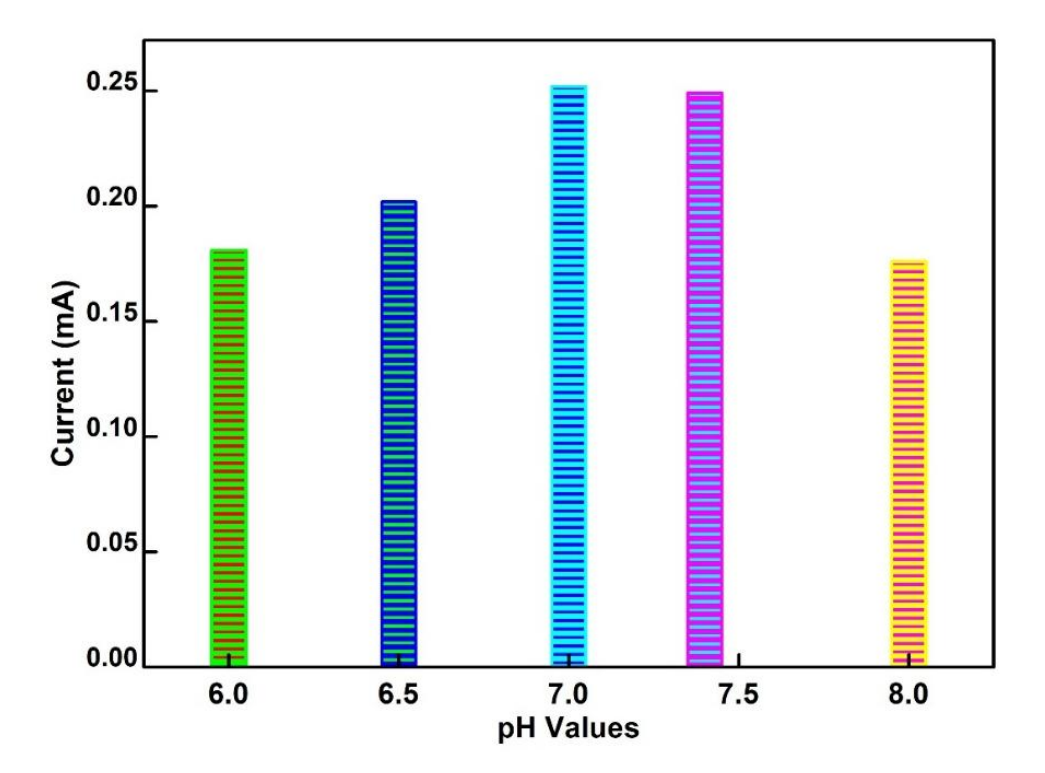


Figure 4.13: The influence of pH within the 6.0 to 8.0 range on the electrochemical peak current of the Anti-CEA/h-BNNS/ITO immunoelectrode was conducted to optimize antibody-antigen interaction efficiency.

The optimum peak current was observed at neutral pH 7.0, indicating that neutral pH provides the most favorable environment for antibodies to achieve an oriented and stable configuration essential for effective covalent immobilization. At this pH, the antibodies maintain their native conformation, ensuring that their active sites remain accessible for antigen binding, which is crucial for the high sensitivity and specificity of the immunosensor. This finding aligns with established knowledge that biomolecules tend to preserve their natural structural integrity at neutral pH, whereas exposure to acidic or basic conditions often leads to denaturation and loss of biological function, negatively impacting sensor performance.

Supporting this, Oregioni et al. reported that the  $\alpha$ -amino (N-terminus) groups, which are abundantly present throughout the antibody structure, exhibit significant chemical

reactivity specifically at pH 7.0. The conducive buffer environment led to optimum electrochemical reactivity by promoting efficient covalent bonding between the antibody and the nano-biosensor interface, thereby demonstrating robust immobilization and stable bio-recognition interfaces. Furthermore, the conformational orientation and effective binding efficiency of antibodies at neutral pH eventually improve electron transfer dynamics, depicted in a bar graph by the heightened peak current response through electrochemical measurements.

To ensure clinical selectivity towards targeted affinity biomarkers, carcinoembryonic antigen (CEA) in the presence of an intricate biological environment exhibiting possible interfering biomolecules frequently found in the complex serum matrix of non-small cell lung cancer (NSCLC) patients. Therefore, a detailed selectivity study was conducted to evaluate the capability of the fabricated BSA/Anti-CEA/h-BNNS/ITO immunoelectrode to discriminate CEA from potential co-existing interferents. These interferents included endothelin-1 (ET-1) [47], C-reactive protein (CRP) [48], neuron-specific enolase (NSE) [49], cardiac troponin-I (cTnI) [50], sodium chloride (NaCl), and others that may be co-expressed in patient serum.

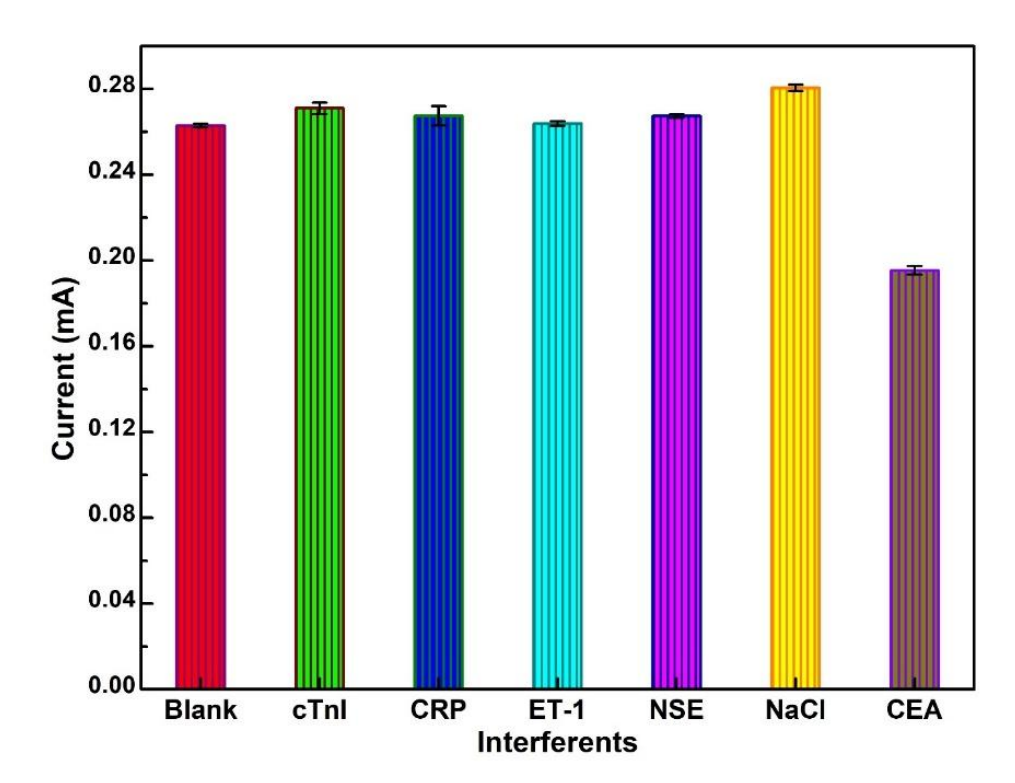


Figure 4.14: Bar graph depicting the selectivity study conducted using DPV measurements to investigate the effect of various interferents relevant to NSCLC patients on the electrochemical performance of the BSA/Anti-CEA/h-BNNS/ITO immunosensor.

To evaluate the cross-reactivity of the h-BNNS nano-biosensor interface apart from the intrinsic affinity interactions between antigen—antibody, the electrochemical investigations were carried out by obtaining DPV response from potential interferents present in serum with physiologically appropriate concentrations (**Fig. 4.14**). Initially, control test was conducted to obtain a stable baseline of the BSA/Anti-CEA/h-

BNNS/ITO immunoelectrode without CEA (0 ng/mL) signal. For selectivity assessment, a distinct potential interferents was introduced individually to the BSA/Anti-CEA/h-BNNS/ITO platform, with a 30-minute incubation preceding DPV analysis to enable potential binding. Post-incubation, the electrochemical response was then monitored to assess any deviation in peak current intensity from the baseline. As shown in Fig. 4.14, this study confirms whether or not non-specific biomolecules induce any significant response, thereby validating the selective recognition capability of the designed nano-biosensing platform. The resulting DPV responses showed negligible change in the peak current compared to the blank electrode, indicating no significant non-specific interaction or signal suppression caused by these interferents. In contrast, upon the introduction of 4 ng/mL of CEA, a marked decrease in the peak current was observed in the DPV response. This substantial drop in current can be attributed to the successful and specific binding between the immobilized Anti-CEA antibodies and the target CEA antigen. The formation of the antibody-antigen complex on the electrode surface creates an insulating biological layer, which hinders electron transfer and thereby suppresses the redox signal. This pronounced current reduction, observed only in the presence of CEA and not with other interfering biomolecules, strongly validates the immunoelectrode's high specificity and selective recognition capability for CEA. Such selective electrochemical behaviour confirms the sensor's potential for accurate and reliable detection of CEA in clinically relevant samples.

To validate the reliability and consistency of the fabricated BSA/Anti-CEA/h-BNNS/ITO immunoelectrode, a reproducibility study was systematically conducted. The primary objective of this investigation was to evaluate the degree of uniformity in the electrochemical response across multiple independently prepared electrodes under identical experimental conditions. Reproducibility is a critical performance parameter that reflects the robustness and fabrication stability of an electrochemical biosensor, especially for practical diagnostic applications. In this study, four separate immunoelectrodes were fabricated using an identical protocol, wherein each electrode surface was modified with a fixed concentration of carcinoembryonic antigen (CEA, 8 ng/mL) following immobilization of Anti-CEA monoclonal antibodies and BSA blocking. Differential Pulse Voltammetry (DPV) measurements were recorded for each electrode, and the peak current responses were analyzed to assess variation among them (Fig. 4.15).

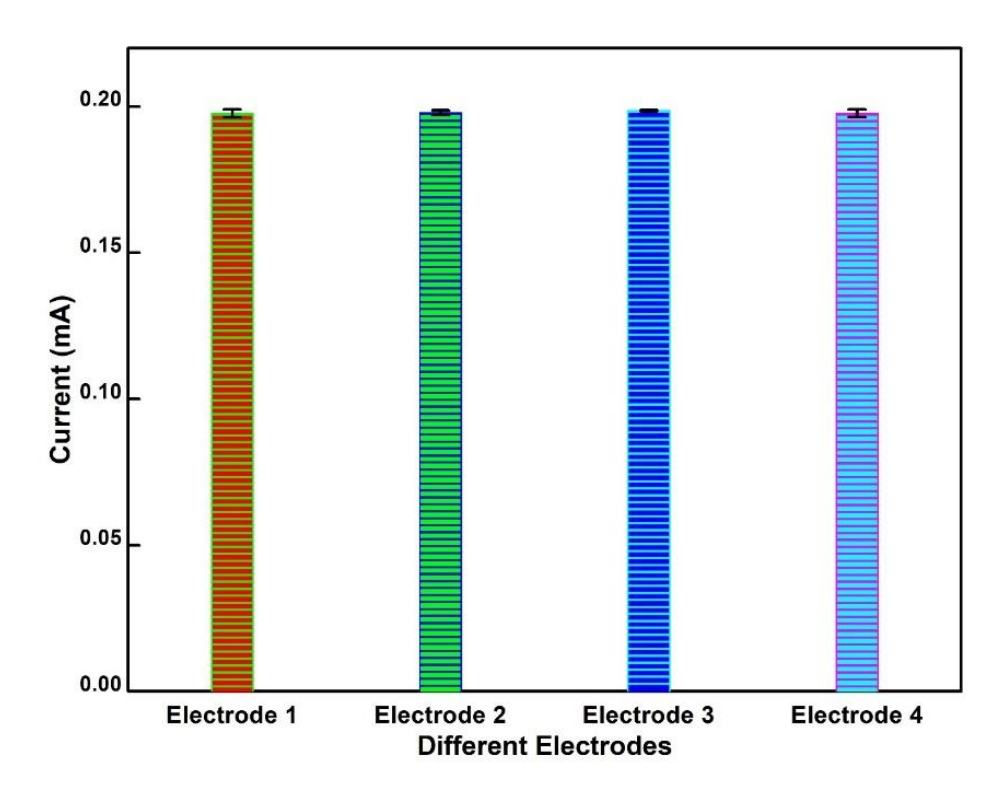


Figure 4.15: Reproducibility was evaluated using four independently fabricated BSA/Anti-CEA/h-BNNS/ITO immunoelectrodes prepared under identical protocols.

The relative standard deviation (RSD) calculated from the DPV responses of the four electrodes was found to be 0.232%, which is significantly lower than the acceptable threshold of 5% for analytical reproducibility. This minimal RSD value reflects not only the uniform functionalization of the immunoelectrode surface but also confirms the consistency of the bio-recognition interface and the stability of the electrode fabrication process. This outcome substantiates that the immunoelectrode platform provides stable, uniform, and excellent reproducibility of the BSA/Anti-CEA/h-BNNS/ITO immunosensing platform and strongly supports its potential for scalable production and deployment in reliable point-of-care diagnostic systems.

Shelf-life evaluation plays a critical role in assessing the long-term stability and practical applicability of the developed h-BNNS-based immunosensor, particularly for clinical diagnostics and industrial deployment where reliable storage and reusability are essential. A stable shelf life ensures that the sensor can retain its functionality over time during storage, which is critical for real-world applications. To determine the shelf-life performance, the fabricated CEA/BSA/Anti-CEA/h-BNNS/ITO immunoelectrode was subjected to a systematic aging study. The immunoelectrode, modified with 6 ng/mL of carcinoembryonic antigen (CEA), was stored under refrigerated conditions at 4 °C, and its electrochemical performance was monitored over a 6-week period using differential pulse voltammetry (DPV) at regular weekly intervals (as illustrated in **Fig. 4.16**).

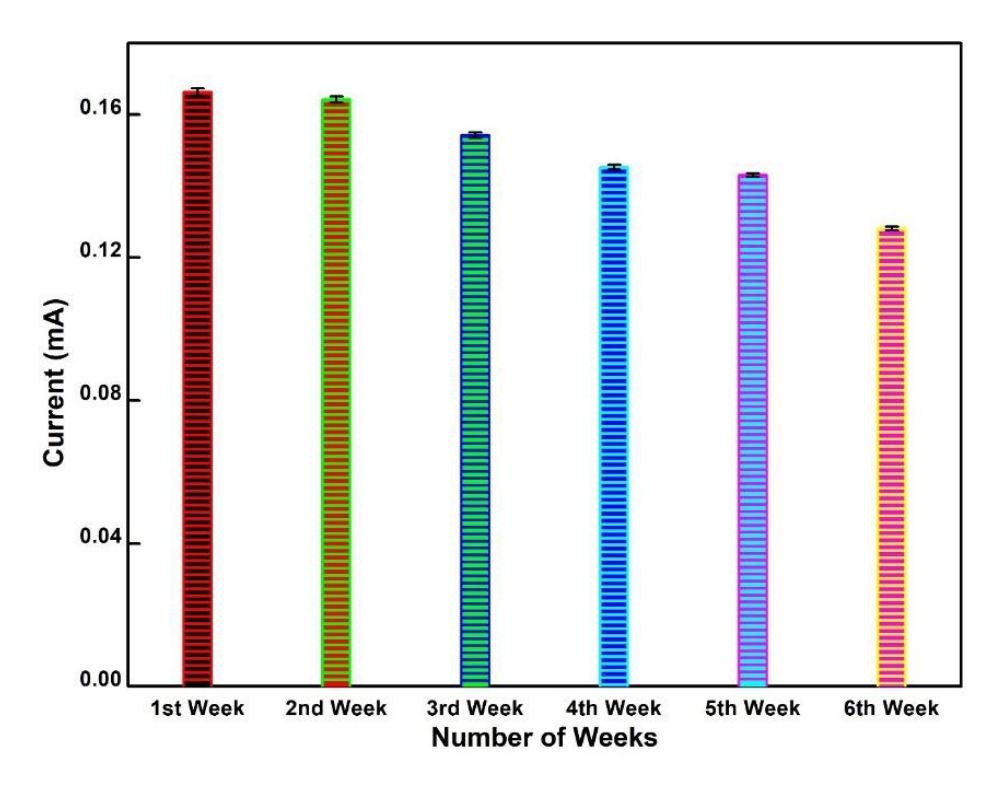


Figure 4.16: Differential pulse voltammetry (DPV) investigation to systematically evaluate the shelf-life stability of the CEA/BSA/Anti-CEA/h-BNNS/ITO immunoelectrode, monitored over six weeks with regular weekly intervals.

Throughout the first five weeks, the sensor maintained a stable DPV current response, indicating negligible stable antibody-antigen interaction and effective preservation of the bio-recognition layer. Specifically, 86.01% of the initial DPV signal was retained by the end of the fifth week, with a relative standard deviation (RSD) of 6.8%, confirming the high stability, consistent performance, and storage tolerance of the immunoelectrode over this period. However, a marked decline in the peak current was observed at the beginning of the sixth week, which is attributed to the gradual leaching or denaturation of the immobilized antibody and antigen molecules. This decline signals the onset of functional degradation of the biosensor, thereby defining the effective operational shelf-life to be up to five weeks under refrigerated storage. These results confirm that the developed h-BNNS-based immunoelectrode demonstrates excellent storage stability, making it a promising candidate for real-world clinical and industrial applications that require extended usability with minimal performance loss.

To establish the clinical utility together with a reliable diagnostic response of the asfabricated h-BNNS nano-biosensing interface, its electrochemical detection of CEA was investigated by spiking the CEA concentrations in human serum samples. This study was conducted to assess the cross-reactivity of the prepared BSA/Anti-CEA/h-BNNS/ITO immune-interface in the serum sample, which offers complex biological environments comprising various proteins and biomolecules that may interfere with detection. Determination of consistent functionality of hBNNS nano-biointerface, the electrochemical response for the standard CEA (A) was compared with that of human serum samples artificially spiked with identical CEA concentrations (S). The comparative analysis, detailed in **Fig. 4.17**, highlights the immunoelectrode's precision and suitability in complex biological matrices for application in clinical diagnostics.

Table 4.4: Quantitative determination of relative standard deviation (RSD%) and recovery rates for CEA in spiked serum, with reference to actual CEA concentration values.

CEA Concentration (ng/mL)	Peak Current Associated with Actual Sample (A, in mA)	Peak Current Associated with Spiked Sample (S, in mA)	RSD %	Recovery %
1	0.244753	0.24784	0.886168	101.26
4	0.19577	0.198487	0.974479	101.38
8	0.106403	0.107453	0.694355	100.98

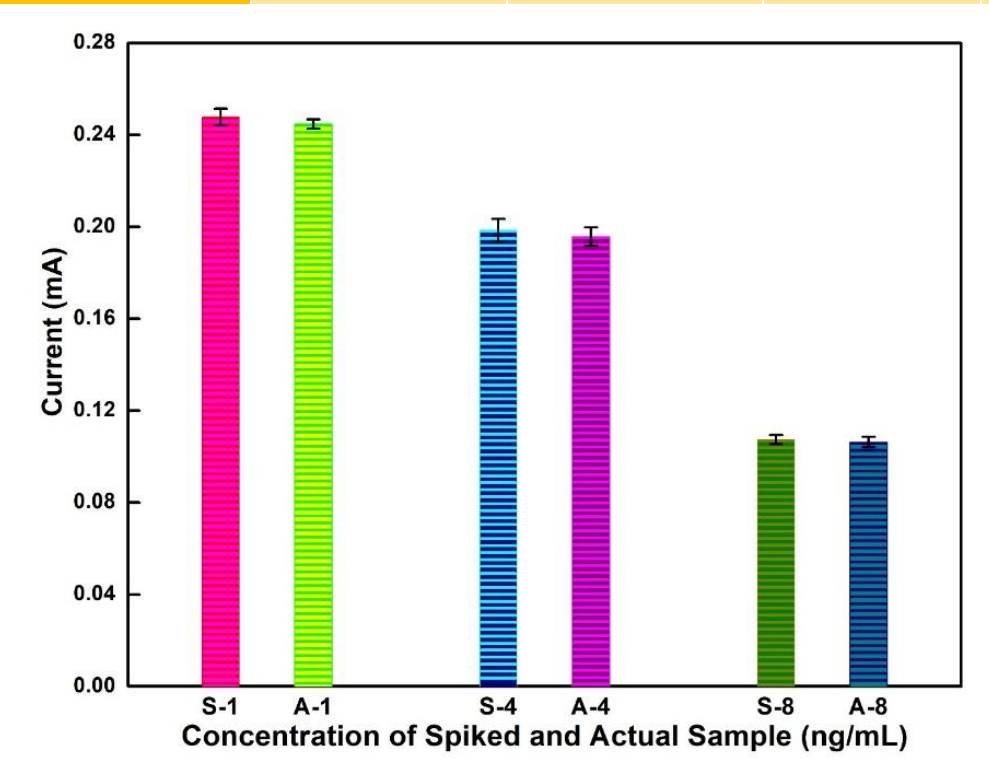


Figure 4.17: Evaluation of the CEA/BSA/Anti-CEA/h-BNNS/ITO immunoelectrode using spiked serum sample analysis, to comprehensively test the sensitivity and accuracy of as-fabricated immunoelectrodes' applicability for real sample analysis.

The results, summarized in **Table 4.4**, present the corresponding current responses, indicating that the peak current values obtained from the serum samples (A) closely aligned with standard CEA concentrations (S). Specifically, the relative standard deviation (RSD) values for CEA concentrations of 1, 4, and 8 ng/mL were exceptionally low, at 0.886%, 0.974%, and 0.694%, respectively. These minimal deviations reflect the high precision and robustness of the immunoelectrode, even in the presence of potential interferents found in serum. These results strongly validate that the developed immunoelectrode retains its bio-recognition efficiency and electrochemical

responsiveness in clinically relevant human serum, exhibiting the complex nature. Thus, the sensor demonstrates excellent potential for reliable, efficient, and real-time detection of CEA in human serum, making it a promising candidate for point-of-care cancer diagnostics and clinical monitoring.

#### Conclusion

This study demonstrated the development of a next-generation, label-free electrochemical immunosensor for the sensitive and selective detection of Carcinoembryonic Antigen (CEA), a clinically relevant biomarker associated with nonsmall cell lung cancer (NSCLC). The research harnesses the hydrothermally nanoengineered ultrathin hexagonal boron nitride nanosheets (h-BNNS) to construct a highly stable, biocompatible, and efficient nano-biointerface. This study demonstrated the development of a next-generation, label-free electrochemical immunosensor for the sensitive and selective detection of Carcinoembryonic Antigen (CEA), a clinically relevant biomarker associated with non-small cell lung cancer (NSCLC). The research harnesses the hydrothermally nano-engineered ultrathin hexagonal boron nitride nanosheets (h-BNNS) to construct a highly stable, biocompatible, and efficient nanobiointerface. Its key importance lies in addressing the urgent need for early, accurate, and reliable NSCLC diagnostics, offering a sustainable, high-performance biosensing interface that outperforms conventional platforms through its exceptional sensitivity, low detection limit, and robust selectivity in complex biological matrices. This work comprehensively discusses the core scientific importance of nanostructure engineering carried out utilizing hydrothermal exfoliation of bulk h-BN into few-layered nanosheets. Successful nucleation of hexagonal structure in hBNNS was attributed to the synergistic interplay of temperature-time optimization, the partially ionic nature of B-N bonds, intercalating agent dynamics, and Lewis acid-base complexation chemistry. These conditions facilitated the formation of well-exfoliated, ultrathin, hexagonal nanostructures with high surface-to-volume ratio, essential for effective biofunctionalization and signal transduction. Furthermore, the covalent immobilization of biomolecules (CEA antibody, BSA, and target antigen) on the engineered h-BNNS/ITO platform was thoroughly validated through FT-IR spectral analysis. Effective nanobiointerface formation was assessed by the appearance and modulation of amide I and II bands, as depicted in FT-IR study. This led to the fabrication of a robust sensing interface capable of high-affinity and specific bio-recognition.

The electrochemical performance of the fabricated CEA/BSA/Anti-CEA/h-BNNS/ITO immunoelectrode was systematically evaluated using differential pulse voltammetry (DPV) across a physiological CEA concentration range (0–50 ng/mL). It demonstrated an exceptional sensitivity of 24.84  $\mu$ A·mL/ng·cm², an ultra-low detection limit of 22.5 pg/mL, enabling ultra-trace level detection suitable for early-stage cancer diagnostics. The immunoelectrode exhibited exceptional reproducibility, with a relative standard deviation (RSD) of 0.232%, and demonstrated unparalleled selectivity against interferents such as endothelin (ET-1), C-reactive protein (CRP), neuron-specific enolase (NSE), cardiac troponin-I (cTnI), and NaCl, attributed to specific antibody–antigen interactions and BSA passivation. In addition, it exhibited outstanding long-term storage stability, retaining over 86% of its original signal after five weeks at 4 °C. To validate clinical relevance, the biosensor's performance was assessed using CEA-

spiked human serum samples. The sensor maintained precise and reproducible current responses, closely matching those obtained with standard CEA solutions. These findings were supported by low relative standard deviations (RSD) of 0.886%, 0.974%, and 0.694% for 1, 4, and 8 ng/mL CEA concentrations, respectively, confirming the sensor's reliability and robustness in complex biological matrices. The key importance of this study lies in establishing ultrathin h-BNNS as a transformative material for immunosensing applications. It not only showcases a facile and scalable synthesis approach but also validates the material's bio-functional utility, electrochemical responsiveness, and clinical diagnostics potential. The outcomes of this work pave the way for the practical utility of h-BNNS-based point-of-care diagnostic devices and highlight the clinical feasibility of deploying this sensor platform for early cancer detection technologies.

#### References

- [1] S. Malik, K. Muhammad, Y. Waheed, Nanotechnology: A Revolution in Modern Industry, Molecules, 28 (2023) 661.
- [2] R. Renneberg, D. Pfeiffer, F. Lisdat, G. Wilson, U. Wollenberger, F. Ligler, A.P. Turner, Frieder Scheller and the short history of biosensors, Biosensing for the 21st Century, (2007) 1-18.
- [3] P. Malik, V. Katyal, V. Malik, A. Asatkar, G. Inwati, T.K. Mukherjee, Nanobiosensors: Concepts and Variations, International Scholarly Research Notices, 2013 (2013) 327435.
- [4] W. Wen, Y. Song, X. Yan, C. Zhu, D. Du, S. Wang, A.M. Asiri, Y. Lin, Recent advances in emerging 2D nanomaterials for biosensing and bioimaging applications, Materials Today, 21 (2018) 164-177.
- [5] K. Zhang, Y. Feng, F. Wang, Z. Yang, J. Wang, Two dimensional hexagonal boron nitride (2D-hBN): synthesis, properties and applications, Journal of Materials Chemistry C, 5 (2017) 11992-12022.
- [6] Z. Zhen, H. Zhu, 1 Structure and Properties of Graphene, in: H. Zhu, Z. Xu, D. Xie, Y. Fang (Eds.) Graphene, Academic Press, 2018, pp. 1-12.
- [7] G. Ban, Y. Hou, Z. Shen, J. Jia, L. Chai, C. Ma, Potential Biomedical Limitations of Graphene Nanomaterials, International Journal of Nanomedicine, 18 (2023) 1695-1708.
- [8] L.H. Li, J. Cervenka, K. Watanabe, T. Taniguchi, Y. Chen, Strong Oxidation Resistance of Atomically Thin Boron Nitride Nanosheets, ACS Nano, 8 (2014) 1457-1462.
- [9] D. Pacile, J. Meyer, Ç. Girit, A. Zettl, The two-dimensional phase of boron nitride: Few-atomic-layer sheets and suspended membranes, Applied Physics Letters, 92 (2008).
- [10] Z. Liu, Y. Gong, W. Zhou, L. Ma, J. Yu, J.C. Idrobo, J. Jung, A.H. MacDonald, R. Vajtai, J. Lou, Ultrathin high-temperature oxidation-resistant coatings of hexagonal boron nitride, Nature communications, 4 (2013) 2541.
- [11] X. Yu, M. Xue, Z. Yin, Y. Luo, Z. Hong, C. Xie, Y. Yang, Z. Ren, Flexible boron nitride composite membranes with high thermal conductivity, low dielectric constant and facile mass production, Composites Science and Technology, 222 (2022) 109400.
- [12] Q. Cai, A. Du, G. Gao, S. Mateti, B.C.C. Cowie, D. Qian, S. Zhang, Y. Lu, L. Fu, T. Taniguchi, S. Huang, Y. Chen, R.S. Ruoff, L.H. Li, Molecule-Induced Conformational Change in Boron Nitride Nanosheets with Enhanced Surface Adsorption, Advanced Functional Materials, 26 (2016) 8202-8210.
- [13] C. Sun, J. Zhao, D. Zhang, H. Guo, X. Wang, H. Hu, Covalent functionalization of boron nitride nanosheets via reductive activation, Nanoscale, 12 (2020) 18379-18389.
- [14] G. Yang, S.-J. Park, Conventional and Microwave Hydrothermal Synthesis and Application of Functional Materials: A Review, Materials, 12 (2019) 1177.
- [15] J. Cairns, The origin of human cancers, Nature, 289 (1981) 353-357.

- [16] H. Sung, J. Ferlay, R.L. Siegel, M. Laversanne, I. Soerjomataram, A. Jemal, F. Bray, Global Cancer Statistics 2020: GLOBOCAN Estimates of Incidence and Mortality Worldwide for 36 Cancers in 185 Countries, CA: A Cancer Journal for Clinicians, 71 (2021) 209-249.
- [17] R.A. de Mello, A.F. Veloso, P. Esrom Catarina, S. Nadine, G. Antoniou, Potential role of immunotherapy in advanced non-small-cell lung cancer, OncoTargets and Therapy, 10 (2016) 21-30.
- [18] Y. Alduais, H. Zhang, F. Fan, J. Chen, B. Chen, Non-small cell lung cancer (NSCLC): A review of risk factors, diagnosis, and treatment, Medicine, 102 (2023) e32899.
- [19] G. Curigliano, Cancer Patients and Risk of Mortality for COVID-19, Cancer Cell, 38 (2020) 161-163.
- [20] A.K. Ganti, J.L. Mulshine, Lung Cancer Screening, The Oncologist, 11 (2006) 481-487.
- [21] S.K. Arya, S. Bhansali, Lung Cancer and Its Early Detection Using Biomarker-Based Biosensors, Chemical Reviews, 111 (2011) 6783-6809.
- [22] P. Sharma, M.R. Hasan, M. Khanuja, R. Rawal, Shivani, R. Pilloton, J. Narang, Aptamer-based silver nanoparticle decorated paper platform for electrochemical detection ovarian cancer biomarker PDGF, Materials Chemistry and Physics, 306 (2023) 128114.
- [23] I.E. Tothill, Biosensors for cancer markers diagnosis, Seminars in Cell & Developmental Biology, 20 (2009) 55-62.
- [24] D.S. Lee, S.J. Kim, J.H. Kang, S.H. Hong, E.K. Jeon, Y.K. Kim, R. Yoo Ie, J.G. Park, H.S. Jang, H.C. Lee, Y.S. Kim, Serum Carcinoembryonic Antigen Levels and the Risk of Whole-body Metastatic Potential in Advanced Non-small Cell Lung Cancer, J Cancer, 5 (2014) 663-669.
- [25] M. Okada, W. Nishio, T. Sakamoto, K. Uchino, T. Yuki, A. Nakagawa, N. Tsubota, Prognostic significance of perioperative serum carcinoembryonic antigen in non-small cell lung cancer: analysis of 1,000 consecutive resections for clinical stage I disease, The Annals of Thoracic Surgery, 78 (2004) 216-221.
- [26] B. Singh, G. Kaur, P. Singh, K. Singh, B. Kumar, A. Vij, M. Kumar, R. Bala, R. Meena, A. Singh, A. Thakur, A. Kumar, Nanostructured Boron Nitride With High Water Dispersibility For Boron Neutron Capture Therapy, Scientific Reports, 6 (2016) 35535.
- [27] E.B. Aydın, M.K. Sezgintürk, Indium tin oxide (ITO): A promising material in biosensing technology, TrAC Trends in Analytical Chemistry, 97 (2017) 309-315.
- [28] S.K. Vashist, Comparison of 1-Ethyl-3-(3-Dimethylaminopropyl) Carbodiimide Based Strategies to Crosslink Antibodies on Amine-Functionalized Platforms for Immunodiagnostic Applications, Diagnostics, 2 (2012) 23-33.
- [29] W. Sun, Y. Meng, Q. Fu, F. Wang, G. Wang, W. Gao, X. Huang, F. Lu, High-Yield Production of Boron Nitride Nanosheets and Its Uses as a Catalyst Support for Hydrogenation of Nitroaromatics, ACS Applied Materials & Interfaces, 8 (2016) 9881-9888.
- [30] L. Hua Li, Y. Chen, B.-M. Cheng, M.-Y. Lin, S.-L. Chou, Y.-C. Peng, Photoluminescence of boron nitride nanosheets exfoliated by ball milling, Applied Physics Letters, 100 (2012).
- [31] R.V. Gorbachev, I. Riaz, R.R. Nair, R. Jalil, L. Britnell, B.D. Belle, E.W. Hill, K.S. Novoselov, K. Watanabe, T. Taniguchi, A.K. Geim, P. Blake, Hunting for Monolayer Boron Nitride: Optical and Raman Signatures, Small, 7 (2011) 465-468.
- [32] T. Yuzuriha, D. Hess, Structural and optical properties of plasma-deposited boron nitride films, Thin Solid Films, 140 (1986) 199-207.
- [33] M. Boulet-Audet, B. Byrne, S.G. Kazarian, High-Throughput Thermal Stability Analysis of a Monoclonal Antibody by Attenuated Total Reflection FT-IR Spectroscopic Imaging, Analytical Chemistry, 86 (2014) 9786-9793.
- [34] J.G. Kelly, J. Trevisan, A.D. Scott, P.L. Carmichael, H.M. Pollock, P.L. Martin-Hirsch, F.L. Martin, Biospectroscopy to metabolically profile biomolecular structure: a multistage approach linking computational analysis with biomarkers, Journal of Proteome Research, 10 (2011) 1437-1448.

- [35] O. Suys, A. Derenne, E. Goormaghtigh, ATR-FTIR Biosensors for Antibody Detection and Analysis, International Journal of Molecular Sciences, 23 (2022) 11895.
- [36] A. Sibai, K. Elamri, D. Barbier, N. Jaffrezic-Renault, E. Souteyrand, Analysis of the polymer-antibody-antigen interaction in a capacitive immunosensor by FTIR difference spectroscopy, Sensors and Actuators B: Chemical, 31 (1996) 125-130.
- [37] L. Tolosa, M.T. Donato, M.J. Gómez-Lechón, General Cytotoxicity Assessment by Means of the MTT Assay, in: M. Vinken, V. Rogiers (Eds.) Protocols in In Vitro Hepatocyte Research, Springer New York, New York, NY, 2015, pp. 333-348.
- [38] N. Elgrishi, K.J. Rountree, B.D. McCarthy, E.S. Rountree, T.T. Eisenhart, J.L. Dempsey, A Practical Beginner's Guide to Cyclic Voltammetry, Journal of Chemical Education, 95 (2018) 197-206.
- [39] H. Liang, Y. Luo, Y. Li, Y. Song, L. Wang, An Immunosensor Using Electroactive COF as Signal Probe for Electrochemical Detection of Carcinoembryonic Antigen, Analytical Chemistry, 94 (2022) 5352-5358.
- [40] M. Pavithra, S. Muruganand, C. Parthiban, Development of novel paper based electrochemical immunosensor with self-made gold nanoparticle ink and quinone derivate for highly sensitive carcinoembryonic antigen, Sensors and Actuators B: Chemical, 257 (2018) 496-503.
- [41] Q.-L. Wang, H.-F. Cui, X. Song, S.-F. Fan, L.-L. Chen, M.-M. Li, Z.-Y. Li, A label-free and lectin-based sandwich aptasensor for detection of carcinoembryonic antigen, Sensors and Actuators B: Chemical, 260 (2018) 48-54.
- [42] M. Jozghorbani, M. Fathi, S.H. Kazemi, N. Alinejadian, Determination of carcinoembryonic antigen as a tumor marker using a novel graphene-based label-free electrochemical immunosensor, Analytical Biochemistry, 613 (2021) 114017.
- [43] C. Amarasiri, T.B. Nguyen, L.T. Nguyen, V.T. Thu, N.T.M. Thuy, T. Dai Lam, Electrochemical Immunosensor Based on Fe3O4/PANI/AuNP Detecting Interface for Carcinoembryonic Antigen Biomarker, Journal of Electronic Materials, 46 (2017) 5755-5763.
- [44] S. Kumar, M. Umar, A. Saifi, S. Kumar, S. Augustine, S. Srivastava, B.D. Malhotra, Electrochemical paper based cancer biosensor using iron oxide nanoparticles decorated PEDOT:PSS, Analytica Chimica Acta, 1056 (2019) 135-145.
- [45] S. Kumar, S. Kumar, C.M. Pandey, B.D. Malhotra, Conducting paper based sensor for cancer biomarker detection, Journal of Physics: Conference Series, 704 (2016) 012010.
- [46] S. Kumar, A. Sen, S. Kumar, S. Augustine, B.K. Yadav, S. Mishra, B.D. Malhotra, Polyaniline modified flexible conducting paper for cancer detection, Applied Physics Letters, 108 (2016).
- [47] J.L. Chen, X.D. Lv, H. Ma, J.R. Chen, J.A. Huang, Detection of cancer embryo antigen and endothelin-1 in exhaled breath condensate: A novel approach to investigate non-small cell lung cancer, Mol Clin Oncol, 5 (2016) 124-128.
- [48] H. Aref, S. Refaat, CRP evaluation in non-small cell lung cancer, Egyptian Journal of Chest Diseases and Tuberculosis, 63 (2014) 717-722.
- [49] H. Satoh, H. Ishikawa, K. Kurishima, Y.T. Yamashita, M. Ohtsuka, K. Sekizawa, Cut-off levels of NSE to differentiate SCLC from NSCLC, Oncol Rep, 9 (2002) 581-583.
- [50] C. Chen, J.B. Liu, Z.P. Bian, J.D. Xu, H.F. Wu, C.R. Gu, Y. Shi, J.N. Zhang, X.J. Chen, D. Yang, Cardiac troponin I is abnormally expressed in non-small cell lung cancer tissues and human cancer cells, Int J Clin Exp Pathol, 7 (2014) 1314-1324.

## Chapter 5

Construction of Engineered 2D-2D Hybrid Nanocomposite based rGO-integrated hBNNS through Strategic Organic—Inorganic Interfacial Chemistry for High-Performance Electrocatalytic Detection of Carcinoembryonic Antigen.

In this chapter, the concept of nanostructure engineering is introduced to fabricate organic-inorganic hybrid nanocomposites (OIHNs) with strategically tailored surface functionalities, enabling the construction of ultrasensitive nano-biosensing platforms capable of detecting trace-level target analytes to be comprehensively detailed. A synergistically cross-linked nano-biosensor harnessing reduced graphene oxide (rGO)decorated hexagonal boron nitride nanosheets (hBNNS) was developed for highperformance detection of carcinoembryonic antigen (CEA). The controlled in-situ hydrothermal approach was utilized to synthesize rGO-hBNNS hybrid nanocomposite, with extensive spectroscopic and microscopic analyses validating structural integrity, uniform nanosheet distribution and optimal hybridization. Electrophoretic deposition (EPD) technique at a low DC potential of 15 V was employed to fabricate high-quality micro-electrodes on pre-hydrolyzed ITO substrates, ensuring reproducible electrode coverage and enhanced electron-transfer pathways. Imperative fabrication and operational parameters, including antibody incubation time, electrolyte pH, and electrode preparation, were systematically optimized to maximize sensor performance. Electrocatalytic activity of rGO-hBNNS hybrid nanocomposite improved 29% relative to bare hBNNS, thereby highlighting the role of rGO in facilitating accelerated electron transport and enhancing electrochemical performance. Numerous functional moieties emerged on the electroactive sites of the nanocomposite, enabling dense, abundant sitespecific anchoring of Anti-CEA antibodies thereby enhancing binding specificity and sensitivity. The rGO-hBNNS-based nano-biointerface achieved a remarkable detection limit of 5.47 pg/mL with an R<sup>2</sup> value of 0.99963 depicting ~4.1 times enhanced LOD in comparison to hBNNS based immunoelectrodes in operated efficiently across a dynamic range of 0-50 ng/mL. Extensive clinical validations confirmed its prolonged storage stability, high selectivity against potential interferents, and excellent recovery rates in spiked human serum samples, establishing this rGO-hBNNS/ITO platform as a robust, highly sensitive, and clinically applicable tool for early detection and monitoring of CEA in NSCLC diagnostics.

The research findings detailed in this chapter have been published in a scientific journal: "Fabrication of rGO-decorated hBNNS hybrid nanocomposite via organic—inorganic interfacial chemistry for enhanced electrocatalytic detection of carcinoembryonic antigen" Analytical and Bioanalytical Chemistry, 2024 (416) 4789-4805

#### 5.1 Introduction

Two-dimensional (2D) nanomaterials constitute a rapidly advancing class of nanostructures characterized by their unique sheet-like morphology, in which the lateral dimensions typically exceed 100 nm and may extend up to several micrometers or even larger, while maintaining an exceptionally small thickness on the order of a single atomic layer or just a few atoms, generally < 5 nm often referred as ultrathin morphology [1]. This extreme aspect ratio gives rise to exceptional structural and functional attributes, including superior mechanical flexibility, high specific surface area, and tunable electronic band structures. The synergy of these features enables their integration into diverse technological domains such as high-performance nanoelectronics, optoelectronics, biosensing, and heterogeneous catalysis, where their atomic-scale thickness and extended lateral dimensions play a pivotal role in optimizing interfacial interactions and enhancing device performance.

Despite significant variations in their chemical compositions and crystallographic arrangements, nanomaterials can fundamentally be classified into *layered* and *non-layered* structural types [2]. Layered materials exhibit a highly ordered architecture in which atoms within each individual layer are interconnected by strong intralayer bonds typically covalent or ionic—ensuring high structural stability in the plane of the layer. The in-plane architectures of the layered materials are stacked upon each other to form the bulk state based on relatively weak van der Waals forces that contribute to the minimization of the exfoliation energy into laterally large 2D nanostructures. Whereas, the strong intra-layer bonding endows remarkable tensile strength that promotes preservation of their intrinsic atomic structure. This peculiar bonding structure of layered two-dimensional (2D) materials connected together by strong covalent bonds within the intra-layer domain and weak vdW forces in inter-layer space distinguishes them as van der Waals (vdW) materials.

The advent of graphene, exhibiting atomic-scale nanosheets, stimulated global surge into the layered 2D nanomaterials domain, revealing a spectrum of novel physical phenomena absent in conventional materials, establishing them as exceptional platforms for advanced applications. Their inherent structural versatility facilitates the assembly of heterostructures with precise rotational and translational alignments, enabling tuneable band structures owing to layer number and correlation effects induced by flat bands, arising from diverse interlayer coupling mechanisms. The peculiar interlayer coupling interactions, including charge transfer, orbital hybridization, and long-range dipolar interactions positions 2D vdW materials as a transformative platform for advanced device architectures in high-speed electronics, low-power optoelectronics, quantum computation, and nanoscale sensing [3]. Thus, atomically-thin layered two-dimensional (2D) nanomaterials present vast opportunities for engineering high-performance devices capable of meeting modern technological demands.

Within the spectrum of van der Waals layered compounds, hexagonal boron nitride (h-BN), often referred to as "white graphene," distinguishes itself as a structurally lightweight material with graphene-isoelectronic structure. Its atomic arrangement consists of an alternating boron–nitrogen hexagonal sublattice, where atoms are primarily linked by strong covalent bonds with a partial ionic component arising from

the B–N electronegativity difference [4]. This asymmetric electron density distribution imparts significant lattice polarization and an inherently large bandgap in the range of 5–6 eV, positioning h-BN as an electrical insulator with surprisingly robust electroanalytical behaviour. The sp²-hybridized lattice imparts strong chemical inertness and stability against oxidation in ambient environments, additionally sustains exceptional thermal resilience, making h-BN a prime candidate for high-performance nano-electronic, sensing, and protective coating applications.

Hexagonal boron nitride (hBN) exhibits exceptionally high thermal conductivity, making it highly suitable for applications in harsh and high-temperature operational environments. Its inherent wide bandgap confers remarkable chemical inertness, in addition minimizing interference and background noise during signal acquisition, thereby ensuring high precision in real-time sensing applications. However, this same chemical inertness poses a significant limitation for large-scale functionalization, restricting the anchoring of active sites and consequently diminishing the biosensing efficiency [5]. To overcome this limitation, advanced surface modification strategies are essential. These include the decoration of hBN nanosheets with hierarchical nanostructures, which can create abundant electroactive sites, and the formation of nano-hybrid composites that integrate hBN with conductive or catalytically active nanomaterials. Such engineered interfaces can substantially enhance charge transfer kinetics, increase biomolecule immobilization density, and ultimately elevate the sensitivity, selectivity, and operational stability of hBN-based nano-biosensors.

Emergence of nano-engineering innovations has significantly advanced bio-analytical device fabrication by enabling defect induction, tailored functionalization, controlled morphological structuring, and the development of hybrid nanocomposites [6]. While, engineered nanostructures obtained through structural, morphological, and defect engineering offer powerful avenues for enhancing the functional attributes of nanomaterials, yet face persistent challenges under ambient operating conditions, where they are prone to instability, progressive degradation, and surface transformations that compromise their designed functionalities.

Achieving the required level of structural precision with controlled layer thickness, defect density, and particle alignment demands complex fabrication methodologies that are not only labour-intensive but also sensitive to minor variations in process parameters. This complexity often translates into high production costs and limits scalability. Furthermore, maintaining the engineered properties over prolonged operational periods is difficult, particularly when exposed to fluctuating environmental factors like humidity, temperature, and chemical contaminants. Another significant constraint is the potential compromise in chemical and biological compatibility, as surface modifications and defect manipulations may inadvertently introduce reactive sites or impurities that disrupt interactions with biological systems or chemically sensitive environments. These limitations necessitate the development of robust modification strategies and hybrid material architectures that integrate stability enhancement, simplified fabrication routes, and compatibility optimization to fully exploit the potential of nanomaterials in sensing, catalysis, energy storage, and biomedical applications [7].

Synergistically integrated organic-inorganic hybrid nanocomposites (OIHNs), strategically constructed through functionalization and guided by host-guest chemistry principles in biphasic nano-confined matrices, offer a highly efficient pathway to transcend the individual drawbacks of organic and inorganic components [8, 9]. The organic phase provides structural adaptability, low density, and processability, yet is often constrained by fragility, thermal instability, and chemical reactivity under elevated temperatures [10]. The inorganic phase contributes exceptional mechanical robustness, chemical inertness, and thermal endurance, but its inherent limitations include minimal surface functionality, restricted catalytic efficiency, and the need for energy-intensive or intricate synthesis protocols [11]. Through deliberate nanoscale interfacial engineering, OIHNs achieve an optimized combination of strength, stability, and multifunctional performance. This architecture enhances electrical and optical tunability, supports the introduction of targeted functional groups, and enables controlled porosity for improved mass transport. Importantly, the hybrid structure promotes synergistic effects where the organic phase modulates flexibility and functional diversity, while the inorganic phase anchors stability and durability [12]. This synergy extends to catalysis, where enhanced electron transfer pathways and interfacial active sites dramatically improve catalytic turnover rates. By uniting these attributes, OIHNs emerge as a versatile material platform capable of meeting the complex demands of next-generation applications.

Two-dimensional (2D) nanomaterials represent a highly promising class of materials, uniquely positioned to address advanced biosensing and catalytic challenges due to their combination of structural adaptability and physicochemical versatility. Their abundant surface-active sites enable efficient immobilization of biomolecules, while their exceptional catalytic efficiency and tunable electronic properties—particularly bandgap modulation—allow precise optimization for targeted applications. In the context of Organic-Inorganic Hybrid Nanostructures (OIHN), layered van der waals (vdW) materials are particularly valuable as scalable sources for obtaining 2D morphologies. Organic-layered nanostructures, such as reduced graphene oxide (rGO) [13], exhibit an exceptionally high aspect ratio, providing vast surface adsorption areas and a semiconducting bandgap that not only enhances electrocatalytic activity but also facilitates controlled charge transfer. The high defect density in rGO introduces additional active sites, significantly boosting bio-catalytic efficiency. In contrast, inorganic layered nanomaterials such as hexagonal boron nitride (hBN)—often referred to as "inorganic graphite"—offer complementary advantages. hBN possesses lattice parameters closely matching those of rGO, thereby minimizing strain-induced deformation in hybrid composites [14]. Furthermore, it exhibits outstanding mechanical strength, superior thermal and chemical stability, and resistance to environmental degradation, ensuring reliability under diverse operational conditions. These complementary attributes of rGO and hBN make them ideal building blocks for hybrid nanocomposite systems, where the organic component contributes exceptional electrochemical responsiveness and the inorganic counterpart imparts structural robustness, long-term stability, and resistance to harsh environments. Within organic nanomaterials, reduced graphene oxide (rGO) possesses a distinctive electronic arrangement, where electrons are uniformly delocalized across all carbon atoms, generating an extensive network of redox-active sites. This intrinsic abundance of redox centers enhances electron transfer kinetics, making rGO highly advantageous for

integration into OIHN-based nano-biosensors. Conversely, in hexagonal boron nitride (hBN), electron density shifts preferentially toward nitrogen atoms due to their high electronegativity, consequently leaving boron atoms with vacant p-orbitals, a property that imparts unique electronic and catalytic behavior when coupled with conductive nanomaterials[15].

The tailored electronic structure inherent in rGO and hBNNS creates a unique chemical architecture for engineering high-strength interfacial bonds, resulting in a remarkably resilient crosslinking chemistry. This engineered interfacial synergy promotes the creation of a superior hybrid nanocomposite wherein the distinct electronic and structural properties of each component are optimally harnessed. The resulting crosslinked interface is richly decorated with multifunctional adsorption sites, which play a pivotal role in facilitating strong, specific, and stable conjugation with biomolecules and bioconjugates. Compared to conventional immobilization strategies—such as entrapment, physical adsorption, covalent binding without interfacial optimization, or sandwich incubation—the crosslinking approach decisively mitigates inherent drawbacks, including elevated diffusion barriers, instability in protein interactions, restricted conformational flexibility essential for catalytic function, low protein adsorption efficiency, and diminished electron transfer kinetics. By contrast, interfacial crosslinking actively enhances surface functionalization, ensuring efficient bridging between linker molecules and adjacent protein biomarkers. Through selective surface functionalization, crosslinking preserves robust connections between linking agents and protein biomarkers while enhancing protein bioactivity, allows for recyclability without significant loss of catalytic efficiency, maintains a highly ordered protein conformation aligned for optimal electron transport, and delivers an economical, scalable technique adaptable to a range of biosensing platforms. The strategic application of crosslinking thus ensures a high-performance nanointerface capable of long-term stability and consistent analytical performance in complex biological environments.

The strategic engineering of interfacial kinetics in organic–inorganic hybrid nanocomposites (OIHNs) exerts a decisive influence on charge transfer dynamics. Interphase interactions are broadly categorized into Class I and Class II, where Class I encompasses weak bonds—such as van der Waals forces, hydrogen bonding, and hydrophobic–hydrophilic interactions—while Class II comprises strong covalent or iono-covalent bonds [16]. This classification governs molecular dynamics and ultimately dictates sensing performance. Class II OIHNs, formed through robust bonding chemistry between constituent materials, exhibit superior structural stability, precise modulation of physicochemical properties, enhanced interfacial charge transfer through efficient crosslinking, and the incorporation of multifunctional groups that substantially improve protein biomarker immobilization.

Despite their potential, the synthesis of such nanocomposites remains challenging due to inherent limitations of conventional methods such as scalability issues, procedural complexity, and the requirement for elevated reaction temperatures [17]. Addressing these constraints, the present study adopted a one-pot hydrothermal synthesis route capable of concurrently reducing graphene oxide (GO), exfoliating hexagonal boron nitride nanosheets (hBNNS), and reinforcing rGO–hBNNS interfacial crosslinking. This process, conducted under high pressure at relatively low temperatures, mitigates

agglomeration, prevents layer restacking, and maintains nanosheet integrity. Through optimized hydrothermal parameters and selective reducing agents, simultaneous reduction of substantially reactive GO nanosheets alongside precise bond tailoring, yielding a structurally stable rGO-hBNNS hybrid nanocomposite with enhanced electrochemical performance was achieved.

The present work harnesses the inherent synergy of organic–inorganic hybrid nanomaterial (OIHN) interfacial chemistry to fabricate, via a hydrothermal route, an rGO–hBNNS hybrid nanocomposite with superior electrocatalytic efficiency for the label-free detection of CEA biomarkers. Functional amine and carboxyl terminal groups on the rGO-decorated hBNNS nano-matrix serve as effective anchoring sites for monoclonal Anti-CEA Fc receptors through EDC–NHS-mediated crosslinking, thereby replacing conventional, expensive, and complex labeling procedures. Through tailored optimization of the immuno-interface microenvironment, the binding interactions between Anti-CEA and the rGO–hBNNS nano-matrix are significantly enhanced, yielding amplified electrochemical responses and high detection sensitivity. This architecture enables precise Anti-CEA–CEA recognition with a detection limit as low as 5.47 pg/mL. Demonstrating excellent selectivity, stability, reproducibility, and reliability in spiked serum analysis, the rGO–hBNNS hybrid nano-biosensor meets the operational and regulatory requirements of clinical diagnostic platforms.

#### **5.2** Experimental Section:

#### 5.2.1 Chemical, Reagents and Instrumentation:

The study utilized high-purity analytical-grade chemicals and reagents to ensure maximum precision, reliability and reproducibility. Materials procured from Sigma-Aldrich included graphite powder (< 20 μm), bovine serum albumin (BSA), hexagonal boron nitride (h-BN) powder (98%, 5 µm), 1-(3-(dimethylamino)propyl)-3ethylcarbodiimide hydrochloride (EDC), carcinoembryonic antigen (CEA), Nhydroxysuccinimide (NHS), and monoclonal anti-CEA antibodies. From Thermo-Fisher Scientific and Merck provided potassium permanganate (KMnO<sub>4</sub>), sulfuric acid (H<sub>2</sub>SO<sub>4</sub>), hydrazine hydrate (N<sub>2</sub>H<sub>4</sub>·H<sub>2</sub>O, >99%), isopropanol ((CH<sub>3</sub>)<sub>2</sub>CHOH), hydrogen peroxide (30% w/v H<sub>2</sub>O<sub>2</sub>), potassium ferrocyanide (K<sub>4</sub>[Fe(CN)<sub>6</sub>]·3H<sub>2</sub>O), acetonitrile (CH<sub>3</sub>CN), hydrochloric acid (HCl), sodium phosphate monobasic dihydrate (NaH<sub>2</sub>PO<sub>4</sub>·2H<sub>2</sub>O), ethanol (C<sub>2</sub>H<sub>5</sub>OH), potassium ferricyanide (K<sub>3</sub>[Fe(CN)<sub>6</sub>]), and sodium phosphate dibasic dihydrate (Na<sub>2</sub>HPO<sub>4</sub>·2H<sub>2</sub>O). Ultrapure Milli-Q water was employed for all solution preparation and washing procedures. Fresh Phosphate buffer saline (PBS) buffers of different pH values were prepared by mixing solution A (NaH<sub>2</sub>PO<sub>4</sub>·2H<sub>2</sub>O) with solution B (Na<sub>2</sub>HPO<sub>4</sub>·2H<sub>2</sub>O) in Milli-Q water and stored at 4 °C until further use. Human serum samples were obtained from AIIMS, New Delhi, following ethical approval.

Multiple complementary analytical techniques were employed to systematically characterize the hBNNS, GO, and rGO-hBNNS powder samples. Phase purity and crystallographic structure were examined using X-ray diffraction (XRD, Bruker Advance D-8), enabling identification of interlayer spacing, crystal defects, and any phase transformations induced during synthesis. Surface morphology and microstructural features were visualized via scanning electron microscopy (SEM, EVO18 Zeiss), while layer thickness, exfoliation quality, and nanoscale structural

integrity were investigated using high-resolution transmission electron microscopy (TEM, TECNAI, 200 kV). Elemental composition and spatial distribution were determined using energy-dispersive X-ray spectroscopy (EDX), while chemical bonding, functional group incorporation, and defect-related vibrations were probed by Fourier transform infrared spectroscopy (FTIR, Spectrum II-Perkin Elmer). Vibrational and phonon-related properties, along with structural strain and defect density, were analyzed through Raman spectroscopy (WITec,  $\lambda = 532$  nm). Optical absorption characteristics and possible bandgap modifications were evaluated via UVvisible spectroscopy (Perkin Elmer 950). Electrochemical properties were examined using an Autolab Galvanostat/Potentiostat (Metrohm, Netherlands), performing differential pulse voltammetry (DPV) and cyclic voltammetry (CV) to assess charge transfer kinetics and sensor response. The electrochemical setup consisted of an rGOhBNNS-modified ITO working electrode, a platinum rod counter electrode, and an Ag/AgCl reference electrode (in 3 M KCl). All biosensing studies were conducted in a ferro-/ferricyanide ([Fe(CN)<sub>6</sub>]<sup>3-/4-</sup>, 5 mM) redox couple in phosphate-buffered saline (PBS, 50 mM, 0.9% NaCl, pH 7.0), chosen for its well-defined one-electron heterogeneous transfer characteristics.

### 5.2.2 Sustainable and Efficient Synthesis of Graphene Oxide Using Modified Hummer's Approach

The eco-friendly synthesis of graphene oxide (GO) was conducted by oxidizing natural graphite powder through a modified Hummer's method (Fig. 5.1), incorporating slight adjustments to enhance covalent functionalization on the exfoliated GO nanosheets, thereby improving their reactivity and compatibility for advanced applications. Firstly, the process of pre-oxidizing 3 grams of analytical-grade natural graphite with 70 mL of sulfuric acid (H2SO4) and 9 grams of potassium permanganate (KMnO4), which serves as a strong oxidant to intercalate and expand the graphite layers for effective oxidation. Upon adding KMnO4, a temperature increase to 40°C was observed due to the exothermic reaction, necessitating careful control to avoid uncontrolled heat buildup. The mixture was then subjected to controlled and gentle stirring at <300 RPM for 30 mins, ensuring uniform dispersion of graphite with the chemicals while preventing potential exothermic ignition from reactive interactions, thus prioritizing safety and homogeneity. After the temperature stabilization post-stirring, 150 mL of deionized (DI) water was introduced slowly to the uniform dispersion under constant stirring for 15 minutes, maintaining the hot plate at 95°C to facilitate controlled dilution and further oxidation, while mitigating risks of sudden explosive boiling. Further, 500 mL of DI water was added, followed by 15 mL of 30% hydrogen peroxide (H2O2), which terminated the oxidation reaction and reduced excess KMnO4, resulting in a color change from dark brown to yellow that indicates successful formation of GO. In the subsequent step, 250 mL was incorporated into a solution comprising HCl and DI water in a 1:10 ratio under stirring for 2 hours, effectively removing metal ions to streamline filtration and enhance the electrochemical activity of the final product by eliminating catalytic residues that could impede performance. After completion of the reaction, the mixture was allowed to settle overnight, enabling gravitational separation of oxidized graphite particles from the supernatant for easier isolation. Next, the decantation of the remaining solvents and washing the settled particles with DI water was carried out until achieving a neutral pH of 7.0, thoroughly purifying the GO to remove acidic residues and impurities that might affect stability and functionality. Finally, the resultant sample

was dried in a vacuum oven at 65°C for 24 hours, evaporating residual moisture to yield GO nanosheets with high colloidal stability and abundant surface functionalities ready for storage or further use.

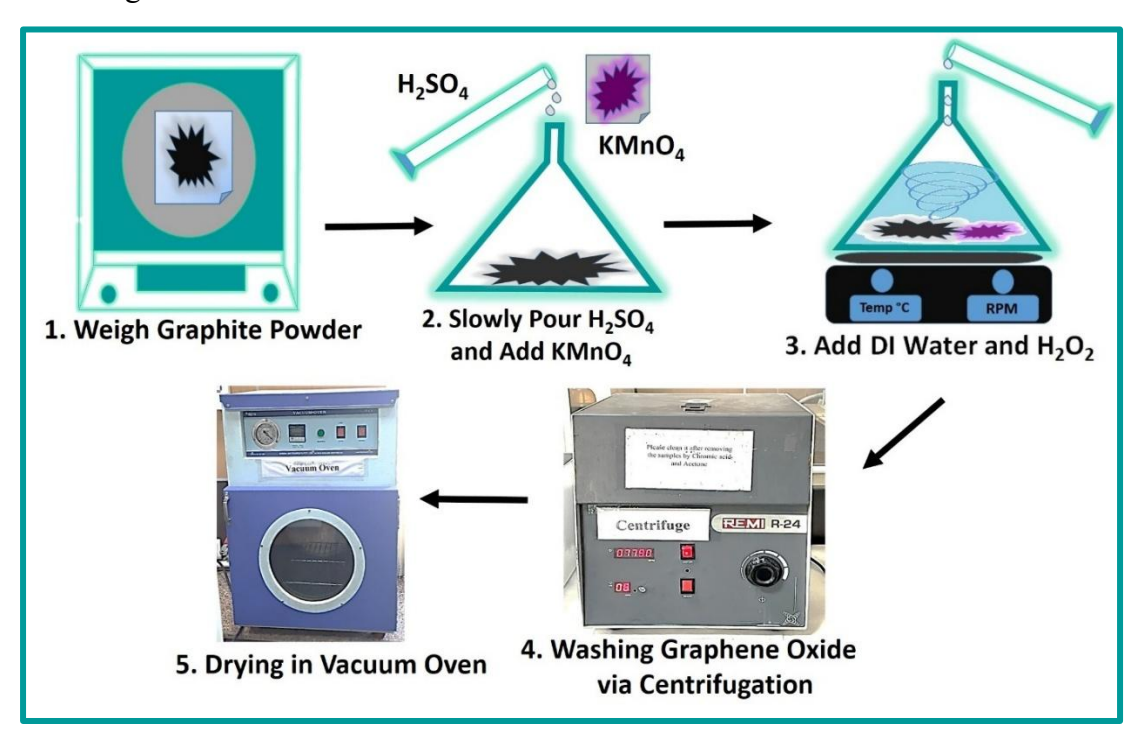


Figure 5.1: Diagram illustrating the eco-friendly modified Hummer's route for the synthesis of graphene oxide (GO) from natural graphite powder

### **5.2.3** Facile One-Pot Hydrothermal Route for Producing rGO-hBNNS Hybrid Nanocomposites with Enhanced Interfacial Integration

Ultrathin multifunctional hexagonal boron nitride nanosheets (hBNNS) were synthesized via a facile hydrothermal route, following previously reported methodology [21]. Unlike bulk hBN, which exhibits poor dispersibility and exfoliation due to its partially ionic B-N bonds—thereby limiting interfacial interactions with other precursors, hBNNS were selected for nanocomposite fabrication to enhance dispersion and reactivity. In the initial step, 122 mg of hBNNS powder was dispersed in 10 mL deionized (DI) water, while 90 mg of graphene oxide (GO), synthesized via an ecofriendly improved Hummers' method, as illustrated in Fig. 5.2, was separately dispersed in 10 mL DI water. Both dispersions underwent ultrasonication-assisted pretreatment for 1 h at room temperature, which promoted hydroxyl ion intercalation, thereby expanding the interlayer spacing while preserving the intrinsic crystalline framework. GO readily dispersed due to its hydrophilic nature, imparted by covalently bound oxygen-containing groups, ensuring high colloidal stability ensuring a homogeneous base for integration. The well-dispersed GO suspension was combined with the hBNNS dispersion, followed by ultrasonication step for 1 h to strengthen precursor-precursor intercalation and interface reinforcement. Subsequently, 1 mL hydrazine hydrate and 15 mL DI water were introduced as the reducing system, enabling conversion of GO to rGO while maintaining uniform dispersion.

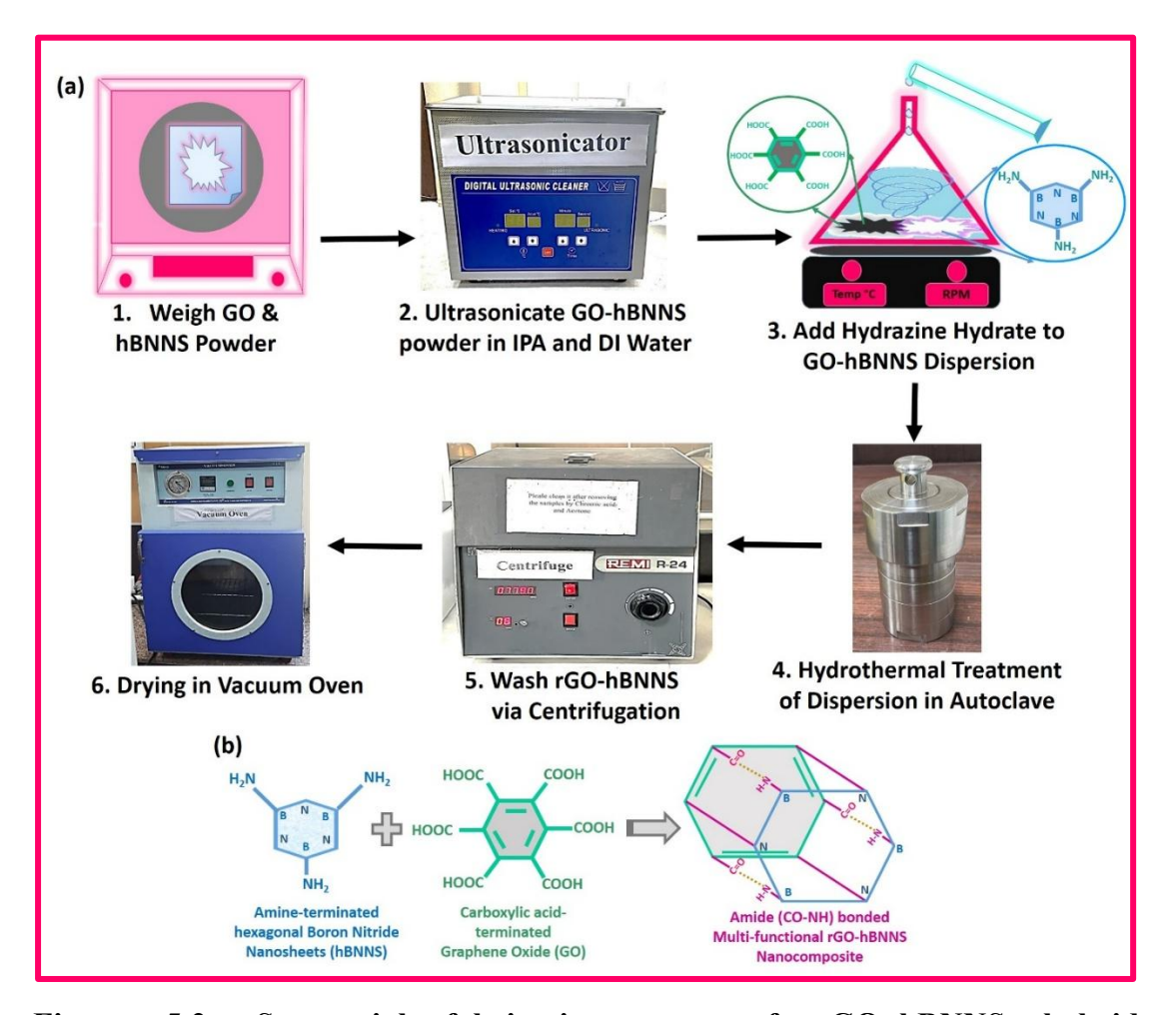


Figure 5.2: Sequential fabrication steps of rGO-hBNNS hybrid nanocomposite via one-pot hydrothermal synthesis route. and Schematic representation interfacial chemistry driving rGO-hBNNS Nanocomposite formation

The mixture was stirred at 270 rpm for 6 h at room temperature to ensure complete reduction and homogeneous distribution. The resulting dispersion was transferred into a 50 mL Teflon liner, sealed within a stainless-steel autoclave, and subjected to hydrothermal treatment at 180 °C for 12 h, facilitating chemical reduction, nanosheet interlocking, and hybrid nanocomposite growth. The presence of electron-deficient boron sites (Lewis acid) on hBNNS, capped with amine groups (Lewis bases), established strong bonding affinity toward electrophilic GO nanosheets, driving the formation of the rGO-hBNNS hybrid. The obtained nanocomposite was washed repeatedly with DI water through centrifugation at 7000 rpm until the supernatant reached pH 7.0, ensuring removal of ionic impurities. Finally, the product was vacuum-dried at 85 °C for 24 h to yield the rGO-hBNNS hybrid nanocomposite.

## 5.2.3 Fabrication of Functionalized rGO-hBNNS/ITO Immunoelectrodes via Controlled Electrophoretic Deposition (EPD) and Nano-interface Engineering enabled Covalent Antibody Immobilization

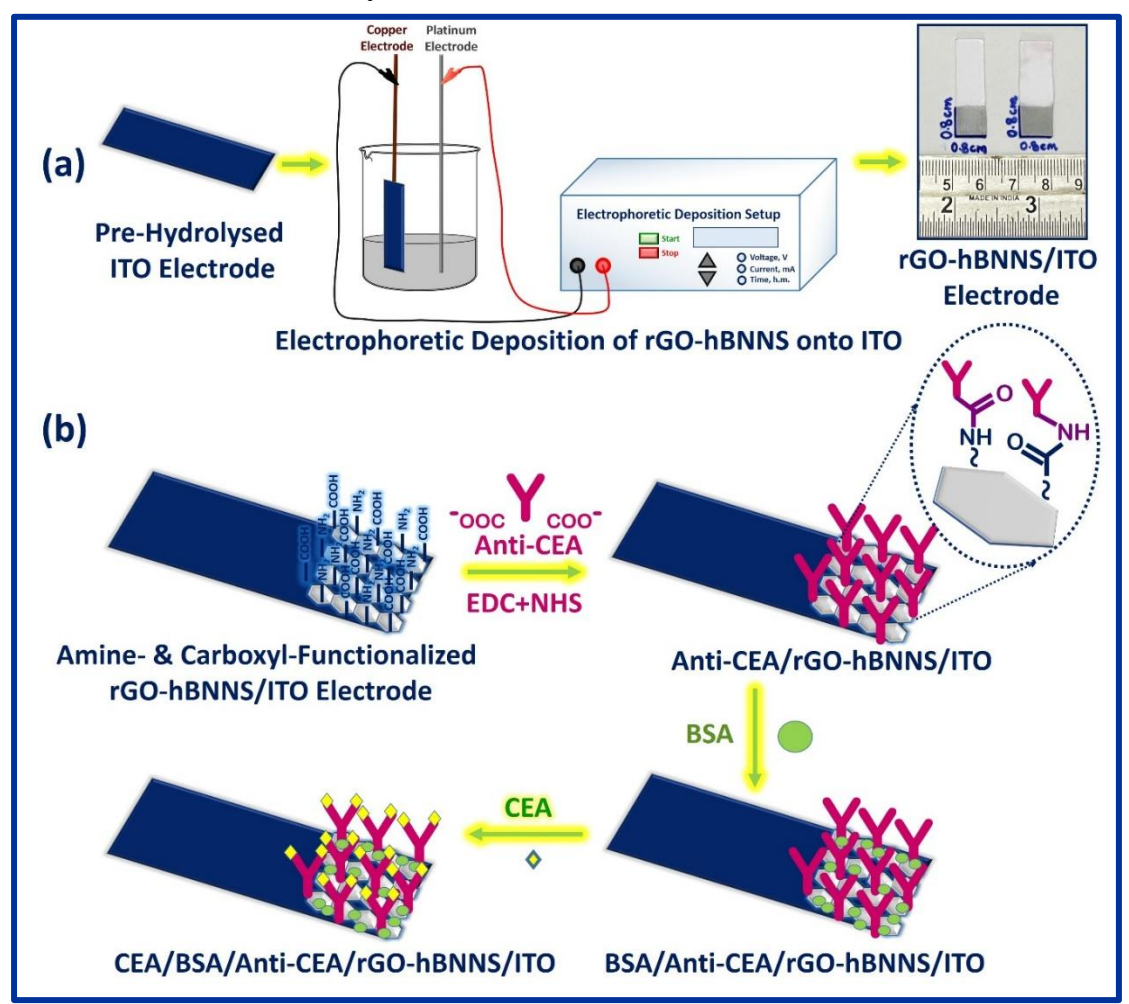


Figure 5.3: Diagrammatic representation of (a) electrophoretic fabrication of rGO-hBNNS-coated ITO electrode, and (b) stepwise biointerface engineering using Anti-CEA immobilization, BSA passivation, and CEA conjugation to produce the nano-biosensing interface.

The rGO-hBNNS/ITO electrodes were fabricated using the electrophoretic deposition (EPD) technique, which leverages the combined effects of colloidal dispersion stability and voltage-driven particle migration to achieve a uniform coating (**Fig. 5.3(a)**). A stable colloidal suspension of 0.25 mg/mL rGO-hBNNS in acetonitrile (CH<sub>3</sub>CN) was prepared by adding 300 μL of magnesium nitrate (Mg(NO<sub>3</sub>)<sub>2</sub>, 1 mg/mL). Magnesium nitrate [Mg(NO<sub>3</sub>)<sub>2</sub>] acts as a dual-function additive, serving both as a surface charge modulator and electrolytic conductivity promoter. Upon dissolution in acetonitrile, it releases Mg<sup>2+</sup> and NO<sub>3</sub><sup>-</sup> ions, increasing the ionic strength of the acetonitrile suspension and imparting a positive surface charge to rGO-hBNNS particles by cation adsorption. This promotes stable dispersion, prevents agglomeration, and enables uniform particle migration under the electric field, resulting in a compact, well-adhered coating on the ITO substrate. The suspension was ultrasonicated for 1 h to ensure uniform particle distribution and prevent premature aggregation and enhance suspension homogeneity.

This well-dispersed suspension was transferred into a two-electrode cell, consisting of pre-hydrolyzed ITO ( $0.8~\rm cm \times 2.5~cm$ ) as the working electrode (positive terminal) and a platinum rod as the counter electrode (negative terminal). Prior to deposition, ITO substrates were hydrolyzed in a 1:1:5 mixture of hydrogen peroxide, ammonia, and DI water, activating surface radical groups to enhance film adhesion and binding affinity of the nanocomposite layer. A homogeneous rGO-hBNNS film ( $0.8~\rm cm \times 0.8~cm$ ) was deposited at 15 V DC for 1 min, yielding a uniform conductive layer.

Figure 5.4: Depiction of molecular interactions involving amide bond formation: (a) L-glutamic acid with amine-functional hBNNS, (b) L-lysine with epoxide-functional rGO, and (c) L-lysine with carboxyl-functional rGO. The nano-biosensor platform was engineered by covalently anchoring monoclonal Anti-CEA onto rGO-hBNNS-modified ITO surfaces using EDC-NHS chemistry (Fig. 5.3(b)). Firstly, monoclonal Anti-CEA stock solution was prepared in PBS buffer (pH 7.4) by activating its -COOH and -NH₂ groups via carbodiimide-based EDC-NHS chemistry (Fig. 5.3(b)) [18]. Specifically, Anti-CEA (50 μg/mL) was reacted with EDC (0.2 M) and NHS (0.05 M) in a 2:1:1 molar ratio at room temperature for 30 min. EDC, acting as a zero-length crosslinker, covalently activated the carboxyl-terminated Fc region (L-glutamic acid) of Anti-CEA to form an unstable O-acylisourea ester, which was stabilized into an amine-reactive NHS ester [19]. This intermediate efficiently

crosslinked the Fc region to amine-terminated hBNNS interfaces, producing robust amide bonds (**Fig. 5.4(a)**). Additionally, lysine residues on Anti-CEA provided sidechain amino groups that conjugated with C–O–C and –COOH groups on rGO surfaces through the same EDC–NHS mechanism (**Fig. 5.4(b–c)**) [20]. Subsequently, 20  $\mu$ L of Anti-CEA was immobilized onto the rGO–hBNNS film for 24 h in a controlled humid chamber, ensuring uniform antibody orientation and high binding affinity. BSA (10  $\mu$ L, 1% w/w) was then applied to passivate unbound active sites, reducing nonspecific adsorption. Finally, CEA antigen (10  $\mu$ L) was incubated for 30 min, enabling specific antigen–antibody interaction. The resulting immunoelectrodes were stored at 4 °C to preserve biological activity.

#### 5.3 Experimental Results & Analysis:

#### 5.3.1 Analytical Nanomaterial Characterizations:

### 5.3.1.1 Comprehensive Crystallographic Characterization of rGO-hBNNS Hybrid Nanocomposite Using X -Ray Diffraction (XRD) Analysis:

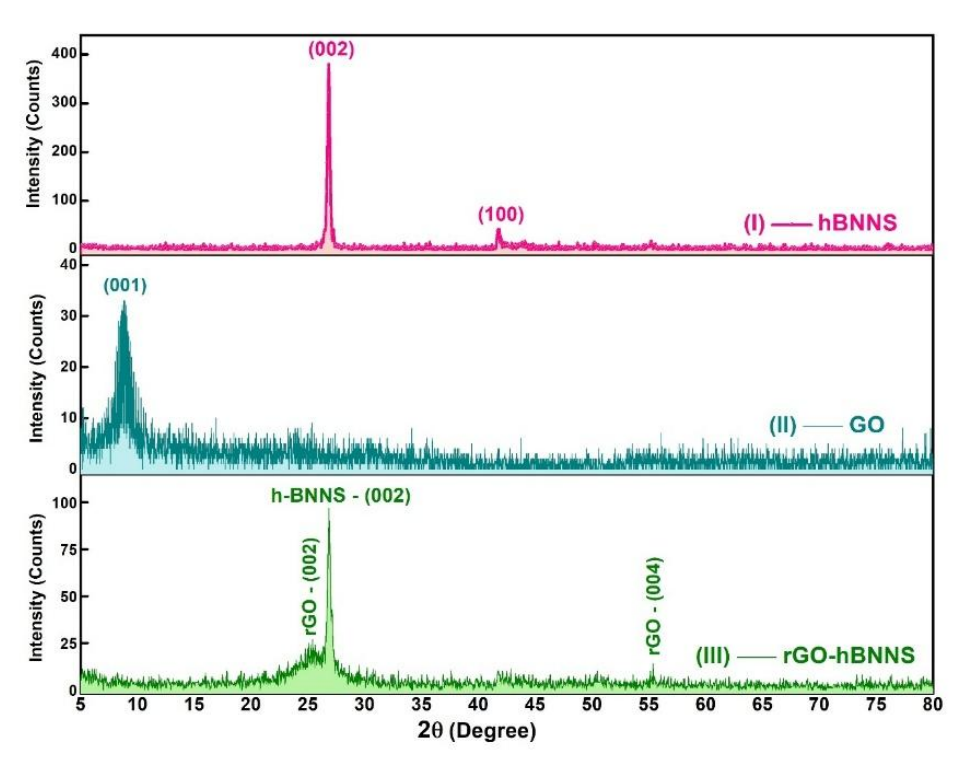


Figure 5.5: Powder X-ray diffraction patterns of (I) hBNNS, (II) GO, and (III) rGO-hBNNS nanocomposite obtained across the  $2\theta$  range of  $5^{\circ}-80^{\circ}$ , demonstrating key crystallographic attributes.

A comprehensive XRD analysis was performed across a  $2\theta$  range of  $5^{\circ}$ – $80^{\circ}$  to systematically evaluate the phase formation, phase purity, and crystallinity of three materials: (I) hBNNS, (II) GO, and (III) rGO-hBNNS nanocomposite, as illustrated in **Fig. 5.5(a)**. This analytical approach scanning wide  $2\theta$  range ensures accurate identification of characteristic peaks, all relevant Bragg reflection, and verifies the structural homogeneity of each sample. The optimized hydrothermal synthesis conditions, combined with the effective intercalation–exfoliation mediated by isopropanol (IPA) and hydrazine hydrate, facilitated the synthesis of high-purity

hexagonal boron nitride nanosheets (hBNNS). This structural integrity was confirmed by two sharp and well-defined diffraction peaks observed at 26.84° and 41.72° in **Fig. 5.5(a)-(I)**, which correspond to the (002) and (100) crystallographic planes of hexagonal BN, respectively. The match with reference data [**JCPDS Card No. 034–0421**] provides conclusive evidence of phase purity and the absence of crystallographic distortions [21].

The XRD pattern of GO, presented in Fig. 5.5(a)-(II), displays a distinct, intense, and broad diffraction peak positioned at  $2\theta = 8.8^{\circ}$ , markedly down-shifted to a lower angle compared to pristine graphite. This peak corresponds to the (001) crystallographic plane (**Table 5.1**) and is a strong indicator of extensive oxidation of bulk graphite powder. Such oxidation was achieved through the action of aggressive chemical precursors, specifically KMnO<sub>4</sub> and H<sub>2</sub>SO<sub>4</sub>, which facilitated deep structural transformation [22]. The observed down-shift in diffraction angle, combined with a significantly enlarged interlayer spacing of d(001) = 1.004 nm calculated via Bragg's Equation. (Eq. [5.1]), confirms the intercalation of oxygen-rich functional groups—hydroxyl, carboxyl, carbonyl, and epoxy—into the graphite layers. This intercalation not only disrupted the  $\pi$ -bonded planar stacking but also enabled efficient exfoliation, thereby enhancing GO oxidation. FT-IR analysis corroborates the presence of these oxygen functionalities. For the rGO-hBNNS nanocomposite, the XRD pattern in Fig. 5.5(a)-(III) reveals a dominant peak at 26.84°, indexed to the (002) plane of hBNNS, alongside two weaker peaks at 25.4° and 55.3°, corresponding to the (002) and (004) planes of rGO. These results imply that hydrothermal synthesis favored the growth of rGO with relatively poor crystallinity on the surface of highly crystalline hBNNS nanostructures.

Bragg's Relation: 
$$2d \times Sin\theta = n\lambda$$
 [5.1]

According to Bragg's principle, d denotes the interplanar spacing in nanometers, revealing the scale of periodicity within the crystal structure. The angle  $\theta$  (in radians) corresponds to the Bragg diffraction angle at which coherent scattering produces a measurable peak. The integer n designates the diffraction order, identifying the number of whole wavelengths accommodated in the path difference between scattered waves. The term  $\lambda$  signifies the wavelength of the incident beam, whether electron or X-ray which fundamentally determines the spatial resolution achievable in diffraction analysis.

Table 5.1: Intense diffraction peaks, corresponding *hkl* planes, peak positions, full width at half maximum (FWHM), calculated crystallite sizes, and interplanar spacings for hBNNS, GO, and rGO-hBNNS nanocomposite samples.

S.No.	Sample		Intense (hkl) Planes	Peak Position, 2θ (°)	FWHM (°)	Crystallite Size (D, nm)	d-spacing (nm)
1.	Hexagonal Boron Nitride Nanosheets, hBNNS		(002)	26.84	0.2392	34.171	0.332
2.	Graphene Oxide, GO		(100)	8.8	1.205	6.616	1.004
3.	rGO-hBNNS	hBNNS	(002)	26.84	0.3187	25.640	0.332
	Nanocomposite	rGO	(002)	25.4	1.089	7.483	0.350

The XRD analysis revealed the emergence of two distinct diffraction planes in reduced graphene oxide (rGO) alongside a pronounced reduction in interplanar spacing during the hydrothermal conversion of graphene oxide (GO) into rGO. Specifically, the dspacing decreased from 1.004 nm for the (100) plane in GO to 0.350 nm for the (002) plane in rGO, reflecting the re-establishment of the graphitic framework and a higher degree of  $\pi$ - $\pi$  stacking. This transition signifies a disordered stacking of layered nanostructures, a characteristic outcome of restoring sp<sup>2</sup> domains in rGO after chemical reduction. In the rGO-hBNNS hybrid nanocomposite, the hexagonal boron nitride nanosheets (hBNNS) displayed a highly crystalline morphology, predominantly aligned along the (002) plane, with complete suppression of the (100) plane, indicating preferential layer-by-layer stacking. Furthermore, in situ hydrothermal intercalation, nucleation, and growth of rGO nanosheets promoted a stronger quantum confinement effect, as evidenced by a substantial reduction in crystallite size, from 34.17 nm in pure hBNNS to 25.64 nm in the nanocomposite, while preserving the intrinsic d-spacing of hBNNS. These nanoscale refinements indicate the formation of ultra-thin hBNNS flakes with fewer layers within the composite matrix. In contrast, the crystallite size (Eq. [5.2]) of rGO increased from 6.616 nm in GO to 7.483 nm in the nanocomposite, which is attributed to enhanced stacking in rGO's crystallographic planes to reconcile the d-spacing mismatch between rGO and hBNNS, thereby achieving a stable nanoconfined architecture, as depicted in Table 5.1.

Debye-Scherrer's Formula: 
$$D = \frac{0.9 \lambda}{\beta \times Cos\theta}$$
 [5.2]

In the Debye–Scherrer Equation, D represents the average crystallite size (nm),  $\lambda$  is the wavelength of incident X-rays (nm),  $\beta$  corresponds to the full-width at half-maximum of the diffraction peak (radians), and  $\theta$  is the associated Bragg diffraction angle (radians). This quantitative relationship allows precise determination of nanoscale structural dimensions based on X-ray diffraction data. The measured interplanar spacing for rGO at the (002) plane was 0.350 nm, which exactly matched the d-spacing value for crystalline graphite, signifying a successful restoration of extended sp²-hybridized graphitic domains in the basal planes following reduction [22]. This structural reinstatement further implies that residual oxygen-containing functional groups, particularly hydroxyl and carboxyl moieties, preferentially adsorb onto the surface of rGO sheets rather than embedding within the interlayer galleries, preserving the compact stacking of graphene layers while maintaining hydrophilic character for improved dispersibility.

# 5.3.1.2 Integrated High-Resolution Electron Microscopy and EDAX-Based Elemental Investigation for Detailed Morphological and Compositional Analysis of rGO-hBNNS Hybrid Nanocomposite

The detailed micro- and nano-scale structural characteristics, together with elemental composition, of the as-synthesized (I) hBNNS, (II) GO, and (III) rGO-hBNNS hybrid nanocomposite were thoroughly examined via scanning electron microscopy (SEM), transmission electron microscopy (TEM), and energy-dispersive X-ray analysis (EDAX), as illustrated in Fig. 5.6(a)–(c). The SEM micrograph in Fig. 5.6(a-I) reveals densely nucleated, enlarged, and highly ordered flaky nanosheets of hexagonal boron nitride nanosheets (hBNNS), signifying efficient nucleation, with a high degree of planar uniformity and lateral growth during synthesis, reflecting effective exfoliation

from bulk h-BN. In contrast, the GO surface morphology in **Fig. 5.6(a-II)** exhibits pronounced corrugated edges and stacked sheet-like formations, a direct consequence of the "extensive peeling" of bulk graphite powder through oxidative exfoliation. These curled and folded sheet edges point to the inherent flexibility and disruption of sp² domains by oxygen functional groups onto GO nanosheets, which is crucial for hybrid composite integration. The rGO-hBNNS nanocomposite in **Fig. 5.6(a-III)** exhibits a heterogeneous contrast pattern dark, wavy, wrinkled rGO nanosheets intertwined with lighter, sleek, disc-shaped hBNNS. This arrangement reflects a thermodynamically driven aggregation aimed at reducing overall surface energy by passivating dangling surface bonds.

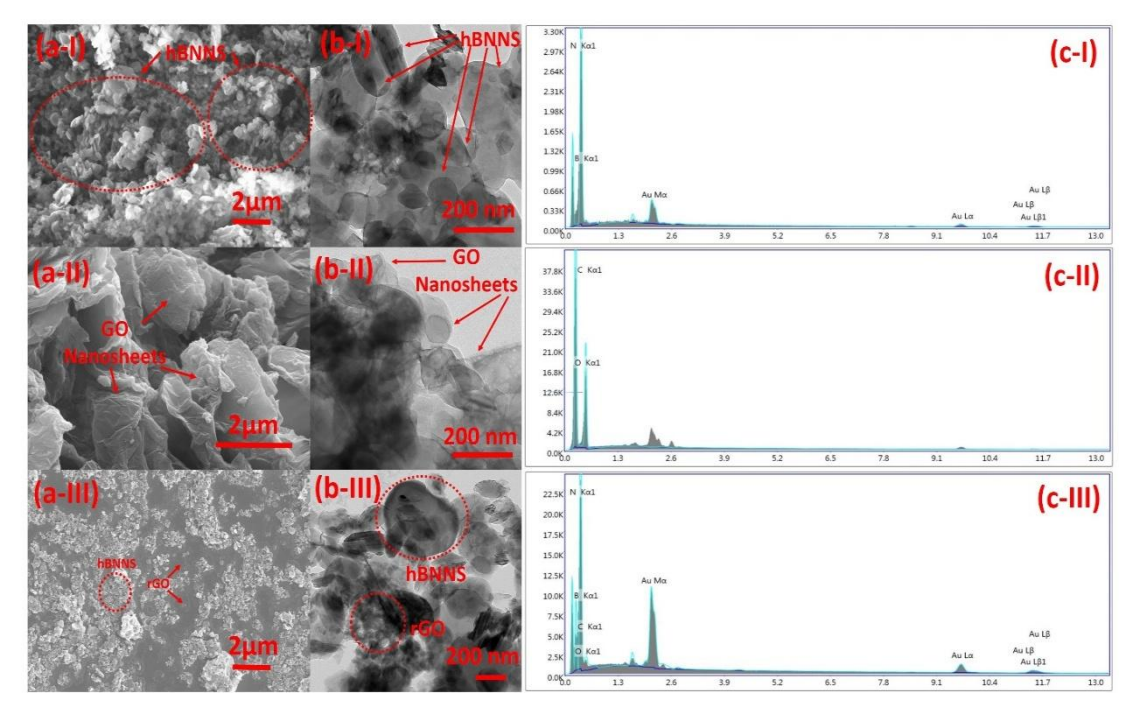


Figure 5.6: Morphological and elemental characterization conducted using (a) Scanning electron microscopy (SEM) images at 2  $\mu$ m resolution capturing surface topography, (b) transmission electron microscopy (TEM) images at 200 nm resolution detailing nanoscale morphology, and (c) energy-dispersive X-ray analysis (EDAX) spectra highlighting elemental composition, presented for (I) hBNNS, (II) GO, and (III) rGO-hBNNS nanocomposite

High-resolution TEM imaging provided detailed insight into the nanoscale architecture of the materials, as shown in **Fig. 5.6(b-I)**, where hBNNS appears as highly transparent, circular nanosheets with exceptionally low thickness, affirming the successful synthesis of ultrathin two-dimensional layers with minimal stacking. **Fig. 5.6(b-II)** presents GO nanosheets that are wrinkled, semi-transparent, and clearly exhibit corrugated interlayer spacing, a structural consequence of oxygen-containing functional groups intercalated between graphene layers, which not only disrupts  $\pi$ – $\pi$  stacking but also enhances chemical reactivity. In **Fig. 5.6(b-III)**, the rGO–hBNNS hybrid reveals nanoscale domains of rGO intricately intertwined with hBNNS flakes, a configuration that demonstrates uniform dispersion, forming a continuous network that confirms their strong interfacial bonding and coherent integration into a hybrid nanocomposite with well-defined nanoscale architecture. This arrangement confirms the formation of a

structurally stable, strong interfacial compatibility, enabling effective stress transfer and electronic coupling in the nanocomposite matrix.

Table 5.2: Elemental analysis presenting atomic and weight percentages, as well as B/N and C/O ratios, for (I) hBNNS, (II) GO, and (III) the synthesized rGO-hBNNS hybrid nanocomposite.

S.No.	Sample	Elements	Atomic %	Weight %	B/N Ratio	C/O Ratio	
1.		Boron	49.59	41.02	0.99		
	hBNNS	Nitrogen	50.06	53.66		-	
		AuL	0.35	5.31			
2	GO	Carbon	66.64	60		1.99	
2.	GO	Oxygen	33.36	40	-		
3.		Boron	36.49	28.20	0.83	Ratio -	
	CO	Nitrogen	43.81	43.46			
	rGO-	Carbon	16.81	14.43			
	hBNNS	Oxygen	2.11	2.41			
		AuL	0.79	11.10			

Elemental analysis derived from EDX spectra, corresponding to Fig. 5.6(I–III), decisively confirms the successful synthesis of pure hBNNS, GO, and the rGO-hBNNS nanocomposite (Table 5.2). For GO, the measured C/O atomic ratio was 1.997, reflecting a high degree of oxidation with abundant oxygenated functional groups on the graphene lattice by disruption of  $\pi$ - $\pi$  stacking which promotes hydrophilicity but limits electrical conductivity. Upon nanocomposite synthesis, this ratio increased markedly to 7.966, indicating a substantial elimination of oxygen-containing functional groups and the restoration of the conjugated sp<sup>2</sup> carbon network in rGO. Furthermore, the rGO-hBNNS composite displayed a notable C/N ratio of 0.371, alongside a higher atomic % and weight % of nitrogen compared to pristine hBNNS. This nitrogen enrichment is directly attributed to the hydrazine hydrate-assisted chemical reduction process, wherein nitrogen atoms participate in covalent or semi-covalent bonding between rGO sheets and hBNNS flakes. The nitrogen-mediated crosslinking strengthens the hybrid structure and ensures stable integration, thereby creating a reinforced network that optimizes interfacial adhesion within the composite matrix, facilitates stress transfer, improves mechanical resilience, and promotes facile electron transport in two nanomaterial components.

### 5.3.1.3 Spectroscopic Band Structure and Optical Transition Investigation of rGO-hBNNS Hybrid Nanocomposite Using UV-Visible Absorption Analysis

UV–Visible spectroscopy was employed to systematically analyze the absorption spectra of the materials pre- and post-synthesis of rGO-hBNNS hybrid nanocomposite, enabling precise insights into the interaction dynamics, electronic band restructuring and structural transformations responsible for both bandgap modulation and absorption peak shifts (**Fig. 5.7**). Upon formation of the rGO-hBNNS nanocomposite, a distinct red-shift was detected in the sharp absorption edge of hBNNS, shifting from 185 nm (6.534 eV) in pristine hBNNS to 186 nm (3.726 eV), indicating a notable reduction in optical bandgap (**Fig. 5.7(I, II, V, VI)**). In contrast, highly disordered GO nanosheets displayed two prominent absorption peaks at 229 nm (3.679 eV) and 316 nm (2.969 eV), corresponding to  $\pi$ – $\pi$ \* electronic transitions from C=C bonds and n– $\pi$ \* transitions from C=O bonds, respectively (**Fig. 5.7(III, IV)**). Hydrothermal reduction of GO

caused a pronounced blue-shift of the  $\pi$ - $\pi$ \* peak to 193 nm (3.233 eV), while the n- $\pi$ \* peak remained near 318 nm (2.789 eV), and an additional absorption band emerged at 562 nm (2.049 eV), indicating new electronic states introduced during composite formation (**Fig. 5.7(V, VI)**) [23]. The bandgaps of all samples were quantified using Tauc's plot by extrapolating the linear region in the ( $\alpha$ hv)² versus hv curve [24]. This analysis revealed significant bandgap narrowing—from 5.34 eV in pure hBNNS to 3.726 eV, and from 3.679 eV in GO to 3.233 eV in the rGO-hBNNS hybrid—directly linked to the removal of oxygenated functional groups and the strong interlayer coupling between rGO and hBNNS. These structural interactions facilitated electronic band dispersion, thereby confirming effective band structure engineering in the nanocomposite due to enhanced charge delocalization and electronic band dispersion (**Fig. 5.7(II, IV, VI)**).

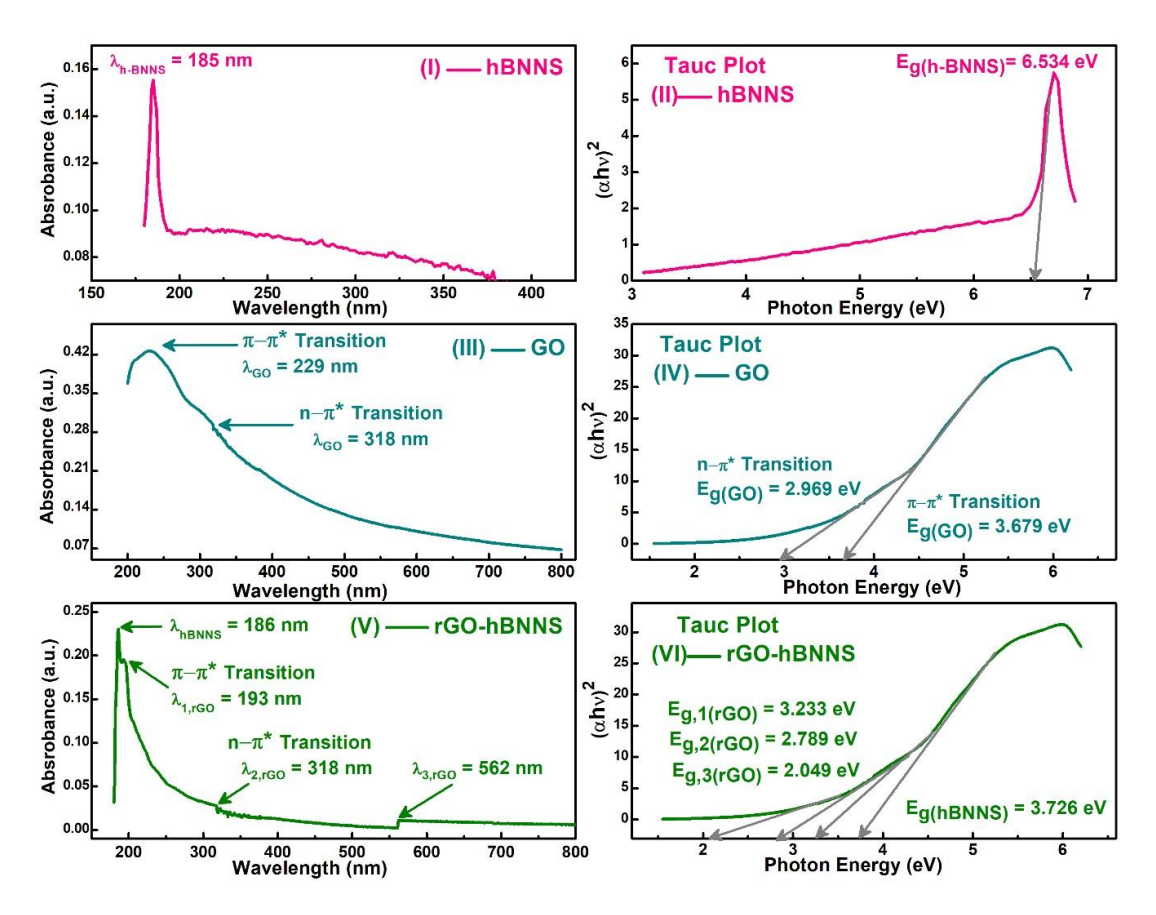


Figure 5.7: Detailed UV-visible absorption spectra and associated Tauc plots for (I) hBNNS (Pink), (II) GO (Cyan), and (III) rGO-hBNNS (Green), to estimate the optical band gap energies by analyzing their electronic transitions.

### 5.3.1.4 Raman Spectroscopy Elucidating Phonon Dynamics, Vibrational Modes, and Electronic Interactions in the rGO-hBNNS Hybrid Nanocomposite

Raman spectroscopy, a powerful non-destructive analytical technique, is pivotal for assessing the electronic structure, nanocomposite formation, and layer ordering within advanced materials by meticulously examining vibrational modes, shifts in peak positions, variations in peak intensity, full-width at half-maximum (FWHM), and

defect densities. In the present study, Raman spectra were obtained for the assynthesized samples: (I) hexagonal boron nitride nanosheets (hBNNS), (II) graphene oxide (GO), and (III) reduced graphene oxide-hBNNS (rGO-hBNNS) hybrid nanocomposite, as shown in **Fig. 5.8**.

The spectrum of pure hBNNS (**Fig. 5.8(I**)) prominently features a sharp and intense peak at 1368.43 cm<sup>-1</sup>, which corresponds to the in-plane E2g phonon vibration mode. This mode is characteristic of the highly ordered hexagonal lattice of boron and nitrogen atoms, reflecting the crystalline integrity of hexagonal lattice vibrations and structural ordering within the ultrathin nanosheets.

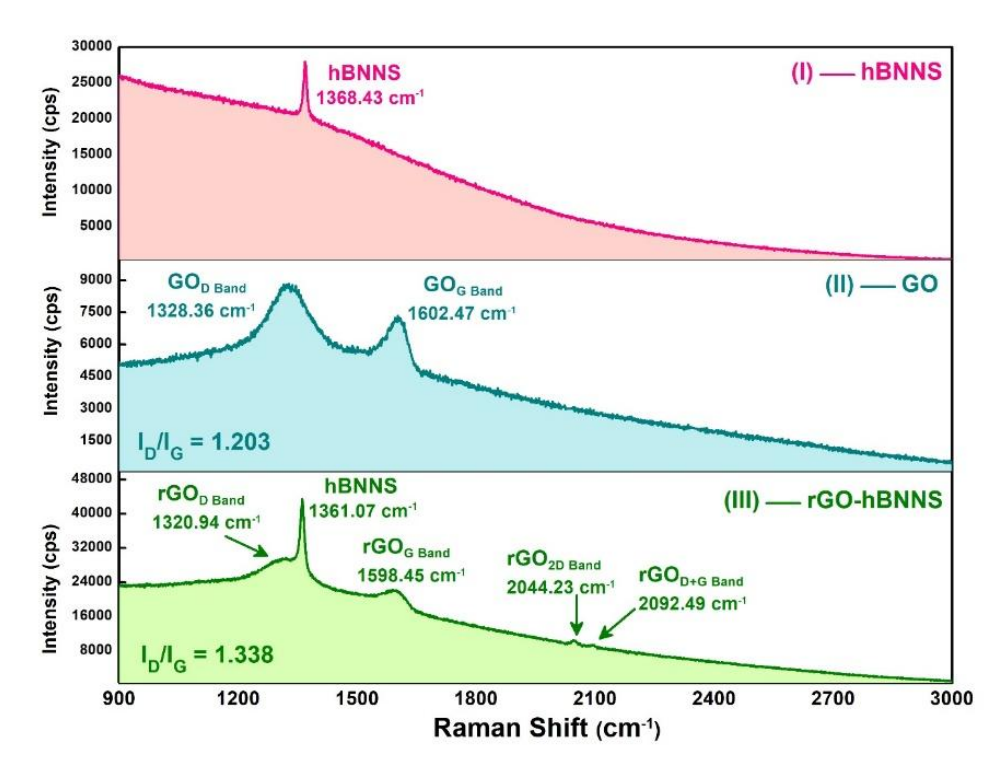


Figure 5.8: Raman spectroscopic analysis conducted on (I) hBNNS (Pink), (II) GO (Cyan), and (III) rGO-hBNNS (Green) across the 900-3000 cm<sup>-1</sup> wavenumber range to evaluate their distinct vibrational modes.

The Raman spectrum of GO (**Fig. 5.8(II**)) distinctly displays two significant peaks at approximately 1328.36 cm<sup>-1</sup> and 1602.47 cm<sup>-1</sup>. The peak at 1328.36 cm<sup>-1</sup> represents the D-band, arising from first-order breathing modes of k-point phonons with A1g symmetry; this band is directly linked to sp<sup>3</sup> hybridized carbon atoms induced by structural defects and disorder in the GO nanosheets. The peak at 1602.47 cm<sup>-1</sup> corresponds to the G-band, originating from the E2g phonon mode related to sp<sup>2</sup> hybridized carbon atoms in the graphene lattice, signifying graphitic domains [25]. Notably, the absence of the 2D band (or G'-band), an overtone of the D-band, indicates the high defect density and the lack of ordered stacking along the c-axis in the GO sheets [26]. This absence highlights the disrupted  $\pi$ -electron conjugation and the dominance of defect-induced states in GO.

Upon formation of the rGO-hBNNS hybrid nanocomposite, the Raman spectrum (**Fig. 5.8(III)**) exhibits three distinctly red-shifted peaks at 1320.94 cm<sup>-1</sup>, 1361.07 cm<sup>-1</sup>, and

1598.41 cm<sup>-1</sup>, which correspond respectively to the D-band of rGO, the in-plane E2g vibrational mode of hBNNS, and the G-band of rGO. The subtle shifts in these peaks relative to the individual components suggest a strong interfacial interaction and electronic coupling between rGO and hBNNS within the hybrid structure. This hybridization facilitates partial restoration of the graphitic domains and modulates the phonon behavior due to chemical bonding and charge transfer effects.

Additionally, two diminished peaks observed at 2044.23 cm<sup>-1</sup> and 2092.49 cm<sup>-1</sup> in the rGO-hBNNS spectrum correspond to significantly red-shifted 2D and D + G bands, respectively [26, 27]. These features are indicative of the restoration of ordered stacking in rGO nanosheets, which are now preferentially aligned along the (002) crystallographic plane of hBNNS oriented along the c-axis. The pronounced red shift in the 2D band is attributed to electron cloud density transfer from rGO to functionalized hBNNS, which strengthens the bond alignment in defect-induced domains, thereby stabilizing the hybrid nanocomposite's structural framework [28]. This charge redistribution and strong electronic interaction enhance the overall crystalline coherence and electronic properties of the rGO-hBNNS system.

The observed prominent red-shift in the Raman spectra of reduced graphene oxide (rGO) within the rGO-hBNNS nanocomposite, specifically about 7.42 cm<sup>-1</sup> for the D-band and 4.06 cm<sup>-1</sup> for the G-band, signifies the successful and near-complete reduction of graphene oxide (GO) to rGO [29]. This shift is a direct consequence of the restoration and reorganization of graphitic sp<sup>2</sup> hybridized carbon domains, which enhances electron delocalization and increases electron density within the nanostructure and strong interfacial coupling with hBNNS, facilitated by pronounced tensile strain arising during nanocomposite synthesis. Moreover, this red-shift confirms strong interfacial coupling, between rGO and hexagonal boron nitride nanosheets (hBNNS). This transition involves restoration of sp<sup>2</sup> graphitic nanostructures, increased electronic density, and strong interfacial coupling with hBNNS, facilitated by an exceptional tensile strain imparted during the hydrothermal synthesis process, which drives intimate bonding and electronic interactions between the components [30].

Simultaneously, the hBNNS component exhibits a red-shift of approximately 7.36 cm<sup>-1</sup> upon nanocomposite formation. This spectral shift reveals the evolution of improved crystalline nanostructures in hBNNS, characterized by a significant reduction in layer thickness and lateral expansion of nanosheet morphology. These morphological refinements stem from intrinsic tensile strain developed under hydrothermal treatment conditions, which promotes rearrangement of atomic layers and enhanced crystallinity within the nanosheets.

A critical parameter supporting these structural transformations is the increase in the intensity ratio of the D-band to G-band ( $I_D/I_G$ ) from 1.203 in GO to 1.338 in the rGO-hBNNS nanocomposite. This increase reflects the high-temperature induced hydrothermal reduction process, which restored  $sp^2$  carbon networks in rGO, simultaneously introducing defects and vacancies due to structural reorganization and removal of oxygen-containing groups. These defects, instead of diminishing material architecture, contribute to enhanced layered stacking between rGO and hBNNS, as corroborated by the corresponding increase in crystallite size observed from X-ray diffraction (XRD) analysis. The higher  $I_D/I_G$  ratio thus substantiates the red-shift

phenomena in the Raman peaks, indicating a controlled defect landscape essential for forming a chemically stable interface between rGO and hBNNS.

Furthermore, the intensity ratio of the 2D-band to G-band ( $I_{2D}/I_{G}$ ) increases appreciably to 0.472 in the rGO-hBNNS nanocomposite, signifying a partial restoration of graphitic crystallinity and a reduction in the extent of layer stacking compared to pristine GO. This change reflects the remarkable exfoliation and decreased layer stacking in the rGO-hBNNS composite upon reduction and integration, which enhances the electronic and mechanical properties of the hybrid material [30].

Importantly, the Raman spectra of the synthesized nanocomposite reveal no extraneous peaks beyond those assigned to rGO and hBNNS, underscoring the exceptional phase purity and homogeneous integration of the two components in the hybrid structure. This purity ensures that the nanocomposite's properties are intrinsic to the well-ordered materials rather than arising from impurities or secondary phases, validating the efficacy of the synthesis process. The detailed Raman analysis highlights critical structural and electronic evolutions during nanocomposite formation, including restoration of graphitic domains, defect modulation, enhanced interfacial bonding, morphological refinement of hBNNS, and overall phase purity, factors collectively contributing to the superior functional performance of the rGO-hBNNS hybrid nanocomposite.

# 5.3.1.5 FT-IR Spectroscopy—Driven Investigation of Molecular Bond Dynamics and Sequential Protein Immobilization Mechanisms in rGO-hBNNS Hybrid Nanocomposites

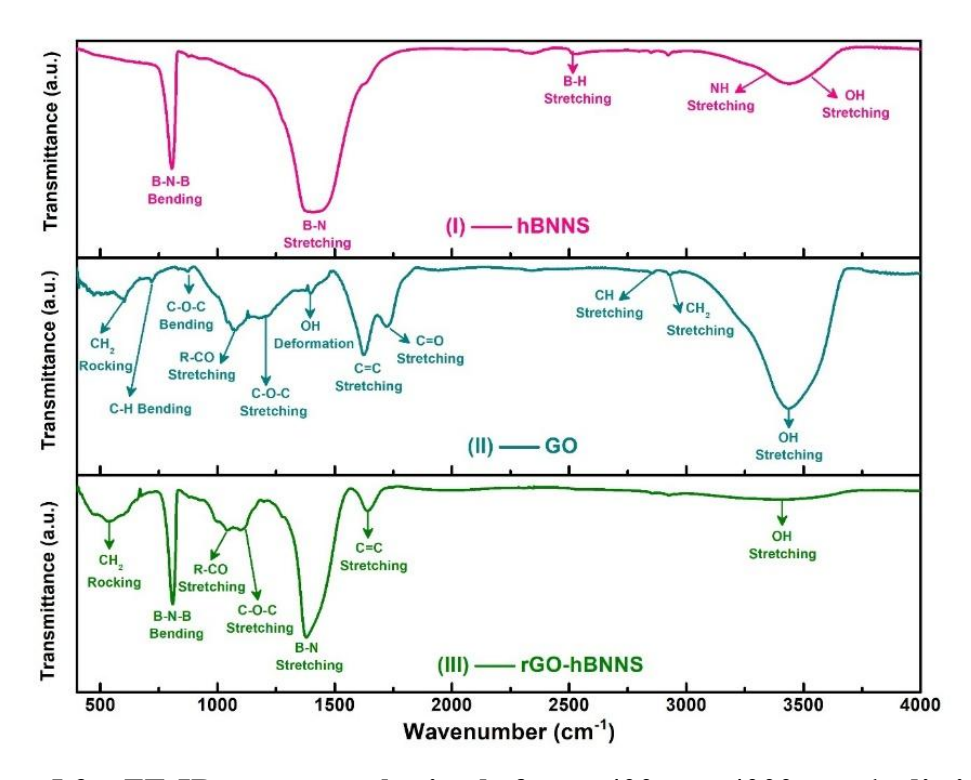


Figure 5.9: FT-IR spectra obtained from 400 to 4000 cm<sup>-1</sup> distinctly demonstrate the characteristic molecular features of h-BNNS, GO, and rGO-hBNNS, confirming successful synthesis and hybridization at the molecular level.

The intricate chemical bond formation and surface functionalization of the assynthesized nanomaterials were comprehensively analyzed through FT-IR spectroscopy, which provides vibrational evidence of compositional and structural modifications, as illustrated in **Fig. 5.9**. In the FT-IR spectrum of hBNNS (**Fig. 5.9(I)**), the transmittance spectra displayed distinct fingerprint peaks at 804 cm<sup>-1</sup> and 1413 cm<sup>-1</sup>, corresponding to B–N–B bending and B–N stretching vibrations, which confirm the structural integrity of hexagonal boron nitride nanosheets. Additional broad peaks at 2500 cm<sup>-1</sup>, 3200–3500 cm<sup>-1</sup>, and above 3500 cm<sup>-1</sup> were attributed to B–H stretching, N–H stretching, and O–H stretching vibrations, respectively [21], indicating residual surface functionalities that enhance potential chemical reactivity.

Table 5.3: Assigned FT-IR vibrational peaks validating the successful synthesis of (I) hBNNS, (II) GO, and (III) rGO-hBNNS hybrid nanocomposite, confirming the preservation of key functional groups and the emergence of composite-specific features.

S.NO.	Sample	Wavenumber (cm <sup>-1</sup> )	<b>Assigned Bands</b>	Reference	
		806	B-N-B Bend		
1.	Hexagonal Boron Nitride Nanosheets, (hBNNS)	1405	B-N Stretch	ra41	
		2518	B-H Stretch	[21]	
		3200-3500	N-H Stretch		
		>3500	OH Stretch		
	Graphene Oxide Nanosheets, (GO)	603	CH <sub>2</sub> Rock		
		819	C-H Bend		
		874	C-O-C Bend		
		1074	R-CO Stretch		
		1216	C-O-C Stretch		
2.		1398	OH Deformation	[31, 32]	
		1621	C=C Stretch		
		1729	C=O Stretch		
		2832	C-H Symmetric Stretch		
		2855	CH <sub>2</sub> Asymmetric Stretch		
		3437	OH Stretch		
	Reduced Graphene	546	CH <sub>2</sub> Rock		
3.	Oxide – Hexagonal	808	B-N-B Bend		
	Boron Nitride	1036	R-CO Stretch	[21, 31,	
	Nanosheets based	1109	C-O-C Stretch	32]	
	Nanocomposite	1379	B-N Stretch		
	(rGO-hBNNS)	1637	C=C Stretch		

For GO (**Fig. 5.9(II**)), a sharp skeletal vibration peak at 1621 cm<sup>-1</sup> was observed, representing the retained sp<sup>2</sup> hybridized graphitic carbon backbone, pivotal for its electronic properties [33]. The bonding configuration further revealed pronounced hydrophilic oxygen-containing peaks, including epoxy groups at 874 cm<sup>-1</sup> and 1216 cm<sup>-1</sup>, alkoxy at 1074 cm<sup>-1</sup>, carboxyl at 1729 cm<sup>-1</sup>, and hydroxyl groups at 1398 cm<sup>-1</sup> and 3437 cm<sup>-1</sup>, as detailed in **Table 5.3** [31]. The GO spectrum also exhibited hydrocarbon-related functional peaks such as CH<sub>2</sub> rocking at 603 cm<sup>-1</sup>, C–H out-of-plane bending at 819 cm<sup>-1</sup>, and symmetric (2832 cm<sup>-1</sup>) and asymmetric (2855 cm<sup>-1</sup>)

alkyl stretching modes, signifying surface contamination or residual synthesis byproducts.

In the rGO-hBNNS nanocomposite (**Fig. 5.9(III)**), the FT-IR spectrum displayed the unique coexistence of material-specific peaks. These included the hBNNS-related B-N-B bending at 808 cm<sup>-1</sup> and B-N stretching at 1379 cm<sup>-1</sup>, alongside the C=C skeletal vibration of graphitic domains in rGO at 1637 cm<sup>-1</sup>, confirming strong hybridization between the two phases [21]. Despite the exceptional efficiency of hydrothermal reduction in removing oxygen functionalities from GO, residual oxygen-bearing groups persisted, indicated by peaks at 1036 cm<sup>-1</sup>, 1079 cm<sup>-1</sup>, and 3392 cm<sup>-1</sup>, along with an alkyl-related peak at 546 cm<sup>-1</sup>. This partial retention of oxygen moieties suggests a controlled reduction process, preserving functional sites that can aid in further chemical modifications and interfacial bonding in the nanocomposite structure.

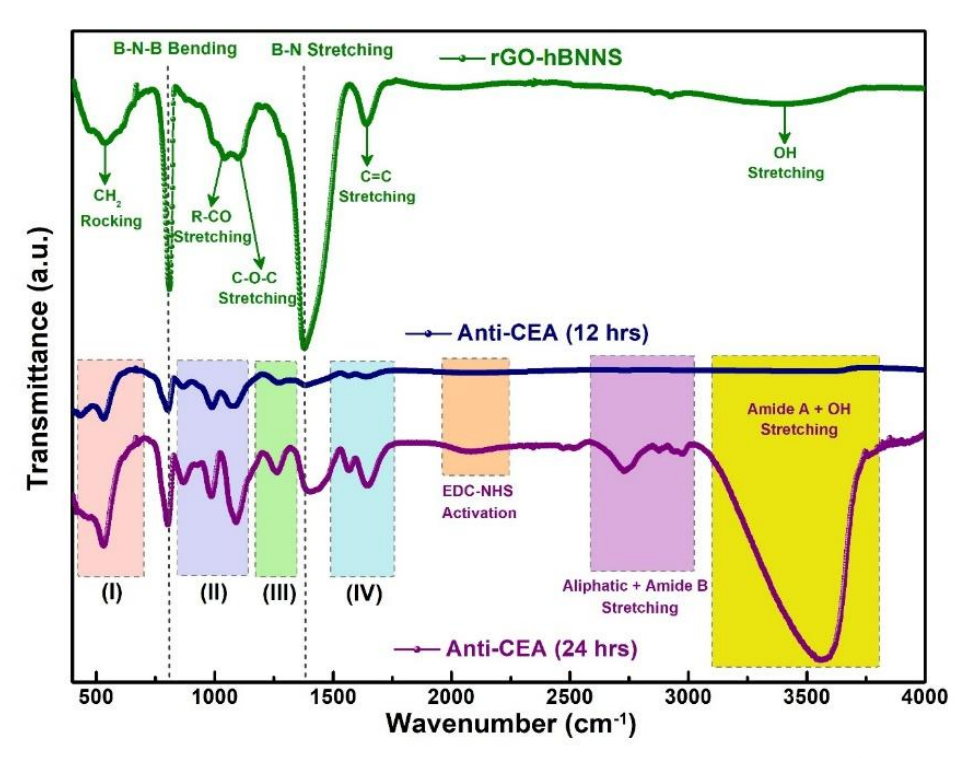


Figure 5.10: FT-IR Spectroscopic Analysis for Time-Dependent Optimization of Anti-CEA Immobilization on rGO-hBNNS Hybrid Nanocomposite

To determine the optimum time-dependent immobilization efficiency of Anti-CEA on rGO-hBNNS/ITO electrodes, FT-IR spectroscopy was employed to systematically to obtain vibrational spectra after 12 h (blue) and 24 h (purple) incubation periods (**Fig. 5.10**). Before Anti-CEA immobilization, the nanocomposite exhibited characteristic peaks assigned to B-N-B bending, B-N stretching, C = C skeletal vibrations, alkyl rocking, alkoxy stretching, and epoxy stretching, demonstrating the chemical framework and functional moieties available for conjugation. Upon introducing Anti-CEA, distinct protein-derived peaks emerged in specific wavenumber regions—phosphorylation (869 cm<sup>-1</sup>), amide III (NH bending, 1264 cm<sup>-1</sup>), amide II (C-N stretching, 1567 cm<sup>-1</sup>), and amide I (C = O stretching, 1647 cm<sup>-1</sup>)—providing molecular evidence of antibody binding to the nanocomposite surface [21].

Extending the immobilization to 24 h induced additional diagnostic peaks, including those for EDC–NHS mediated activation (2081 cm<sup>-1</sup>), aliphatic C–H stretching modes (2729 cm<sup>-1</sup>, 2877 cm<sup>-1</sup>), amide B stretching (2978 cm<sup>-1</sup>), amide A stretching (3300 cm<sup>-1</sup>), and intense O–H stretching (> 3500 cm<sup>-1</sup>), signifying complete covalent linkage and structural stabilization of Anti-CEA [21, 33]. Conversely, the 12 h treatment, while showing amide and phosphorylation features, lacked the unique coupling EDC–NHS, high-intensity amide peaks, strong aliphatic, extended hydrogen-bonding signals, and stabilization signals, confirming that only partial immobilization occurred under shorter incubation. This comparative analysis decisively establishes 24 h as the optimal immobilization duration for achieving maximum protein loading and stable biochemical activity.

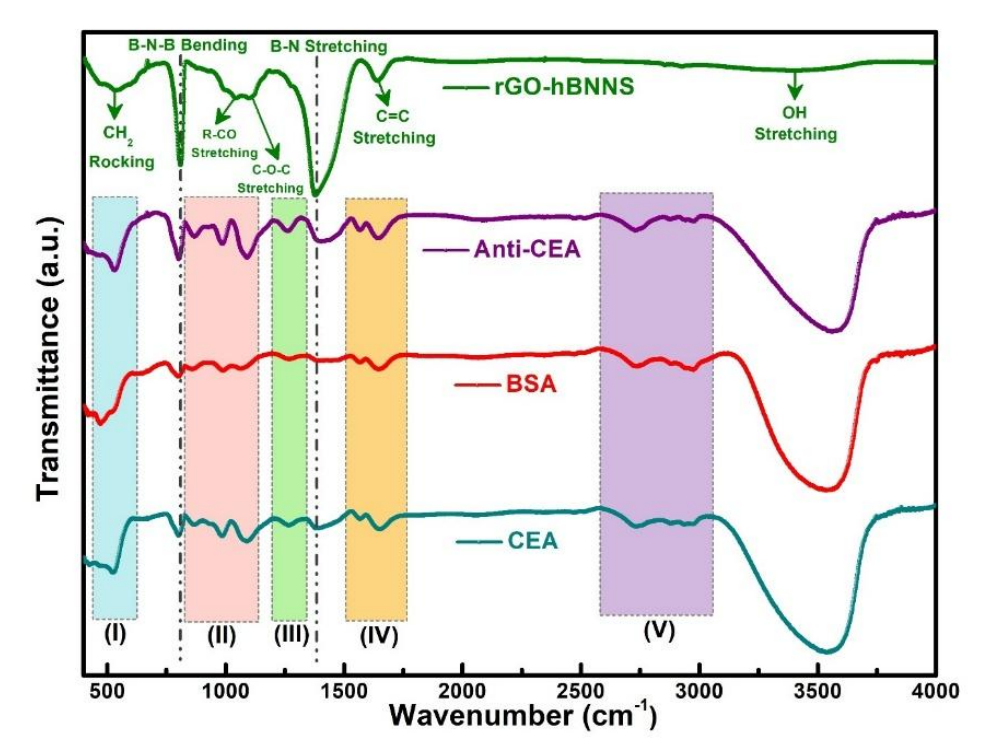


Figure 5.11: Distinct FT-IR analysis over 400–4000 cm<sup>-1</sup> depicting the characteristic vibrational fingerprints of rGO-hBNNS and progressive bioconjugation process, confirming the stepwise achievement of antibody coupling, protein blocking, and antigen binding with high precision.

The progressive construction of the immunosensing platform on the rGO-hBNNS nanocomposite was meticulously monitored using FT-IR spectroscopy to confirm molecular-level binding events (Fig. 5.11). The attachment of EDC-NHS-activated Anti-CEA was clearly validated by the appearance of amide-I, II, and III bands, signifying preserved protein structural integrity, while characteristic hBNNS peaks persisted, indicating that nanocomposite features remained intact biofunctionalization [34]. Upon the subsequent deposition of BSA (10 μL) onto the Anti-CEA/rGO-hBNNS interface, a marked a substantial drop in FT-IR transmittance intensity within spectral regions II, III, IV, and V indicated effective blocking of nonspecifically bound antibodies, ensuring improved selectivity and minimized background interference [21]. Finally, the immobilization of CEA antigens onto the BSA/Anti-CEA/rGO-hBNNS layer not only restored transmittance intensity but also

shifted peaks within regions III, IV, V, and VI, signifying robust and targeted antigen—antibody binding [35]. These results collectively confirm that the fabrication process achieved precise biomolecular assembly, optimized surface passivation, and stable immunorecognition capability.

#### **5.3.2** Electrochemical Profiling and Analysis:

### **5.3.2.1** Interfacial Electrochemical Kinetics of rGO-hBNNS/ITO Electrodes on Sequential Protein Immobilization

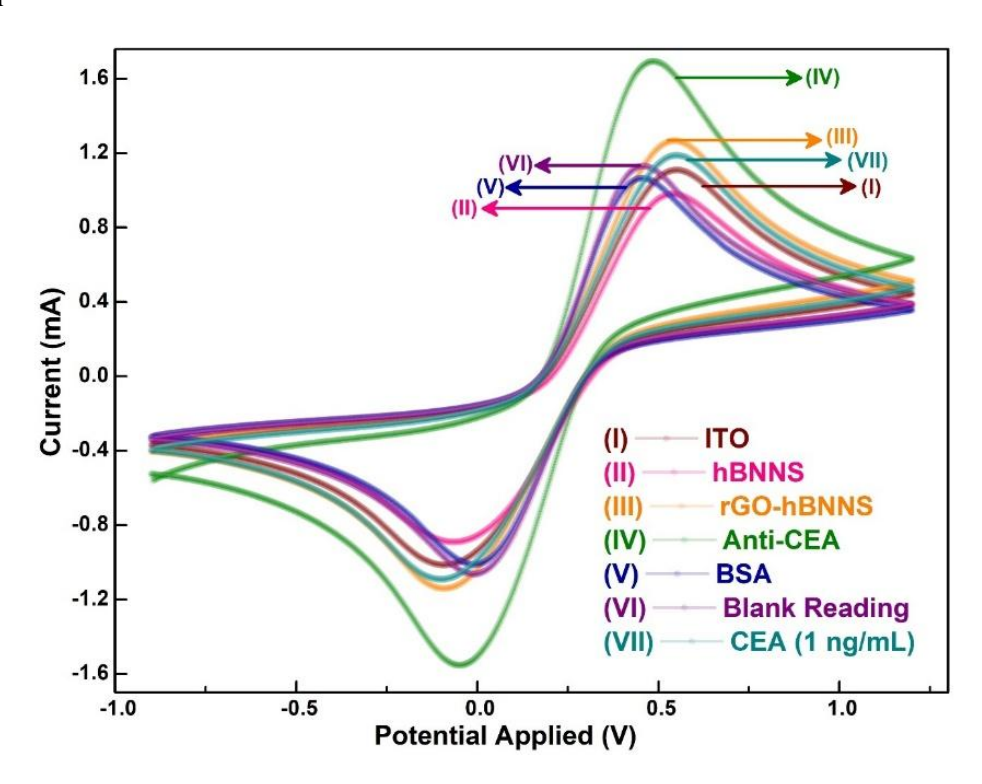


Figure 5.12: Cyclic voltammetry (CV) analysis, conducted over a potential range of -0.9 to 1.2 V, provides clear and detailed evidence of successful stepwise modification of the rGO-hBNNS/ITO electrode with protein biomolecules, highlighting the progressive formation of an efficient biointerface.

A comprehensive electrochemical assessment was performed using cyclic voltammetry (CV, Fig. 5.12) and differential pulse voltammetry (DPV, Fig. 5.13) following each sequential stage of immunosensor construction, reinforcing the structural and functional observations made via FT-IR spectroscopy.CV investigations after each biomolecular immobilization step yielded critical data for calculating the diffusion coefficients (Table 5.4) using the Randles–Sevcik Equation (Eq. [5.3]). This quantification provided a meticulous understanding of interfacial electron-transfer kinetics, further confirming the influence of molecular architecture of the bio-interface for maximized electrochemical performance and sensing accuracy [36].

$$I_p = (2.69 \times 10^5) n^{3/2} A C D^{1/2} \sqrt{\nu}$$
 [5.3]

The Randles–Sevcik relationship defines  $I_p$  as the peak current (anodic or cathodic), n as the number of electrons involved in the redox process (n = 1), A as the electroactive

area of the working electrode (0.64 cm<sup>2</sup>), C as the molar concentration of the electroactive species (5 × 10<sup>-3</sup> mol·cm<sup>-3</sup>), D as the diffusion coefficient, and v as the applied scan rate (50 mV·s<sup>-1</sup>).

Electrophoretic deposition (EPD) of the rGO–hBNNS nanocomposite onto ITO electrodes yielded markedly enhanced electrochemical parameters, with anodic peak current of  $1.25 \pm (1.3 \times 10^{-2})$  mA, DPV current of  $0.177 \pm (3.7 \times 10^{-4})$  mA, and diffusion coefficient of  $4.23 \times 10^{-7} \pm (8.6 \times 10^{-9})$  cm<sup>2</sup>·s<sup>-1</sup>, respectively. These values represent substantial performance gains of approximately 29%, 29%, and 68% over electrodes modified with hBNNS alone, which exhibited anodic peak current, DPV current, and diffusion coefficient of  $0.964 \pm (1.6 \times 10^{-2})$  mA,  $0.138 \pm (1.1 \times 10^{-4})$  mA, and  $0.138 \pm (1.$ 

Table 5.4: Evaluation of interfacial electron transfer from peak anodic current (CV), diffusion coefficient, and DPV current monitored throughout sequential fabrication of the immunoelectrode.

Stepwise Electrode Modification	Anodic Peak Current (I <sub>pa</sub> , mA)	Diffusion Coefficient (D, cm <sup>2</sup> ·s <sup>-1</sup> )	DPV Current (mA)
ITO	$1.108 \pm (1.01 \times 10^{-2})$	$3.316 \times 10^{-7} \pm (6.07 \times 10^{-9})$	$0.154 \pm (1.14 \times 10^{-3})$
hBNNS	$0.965 \pm (1.65 \times 10^{-2})$	$2.512 \times 10^{-7} \pm (8.60 \times 10^{-9})$	$0.138 \pm (1.08 \times 10^{-4})$
rGO-hBNNS	$1.251 \pm (1.27 \times 10^{-2})$	$4.229 \times 10^{-7} \pm (8.64 \times 10^{-9})$	$0.177 \pm (3.66 \times 10^{-4})$
Anti-CEA	$1.672 \pm (1.91 \times 10^{-2})$	$7.546 \times 10^{-7} \pm (1.73 \times 10^{-8})$	$0.238 \pm (4.63 \times 10^{-4})$
BSA	$1.066 \pm (0.15 \times 10^{-2})$	$3.069 \times 10^{-7} \pm (8.86 \times 10^{-10})$	$0.149 \pm (1.80 \times 10^{-4})$
Blank Reading	$1.128 \pm (0.15 \times 10^{-2})$	$3.436 \times 10^{-7} \pm (9.36 \times 10^{-10})$	$0.165 \pm (9.16 \times 10^{-5})$
CEA	$1.188 \pm (1.08 \times 10^{-2})$	$3.810 \times 10^{-7} \pm (5.18 \times 10^{-10})$	$0.171\pm(5.50\times10^{-4})$

The substantial enhancements in current response and mass transport characteristics highlight the exceptional electrochemical behavior of electrophoretically deposited rGO-hBNNS films on ITO compared to electrodes modified solely with hBNNS deposition. This superior performance originates from the electron-rich nature of rGO nanosheets comprising a delocalized  $\pi$ -electron network, which provides an extensive network of conductive channels and facilitates rapid electron transfer across the interface. By integrating rGO with hBNNS, the composite not only boosts electrocatalytic activity but also improves mass transport dynamics, ensuring faster redox reactions and enhanced sensing efficiency. Such a synergistic structure creates an electrochemically active surface with high charge mobility, making it exceptionally suitable for sensitive and selective electrochemical detection. Upon immobilization of Anti-CEA antibodies, the anodic peak current and DPV current rose to  $1.67 \pm (1.9 \times 10^{-2})$  mA and  $0.238 \pm (4.6 \times 10^{-4})$  mA, marking ~33% and ~34% increases, respectively, over the rGO-hBNNS/ITO baseline. Simultaneously, the diffusion coefficient surged to  $7.55 \times 10^{-7} \pm (1.7 \times 10^{-8})$  cm<sup>2</sup>·s<sup>-1</sup>, representing a ~78%

improvement. These advancements is attributed to the high-density binding sites (COOH, -NH<sub>2</sub>) available on the rGO-hBNNS surface, which, when activated by EDC-NHS coupling, enable dense loading density, optimal orientation, and stable antibody attachment for rapid, selective antigen recognition. The result is a highly conductive, biocompatible, and structurally optimized sensing platform capable of supporting high electron-transfer rates for highly robust, sensitive, and precise biosensing operations. The deposition of BSA onto the Anti-CEA/rGO-hBNNS/ITO immunoelectrode induced a substantial decline in electrochemical performance, with anodic peak current, DPV current, and diffusion coefficient measured at  $1.07 \pm (0.15 \times 10^{-2})$  mA,  $0.149 \pm (1.8 \times 10^{-4})$  mA, and  $3.07 \times 10^{-7} \pm (8.9 \times 10^{-10})$  cm<sup>2</sup>·s<sup>-1</sup>, respectively.

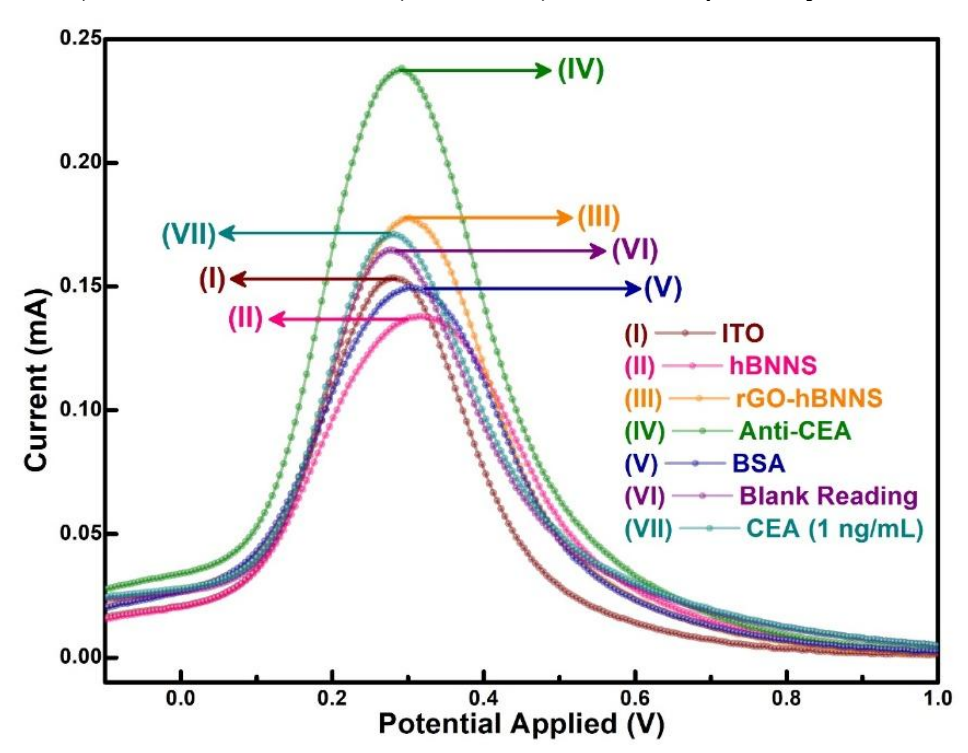


Figure 5.13: Differential Pulse Voltammetry (DPV) performed within the -0.2 to 1.2 V potential window reveals the progressive biofunctionalization of rGO-hBNNS/ITO electrodes, enabling precise monitoring of electron transfer dynamics and successful protein modification at each fabrication step.

This decline in electrochemical response indicates effective passivation of non-specifically oriented or unbound antibodies on incorporating globular BSA protein molecules to exposed binding sites, thereby minimizing non-specific interactions and enhancing the electrode's operational stability and selectivity for CEA detection. Such controlled passivation reinforces the structural integrity of the bio-interface, reducing background noise, and ensuring that subsequent current changes arise predominantly from specific CEA recognition. Such passivation enhances the electrode's specificity toward the target analyte (CEA) and stabilizes the bio-interface, reducing false positives in subsequent measurements. Following this passivation, the blank reading (0 ng/mL CEA) produced a measurable recovery in electrochemical activity, with anodic peak current, DPV current, and diffusion coefficient rising to  $1.13 \pm (0.15 \times 10^{-2})$  mA,  $0.165 \pm (9.2 \times 10^{-5})$  mA, and  $3.44 \times 10^{-7} \pm (9.4 \times 10^{-10})$  cm<sup>2</sup>·s<sup>-1</sup>, respectively. This resurgence in analytical response indicates restoration of electron transfer pathways upon specific

molecular recognition events at the biofunctionalized surface, despite BSA passivation, validating the effective antigen-binding capability of as-fabricated nano-biosensor and the functional readiness for sensitive CEA quantification.

The observed rise in anodic peak current, DPV current, and diffusion coefficient following the blank measurement can be attributed to the active participation of ions present in the phosphate buffer solution (PBS, pH 7.4). These ions facilitate charge transport by enhancing the conductivity of the electrolyte and reducing the interfacial charge-transfer resistance, thereby accelerating electron transfer processes at the electrode–electrolyte interface. This finding elucidates the function of the buffer in maintaining a stable ionic environment, mitigating potential fluctuations, and ensuring high reproducibility in electrochemical measurements. Furthermore, the buffer solution contributes to optimal pH conditions that preserve antibody and antigen structural integrity, enabling more efficient binding interactions.

Upon subsequent immobilization of the CEA antigen onto the BSA/Anti-CEA/rGO-hBNNS/ITO immunoelectrode, a marked increase in anodic peak current, DPV current, and diffusion coefficient was recorded, measuring  $1.19 \pm (0.08 \times 10^{-2})$  mA,  $0.171 \pm (5.5 \times 10^{-4})$  mA, and  $3.81 \times 10^{-7} \pm (5.2 \times 10^{-10})$  cm<sup>2</sup>·s<sup>-1</sup>, respectively. This pronounced enhancement confirms the successful formation of the highly specific antibody–antigen complex, which modifies the interfacial electron-transfer dynamics through the introduction of an organized biomolecular layer. The result demonstrates selective CEA recognition capability, exceptional sensitivity and operational robustness of the BSA/Anti-CEA/rGO-hBNNS/ITO biosensing interface.

## 5.3.2.2 Assessment of Scan Rate-Dependent Interfacial Electron Transfer Behavior in rGO-hBNNS/ITO-Based Nano-Biosensors Using Cyclic Voltammetry Measurements

To investigate the interfacial charge-transfer kinetics of the BSA/Anti-CEA/rGO-hBNNS/ITO nano-biosensor, cyclic voltammetry (CV) was employed to systematically monitor the peak anodic current (Ipa) and cathodic current (Ipc) as the scan rate was progressively varied from 10 mV/s to 150 mV/s, as depicted in **Fig. 5.14**. This approach enables precise evaluation of the redox behavior at the electrode–electrolyte interface, capturing subtle variations in electron-transfer efficiency under different dynamic conditions. Analysis revealed that both the redox peak currents (Ipa and Ipc) and corresponding peak potentials (Epa and Epc) exhibited a direct linear correlation with the square root of the scan rate, as illustrated in **Fig. 5.15**.

```
\begin{split} E_{pa} &= [\ 3.\,668 \times 10^{-4}\ V +\ 2.\,356\ \times 10^{-5}\ V\sqrt{s/mV}\ \times \sqrt{Scan\ Rate[mV/s]}\ ]\ ; \\ R^2 &= 0.998 \quad [5.4] \\ E_{pc} &= [\ 0.\,826 \times 10^{-4}\ V - 2.\,425 \times 10^{-5}\ V\sqrt{s/mV} \times \sqrt{Scan\ Rate[mV/s]}\ ]\ ; \\ R^2 &= 0.996 \quad [5.5] \\ I_{pa} &= [\ 3.\,316 \times 10^{-4}A +\ 1.\,117 \times 10^{-4}\ A\sqrt{s/mV}\ \times \sqrt{Scan\ Rate[mV/s]}\ ]\ ; \\ R^2 &= 0.998 \quad [5.6] \\ I_{pc} &= [\ -3.\,556 \times 10^{-4}A -\ 1.\,003\ \times 10^{-4}\ A\sqrt{s/mV} \times \sqrt{Scan\ Rate[mV/s]}\ ]; \\ R^2 &= 0.999 \quad [5.7] \end{split}
```

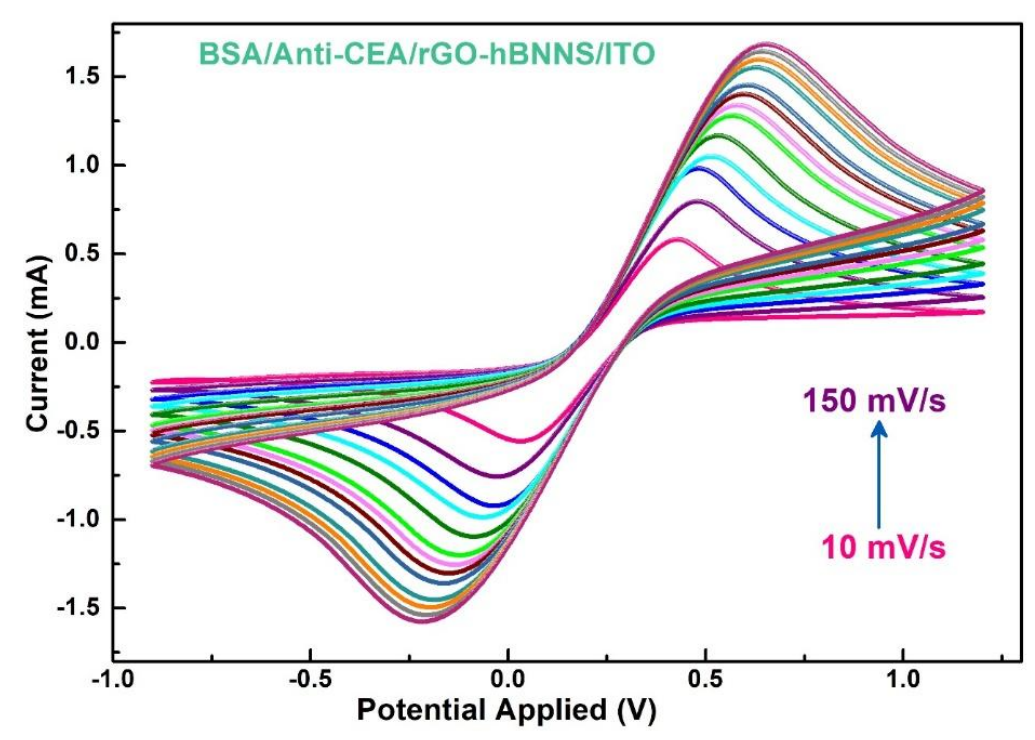


Figure 5.14: Influence of Scan Rate on the Cyclic Voltammetric Response of BSA/Anti-CEA/rGO-hBNNS/ITO Immunoelectrode in Presence of  $[Fe(CN)_6]^{3-/4-}$  electrolyte for scan rate ranging from 10-150 mV/s

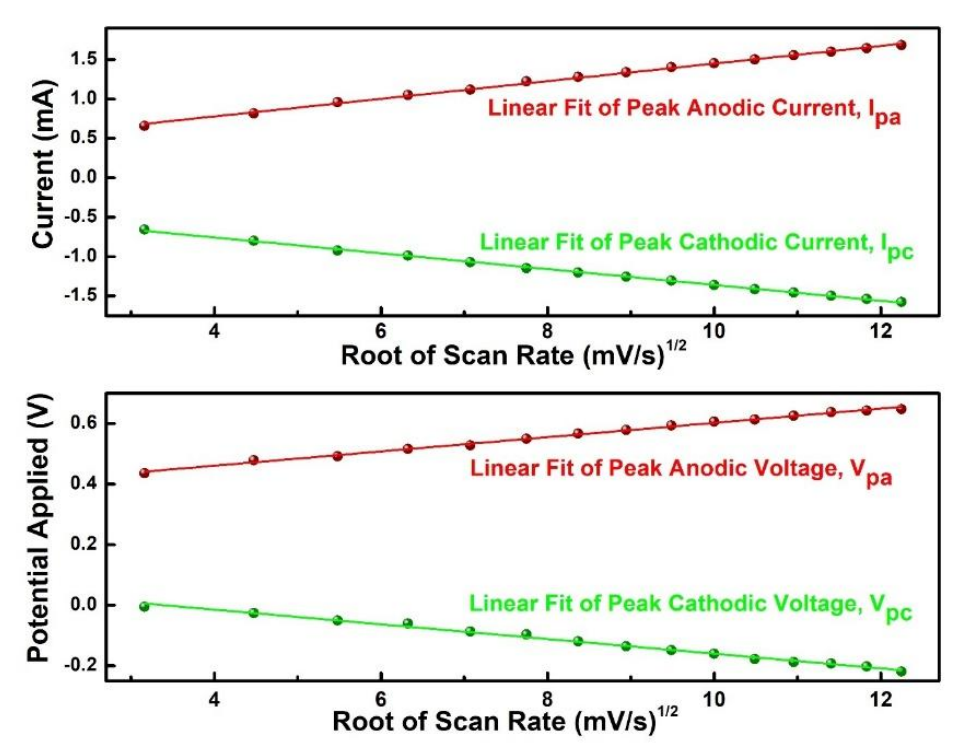


Figure 5.15: Quantitative Linear Relationship derived between Peak Currents and Potentials response with the Square Root of Scan Rate for BSA/Anti-CEA/rGO-hBNNS/ITO Immunoelectrode in the Presence of  $[Fe(CN)_6]^{3-/4-}$  electrolyte.

This relationship, described quantitatively by **Eq.** [5.4-5.7], describes the transport of electroactive species through the electrolyte that limits the rate of electron exchange at the electrode surface for the effective electrochemical mechanism. The observed proportionality between peak current and the square root of scan rate confirms a diffusion-controlled electron-transfer process, where the transport of redox species from the bulk electrolyte to the electrode surface governs the kinetics. The linear dependence of both redox peak currents and their associated potentials (Epa and Epc) indicates that electrochemical behavior is dominated by mass transport rather than surface kinetics, where the rate-limiting factor is the migration of redox-active molecules from the bulk electrolyte to the modified electrode surface. This result affirms the stability and homogeneity of the rGO-hBNNS nano-biointerface and highlights its capacity for predictable electron-transfer responses. Based on this analysis, the scan rate range of 10–150 mV/s is validated as optimal for subsequent electrochemical measurements, ensuring efficient charge-transfer kinetic while maintaining measurement reproducibility and minimizing capacitive interference.

### **5.3.2.3** Electrochemical Calibration Strategy for CEA Detection on Functionalized rGO-hBNNS/ITO Nano-Biosensors

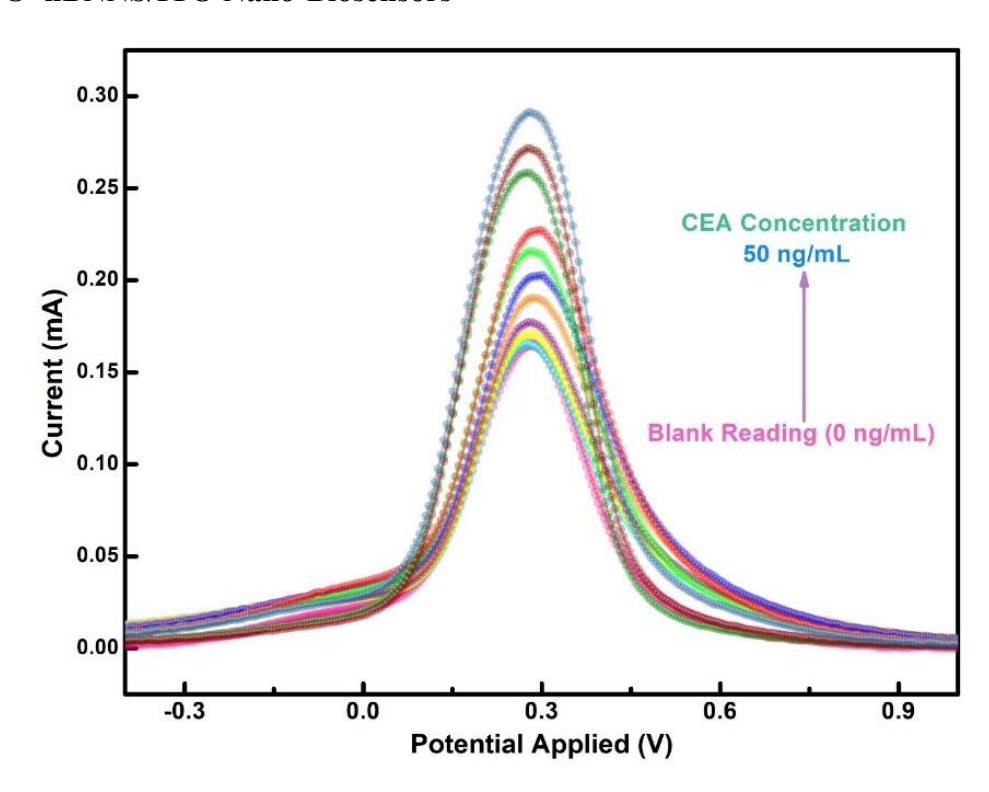


Figure 5.16: Differential pulse voltammetry (DPV) response upon successive addition of CEA in the range 0-50 ng/mL onto BSA/Anti-CEA/rGO-hBNNS/ITO immunoelectrode

A robust calibration curve obtained through differential pulse voltammetry (DPV) analysis, examining the sequential binding of carcinoembryonic antigen (CEA) at concentrations spanning the physiological interval of 0 to 50 ng/mL, as depicted in **Fig. 5.16**. This selection of clinically relevant physiological spectrum from 0 to 50 ng/mL is due to the well-established elevation of CEA levels exceeding 5 ng/mL in non-small

cell lung cancer (NSCLC) patients, highlighting the platform's precision in identifying pathological deviations and its potential for transformative clinical applicability in early detection and monitoring of oncogenic biomarkers.

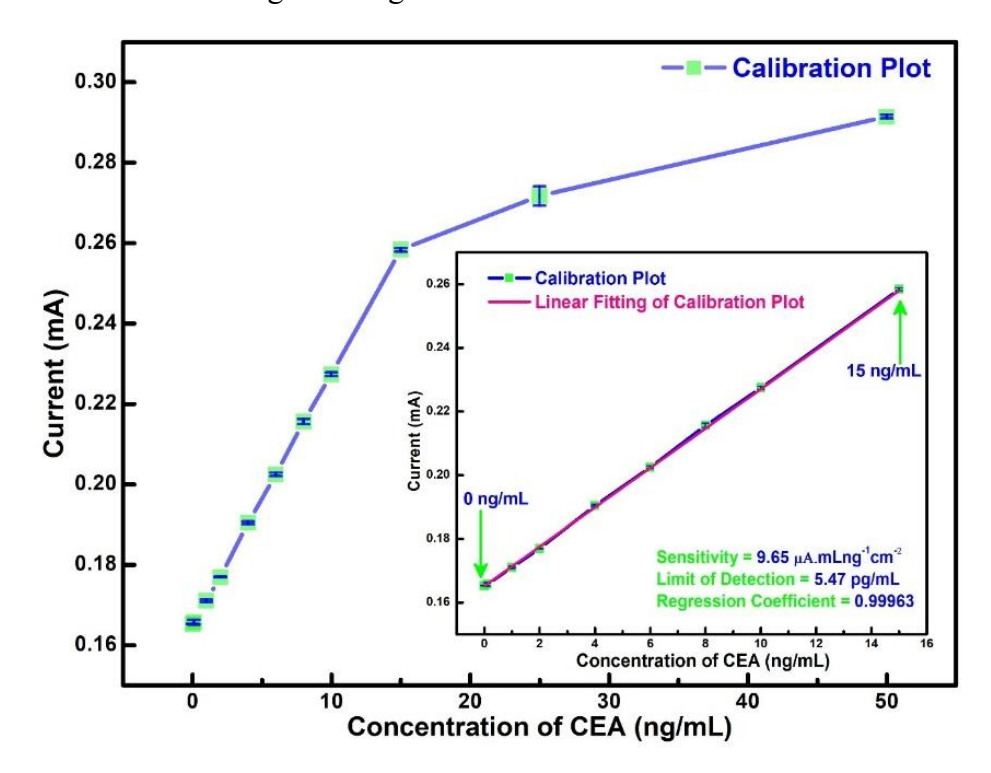


Figure 5.17: Linear calibration graph correlating peak DPV current as a function of CEA concentration, validating the performance and quantitative detection capability of the rGO-hBNNS-based immunosensor.

The DPV current exhibits a pronounced and proportional increase with rising CEA concentrations up to 15 ng/mL, clearly demonstrating a linear correlation between analyte concentration and electrochemical response (Fig. 5.17). This linearity arise from enhanced electron transfer kinetics facilitated by the abundant surface-active sites on the rGO-hBNNS nanocomposite, which efficiently mediate antibody-antigen interactions at the engineered nano-biointerface. The optimized surface chemistry and high-density functional moieties of the BSA/Anti-CEA/rGO-hBNNS/ITO electrode enable a robust and sensitive bio-recognition process, ensuring precise signal transduction. Beyond 15 ng/mL, however, the current response begins to deviate from linearity, reflecting the saturation of available binding and crosslinking sites on the nano-biointerface. This saturation effect results from the optimized occupancy of surface functional groups, which limits further antibody-antigen complex formation and thus constrains the electron transfer enhancement. Consequently, the observed plateau underscores the importance of surface site availability and indicates the practical upper detection limit of the sensor under the given experimental conditions. Overall, this data confirms the high sensitivity, selectivity, and operational stability of the immunosensor platform for quantitative CEA detection in clinically relevant concentrations.

The calibration curve presented in Fig. 5.17 was meticulously fitted with a linear regression model to quantitatively evaluate the sensing performance parameters of the as-fabricated nano-biosensor based on the rGO-hBNNS/ITO electrode platform. This linear fit, spanning the critical concentration range of 0 to 15 ng/mL, yielded a regression Equation of the form y = mx + c, where y represents the measured current response and x corresponds to the CEA concentration. This strong correlation coefficient of determination (R<sup>2</sup> =0.99963) reflects an almost perfect linearity, indicating the high precision and reliability of the immunosensor within this range. The robust linear relationship confirms the sensor's capability to provide consistent, reproducible, and accurate quantification of CEA at physiologically relevant levels. Furthermore, the detailed regression analysis enables extraction of crucial analytical metrics such as sensitivity, limit of detection, and dynamic range, which are vital for benchmarking the sensor's clinical applicability. The outstanding linearity also indicates minimal interference from nonspecific binding or matrix effects, reinforcing the effective nano-biointerface engineering of the rGO-hBNNS/ITO electrode. Eq. [5.8] succinctly encapsulates this linear dependence, serving as a foundational mathematical model for interpreting sensor responses and facilitating calibration for practical diagnostic applications.

### $I(mA) = [9.65 \,\mu A \cdot mL \cdot ng^{-1} \cdot cm^{-2} \times (CEA\ Concentration) + 0.165\ mA]$ [5.8]

Utilizing the slope from the linear fit, the sensitivity of the rGO-hBNNS-based immunosensor was calculated to be 9.65 µA·mL·ng<sup>-1</sup>·cm<sup>-2</sup> by dividing the slope by the electroactive surface area of 0.64 cm<sup>2</sup>. This high sensitivity reflects the immunosensor's exceptional ability to transduce minute changes in carcinoembryonic antigen concentration into measurable electrical signals, underscoring the efficiency of the rGO-hBNNS nanocomposite in facilitating electron transfer and biomolecular recognition. Further, by integrating the sensor's sensitivity with the experimentally obtained standard deviation at the BSA/Anti-CEA/rGO-hBNNS/ITO nanobiointerface, the lower limit of detection was accurately computed according to the relation in **Eq. [5.9]**. This detailed methodology substantiates the sensor's capability to detect minute concentrations of CEA with high precision and reliability, validating its potential for early-stage detection and precise clinical diagnostics [37].

#### Limit of Detection = $3\sigma/m$ [5.9]

In this context, σ represents the standard deviation calculated from measurements of the blank immunoelectrode (BSA/Anti-CEA/rGO-hBNNS/ITO), which depicts a critical indicator of baseline noise and variability inherent to the sensor platform. The variable m denotes the sensitivity of the biosensor, defined as the slope of the calibration curve reflecting the current response per unit concentration of the target analyte. The integration of these parameters into the detection limit formula enables precise quantification of the sensor's lower limit of detection (LOD), with exceptionally low value at 5.47 pg/mL. This remarkable sensitivity is attributed to the synergistic interplay between the organic functionalities of reduced graphene oxide (rGO) and the inorganic hexagonal boron nitride nanosheets (hBNNS), which collectively enhance electron transfer kinetics, surface area for biomolecule immobilization, and overall signal transduction efficiency.

Moreover, the as-fabricated immunosensor based on the rGO-hBNNS hybrid nanocomposite demonstrates superior performance when compared against a broad spectrum of existing rGO-based immunosensors reported in the literature for biosensing applications (**detailed in Table 5.5**). This enhanced performance encompasses key parameters such as sensitivity, detection limit, response time, and stability, highlighting the innovative material design and optimized fabrication strategy employed. The results remarkably position the rGO-hBNNS nanocomposite as a highly promising candidate for ultrasensitive, reliable, and rapid detection of carcinoembryonic antigen (CEA), offering significant potential for early-stage cancer diagnostics and detecting trace biomarkers in clinical oncology, as comprehensively detailed in **Table 5.5**.

Table 5.5: Evaluation and comparison of rGO-hBNNS-based nano-biosensor metrics with conventional immunosensors.

Sensing Matrix	<b>Detection Technique</b>	Linear Range (ng/mL)	<b>Limit of Detection</b>	Sensitivity	Stability	Ref.
APTES-nYZR	DPV	0.01-50	7.2 pg/mL	0.2 mA·ng <sup>-1</sup> ·mL·mm <sup>-2</sup>	56 Days	[38]
BN-Nanosheets/GCE	EIS	0.1-500	0.017 ng/mL	17 pg/mL	60 days	[39]
PtNP(PPy-PPa)-RGO	EIS	10 - 1000	4 ng/mL	107.08 Ω·cm <sup>2</sup> ·decade <sup>-1</sup>	30 Days	[40]
rGO-PEI-Ag-Nf	DPV	0.5 - 500	0.38 ng/mL	25.29 μA·(log ng/mL) <sup>-1</sup>	28 Days	[41]
AuNP/PEI/rGO	CV, DPV	1 - 50	0.219 ng/mL	0.860 μA·mL·ng <sup>-1</sup> ·cm <sup>-2</sup>	7 Days	[42]
AuNP-rGO	DPV	0.0005 - 4	72.73 ng/mL	7.31 mA·mL·pg <sup>-1</sup>	3 Months	[43]
PS/rGO-MNP-PDA ENF	CV, DPV, EIS	0.5 - 60	0.33 ng/mL	0.354 μA·mL·ng <sup>-1</sup>	-	[44]
L-Methionine/ZrO <sub>2</sub> -RGO	CV, DPV	1 - 20	0.079 ng/mL	4.8 μA·mL·ng <sup>-1</sup> ·cm <sup>-2</sup>	9 Weeks	[45]
Pd <sub>nano</sub> /rGO/PEDOT	EIS, CV	0.2 - 20	0.2 ng/mL	0.375 mA·mL·ng <sup>-1</sup>	8 Weeks	[46]
nHfO <sub>2</sub> -RGO	DPV	0 - 30	0.16 ng/mL	18.24 μA·mL·ng <sup>-1</sup>	27 Days	[47]
ZrO <sub>2</sub> -RGO	CV, DPV	2 - 22	0.122 ng/mL	0.756 μA·mL·ng <sup>-1</sup>	8 Weeks	[37]
h-BNNS/ITO	CV, DPV	0 – 10	22.5 pg/mL	24.84 μA·mL·ng <sup>-1</sup> ·cm <sup>-2</sup>	5 Weeks	[21]
rGO-hBNNS/ITO	DPV, CV	0 - 15	5.47 pg/mL	9. 65 μA·mL·ng <sup>-1</sup> ·cm <sup>-2</sup>	8 Weeks	Present Work

Keywords: CV-Cyclic Voltammetry, DPV- Differential Pulse Voltammetry, EIS- Electrochemical Impedance spectroscopy, nYZR- yttria-doped zirconia-reduced graphene oxide nanocomposite, PS-Polystyrene, MNP-Magnetic Nanoparticle (Fe<sub>3</sub>O<sub>4</sub>), PDA- Polydopamine, ENF- Electrospun Nanofibers.

### **5.3.2.4** Detailed Systematic Investigation of Electroanalytical Performance of rGO-hBNNS/ITO Nano-Biosensor

A extensive series of experiments was carried out to rigorously evaluate the real-time analytical applicability of the BSA/Anti-CEA/rGO-hBNNS/ITO nano-biosensor. These investigations focused on verifying the sensor's enhanced electrochemical performance under the pre-optimized working pH, ensuring reproducibility and consistency of current responses across multiple immunoelectrodes fabricated under identical conditions, and systematically distinguishing appropriate signals from potential false positives. In addition, the studies explored the selectivity of nano-biosensor by examining its response in the presence of various interferents commonly found in real biological samples, assessed its operational stability over extended time periods, and quantitatively analyzed its ability to detect spiked concentrations of CEA antigens in authentic clinical specimens, thereby validating its practical feasibility for accurate and sensitive clinical diagnostics.

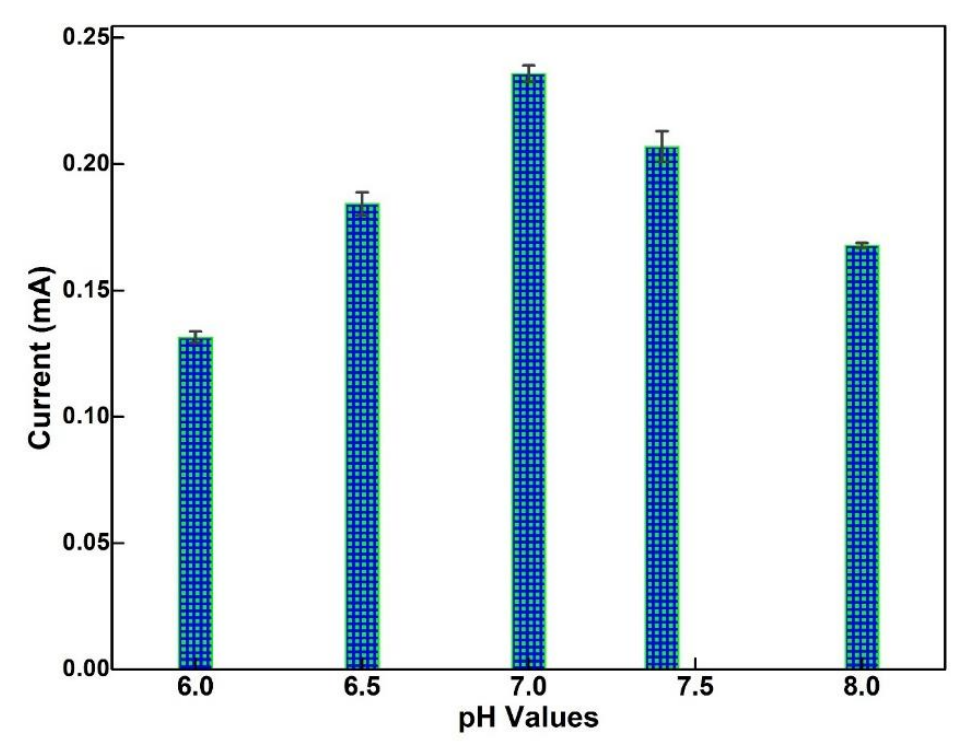


Figure 5.18:Influence of buffer pH on peak DPV current of the Anti-CEA/rGO-hBNNS/ITO immunosensor, demonstrating sensitivity and stability across physiologically relevant pH ranges for optimal electrochemical performance.

Conducting a pH study is a critical prerequisite for the development of a operational, reliable, and practical immunosensor, as it ensures optimal conditions for signal transduction by providing the biochemical environment necessary for optimal antigenantibody interaction (Fig. 5.18). A functional immunosensor converts specific antigenantibody binding events into measurable signals such as electrical, optical, piezoelectric, or calorimetric—through efficient and reversible electron transfer between the electrode surface and the analyte. Achieving this requires high sensitivity in addition to stability in the measured response to the binding event. For this

conversion to be accurate and reproducible, the antibodies immobilized on the sensing surface must operate under conditions that maximize their binding affinity and activity. Therefore, selecting an appropriate buffer system is essential to maintain the structural integrity and reactivity of the immobilized antibodies, ensuring maximal receptivity and precise detection of the target analyte.

A systematic pH optimization study was carried out using differential pulse voltammetry (DPV) at a scan rate of 50 mV/s across a series of phosphate buffer saline (PBS) solutions, each with a concentration of 50 mM and 0.9% NaCl, containing the redox probe Ferro-ferricyanide [5 mM, {Fe(CN)<sub>6</sub><sup>3-/4-</sup>]. The pH of these buffers was carefully varied from 6.0 to 8.0 to investigate the effect of proton concentration on electron transfer kinetics at the electrode interface. The DPV measurements revealed that the maximum anodic peak current was consistently observed at pH 7.0, indicating the most favorable electrochemical environment for electron transfer. In addition, this neutral pH was found to be optimal for maintaining the structural integrity and functional activity of the immobilized biomolecules, ensuring that antibodies and antigens retained their native conformation and reactivity. Consequently, PBS at pH 7.0 was selected as the standardized buffer system for all subsequent electrochemical experiments, providing a stable and reproducible environment for the rGO-hBNNS-based immunosensor and ensuring high sensitivity, reproducibility, and reliability in carcinoembryonic antigen detection.

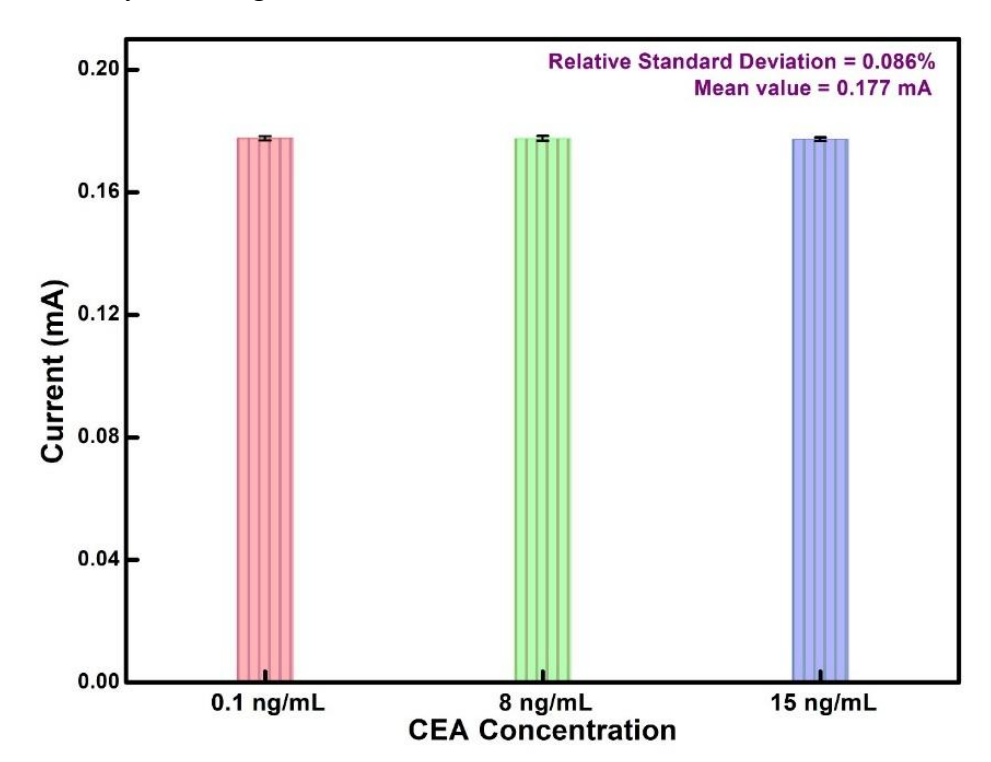


Figure 5.19: Bar graph illustrating the control experiment on rGO-hBNNS/ITO electrodes depicting the negligible electrochemical response upon addition of different CEA concentrations.

To evaluate potential false responses, the behavior of the rGO-hBNNS/ITO electrode without antibody functionalization was examined against that of the BSA/Anti-CEA/rGO-hBNNS/ITO immunoelectrode (**Fig. 5.19**). In this control experiment, three

concentrations of CEA (0.1, 8, and 15 ng/mL) were immobilized on bare rGO-hBNNS/ITO electrodes, shown in Fig. 8a, and the average current response was measured at 0.177 mA. This stable signal confirms that the bare electrode does not respond to antigen binding, verifying that the current changes observed in functionalized immunoelectrodes are solely due to specific antibody-antigen interactions. The low RSD of 0.08% further highlights the high reproducibility and reliability of the electrode, establishing its suitability as a robust baseline for accurate and precise electrochemical biomarker detection.

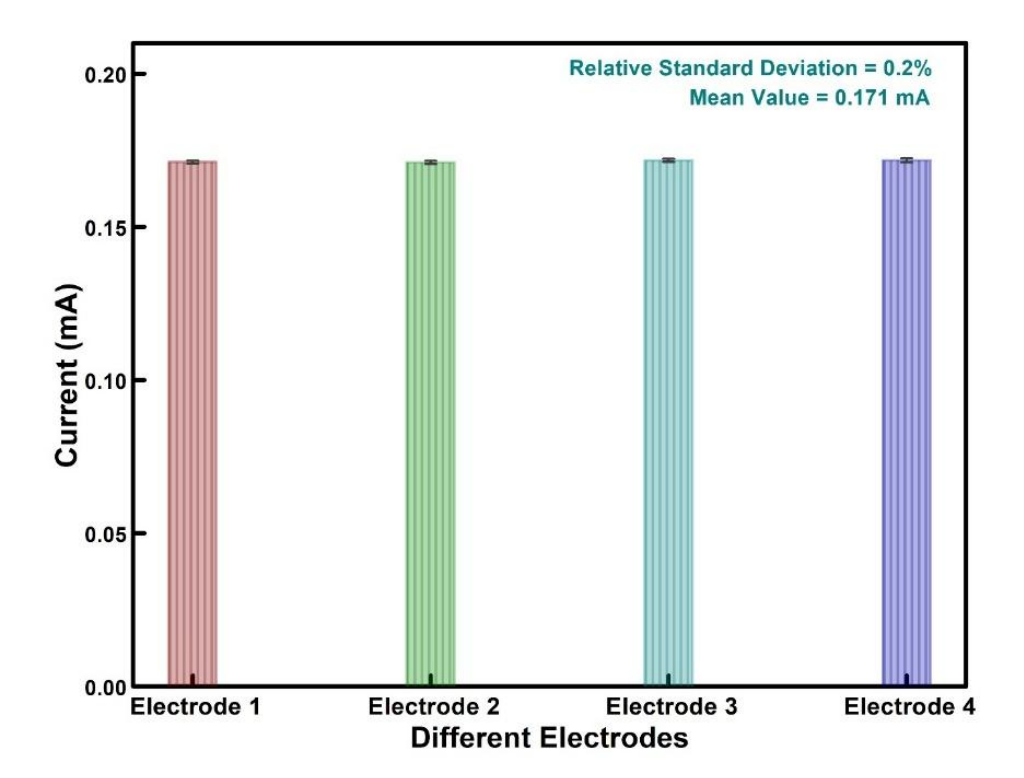


Figure 5.20: Bar graph illustrating the reproducibility of DPV current responses across multiple independently fabricated BSA/Anti-CEA/rGO-hBNNS/ITO immunoelectrodes.

A comprehensive reproducibility assessment was performed to evaluate the consistency and reliability of the electrochemical response of the as-fabricated BSA/Anti-CEA/rGO-hBNNS/ITO immunosensor (Fig. 5.20). Differential pulse voltammetry (DPV) measurements were systematically recorded on four independently fabricated immunoelectrodes after immobilizing a standardized 1 ng/mL concentration of CEA onto each electrode, as illustrated in Fig. 8b. The measured DPV responses demonstrated minimal variation, with an average peak current of 0.171 mA across all four electrodes, reflecting uniform electrochemical performance. Further quantitative analysis revealed a relative standard deviation (RSD) of just 0.2%, which is significantly below the widely accepted threshold of 5% for reproducibility in biosensing applications. This exceptionally low RSD indicates the precise fabrication and uniform surface functionalization of the immunoelectrodes in addition to their ability to deliver consistent, reliable, and repeatable measurements under identical experimental conditions. These findings contribute towards the robustness of the

immunosensor platform and confirm its suitability for repeated, accurate detection of CEA for practical diagnostic applications.

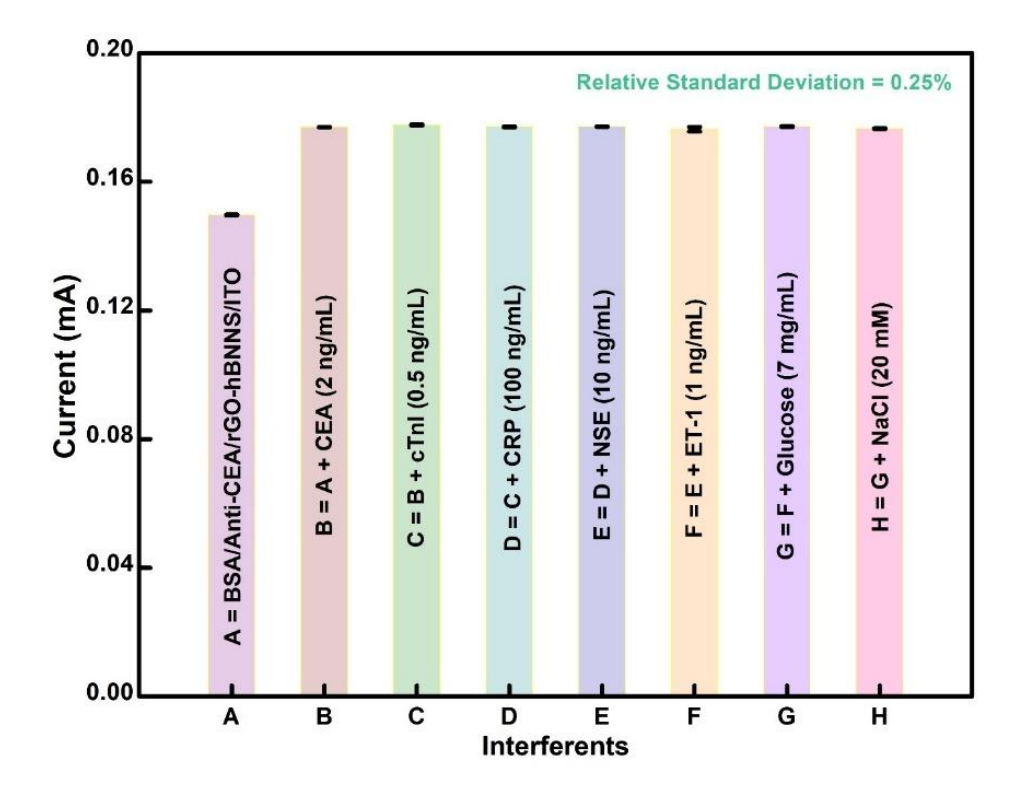


Figure 5.21: Quantitative bar representation of Sequential selectivity evaluation of the BSA/Anti-CEA/rGO-hBNNS/ITO immunoelectrode with stepwise addition of target CEA and potential interferents: (A) BSA/Anti-CEA/rGO-hBNNS/ITO, (B) + CEA (2 ng/mL), (C) + cTnI (0.5 ng/mL), (D) + CRP (100 ng/mL), (E) + NSE (10 ng/mL), (F) + ET-1 (1 ng/mL), (G) + Glucose (7 ng/mL), and (H) + NaCl (20 mM).

Accurate detection of carcinoembryonic antigen (CEA) in human serum requires high selectivity, as serum contains multiple analytes that may interfere with antigenantibody interactions (Fig. 5.21). To ensure clinical relevance, it was imperative to evaluate the specificity of the rGO-hBNNS-based immunosensor for carcinoembryonic antigen (CEA) in the presence of potential interfering biomolecules, including cardiac troponin I (cTnI), C-reactive protein (CRP), neuron-specific enolase (NSE), endothelin-1 (ET-1), glucose, and sodium chloride (NaCl). These interferents, commonly present in serum, could potentially disrupt the precise binding interaction between CEA and the BSA/Anti-CEA/rGO-hBNNS/ITO immunoelectrode, thereby compromising detection accuracy. To rigorously assess selectivity, the immunosensor was systematically tested by introducing successive concentrations of these interfering analytes, and the differential pulse voltammetry (DPV) technique was employed to monitor any deviations in the electrochemical response, as illustrated in Fig. 8c. Table S3, further corroborates the exceptional selectivity of the fabricated immunosensor toward CEA, demonstrating that the current response of the CEA/BSA/Anti-CEA/rGOhBNNS/ITO interface remained stable and unaffected despite the presence of interfering substances. The observed relative standard deviation (RSD) of 0.25%

depicts the highly selective and reproducible behavior of the immunosensor, confirming that it can reliably distinguish the target antigen from other coexisting biomolecules in complex biological matrices. This analysis highlights that the rGO-hBNNS-based nano-biosensor not only ensures precise and specific detection of CEA but also maintains robustness, stability, and practical applicability in clinical diagnostics, reinforcing its potential as a reliable platform for real-time serum analysis.

Table 5. 6: Differential pulse voltammetry (DPV) response and corresponding relative standard deviation (RSD%) upon sequential addition of various interfering analytes to evaluate the selectivity of the fabricated rGO-hBNNS/ITO nano-biosensor.

Crossing Reagents	Concentration of Interferent Added	Current Change (mA)			Average Response	RSD (10 <sup>-3</sup> ,
		1	2	3		<b>%</b> )
A = BSA/Anti- CEA/rGO- hBNNS/ITO	-	0.1498	0.1496	0.1494	$0.1496 \pm (1.80 \times 10^{-4})$	-
$\mathbf{B} = \mathbf{A} + \mathbf{CEA}$	2 ng/mL	0.1769	0.1770	0.1768	$0.1769 \pm (1.35 \times 10^{-4})$	0.76
C = B + cTnI	0.5 ng/mL	0.1779	0.1774	0.1774	$0.1776 \pm (3.01 \times 10^{-4})$	1.70
$\mathbf{D} = \mathbf{C} + \mathbf{CRP}$	100 ng/mL	0.1768	0.1769	0.1773	$0.1770 \pm (2.43 \times 10^{-4})$	1.37
$\mathbf{E} = \mathbf{D} + \mathbf{NSE}$	10 ng/mL	0.1771	0.1772	0.1770	$0.1771 \pm (9.50 \times 10^{-5})$	0.53
$\mathbf{F} = \mathbf{E} + \mathbf{ET-1}$	1 ng/mL	0.1753	0.1758	0.1777	$0.176 \pm (1.24 \times 10^{-3})$	7.00
G = F+Glucose	7 mg/mL	0.1769	0.1772	0.1772	$0.1771 \pm (2.05 \times 10^{-4})$	1.16
H = G + NaCl	20 mM	0.1766	0.1761	0.1766	$0.1764 \pm (2.67 \times 10^{-4})$	1.51

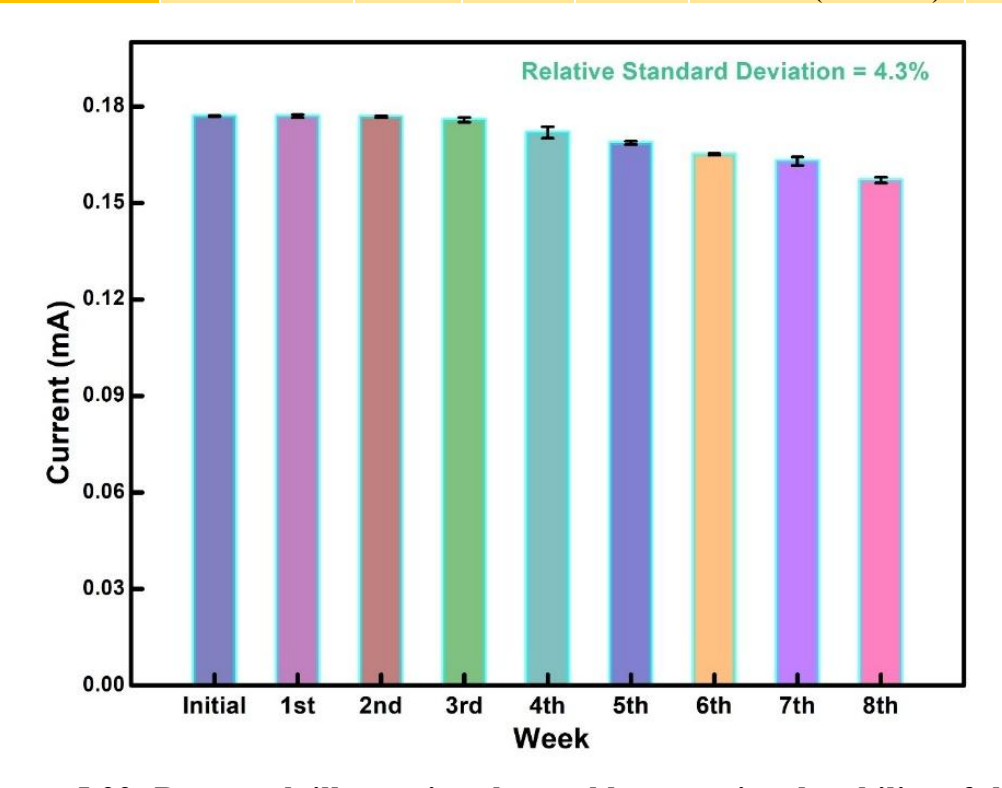


Figure 5.22: Bar graph illustrating the weekly operational stability of the asfabricated BSA/Anti-CEA/rGO-hBNNS/ITO immunosensor, confirming sustained sensor activity.

To ascertain the long-term shelf-life and clinical storage stability of the CEA-immobilized BSA/Anti-CEA/rGO-hBNNS/ITO immunoelectrode, a comprehensive shelf-life study was evaluated using differential pulse voltammetry (DPV), as illustrated in Fig. 5.22. The immunosensor was stored under controlled conditions at 4 °C, and weekly DPV measurements were conducted to monitor the preservation of its electrochemical response over time, ensuring its suitability for long-term real-time applications. Over the eight-week period, the DPV current retained 88.74% of its initial magnitude, indicating minimal degradation in sensor performance. The associated relative standard deviation (RSD) was calculated to be 4.3%, which falls well within the acceptable threshold of <5%, demonstrating the consistency and reliability of the fabricated nano-biosensor. These findings conclusively depict the exceptional storage robustness and operational longevity of the immunosensor, highlighting its potential for practical clinical applicability with enhanced reproducibility and stability over extended periods.

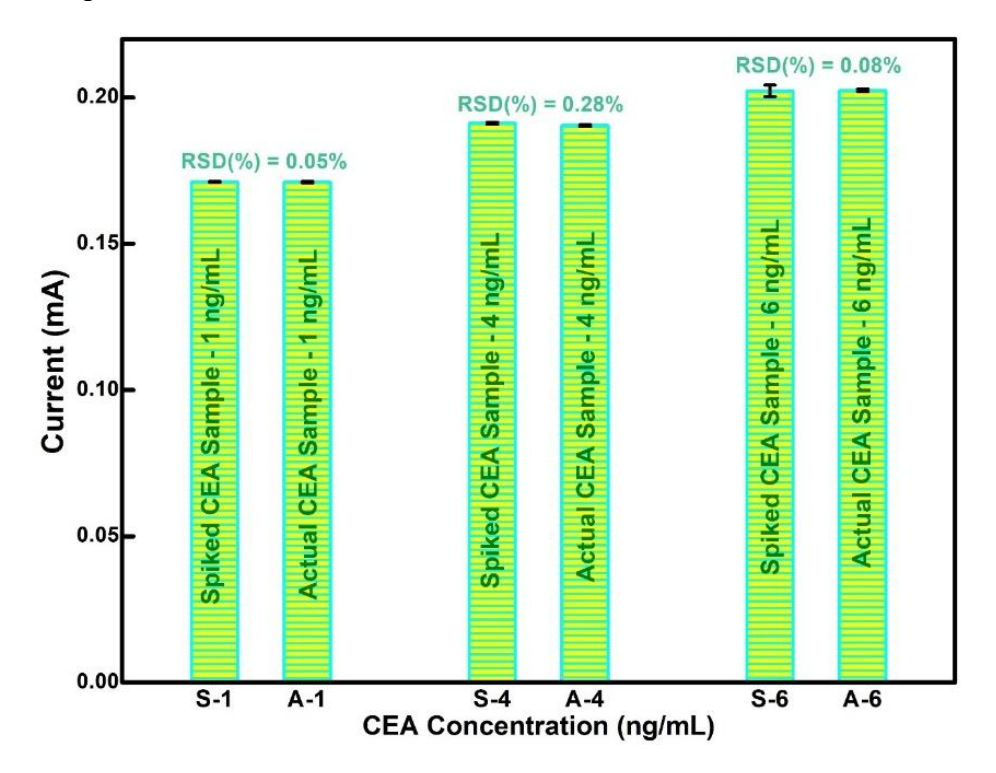


Figure 5.23: Real-sample validation of the CEA/BSA/Anti-CEA/rGO-hBNNS/ITO immunoelectrode through controlled spiked serum experiments to quantify its sensitivity, reproducibility, and reliability for clinical applications.

To evaluate the real-time clinical applicability of the BSA/Anti-CEA/rGO-hBNNS/ITO immunoelectrode, human serum samples were first verified for authenticity and compositional integrity (**Fig. 5.23**). The study focused on assessing the immunosensor's capacity to detect CEA within a biologically relevant environment containing various endogenous analytes. Known concentrations of CEA were spiked into these serum samples, and the DPV response of the spiked samples (S) was meticulously compared against the DPV response from the actual CEA concentrations (A). This comparative analysis provided a detailed understanding of the sensor's

accuracy, sensitivity, and reliability in detecting target antigens under realistic conditions. As shown in **Fig. 5.23**, the consistent peak currents across actual and spiked samples underscore the immunoelectrode's excellent performance, highlighting its robustness in maintaining precise antigen-antibody interactions and stable electron transfer, while demonstrating its readiness for deployment in clinical diagnostics and point-of-care applications.

Table 5.7: Quantitative evaluation of recovery currents and RSD (%) for spiked CEA concentrations in human serum with actual concentrations, illustrating the capability of the BSA/Anti-CEA/rGO-hBNNS/ITO immunoelectrode to achieve consistent, precise, and clinically relevant measurements.

CEA Concentration (ng/mL)	Average Current for Standard CEA Sample (A, in mA)	Average Current for Spiked CEA Sample (S, in mA)	RSD (%)	Recovery %
1	$0.17106 \pm (5.50 \times 10^{-4})$	0.17118± (3.65 × 10 <sup>-4</sup> )	0.04	100.07
4	$0.19041\pm (5.82 \times 10^{-4})$	0.19116± (6.68 × 10 <sup>-4</sup> )	0.27	100.39
6	$0.20246 \pm (7.31 \times 10^{-4})$	$0.20223\pm (3.43 \times 10^{-3})$	0.08	99.88

A detailed analysis of the DPV current responses, presented in **Table 5.7**, demonstrates a striking agreement between standard CEA solutions and CEA spiked into human serum samples, affirming the exceptional analytical performance of the BSA/Anti-CEA/rGO-hBNNS/ITO immunoelectrode in clinically relevant conditions. For standard concentrations of 1, 4, and 6 ng/mL, the average peak currents recorded were  $0.171 \pm (5.5 \times 10^{-4})$  mA,  $0.190 \pm (5.8 \times 10^{-4})$  mA, and  $0.202 \pm (7.3 \times 10^{-4})$  mA, respectively, while the corresponding spiked serum samples produced peak currents of  $0.171 \pm (3.7 \times 10^{-4})$  mA,  $0.191 \pm (6.7 \times 10^{-4})$  mA, and  $0.202 \pm (3.4 \times 10^{-3})$  mA, reflecting near-perfect correspondence between standard and real-sample measurements. The exceptionally low RSD values of 0.05%, 0.28%, and 0.08% further confirm the precision, reproducibility, and stability of the immunosensor across repeated measurements. These results clearly indicate that the fabricated BSA/Anti-CEA/rGO-hBNNS/ITO nano-biosensor maintains high sensitivity and specificity for CEA detection, effectively minimizing errors due to sample variability or interfering biomolecules in complex clinical serum matrices. Consequently, the BSA/Anti-CEA/rGO-hBNNS/ITO immunoelectrode demonstrates robust performance for clinical diagnostics, ensuring minimal interference from endogenous analytes, which is vital for reliable NSCLC prognosis and monitoring.

### **Conclusion**

In summary, the present study strategically leverages the synergistic integration of organic-inorganic hybrid nanocomposites to construct an advanced nano-biosensing platform tailored for the ultrasensitive, rapid, cost-effective, and label-free detection of serum tumor markers associated with non-small cell lung cancer (NSCLC). The

hydrothermally synthesized rGO-hBNNS hybrid nanocomposite demonstrated a substantial enhancement in electrocatalytic activity, approximately ~29% higher than bare hBNNS, attributable to optimized crosslinking kinetics and superior electron transfer at the nano-biointerface. The combination of amine-terminated hBNNS with carboxyl-functionalized rGO nanosheets generated an interface densely populated with reactive surface sites, which facilitated the efficient and stable immobilization of Anti-CEA antibodies. This structured nano-biointerface significantly amplified the antibody loading capacity, directly translating into exceptional sensitivity of the immunosensor. Remarkably, this optimized design enabled the detection of carcinoembryonic antigen (CEA) at an ultralow limit of 5.47 pg/mL, ensuring applicability for early-stage NSCLC monitoring. In addition, the BSA/Anti-CEA/rGO-hBNNS/ITO immunoelectrode exhibited outstanding storage stability over 8 weeks under standard conditions and maintained high selectivity even in the presence of multiple potential serum interferents, including proteins and ions. Clinical relevance was further corroborated through spiked human serum sample analyses, which yielded excellent recovery rates, confirming the robustness and reliability of the sensor in real-world biological matrices. Overall, these findings establish the rGO-hBNNS-based nano-biosensor as a robust, highly sensitive, and clinically applicable platform capable of facilitating accurate, realtime monitoring of critical tumor biomarkers in biological fluids, representing a significant advancement in the development of next-generation diagnostic tools for NSCLC.

#### References

- [1] N.B. Singh, S.K. Shukla, Chapter 3 Properties of two-dimensional nanomaterials, in: R. Khan, S. Barua (Eds.) Two-Dimensional Nanostructures for Biomedical Technology, Elsevier, 2020, pp. 73-100.
- [2] H. Ma, Y. Xing, B. Cui, J. Han, B. Wang, Z. Zeng, Recent advances in two-dimensional layered and non-layered materials hybrid heterostructures, Chinese Physics B, 31 (2022) 108502.
- [3] A.K. Geim, I.V. Grigorieva, Van der Waals heterostructures, Nature, 499 (2013) 419-425.
- [4] K. Zhang, Y. Feng, F. Wang, Z. Yang, J. Wang, Two dimensional hexagonal boron nitride (2D-hBN): synthesis, properties and applications, Journal of Materials Chemistry C, 5 (2017) 11992-12022.
- [5] A.E. Naclerio, P.R. Kidambi, A Review of Scalable Hexagonal Boron Nitride (h-BN) Synthesis for Present and Future Applications, Advanced Materials, 35 (2023) 2207374.
- [6] T.A. Shifa, F. Wang, Y. Liu, J. He, Heterostructures Based on 2D Materials: A Versatile Platform for Efficient Catalysis, Advanced Materials, 31 (2019) 1804828.
- [7] H. Chen, D.-e. Jiang, Z. Yang, S. Dai, Engineering Nanostructured Interfaces of Hexagonal Boron Nitride-Based Materials for Enhanced Catalysis, Accounts of Chemical Research, 56 (2023) 52-65.
- [8] P. Gomez-Romero, Hybrid Organic-Inorganic Materials—In Search of Synergic Activity, Advanced Materials, 13 (2001) 163-174.
- [9] S. Wang, Y. Kang, L. Wang, H. Zhang, Y. Wang, Y. Wang, Organic/inorganic hybrid sensors: A review, Sensors and Actuators B: Chemical, 182 (2013) 467-481.
- [10] A.C. Grimsdale, K. Müllen, The Chemistry of Organic Nanomaterials, Angewandte Chemie International Edition, 44 (2005) 5592-5629.
- [11] Y. Guo, K. Xu, C. Wu, J. Zhao, Y. Xie, Surface chemical-modification for engineering the intrinsic physical properties of inorganic two-dimensional nanomaterials, Chemical Society Reviews, 44 (2015) 637-646.

- [12] B.H. Alshammari, M.M.A. Lashin, M.A. Mahmood, F.S. Al-Mubaddel, N. Ilyas, N. Rahman, M. Sohail, A. Khan, S.S. Abdullaev, R. Khan, Organic and inorganic nanomaterials: fabrication, properties and applications, RSC Advances, 13 (2023) 13735-13785.
- [13] M. Sarno, D. Scarpa, A. Senatore, W. Ahmed Abdalglil Mustafa, rGO/GO Nanosheets in Tribology: From the State of the Art to the Future Prospective, Lubricants, 8 (2020) 31.
- [14] M.J. Molaei, M. Younas, M. Rezakazemi, A Comprehensive Review on Recent Advances in Two-Dimensional (2D) Hexagonal Boron Nitride, ACS Applied Electronic Materials, 3 (2021) 5165-5187.
- [15] A.F. Khan, D.A.C. Brownson, E.P. Randviir, G.C. Smith, C.E. Banks, 2D Hexagonal Boron Nitride (2D-hBN) Explored for the Electrochemical Sensing of Dopamine, Analytical Chemistry, 88 (2016) 9729-9737.
- [16] A. Batool, T.A. Sherazi, S.A.R. Naqvi, Organic–Inorganic Nanohybrid-Based Electrochemical Biosensors, in: K. Rizwan, M. Bilal, T. Rasheed, T.A. Nguyen (Eds.) Hybrid Nanomaterials: Biomedical, Environmental and Energy Applications, Springer Nature Singapore, Singapore, 2022, pp. 151-173.
- [17] T. Mousavand, S. Takami, M. Umetsu, S. Ohara, T. Adschiri, Supercritical hydrothermal synthesis of organic-inorganic hybrid nanoparticles, Journal of Materials Science, 41 (2006) 1445-1448.
- [18] N.G. Welch, J.A. Scoble, B.W. Muir, P.J. Pigram, Orientation and characterization of immobilized antibodies for improved immunoassays (Review), Biointerphases, 12 (2017).
- [19] F. Vivanco-Martínez, R. Bragado, J.P. Albar, C. Juarez, F. Ortíz-Masllorens, Chemical modification of carboxyl groups in human Fc $\gamma$  fragment: Structural role and effect on the complement fixation, Molecular Immunology, 17 (1980) 327-336.
- [20] S.K. Vashist, Comparison of 1-Ethyl-3-(3-Dimethylaminopropyl) Carbodiimide Based Strategies to Crosslink Antibodies on Amine-Functionalized Platforms for Immunodiagnostic Applications, Diagnostics, 2 (2012) 23-33.
- [21] K. Sharma, N.K. Puri, B. Singh, An efficient electrochemical nano-biosensor based on hydrothermally engineered ultrathin nanostructures of hexagonal boron nitride nanosheets for label-free detection of carcinoembryonic antigen, Applied Nanoscience, (2023) 1-14.
- [22] S. Yang, W. Yue, D. Huang, C. Chen, H. Lin, X. Yang, A facile green strategy for rapid reduction of graphene oxide by metallic zinc, RSC Advances, 2 (2012) 8827-8832.
- [23] R. Debbarma, S. Behura, P. Nguyen, T.S. Sreeprasad, V. Berry, Electrical Transport and Network Percolation in Graphene and Boron Nitride Mixed-Platelet Structures, ACS Applied Materials & Interfaces, 8 (2016) 8721-8727.
- [24] K. Sharma, N.K. Puri, Enhanced electrochemical performance of hydrothermally exfoliated hexagonal boron nitride nanosheets for applications in electrochemistry, Journal of The Electrochemical Society, 168 (2021) 056512.
- [25] A.C. Ferrari, J. Robertson, Interpretation of Raman spectra of disordered and amorphous carbon, Physical Review B, 61 (2000) 14095-14107.
- [26] M.A. Pimenta, G. Dresselhaus, M.S. Dresselhaus, L.G. Cançado, A. Jorio, R. Saito, Studying disorder in graphite-based systems by Raman spectroscopy, Physical Chemistry Chemical Physics, 9 (2007) 1276-1290.
- [27] K. Krishnamoorthy, M. Veerapandian, K. Yun, S.J. Kim, The chemical and structural analysis of graphene oxide with different degrees of oxidation, Carbon, 53 (2013) 38-49.
- [28] H. Purwaningsih, N.M.I.P. Suari, W. Widiyastuti, H. Setyawan, Preparation of rGO/MnO2 Composites through Simultaneous Graphene Oxide Reduction by Electrophoretic Deposition, ACS Omega, 7 (2022) 6760-6767.
- [29] Y.-H. Yao, J. Li, H. Zhang, H.-L. Tang, L. Fang, G.-D. Niu, X.-J. Sun, F.-M. Zhang, Facile synthesis of a covalently connected rGO–COF hybrid material by in situ reaction for enhanced visible-light induced photocatalytic H2 evolution, Journal of Materials Chemistry A, 8 (2020) 8949-8956.

- [30] M.F.R. Hanifah, J. Jaafar, M.H.D. Othman, A.F. Ismail, M.A. Rahman, N. Yusof, W.N.W. Salleh, F. Aziz, Facile synthesis of highly favorable graphene oxide: Effect of oxidation degree on the structural, morphological, thermal and electrochemical properties, Materialia, 6 (2019) 100344.
- [31] A. Mathkar, D. Tozier, P. Cox, P. Ong, C. Galande, K. Balakrishnan, A. Leela Mohana Reddy, P.M. Ajayan, Controlled, stepwise reduction and band gap manipulation of graphene oxide, The journal of physical chemistry letters, 3 (2012) 986-991.
- [32] G. Socrates, Infrared and Raman characteristic group frequencies: tables and charts, John Wiley & Sons, 2004.
- [33] A. Martínez Cortizas, O. López-Costas, Linking structural and compositional changes in archaeological human bone collagen: an FTIR-ATR approach, Scientific Reports, 10 (2020) 17888.
- [34] O. Suys, A. Derenne, E. Goormaghtigh, ATR-FTIR Biosensors for Antibody Detection and Analysis, International Journal of Molecular Sciences, 23 (2022) 11895.
- [35] A. Sibai, K. Elamri, D. Barbier, N. Jaffrezic-Renault, E. Souteyrand, Analysis of the polymer-antibody-antigen interaction in a capacitive immunosensor by FTIR difference spectroscopy, Sensors and Actuators B: Chemical, 31 (1996) 125-130.
- [36] N. Elgrishi, K.J. Rountree, B.D. McCarthy, E.S. Rountree, T.T. Eisenhart, J.L. Dempsey, A Practical Beginner's Guide to Cyclic Voltammetry, Journal of Chemical Education, 95 (2018) 197-206.
- [37] S. Kumar, J.G. Sharma, S. Maji, B.D. Malhotra, Nanostructured zirconia decorated reduced graphene oxide based efficient biosensing platform for non-invasive oral cancer detection, Biosensors and Bioelectronics, 78 (2016) 497-504.
- [38] S. Kumar, N. Gupta, B.D. Malhotra, Ultrasensitive biosensing platform based on yttria doped zirconia-reduced graphene oxide nanocomposite for detection of salivary oral cancer biomarker, Bioelectrochemistry, 140 (2021) 107799.
- [39] B. Öndeş, U. Kilimci, M. Uygun, D.A. Uygun, Determination of carcinoembryonic antigen (CEA) by label-free electrochemical immunosensor using functionalized boron nitride nanosheets, Bioelectrochemistry, (2024) 108676.
- [40] N. Puri, S.K. Mishra, A. Niazi, A.K. Srivastava, Rajesh, Physicochemical characteristics of reduced graphene oxide based Pt-nanoparticles-conducting polymer nanocomposite film for immunosensor applications, Journal of Chemical Technology & Biotechnology, 90 (2015) 1699-1706.
- [41] Y. Wang, D. Ma, G. Zhang, X. Wang, J. Zhou, Y. Chen, X. You, C. Liang, Y. Qi, Y. Li, An electrochemical immunosensor based on SPA and rGO-PEI-Ag-Nf for the detection of arsanilic acid, Molecules, 27 (2021) 172.
- [42] X. Liu, L.-Y. Lin, F.-Y. Tseng, Y.-C. Tan, J. Li, L. Feng, L. Song, C.-F. Lai, X. Li, J.-H. He, Label-free electrochemical immunosensor based on gold nanoparticle/polyethyleneimine/reduced graphene oxide nanocomposites for the ultrasensitive detection of cancer biomarker matrix metalloproteinase-1, Analyst, 146 (2021) 4066-4079.
- [43] S. Verma, A. Singh, A. Shukla, J. Kaswan, K. Arora, J. Ramirez-Vick, P. Singh, S.P. Singh, Anti-IL8/AuNPs-rGO/ITO as an immunosensing platform for noninvasive electrochemical detection of oral cancer, ACS applied materials & interfaces, 9 (2017) 27462-27474.
- [44] S. Ketmen, S. Er Zeybekler, S.S. Gelen, D. Odaci, Graphene Oxide-Magnetic Nanoparticles Loaded Polystyrene-Polydopamine Electrospun Nanofibers Based Nanocomposites for Immunosensing Application of C-Reactive Protein, Biosensors, 12 (2022) 1175.
- [45] P.K. Gupta, S. Tiwari, Z.H. Khan, P.R. Solanki, Amino acid functionalized ZrO 2 nanoparticles decorated reduced graphene oxide based immunosensor, Journal of Materials Chemistry B, 5 (2017) 2019-2033.

- [46] S. Gupta, U. Jain, B.T. Murti, A.D. Putri, A. Tiwari, N. Chauhan, Nanohybrid-based immunosensor prepared for Helicobacter pylori BabA antigen detection through immobilized antibody assembly with@Pdnano/rGO/PEDOT sensing platform, Scientific Reports, 10 (2020) 21217.
- [47] S. Kumar, S. Kumar, S. Augustine, S. Yadav, B.K. Yadav, R.P. Chauhan, A.K. Dewan, B.D. Malhotra, Effect of Brownian motion on reduced agglomeration of nanostructured metal oxide towards development of efficient cancer biosensor, Biosens. Bioelectron., 102 (2018) 247-255.

## Chapter 6

# Fabrication of a Self-assembled 3D-2D Nano-Hybrid Composite combining hBNNS and $Cu/Cu_XO$ nanoflowers for High-Performance Electrochemical detection of the CEA Biomarker

This chapter explores the potential of nano-hybrid composites (NHCs), which synergistically integrate metallic nanoflowers and semiconducting nanosheets, demonstrating unparalleled promise in the development of nano-biosensors with superior stability, sensitivity, and selectivity. This study reports the fabrication of a 3D-2D self-assembled NHC comprising hydrothermally copper/copper oxide nanoflowers (CuxO) integrated with hexagonal boron nitride nanosheets (Cu/Cu<sub>X</sub>O-hBNNS) for label-free detection of carcinoembryonic antigen (CEA). A comprehensive characterization of Cu<sub>X</sub>O-NF, hBNNS, and Cu/Cu<sub>X</sub>OhBNNS NHC was performed using advanced spectroscopic techniques and nanoscale imaging. Uniform films of Cu/Cu<sub>X</sub>O-hBNNS were successfully deposited onto prehydrolyzed ITO electrodes via electrophoretic deposition (EPD) at a low DC potential of 15V. Optimization of key parameters, including antibody incubation time, electrolyte pH, and the reduction of negative control, ensured high immunoelectrode efficiency. The Cu/Cu<sub>X</sub>O-hBNNS platform demonstrated approximately 74% and 31% enhancements in cyclic voltammetry (CV) and differential pulse voltammetry (DPV) responses, respectively, along with a three-fold increase in diffusion coefficient compared to bare hBNNS. These improvements were driven by the superior electrocatalytic activity of Cu<sub>X</sub>O-NFs. The porous architecture of Cu/Cu<sub>X</sub>O-hBNNS, coupled with multifunctional groups, facilitated high-density immobilization, enhanced binding affinity, and site-specific anchoring of Anti-CEA. The BSA/Anti-CEA/Cu/Cu<sub>X</sub>OhBNNS/ITO nano-biosensor exhibited a wide dynamic range (0-50 ng/mL) and achieved an ultralow detection limit of 3.22 pg/mL ( $R^2 = 0.99998$ ), demonstrating  $\sim 7$ times improved LOD in comparison to hBNNS-based immunosensors utilizing [Fe(CN)<sub>6</sub>]<sup>3-/4-</sup> as a redox probe. Clinical studies further validated the sensor's remarkable shelf life, minimal cross-reactivity, and robust recovery rates in human serum, highlighting its potential for precise and reliable early-stage cancer detection.

The research findings detailed in this chapter have been published in a scientific journal: "Self-assembled nano-hybrid composite based on Cu/CuxO nanoflower decorated onto hBNNS for high-performance and ultra-sensitive electrochemical detection of CEA biomarker" Bioelectrochemistry, 2025 (165) 108993

#### 6.1 Introduction

Cutting-edge nano-biosensors, synergistically integrating nanotechnology with bioanalytical sensing, have emerged as transformative tools for achieving rapid, highly precise, and ultra-sensitive point-of-care diagnostics [1, 2]. These systems are revolutionizing early disease detection, real-time monitoring, and personalized therapeutic interventions by offering unprecedented speed and sensitivity in biomarker quantification. The remarkable progress in this field has been fueled by continuous advancements in nano-engineering techniques, including the fabrication of multifunctional nano-hybrid composites [3], modulation of interfacial properties [4], strategic defect engineering [5], hierarchical structural optimization [6], and targeted surface functionalization [7]. Each of these approaches contributes uniquely to enhancing sensor performance by improving charge transfer kinetics, maximizing binding affinity, and expanding the structural versatility of biosensing interfaces. Among the various strategies, the development of self-assembled nano-hybrid composites (NHCs) has gained significant attention as they provide a powerful means of integrating nanostructures with varied morphologies, sizes, and compositions into a single functional platform [8]. This integration fosters synergistic interactions that amplify the mechanical stability, electronic conductivity, and catalytic reactivity of the biosensor. The principle of self-assembly is particularly advantageous, as it relies on thermodynamically favorable interactions such as hydrogen bonding, van der Waals forces, coordination chemistry, and electrostatic interactions, which collectively enable spontaneous organization of nanoscale components without the need for external intervention. Beyond structural integration, self-assembly provides a finely tuned microenvironment that facilitates the optimal orientation and immobilization of antibodies, particularly the fragment crystallizable (Fc) region, thereby ensuring improved antigen recognition and enhanced signal transduction. By reinforcing Fc binding interactions on the biosensing interface, this approach significantly boosts electrocatalytic activity while maintaining long-term operational stability. Consequently, this research emphasizes the deliberate use of self-assembly principles to advance next-generation nano-biosensors capable of delivering reliable and clinically relevant diagnostic outcomes.

To develop nano-biosensors with long-term operational stability, hexagonal boron nitride nanosheets (hBNNS), widely recognized as "white graphene," have emerged as a highly promising inorganic layered material. As a lightweight group III-nitride compound, hBNNS represents a lightweight and robust compound that exhibits remarkable potential for sustainable electrochemical applications. Its exceptional chemical and thermal stability, withstanding temperatures up to ~1100 °C, combined with superior mechanical strength, makes it an ideal platform for applications requiring durability and consistency [9, 10]. Unlike many conventional nanomaterials prone to oxidation, degradation, or agglomeration, hBNNS provides intrinsic resistance against these challenges, thereby ensuring persistent electrochemical performance, structural integrity, long-term durability, and reproducible catalytic performance for promising nano-biosensing performance.

Furthermore, hBNNS possesses a wide bandgap strengthens electrochemical performance by minimizing undesirable electronic interactions and interference during electrochemical measurements [11], thereby increasing the accuracy and selectivity of

biosensor performance. Its inherently high surface area contributes to the exposure of abundant active sites, significantly enhancing sensitivity, catalytic efficiency, and analyte binding capacity [12]. Complementing these advantages, the material's low dielectric constant plays a key role in reducing energy dissipation, maintaining signal integrity, and suppressing background noise, which is particularly important for detecting trace-level biomarkers [13]. Additionally, the robust barrier properties of hBNNS offer protection against environmental degradation from moisture, oxygen, and other contaminants, reinforcing its robustness under practical conditions [14].

Nevertheless, despite these superior physicochemical attributes, hBNNS suffers from limitations arising from its wide bandgap and strong intralayer covalent bonding, which significantly hinder charge transfer kinetics and restrict its ability to immobilize biomolecules such as antibodies. To overcome these inherent challenges, researchers have developed several modification strategies to enhance its electro-catalytic properties, with the incorporation of hybrid metal and metal oxide nanostructures proving especially effective. Among these, Cu/Cu<sub>X</sub>O hybrids have gained significant attention owing to their synergistic physicochemical characteristics [15, 16]. These hybrid structures exhibit outstanding electrocatalytic activity, high surface sensitivity, and superior electrical conductivity while simultaneously introducing bandgap tunability and structural stability into the composite system.

The unique contribution of copper lies in its abundance, cost-effectiveness, and favorable electronic configuration. Metallic copper (Cu), with its [Ar]  $3d^{10}$   $4s^1$  configuration, facilitates rapid electron transfer by minimizing charge transfer resistance, thereby boosting electrochemical responsiveness. Meanwhile, copper oxides (Cu<sub>X</sub>O), leveraging the [Ar]  $3d^9$  and [Ar]  $3d^{10}$  redox states of Cu<sup>+</sup>/Cu<sup>2+</sup>, catalyze oxidation reactions of biomolecules with high efficiency. Together, these complementary mechanisms provide a synergistic effect that not only compensates for the limitations of pristine hBNNS but also significantly improves the overall functionality of the hybrid material.

By coupling hBNNS with Cu/Cu<sub>X</sub>O nanostructures, the resulting hybrid system demonstrates enhanced electrocatalytic activity, improved stability, and superior electron transfer kinetics, making it a robust platform for biosensing applications. The integrated properties of structural stability, conductivity, biocompatibility, and redox efficiency position Cu/Cu<sub>X</sub>O-hBNNS hybrids as a breakthrough material system for developing reliable, long-lasting, and ultra-sensitive biosensors tailored for point-of-care clinical and diagnostic environments.

The development of a high-performance electrochemical nano-biosensor integrating three-dimensional (3D) Cu/Cu<sub>X</sub>O nanoflowers with two-dimensional (2D) hexagonal boron nitride nanosheets (hBNNS) represents a significant advancement in the field of diagnostic technologies. This hierarchical nanostructure harnesses the complementary physicochemical properties of both components: the Cu/Cu<sub>X</sub>O nanoflowers contribute abundant porous channels and reactive sites for biomolecule immobilization, while hBNNS provides a chemically stable, wide-surface-area platform with exceptional structural integrity. Together, they create a robust self-assembled nano-hybrid composite capable of ultra-sensitive, label-free detection of the CEA biomarker, a crucial indicator in early cancer diagnosis.

Fabrication of the Cu/Cu<sub>X</sub>O-hBNNS hybrid composite was accomplished through a hydrothermal synthesis approach, which exploited autogenous temperature and pressure conditions to drive spontaneous self-assembly of nanoscale components [17]. This method ensured the production of highly pure, crystalline, and functionalized nanomaterials at relatively low synthesis temperatures, mitigating risks of nanostructure loss or deterioration. The ordered assembly was governed by molecular interactions such as Cu–N, Cu–H, N–H, and B–H bonding, which stabilized the hybrid architecture. FTIR spectroscopy provided critical evidence of these interactions, confirming successful functionalization and structural integration of the composite. The resulting material exhibits both mechanical resilience and chemical durability, making it suitable for long-term biosensing applications.

To enhanced bio-affinity of nano-biointerface, Cu/CuxO-hBNNS surface provides abundant surface active sites that enables efficient immobilization of Anti-CEA antibodies by directly conjugating their fragment crystallizable (Fc) regions. This strong adsorption-driven anchoring ensures improved antibody orientation, reduced steric hindrance, and enhanced accessibility of antigen-binding sites, thereby maximizing the efficiency of antigen-antibody interactions. The 3D Cu/Cu<sub>X</sub>O nanoflowers further accelerate electrocatalytic activity by facilitating rapid electron transfer, lowering overpotential, and amplifying the electrochemical signal response, while hBNNS maintains stability by preventing degradation or denaturation of immobilized biomolecules. The Cu/Cu<sub>X</sub>O-hBNNS nano-biosensor under optimized experimental conditions exhibits a remarkable sensitivity, achieving an exceptionally low detection limit that extends well within the physiological concentration range of the CEA biomarker. Its performance surpasses that of conventional biosensors fabricated from metals, metal oxides and semiconductors but also ensures operational reliability, cost-effectiveness, and scalability. By effectively combining nanoscale selfassembly, hierarchical architecture, and precision bio-functionalization, the Cu/Cu<sub>X</sub>OhBNNS-based biosensor establishes a new paradigm for advanced cancer diagnostics.

### **6.2** Experimental Section:

#### **6.2.1** Chemical, Reagents and Instrumentation:

To implement the experiments in this study, only analytical-grade chemicals and reagents of verified purity were selected to eliminate potential contamination sources and ensure high-precision measurements. The essential chemicals and reagents, including bovine serum albumin (BSA, >96%), ethylene glycol (OHCH2CH2OH, >99%), h-BN powder (98%, 5µm-particle size), sodium chloride (NaCl, >99%), 1-(3-(dimethylamino)-propyl)-3-ethylcarbodiimide hydrochloride (EDC, >98%), potassium bromide (KBr, >99%), carcinoembryonic antigen (CEA), N-hydroxysuccinimide (NHS, 96%), and monoclonal antibodies of CEA were obtained from Sigma Aldrich. While, additional significant chemical compounds were provided by Thermo-Fisher Scientific and Merck, such as cupric acetate monohydrate (Cu(CH<sub>3</sub>COO)<sub>2</sub>·H<sub>2</sub>O), hydrazine hydrate (N<sub>2</sub>H<sub>4</sub>H<sub>2</sub>O, 80%), polysorbate 20 (Tween 20), isopropanol potassium ((CH<sub>3</sub>)<sub>2</sub>CHOH, >99%), hexacyano ferrate (II)trihydrate (K<sub>4</sub>[Fe(CN)<sub>6</sub>]·3H<sub>2</sub>O, >98.5%), acetonitrile (CH<sub>3</sub>CN, >99.9%), sodium phosphate monobasic dihydrate (NaH<sub>2</sub>PO<sub>4</sub>·2H<sub>2</sub>O, 98-100.5%), ethanol (C<sub>2</sub>H<sub>5</sub>OH, 99%), potassium hexacyano ferrate (III) (K<sub>3</sub>[Fe(CN)<sub>6</sub>], >98.5%), and sodium phosphate dibasic dihydrate (Na<sub>2</sub>HPO<sub>4</sub>·2H<sub>2</sub>O, 98-100.5%). Ultrapure Milli-Q water served as an

important medium for solution preparation and sample washing. A series of fresh phosphate buffer saline (PBS) solutions were prepared at various pH levels by combining solution A (NaH<sub>2</sub>PO<sub>4</sub>·2H<sub>2</sub>O), solution B (Na<sub>2</sub>HPO<sub>4</sub>·2H<sub>2</sub>O), and ultrapure Milli-Q water, storing them at 4 °C for subsequent applications. The sandwich-assay ELISA kit was obtained from Amplicon Biotech, India.

Comprehensive physicochemical characterization of the synthesized Cu<sub>X</sub>O, hBNNS, and Cu/Cu<sub>X</sub>O-hBNNS powders was achieved using multiple advanced techniques. Phase composition and crystalline structure were determined with high precision using X-ray diffraction (XRD, Bruker Advance D-8). Micro- and nano-morphological features were elucidated via Scanning Electron Microscopy (SEM, EVO18 Zeiss) and Transmission Electron Microscopy (TEM, TECNAI 200 KV), with quantitative size analysis performed using ImageJ 1.54f software. Fourier-transform infrared spectroscopy (FTIR, Spectrum II-Perkin Elmer, 400–4000 cm<sup>-1</sup>) revealed the nature of chemical bonds within the samples, while Raman spectroscopy (Renishaw,  $\lambda = 785$  nm) and UV-Visible spectroscopy (Perkin Elmer 950) provided insight into vibrational, electronic, and optical transitions. Electrochemical characterization, including Cyclic Voltammetry (CV) and Differential Pulse Voltammetry (DPV), was performed using an Autolab Potentiostat/Galvanostat (Metrohm, Netherlands) in a three-electrode configuration: Cu/Cu<sub>X</sub>O-hBNNS/ITO as the working electrode, a platinum rod as the counter electrode, and Ag/AgCl (3 M KCl) as the reference. Immunosensing studies were conducted in phosphate-buffered saline (PBS, 50 mM, 0.9% NaCl, pH 7.0) containing 5 mM ferro/ferricyanide ([Fe(CN)<sub>6</sub>]<sup>3-/4-</sup>) to facilitate single-electron heterogeneous transfer.

### 6.2.2 Facile One-Step Polyol-Mediated Synthesis of Dandelion-Like CuxO Nanoflowers:

Dandelion-like copper oxide (CuxO) nanoflowers were synthesized through a precisely controlled one-step polyol-mediated process, as schematically represented in **Fig. 6.1**. This approach utilized ethylene glycol (EG) as both a high-boiling-point solvent and a mild reducing agent, enabling a controlled nucleation and anisotropic growth pathway that favored the formation of intricate flower-like morphologies. Initially, 0.15 M cupric acetate monohydrate [Cu(CH<sub>3</sub>COO)<sub>2</sub>·H<sub>2</sub>O] was completely dissolved in 30 mL of EG under continuous magnetic stirring at 200 rpm. The moderate stirring rate maintained a uniform dispersion of Cu<sup>2+</sup> cations and acetate anions while minimizing vortex-induced vibrations that could rapidly activate heterogeneous nucleation. The strategic choice of EG offered high viscosity to help slow down particle growth, yet its reducing capacity facilitates the gradual conversion of Cu<sup>2+</sup> to lower oxidation states under thermal conditions, ensuring a balance between nucleation and growth stages.

To modulate the reaction kinetics and promote the morphological evolution, 10 mL of polysorbate-20 (Tween 20) was introduced into the solution. Here, Tween 20 provided a hydrophilic–lipophilic balance (HLB) that enabled efficient adsorption onto growing nanocrystal surfaces, providing steric hindrance that prevented uncontrolled agglomeration. Additionally, it also acted as a soft templating agent, promoting the radial alignment of nanosheets from a central nucleation core, thereby generating the characteristic "dandelion-like" architecture. Interestingly, the long hydrophobic chains of surfactant interacted with specific crystallographic planes of Cu<sub>X</sub>O, retarding their

growth while allowing other planes to extend more rapidly, an essential factor for anisotropic flower-like structuring.

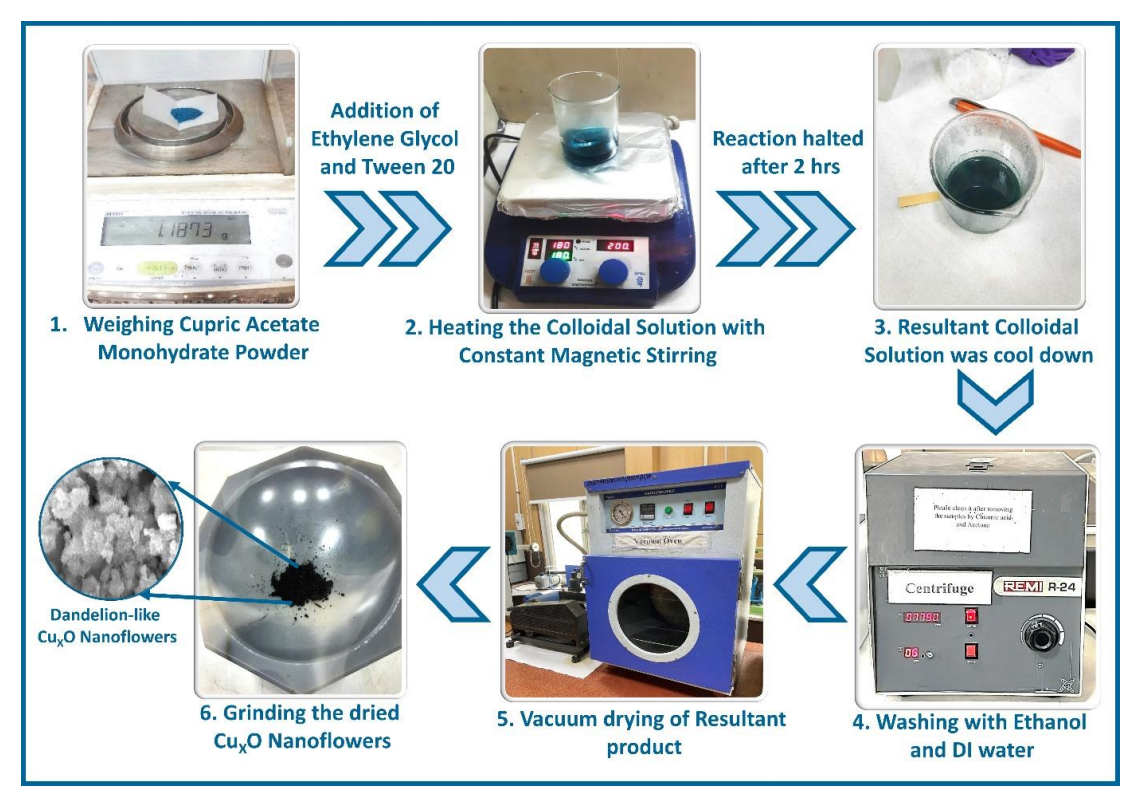


Figure 6.1: Schematic illustration of the sequential steps followed in the polyol-assisted synthesis of dandelion-shaped CuxO nanoflowers.

The reaction mixture was then transferred to a temperature-controlled hot plate and heated to  $180~^{\circ}\text{C}$  for 2 h under an ambient environment. At this elevated temperature, EG began to partially reduce Cu²+ ions to Cu+, triggering the co-precipitation of Cu2O and CuO phases through hydrolysis—oxidation—reduction equilibria. The controlled reaction duration allowed for the self-assembly of nanosheets into hierarchical nanoflowers without excessive development, while also preventing the collapse of subtle structures due to Ostwald ripening effects. During this stage, the solution color gradually transitioned from turquoise blue to dark green, visually confirming the formation of CuxO nanostructures and the progression of the reduction process.

Following synthesis, the mixture was allowed to cool naturally to ambient temperature to minimize structural stress that could induce cracking or partial detachment of nanosheets from the nanoflower core. The product was then subjected to a multi-step purification sequence involving repeated centrifugation at 10,000 rpm with alternating washes of ethanol and deionized water. This rigorous washing protocol served to remove unreacted precursors, excess surfactant molecules, and any soluble byproducts, while also restoring the surface chemistry to a neutral pH, thereby improving stability. The purified material was vacuum-dried at a sufficiently low temperature of 50 °C for 24 h to preserve the delicate nanoarchitecture while ensuring complete solvent removal. The dried product was subsequently ground into a fine, homogeneously textured powder, eliminating the possibility of macroscopic aggregates and ensuring a narrow particle size distribution. The resulting CuxO nanoflowers exhibited high purity, well-

defined morphology, and a large specific surface area, making them highly suitable for applications requiring enhanced electron transport and abundant active sites as critical performance determinants. The controlled polyol synthesis protocol for  $Cu_XO$  nanoflowers using Tween 20 as a steric stabilizer and ethylene glycol as both solvent and reducing agent is rigorously described in the subsequent mechanism.

Dissolution of Copper(II) Acetate Monohydrate in Ethylene Glycol:

$$Cu(CH_3COO)_2 \cdot H_2O \rightarrow Cu^{2+} + 2CH_3COO^{-} + H_2O$$

Steric Stabilization of Copper ions (Cu<sup>2+</sup>) on Complexation with Tween 20:

 $Cu^{2+}$  + Tween 20  $\rightarrow$  Cu - Tween 20 Complex

Partial reduction of Copper ions to Cuprous Oxide using Ethylene Glycol:

$$Cu^{2+} + OHCH_2CH_2OH \rightarrow Cu_2O + OHCH_2COOH + 2H^+$$

Complete oxidation to Cupric Oxide in ambient atmosphere:

 $Cu_2O + \frac{1}{2}O_2 \rightarrow 2CuO$ 

**Overall Reaction:** 

 $2Cu(CH_3COO)_2 \cdot H_2O + 2OHCH_2CH_2OH + \frac{1}{2}O_2 \rightarrow CuO + Cu_2O + 2OHCH_2COOH + 4CH_3COOH + 2H_2O$ 

### 6.2.2 Stepwise In-situ Hydrothermal Approach for the Synthesis of Cu/CuxO-hBNNS Nano-hybrid Composite

The  $Cu/Cu_XO$ -decorated hBNNS nano-hybrid composite, as shown in **Fig. 6.2**, was synthesized through a facile in-situ hydrothermal methodology, employing  $Cu_XO$  nanoflowers and hBNNS as the precision-engineered precursors. The reason behind employing hBNNS instead of bulk hBN lies in the substantial interlayer ionic interaction between boron and nitrogen atoms in the bulk form, which severely impedes the critical synthesis factors of interfacial intercalation, dispersibility, and exfoliation. In contrast, hBNNS exhibits ultrathin morphology with greater lateral exposure, and improved chemical accessibility that facilitates extensive contact with  $Cu_XO$  nanostructures, thereby ensuring efficient nucleation, uniform decoration, and superior nanocomposite formation.

In a standard synthesis protocol, the preparation of the  $Cu/Cu_XO$ –hBNNS nano-hybrid composite was initiated with the formation of two separate, highly uniform dispersions. In two different beaker, precisely weighed quantities of 130 mg of ultrathin hexagonal boron nitride nanosheets (hBNNS) and 100 mg of copper oxide nanoflowers ( $Cu_XO$  NFs) are each dispersed in 10 mL of deionized (DI) water. These dispersions are individually subjected to ultrasonication for 1 hour, a step that facilitates complete exfoliation of hBNNS layers, disaggregation of  $Cu_XO$  nanoflowers, and homogeneous particle distribution throughout the solvent. Ultrasonication also disrupts weak van der Waals interactions and enhances the surface accessibility of functional groups on both nanomaterials.

After this pre-treatment, the two stable dispersions are combined in a single beaker to initiate the precursor interaction stage. To the mixture, 10 mL of isopropyl alcohol (IPA) is introduced, which help in lowering the overall surface tension of the aqueous

system, thereby promoting intimate contact between hydrophilic and hydrophobic regions of the nanostructures. In addition, it acts as a mild reducing agent in the subsequent steps, providing favorable environment for surface modification of Cu<sub>x</sub>O. The resulting dispersion containing both hBNNS and Cu<sub>x</sub>O precursors is thoroughly mixed to achieve compositional homogeneity, by mitigating particle aggregation through polarity adjustment of the solvent environment.

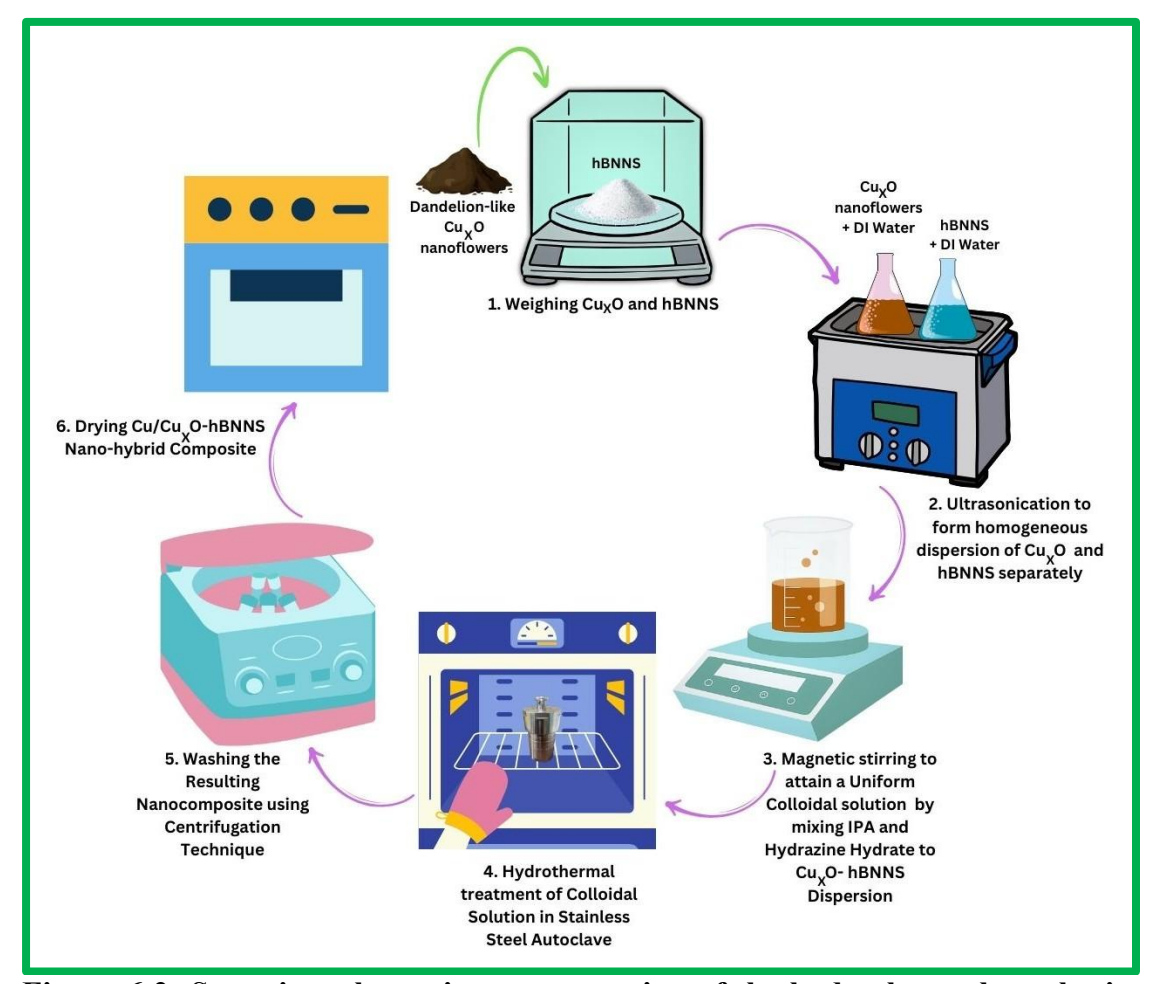


Figure 6.2: Stepwise schematic representation of the hydrothermal synthesis route employed for the fabrication of Cu/CuxO-hBNNS nano-hybrid composite.

To initiate selective reduction and functional interlinking, 5 mL of hydrazine hydrate (N<sub>2</sub>H<sub>4</sub>·H<sub>2</sub>O), a strong reducing agent, was added to the well-mixed dispersion. This addition initiates a partial reduction process wherein a portion of Cu<sup>2+</sup> ions present in the Cu<sub>x</sub>O nanoflowers are reduced to metallic copper (Cu<sup>0</sup>). The reduction mechanism is further aided by the presence of IPA, which can synergistically accelerate electron transfer to Cu<sup>2+</sup> species. The emergence of Cu<sup>0</sup> on the surface of the Cu<sub>x</sub>O nanoflowers enhances their chemical reactivity, enabling selective covalent and coordinative bonding with amino functionalities present on defect sites and edges of the hBNNS sheets. This step effectively seeds the formation of a 3D–2D hybrid nanoarchitecture through interfacial complexation and spatial anchoring of metallic copper sites onto hBNNS surfaces. To ensure complete interaction and bonding, the reaction mixture is subjected to magnetic stirring at a constant speed of 270 rpm for 1 hour. This dynamic

mixing promotes sustained contact between reactive interfaces with consistent collision frequency between particles, preventing aggregation and enabling uniform nucleation of Cu<sup>o</sup> over hBNNS. Subsequently, the well-dispersed solution is transferred into a 50 mL Teflon-lined stainless-steel autoclave. The sealed autoclave is placed in a high-temperature oven and subjected to hydrothermal treatment at 180 °C for 18 hours. During this period, the elevated temperature and pressure-assisted growth enhance interfacial adhesion strengthening and structural stabilization of the Cu/Cu<sub>x</sub>O-hBNNS nano-hybrid, while also improving crystallinity and adhesion at the nano junctions.

Upon completion of the hydrothermal process, the autoclave was allowed to cool naturally to room temperature to prevent thermal shock-induced structural deformation. The resultant dispersion is then rigorously washed multiple times with DI water to eliminate any unreacted precursors, loosely bound residues, and excess hydrazine hydrate. The washing process is followed by high-speed centrifugation at 9000 rpm, repeated until the supernatant attains a neutral pH, indicating the removal of ionic contaminants. This step is critical to ensuring the chemical purity and stability of the final product. Finally, the purified nanocomposite is dried at 90 °C in a low-temperature oven to evaporate residual moisture and solvent without inducing thermal degradation or oxidation of the nanostructures, while preserving the structural and chemical stability of the nano-hybrid composite. The resultant product of dry, fine powder of the Cu/Cu<sub>x</sub>O-hBNNS nano-hybrid composite was obtained. The ionic mechanism describes the partial reduction of Cu<sup>2+</sup> to Cu<sup>0</sup> with hydrazine hydrate acting as a primary reductant, donating electrons to Cu<sup>2+</sup> centers and producing nitrogen gas as a byproduct. Concurrently, IPA assists in electron donation and stabilizes the reduced metallic sites, preventing uncontrolled aggregation. The presence of defect-rich ultrathin hBNNS, with its exposed nitrogen sites and residual amino functionalities, facilitates selective complexation of Cu<sup>o</sup> via coordinate covalent bonding. The sequential chemical reduction, surface modification, and hydrothermal consolidation results in a structurally robust, chemically stable, and catalytically active nano-hybrid composite with synergistic 3D–2D interactions as mentioned in the chemical equations below:

Dissociation of Hydrazine Hydrate carried partial reduction of Cupric to Cuprous state:

$$N_2H_4$$
 +  $H_2O \leftrightarrow N_2H_5$  +  $OH^-$   
 $CuO + H_2O + e^- \rightarrow Cu_2O + OH^-$ 

Dissociation of Isopropanol for effective intercalation and partial reduction of Cuprous state to Zero-valent Copper (Cu<sup>0</sup>):

$$(CH_3)_2CHOH + H_2O \rightarrow (CH_3)_2CO + 2H^+ + 2e^-$$

$$Cu_2O+ H_2O + 2e^- \rightarrow 2Cu + 2OH^-$$

**Reduction of Copper Oxide Nanoflowers:** 

$$Cu_2O + N_2H_4 + H_2O \rightarrow 2Cu + N_2 + 2OH^-$$

$$Cu_2O + (CH_3)_2CHOH + H_2O \rightarrow 2Cu + (CH_3)_2CO + 2OH^{-1}$$

### Binding of Copper Nanoflowers and Ultrathin hBNNS for Nanocomposite Synthesis:

#### Cu/Cu<sub>x</sub>O + hBNNS → Cu/Cu<sub>x</sub>O-hBNNS Nanocomposite

### 6.2.3 Electrophoretic deposition (EPD) of Cu/CuxO-hBNNS film onto ITO substrates:

Electrophoretic Deposition (EPD) was strategically employed to fabricate Cu/Cu<sub>X</sub>O-hBNNS/ITO micro-electrodes with high precision and reproducibility in film formation. This method harnessed the synergistic role of a stable colloidal medium and the directed drift of nanoparticles under an applied electric field to achieve controlled deposition (**Fig. 6.3(I)**). A homogeneous suspension was first prepared by dispersing 0.5 mg/mL of Cu/Cu<sub>X</sub>O-hBNNS in acetonitrile (CH<sub>3</sub>CN), which served as an effective polar solvent due to its high dielectric constant and low viscosity, thereby ensuring efficient particle migration. To further enhance suspension stability and prevent agglomeration, 300 μL of magnesium nitrate (Mg(NO<sub>3</sub>)<sub>2</sub>, 1 mg/mL) was introduced as a charging and stabilizing agent, imparting positive surface charge to the nanocomposite. This mixture was then ultrasonicated for 1 hour, where acoustic cavitation promoted complete exfoliation, uniform distribution, and prevention of particle clustering, ensuring electrokinetic uniformity during deposition.

The prepared colloidal dispersion was transferred to a beaker containing a twoelectrode assembly. The working electrode was a pre-hydrolyzed ITO substrate (0.8 cm × 2.5 cm), utilized for its transparency, high conductivity, and strong interfacial bonding with the nanocomposite. The ITO substrate was connected to the negative terminal, while a platinum rod, owing to its high stability and conductivity, acted as the counter electrode and was connected to the positive terminal. Prior to deposition, the ITO electrodes were hydrolyzed using a solution of hydrogen peroxide, ammonia, and deionized water (1:1:5). This step was essential as it activated surface hydroxyl groups, introduced radical functionalities, and increased surface roughness, thereby enhancing electrostatic attraction and film adhesion of the nanocomposite. During deposition, an external DC voltage of 15 V was applied for 1 minute, generating an electric field that induced electrophoretic migration of the charged Cu/Cu<sub>X</sub>O-hBNNS nanoparticles towards the ITO surface. This controlled migration facilitated the uniform deposition of a 0.8 cm × 0.8 cm homogeneous nanocomposite film. The outcome was a darkbrown Cu/Cu<sub>X</sub>O-hBNNS/ITO micro-electrode, indicating dense and consistent coverage (Fig. 6.3(III)-(a)). Upon electrochemical evaluation, the electrode color shifted from dark-brown to light-brown (Fig. 6.3(III)-(b)), a clear signature of dynamic surface-charge participation. This transformation reflected redox-induced modulation of the Cu/Cu<sub>X</sub>O states within the hybrid nanocomposite, validating its electroactive behaviour in PBS medium and confirming efficient electron transfer kinetics at the electrode-electrolyte interface.

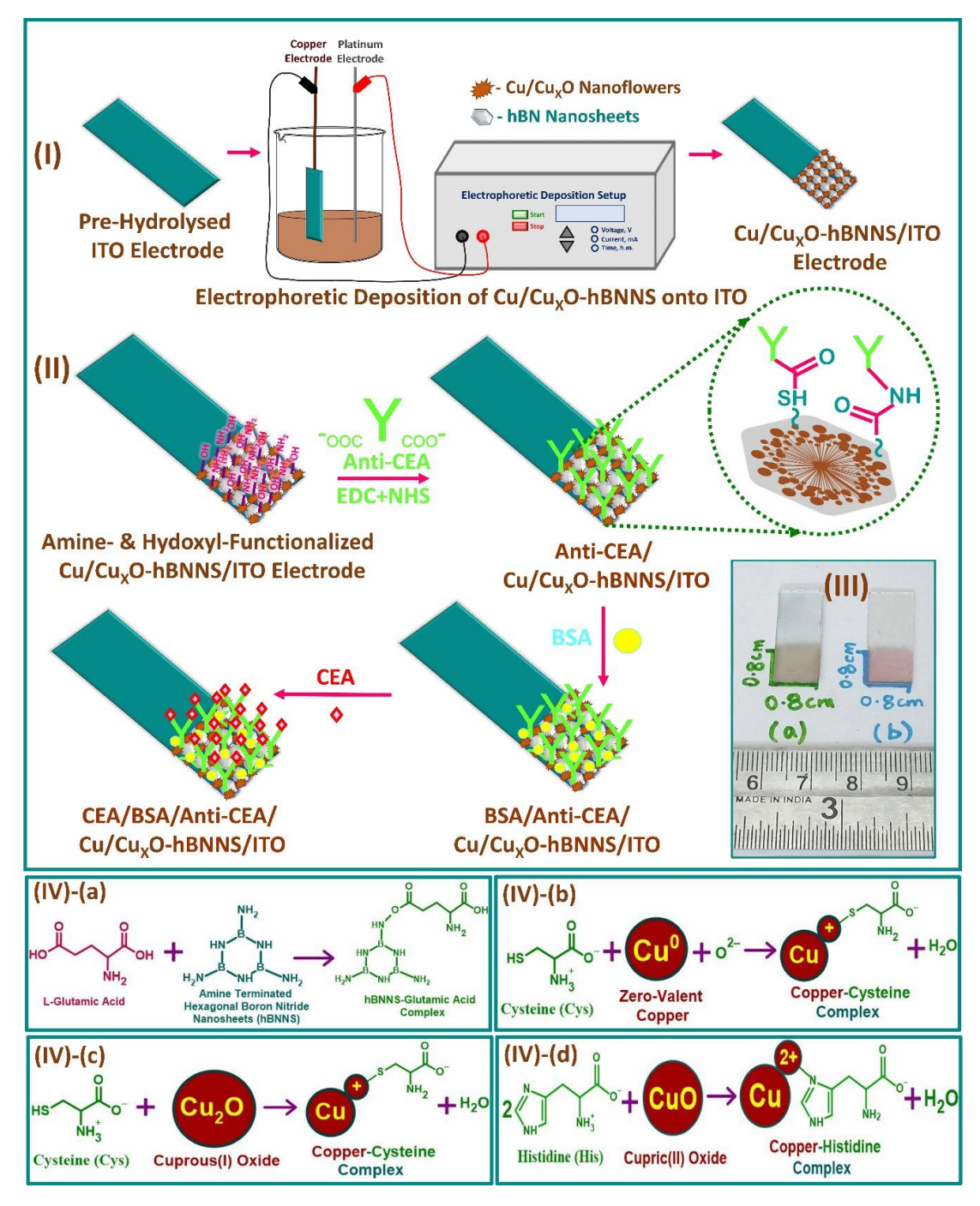


Figure 6.3: (I) Pictorial illustration of Cu/Cu<sub>X</sub>O-hBNNS film deposition via electrophoretic deposition (EPD); (II) Schematic representation of sequential steps involved in the fabrication of the Cu/Cu<sub>X</sub>O-hBNNS-based nanobiosensor; (III) Optical images of Cu/Cu<sub>X</sub>O-hBNNS/ITO micro-electrodes (a) prior to and (b) following electrochemical characterization; (IV) Proposed mechanistic pathway for amide bond formation: (a) between L-glutamic acid and amine-functionalized hBNNS, (b) between cysteine and zero-valent copper, (c) between cysteine and cuprous oxide, and (d) between histidine and cupric oxide.

#### 6.2.4 Fabrication of Cu/CuxO-hBNNS based immunosensor:

The development of the Cu/Cu<sub>X</sub>O-hBNNS-based immunoelectrode was carried out with meticulous precision to ensure robust electrochemical performance and long-term stability of the biosensing platform. The initial step involved decorating pre-hydrolyzed ITO electrodes with a Cu/Cu<sub>X</sub>O-hBNNS matrix, as illustrated in **Fig. 6.3(II)**, under systematically optimized synthesis conditions. This structural integration provided a 3D nano-architectured surface enriched with catalytic sites and strong conductive pathways. The nanohybrid composite-based interface exhibiting Cu/Cu<sub>X</sub>O nanoflowers onto hBNNS, facilitating efficient electron transfer processes and enhancing the immobilization efficiency of bio-recognition elements.

The site-directed immobilization of monoclonal Anti-CEA antibodies, illustrated in Fig. 6.3(IV-V), was achieved through the preparation of a stock antibody solution in phosphate buffer saline (PBS, pH 7.4), utilizing EDC-NHS chemistry to ensure selective activation of functional groups. Specifically, the carboxyl and amine groups present on the antibody were activated by conjugating 50 µg·mL<sup>-1</sup> Anti-CEA with freshly prepared EDC (0.2 M) and NHS (0.05 M) in a 2:1:1 ratio at room temperature, and the mixture was incubated for 30 minutes to allow formation of reactive intermediates. The immobilization step involved the deposition of 20 µL of activated Anti-CEA solution onto the Cu/Cu<sub>X</sub>O-hBNNS film, which was uniformly distributed on the ITO electrode surface. To ensure strong and specific anchoring, the electrode was maintained in a humid chamber for 24 hours, thereby permitting gradual and complete binding interactions. Post-immobilization, 10 µL of 1% BSA solution (w/v in ultrapure Milli-Q water) were applied to the immunoelectrode, effectively blocking nonspecific binding sites and thereby enhancing biosensor selectivity. Subsequently, 10 μL of CEA solution at appropriate concentrations were incubated for 30 minutes onto the BSA/Anti-CEA/Cu/Cu<sub>X</sub>O-hBNNS/ITO interface, resulting in the final functional immunoelectrode configuration. The prepared electrode was stored at 4°C to preserve its bioactivity for subsequent analytical use.

At the molecular scale, the chemistry underlying these nano-bio coupling interactions is highly significant. The EDC molecule, a zero-length cross-linker, initially reacts with the carboxyl-terminated Fc region (L-Glutamic Acid residues) of Anti-CEA to form a reactive O-acylisourea ester [18]. This unstable intermediate is subsequently stabilized by NHS, yielding a more durable NHS ester that couples efficiently with amine groups present on the hBNNS matrix, forming robust covalent amide linkages (Fig. 6.3(IV)-(a)). Furthermore, additional stabilization and electron-rich conjugation are achieved through thiol groups from cysteine residues in Anti-CEA, which interact strongly with the Cu<sup>o</sup> nanoparticles [19] (Fig. 6.3(IV)-(b)) and cuprous oxide (Cu<sub>2</sub>O) domains [20] (Fig. 6.3(IV)-(c)) at the hybrid nano-biointerface. These interactions, validated through FTIR analysis, further reinforce the intimate bonding between the metallic copper domains and the antibody. In parallel, the imidazole nitrogen from histidine residues of Anti-CEA engages in stable coordination with CuO species at the interface (Fig. 6.3(IV)-(d)) [20], thereby providing multipoint binding stability and enhancing overall structural integrity of the immunoelectrode. This synergistic multi-interaction binding—comprising covalent bonds, coordination complexes, and electrostatic stabilization—confers superior durability, enhanced biorecognition fidelity, and remarkable electrocatalytic performance to the final biosensing platform.

### **6.3** Experimental Results & Analysis:

#### **6.3.1** Analytical Nanomaterial Characterizations:

### 6.3.1.1 In-depth Structural and Crystallographic Insights into Cu/Cu<sub>X</sub>O-hBNNS Hybrid Nanocomposite Using Advanced XRD Analysis

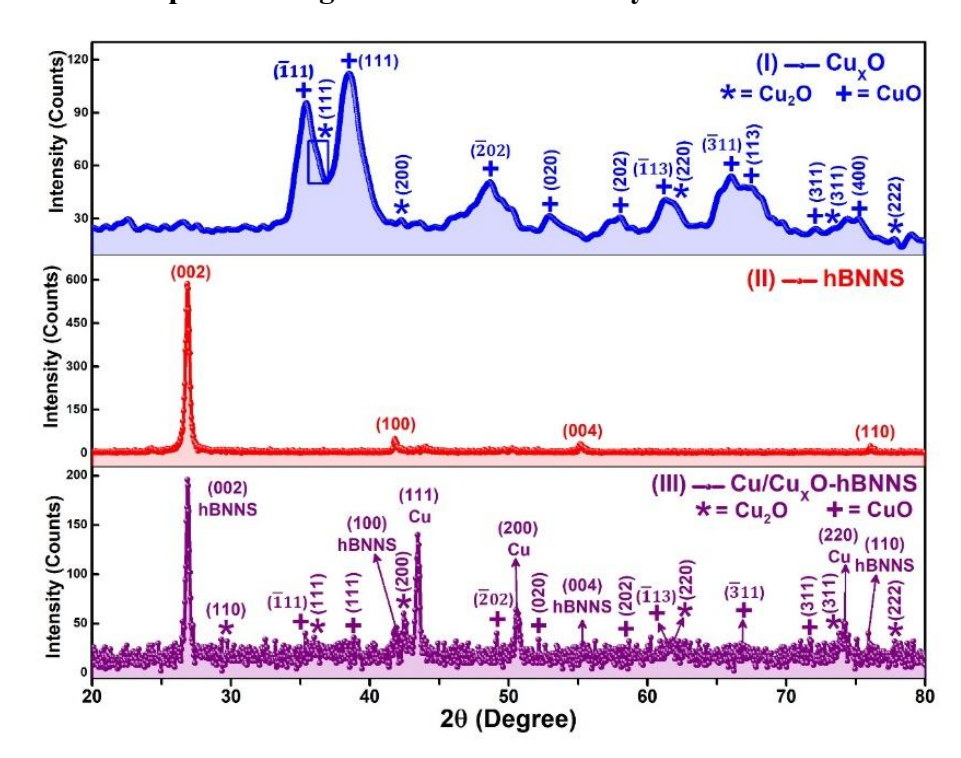


Figure 6.4: X-ray diffraction (XRD) analysis was performed on (I) CuxO Nanoflowers, (II) hBNNS, and (III) Cu/CuxO-hBNNS nano-hybrid composite, recording diffraction patterns within the 2θ range of 10°-80°.

A detailed X-ray diffraction (XRD) investigation, conducted over a 2θ range of 20°–80° was performed to comprehensively analyze the phase composition, crystal structure, crystallite size, and interlayer spacing of the synthesized nanomaterials, namely: (I) Cu/Cu<sub>X</sub>O nanostructures, (II) hBNNS, and (III) Cu/Cu<sub>X</sub>O-hBNNS nanohybrid composite (NHC), as presented in **Fig. 6.4(a)**. The crystallographic assessment further allowed evaluation of intrinsic strain and dislocation density, providing deeper insights into lattice imperfections and structural quality.

The CuxO nanoflowers fabricated through a one-step polyol method exhibited distinct and sharp diffraction peaks positioned at 35.42°, 52.94°, 58.04°, 61.32°, 66.04°, 67.5°, 72.12°, 75.18°, 38.52°, and 48.66°, corresponding to the (111), (111), (202), (020), (202), (113), (311), (113), (311), and (400) crystallographic planes of monoclinic CuO, respectively, in accordance with **JCPDS card no. 96-901-55569** [21]. In addition, the appearance of relatively fewer but well-defined diffraction peaks located at 36.36°, 42.26°, 61.8°, 73.46°, and 77.78° were attributed to the (111), (200), (220), (311), and (222) planes of cuprous oxide (Cu<sub>2</sub>O), as verified by **JCPDS card no. 5-667** [22]. Remarkably, two highly intense reflections observed at 35.42° and 38.52° indicated a preferential crystallographic orientation, with dominant alignments along the (1<sup>-</sup>11) and (111) planes of CuO, underscoring the strong anisotropic growth tendency of the nanoflowers. Employing the Debye–Scherrer equation (Eq. [6.2]) the crystallite size

corresponding to the most intense (111) peak was calculated as 4.38 nm, whereas the d-spacing determined through Bragg's relation (Eq. [6.1]) yielded 0.233 nm.

Bragg's Relation: 
$$2d \times Sin\theta = n\lambda$$
 [6.1]

In Bragg's relation, d represents the interplanar spacing between successive crystallographic planes, expressed in nanometers (nm), which is a direct indicator of the compactness of atomic arrangements within the lattice. The parameter  $\theta$  denotes the Bragg's diffraction angle, measured in radians, signifying the angular position at which constructive interference of X-rays occurs due to lattice periodicity. The variable n corresponds to the order of reflection, indicating the multiple levels of diffracted beams generated when the Bragg condition is satisfied. Meanwhile,  $\lambda$  is the wavelength of the incident X-ray beam, which fundamentally governs the resolution of diffraction analysis and directly influences the accuracy of determining lattice constants and crystallographic details. Each parameter altogether influences this relationship and forms the basis of Bragg's Law, which is effective in revealing the structural integrity, orientation, and crystalline perfection of nanomaterials.

Debye-Scherrer's Formula: 
$$D = \frac{0.9 \lambda}{\beta_{hkl} \times Cos\theta}$$
 [6.2]

In Debye Scherrer equation, D signifies the average crystallite size, expressed in nanometers (nm), which directly reflects the nanoscale dimensions of coherently diffracting domains within the material. The parameter  $\lambda$  denotes the wavelength of the incident X-rays, measured in nanometers, serving as a fundamental constant that determines the resolution and interaction depth of the diffraction process. The variable  $\beta$  corresponds to the full width at half maximum (FWHM) of the diffraction peak, expressed in radians, which is a critical measure of peak broadening influenced by both crystallite size and lattice strain. Finally,  $\theta$  represents the diffraction angle, also expressed in radians, at which constructive interference occurs, directly connecting the structural arrangement of atoms with the observable diffraction pattern. Collectively, these parameters underpin the Scherrer equation, a vital tool for estimating nanoscale crystallite sizes and correlating structural broadening with the intrinsic properties of crystalline materials.

Furthermore, the dislocation density ( $\delta$ ), a critical measure of lattice imperfections, was estimated using the relation  $\delta = 1/D^2$  (**Eq. [6.3]**), signifying a relatively high density of dislocations arising from nanoscale crystallinity and structural distortions. Such detailed crystallographic features collectively confirmed the coexistence of mixed-valence  $Cu_XO$  phases and validated the nanoscale structural uniformity of the synthesized material system.

Dislocation Density: 
$$\delta = \frac{1}{D^2}$$
 [6.3]

In this context,  $\delta$  represents the dislocation density, expressed in nm<sup>-2</sup>, which quantifies the number of dislocations present per unit area of the crystal lattice and serves as a direct measure of lattice imperfections and defect concentration within the nanomaterial. Meanwhile, D denotes the crystallite size in nanometers (nm), reflecting the average dimension of coherently diffracting domains. The inverse relationship between these two parameters indicates that smaller crystallite sizes typically

correspond to higher dislocation densities, which profoundly influence the mechanical strength, electronic behaviour, and overall functional properties of the nanomaterial.

In polyol-synthesized Cu<sub>X</sub>O nanoflowers, the reduction in crystallite size directly contributed to a relatively high dislocation density of  $5.2 \times 10^2$  nm<sup>-2</sup>, as calculated using Eq. [6.3]. This elevated density of dislocations arises due to multiple concurrent factors: the accelerated crystal growth rate under polyol conditions, the viscosityinduced chemical stresses generated by ethylene glycol during the reaction, and the additional mechanical stresses introduced by vigorous stirring. These combined stresses create lattice distortions that intensify structural disorder, thereby increasing the defect concentration within the crystal lattice. Such a high dislocation density corresponded to a micro-strain of  $2.39 \times 10^2$ , as determined using Eq. [6.4], highlighting the substantial lattice strain embedded in the nanostructure. This strain plays a critical role in hindering the orderly nucleation and subsequent growth of crystallites, which restricts the formation of well-defined and defect-free crystal domains. Consequently, the crystallographic quality of the Cu<sub>X</sub>O nanoflowers is compromised, with smaller crystallites exhibiting a higher fraction of disordered grain boundaries and defect-rich regions. These imperfections significantly reduce the number of stable and efficient active sites available for catalytic reactions, thereby diminishing the structural integrity and long-term reliability of the nanostructures. To address these inherent limitations, been directed toward engineering Cu/Cu<sub>x</sub>O-hBNNS nanocomposites, which integrate the catalytic potential of Cu/Cu<sub>X</sub>O-based nanostructures with the structural stability and large surface area of hBN nanosheets. This synergistic hybridization enhances the density of accessible surface-active sites while simultaneously suppressing defect-driven instability, thereby ensuring superior catalytic efficiency and durability.

Microstrain: 
$$\varepsilon = \frac{\beta_{hkl}}{4 \times \sin \theta}$$
 [6.4]

n this context,  $\beta$ hkl denotes the full width at half maximum (FWHM) of the diffraction peak corresponding to a specific crystallographic plane (hkl), measured in radians. This parameter is a critical indicator of peak broadening in X-ray diffraction patterns, which is directly associated with nanoscale effects such as crystallite size reduction, microstrain, and lattice imperfections. Similarly,  $\theta$  represents the Bragg diffraction angle, also expressed in radians, which defines the angular position of the diffracted X-rays and plays a fundamental role in evaluating interplanar spacings, lattice constants, and structural distortions within the material. Together,  $\beta$ hkl and  $\theta$  provide vital insights into the degree of crystallinity, structural integrity, and nanoscale phenomena governing the material's physical properties.

In **Fig. 6.4(a)-II**, the hydrothermally synthesized hexagonal boron nitride nanosheets (hBNNS) exhibit distinct diffraction peaks at 26.88°, 41.8°, 55.16°, and 76.08°, which correspond to the (002), (100), (004), and (110) crystallographic planes, respectively, as confirmed by **JCPDS Card No. 034–0421** [23]. The emergence of these peaks confirms the successful exfoliation and crystallization of hBNNS into a well-defined hexagonal phase. To achieve large lateral-sized, functionalized nanosheets, precise Lewis acid–base complexation chemistry was employed to initiate the intercalation–exfoliation process, thereby ensuring the formation of a pure crystalline lattice with minimal defects. Among the observed peaks, the prominent diffraction at 26.88 highlights the preferential alignment of hBNNS along the (002) hkl plane, a feature that

signifies the layered arrangement and structural uniformity of the material. Furthermore, Fig. 6.4(a)-III presents the XRD spectrum of the Cu/Cu<sub>X</sub>O-hBNNS nanohybrid composite (NHC), which demonstrates characteristic diffraction peaks of both hBNNS and Cu/Cu<sub>x</sub>O nanoflowers. The presence of well-defined peaks at 26.88°, 42.44°, and 75.92°, indexed to the (002), (100), and (110) planes of hBNNS, further validates the retention of the parent lattice structure, as corroborated by JCPDS Card No. 034–0421 [32]. Importantly, the persistence of the (002) reflection at  $2\theta = 26.88^{\circ}$ in the nanocomposite confirms that hydrothermal conditions did not disrupt the interplanar spacing (d(002) = 0.331 nm, Table S1) or compromise the intrinsic lattice stability of hBNNS. This resilience under synthesis conditions underscores the suitability of hBNNS as a robust structural scaffold capable of maintaining its crystalline framework, thereby enhancing the stability and long-term reliability of the nanohybrid system. Nevertheless, a measurable increase in crystallite size from 25.37 nm to 31.42 nm in hBNNS after nanocomposite formation suggests effective diffusion and intercalation of Cu/Cu<sub>X</sub>O atoms into the nanosheet matrix at elevated temperatures, promoting enhanced crystallinity and stronger interfacial bonding.

The larger crystallite size of hBNNS significantly contributed to lowering micro-strain and dislocation density, which in turn minimized structural defects, enhanced mechanical stability, and improved the overall structural integrity of the Cu/Cu<sub>X</sub>O nanoflowers integrated within the hybrid system. This structural refinement directly strengthened the durability and functionality of the nanocomposite. Furthermore, the prominent and sharp diffraction peaks observed in the Cu/Cu<sub>x</sub>O-hBNNS nanohybrid composite (NHC) at 43.44°, 50.52°, and 74.12° are distinctly associated with the (111), (200), and (220) crystallographic planes of the pure face-centered cubic (FCC) phase of metallic copper, as indexed by JCPDS Card No. 04-0836. This clearly confirms the successful hydrothermal reduction of CuxO nanoflowers into stable metallic copper nanostructures. Additionally, the diffraction peaks corresponding to Cu<sub>2</sub>O (35.36°, 41.88°) and CuO (49.16°, 52.16°) were notably intense, establishing the effective reinforcement and strong hybridization of Cu/Cu<sub>X</sub>O structures onto the hBNNS matrix [21, 22]. Importantly, the (111) crystallographic plane of Cu nanoflowers, owing to its inherently low surface energy, exhibited remarkable stability, which not only reduced agglomeration tendencies but also ensured a more uniform distribution of nanostructures, thereby improving both structural integrity and catalytic efficiency [24]. Moreover, hydrothermal reduction brought about substantial modifications in structural parameters: the interplanar spacing of Cu/Cu<sub>X</sub>O nanoflowers (d(111) = 2.08 nm) was reduced compared to  $Cu_XO$  nanoflowers (d(111) = 0.233 nm), suggesting a denser atomic packing as a result of partial oxygen removal during the reduction. Simultaneously, the crystallite size of Cu/Cu<sub>X</sub>O nanoflowers (D = 29.19 nm) was drastically larger than that of Cu<sub>X</sub>O nanoflowers (D = 4.38 nm), indicating that the reduction process facilitated not just oxygen removal but also induced the coalescence of smaller crystallites, driving the formation of well-defined nanoflower morphologies. Consequently, this coarsening effect not only optimized the hierarchical structure but also contributed to improved catalytic functionality, enhanced chemical stability, and superior structural resilience of the Cu/Cu<sub>X</sub>O-hBNNS nanohybrid system.

Table 6.1: Evalution of microstrain and dislocation density in as-synthesized (I) Cu<sub>X</sub>O, (II) hBNNS, (III) Cu/Cu<sub>X</sub>O-hBNNS samples respectively.

S.No.	S.No. Sample		Intense (hkl) Planes	Peak Position, 20 (°)	FWHM (°)	Crystallite Size (D, nm)	d-spacing (d, nm)	Micro Strain (ε)	Dislocation Density (δ, nm <sup>-2</sup> )
1.	CuxO		(111)	38.52	1.92	4.38	0.233	$2.39 \times 10^{-2}$	$5.2 \times 10^{-2}$
2.	2. hBNNS		(002)	26.88	0.32	25.37	0.331	$5.88 \times 10^{-3}$	$1.55 \times 10^{-3}$
Cu/Cu <sub>x</sub> O - hBNNS NHC	Cu/Cu <sub>X</sub> O	(111)	50.52	0.29	29.19	0.208	$3.21 \times 10^{-3}$	$1.17 \times 10^{-3}$	
	hBNNS	(002)	26.88	0.26	31.42	0.331	$4.75 \times 10^{-3}$	1.01 10 <sup>-3</sup>	

## 6.3.1.2 Morphological Assessment and Microstructural Insights into CuxO, hBNNS, and Cu/CuxO-hBNNS Using High-Resolution SEM and TEM Techniques

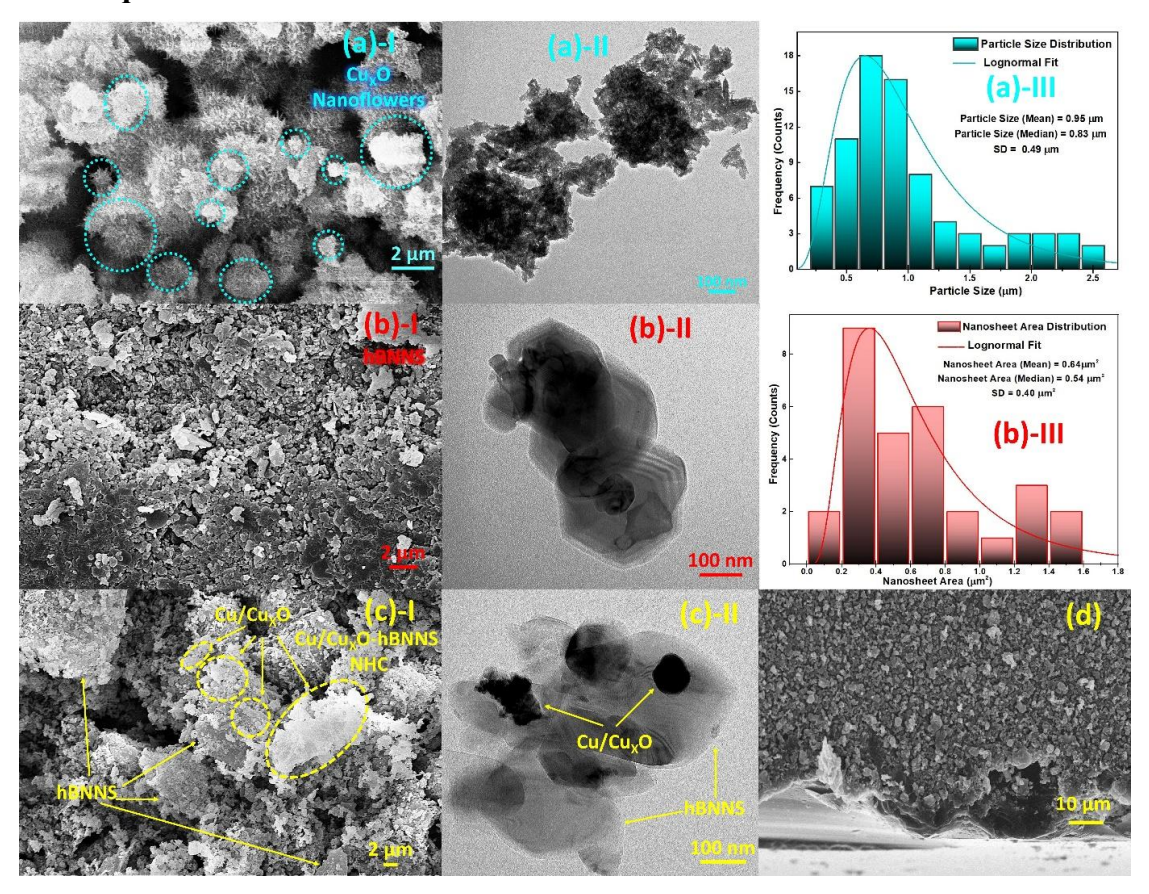


Figure 6.5: (I) Scanning electron microscopy (SEM), (II) transmission electron microscopy (TEM), and (III) particle size distribution curves corresponding to (a)  $Cu_XO$ , (b) hBNNS, and (c)  $Cu/Cu_XO$ -hBNNS nanohybrid composite (NHC); (d) SEM micrograph depicting the surface morphology of the as-fabricated  $Cu/Cu_XO$ -hBNNS/ITO electrode.

SEM micrographs illustrated in **Fig. 6.5(a)-I, 6.5(b)-I, and 6.5(c)-I** provided a comprehensive evaluation of the morphology of  $Cu_XO$ , hBNNS, and  $Cu/Cu_XO$  nanostructures, respectively, while **Fig. 6.5(d)** presented the surface features of the fabricated  $Cu/Cu_XO$ -hBNNS/ITO electrode. The particle size distribution curve of  $Cu_XO$  (**Fig. 6.5(a)-III**) revealed dandelion-like nanoflowers with dimensions spanning from 0.1 to 2.5  $\mu$ m, possessing an average particle size of 0.95  $\mu$ m and a median size of 0.83  $\mu$ m. This morphology, distinctly observed in **Fig. 6.5(a)-I**, is characterized by a highly porous architecture that originates from the preferential radial growth of  $Cu_XO$  nanostructures, a process promoted by ethylene glycol and Tween 20 during the polyol synthesis route. These findings were corroborated by TEM micrographs at a 100 nm scale (**Fig. 6.5(a)-II**), which confirmed an average particle size of 0.66  $\mu$ m, demonstrating consistency with the SEM results and ensuring the accuracy of the morphological assessment.

Hydrothermally exfoliated hBNNS, as presented in Fig. 6.5(b)-I and validated through the nanosheet area distribution curve (Fig. 6.5(b)-III), displayed lateral dimensions

ranging from 0.1 to  $1.6~\mu m^2$ , with an average nanosheet area of  $0.64~\mu m^2$  and a median area of  $0.54~\mu m^2$ . These nanosheets exhibited ultrathin features and smooth lateral edges, supporting their effective role as a two-dimensional support matrix. The integration of Cu/Cu<sub>X</sub>O nanoflowers onto hBNNS, shown in **Fig. 6.5(c)-I** (SEM) and **Fig. 6.5(c)-II** (TEM), demonstrated a homogeneous distribution of nanoflowers across the nanosheet surface, confirming the successful synthesis of the Cu/Cu<sub>X</sub>O-hBNNS nanohybrid composite (NHC). This hybridization was achieved through hydrothermal reduction of copper salts under high-pressure and high-temperature conditions, a process orchestrated by hydrazine hydrate and IPA that regulated nucleation and growth of Cu/Cu<sub>X</sub>O nanoflowers into a porous, dandelion-like architecture.

The successful anchoring of Cu/Cu<sub>X</sub>O nanoflowers on hBNNS nanosheets is primarily attributed to van der Waals forces and electrostatic interactions, which stabilize the hybrid architecture and promote uniform coverage. The SEM and TEM analyses collectively validate this integration, highlighting the synergistic interplay between the 0D–3D Cu/Cu<sub>X</sub>O nanoflowers and the 2D hBNNS support. Finally, the as-fabricated Cu/Cu<sub>X</sub>O-hBNNS/ITO electrode, illustrated in **Fig. 6.5(d)**, revealed a rough and porous surface morphology endowed with plentiful surface-active sites, which enhance biomolecule immobilization and electron transfer kinetics, thereby ensuring its superior performance as an efficient nano-biosensor interface.

## 6.3.1.3 Investigation of Electronic Band Structure, Optical Transition Mechanisms, and Urbach Energy in Cu/CuxO-hBNNS Hybrid Nanocomposite Using UV-Vis Spectroscopy

To evaluate the bandgap tuning and the nature of electronic transitions, the absorption spectra of the as-synthesized sample were recorded in the UV-Visible region, as presented in **Fig. 6.6(c)**. The optical bandgap energy (Eg) was further determined using Tauc's method, expressed mathematicallyby **Eq. (6.5)**:

$$(\alpha h v)^{1/n} = A(h v - E_g)$$
 [Eq. 6.5]

In this equation, the absorption coefficient ( $\alpha$ ) provides a direct measure of how efficiently the material absorbs light within a specific wavelength range, thereby offering insights into the density of allowed electronic states and transition probabilities. The photon energy (hv) drives electron excitation, and the bandgap energy (Eg) acts as the minimum energy threshold for an electron to move from the valence band to the conduction band. The parameter A is a material-dependent proportionality constant that remains relatively stable across the spectral range of interest. A key factor in this analysis is the exponent n, which indicates the type of electronic transition. For direct transitions (n = 1/2), the process involves a straightforward photon-to-electron energy transfer without the need for additional energy mediation. This mechanism has been reported in systems such as mixed-valence Cu<sub>X</sub>O [25], few-layered hexagonal boron nitride nanosheets (hBNNS) [26], and Cu/Cu<sub>X</sub>O-hBNNS hybrid structures [22, 27], where direct optical transitions dominate the absorption behavior. Conversely, for indirect transitions (n = 2), electron excitation requires not only photon energy but also assistance from phonons, which provide the necessary momentum compensation. This distinction between direct and indirect transitions is essential for interpreting the optical behavior of semiconductors and for tailoring materials toward specific optoelectronic applications.

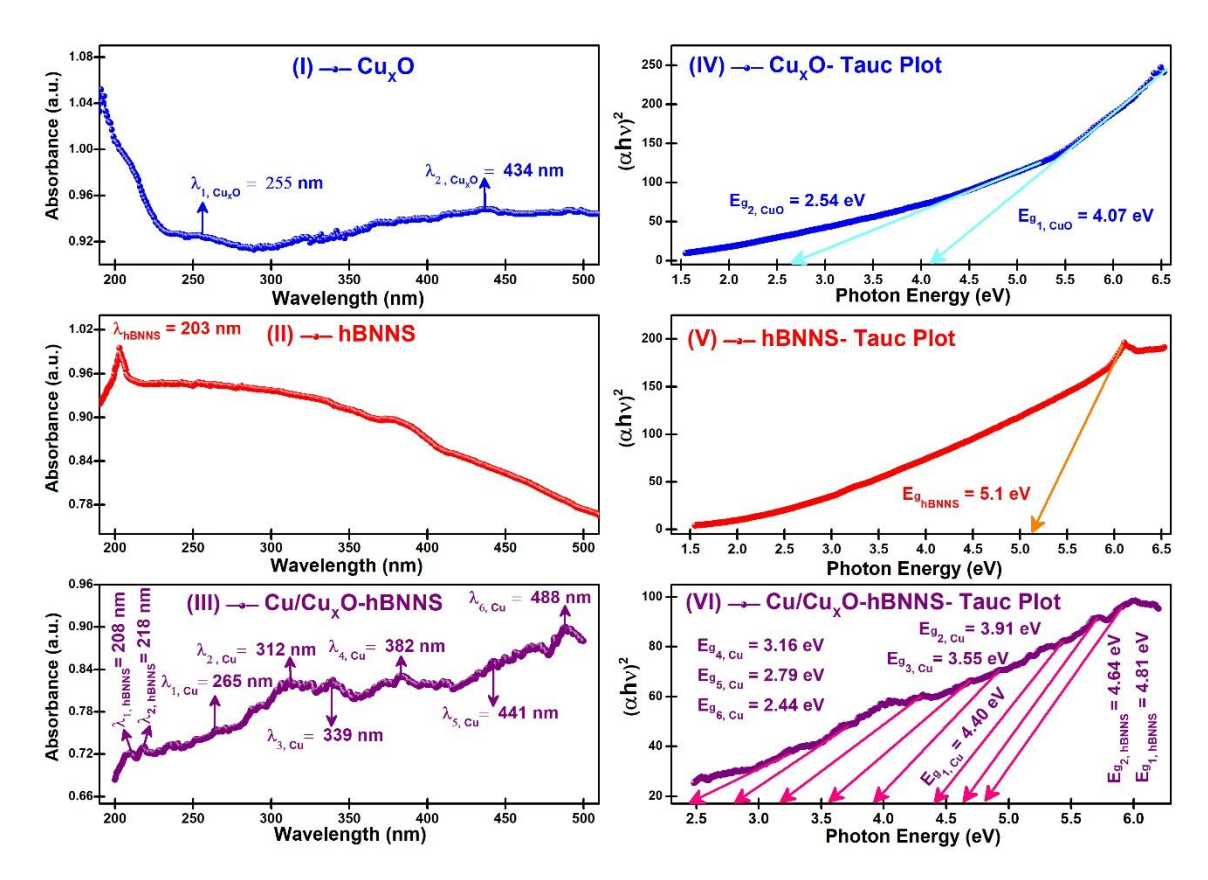


Figure 6.6: UV-Vis spectroscopic absorption data with corresponding Tauc plots, highlighting the electronic transition and bandgap estimation in CuxO (Blue), hBNNS (Red), Cu/CuxO/hBNNS (Purple)

The absorption spectrum of Cu<sub>x</sub>O nanoflowers (Fig. 6.6(c)-I) revealed a strong peak centered at 255 nm, positioned within the ultraviolet region of the spectrum. This feature is directly associated with the intrinsic electronic structure of CuXO, yielding a direct bandgap value (Eg,CuxO) of 4.07 eV (Fig. 6.6(c)-IV). The origin of this absorption is attributed to a ligand-to-metal charge transfer (LMCT) transition, where an electron is promoted from the oxygen p-orbitals (acting as the ligand) into the copper d-orbitals (metal ion states) [28]. Such LMCT processes are characteristic of transition metal oxides and underline the strong coupling between oxygen and copper states, which significantly influences the optical activity of the nanostructures. Another welldefined absorption band was observed at 434 nm in the visible region, corresponding to a narrower optical bandgap of 2.54 eV (Fig. 6.6(c)-IV). This feature arises from dd electronic transitions within Cu<sup>2+</sup> ions, specifically involving excitation from the lower-energy T<sub>2</sub>g orbital to the higher-energy E<sub>2</sub>g orbital [29]. The presence of this transition highlights the contribution of localized electronic states in modulating the optical response of CuxO nanoflowers, thereby enhancing their capacity to interact with visible light—a property highly desirable for applications in photocatalysis and optoelectronics.

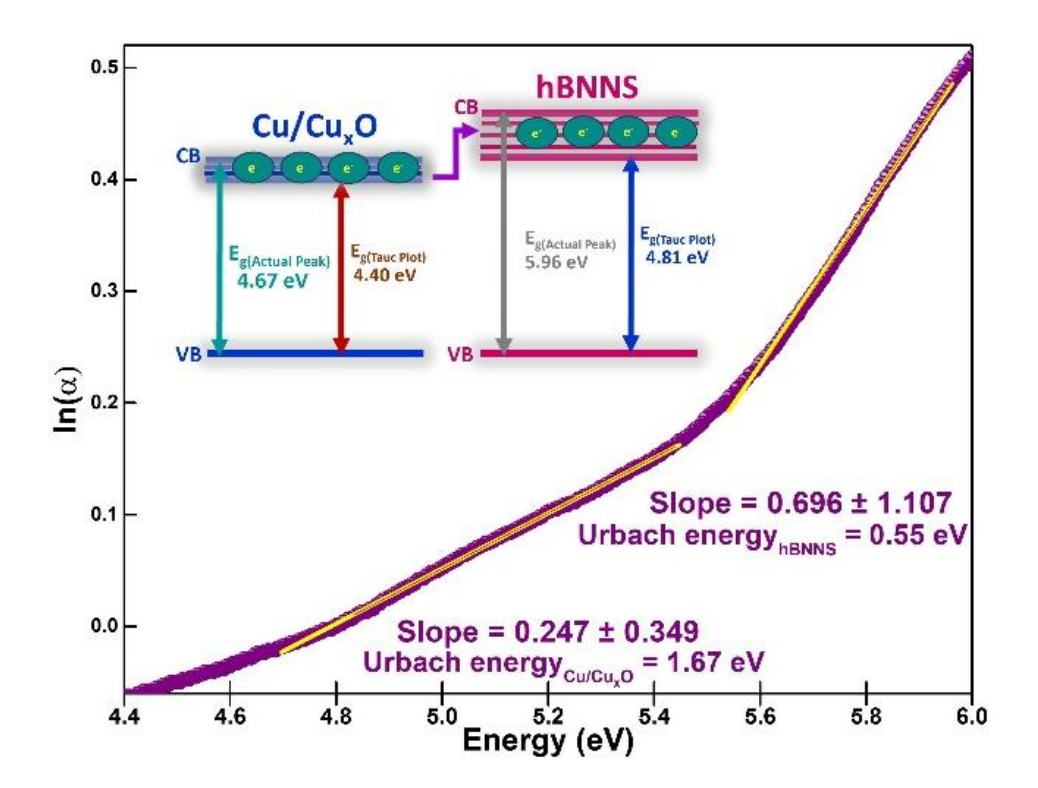


Figure 6.7: Urbach Energy evaluation for Cu/Cu<sub>X</sub>O-hBNNS Nano-hybrid Composite

In addition, the absorption spectrum of hBNNS (Fig. 6.6(c)-II) displayed a peak at 203 nm, characteristic of transitions involving excitonic states within its wide bandgap structure. The bandgap of hBNNS was calculated to be 5.1 eV (Fig. 6.6(c)-V), which reflects its insulating nature and exceptional stability [30]. Such wide-bandgap behavior, along with robust excitonic features, makes hBNNS an attractive sensing platform and a suitable host for hybrid nanocomposites. Upon the formation of Cu/Cu<sub>X</sub>O-hBNNS nanohybrids (NHCs) (Fig. 6.6(c)-III), substantial modifications in the optical spectrum were evident. The primary absorption band of hBNNS underwent a red-shift and split into two distinct peaks at 208 nm and 218 nm. This splitting signifies a profound alteration in the electronic environment caused by the incorporation of Cu and Cu<sub>X</sub>O nanoparticles into the hBNNS framework. The hybridization of copper states with the boron nitride matrix leads to the generation of new defect states and electronic pathways, effectively tuning the absorption edge and broadening the optical response of the system. To gain further insights into the localized defect states and disorder introduced within the hybrid system, the Urbach energy was evaluated using Eq. [6.6]–[6.7], as shown in Fig. 6.7 [31]. The Urbach energy analysis quantifies the width of the band-tail states and provides a direct measure of defect density, thereby offering a deeper understanding of how nanoscale heterostructuring influences optical absorption, defect engineering, and potential optoelectronic performance.

$$\alpha = \alpha_o \exp(\frac{E - E_g}{E_{ij}})$$
 [6.6]

$$\ln(\alpha) = \ln(\alpha_0) + \frac{(E - E_g)}{E_u}$$
 [6.7]

a denotes the absorption coefficient that governs the interaction of photons with the material, while αω is a material-dependent pre-exponential factor. The incident photon energy is represented as E = hv, where h is Planck's constant and v is the frequency of incident light. The bandgap energy Eg defines the threshold for electronic excitation at a specific temperature (T), whereas the Urbach energy (Eu), determined from the inverse slope of the linear fit in the plot of  $ln(\alpha)$  versus E, quantifies the width of the band-tail states generated by structural disorder or defect-induced localized states. For pristine hBNNS, the Urbach energy (Eu,hBNNS) was calculated to be 0.55 eV (Fig. **6.67**), indicating a moderate density of tail states. This energy tail broadening reflects the material's ability to incorporate and stabilize Cu/Cu<sub>X</sub>O nanoflowers at its active surface sites, suggesting that defect accommodation is essential for the self-assembly of hybrid nanostructures. Upon hybridization, the introduction of Cu/Cu<sub>X</sub>O nanoflowers led to profound modifications in the absorption features. The absorption spectrum of Cu/Cu<sub>X</sub>O-hBNNS displayed a red-shifted Cu/Cu<sub>X</sub>O peak at 265 nm (Fig. 6.6(c)-III), accompanied by a significantly higher Urbach energy (Eu,Cu/Cu<sub>X</sub>O) of 1.67 eV (Fig. 6.7). This dramatic increase points toward the onset of surface plasmon resonance (SPR) phenomena in Cu/Cu<sub>X</sub>O nanoflowers, where incident light stimulates collective oscillations of conduction electrons on nanoparticle surfaces [32]. Such plasmonic excitations alter the local electromagnetic field, enhance light absorption, and strongly influence charge carrier generation and transfer across the hybrid interface.

Additional absorption features were observed at 312 nm (Eg2 = 3.91 eV), 339 nm (Eg3 = 3.55 eV), and 382 nm (Eg4 = 3.16 eV) (**Fig. 6.6(c)-III, VI**). These excitations correspond to defect-mediated excitonic transitions, where photogenerated excitons are stabilized by defect states, thereby facilitating efficient charge transfer within the hybrid composite. The existence of multiple transitions with Eg > 3 eV highlights the role of defect engineering in tuning the optical response and charge dynamics of the hybrid [28]. Moreover, a broad absorption edge extending into the visible region at 441 nm and 488 nm was identified, attributed to metal-centered transitions in metallic Cu<sup>0</sup> nanostructures. These features are linked to inter-band transitions between the Cu (2Eg) and hBNNS (2T2g) states, synergistically coupled with the plasmonic response of Cu<sub>X</sub>O nanoparticles. Such hybridized transitions demonstrate that the Cu/Cu<sub>X</sub>O-hBNNS nanohybrid composite sustains highly efficient electronic coupling between metal and semiconductor components[33, 34].

# 6.3.1.4 Raman Spectroscopic Analysis of Phonon Dynamics, Vibrational Signatures, and Electronic Interactions in Cu/CuxO-hBNNS Nano-Hybrid Nanocomposites

The vibrational and structural properties of (I)  $Cu_XO$ , (II) hBNNS, and (III)  $Cu/Cu_XO$ -hBNNS nanohybrids were analyzed through surface-enhanced Raman spectroscopy (SERS), with results shown in **Fig. 6.8**. Owing to its monoclinic lattice,  $Cu_XO$  exhibits a phonon spectrum far more intricate than cubic or hexagonal oxides. At the  $\Gamma$  point, a CuO unit cell (with two copper and two oxygen atoms) yields 12 vibrational modes, represented as:

$$\Gamma = A_g + 2B_g + 4A_u + 5B_u$$

This includes six infrared-active modes (3Au + 3Bu), three acoustic modes (Au + 2Bu), and three Raman-active modes (Ag + 2Bg). Importantly, within this monoclinic

symmetry, Cu atoms remain stationary due to their site constraints, leaving oxygen atoms as the primary contributors to Raman-active vibrations.

In **Fig. 6.8-I**, the characteristic Raman bands of CuO are observed at 281 cm<sup>-1</sup> (Ag), 331 cm<sup>-1</sup> (B1g), and 599 cm<sup>-1</sup> (B2g). The notable red-shift of the Ag mode to 281 cm<sup>-1</sup> reflects the in-phase and out-of-phase rotational vibrations of CuO units, indicative of changes in lattice dynamics arising from intrinsic defects, strain, or size confinement effects, corroborated by XRD findings [35]. Similarly, the B1g mode at 331 cm<sup>-1</sup>, associated with Cu–O bond bending vibrations, demonstrates alterations in bond strength and lattice parameters, while the B2g mode at 599 cm<sup>-1</sup> suggests modifications in the local oxygen environment, likely induced by distortions or oxygen vacancies. Such systematic red-shifting of Raman-active modes can also be attributed to the 785 nm laser excitation wavelength, which is known to generate localized heating effects in transition metal oxides, thereby enhancing anharmonic interactions [36].

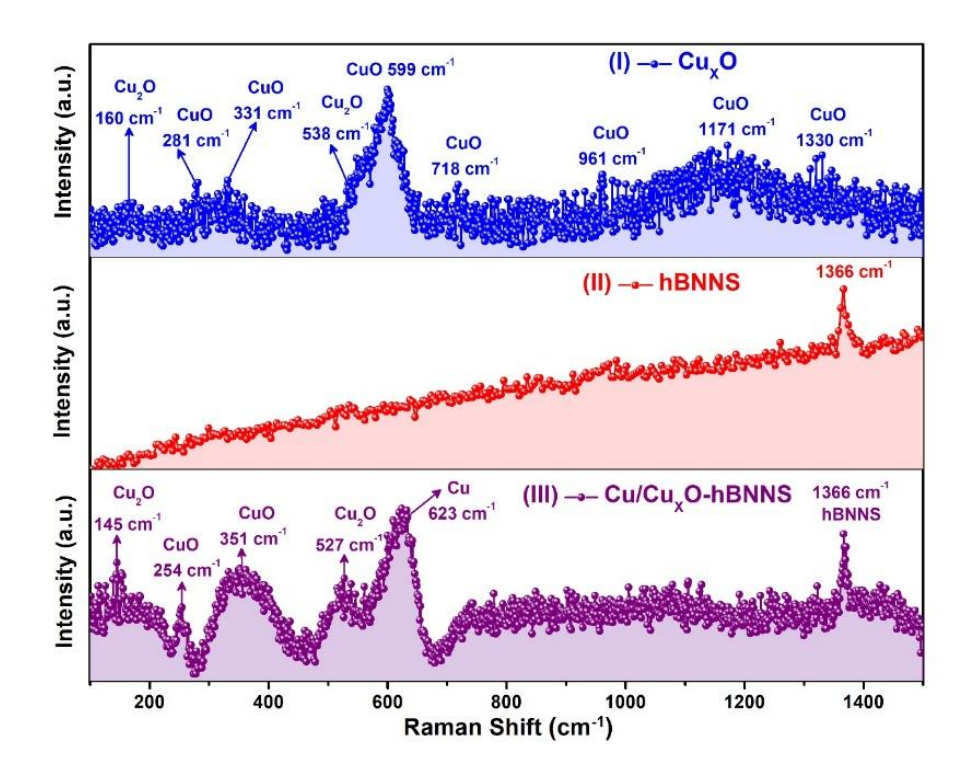


Figure 6.8: Raman spectroscopic response for  $Cu_XO$  (Blue), hBNNS (Red), and  $Cu/Cu_XO$ -hBNNS (Purple)

The additional high-frequency phonon modes observed at 718 cm<sup>-1</sup>, 961 cm<sup>-1</sup>, 1171 cm<sup>-1</sup>, and 1330 cm<sup>-1</sup> correspond to second-order overtones and combination bands of lattice vibrations, thereby confirming the crystalline quality of Cu<sub>X</sub>O [37]. The emergence of blue-shifted peaks at 160 cm<sup>-1</sup> and 538 cm<sup>-1</sup> reflects contributions from T<sub>1u</sub> and T<sub>2g</sub> vibrational symmetries, characteristic of Cu<sub>2</sub>O domains embedded within the Cu<sub>X</sub>O matrix [38]. The coexistence of these CuO and Cu<sub>2</sub>O phases within nanoflowers underscores the mixed-valence nature of copper oxides, which enriches their electronic complexity and fosters stronger electron–phonon interactions. This observation points toward a partial coexistence of CuO and Cu<sub>2</sub>O phases in Cu<sub>X</sub>O nanoflowers, a phenomenon frequently observed in mixed-valence copper oxides

where redox dynamics stabilize multiple oxidation states. These factors validate the successful synthesis of Cu<sub>X</sub>O nanostructures and highlight the hybrid's potential exhibiting the density of electronic states and promote synergistic charge-transfer mechanisms for plasmonic activity, defect-mediated charge transfer, and multifunctional applications in photocatalysis, sensing, and energy devices.

The Raman spectrum of hBNNS, displayed in Fig. 6.8-(II), is dominated by a welldefined E<sub>2</sub>g mode at 1366 cm<sup>-1</sup>, a characteristic phonon vibration of hexagonal boron nitride. The red-shift relative to bulk hBN signifies that hydrothermal synthesis induced tensile strain, leading to a measurable increase in interlayer spacing. This strain facilitates layer exfoliation, thereby reducing thickness while enhancing lateral size. Simultaneously, the process improves crystalline order, diminishes the defect density, and ensures the production of high-quality nanosheets [18]. Upon forming the Cu/Cu<sub>X</sub>O-hBNNS nanocomposite, the position of the E<sub>2</sub>g band remains fixed, as seen in Fig. 6.8-(III). This stability indicates that the interlayer separation and overall layered structure of hBNNS are structurally robust, even under the influence of Cu/Cu<sub>X</sub>O nanoparticle incorporation. Reinforcement from XRD patterns, which show unaltered d-spacing values, further affirms that the integrity of hBNNS was maintained. The hybrid spectrum also highlights a strong band at 623 cm<sup>-1</sup>, assigned to metallic Cu<sup>0</sup> vibrational modes. The presence of Cu<sup>0</sup> is critical as it underpins plasmonic activity and electron–phonon interactions within the composite [39]. Complementary weaker peaks detected through SERS at 145 cm<sup>-1</sup> and 527 cm<sup>-1</sup> (attributed to Cu<sub>2</sub>O) and 254 cm<sup>-1</sup> and 351 cm<sup>-1</sup> (attributed to CuO) demonstrate partial oxidation of metallic copper. The coexistence of these phases not only validates XRD observations but also points to dynamic redox behavior, where Cu<sup>0</sup> undergoes oxidation into Cu<sup>+</sup> and Cu<sup>2+</sup> states [38]. The multiphase coexistence enhances the composite's capacity for charge-transfer interactions, contributing to its optoelectronic and catalytic efficiency.

# 6.3.1.5 FT-IR Spectroscopy elucidating Molecular Bond Dynamics and Protein Immobilization Mechanisms in Cu/Cu<sub>X</sub>O-hBNNS Hybrid Nanocomposites

FTIR spectroscopy was employed to qualitatively examine chemical interactions, bond formation, and the presence of functional groups, offering molecular-level insights into the structural composition of the studied materials (Table 6.2). As shown in Fig. 6.9(e)-I, the FTIR spectrum of polyol-synthesized CuXO nanoflowers exhibited distinct vibrational bands at 425 cm<sup>-1</sup>, 531 cm<sup>-1</sup>, and 587 cm<sup>-1</sup>, corresponding to the Au, Blu, and B2u modes of Cu–O stretching, respectively [40]. Specifically, the Au mode at 425 cm<sup>-1</sup> represents Cu-O stretching along the [101] plane, whereas the Bu modes at 531 cm<sup>-1</sup> and 587 cm<sup>-1</sup> denote Cu–O stretching vibrations along the same crystallographic direction [40]. Additional absorption bands at 881 cm<sup>-1</sup>, 1385 cm<sup>-1</sup>, and 1619 cm<sup>-1</sup> were assigned to Cu-OH bending, in-plane CuO rocking, and out-of-plane CuO rocking vibrations, respectively, verifying the successful functionalization of CuxO nanoflowers [41, 42]. Furthermore, two prominent transmittance peaks at 2853 cm<sup>-1</sup> and 2922 cm<sup>-1</sup>, attributed to symmetric and asymmetric stretching of the -CH<sub>2</sub> methylene groups, confirm the presence of residual Tween 20 and ethylene glycol (EG) used during the polyol synthesis [43]. In addition, a well-defined band at 1086 cm<sup>-1</sup> was identified as the C-O stretching vibration, a characteristic feature of EG. Collectively, these peaks confirm the interaction of Cu<sub>X</sub>O nanoflower surface-active sites with Tween 20 and EG molecules, leading to surface functionalization that influenced both the molecular structure and physicochemical composition of the nanoflowers. Meanwhile, the FTIR spectrum of hBNNS (**Fig. 6.9(e)-II**) revealed characteristic vibrational fingerprints of boron nitride. Specifically, a band at 806 cm<sup>-1</sup> represents B–N–B out-of-plane bending ( $A_{2u}$  mode), and the 1387 cm<sup>-1</sup> band corresponds to B–N in-plane stretching ( $E_{1u}$  mode). Additional absorption bands were observed at 2526 cm<sup>-1</sup> (B–H stretching), in the 3200–3500 cm<sup>-1</sup> region (N–H stretching), and above 3500 cm<sup>-1</sup> (O–H stretching), indicating the incorporation of hydrogenated and hydroxyl groups [18]. These features confirm that hydrothermal treatment not only preserved the intrinsic vibrational identity of hBN but also introduced surface functionalization, enhancing the nanosheets' chemical reactivity and structural adaptability.

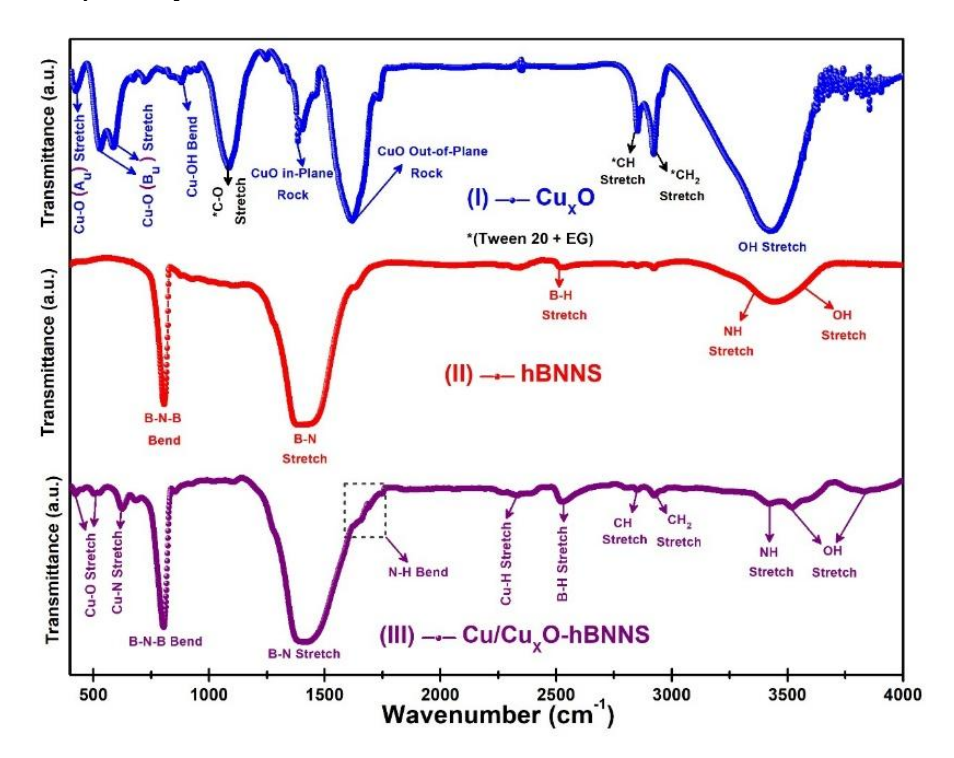


Figure 6.9: FTIR spectra of CuxO (Blue), hBNNS (Red), and Cu/CuxO-hBNNS (Purple)

The integration of Cu/Cu<sub>X</sub>O nanostructures with hBNNS during nanocomposite formation induced a systematic red shift of the characteristic FT-IR peaks of hBNNS to 802 cm<sup>-1</sup> and 1455 cm<sup>-1</sup>, serving as compelling evidence of Cu/Cu<sub>X</sub>O incorporation into the layered hBNNS matrix. This shift arises from synergistic effects including charge transfer processes, electrostatic interactions, coordination bond formation, and lattice strain introduced into the nanohybrid composite (NHC). A strong vibrational signature at 630 cm<sup>-1</sup> in the Cu/Cu<sub>X</sub>O-hBNNS spectrum is specifically attributed to Cu-N bond formation, indicating the establishment of coordinate covalent interactions wherein Cu/Cu<sub>X</sub>O behaves as a Lewis acid while nitrogen from hBNNS [44] or hydrazine hydrate molecules function as Lewis bases [45]. Such bonding interactions at surface-active sites promote ordered self-assembly and significantly reinforce the stability of the hybrid system. Subtle absorption features detected at 424 cm<sup>-1</sup> and 505 cm<sup>-1</sup> correspond to copper-oxygen vibrations, pointing toward partial oxidation of Cu/Cu<sub>X</sub>O nanoparticles, consistent with their high surface reactivity. These peaks align

well with Raman and XRD analyses, jointly verifying the coexistence of copperoxygen bonds. Beyond these fundamental interactions, hydrothermal functionalization introduced additional spectral bands at 1661 cm<sup>-1</sup> (N–H bending), 2332 cm<sup>-1</sup> (Cu–H stretching), 2526 cm<sup>-1</sup> (B–H stretching), 2852 cm<sup>-1</sup> (symmetric CH<sub>2</sub> stretching), 2925 cm<sup>-1</sup> (asymmetric CH<sub>2</sub> stretching), and 3422 cm<sup>-1</sup> (N–H stretching). These vibrational fingerprints provide evidence of chemical bonding, transient interactions, and cooperative self-assembly mechanisms that govern the molecular organization and stability of the Cu/Cu<sub>X</sub>O–hBNNS nanocomposite [46, 47].

Table 6.2: FT-IR band assigned to (I) CuxO, (II) hBNNS, and (III) Cu/CuxO-hBNNS samples respectively.

S.NO.	Sample	Wavenumber (cm <sup>-1</sup> )	Assigned Bands
	Cu <sub>X</sub> O	425	Au mode Cu-O Stretch
		531	B <sub>u</sub> mode Cu-O Stretch
		587	B <sub>u</sub> <sup>2</sup> mode Cu-O Stretch
		881	Cu-OH Bend
		1086	C-O Stretch
1.		1385	CuO in-plane Rocking Vibration
1.		1619	CuO Out-of-plane Rocking Vibration
		2354	Cu-H Stretch
		2853	CH Stretch
		2922	CH <sub>2</sub> Stretch
		3432	OH Stretch
	hBNNS	806	B-N-B Bend
		1387	B-N Stretch
2.		1628	N-H Bend
2.		2526	B-H Stretch
		3200-3500	N-H Stretch
		>3500	OH Stretch
	Cu/Cu <sub>x</sub> O-hBNNS	424, 505	Cu-O Stretch
		625	Cu-N Stretch
		804	B-N-B Bend
		1408	B-N Stretch
		1661	N-H Bend
3.		2332	Cu-H Stretch
3.		2526	B-H Stretch
		2852	CH <sub>2</sub> (Symmetric) Stretch
		2925	CH <sub>2</sub> (Asymmetric) stretch
		3422	N-H Stretch
		3521, 3827 (>3500)	OH Stretch

Optimizing the electrocatalytic efficiency of the Cu/Cu<sub>X</sub>O-hBNNS nano-biosensor fundamentally depends on the precise engineering of a nano-biointerface. To attain this optimization, the precise adjustment of antibody immobilization time, which ensures maximum occupation of surface-active sites, thereby enhancing the sensor's sensitivity toward trace analyte concentrations, reducing response time, and improving the reliability of bioanalytical outputs. FTIR spectra presented in **Fig. 6.10** compare the Cu/Cu<sub>X</sub>O-hBNNS/ITO electrode (purple) before modification with Anti-CEA immobilization after 12 h (orange) and 24 h (dark cyan).

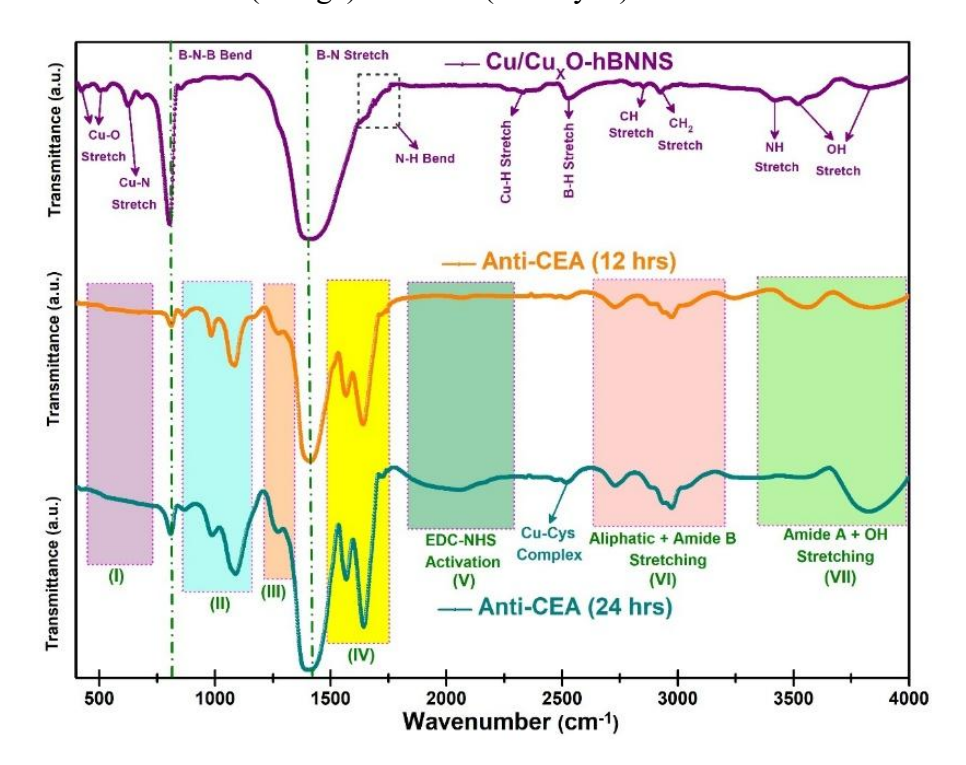


Figure 6.10: Immobilization of Anti-CEA antibodies on Cu/CuxO-hBNNS/ITO electrodes monitored by FTIR spectroscopy at 12 hours (Orange) and 24 hours (Cyan), demonstrating stepwise enhancement of biomolecular attachment.

Upon antibody immobilization, the FTIR profile shows the retention of a less intense B–N–B bending vibration and a distinct B–N stretching vibration, while the characteristic peaks corresponding to Cu–N, Cu–H, and B–H stretching modes disappear. Their absence confirms their active involvement in amide bond formation via EDC–NHS activation chemistry, enabling covalent anchoring of antibodies. Notably, prolonged immobilization for 24 h resulted in a clear intensification of protein-related vibrational signatures: region II (protein phosphorylation at 868 cm<sup>-1</sup>, symmetric phosphate stretching at 988 cm<sup>-1</sup>, polysaccharide stretching at 1090 cm<sup>-1</sup>), region III (NH bending at 1273 cm<sup>-1</sup>), region IV (Amide II at 1568 cm<sup>-1</sup>, Amide I at 1643 cm<sup>-1</sup>). Similarly, increased peak intensities were observed in region VI (aliphatic CH stretching at 2727 cm<sup>-1</sup>, CH<sub>2</sub> stretching at 2879 cm<sup>-1</sup>, Amide B stretching at 2975 cm<sup>-1</sup>) and region VII (Amide A stretching at 3560 cm<sup>-1</sup>, OH stretching >3500 cm<sup>-1</sup>), highlighting robust antibody adsorption. Furthermore, a distinct absorption band at 2059 cm<sup>-1</sup> validated EDC–NHS-mediated activation of –COOH and –NH<sub>2</sub> groups in

antibodies, enabling efficient crosslinking. An additional peak at 2518 cm<sup>-1</sup> was assigned to the interaction of Anti-CEA with Cu/Cu<sub>X</sub>O nanostructures, signifying strong complexation with cysteine residues in monoclonal IgG antibodies [18, 48]. Collectively, these findings confirm that 24 h incubation establishes an optimal biointerface for superior biosensing performance.

Sequential protein immobilization on the Cu/Cu<sub>X</sub>O-hBNNS/ITO immunoelectrode was systematically validated by FTIR spectroscopy, as illustrated in **Fig. 6.11**. After the optimized conjugation of EDC-NHS activated Anti-CEA onto the Cu/Cu<sub>X</sub>O-hBNNS/ITO electrode, 10 μL of BSA was introduced to passivate the biosensing matrix. This passivation step was critical, as the globular BSA protein effectively blocked unoccupied sites, preventing nonspecific antibody adsorption. In the FTIR spectra, the immobilization of BSA was confirmed by the emergence of characteristic peaks in region IV (1560 cm<sup>-1</sup>, 1645 cm<sup>-1</sup>, 1749 cm<sup>-1</sup>) and a distinct band at 3258 cm<sup>-1</sup>, corresponding to amide I vibrations and hydrogen-bonded N–H stretching [49]. These features indicated that BSA maintained a stable secondary structure upon immobilization. Moreover, the marked decrease in transmittance intensities across regions II–V further validated the efficient suppression of nonspecific background signals, thereby enhancing sensitivity, specificity, and the overall reliability of the nano-biointerface.

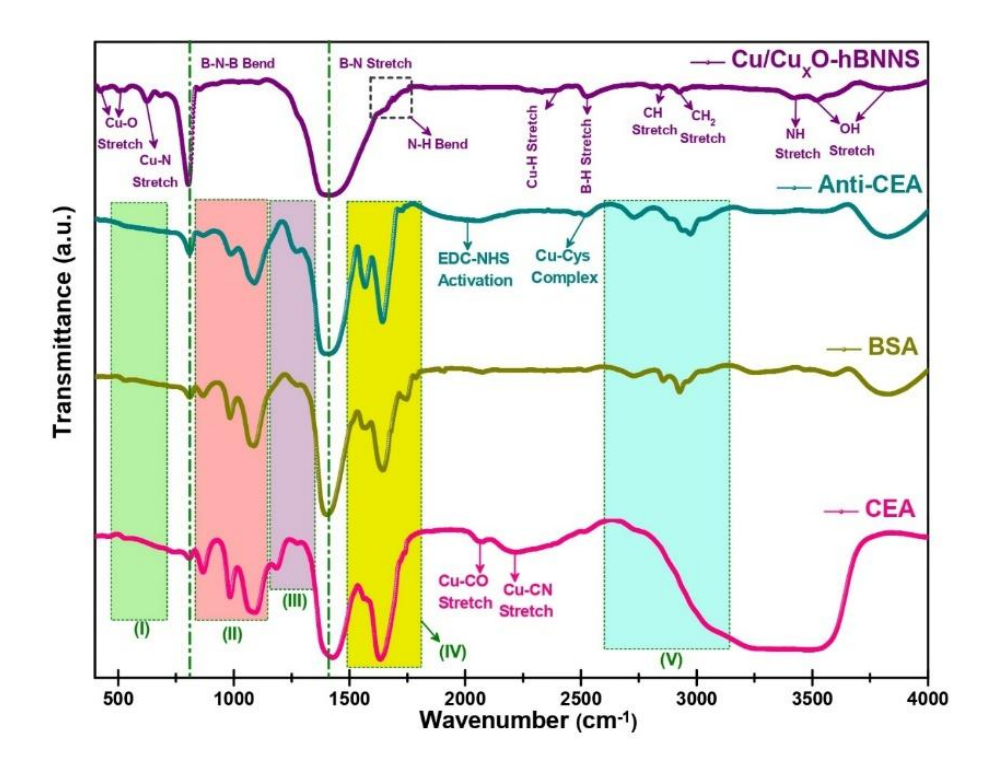


Figure 6.11: Stepwise fabrication of the Cu/CuxO-hBNNS based immunoelectrode evaluated using FTIR spectroscopy

Following this, immobilization of the target antigen CEA on the BSA/Anti-CEA/Cu/Cu<sub>X</sub>O-hBNNS/ITO assembly was clearly evident through the pronounced amplification of characteristic transmittance peaks in regions II–V, signifying successful antibody-antigen binding. A progressive reduction in the intensity of the B-N-B bending peak during sequential addition of BSA and CEA highlighted the

increased utilization of surface-active sites on hBNNS for crosslinking of antibody–antigen complexes [23]. Additionally, the appearance of two distinct peaks at 2074 cm<sup>-1</sup> and 2221 cm<sup>-1</sup>, corresponding to Cu–CO and Cu–CN bonds, confirmed Cu/Cu<sub>X</sub>O-mediated conjugation pathways facilitating protein immobilization [46, 50]. The broad absorption band in region V conclusively marked the immobilization of CEA, arising from overlapping contributions of aliphatic chains, amide groups, and hydroxyl groups, which collectively demonstrated the establishment of a stable and functionally active bio-recognition interface.

### **6.3.2** Electrochemical Profiling and Analysis:

### 6.3.2.1 Electrochemical Behaviour and Interfacial Kinetics of Sequential Protein Immobilization in Cu/CuxO-hBNNS Electrodes

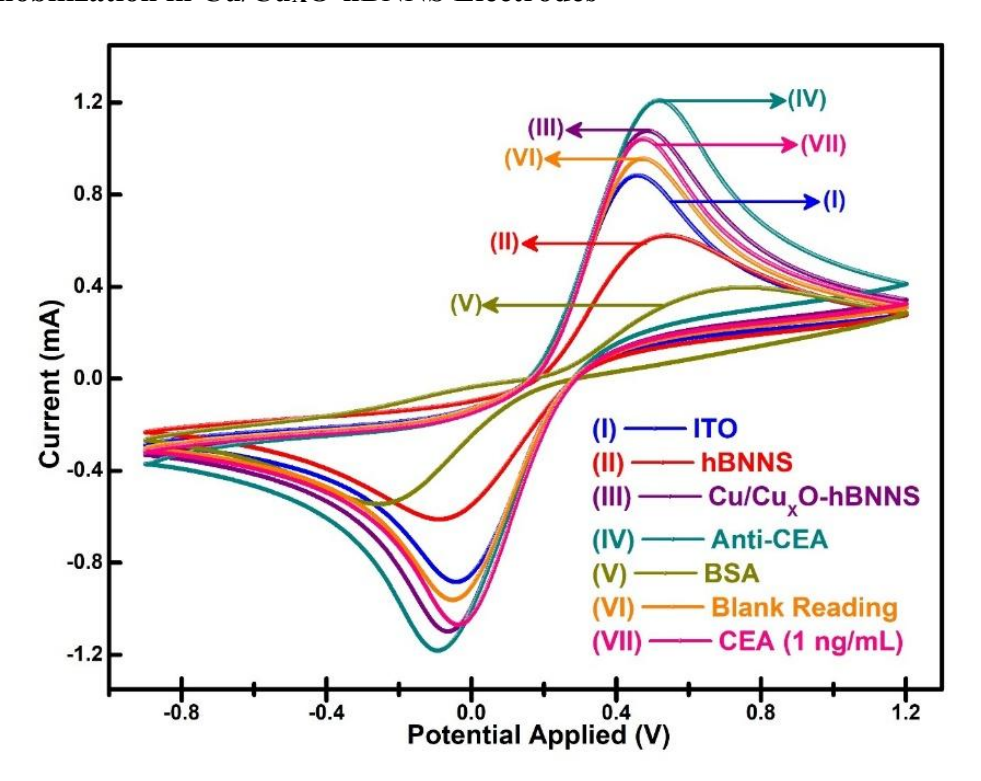


Figure 6.12: The progressive preparation of the Cu/Cu<sub>X</sub>O-hBNNS based immunoelectrode was validated using cyclic voltammetry (CV) analysis

Upon achieving optimized sensing conditions, the progressive fabrication stages of the Cu/Cu<sub>X</sub>O-hBNNS nano-biosensor were rigorously characterized using cyclic voltammetry (CV, **Fig. 6.12**) and differential pulse voltammetry (DPV, **Fig. 6.13**). These electrochemical measurements not only validated the FTIR results but also revealed substantial changes in anodic peak current (Ipa), DPV current response, and diffusion coefficients upon sequential immobilization of Anti-CEA, BSA, and CEA on the Cu/Cu<sub>X</sub>O-hBNNS/ITO electrode (**Table 6.3**). Furthermore, the diffusion coefficients at each immobilization stage were quantitatively determined using the Randle–Sevcik equation (**Eq. [6.8]**), offering direct insights into the evolving interfacial electron transfer kinetics throughout immunoelectrode construction.

$$I_p = (2.69 \times 10^5) n^{3/2} A C D^{1/2} \sqrt{\nu}$$
 [6.8]

Electrochemical investigations of the Cu/Cu<sub>X</sub>O-hBNNS/ITO electrode, guided by the Randles–Sevcik formalism, demonstrated remarkable improvements in interfacial charge transfer dynamics and overall biosensing capability. According to the equation, Ip represents the peak current (anodic/cathodic), n the number of electrons exchanged (n = 1), A the electroactive surface area (0.64 cm<sup>2</sup>), C the redox species concentration (5 × 10<sup>-3</sup> M), D the diffusion coefficient, and v the scan rate (50 mVs<sup>-1</sup>). Upon deposition of the Cu/Cu<sub>X</sub>O-hBNNS film onto the ITO substrate, electrochemical performance was significantly boosted, with ~74% enhancement in CV peak current, ~31% increase in DPV current, and a nearly threefold rise in the diffusion coefficient, relative to baseline hBNNS/ITO electrodes.

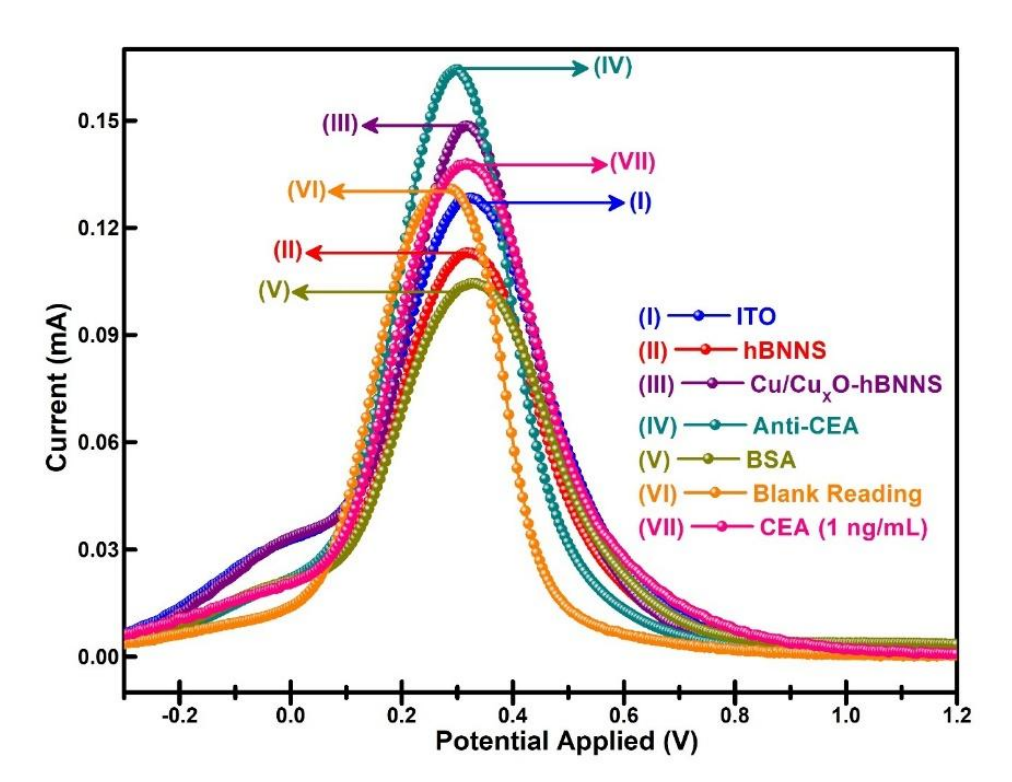


Figure 6.13: Monitoring of Cu/CuxO-hBNNS based immunoelectrode construction was performed through DPV response analysis.

The observed disparity between CV and DPV signals stems from their distinct mechanisms of current generation: CV encompasses both capacitive (non-faradaic) and faradaic contributions, yielding higher peak responses, while DPV isolates faradaic currents by attenuating background interference, thereby delivering more accurate and quantitative outcomes [51, 52]. The improvements in electrochemical behaviour of the Cu/Cu<sub>X</sub>O nanoflowers is due to the unique physicochemical properties, which introduce high-density surface-active sites, broaden electron transport pathways, and exhibit robust catalytic activity. Their hybridization with hBNNS creates a synergistic architecture that accelerates electron kinetics, improves surface charge distribution, and stabilizes the electrode matrix, culminating in superior electrochemical efficiency. Sequential functionalization experiments revealed that the immobilization of Anti-CEA antibodies increased the CV and DPV responses by 10% and 12%, respectively, alongside a 22% rise in diffusion coefficient, underscoring the efficiency of EDC-NHS

mediated coupling in exploiting the porous, multifunctional Cu/Cu<sub>X</sub>O nanostructures (**Table 6.3**).

However, subsequent incubation with BSA induced a significant decline in current response, a direct consequence of protein passivation, where bulky BSA molecules occupy available surface-active sites and obstruct the catalytic channels within the Cu/CuxO nanoflowers. This selective blocking effect confirmed effective suppression of non-specific antibody interactions, thereby enhancing biosensor reliability. Interestingly, blank PBS solution elicited a modest increase in current, highlighting the contributory role of ionic conduction in modulating electrode response. Ultimately, the immobilization of CEA antigens produced a marked rise in current intensity, attributed to the robust formation of antibody—antigen complexes and their electron-coupled interactions with Cu/CuxO nanostructures. This distinct electrochemical signature validates the successful biofunctionalization of the immunoelectrode, evidencing its potential for high-sensitivity detection through the efficient translation of biorecognition events into amplified electrochemical signals.

## 6.3.2.2 Quantitative Evaluation of Scan Rate-Controlled Interfacial Electron Transport in Cu/Cu<sub>X</sub>O-hBNNS/ITO-Based Nano-Biosensors

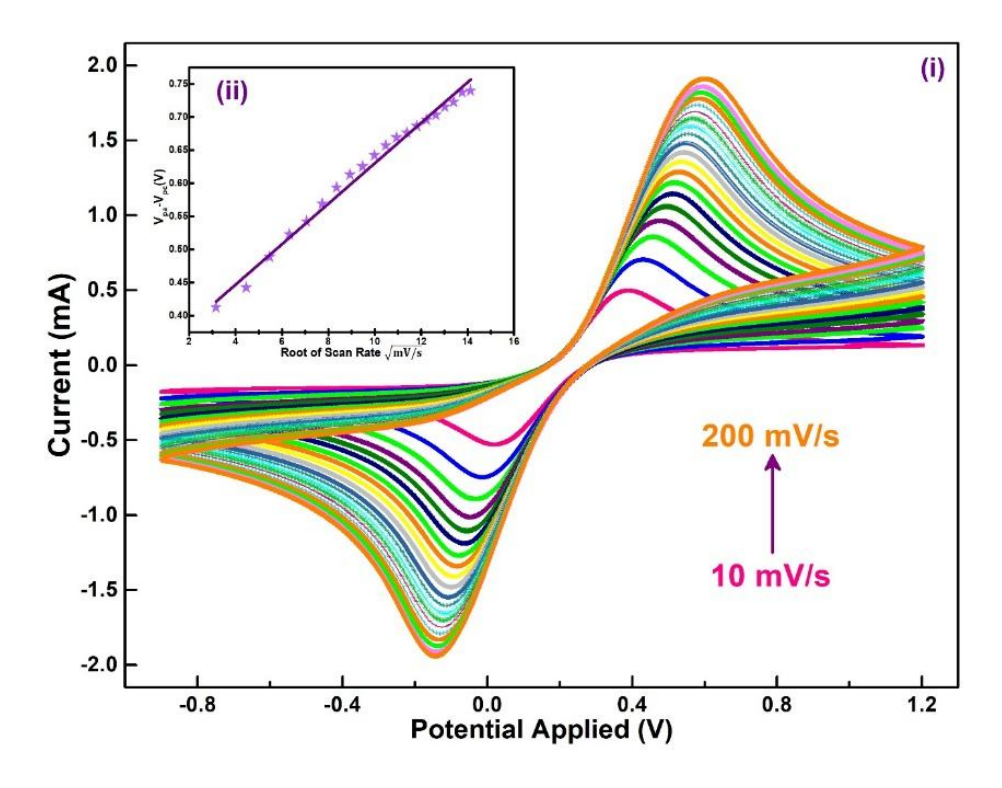


Figure 6.14: Scan rate-dependent cyclic voltammetric investigation of BSA/Anti-CEA/Cu/CuxO-hBNNS/ITO immunoelectrodes, measured across 10–200 mV/s; inset demonstrates the linear relationship between  $\Delta$ Vp and  $\sqrt{s}$ can rate.

The interfacial kinetics of the as-fabricated BSA/Anti-CEA/Cu/Cu<sub>X</sub>O-hBNNS/ITO nano-biosensor were comprehensively examined in PBS buffer (pH 7.0, 50 mM, 0.9% NaCl) using cyclic voltammetry (CV) across an extended scan rate range from 10 mV/s to 200 mV/s, as shown in **Fig. 6.14**. The CV curves revealed a pronounced increase in

both anodic and cathodic peak currents (Ipa, Ipc) with increasing scan rate, accompanied by systematic shifts in anodic and cathodic peak potentials (Vpa, Vpc). A linear correlation was observed between Ipa/Ipc and the square root of the scan rate, as demonstrated in **Fig. 6.15**, signifying that the electron transfer processes at the BSA/Anti-CEA/Cu/CuxO-hBNNS/ITO nano-biointerface were dominantly diffusion-controlled (**Eq. [6.9]-[6.12]**) This implies that the redox-active species near the electrode surface rely primarily on their diffusion rate for effective charge transfer. Moreover, the gradual increase in current magnitude with scan rate suggests a higher flux of redox species toward the electrode interface, while the near-linear dependence of potential shift with scan rate highlights the reversible nature of the redox processes involved. These findings clearly confirm that the biosensor's interfacial electron transfer kinetics are governed by diffusion phenomena, ensuring reliable and sensitive electrochemical responses.

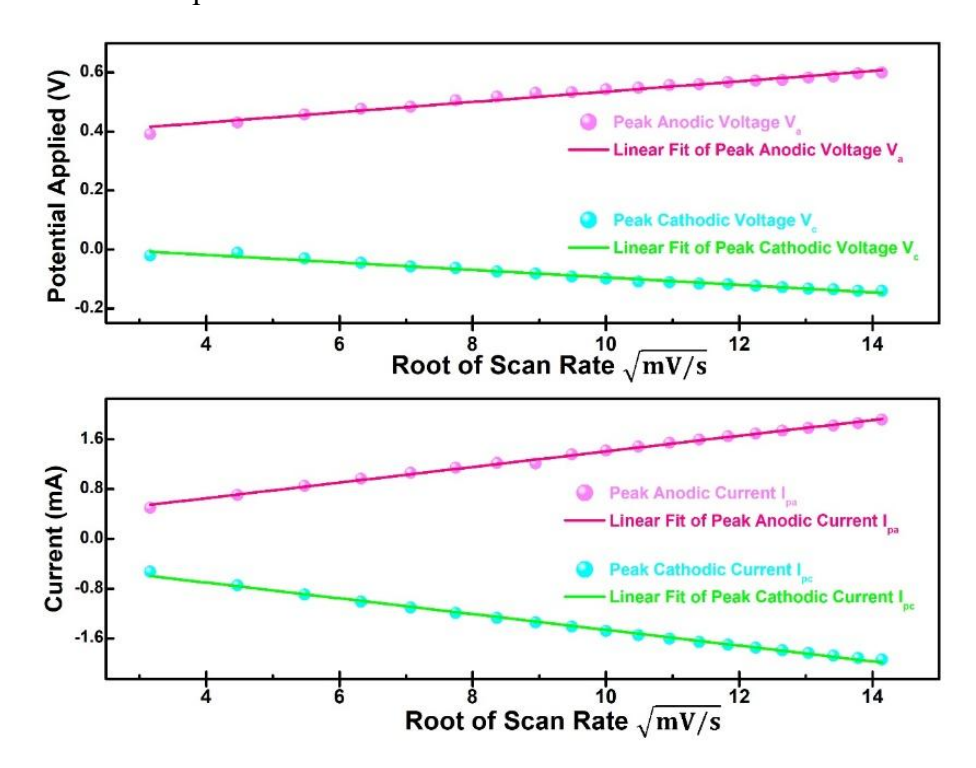


Figure 6.15: Linear correlation established between (i) applied potential and (ii) current response with respect to the square root of scan rate for BSA/Anti-CEA/Cu/CuxO-hBNNS/ITO immunoelectrode.

$$V_{pa} = [\ 3.601 \times 10^{-1} \ V + \ 1.75 \times 10^{-2} \ V \sqrt{s/mV} \times \sqrt{Scan \ Rate[mV/s]} \ ];$$
 
$$R^2 = 0.987 \qquad [Eq. 6.9]$$

$$\begin{aligned} V_{pc} &= [\ 3.\ 227 \times 10^{-2}\ V - 1.\ 271 \times 10^{-2}\ V \sqrt{s/mV} \times \sqrt{Scan\ Rate[mV/s]}\ ]; \\ R^2 &= 0.991 \quad [Eq.\ 6.10] \end{aligned}$$

$$I_{pa} = [\ 1.509 \times 10^{-4} A + \ 1.255 \times 10^{-4} \ A \sqrt{s/mV} \times \sqrt{Scan\ Rate[mV/s]}];$$
 
$$R^2 = 0.998 \qquad [Eq.\ 6.11]$$

$$I_{pc} = [-1.952 \times 10^{-4} A - 1.266 \times 10^{-4} A \sqrt{s/mV} \times \sqrt{Scan Rate[mV/s]}];$$
 R<sup>2</sup> = 0.998 [Eq. 6.12]

The interfacial electron transfer efficiency of the BSA/Anti-CEA/Cu/CuxOhBNNS/ITO immunoelectrode was further substantiated by analyzing the difference between the anodic and cathodic peak potentials ( $\Delta Vp$ ). As shown in Fig. 6.14(Inset), ΔVp displayed a well-defined linear correlation with the square root of the scan rate  $(\sqrt{v})$ , in accordance with Eq. [6.13], signifying that the redox process was largely diffusion-controlled and kinetically unhindered at the electrode interface. This behavior underscores a highly conductive and electroactive surface, where the immobilized biomolecules effectively facilitate charge transport with the ferro/ferricyanide  $[Fe(CN)6]^{3-/4-}$  redox couple in PBS electrolyte. The minimal separation in  $\Delta Vp$  at lower scan rates provides strong evidence of fast electron transfer kinetics, reversible charge transport, and negligible resistive losses. At higher scan rates beyond 150 mV/s, however, slight deviations in  $\Delta Vp$  were detected, which can be explained by complex electrochemical dynamics such as incomplete diffusion layer relaxation, sluggish electron hopping rates, solution ohmic resistance, enhanced capacitive contributions from the electrical double layer, and inherent limitations in instrumental response time. These deviations, while minor, do not compromise the overall performance of the immunoelectrode but rather reflect the natural limitations of high-frequency electrochemical interrogation. Taken together, the findings demonstrate that the BSA/Anti-CEA/Cu/Cu<sub>X</sub>O-hBNNS/ITO nano-biosensor exhibits highly efficient, rapid, and reversible electron transfer properties under practical operating conditions, which directly contribute to its sensitivity, stability, and reliability in biosensing applications.

# 6.3.2.3 Assessment of the Sensing Performance and Electrochemical Response Dynamics of Cu/CuxO-hBNNS-Based Immunoelectrodes

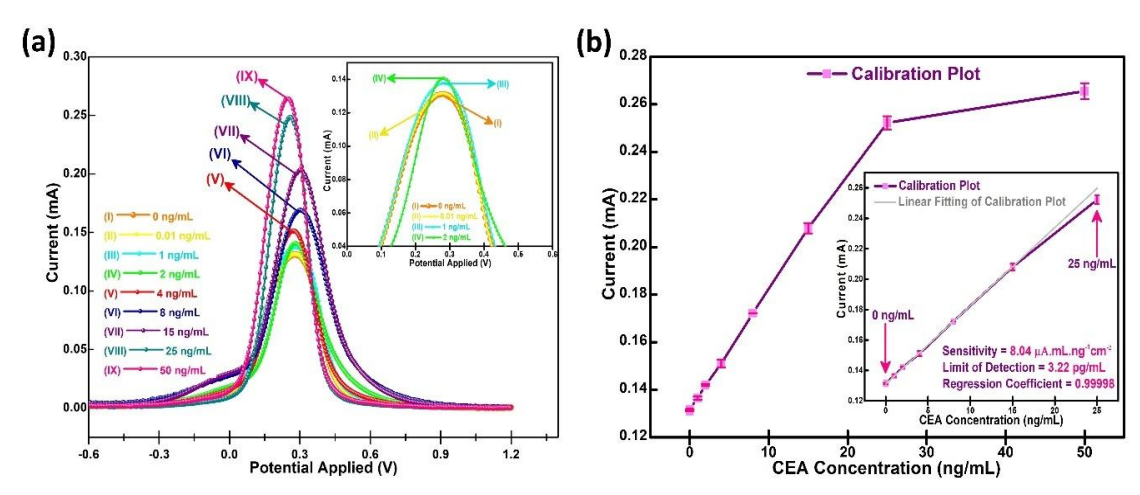


Figure 6.16: (a) Differential Pulse Voltammetry (DPV) responses recorded for varying CEA concentrations (0–50 ng/mL) on the BSA/Anti-CEA/Cu/CuxO-hBNNS/ITO immunoelectrode; (b) Corresponding calibration curve illustrating the linear correlation between DPV current signals and CEA concentration.

Under precisely optimized experimental conditions, the sensing capability of the BSA/Anti-CEA/Cu/Cu<sub>x</sub>O-hBNNS/ITO nano-biosensor was examined for ultrasensitive and quantitative detection of the carcinoembryonic antigen (CEA) biomarker, a critical clinical marker associated with non-small cell lung cancer (NSCLC). While the serum concentration of CEA in healthy individuals generally remains below 5 ng/mL, elevated levels are widely recognized as an indicator of malignant progression in NSCLC patients. To establish the diagnostic potential, the differential pulse voltammetry (DPV) current response of the Cu/Cu<sub>X</sub>O-hBNNS-based immunosensor was carefully monitored across a wide concentration range of CEA (0-50 ng/mL), as shown in Fig. 6.16(a). A distinct, progressive enhancement in DPV current was observed up to 25 ng/mL, reflecting accelerated electron transfer kinetics mediated through the electrocatalytically active porous Cu/CuxO nanoflowers uniformly distributed across the hBNNS substrate. Density functional theory (DFT) simulations further corroborated these observations, highlighting that Cu/Cu<sub>X</sub>O decoration modulates bandgap states of hBN while redistributing charge density to highly electronegative nitrogen atoms, ultimately facilitating efficient charge transport [53]. This behavior is also influenced by conformational rearrangements in the immobilized BSA/Anti-CEA matrix, wherein antibody-antigen interactions generate spatially oriented conductive pathways, further amplifying signal intensity. Beyond 25 ng/mL, DPV signals approached saturation, suggesting maximal utilization of active binding moieties on the immunoelectrode interface.

Subsequently, a precise calibration curve was constructed (**Fig. 6.16(b)**), fitted using a linear regression model to define performance parameters of the nano-biosensor. Each experimental point was validated through triplicate measurements (n = 3) to ensure reproducibility. The curve delineated a strong linear response over the 0–25 ng/mL concentration window, represented by the regression equation y = mx + c with an exceptional regression coefficient ( $R^2 = 0.99998$ ), confirming the biosensor's outstanding linearity, sensitivity, and reliability as detailed in **Eq. [6.14]**.

$$I~(mA) = [~8.~04~\mu A.~mL.~ng^{-1}.~cm^{-2}~\times (CEA~Concentration) + 0.~131~mA~] \\ [6.14]$$

The slope extracted from the linear calibration curve was critically employed in quantifying the sensitivity of the Cu/Cu<sub>x</sub>O-hBNNS/ITO-based immunosensor, which was determined to be 8.04 µA·mL·ng<sup>-1</sup>·cm<sup>-2</sup>. This sensitivity value was derived using the well-established formula Slope/Surface Area, where the effective electroactive surface area of the electrode was calculated as 0.64 cm<sup>2</sup>. The high slope value reflects the remarkable electron transfer efficiency and the strong affinity binding interaction between the immobilized Anti-CEA antibodies and their target antigen, CEA, which collectively enhance the signal response of the fabricated nano-biosensor. Importantly, the determination of sensitivity is not only a measure of performance but also serves as a foundation for evaluating the analytical strength of the immunoelectrode in distinguishing minute variations in biomarker concentrations, a critical factor for early cancer diagnostics.

Furthermore, the lower limit of detection (LOD) was meticulously calculated by combining the standard deviation ( $\sigma$ ) of the blank response with the sensor's sensitivity, following the relationship outlined in **Eq. [6.15]**. This approach integrates both the baseline electrochemical noise level and the sensor's signal amplification capability,

thus offering a statistically reliable threshold for the smallest concentration of CEA that can be consistently detected. Such integration ensures that the derived LOD is not an arbitrary quantity but a reflection of the actual signal-to-noise dynamics inherent to the immunosensor system. The exceptionally low LOD achieved validates the robustness and reproducibility of the Cu/CuxO-hBNNS/ITO nano-biosensor, underscoring its potential in detecting trace concentrations of CEA even within the clinical range where early disease markers are often found. The sensitivity and LOD outcomes affirm the superior analytical performance of this nanostructured platform, positioning it as a reliable candidate for precise biomarker quantification in clinical diagnostics [54].

### Limit of Detection = $(3 \times \sigma)/m$ [6.15]

The determination of the lower limit of detection (LOD), where  $\sigma$  reflects the standard deviation of the blank response and m denotes the sensitivity, revealed that the Cu/CuxO-hBNNS/ITO immunosensor attained an extraordinarily low LOD of 3.22 pg/mL. This performance is directly attributed to the synergistic integration of hierarchical Cu/CuXO nanoflowers with the layered hBNNS matrix, which enhances surface functionality, maximizes electroactive sites, and drives accelerated charge transfer dynamics. Such a hybrid configuration ensures a highly sensitive, stable, and reproducible biosensing platform capable of detecting trace CEA levels that are often undetectable using conventional electrode materials. Importantly, this LOD surpasses the detection thresholds reported for traditional metal- and semiconductor-based nanocomposites, establishing Cu/CuxO-hBNNS as a next-generation material system for advanced immunosensing. The ability to detect CEA at such low concentrations significantly advances early-stage cancer diagnostics, reaffirming the superiority of this biosensor design, as summarized in **Table 6.3**.

Table 6.3: Comparison of sensing characteristics of Cu/CuxO-hBNNS based nano-biosensor with existing metal- and semiconductor-based immunosensors.

semiconductor-based infinunosensors.								
Sensing	Sensing Matrix	<b>Detection Technique</b>	Linear	Limit of	Sensitivity	<b>Stability</b>	Ref.	
Platform			Range	Detection				
			(ng/mL)					
Immunosensor	Cu/UiO-66	Fluorescence	0.01 - 0.3	0.01 ng/mL	1681 ΔF·mL·ng <sup>-1</sup>	-		
Immunosensor	CP/ZIF-8/PDA	Fluorescence	0.01 - 20	7.6 pg/mL	2154.8 ΔF	16 days		
					·(decade)-1			
Immunosensor	AuNPs-Cu <sup>2+</sup> -Cys	Photothermal	3.0 - 48.0	1.3 ng/mL	0.232 (°C-	-		
					¹)·mL·ng-¹			
Immunosensor	Ag/Au-DN-Graphene	Electrochemical	0.01 - 120	8 pg/mL	0.494	-		
					μA·(decade) <sup>-1</sup>			
Immunosensor	3D-G/AuNP	Electrochemical	0.5 - 200	0.31 ng/mL	-0.026 μA·mL·ng	30 days		
					1			
Immunosensor	Ag@SiO <sub>2</sub> NPs	Electrochemical	0.5 - 10	0.01 ng/mL	-	6 weeks		
Immunosensor	AgNCs@Apt@UiO66	Electrochemical	0.01 - 10	4.93 pg/mL	6.08 μA·(decade)-1	11 days		
Immunosensor	NCMTs@Fe <sub>3</sub> O <sub>4</sub> @Cusilicate	Electrochemical	0.03 - 6	5.38 pg/mL	-	30 days		
Immunosensor	CeO <sub>2</sub> /CdS	Photoelectrochemical	0.1 - 10	0.057 ng/mL	-	-		
Immunosensor	h-BNNS	Electrochemical	0 - 10	22.5 pg/mL	24.84	5 weeks		
					μA·mL·ng <sup>-1</sup> ·cm <sup>-2</sup>			
Immunosensor	rGO-hBNNS	Electrochemical	0 - 15	5.47 pg/mL	9. 65	8 weeks		
					μA·mL·ng <sup>-1</sup> ·cm <sup>-2</sup>			
Immunosensor	Cu/Cu <sub>x</sub> O-hBNNS	Electrochemical	0 - 25	3.22 pg/mL	8. 04	60 days	Present	
					μA·mL·ng <sup>-1</sup> ·cm <sup>-2</sup>		Work	

Keywords: Cu -Copper, UiO-66 -Zr-MOF (Metal organic framework), NF -Nanoflower, CP -Copper peroxide, ZIF -Zeolitic imidazolate framework, PDA -Polydopamine nanoparticles, MNP -Magnetic Nanoparticle (Fe<sub>3</sub>O<sub>4</sub>), PDA -Polydopamine, ENF -Electrospun Nanofibers, NP-Nanoparticles, Au- Gold, Ag-Silver, DN -1,5-diaminonaphthalene, 3D-G -Three-dimensional graphene, SiO<sub>2</sub> -Silicon dioxide, Apt -Aptamer, NMCT -N-doped magnetic carbon microtubes,  $\Delta F$  = Relative Fluorescent Unit (RFU).

### 6.3.2.4 Comprehensive Evaluation of the Electroanalytical Performance of $Cu/Cu_XO-hBNNS/ITO-Based$ Nano-Biosensors

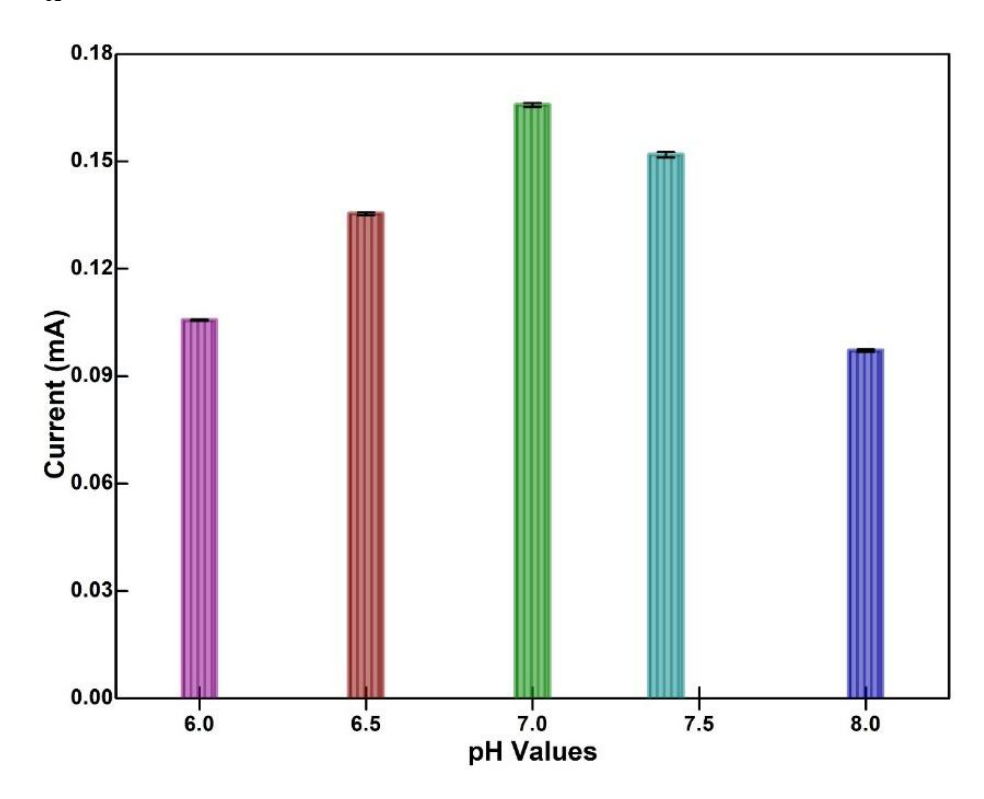


Figure 6.17: Bar graph representation of the DPV responses of the Anti-CEA/Cu/Cu<sub>X</sub>O-hBNNS/ITO immunoelectrode across varying buffer pH values (6.0-8.0), highlighting the influence of pH on electrochemical performance.

To establish the practical applicability and stability of the developed nano-biosensor, a systematic evaluation of the influence of pH on the electrochemical response was carried out using differential pulse voltammetry (DPV) at a fixed scan rate of 50 mV/s. This investigation was critical to determine the most favourable pH conditions for the effective functioning of the Anti-CEA/Cu/Cu<sub>X</sub>O-hBNNS/ITO immunoelectrode. A wide pH window ranging from 6.0 to 8.0 was explored using phosphate buffer saline (PBS) solutions containing the ferro/ferricyanide redox couple [5 mM,  $\{Fe(CN)_6^{3-/4-}\}$ ]. As illustrated in Fig. 6.17, the immunoelectrode displayed a distinct pH-dependent response, with the maximum DPV current observed at pH 7.0. This result underscores the significance of maintaining a neutral pH environment, which provides optimal electrochemical conditions by ensuring the stability, structural integrity, and native conformations of biomolecules immobilized at the sensor interface. At lower pH values (pH 6.0-6.5), partial denaturation and loss of antibody-antigen binding affinity may occur due to proton-induced alterations in the biomolecular architecture, thereby reducing electrochemical performance. Conversely, at higher alkaline conditions (pH 7.5-8.0), excessive deprotonation could destabilize surface chemistry and impede efficient electron transfer pathways. Therefore, neutral PBS (pH 7.0) was identified as the most suitable medium, balancing the preservation of bioactivity with maximized electron transfer kinetics. Consequently, PBS at pH 7.0 was employed as the standard

electrolyte in all subsequent electrochemical experiments to ensure reliability, reproducibility, and optimal sensor performance.

A comprehensive negative control study was performed to confirm that the observed electrochemical responses originate solely from specific antigen-antibody interactions and not from nonspecific adsorption processes. For this purpose, the bare Cu/Cu<sub>X</sub>OhBNNS/ITO electrode was exposed to incremental concentrations of CEA antigen (0.01, 4, 8, and 15 ng/mL), followed by DPV analysis to track the current response. As shown in Fig. 6.18, the bare electrode exhibited a steady DPV current of 0.148 mA, which remained virtually unchanged across all tested concentrations. The absence of measurable signal enhancement, corroborated by data presented in Table S3, underscores that the Cu/Cu<sub>X</sub>O-hBNNS/ITO framework alone does not exhibit affinity toward CEA. This strongly rules out the possibility of nonspecific complexation or random physical adsorption of the antigen onto the nanostructured electrode surface. Instead, the experimental results clearly demonstrate that the selective and measurable electrochemical signal is only established when the electrode is biofunctionalized with Anti-CEA antibodies and stabilized with BSA, thereby forming the BSA/Anti-CEA/Cu/Cu<sub>X</sub>O-hBNNS/ITO immunoelectrode. Such findings not only validate the robustness and specificity of the sensing platform but also reinforce its diagnostic reliability by eliminating the risk of false positive responses. The results highlight that the porous, electrocatalytically active Cu/Cu<sub>x</sub>O nanostructures anchored onto hBNNS provide an excellent conductive substrate while remaining chemically inert toward nonspecific binding, thereby ensuring that only true antigen recognition contributes to the biosensor's electroanalytical output.

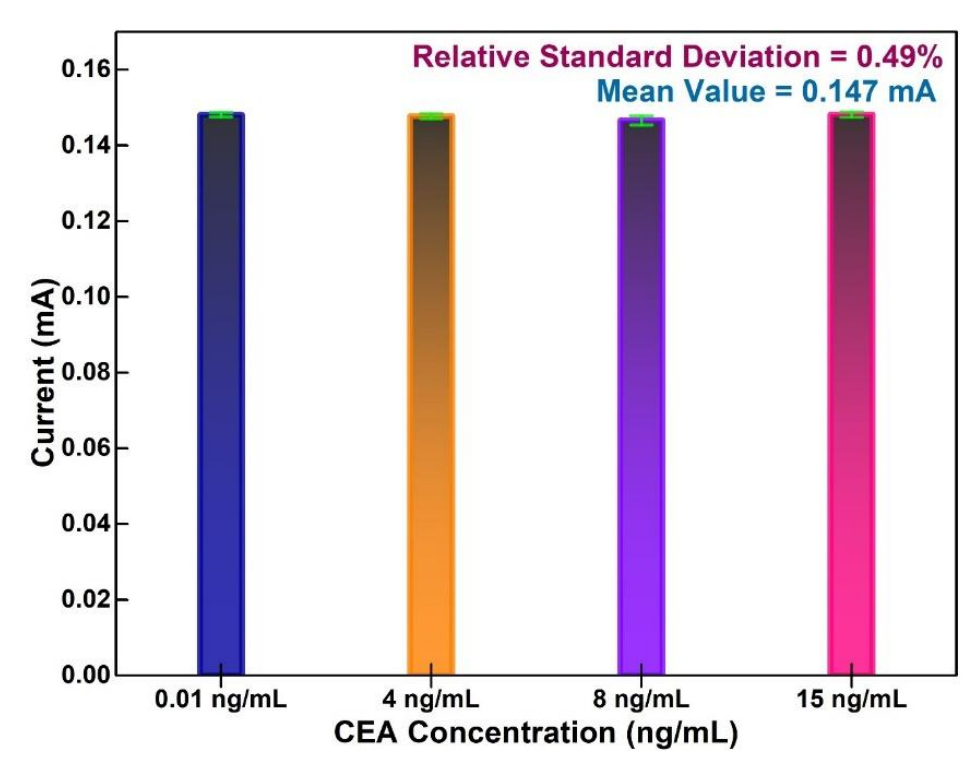


Figure 6.18: Control study illustrated through a bar graph, depicting the DPV current variations of the Cu/CuxO-hBNNS/ITO electrode in response to CEA concentrations of 0.01, 4, 8, and 15 ng/mL.

A comprehensive reproducibility study was carried out to validate the consistency and reliability of the electrochemical performance of the Cu/Cu<sub>X</sub>O-hBNNS-based immunosensor. Multiple electrodes were fabricated under identical experimental conditions and systematically tested to assess whether their electrochemical responses remained stable across different samples. As shown in Fig. 6.19, four independent immunoelectrodes were prepared and subjected to Differential Pulse Voltammetry (DPV) measurements. Each electrode was tested in triplicate (n = 3), ensuring statistical robustness of the data set. The recorded results demonstrated an average peak current of 0.169 mA with an exceptionally low relative standard deviation (RSD) of 0.71%. This narrow deviation highlights the uniformity in fabrication, precise immobilization of biomolecules, and reproducible electrode-electrolyte interfacial characteristics. Importantly, the electrochemical responses obtained were consistent with those observed in the initial characterization studies, confirming that the as-developed sensor platform can reliably deliver steady performance over multiple independent trials. The low RSD value also reflects strong control over nanostructure growth and functionalization, which is critical for ensuring dependable signal output in biosensing applications. Collectively, these findings affirm that the Cu/CuxO-hBNNS-based immunosensor exhibits excellent reproducibility, a vital parameter for transitioning such devices toward real-world diagnostic applications.

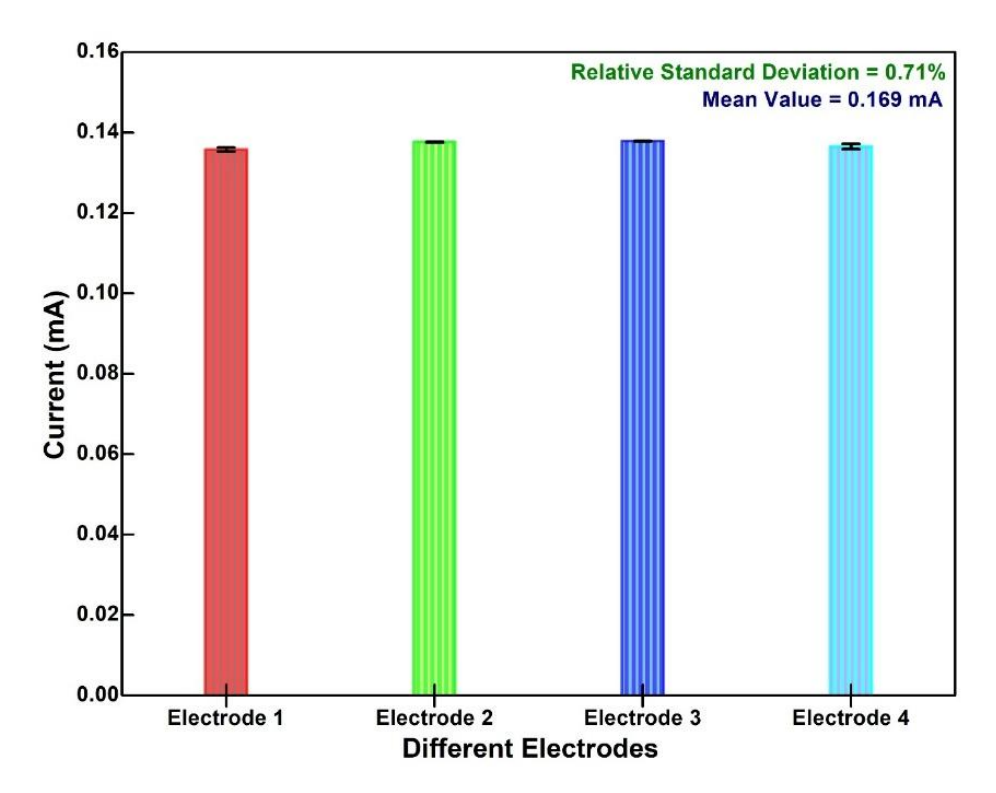


Figure 6.19: Evaluation of the reproducibility of electrochemical current response in the as-prepared CEA/BSA/Anti-CEA/Cu/CuxO-hBNNS/ITO immunoelectrode.

The specificity of the Cu/Cu<sub>X</sub>O-hBNNS-based electrochemical nano-biosensor was thoroughly investigated to ensure its ability to selectively detect the Carcinoembryonic Antigen (CEA) biomarker in complex biological environments where several coexisting proteins and serum components are present. To achieve this, Differential

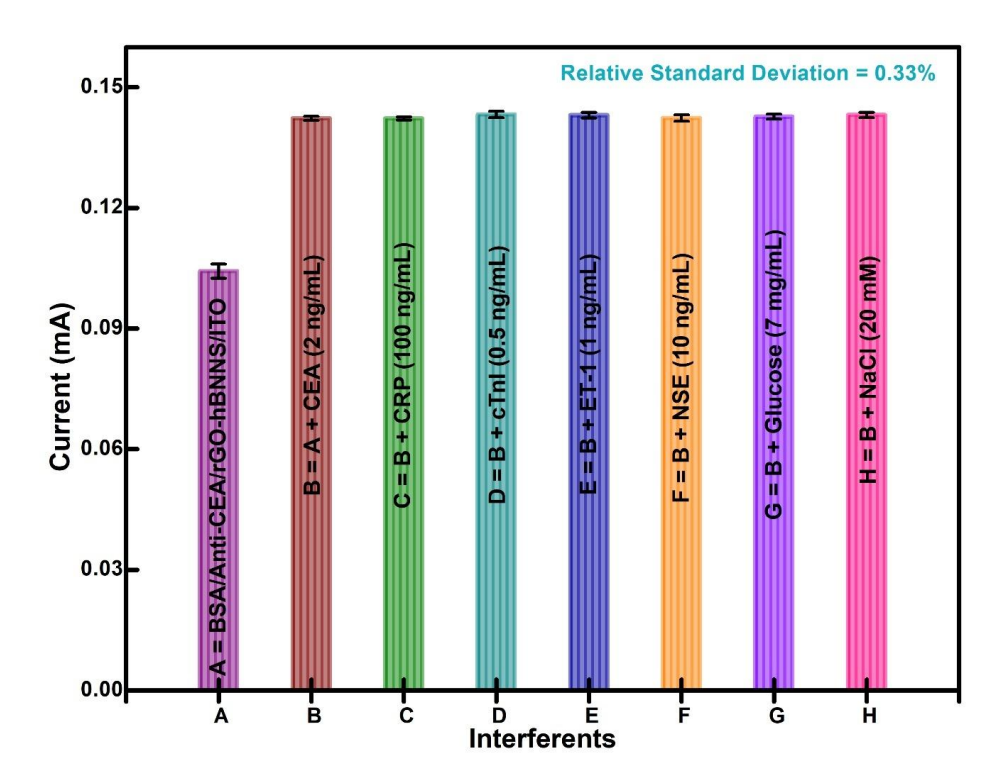


Figure 6.20: Selectivity analysis illustrated by bar chart, demonstrating the electrochemical response of the BSA/Anti-CEA/Cu/CuxO-hBNNS/ITO immunoelectrode in the presence of CEA and potential interfering biomolecules: (A) electrode baseline, (B) + CEA (2 ng/mL), (C) + CRP (100 ng/mL), (D) + cTnI (0.5 ng/mL), (E) + ET-1 (1 ng/mL), (F) + NSE (10 ng/mL), (G) + Glucose (7 ng/mL), and (H) + NaCl (20 mM).

Pulse Voltammetry (DPV) responses were systematically measured against a panel of potential interferents commonly found in blood serum, as illustrated in Fig. 6.20. These interferents included clinically relevant proteins such as C-Reactive Protein (CRP, 100 ng/mL), Endothelin-1 (ET-1, 1 ng/mL), Cardiac Troponin I (cTnI, 0.5 ng/mL), and Neuron-Specific Enolase (NSE, 10 ng/mL), each known to coexist with or mimic biomolecular signals in diseased states. Moreover, abundant serum components such as glucose (7 mg/mL) and sodium chloride (NaCl, 20 mM) were introduced to evaluate potential cross-reactivity. In each case, the interferent was individually spiked into a PBS solution containing a fixed concentration of CEA (2 ng/mL), and the resulting DPV currents were recorded (Table 6.4). The results demonstrated that the presence of these interferents caused only negligible variations in the peak current, with a relative standard deviation (RSD) of merely 0.33% compared to the baseline CEA response. This exceptionally low deviation underscores the superior specificity and minimal cross-sensitivity of the BSA/Anti-CEA/Cu/Cu<sub>X</sub>O-hBNNS/ITO immunoelectrode. The observed behavior validates the robust antibody-antigen binding affinity, which resists nonspecific adsorption or competitive binding from structurally unrelated biomolecules. Importantly, these results align with earlier findings by Nap et al., who demonstrated the high selectivity of monoclonal CEA antibodies in recognizing CEA epitopes over other serum proteins [55]. This study highlights that the fabricated immunoelectrode achieves outstanding specificity, a critical prerequisite for accurate

biomarker detection in clinical diagnostics, especially in the presence of complex serum matrices.

Table 6.4: Tabular representation of stepwise fabrication of Cu/Cu<sub>x</sub>O-hBNNS based Nano-biosensor examined by Anodic Peak Current, Diffusion Coefficient, and DPV Current respectively.

		~ P J -	
Stepwise	Anodic Peak Current	Diffusion Coefficient ±	
Electrode	± SD	SD	DPV Current $\pm$ SD (mA)
Modification	(I <sub>pa</sub> , mA)	$(D, cm^2 s^{-1})$	
ITO	$0.87 \pm (0.9 \times 10^{-2})$	$2.06 \times 10^{-11} \pm (4.5 \times 10^{-13})$	$0.128 \pm (1.2 \times 10^{-3})$
hBNNS	$0.62 \pm (0.1 \times 10^{-2})$	$1.04 \times 10^{-11} \pm (4.1 \times 10^{-14})$	$0.113 \pm (0.5 \times 10^{-3})$
Cu/CuXO- hBNNS	$1.08 \pm (0.4 \times 10^{-3})$	$3.13 \times 10^{-11} \pm (0.3 \times 10^{-14})$	$0.148 \pm (0.9 \times 10^{-3})$
Anti-CEA	$1.19 \pm (0.1 \times 10^{-2})$	$3.82 \times 10^{-11} \pm (6.7 \times 10^{-14})$	$0.166 \pm (1.4 \times 10^{-3})$
BSA	$0.39 \pm (0.05 \times 10^{-2})$	$4.24 \times 10^{-12} \pm (1.1 \times 10^{-14})$	$0.106 \pm (2.1 \times 10^{-3})$
Blank Reading	$0.95 \pm (0.6 \times 10^{-2})$	$2.43 \times 10^{-11} \pm (3.2 \times 10^{-13})$	$0.131 \pm (0.2 \times 10^{-3})$
CEA	$1.03 \pm (0.3 \times 10^{-2})$	$2.91 \times 10^{-11} \pm (1.5 \times 10^{-13})$	$0.137(0.9 \times 10^{-3})$

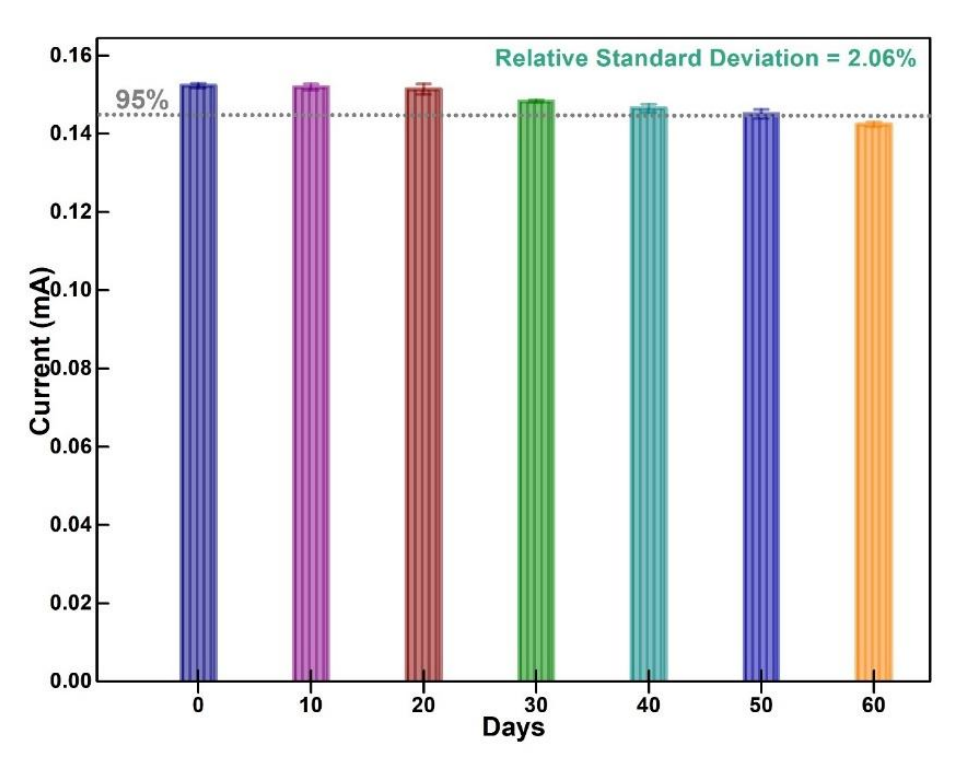


Figure 6.21: Current stability analysis of the CEA/BSA/Anti-CEA/Cu/CuxO-hBNNS/ITO immunoelectrode, evaluated over a period of 10 days at regular time intervals.

The long-term stability of the  $Cu/Cu_XO$ -hBNNS-based immunosensor was comprehensively assessed, as depicted in **Fig. 6.21**, through repeated DPV measurements performed every 10 days under consistent storage conditions at 4 °C. This approach ensured that variations in electrochemical response were attributable solely to time-dependent changes in the biosensor rather than external factors. Remarkably, the immunosensor maintained nearly constant activity for up to 50 days, with only a 4.7% decrease in peak current compared to its initial baseline value. Such minimal degradation strongly validates the robustness of the  $Cu/Cu_XO$ -hBNNS

functional layer and its ability to preserve antibody-antigen recognition efficiency over prolonged durations. After 60 days, however, the decline became more evident, with total reduction surpassing 6.5%, signalling the threshold at which sensor performance becomes compromised. This systematic evaluation not only confirms the high stability and durability of the as-fabricated immunoelectrode but also emphasizes the critical role of storage strategies and periodic monitoring in ensuring its long-term clinical viability.

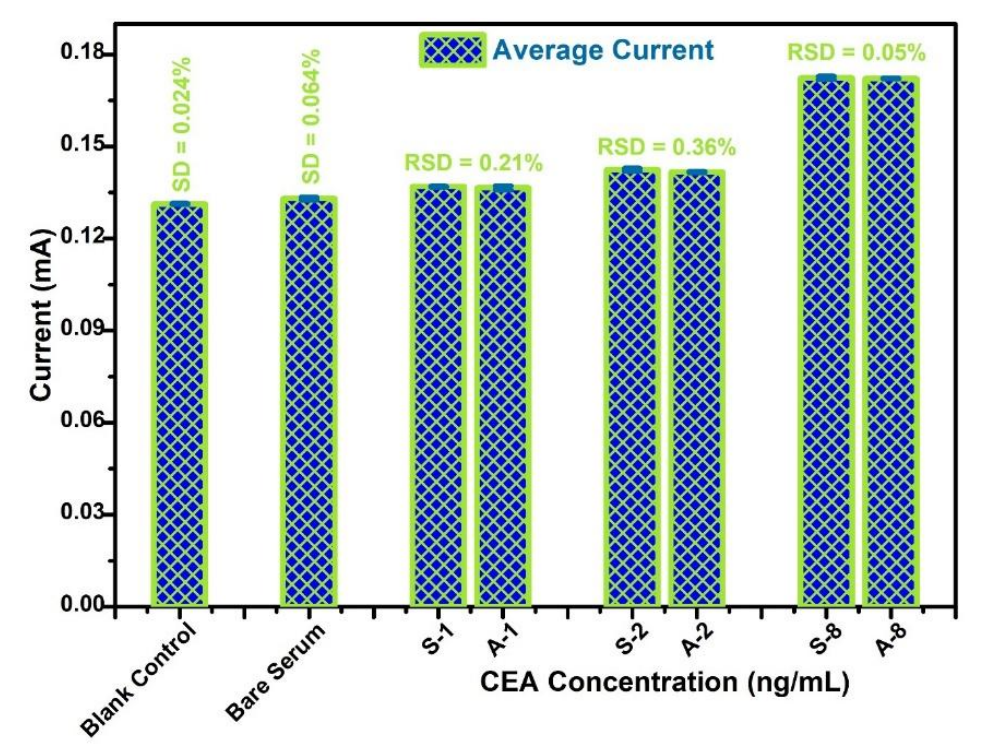


Figure 6.22: Bar chart representation of differential DPV responses obtained from blank control, pure serum, and CEA-spiked serum samples, confirming the detection capability of the as-fabricated immunoelectrode.

The analytical efficacy of the Cu/Cu<sub>X</sub>O-hBNNS/ITO-based nano-biosensor to detect spiked carcinoembryonic antigen (CEA) in real human serum was rigorously examined using DPV, as presented in Fig. 6.22. For this evaluation, serum samples were spiked with defined CEA concentrations by mixing equal volumes (10 µL each) of serum and antigen solution, homogenized through repeated pipetting, and incubated for 30 minutes prior to immobilization on the BSA/Anti-CEA/Cu/CuxO-hBNNS/ITO immunoelectrode. Since physiological CEA concentrations in healthy individuals remain below 5 ng/mL, the ability to accurately detect elevated levels is clinically critical for early cancer diagnostics. The DPV current responses corresponding to known CEA concentrations (A) were recorded and compared against responses obtained from identically spiked serum samples (S), revealing excellent agreement between experimental and reference signals. To further validate these results, quantification was performed in triplicate using both the immunoelectrode and standard sandwich ELISA. The ELISA assay, conducted with Anti-CEA pre-coated wells and absorbance recorded at 450 nm, yielded values consistent with DPV measurements. The strong correlation between ELISA and electrochemical data demonstrates the exceptional sensitivity and precision of the Cu/Cu<sub>X</sub>O-hBNNS/ITO immunoelectrode, confirming its robust, accurate, and sensitive applicability for clinical biomarker monitoring and early cancer diagnostics.

Table 6.5: Evaluation of recovery current and relative standard deviation (RSD, %) for detecting spiked CEA concentrations in human serum samples, relative to the actual CEA concentration and estimation of bare serum concentration using DPV and ELISA techniques respectively.

CEA Concentration (ng/mL)	Average Current ± SD for Standard CEA Sample (A, in mA)	Average Current ± SD for Spiked CEA Sample (S, in mA)	RSD (%)	Recovery %	Bare Serum Concentration (ng/mL)	
1	$0.136 \pm (1.2 \times 10^{-3})$	$0.136 \pm (1.9 \times 10^{-4})$	0.21	100.29		ELISA- 0.287
2	$0.142 \pm (2.7 \times 10^{-4})$	$0.142 \pm (7.8 \times 10^{-4})$	0.36	100.51	DPV- 0.259	
8	$0.172 \pm (4.6 \times 10^{-5})$	$0.172 \pm (8.8 \times 10^{-4})$	0.05	100.07		

The results summarized in **Table 6.5** highlight the exceptional precision and reproducibility of the developed BSA/Anti-CEA/Cu/Cu<sub>X</sub>O-hBNNS/ITO immunoelectrode. For standard CEA concentrations of 1, 2, and 8 ng/mL, the average DPV peak currents were determined as  $0.136 \pm (1.2 \times 10^3)$ ,  $0.142 \pm (2.7 \times 10^4)$ , and  $0.172 \pm (4.6 \times 10^{5})$  mA, respectively. These values exhibited an almost identical correlation with the currents obtained for CEA-spiked human serum samples, which measured  $0.136 \pm (1.9 \times 10^4)$ ,  $0.142 \pm (7.8 \times 10^4)$ , and  $0.172 \pm (8.8 \times 10^4)$  mA. The relative standard deviations at these concentrations were notably minimal, calculated as 0.21 %, 0.36 %, and 0.05 %, underscoring the stability and reliability of the DPV technique. This remarkable consistency across both standard and spiked samples validates the immunoelectrode's capacity to deliver accurate, reproducible, and clinically meaningful detection of CEA in human serum.

#### **Conclusion:**

This research comprehensively establishes the successful fabrication of an advanced metal—semiconductor nano-hybrid composite (NHC) consisting of self-assembled 3D Cu/Cu<sub>X</sub>O nanoflowers anchored onto hBNNS nanosheets, engineered specifically for the ultrasensitive detection of carcinoembryonic antigen (CEA). The fabrication process was strategically optimized, with each modification step validated through FT-IR spectroscopy and electrochemical assessments, ensuring accurate monitoring of structural and functional enhancements. The porous dandelion-like Cu/Cu<sub>X</sub>O nanoflowers, reinforced onto the high-surface-area hBNNS scaffold, provided a unique structural synergy by offering abundant catalytic active sites, multifunctional chemical groups, and interconnected porous channels. These features facilitated efficient immobilization of Anti-CEA antibodies, improved binding orientation, and promoted stronger affinity interactions with target CEA molecules. Moreover, the integration of Cu/Cu<sub>X</sub>O nanoflowers substantially elevated the electrochemical performance by

lowering the activation energy for redox processes, enhancing electron transfer efficiency, and enriching the electrode surface with hierarchically distributed reactive sites. As a result, the immunoelectrode achieved an extraordinary limit of detection (3.22 pg/mL) and a wide linear detection range (0–25 ng/mL), which are both critical for early and precise detection of trace-level biomarkers. Importantly, the biosensor demonstrated excellent reproducibility, operational stability for over 60 days of storage at 4 °C, and superior selectivity against interfering biomolecules such as CRP, ET-1, and glucose, ensuring high diagnostic fidelity even in complex biological matrices. Validation in spiked human serum samples revealed excellent recovery rates, further highlighting its translational capability in real clinical contexts. These outcomes collectively establish the Cu/Cu<sub>x</sub>O-hBNNS-based nano-hybrid composite as a powerful and versatile platform, not only advancing cancer biomarker detection but also opening new avenues for the development of multifunctional biosensors adaptable to a wide range of biomedical applications.

#### **References:**

- [1] Z. Yu, G. Cai, X. Liu, D. Tang, Pressure-Based Biosensor Integrated with a Flexible Pressure Sensor and an Electrochromic Device for Visual Detection, Analytical Chemistry, 93 (2021) 2916-2925.
- [2] L. Lu, R. Zeng, Q. Lin, X. Huang, D. Tang, Cation Exchange Reaction-Mediated Photothermal and Polarity-Switchable Photoelectrochemical Dual-Readout Biosensor, Analytical Chemistry, 95 (2023) 16335-16342.
- [3] R. Batool, A. Rhouati, M.H. Nawaz, A. Hayat, J.L. Marty, A review of the construction of nano-hybrids for electrochemical biosensing of glucose, Biosensors, 9 (2019) 46.
- [4] H. Chen, D.-e. Jiang, Z. Yang, S. Dai, Engineering nanostructured interfaces of hexagonal boron nitride-based materials for enhanced catalysis, Accounts of Chemical Research, 56 (2022) 52-65.
- [5] I.H. Abidi, N. Mendelson, T.T. Tran, A. Tyagi, M. Zhuang, L.-T. Weng, B. Özyilmaz, I. Aharonovich, M. Toth, Z. Luo, Selective Defect Formation in Hexagonal Boron Nitride, Advanced Optical Materials, 7 (2019) 1900397.
- [6] J.H. Ramirez Leyva, G. Vitale, A. Hethnawi, A. Hassan, M.J. Perez-Zurita, G.U. Ruiz-Esparza, N.N. Nassar, Mechanism of Hierarchical Porosity Development in Hexagonal Boron Nitride Nanocrystalline Microstructures for Biomedical and Industrial Applications, ACS Applied Nano Materials, 1 (2018) 4491-4501.
- [7] W. Jin, W. Zhang, Y. Gao, G. Liang, A. Gu, L. Yuan, Surface functionalization of hexagonal boron nitride and its effect on the structure and performance of composites, Applied Surface Science, 270 (2013) 561-571.
- [8] R.D. Crapnell, A. Tridente, C.E. Banks, N.C. Dempsey-Hibbert, Evaluating the Possibility of Translating Technological Advances in Non-Invasive Continuous Lactate Monitoring into Critical Care, Sensors, 21 (2021) 879.
- [9] Z. Liu, Y. Gong, W. Zhou, L. Ma, J. Yu, J.C. Idrobo, J. Jung, A.H. MacDonald, R. Vajtai, J. Lou, Ultrathin high-temperature oxidation-resistant coatings of hexagonal boron nitride, Nature communications, 4 (2013) 2541.
- [10] S.C. Yoo, J. Kim, W. Lee, J.Y. Hwang, H.J. Ryu, S.H. Hong, Enhanced mechanical properties of boron nitride nanosheet/copper nanocomposites via a molecular-level mixing process, Composites Part B: Engineering, 195 (2020) 108088.
- [11] K. Ba, W. Jiang, J. Cheng, J. Bao, N. Xuan, Y. Sun, B. Liu, A. Xie, S. Wu, Z. Sun, Chemical and bandgap engineering in monolayer hexagonal boron nitride, Scientific reports, 7 (2017) 45584.

- [12] S.M. Kim, A. Hsu, M.H. Park, S.H. Chae, S.J. Yun, J.S. Lee, D.-H. Cho, W. Fang, C. Lee, T. Palacios, Synthesis of large-area multilayer hexagonal boron nitride for high material performance, Nature communications, 6 (2015) 8662.
- [13] X. Yu, M. Xue, Z. Yin, Y. Luo, Z. Hong, C. Xie, Y. Yang, Z. Ren, Flexible boron nitride composite membranes with high thermal conductivity, low dielectric constant and facile mass production, Composites Science and Technology, 222 (2022) 109400.
- [14] S. Roy, X. Zhang, A.B. Puthirath, A. Meiyazhagan, S. Bhattacharyya, M.M. Rahman, G. Babu, S. Susarla, S.K. Saju, M.K. Tran, Structure, properties and applications of two-dimensional hexagonal boron nitride, Advanced Materials, 33 (2021) 2101589.
- [15] E. Bahrami, R. Amini, S. Vardak, Electrochemical detection of dopamine via pencil graphite electrodes modified by Cu/CuxO nanoparticles, Journal of Alloys and Compounds, 855 (2021) 157292.
- [16] H.T. Le, D.T. Tran, T.L. Luyen Doan, N.H. Kim, J.H. Lee, Hierarchical Cu@CuxO nanowires arrays-coated gold nanodots as a highly sensitive self-supported electrocatalyst for L-cysteine oxidation, Biosensors and Bioelectronics, 139 (2019) 111327.
- [17] K. Byrappa, T. Adschiri, Hydrothermal technology for nanotechnology, Progress in crystal growth and characterization of materials, 53 (2007) 117-166.
- [18] K. Sharma, N.K. Puri, B. Singh, Fabrication of rGO-decorated hBNNS hybrid nanocomposite via organic–inorganic interfacial chemistry for enhanced electrocatalytic detection of carcinoembryonic antigen, Analytical and Bioanalytical Chemistry, (2024) 1-17.
- [19] A. Rigo, A. Corazza, M.L. di Paolo, M. Rossetto, R. Ugolini, M. Scarpa, Interaction of copper with cysteine: stability of cuprous complexes and catalytic role of cupric ions in anaerobic thiol oxidation, Journal of inorganic biochemistry, 98 (2004) 1495-1501.
- [20] S.M.G. Leite, L.M.P. Lima, S. Gama, F. Mendes, M. Orio, I. Bento, A. Paulo, R. Delgado, O. Iranzo, Copper(II) Complexes of Phenanthroline and Histidine Containing Ligands: Synthesis, Characterization and Evaluation of their DNA Cleavage and Cytotoxic Activity, Inorganic Chemistry, 55 (2016) 11801-11814.
- [21] C. Gherasim, P. Pascariu, M. Asandulesa, M. Dobromir, F. Doroftei, N. Fifere, A. Dascalu, A. Airinei, Copper oxide nanostructures: Preparation, structural, dielectric and catalytic properties, Ceramics International, 48 (2022) 25556-25568.
- [22] A. Serrà, E. Gómez, J. Michler, L. Philippe, Facile cost-effective fabrication of Cu@Cu2O@CuO-microalgae photocatalyst with enhanced visible light degradation of tetracycline, Chemical Engineering Journal, 413 (2021) 127477.
- [23] K. Sharma, N.K. Puri, B. Singh, An efficient electrochemical nano-biosensor based on hydrothermally engineered ultrathin nanostructures of hexagonal boron nitride nanosheets for label-free detection of carcinoembryonic antigen, Applied Nanoscience, (2023) 1-14.
- [24] J.-Y. Pak, I.-S. Kim, R.-H. Kim, H.-S. Jin, Surface energy and its anisotropy for fcc metals: modified embedded atom method study, Indian Journal of Physics, 97 (2023) 1981-1988.
- [25] Y. Yang, D. Xu, Q. Wu, P. Diao, Cu2O/CuO bilayered composite as a high-efficiency photocathode for photoelectrochemical hydrogen evolution reaction, Scientific reports, 6 (2016) 35158.
- [26] D. Pacile, J. Meyer, Ç. Girit, A. Zettl, The two-dimensional phase of boron nitride: Few-atomic-layer sheets and suspended membranes, Applied Physics Letters, 92 (2008).
- [27] M.S. Alqahtani, S. Mohamed, N. Hadia, M. Rabia, M. Awad, Some characteristics of Cu/Cu2O/CuO nanostructure heterojunctions and their applications in hydrogen generation from seawater: effect of surface roughening, Physica Scripta, 99 (2024) 045939.
- [28] T. Berger, A. Trunschke, Optical Properties: UV/Vis Diffuse Reflectance Spectroscopy and Photoluminescence, Metal Oxide Nanoparticles: Formation, Functional Properties, and Interfaces, 2 (2021) 435-482.
- [29] J.J. Bravo-Suarez, B. Subramaniam, R.V. Chaudhari, Ultraviolet–visible spectroscopy and temperature-programmed techniques as tools for structural characterization of Cu in CuMgAlO x mixed metal oxides, The Journal of Physical Chemistry C, 116 (2012) 18207-18221.

- [30] J. Shang, F. Xue, C. Fan, E. Ding, Preparation of few layers hexagonal boron nitride nanosheets via high-pressure homogenization, Materials Letters, 181 (2016) 144-147.
- [31] O.V. Rambadey, A. Kumar, A. Sati, P.R. Sagdeo, Exploring the interrelation between Urbach energy and dielectric constant in Hf-substituted BaTiO3, ACS omega, 6 (2021) 32231-32238.
- [32] A. Singh, S. Kaur, A. Kaur, T. Aree, N. Kaur, N. Singh, M.S. Bakshi, Aqueous-phase synthesis of copper nanoparticles using organic nanoparticles: Application of assembly in detection of Cr3+, ACS Sustainable Chemistry & Engineering, 2 (2014) 982-990.
- [33] S. Sk, A. Tiwari, B.M. Abraham, N. Manwar, V. Perupogu, U. Pal, Constructing Cu/BN@PANI ternary heterostructure for efficient photocatalytic hydrogen generation: A combined experimental and DFT studies, International Journal of Hydrogen Energy, 46 (2021) 27394-27408.
- [34] P. Colomban, H.D. Schreiber, Raman signature modification induced by copper nanoparticles in silicate glass, Journal of Raman Spectroscopy: An International Journal for Original Work in all Aspects of Raman Spectroscopy, Including Higher Order Processes, and also Brillouin and Rayleigh Scattering, 36 (2005) 884-890.
- [35] Y. Deng, A.D. Handoko, Y. Du, S. Xi, B.S. Yeo, In Situ Raman Spectroscopy of Copper and Copper Oxide Surfaces during Electrochemical Oxygen Evolution Reaction: Identification of CuIII Oxides as Catalytically Active Species, ACS Catalysis, 6 (2016) 2473-2481.
- [36] Z. Wang, V. Pischedda, S. Saxena, P. Lazor, X-ray diffraction and Raman spectroscopic study of nanocrystalline CuO under pressures, Solid state communications, 121 (2002) 275-279.
- [37] A. Litvinchuk, A. Möller, L. Debbichi, P. Krüger, M. Iliev, M. Gospodinov, Second-order Raman scattering in CuO, Journal of Physics: Condensed Matter, 25 (2013) 105402.
- [38] B. Purusottam Reddy, K. Sivajee Ganesh, O. Hussain, Growth, microstructure and supercapacitive performance of copper oxide thin films prepared by RF magnetron sputtering, Applied Physics A, 122 (2016) 1-10.
- [39] P. Kumar, M.C. Mathpal, S. Hamad, S.V. Rao, J.H. Neethling, A.J. van Vuuren, E.G. Njoroge, R.E. Kroon, W.D. Roos, H.C. Swart, Cu nanoclusters in ion exchanged soda-lime glass: Study of SPR and nonlinear optical behavior for photonics, Applied Materials Today, 15 (2019) 323-334.
- [40] A. Kuz'menko, D. Van der Marel, P. Van Bentum, E. Tishchenko, C. Presura, A. Bush, Infrared spectroscopic study of CuO: Signatures of strong spin-phonon interaction and structural distortion, Physical Review B, 63 (2001) 094303.
- [41] J. Vieillard, N. Bouazizi, M.N. Morshed, T. Clamens, F. Desriac, R. Bargougui, P. Thebault, O. Lesouhaitier, F. Le Derf, A. Azzouz, CuO nanosheets modified with amine and thiol grafting for high catalytic and antibacterial activities, Industrial & Engineering Chemistry Research, 58 (2019) 10179-10189.
- [42] S.H. Sabeeh, H.A. Hussein, H.K. Judran, Synthesis of a complex nanostructure of CuO via a coupled chemical route, Materials Research Express, 3 (2016) 125025.
- [43] K. Giannousi, I. Avramidis, C. Dendrinou-Samara, Synthesis, characterization and evaluation of copper based nanoparticles as agrochemicals against Phytophthora infestans, RSC advances, 3 (2013) 21743-21752.
- [44] A. Kose, M.F. Fellah, Hydrogen adsorption, desorption, sensor and storage properties of Cu doped/decorated boron nitride nanocone materials: A density functional theory and molecular dynamic study, International Journal of Hydrogen Energy, 79 (2024) 1086-1099.
- [45] R.K. Sithole, L.F.E. Machogo, M.A. Airo, S.S. Gqoba, M.J. Moloto, P. Shumbula, J. Van Wyk, N. Moloto, Synthesis and characterization of Cu3N nanoparticles using pyrrole-2-carbaldpropyliminato Cu(ii) complex and Cu(NO3)2 as single-source precursors: the search for an ideal precursor, New Journal of Chemistry, 42 (2018) 3042-3049.
- [46] J. Coates, Interpretation of infrared spectra, a practical approach, Encyclopedia of analytical chemistry, 12 (2000) 10815-10837.

- [47] K. Liu, Y. Song, S. Chen, Electrocatalytic activities of alkyne-functionalized copper nanoparticles in oxygen reduction in alkaline media, Journal of Power Sources, 268 (2014) 469-475.
- [48] K.M. Dokken, J.G. Parsons, J. McClure, J.L. Gardea-Torresdey, Synthesis and structural analysis of copper (II) cysteine complexes, Inorganica Chimica Acta, 362 (2009) 395-401.
- [49] J. Grdadolnik, Y. Maréchal, Bovine serum albumin observed by infrared spectrometry. I. Methodology, structural investigation, and water uptake, Biopolymers: Original Research on Biomolecules, 62 (2001) 40-53.
- [50] C. Pradier, M. Salmain, S. Boujday, IR spectroscopy for biorecognition and molecular sensing, in: Biointerface Characterization by Advanced IR Spectroscopy, Elsevier, 2011, pp. 167-216.
- [51] A. Molina, J. González, Pulse voltammetry in physical electrochemistry and electroanalysis, Monographs in electrochemistry, (2016).
- [52] O. Gharbi, M.T. Tran, B. Tribollet, M. Turmine, V. Vivier, Revisiting cyclic voltammetry and electrochemical impedance spectroscopy analysis for capacitance measurements, Electrochimica Acta, 343 (2020) 136109.
- [53] B. Balkanlı, N. Yuksel, M.F. Fellah, Neurotransmitter amino acid adsorption on metal doped boron nitride nanosheets as biosensor: DFT study on neural disease prediagnosis system, Sensors and Actuators A: Physical, 366 (2024) 114980.
- [54] S. Augustine, P. Kumar, B.D. Malhotra, Amine-functionalized MoO3@ RGO nanohybrid-based biosensor for breast cancer detection, ACS Applied Bio Materials, 2 (2019) 5366-5378.
- [55] M. Nap, M.-L. Hammarström, O. Börmer, S. Hammarström, C. Wagener, S. Handt, M. Schreyer, J.-P. Mach, F. Buchegger, S. von Kleist, Specificity and affinity of monoclonal antibodies against carcinoembryonic antigen, Cancer research, 52 (1992) 2329-2339.

# Chapter - 7

Integration of hierarchical nanostructures featuring 2D-hBNNS decorated with mixed-phase 1D-TiO<sub>2</sub> nanowires for ultra-sensitive, High-Performance Electrochemical Sensing of Carcinoembryonic Antigen.

This chapter examine the Potential of an innovative nano-hybrid composite (NHC) based on nan-layered transition metal oxide, comprising one-dimensional (1D) TiO<sub>2</sub> nanowires (NWs) integrated with semiconducting hexagonal boron nitride nanosheets (hBNNS), forming TiO<sub>2</sub>-hBNNS nano-interface matrix for label-free, ultra-sensitive detection of carcinoembryonic antigen (CEA). The synthesis of TiO<sub>2</sub>-NWs, hBNNS, and the TiO2-hBNNS NHC was achieved through a hydrothermal approach and systematically demonstrated using advanced material characterization techniques. Furthermore, the fabrication of TiO<sub>2</sub>-hBNNS microelectrodes was accomplished by voltage-driven electrophoretic deposition (EPD) technique onto pre-hydrolyzed indium tin oxide (ITO) electrodes. The pivotal role of optimization parameters employing optimal pH measurement, antibody incubation time, control analysis is described and investigated to ensure high-performance biosensing. The electroanalytical evaluation of the TiO<sub>2</sub>-hBNNS microelectrode demonstrated exceptional sensitivity, achieving a current response of 11.2 mA ng<sup>-1</sup> mL cm<sup>-2</sup>, with an impressively low detection limit of 0.035 pg/mL ( $R^2 = 0.99963$ ) exhibiting detection capacity of target analyte as low as fg/mL in comparison to LOD of pristine hBNNS in pg/mL over a broad dynamic range of 0-50 ng/mL. Clinical assessment of the fabricated electrode further revealed excellent stability, prolonged shelf life, negligible cross-reactivity, and reliable recovery rates in human serum samples. These findings highlight the significant sensing potential of the TiO<sub>2</sub>-hBNNS microelectrode as a robust and precise platform for earlystage cancer biomarker detection.

#### 7.1 Introduction

Structural hierarchy is an intrinsic law of nature, observed consistently across biological and physical systems, from the smallest units of life such as cells to entire ecosystems such as forests [1]. At every level, nature applies recursive principles of assembly, where repeating units integrate into increasingly complex architectures. This hierarchical order imparts functionality, efficiency, and adaptability, ensuring that natural systems are both dynamic and capable of sustaining complex processes. The same principle holds true in material science, where hierarchical structuring within engineered materials can dramatically alter their bulk behaviour and overall properties. By incorporating nature-inspired hierarchical features into nanoscale materials, it becomes possible to transform their fundamental characteristics, thereby unlocking opportunities for enhanced performance in technological fields including energy conversion, catalysis, sensing, environmental remediation, and biomedicine.

At the nanoscale, the integration of hierarchy produces striking transformations in material behaviour. Hierarchical nanostructures are defined as integrated architectures consisting of systematically arranged nanoscale building blocks that can adopt zero-, one-, two-, or three-dimensional morphologies [2]. Typical examples include zerodimensional quantum dots, one-dimensional nanofibers, nanorods, and nanowires, twodimensional nanosheets and thin films, and three-dimensional architectures such as nanoflowers, nanospheres, and porous scaffolds. These architectures may also exist in hybrid forms, where multiple dimensionalities are combined to yield multifunctional systems. The deliberate fabrication of porous hierarchies across multiple scales enables scientists to replicate natural efficiency while introducing properties such as enhanced catalytic activity, controlled diffusion pathways, tuneable optical behaviour, and improved mechanical integrity. A central focus in this domain is the rigorous exploration of the interplay between structural design and functional outcomes, as mastering this relationship is critical for the development of advanced materials with tailored performance. Natural assemblies, although highly intricate and threedimensional, are often constrained by issues of fragility, instability, and vulnerability under harsh operating conditions. By contrast, engineered hierarchical nanostructures emulate the organizational elegance of natural systems and surpass them in robustness and adaptability, making them indispensable in the design of high-performance porous materials.

Hierarchical nanohybrid composites have emerged as superior alternatives to conventional spherical nanoparticles, primarily because their structural design can be rationally controlled, functionalities can be effectively combined, and transport properties can be finely tuned [3]. These advantages enable hierarchical systems to deliver enhanced surface reactivity, optimized charge transfer, and higher catalytic efficiency, thereby outperforming spherical nanoparticle counterparts in various applications. Among the broad spectrum of metal oxides, titanium dioxide (TiO<sub>2</sub>) holds a particularly distinguished position [4]. Its excellent redox potential, strong acid—base properties, and wide electrochemical window have established TiO<sub>2</sub> as one of the most versatile and durable oxides for heterogeneous catalysis, particularly in the field of photocatalysis. TiO<sub>2</sub> is further valued for its high chemical stability, resistance to photocorrosion, non-toxic nature, cost-effectiveness, and commercial availability. These attributes have facilitated its widespread use in diverse applications ranging from its

role as a white pigment in paints, toothpaste, and cosmetics to its utilization in photocatalysis, catalytic supports, photovoltaic devices, and as an electrode material in lithium-ion batteries. In recent years, however, the scientific focus has shifted toward TiO<sub>2</sub> materials designed with hierarchical architectures. Such architectures, compared to simple spherical nanoparticles, exhibit superior properties including enlarged surface area, enhanced porosity, and improved light-harvesting efficiency. Moreover, they offer more active sites for adsorption and reaction, along with shorter charge transport pathways, leading to better photocatalytic performance.

The historical importance of TiO<sub>2</sub> research can be traced back to the pioneering work of Fujishima and Honda in 1972, who first demonstrated the photolysis of water using TiO<sub>2</sub> electrodes [5]. This seminal discovery revolutionized the field of photocatalysis and opened the pathway for TiO<sub>2</sub> to become one of the most extensively studied materials in environmental remediation and clean energy. Its inherent ability to generate reactive oxygen species under light irradiation allows TiO<sub>2</sub> to degrade a wide spectrum of organic pollutants, making it highly relevant for addressing environmental contamination. Consequently, the pursuit of hierarchical TiO<sub>2</sub> nanostructures represents a vital step toward maximizing the material's intrinsic properties while tailoring its architecture for advanced catalytic and photocatalytic applications.

Titanium dioxide (TiO<sub>2</sub>) has established itself as one of the most versatile oxides, finding widespread applications across a diverse range of fields, including photocatalysis, sensors, catalyst supports, lithium-ion batteries, dye-sensitized solar cells (DSSCs), biomaterials, and CO methanation [6]. Its adaptability stems from its structural polymorphism, which includes anatase, rutile, brookite, and amorphous phases. Among these, anatase TiO<sub>2</sub> has consistently demonstrated superior photocatalytic activity due to its favorable electronic structure, high surface energy facets, and efficient charge separation characteristics, making it the preferred phase for advanced applications. The photocatalytic performance of TiO<sub>2</sub> nanoparticles is highly dependent on intrinsic and extrinsic factors such as surface area, morphology, crystallinity, band gap energy, and metal loading. Parameters like shape and size critically influence light absorption and charge transport, while crystal structure governs defect density and electron-hole recombination. Accordingly, TiO<sub>2</sub> nanostructures engineered into various morphologies—such as nanorods, nanotubes, and elongated cylindrical forms—have proven to exhibit enhanced photocatalytic efficiencies compared to commercial benchmarks like Degussa P25. These improvements are attributed to better delocalization of photogenerated electron-hole pairs, higher surface accessibility, and reduced recombination losses.

One-dimensional TiO<sub>2</sub> nanostructures, in particular, have garnered heightened attention compared to their zero-dimensional (0D) and two-dimensional (2D) counterparts [7]. Their higher aspect ratio, extended charge transport pathways, and large specific surface area make them exceptionally suitable for photocatalytic and energy-related applications. Extensive research has focused on optimizing fabrication techniques to further refine their functional properties, including enhanced light absorption, improved charge separation, and maximized surface reactivity. Morphology, exposed crystal planes, and nanoscale dimensions remain decisive factors that control the physicochemical properties of titania, and these parameters have been meticulously studied to guide targeted synthesis. The development of hierarchical TiO<sub>2</sub>

nanostructures at the micro- and nanoscale has been identified as a transformative strategy to overcome fundamental limitations associated with charge carrier recombination and diffusion kinetics. Hierarchically organized porous frameworks allow efficient diffusion of reactants toward active catalytic sites while simultaneously providing improved light-harvesting efficiency and increased surface-to-volume ratio. Such architectures integrate porosity, morphology, and quantum confinement effects to tailor the conduction and valence band edges, thereby tuning photocatalytic activity for specific applications. In addition, by scaling the building blocks of TiO<sub>2</sub> down to the nanometer regime, the quantum size effect comes into play, enabling precise control over electronic band structures. These advancements demonstrate that structural engineering of TiO<sub>2</sub> from the nanoscale to hierarchical architectures is not only crucial for enhancing its photocatalytic efficiency but also pivotal for expanding its role in sustainable energy conversion, environmental remediation, and next-generation nanotechnology applications.

Titanium dioxide [titanium(IV) oxide or titania] is an extensively studied metal oxide with the molecular formula TiO<sub>2</sub> and a molecular weight of 79.87 g/mol [8]. It is well recognized for its non-toxic nature, remarkable chemical stability, and excellent biocompatibility, making it suitable for both industrial and biomedical applications. TiO<sub>2</sub> is also a strong oxidizing agent with a large specific surface area, which greatly contributes to its outstanding photocatalytic activity. In addition to its catalytic merits, TiO<sub>2</sub> is cost-effective due to its abundance in nature, ease of synthesis, low production costs, and high dielectric constant, all of which have contributed to its widespread use in environmental, energy, and medical fields. Titanium dioxide (TiO<sub>2</sub>) crystallizes in four principal polymorphic phases: rutile (tetragonal, thermodynamically stable), anatase (tetragonal, metastable), brookite (rhombohedral), and TiO<sub>2</sub>-B (monoclinic). Each phase exhibits distinct structural and physicochemical characteristics that govern its suitability for specific applications. The interplay between these polymorphs has been the subject of extensive research, as their structural, optical, and electrical properties directly determine TiO2's performance in applications such as photocatalysis, photovoltaics, sensors, and biomaterials. Comparative studies on anatase, rutile, and brookite have systematically outlined differences in lattice parameters, dielectric properties, bandgap energies, and electron transport behaviour, highlighting how controlled synthesis and phase engineering can unlock the full potential of TiO2 [9]. This versatility indicates TiO2 is most investigated and technologically significant oxides in materials science.

Rutile, the most thermodynamically stable phase of TiO<sub>2</sub>, crystallizes in a tetragonal structure containing six atoms per unit cell [10]. Each Ti atom is coordinated in a slightly distorted TiO<sub>6</sub> octahedron, reflecting a minor orthorhombic distortion within the lattice. At particle sizes greater than 14 nm, rutile becomes more stable than anatase, marking it as the energetically favourable polymorph under these conditions. Naturally occurring rutile crystals predominantly expose the (110) surface, which is considered the most stable stoichiometric surface of rutile. Within the unit cell, four oxygen atoms form a partial octahedral environment around titanium, while two titanium atoms, located at [0, 0, 0] and (½, ½, ½) positions, are distinctly available. Each TiO<sub>6</sub> octahedron connects with ten neighbouring octahedra, sharing two edges and eight corners. The edge-sharing octahedra are preferentially aligned along the [001]

crystallographic direction, a configuration that critically influences the anisotropy of rutile's structural and electronic properties.

Anatase TiO<sub>2</sub> is characterized by a pronounced distortion of the TiO<sub>6</sub> octahedra, much larger than that observed in rutile, resulting in a tetragonal structure of lower symmetry approaching orthorhombic geometry [11]. The energy gap between anatase and rutile phases is minimal, typically ranging between 2–10 kJ mol<sup>-1</sup>, suggesting that their thermodynamic stabilities are closely matched. At 0 K, rutile does not exhibit greater thermodynamic favourability than anatase, contrary to its dominance at higher temperatures. The anatase unit cell comprises four titanium atoms situated at positions (½, ½, ½), (0, 0, 0), (½, 0, ¼), and (0, ½, ¼), coordinated by eight oxygen atoms to form distorted TiO<sub>6</sub> octahedra. Each octahedron connects by sharing four of its edges with adjacent octahedra, establishing a distinctive network that plays a pivotal role in governing the charge transport, optical transitions, and photocatalytic behaviour unique to the anatase phase.

Brookite is one of the three naturally occurring polymorphs of TiO<sub>2</sub>, crystallizing in the orthorhombic system. Its unit cell possesses a comparatively larger volume, accommodating eight TiO<sub>2</sub> groups per cell [12]. Among the polymorphs, brookite is the least dense form, lighter than both anatase and rutile, and yet retains photocatalytic activity, making it technologically relevant. Studies have demonstrated that brookite and other TiO<sub>2</sub> phases can be modified under high-pressure treatments to enhance their photocatalytic properties, including metal-free photocatalytic water splitting. Investigations of surface modifications revealed performance variations when conducted on anatase single-crystal facets and wafer slices of the [001] plane, with pressure-driven phase transitions. Furthermore, the phase stability of TiO<sub>2</sub> is highly sensitive to impurities. For example, anatase in powder samples doped with vanadium, molybdenum, or tungsten completely transforms into other polymorphs at approximately 530 °C, 680 °C, and 830 °C, respectively, underscoring how dopants and thermal effects critically dictate phase stability and photocatalytic functionality.

Within the Group III nitride family, hexagonal boron nitride (h-BN), widely known as white graphene, stands as a uniquely lightweight and structurally robust compound exhibiting remarkable electronic and physicochemical characteristics [13]. Its crystalline lattice is defined by the alternating placement of boron and nitrogen atoms arranged in a hexagonal geometry. While the dominant bonding within this lattice is covalent, the substantial electronegativity difference between boron and nitrogen introduces partial ionic character, leading to charge polarization and uneven distribution of electron density. This intrinsic polarity underpins h-BN's exceptionally wide bandgap of approximately 5–6 eV and contributes to its distinct combination of low intrinsic conductivity with superior stability.

The sp²-hybridized bonding network in h-BN ensures structural rigidity while simultaneously conferring unique electroanalytical properties. Unlike graphene, which is characterized by metallic conductivity, h-BN remains electrically insulating but excels in electroanalytical systems due to its ability to suppress background interference [14]. In addition, h-BN demonstrates outstanding resistance to oxidation under ambient conditions and exhibits superior thermal stability, properties that make it highly attractive for applications requiring durability in chemically harsh or high-temperature

environments. Its remarkably high thermal conductivity allows efficient heat dissipation, while its wide bandgap contributes to chemical inertness, ensuring resilience against reactive species. Accordingly, h-BN finds application in diverse areas such as solid lubricants, high-performance protective coatings, and substrates for high-power or high-frequency electronic and optoelectronic devices.

In the context of biosensing, h-BN provides both opportunities and challenges. Its chemical inertness minimizes signal interference, ensuring reliable and precise detection, but simultaneously restricts functionalization efficiency and biomolecule anchoring capacity [15]. To counteract this limitation, researchers employ advanced modification strategies such as covalent surface functionalization, hybridization with conductive nanomaterials (e.g., metals, metal oxides, or carbon allotropes), and hierarchical nanostructure engineering. These approaches not only increase the effective electroactive surface area but also enhance electron transfer dynamics and facilitate high-density biomolecule immobilization. Through such nano-engineering strategies, h-BN is transformed from a chemically inert insulating material into a highly effective sensing interface with excellent sensitivity, selectivity, and operational stability. Therefore, h-BN distinguishes itself as a multifunctional material that merges structural robustness, chemical resistance, and wide bandgap properties with tunable surface chemistry via hybridization. This balance of inherent stability with engineered reactivity positions h-BN as a promising cornerstone in the design and development of high-performance nano-biosensors, particularly for real-time biomedical diagnostics and environmental monitoring applications.

The strategic coupling of one-dimensional (1D) TiO<sub>2</sub> nanowires with two-dimensional (2D) hexagonal boron nitride nanosheets (hBNNS) gives rise to a hierarchical hybrid system with exceptional electrochemical and structural properties [16]. This nanoarchitectured platform exhibits remarkable electrocatalytic activity, robust stability, and accelerated electron transfer kinetics, establishing itself as a reliable candidate for next-generation biosensing applications. The synergy between TiO<sub>2</sub> and hBNNS enables a unique balance of conductivity, biocompatibility, redox efficiency, and structural durability, thereby positioning TiO<sub>2</sub>–hBNNS hybrids as a breakthrough material system for point-of-care diagnostics.

The development of this hybrid nano-biosensor represents a decisive advancement in cancer diagnostics, particularly for the label-free, ultra-sensitive detection of carcinoembryonic antigen (CEA). In this architecture, TiO<sub>2</sub> nanowires provide vertically aligned porous channels and abundant reactive sites for effective biomolecule immobilization, while hBNNS contributes high chemical stability, a wide surface area, and mechanical integrity. The integration of these components results in a self-assembled nanocomposite with superior sensitivity and long-term operational reliability. Fabrication was achieved via a hydrothermal synthesis route that exploited autogenous temperature and pressure to drive spontaneous assembly, ensuring phase-pure crystalline nanomaterials at low temperatures without compromising nanostructure integrity. FTIR spectroscopy validated the strong molecular interactions responsible for stabilizing the hybrid framework, confirming successful structural integration and functionalization. The bio-interface was further optimized by leveraging abundant active sites on TiO<sub>2</sub>–hBNNS for efficient Anti-CEA antibody immobilization through Fc-region conjugation. This ensured improved antibody

orientation, minimized steric hindrance, and enhanced antigen-binding efficiency. The electrochemical performance of this hybrid platform is exceptional: TiO<sub>2</sub> nanowires accelerate electron transfer and amplify electrocatalytic signals, while hBNNS safeguards biomolecular stability against denaturation and degradation. Under optimized conditions, the biosensor achieves an ultra-low detection limit well within the physiological range of CEA, far surpassing the capabilities of conventional metal, metal oxide, or semiconductor-based sensors. This innovation not only advances diagnostic precision but also offers cost-effectiveness, scalability, and long-term stability, establishing a new paradigm in biosensor technology for clinical cancer detection.

### 7.2 Experimental Section:

#### 7.2.1 Chemical, Reagents and Instrumentation:

In the present investigation, a diverse range of high-purity analytical-grade chemicals and reagents were utilized to ensure experimental reliability, reproducibility, and precision. The primary set of reagents procured from Sigma Aldrich included ethylene glycol (OHCH2CH2OH, >99%), bulk h-BN powder (98%, 5µm-particle size), bovine serum albumin (BSA), chloroform (CHCl<sub>3</sub>), sodium chloride (NaCl, >99%), potassium bromide (KBr, >99%), carcinoembryonic antigen (CEA), monoclonal antibodies of 1-(3-(dimethylamino)-propyl)-3-ethylcarbodiimide hydrochloride CEA, >98%), and N-hydroxysuccinimide (NHS, 96%). Various reagents of equally high purity were sourced from Thermo Fisher Scientific and Merck, including Titanium dioxide (TiO<sub>2</sub>), potassium ferrocyanide (K<sub>4</sub>[Fe(CN)<sub>6</sub>]·3H<sub>2</sub>O, >98.5%), isopropanol (CH<sub>3</sub>)<sub>2</sub>CHOH, >99%), hydrazine hydrate (N<sub>2</sub>H<sub>4</sub>H<sub>2</sub>O, >99%), sodium phosphate monobasic dihydrate (NaH<sub>2</sub>PO<sub>4</sub>·2H<sub>2</sub>O<sub>2</sub>, 98–100.5%), sodium hydroxide (NaOH), acetonitrile (CH<sub>3</sub>CN, >99.9%), ethanol (C<sub>2</sub>H<sub>5</sub>OH, 99%), potassium ferricyanide (K<sub>3</sub>[Fe(CN)<sub>6</sub>], >98.5%), hydrochloric acid (HCl) and sodium phosphate dibasic dihydrate (Na<sub>2</sub>HPO<sub>4</sub>·2H<sub>2</sub>O, 98–100.5%). To maintain the integrity of electrochemical and immunological assays, only ultrapure Milli-Q water was used for solution preparation and sample washing. Fresh phosphate buffer saline (PBS) solutions of varying pH values were formulated by combining solution A (NaH<sub>2</sub>PO<sub>4</sub>·2H<sub>2</sub>O), solution B (Na<sub>2</sub>HPO<sub>4</sub>·2H<sub>2</sub>O), and Milli-Q water in precise ratios, followed by storage at 4 °C until use. The immunoassay validation was supported using a sandwich-assay ELISA kit procured from Amplicon Biotech, India.

To establish a detailed interrelationship between their physical structure, chemical composition, and functional performance of the as-synthesized TiO<sub>2</sub>-NW, hBNNS, and TiO<sub>2</sub>-hBNNS samples, an extensive set of characterization procedures systematically investigated. To determine crystallographic phases and assess structural order, X-ray diffraction (XRD, Bruker Advance D-8) was employed. This facilitated precise identification of the crystalline structure, quantification of phase purity, and evaluation of potential lattice strain, which is critical for correlating structural attributes with functional performance. Morphological investigations were carried out using Scanning Electron Microscopy (SEM, EVO18 Zeiss) and Transmission Electron Microscopy (TEM, TECNAI 200 kV), enabling high-resolution visualization of both micro- and nano-scale architectures, particle boundaries, and aggregation tendencies. To ensure accurate quantification of particle size distributions and surface feature dimensions,

ImageJ-1.54f software was used to perform statistical analyses on multiple SEM and TEM images, providing reliable average size estimations and dispersity indices. Chemical bonding and molecular-level interactions within the nano-hybrids were probed using Fourier-Transform Infrared (FTIR) Spectroscopy (Spectrum II, Perkin Elmer) in the range of 400–4000 cm<sup>-1</sup>. This analysis elucidated the presence of functional groups, possible surface modifications, and bonding configurations between the TiO2 and hBNNS phases, which directly influence stability and reactivity. Furthermore, Raman spectroscopy (Renishaw,  $\lambda = 785$  nm) provided vibrational fingerprint data, revealing phonon modes and defect-induced shifts, while UV–Visible spectroscopy (Perkin Elmer 950) enabled evaluation of optical bandgap energies, electronic transitions, and light absorption behavior—critical factors for optoelectronic and sensing performance optimization.

Electrochemical analyses were performed using Cyclic Voltammetry (CV) and Differential Pulse Voltammetry (DPV) on an Autolab Galvanostat/Potentiostat (Metrohm, Netherlands). The system was configured in a classical three-electrode arrangement comprising a TiO2-hBNNS-modified indium tin oxide (ITO) substrate as the working electrode, a platinum rod as the counter electrode, and an Ag/AgCl electrode immersed in 3 M KCl as the reference. This configuration enabled precise control and monitoring of redox processes. Immunosensing evaluations were conducted in phosphate-buffered saline (PBS, 50 mM, 0.9% NaCl, pH 7.0), supplemented with a ferro/ferricyanide redox couple ([Fe(CN)<sub>6</sub>]<sup>3-/4-</sup>, 5 mM) to facilitate rapid and efficient single-electron heterogeneous transfer between the immobilized bioreceptor and the electrode interface. This setup allowed for highly sensitive and selective detection of the carcinoembryonic antigen (CEA), leveraging the synergistic electrocatalytic properties of the TiO2-hBNNS hybrid. The comprehensive integration of structural, morphological, chemical, optical, and electrochemical analyses provides a robust foundation for optimizing this nano-biosensing platform toward clinical-grade performance.

## 7.2.2 Energy-Efficient Solvothermal Approach for the Controlled Growth of One-Dimensional High-Aspect-Ratio TiO<sub>2</sub> Nanowires

A facile, meticulously controlled solvothermal approach was employed to synthesize TiO<sub>2</sub> nanowires, leveraging the synergistic effects of strong alkaline conditions and polyol chemistry to direct anisotropic crystal growth (**Fig. 7.1**). The process initiated by dispersing 500 mg of TiO<sub>2</sub> powder into 30 mL of a concentrated 10 M NaOH solution, followed by ultrasonication for 1 hour. This stage served to achieve homogeneous dispersion, activate surface sites, and initiate crystal lattice loosening through strong hydroxide ion interactions. Subsequently, 5 mL of ethylene glycol (EG) was incorporated into the mixture, and the dispersion was stirred at 270 rpm for 2 hours at 30 °C. EG molecules selectively adsorbed on TiO<sub>2</sub> surfaces, forming stabilizing hydrogen-bond networks that prevented uncontrolled aggregation and simultaneously introduced a morphology-directing effect. In addition, NaOH stimulated hydroxylation, and complexation processes that led to interlayer expansion, defect site activation, and partial exfoliation, producing reactive nanosheet-like precursors required for anisotropic growth.

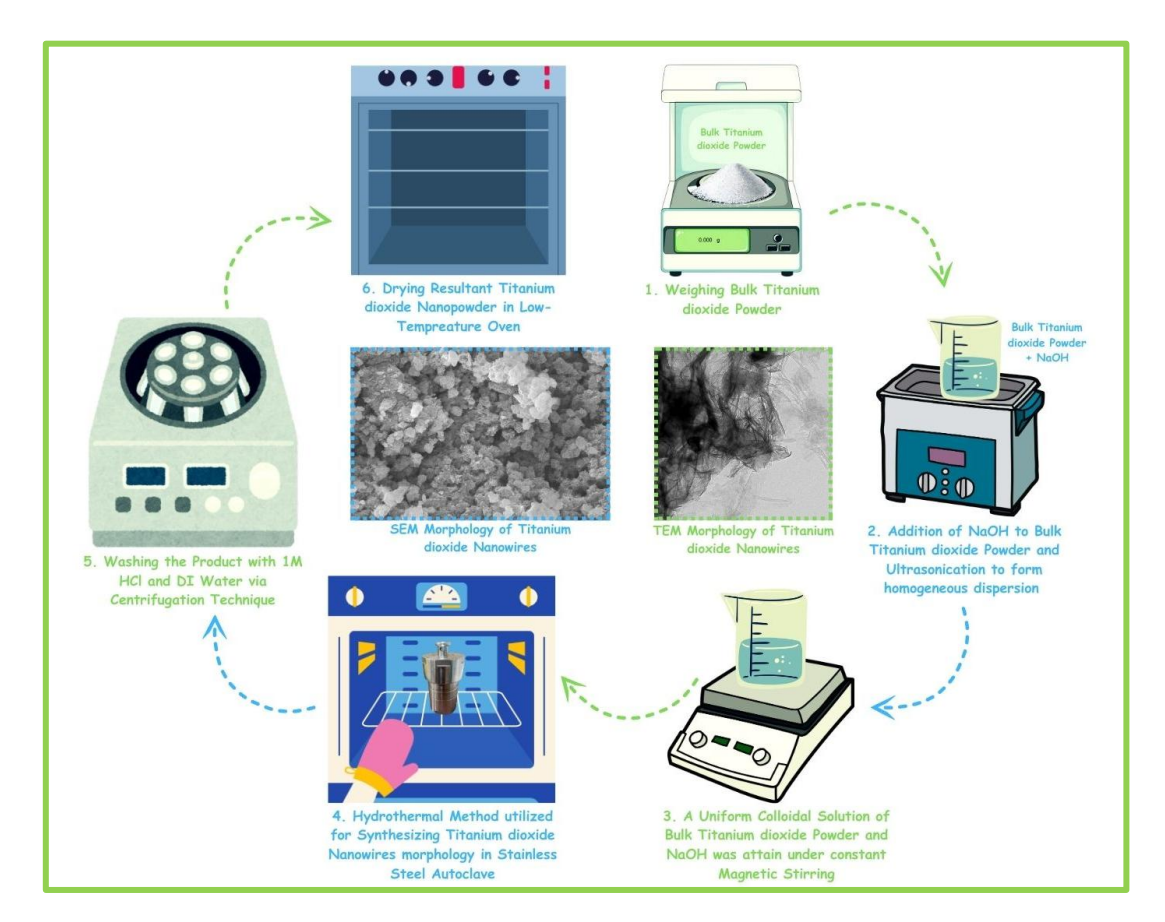


Figure 7.1: Stepwise schematic Illustration for the synthesis of TiO<sub>2</sub> nanowires through the solvothermal method.

This well-dispersed homogeneous mixture was transferred into a 50 mL Teflon-lined stainless-steel autoclave, that exhibits the ability to withstand high pressures and chemically aggressive environments. The autoclave was tightly sealed and subjected to hydrothermal conditions at 180 °C for 24 hours to promote controlled crystal growth kinetics. Under these conditions, NaOH dissociates to release OH<sup>-</sup> ions that penetrate TiO<sub>2</sub> crystal layers, weakening interlayer van der Waals forces and enabling exfoliation into ultrathin structures. Simultaneously, EG molecules adsorb to the reactive site on TiO<sub>2</sub> surface through hydroxyl interactions, functioning both as a soft template and as a steric stabilizer, lowering surface energy barriers and directing the growth axis preferentially along one dimension, thus transforming the intermediate nanosheets into high-aspect-ratio nanowires.

The morphological transformation into nanowires occurs through selective facet growth control—hydroxide ions preferentially bind to specific crystallographic planes, lowering their growth rate and promoting elongation along the axial direction. This anisotropic growth is further stabilized by EG capping, which minimizes surface energy and promotes ordered assembly. The presence of EG also plays a chemical role by forming weak Ti–O–C complexes during solvothermal treatment, thereby introducing surface functional groups to enhance structural stability, catalytic activity, and potential active site exposure.

Post-synthesis, the reaction product was purified with repetitive centrifugation at speeds >5000 rpm, utilizing 1 M hydrochloric acid (HCl) to remove residual Na<sup>+</sup> ions and Milli-Q water to restore pH equilibrium at 7.0, thereby preventing post-synthesis corrosion or uncontrolled precipitation. This dual-step washing removed excess NaOH, eliminated surface-bound EG and soluble reaction by-products, gradually bringing the pH to a neutral value of 7.0, indicating complete neutralization. The washed product was then dried at 60 °C for 24 hours, resulting in phase-pure, crystallographically ordered TiO<sub>2</sub> nanowires, yielding high-quality nanowires with well-preserved aspect ratios and pristine surface chemistry.

## 7.2.3 An In-Situ Strategic Hydrothermal Synthesis of TiO<sub>2</sub>-hBNNS Nano-Hybrid Composite

The in-situ cationic surfactant-mediated hydrothermal fabrication of TiO<sub>2</sub>-decorated hBNNS nano-hybrid composite (**Fig. 7.2**) was strategically carried out by employing TiO<sub>2</sub> nanowires and hBNNS as engineered precursors. Ultrathin hBNNS, selected in preference to bulk hBN, exhibiting high surface-to-volume ratio, enhanced edge activity, and abundant interaction sites, overcoming the limitations posed by strong interatomic B–N ionic bonding in bulk crystals that severely restricts exfoliation, dispersibility, and interfacial compatibility, thereby limiting composite integration.

To initiate the synthesis process, 100 mg of hBNNS and 60 mg of TiO<sub>2</sub> nanowires were weighed and dispersed in 18 mL of deionized water through ultrasonication for 1 hour, ensuring complete exfoliation of nanosheets and disentanglement of nanowires. To further reduce surface energy and support miscibility, 10 mL of IPA was added, which acted as a co-solvent to minimize agglomeration. Continuous ultrasonication allowed equal distribution of both nanostructures and promoted intimate interfacial contact. To strengthen their interactions between precursors, the suspension was further stabilized by 2 mL of hydrazine hydrate, which established amino group-mediated selective binding between TiO<sub>2</sub> nanowires and hBNNS, thereby establishing a robust interfacial network for complexation. Following this, 2 mL of 0.1 M CTAB was introduced. As a cationic surfactant, CTAB provided electrostatic stabilization and functioned as a structure-directing agent, assisting in the ordered alignment of TiO<sub>2</sub> nanowires over the surface of hBNNS while preserving their individual morphologies.

To ensure uniform precursor interaction, the mixture was magnetically stirred at 270 rpm for 2 hours to reinforce uniform molecular-level interaction. The mixture was transferred and sealed in a 50 mL Teflon-lined stainless-steel autoclave. Hydrothermal treatment was conducted at 180 °C for 7 hours, where thermal and pressure-induced conditions promoted the in-situ assembly of TiO<sub>2</sub> onto hBNNS surfaces. After natural cooling, the obtained dispersion, characterized by a high pH (~12), was subjected to meticulous purification. The composite was first washed with chloroform to remove residual organic molecules and then repeatedly rinsed with IPA and deionized water to eliminate unreacted hydrazine and surfactant. The centrifugation process was performed at 5000 rpm until neutral pH was achieved, confirming effective removal of impurities. The resultant precipitate was dried in a hot-air oven at 100 °C for 18 hours, producing a dry TiO<sub>2</sub>-decorated hBNNS nano-hybrid powder.

The purified precipitate was oven-dried at 100 °C for 18 hours to obtain the TiO<sub>2</sub>-decorated hBNNS composite in stable powder form. The overall mechanism of

synthesis was predominantly governed by the synergistic ionic interactions, hydrogen bonding, and surfactant-assisted templating effect of CTAB in conjunction with the interfacial chemistry promoted by IPA and hydrazine hydrate. This approach enabled controlled integration of TiO<sub>2</sub> nanowires into the hBNNS matrix, yielding a nanohybrid composite characterized by enhanced stability, structural robustness, and a well-integrated interfacial framework.



Figure 7.2: Schematic illustration of the engineered solvothermal mechanism facilitating TiO<sub>2</sub> nanowire decoration on hBNNS nano-hybrid composite.

## 7.2.4 Preparation of TiO<sub>2</sub>-hBNNS Functional Films on ITO Surfaces through Electrophoretic Deposition

Electrophoretic deposition (EPD) was employed as a precise and reproducible strategy for fabricating TiO<sub>2</sub>–hBNNS/ITO microelectrodes, ensuring uniform thin-film growth and strong interfacial adhesion. The approach capitalized on the dual advantage of a stable colloidal suspension and the directed drift of charged nanoparticles under an applied electric field, which together enabled highly controlled film formation (**Fig. 7.3**). To prepare the colloidal medium, 0.25 mg/mL of TiO<sub>2</sub>–hBNNS nanocomposite was dispersed in acetonitrile (CH<sub>3</sub>CN), selected for its high dielectric constant and low viscosity that facilitated rapid nanoparticle mobility. For enhanced suspension stability, 300 μL of magnesium nitrate solution (Mg(NO<sub>3</sub>)<sub>2</sub>, 1 mg/mL) was introduced as a charging agent, imparting positive charge to the nanocomposite surface and thereby suppressing agglomeration. The suspension was subjected to ultrasonication for 1 hour, where acoustic cavitation ensured uniform exfoliation, homogeneous particle distribution, and minimized clustering, ultimately maintaining electrokinetic balance during deposition. The prepared colloid was transferred into a two-electrode system,

consisting of a pre-hydrolyzed indium tin oxide (ITO) substrate as the working electrode and a platinum rod as the counter electrode. Hydrolysis of the ITO substrate using a solution of hydrogen peroxide, ammonia, and deionized water (1:1:5) was a critical step that generated hydroxyl-rich functional surfaces, increased roughness, and facilitated enhanced electrostatic attraction between the electrode and nanocomposite. The ITO substrate, measuring  $0.8~\rm cm \times 2.5~cm$ , was connected to the negative terminal, while the platinum electrode was connected to the positive terminal. An external DC voltage of  $20~\rm V$  was applied for 1 minute, inducing directed electrophoretic migration of  $\rm TiO_2$ –hBNNS particles toward the ITO surface. This resulted in the uniform deposition of a  $0.8~\rm cm \times 0.8~cm$  nanocomposite film with dense coverage and consistent morphology.

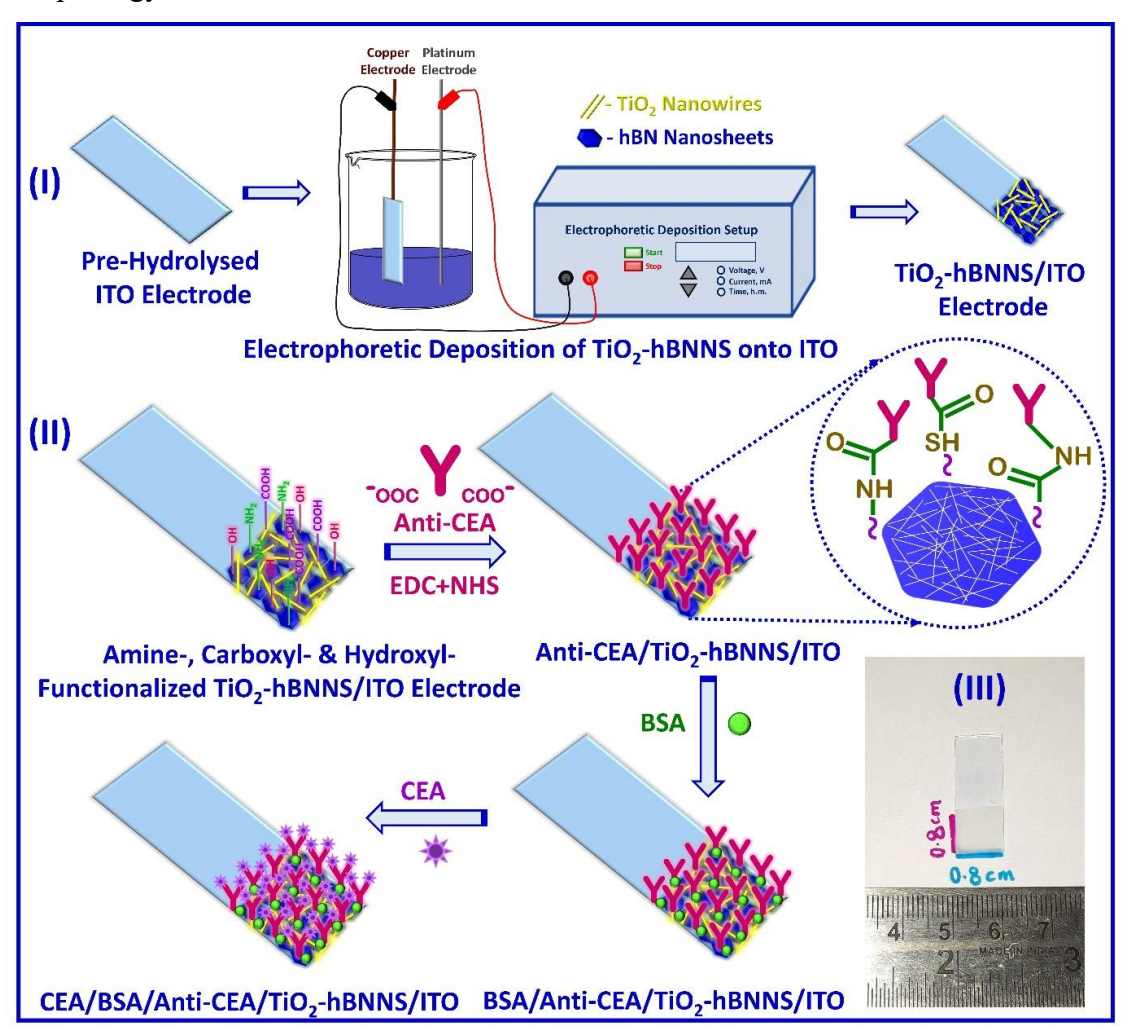


Figure 7.3: (a) Schematic diagram showcasing TiO<sub>2</sub>-hBNNS film deposition through electrophoretic deposition (EPD) technique, (b) Systematic illustration demonstrating sequential steps involved in fabricating TiO<sub>2</sub>-hBNNS-based nano-biosensor.

#### 7.2.5 Preparation of TiO<sub>2</sub>-hBNNS Integrated Immunosensing Electrode

The fabrication of the TiO<sub>2</sub>-hBNNS-based immunoelectrode was executed with rigorous precision to achieve superior electrochemical performance and prolonged

stability. The procedure commenced with the modification of pre-hydrolyzed indium tin oxide (ITO) electrodes using a TiO<sub>2</sub>-hBNNS nanohybrid matrix (Fig. 7.3(II)). This modification yielded a three-dimensional nano-architectured surface enriched with abundant catalytic sites and highly conductive pathways, thus enabling efficient electron transfer and facilitating enhanced immobilization of bio-recognition elements. The site-specific immobilization of monoclonal Anti-CEA antibodies (Fig. 7.3(IV-V)) was performed by preparing a stock solution of antibodies in phosphate-buffered saline (PBS, pH 7.4). EDC-NHS coupling chemistry was employed to selectively activate carboxyl and amine functional groups. Specifically, 50 μg·mL<sup>-1</sup> Anti-CEA was conjugated with freshly prepared EDC (0.2 M) and NHS (0.05 M) in a 2:1:1 ratio at ambient temperature, followed by incubation for 30 minutes to generate reactive intermediates. Subsequently, 20 µL of the activated antibody solution was deposited on the TiO<sub>2</sub>–hBNNS-modified electrode surface and incubated in a humid chamber for 24 hours to ensure robust and specific anchoring. To eliminate nonspecific adsorption, 10 μL of 1% bovine serum albumin (BSA, w/v in Milli-Q water) was applied to block unoccupied active sites. Finally, 10 µL of CEA solution at predetermined concentrations was incubated for 30 minutes on the BSA/Anti-CEA/TiO<sub>2</sub>-hBNNS/ITO interface, thus completing the fabrication of the functional immunoelectrode. The prepared electrode was stored at 4 °C to preserve structural integrity and bioactivity for subsequent electrochemical investigations.

At the molecular level, the immobilization mechanism highlights the robustness and stability of the bio-nano interface by integrating multiple modes of chemical bonding and non-covalent interactions that ensures long-term functionality of the immunoelectrode. This interface is fabricated owing to physical adsorption of biomolecules by an effectively engineered conjugation network that integrates covalent chemistry, electrostatic forces, and coordination bonding to achieve high biorecognition affinity. The activation of the carboxyl groups on the Fc region of Anti-CEA antibodies by EDC initiates the reaction through the formation of a transient Oacylisourea intermediate [17]. Although inherently unstable, this intermediate is stabilized through NHS (N-hydroxysuccinimide) by converting it into a highly reactive NHS-ester, thereby prolonging its lifetime and making it suitable for subsequent coupling. This activated ester then reacts readily with nucleophilic amine functionalities present on the surface-modified hBNNS, forming robust covalent amide bonds. This covalent linkage ensures primary anchoring mechanism, together with a durable, irreversible, and chemically robust conjugation of Anti-CEA with the nanosheet matrix, essential for long-term bio-recognition stability.

In addition to covalent binding, the guanidine moieties of arginine residues in Anti-CEA exhibit strong cationic behaviour [18]. These positively charged groups establish electrostatic interactions with the negatively charged lattice oxygen atoms in both the anatase and rutile phases of TiO<sub>2</sub>. This interaction strengthens the antibody attachment and plays a pivotal role in enhancing electronic communication at the hybrid interface by facilitating charge transfer pathways between the biomolecule and the semiconductor oxide surface. Thus, attain an exceptional boost in the sensor signal response, additionally stabilizing the orientation of Anti-CEA, maximizing its antigenbinding efficiency.

Furthermore, carboxyl groups of aspartic acid residues in the antibody side chains demonstrate a strong affinity for transition metal centers [19]. They form coordination bonds with the surface titanium (Ti) sites in the TiO<sub>2</sub> lattice. These coordination complexes are highly stable and contribute significantly to the reinforcement of the protein–nanomaterial interface, reducing leaching of the antibody, improving electrode longevity under repeated operational cycles, and provide site-specific stabilization, ensuring that the antibody maintains a favourable spatial orientation required for effective antigen recognition.

Moreover, cysteine residues with their reactive thiol (-SH) groups provide another layer of immobilization through chemisorption onto Ti sites of TiO<sub>2</sub> nanoparticles [18]. The strong affinity between sulfur and transition metals ensures a quasi-covalent attachment of the biomolecule, which further strengthens the interfacial architecture. This thiol-Ti binding is particularly beneficial in resisting mechanical disturbances and maintaining sensor integrity under electrochemical cycling.

In addition, amine groups (-NH<sub>2</sub>) from lysine residues form electrostatic bonds with negatively charged oxygen atoms on TiO<sub>2</sub> [20]. These non-covalent interactions serve as supplementary stabilizing forces, providing additional anchoring points for the antibody and enhancing the overall density of immobilized biomolecules at the interface. The combination of lysine amine interactions with stronger covalent and coordination bonds ensures a multi-layered immobilization network that minimizes antibody denaturation or misorientation.

This hybrid immobilization strategy conferred exceptional durability to the immunoelectrode by preventing antibody leaching, while simultaneously preserving its native conformation for precise antigen recognition. The cooperative network of bonds created a bio-nano interface capable of efficient electron transfer, which translated into superior electrocatalytic efficiency during sensing operations. Consequently, the sensor demonstrated high sensitivity, specificity, and long-term operational stability, making it highly suitable for clinical diagnostics.

#### 7.3 Experimental Results & Analysis:

#### 7.3.1 Analytical Nanomaterial Characterizations:

### 7.3.1.1 X-Ray Diffraction Characterization Elucidating Structural Integrity and Phase Evolution in TiO<sub>2</sub>-hBNNS Hybrid Nanocomposite

A detailed XRD examination in the  $2\theta$  range of  $20^{\circ}$ – $80^{\circ}$  was performed to analyze the phase formation, crystal structure, crystallite size, and interlayer spacing of the assynthesized samples: (I) TiO<sub>2</sub>-NW, (II) hBNNS, and (III) TiO<sub>2</sub>-hBNNS nanohybrid composite (NHC), as illustrated in **Fig. 7.4**. The acquired diffractograms enabled an indepth evaluation of crystalline composition, lattice strain and dislocation density, thereby providing critical insights into the structural integrity phase proportion and defect induced in the as-synthesized materials. The XRD diffraction patterns of TiO<sub>2</sub>-NW polymorphs, comprising the three principal crystalline phases, including anatase, rutile, and brookite are illustrated in **Fig. 7.4(I)**. Each polymorph is distinctly is identified through its most prominent crystallographic reflection, providing structural validation and phase distinction. The anatase phase is characterized by the (101) diffraction peak at  $2\theta = 25.48^{\circ}$ , corresponding to **JCPDS card no. 21-1272**, which

represents its most intense and characteristic reflection [21]. The rutile phase is identified by the (110) peak located at  $2\theta = 27.52^{\circ}$ , in agreement with **JCPDS card no. 21-1276** [22], while the brookite phase is distinctly revealed by the (210) reflection at  $2\theta = 25.4^{\circ}$  as indexed by **JCPDS card no. 21-1272 [22]**. These well-defined peaks, arising from the diffraction patterns of the individual phases, provide conclusive evidence for the coexistence of anatase, rutile, and brookite within the TiO2-NW system. The comprehensive diffractogram of the as-synthesized the TiO<sub>2</sub>-NW depicts all essential reflections, thereby validating the presence of a three-phase crystalline framework. The multiphase structures exhibit significant scientific interest, as the coexistence of anatase, rutile, and brookite often enhances interfacial charge transfer, suppresses recombination of photogenerated carriers, and improves overall catalytic activity. In addition to qualitative confirmation, the phase content of each polymorph is determined quantitatively through integrated peak intensity analysis of the anatase (101), rutile (110), and brookite (121) reflections. This quantitative approach, governed by the relations specified in Eq. [7.1]-[7.3], offers a reliable estimation of the respective phase proportions, thereby affirming the multiphase crystalline composition of the TiO<sub>2</sub> nanowire architecture.

$$W_A = \frac{K_A A_A}{K_A A_A + A_R + K_B A_B}$$
 [7.1]

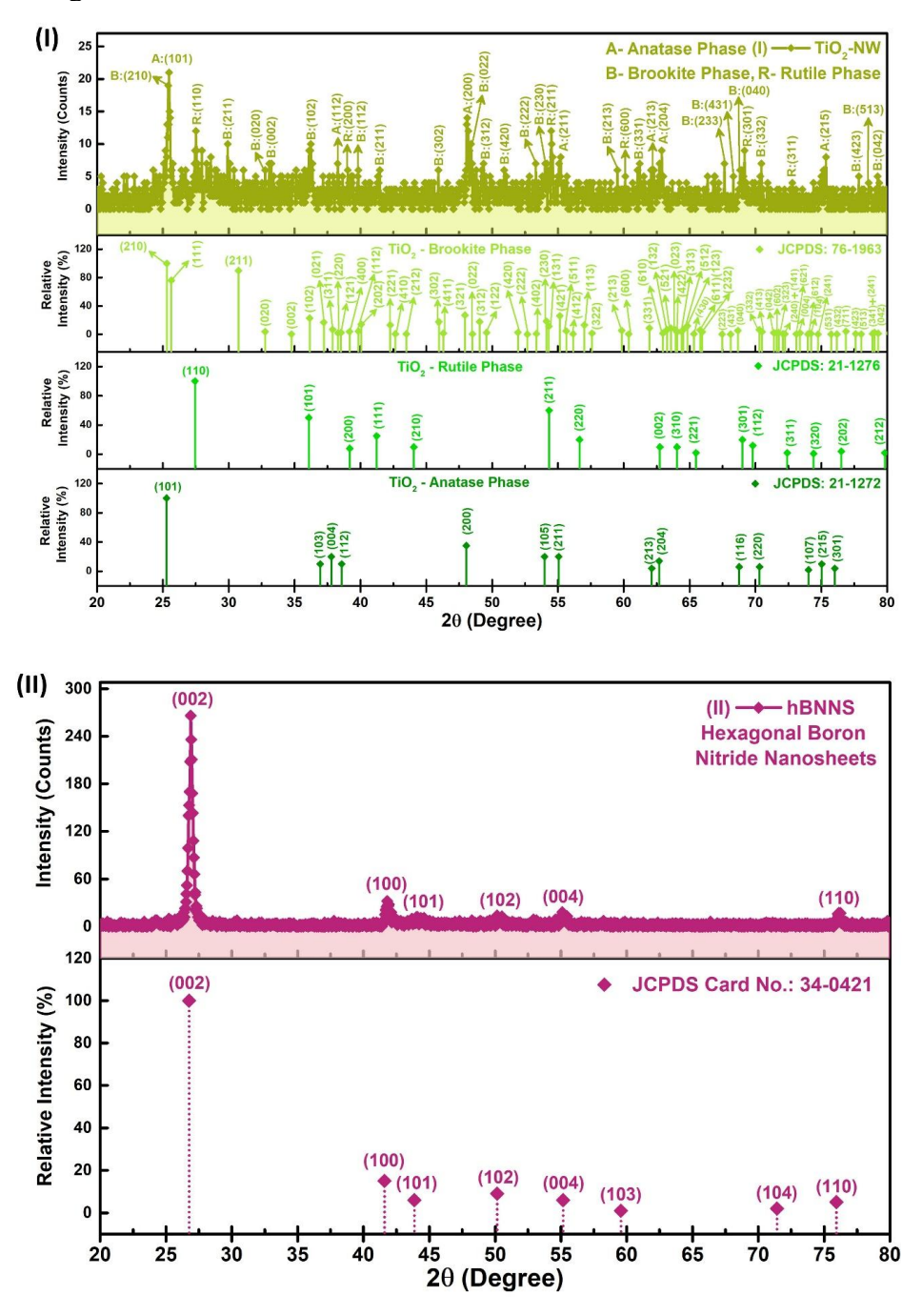
$$W_B = \frac{K_B A_B}{K_A A_A + A_R + K_B A_B}$$
 [7.2]

$$W_R = \frac{A_R}{K_A A_A + A_R + K_B A_B}$$
 [7.3]

In the quantitative determination of the phase composition in the TiO<sub>2</sub> nanowire, the parameters Wa, Wb, and Wr denote the respective mass fractions of anatase, brookite, and rutile phases present within the TiO<sub>2</sub> nanowire system. These mass fractions are determined through comparative evaluation of the characteristic diffraction peak intensities corresponding to each polymorph. The symbols Aa, Ar, and Ab represent the integrated intensities of the most prominent reflections for anatase, rutile, and brookite, respectively, thereby serving as the fundamental parameters for quantitative estimation. To ensure accuracy and account for structural and geometric factors inherent to the different polymorphs, correction coefficients are incorporated into the calculations. Specifically, the coefficients Ka and Kb are employed, with values of 0.886 and 2.721 [23], respectively. These coefficients compensate for differences in scattering power and structural multiplicity between the polymorphs, enabling a more precise determination of their relative contributions. By integrating these factors into the calculation, a robust and reliable quantitative evaluation of the crystalline phase composition is achieved, thereby strengthening the structural analysis of the TiO<sub>2</sub> nanowire sample.

The quantitative phase analysis of mass fractions revealed the crystalline composition of the three polymorphs within the TiO<sub>2</sub> nanowire system was distributed in distinctly measurable proportions. he anatase phase (Wa) was quantified at 22.61%, reflecting its role as a secondary yet significant crystalline component. The brookite phase (Wb) emerged as the most abundant, with a mass fraction of 62.81%, thereby establishing it as the dominant polymorph in the nanowire system. Meanwhile, the rutile phase (Wr) contributed 14.58%, forming the smallest fraction among the three. This distribution

clearly highlights brookite as the predominant phase in the synthesized nanowires, with anatase and rutile existing as secondary contributors. This three-phase composition is highly advantageous in multifunctional nanomaterials, as the synergistic interaction between the polymorphs can facilitate enhanced electron—hole separation, improve structural stability, and broaden application potential in photocatalysis, energy storage, and sensing.



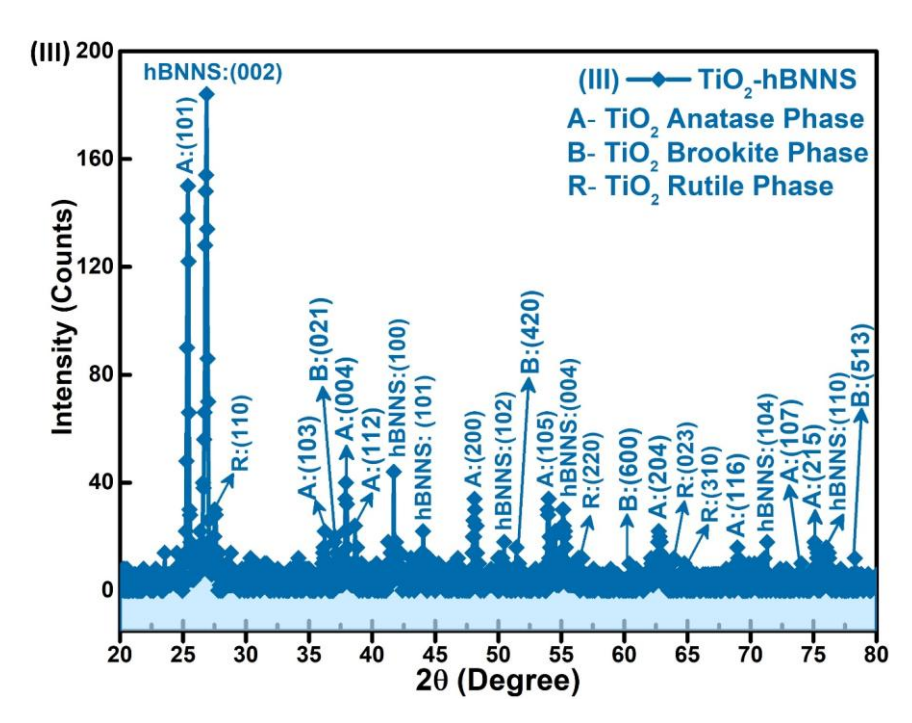


Figure 7.4: X-ray diffraction studies were conducted to investigate the crystalline structure of (I) TiO<sub>2</sub>-NW, (II) hBNNS, and (III) TiO<sub>2</sub>-hBNNS, with diffraction patterns obtained over the 2θ interval spanning 10°-80°.

In Fig. 7.4(II), the XRD diffractogram of the hydrothermally synthesized hexagonal boron nitride nanosheets (hBNNS) displays sharp and well-defined diffraction peaks at 26.88°, 41.8°, 55.16°, 44.12°, 50.16°, 55.12° and 76.12°. These reflections correspond to the (002), (100), (101), (102), (004), and (110) crystallographic planes, respectively, in agreement with the standard reference JCPDS Card No. 034-0421 [24]. The emergence of these characteristic peaks demonstrates successful exfoliation and crystallization of the boron nitride framework into a well-ordered hexagonal phase. The peak at 26.88°, attributed to the (002) reflection, appears with highest intensity, signifying preferential orientation along the basal plane of the layered nanosheets. This alignment highlights the preservation of the intrinsic lamellar structure, which is vital for achieving high aspect ratio nanosheets with uniform thickness and stable interlayer spacing. Furthermore, the synthesis route employed a carefully designed Lewis acidbase complexation mechanism that initiated intercalation—exfoliation, thereby yielding large lateral-sized nanosheets with a high degree of purity and minimal defect density. The presence of well-resolved reflections, particularly the (100) and (110) planes, further confirms the crystalline uniformity and structural integrity of the nanosheets. These structural insights establish that the hydrothermal method effectively facilitated exfoliation and functionalization, producing nanosheets with superior crystallinity, enhanced chemical stability, and well-ordered lattice architecture suitable for highperformance applications.

The quantitative phase analysis clearly demonstrated that the anatase phase (Wa) emerged as the dominant crystalline component in the TiO<sub>2</sub>-hBNNS nanohybrid composite, comprising 61.15% of the total phase composition. This represents a remarkable increase when compared to the TiO<sub>2</sub>-NW sample, where the anatase mass fraction was limited to only 22.60%. Such a significant enhancement in the anatase

proportion after hybridization with hBNNS highlights the profound structural and chemical impact of nano-hybrid composite formation. The incorporation of hBNNS provided a stable two-dimensional support that facilitated controlled nucleation and growth of anatase domains while limiting growth transformation in rutile and brookite phases. Consequently, the anatase phase became the predominant structural component in the composite, a feature of critical importance because anatase-rich TiO<sub>2</sub> systems are widely recognized for their superior photocatalytic efficiency, high electron mobility, and enhanced surface reactivity. The observed increase in anatase content is attributed to be advantageous because anatase exhibits superior photocatalytic activity, high surface reactivity, and excellent electron–hole separation efficiency. Therefore, the transformation from a rutile–brookite competitive system in TiO<sub>2</sub>-NW to an anatase-dominant architecture in the TiO<sub>2</sub>-hBNNS composite underscores the crucial role of hBNNS in tailoring crystalline phase distribution, ultimately enhancing the functional potential of the nanohybrid material for catalytic and sensing applications.

A substantial decline in the brookite phase content was observed upon the formation of the TiO<sub>2</sub>-hBNNS nanohybrid composite, where its proportion reduced dramatically from 62.81% in the pristine TiO<sub>2</sub>-NW sample to 25.04% in the nanohybrid. This remarkable reduction illustrates that the integration of hBNNS effectively disrupted the stability of brookite, which is otherwise a significant component in the unmodified TiO<sub>2</sub> system. Such suppression of brookite formation can be attributed to the strong interfacial interactions between the TiO<sub>2</sub> lattice and the layered hBNNS framework, which guided the crystallization pathway in favour of anatase while simultaneously restricting the growth of brookite domains. Furthermore, the decrease in brookite phase is critical because brookite, although metastable, often coexists with rutile and anatase, thereby creating heterogeneous interfaces that can increase charge recombination and reduce photocatalytic efficiency. By lowering the brookite content to less than half its initial value, the TiO<sub>2</sub>-hBNNS nanohybrid achieved a more phase-pure anatase-rich structure, which is highly desirable for enhancing charge transport and ensuring superior functional performance.

A marginal yet significant reduction in the rutile phase fraction was observed upon the transformation of TiO<sub>2</sub>-NW into the TiO<sub>2</sub>-hBNNS nanohybrid composite, where its relative contribution decreased from 14.57% in the pristine TiO<sub>2</sub>-NW to 13.80% in the hybrid. Although the subtle decrease exhibited limited and subtle impact, but reflects noteworthy restructuring of the crystalline equilibrium driven by the introduction of hBNNS. The nanosheets, with their layered structure and high surface energy, interfered with the stabilization of rutile nuclei during crystallization, leading to a controlled suppression of rutile formation. This phase modulation is important because rutile, while thermodynamically stable, generally exhibits lower photocatalytic efficiency compared to anatase due to higher electron—hole recombination rates. Even a slight decrease in rutile fraction therefore contributes to a more favorable anatase-dominant composition, improving charge separation dynamics and electron transport pathways. The observed reduction highlights how the TiO<sub>2</sub>-hBNNS hybridization subtly adjusts phase proportions to refine structural properties and enhance the functional performance of the composite.

In the TiO<sub>2</sub>-hBNNS nanohybrid composite, the phase modulation is distinctly evident in the TiO<sub>2</sub>-hBNNS nanohybrid composite, which demonstrates a pronounced

dominance of the anatase phase, accompanied by significantly reduced intensities of both brookite and rutile phases. This highlights the preferential stabilization of anatase upon hybrid formation. Moreover, all the characteristic diffraction planes corresponding to hBNNS and TiO<sub>2</sub> were successfully preserved, with only a few reflections appearing with markedly diminished intensity. Such selective attenuation of weaker peaks suggests that the hybridization process enhanced crystallinity in favour of anatase while minimizing less stable phase contributions, thereby confirming the structural coherence and stability of the composite.

# 7.3.1.2 High-Resolution Electron Microscopy for Comprehensive Morphological and Microstructural Evaluation of TiO<sub>2</sub>-NW, hBNNS, and TiO<sub>2</sub>-hBNNS Hybrid Nanocomposite

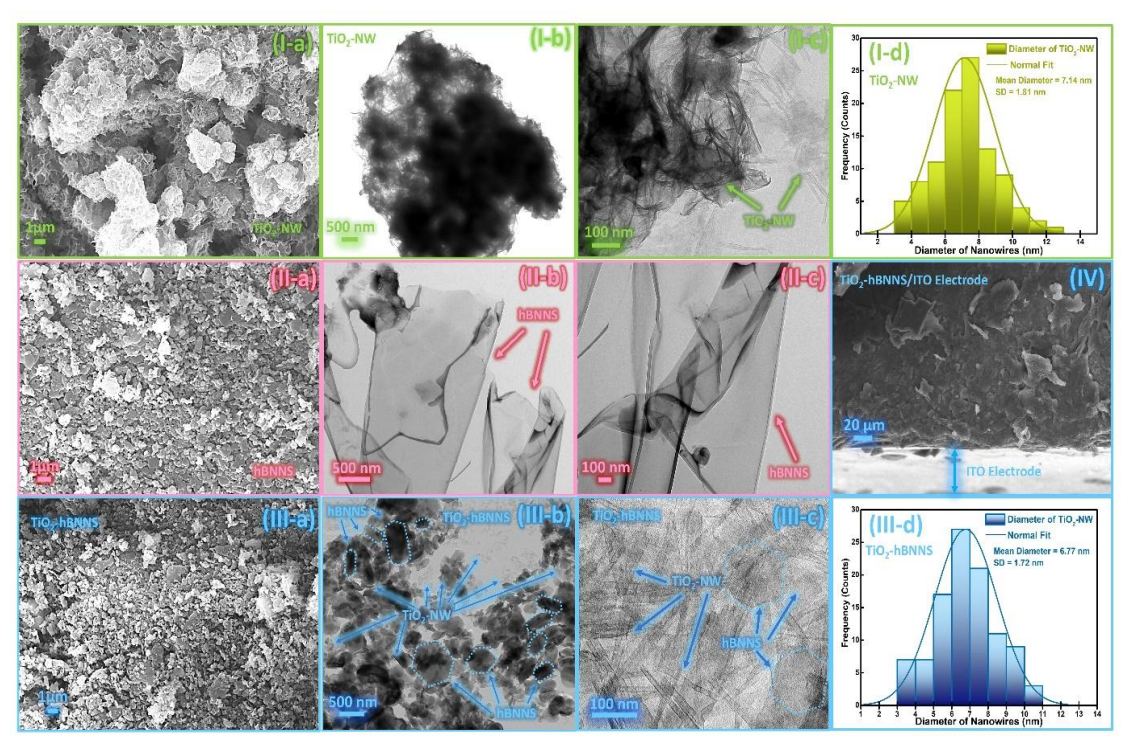


Figure 7.5: Morphological characterization of (I)  $TiO_2$ -NW (green), (II) hBNNS (pink), (III)  $TiO_2$ -hBNNS (blue), and (IV)  $TiO_2$ -hBNNS/ITO electrode: (a) SEM images at 2  $\mu$ m scale, (b) TEM images at 500 nm scale, (c) TEM images at 100 nm scale, and (d) statistical evaluation of  $TiO_2$  nanowire mean diameter before and after nanohybrid composite formation.

SEM micrographs, as illustrated in **Fig. 7.5(I)-a, 7.5(II)-a, and 7.5(III)-a**, provided a comprehensive evaluation of the morphological characteristics of TiO<sub>2</sub> nanowires (TiO<sub>2</sub>-NW), hBNNS, and TiO<sub>2</sub>-hBNNS nanohybrid composites (NHC), respectively. These analyses offered detailed insights into the TiO<sub>2</sub> nanowires diameter size of TiO<sub>2</sub> nanowires (**Fig. 7.5(I)-d**), and TiO<sub>2</sub>-hBNNS (**Fig. 3(III)-d**). TEM imaging at a 500nm and 100 nm scale (**Fig. 7.5(I, II, III)-(b) and (c)**) corroborated these observations, confirming the accuracy of the SEM analyses. The high-aspect-ratio mixed-phase TiO<sub>2</sub> nanowires, analyzed via the distribution curve in **Fig. 7.5(I)-d**, exhibited an average diameter of 7.14 nm, synthesized through a solvothermal approach employing ethylene glycol as a cationic surfactant to regulate growth kinetics and particle uniformity.

Hydrothermally synthesized hBNNS (**Fig. 7.5(II)-b,c**) demonstrated extensive nanosheet areas, with distribution curves reflecting the formation of strong, flexible, and uniformly layered nanosheets capable of providing an ideal support framework. Further analysis through SEM (**Fig. 7.5(III)-a**) and TEM (**Fig. 7.5(III)-b,c**) validated the uniform reinforcement of TiO<sub>2</sub> nanowires onto hBNNS, demonstrating the successful fabrication of the TiO<sub>2</sub>hBNNS nanohybrid composite via hydrothermal synthesis. The synthesis involved aqueous-phase reactions under high-pressure and high-temperature conditions, facilitated by hydrazine hydrate, CTAB, and IPA, which effectively regulated the growth of porous TiO<sub>2</sub> nanowires into a dandelion-like architecture with an average diameter of 6.77 nm. SEM and TEM observations collectively revealed that hBNNS served as a robust support framework, enabling uniform attachment and distribution of TiO<sub>2</sub> nanowires through van der Waals forces and electrostatic interactions. This integration ensured structural stability and maximized accessible surface area.

## 7.3.1.3 Detailed UV-Visible Spectroscopic Analysis of Electronic Band Structure, Optical Transitions, and Urbach Energy in TiO<sub>2</sub>-hBNNS Hybrid Nanocomposite

To comprehensively evaluate the bandgap tuning behaviour and to elucidate the fundamental nature of electronic transitions, the optical absorption spectra of the synthesized  $TiO_2$ –hBNNS hybrid nanocomposite were systematically recorded within the UV–Visible spectral range, as illustrated in **Fig. 7.6(III)-a**. The absorption profile provides crucial insights into the optical response of the material, directly reflecting the energy states involved in photon absorption and subsequent electron excitation. From these spectra, the optical bandgap energy (Eg) was precisely calculated using Tauc's formalism, which establishes the relationship between the absorption coefficient ( $\alpha$ ), incident photon energy (hv), and the type of electronic transition (direct or indirect). The Tauc relation is mathematically represented by **Eq. [7.4]**, thereby enabling accurate determination of the electronic bandgap as well as assessment of transition mechanisms, which are of paramount importance for understanding charge transfer dynamics and optoelectronic performance of the nanocomposite.

$$(\alpha h v)^{1/n} = A(hv - E_g)$$
 [7.4]

In Beer-Lambert's equation, the absorption coefficient ( $\alpha$ ) serves as a critical parameter that quantifies the extent to which the material absorbs incident photons across a defined spectral range. A higher value of  $\alpha$  directly signifies stronger absorption, which is inherently linked to the density of accessible electronic states and the corresponding probability of electronic transitions. The photon energy (hv) represents the driving force for excitation, imparting energy that enables electrons to overcome the energetic barrier between the valence and conduction bands. The bandgap energy (Eg) functions as the defining threshold, representing the minimum energy required for an electron to transition into the conduction band and participate in charge transport processes. The proportionality constant (A) remains largely independent of photon energy, reflecting intrinsic material characteristics such as structural uniformity and electronic configuration, and thereby ensures consistency in the absorption model. Of particular significance is the exponent n, which characterizes the nature of the electronic transition: for direct transitions (n = 1/2), photon energy is directly transferred to electrons without phonon assistance, highlighting an efficient excitation pathway. This

mechanism has been extensively observed in diverse semiconducting systems, including mixed-valence  $TiO_2$  nanowires ( $TiO_2$ -NW), few-layered hexagonal boron nitride nanosheets (hBNNS), and hybrid  $TiO_2$ -hBNNS architectures, where the dominant optical response arises from direct electronic transitions. In such systems, electrons absorb photon energy and are excited directly from the valence band to the conduction band without the necessity of phonon assistance, which ensures a sharp absorption edge, strong optical response, and efficient electron–photon coupling. These characteristics are highly desirable for high-performance optoelectronic devices, as they minimize energy losses while maximizing excitation efficiency. In contrast, indirect transitions (n = 2) are more complex, as they require the combined action of photons and phonons, with phonons supplying the additional momentum necessary to satisfy conservation laws. The fundamental distinction between direct and indirect transitions is therefore critical not only for accurately interpreting semiconductor absorption spectra but also for rationally engineering materials with tailored band structures.

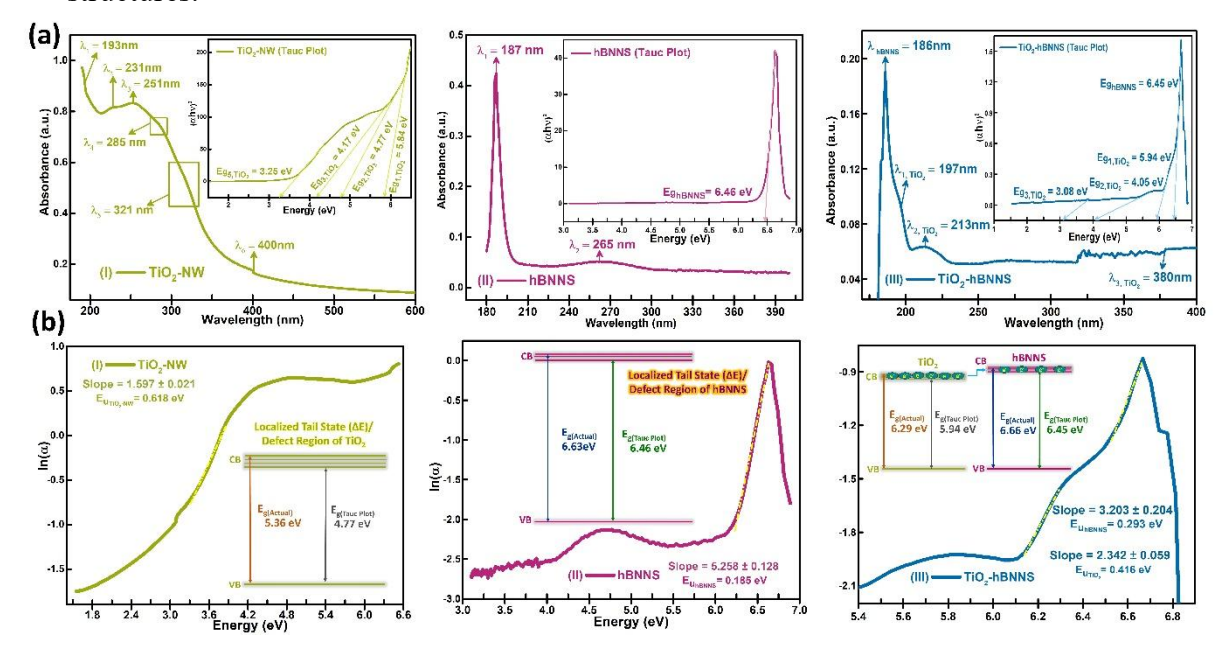


Figure 7.6: Optical characterization depicting (a) UV-Visible absorption spectra (Inset: Tauc plot for bandgap estimation), and (b) Urbach energy estimation for (I) TiO<sub>2</sub>, (II) hBNNS, and (III) TiO<sub>2</sub>-hBNNS samples.

The absorption spectrum of mixed-phase TiO<sub>2</sub> nanowires (TiO<sub>2</sub>-NW) (**Fig. 7.6(I)-a**) displayed pronounced absorption peaks centered at 193 nm, 231 nm, 251 nm, 285 nm, and 321 nm, all distinctly located within the ultraviolet region [25]. The Tauc plot analysis revealed bandgap energies corresponding to the TiO<sub>2</sub>-NW sample, calculated as 5.84 eV, 4.77 eV, 4.17 eV, and 3.25 eV, respectively. These values highlight the presence of multiple optical transitions within the material, indicating contributions from both fundamental and defect-assisted electronic processes. The strong absorption at 193 nm is attributed to the  $E_g(s) \rightarrow T_{2g}(p^*)$  transition reflecting inter-orbital electron transfer between occupied Eg states and unoccupied antibonding  $T_{2g}$  levels [26]. The UV–Visible spectral analysis revealed an extensive absorption region ranging 230–320 nm, indicating strong absorption feature is primarily governed by the  $\pi \rightarrow \pi^*$  electronic transition, which arises from excitations between oxygen 2p bonding orbitals and

titanium 3d antibonding orbitals, consistent with the molecular orbital framework of  $TiO_2$  [27]. Therefore, the second band arises from the  $T2g(p) \rightarrow T2g(p)$  transition\*, which involves electron promotion within the same symmetry class of T2g orbitals, moving from partially filled bonding to higher-energy antibonding states.

The absorption spectrum of hBNNS (Fig. 7.6(II)a exhibited a distinct peak at 187 nm, which is attributed to strong excitonic transitions arising from its wide bandgap configuration [28]. The optical bandgap of hBNNS was precisely determined to be 6.46 eV (Fig. 7.6(II)a-Inset), confirming its intrinsic insulating behaviour and remarkable structural stability. This combination of a wide bandgap and pronounced excitonic characteristics underscores the exceptional suitability of hBNNS as a robust sensing platform and as an ideal host matrix for the development of advanced hybrid nanocomposites.

The formation of TiO<sub>2</sub>-hBNNS nanohybrids (NHCs) (Fig. 7.6(III)a) induced notable modifications in the optical absorption profile, reflecting strong interfacial interactions between TiO<sub>2</sub> nanoparticles and the hBNNS framework. Specifically, the characteristic absorption peak of pristine hBNNS at 187 nm exhibited a slight blue shift to 186 nm, a shift that indicates significant alterations in the local electronic environment upon hybridization. This spectral shift arises from the generation of new defect states and electronic pathways created through the incorporation of TiO<sub>2</sub> into the boron nitride lattice, which effectively tunes the absorption edge and extends the optical response of the nanohybrid. Furthermore, the absorption spectrum of the mixed-phase TiO<sub>2</sub> nanowires within the TiO<sub>2</sub>-hBNNS composite (Fig. 7.6(III)a) demonstrated prominent ultraviolet absorption peaks centered at 197 nm, 213 nm, and 380 nm, confirming the active role of TiO<sub>2</sub> in modulating light-matter interactions. The Tauc plot analysis yielded corresponding bandgap energies of 5.94 eV, 4.05 eV, and 3.08 eV, further validating the band structure modifications induced by hybridization. To evaluate the degree of disorder and defect density introduced within the system, Urbach energy was calculated using Eq. [7.5]-[7.6] (Fig. 7.6(I, II, III)b). The quantified Urbach energy provides direct insight into band-tail states, revealing the extent of defect engineering and its critical influence on optical absorption processes, thus underscoring the enhanced optoelectronic potential of the TiO<sub>2</sub>-hBNNS nanohybrid system.

$$\alpha = \alpha_0 \exp(\frac{E - E_g}{E_u})$$
 [7.5]

$$\ln(\alpha) = \ln(\alpha_0) + \frac{(E - E_g)}{E_u}$$
 [7.6]

The absorption coefficient ( $\alpha$ ) represents the fundamental parameter governing the interaction of incident photons with the electronic structure of the material, while the pre-exponential factor ( $\alpha_0$ ) reflects intrinsic, material-specific constants. The photon energy (E = hv), determined by Planck's constant (h) and the frequency of incident light (v), serves as the driving force for electronic transitions. The bandgap energy (Eg) defines the minimum excitation threshold at a given temperature (T), whereas the Urbach energy (Eu) provides quantitative insight into localized states within the bandgap. Derived from the inverse slope of the linear region in the  $\ln(\alpha)$  versus E plot, Eu quantifies the degree of disorder and defect-induced band-tail broadening. For TiO<sub>2</sub> nanowires (TiO<sub>2</sub>-NW), the Urbach energy (Eu,TiO<sub>2</sub>-NW) was calculated to be 0.618

eV (Fig. 7.6(I)b), suggesting the presence of a moderate density of electronic tail states associated with lattice imperfections and structural defects. In contrast, pristine hBNNS exhibited a significantly lower Urbach energy (Eu,hBNNS) of 0.185 eV, reflecting its highly ordered, insulating character and low defect density (Fig. 7.6(II)b). The relatively narrow tail width in hBNNS highlights its ability to act as a stable scaffold while simultaneously accommodating the structural irregularities of TiO<sub>2</sub> during hybridization. Following the integration of TiO<sub>2</sub> nanowires into the hBNNS framework, the Urbach energies of the composite system were markedly altered, with values of 0.416 eV for TiO<sub>2</sub> and 0.293 eV for hBNNS (Fig. 7.6(III)b). This increase in tail-state density signifies enhanced structural disorder and electronic perturbations, which are closely linked to the onset of surface plasmon resonance (SPR) phenomena in TiO<sub>2</sub> nanowires. Under photon excitation, SPR induces collective oscillations of conduction electrons, thereby amplifying the local electromagnetic field. This plasmonic activity enhances light absorption efficiency, boosts electron-hole generation, and facilitates rapid charge transfer across the TiO2-hBNNS interface. The synergistic effect of defect accommodation and plasmonic resonance demonstrates that hybrid nanostructuring not only modifies the fundamental optical transitions

## 7.3.1.4 Comprehensive Raman Spectroscopic Investigation of Phonon Behaviour, Vibrational Modes, and Electronic Coupling in TiO<sub>2</sub>-hBNNS Nano-Hybrid Composites

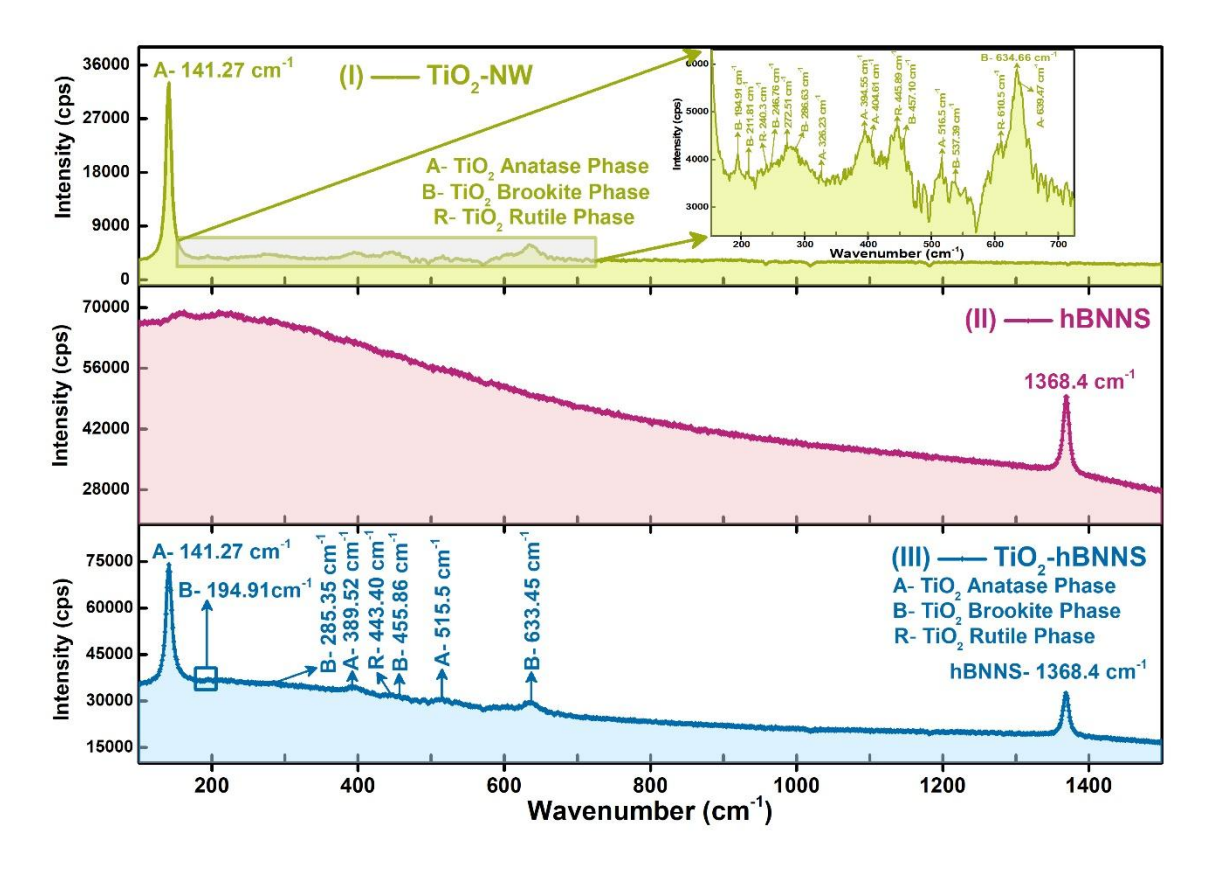


Figure 7.7: Raman spectra of (I) TiO<sub>2</sub>-NW, (II) hBNNS, and (III) TiO<sub>2</sub>-hBNNS was carried out in the 1250–1500 cm<sup>-1</sup> range, providing detailed insights into their vibrational modes and structural interactions.

The Raman spectra of the TiO<sub>2</sub> phases exhibit distinct vibrational signatures that enable phase identification and provide insights into the underlying phonon dynamics. Brookite, a metastable polymorphic modification of TiO<sub>2</sub>, crystallizes in the orthorhombic Pbca space group and contains eight formula units within each unit cell [29]. Due to its lower symmetry compared to anatase and rutile, brookite exhibits a much richer set of vibrational modes. Factor group analysis yields the following irreducible representation Eq. [7.7]:

$$\Gamma opt = 9A_{g}(R) + 9B_{1g}(R) + 9B_{2g}(R) + 9B_{3g}(R) + 9A_{u}(IR inactive) + 8B_{1u}(IR) + 8B_{2u}(IR) + 8B_{3u}(IR)$$
[7.7]

From this decomposition, brookite is predicted to exhibit 36 Raman-active phonon modes and 24 infrared-active modes. Such a complex vibrational spectrum directly reflects the structural complexity of the orthorhombic TiO<sub>6</sub> octahedral network, in which multiple inequivalent oxygen sites contribute to vibrational diversity. Consequently, brookite's Raman spectrum is far more intricate than that of anatase or rutile, making it a sensitive probe for detecting structural distortions, defects, and phase interactions in composite systems. For the brookite phase (Fig. 7.7(I)), the prominent vibrational modes are observed at 194.91, 211.81, 246.86, 286.63, 457.10, 537.19, and 634.66 cm<sup>-1</sup>. The peaks at 194.91 and 211.81 cm<sup>-1</sup> correspond to low-frequency external vibrations associated with lattice translational modes. The band at 246.86 cm<sup>-1</sup> arises from bending vibrations of Ti-O-Ti linkages, while the 286.63 cm<sup>-1</sup> band is linked to internal bending modes within the TiO<sub>6</sub> octahedra. The higher-frequency peaks at 457.10 and 537.19 cm<sup>-1</sup> are attributed to asymmetric Ti-O stretching vibrations, reflecting distortions within the octahedral framework. The intense band at 634.66 cm<sup>-1</sup> represents symmetric stretching of the Ti–O bonds, a fingerprint vibration characteristic of brookite's orthorhombic structure.

In anatase  $TiO_2$ , which crystallizes within the tetragonal  $I4_1$ /amd space group, the unit cell contains Z = 4 formula units, while the primitive cell reduces to two molecular units. Group theoretical analysis yields the irreducible representation for the optical modes as Eq. [7.8],

$$\Gamma \text{opt} = A_{1g}(R) + 2B_{1g}(R) + 3E_{g}(R) + B_{2u}(\text{silent}) + A_{2u}(IR) + 2E_{u}(IR)$$
 [7.8]

The vibrational modes observed experimentally, align well with this prediction and provide a detailed mapping of phonon activity. Oxygen atoms, which play a pivotal role in shaping these dynamics, bridge three titanium atoms in a triply coordinated fashion and occupy positions of C2v symmetry. This bonding arrangement naturally gives rise to three types of vibrational modes: A1, B1, and B2. The B1 modes are associated with out-of-plane deformation motions, while A1 and B2 modes combine the characteristics of Ti–O bond stretching with Ti–O–Ti in-plane deformation vibrations. Such mixed vibrational behaviour reflects the inherent structural complexity of anatase and provides insight into how lattice symmetry governs the coupling of stretching and bending interactions within the Ti–O framework.

For the anatase phase (**Fig. 7.7(I**)), the Raman active modes appear at 141.27, 326.23, 394.55, 404.61, 516.5, and 639.47 cm<sup>-1</sup>. The strongest low-frequency band at 141.27 cm<sup>-1</sup> corresponds to the E\_g mode, reflecting symmetric bending vibrations of oxygen atoms in the TiO<sub>6</sub> octahedra. The peak at 326.23 cm<sup>-1</sup> is assigned to B<sub>1</sub>g bending modes,

while the peaks at 394.55 and 404.61 cm<sup>-1</sup> represent complex bending vibrations involving Ti–O–Ti linkages within the tetragonal lattice. The 516.5 cm<sup>-1</sup> peak is associated with the A<sub>1</sub>g mode, indicating asymmetric Ti–O stretching vibrations. The high-frequency band at 639.47 cm<sup>-1</sup> corresponds to another E\_g symmetric stretching vibration of oxygen atoms, which is a defining signature of the anatase phase.

The rutile polymorph of  $TiO_2$  is a tetragonal crystal structure belonging to the P4<sub>2</sub>/mnm (D<sub>4</sub>h) space group, with two formula units (Z = 2) in the unit cell. Group theoretical analysis predicts the optical phonon modes to follow the irreducible representation (Eq. [7.9]):

$$\Gamma opt = A_{1g}(R) + A_{2g}(silent) + B_{1g}(R) + B_{2g}(R) + E_{g}(R) + A_{2u}(IR) + 2B_{1u}(silent) + 3E_{u}(IR)$$
 [7.9]

Within this distribution, rutile exhibits four Raman-active modes ( $A_{1g}$ ,  $B_{1g}$ ,  $B_{2g}$ ,  $E_{g}$ ), which dominate its vibrational spectrum and are frequently detected in Raman scattering experiments. In addition, infrared activity arises from  $A_{2u}$  and  $E_{u}$  symmetries, while  $A_{2g}$  and  $B_{1u}$  modes remain silent, contributing neither to Raman nor to infrared features. This classification not only defines the spectroscopic behaviour of rutile but also provides a foundation for understanding its phonon-assisted electronic processes, vibrational coupling, and lattice dynamics.

In the case of the rutile phase (**Fig. 7.7(I**)), the observed vibrational bands are positioned at 240.3, 445.89, and 610.5 cm<sup>-1</sup>. The 240.3 cm<sup>-1</sup> band is linked to a B<sub>1</sub>g mode arising from oxygen bending vibrations. The prominent peak at 445.89 cm<sup>-1</sup> corresponds to the E\_g symmetric bending of oxygen atoms, which is strongly characteristic of rutile. Finally, the 610.5 cm<sup>-1</sup> band is assigned to the A<sub>1</sub>g symmetric stretching mode of Ti–O bonds, reflecting the high crystallinity and stability of the rutile tetragonal structure.

The Raman spectrum of hexagonal boron nitride nanosheets (hBNNS) exhibits a dominant E2g vibrational mode at 1368.4 cm<sup>-1</sup>, which serves as a distinct phonon fingerprint of the layered hBN lattice [30] (**Fig. 7.7(II)**). This sharp and intense peak arises from the in-plane stretching vibrations of B–N bonds within the hexagonal framework, a vibrational feature that remains highly stable under different processing conditions. Following the hydrothermal synthesis of TiO2–hBNNS nanohybrids, the E2g mode persists at precisely the same wavenumber, indicating that the structural integrity of the hBNNS is preserved during hybrid formation. The retention of this vibrational feature strongly confirms that the hBN lattice does not undergo significant distortion or decomposition in the presence of TiO2 nanoparticles, thereby validating hBNNS as a robust host matrix capable of sustaining hybridization without compromising its intrinsic phonon dynamics. This stability is particularly important for ensuring reliable electronic and vibrational interactions in hybrid nanocomposites.

In the TiO<sub>2</sub>–hBNNS nanocomposite, the Raman spectrum reveals that the E<sub>2</sub>g vibrational mode of hBNNS remains unshifted, as observed in **Fig. 7.7(III)**. This invariance in peak position clearly demonstrates that the interlayer spacing and layered crystallinity of hBNNS are preserved despite the incorporation of TiO<sub>2</sub> nanoparticles. The structural stability of hBNNS is further confirmed by XRD analysis, which shows consistent d-spacing values with no detectable lattice distortion. This observation underscores the exceptional resilience of hBNNS as a host matrix, capable of

accommodating foreign nanoparticles without compromising its intrinsic phonon dynamics or crystalline framework. Alongside the preserved hBN signature, the spectrum also displays prominent anatase TiO<sub>2</sub> modes at 141.27 cm<sup>-1</sup>, 389.52 cm<sup>-1</sup>, and 515.5 cm<sup>-1</sup>, which are critical for initiating plasmonic resonance and mediating electron–phonon interactions within the hybrid. The presence of anatase is particularly significant, as it is the most photoactive polymorph of TiO2, making it vital for optoelectronic and photocatalytic applications. Additional peaks detected at 194.91 cm<sup>-1</sup>, 285.32 cm<sup>-1</sup>, and 633.45 cm<sup>-1</sup> correspond to brookite, while a band at 443.40 cm<sup>-1</sup> indicates rutile contributions. The coexistence of anatase, brookite, and rutile phases within the hybrid is further corroborated by XRD findings [37], confirming a multiphase system. Such mixed-phase interactions generate synergistic effects, particularly in facilitating charge separation and transfer, thereby enhancing the hybrid's optical absorption, catalytic redox potential, and overall electronic performance. This multiphase composition positions the TiO<sub>2</sub>-hBNNS nanocomposite as a highly efficient platform for advanced photocatalysis, sensing, and energy conversion technologies.

## 7.3.1.5 Comprehensive FT-IR Spectroscopic Investigation of Molecular Bonding Dynamics, Surface Functionalization, and Protein Immobilization Strategies in TiO<sub>2</sub>-hBNNS Hybrid Nanomaterials

FTIR spectroscopy was employed to qualitatively examine chemical interactions, bond formation, and the presence of functional groups, offering molecular-level insights into the structural composition of the studied materials (**Table 7.1**). The FT-IR spectrum of TiO<sub>2</sub> nanowires (TiO<sub>2</sub>-NWs) reveals distinct vibrational bands that confirm both the formation of the TiO<sub>2</sub> lattice and the successful surface functionalization [31] (**Fig. 7.8(I**)). The absorption band at 464 cm<sup>-1</sup> is attributed to the Ti-O-Ti bending mode, a fundamental lattice vibration confirming the crystalline backbone of TiO<sub>2</sub>. This is complemented by the band at 670 cm<sup>-1</sup>, which arises from Ti-O stretching vibrations, further validating the presence of strong Ti-O bonds within the nanowire framework. The sharp band at 809 cm<sup>-1</sup> corresponds to C-O-C stretching vibrations, indicating the incorporation of organic moieties, possibly from residual surfactants or functionalizing agents attached to the nanowire surface. Similarly, the absorption near 912 cm<sup>-1</sup> can be assigned to out-of-plane Ti-OH bending, providing strong evidence of surface hydroxyl groups that are crucial for subsequent chemical modifications and interaction with external molecules.

Additional functionalization is demonstrated by the 1004 cm<sup>-1</sup> band, attributed to R–C–O stretching, and the 1100 cm<sup>-1</sup> peak, which corresponds to C–O stretching vibrations. Together with the 1122 cm<sup>-1</sup> band representing Ti–O–C stretching, these features confirm the formation of Ti–O–C linkages, highlighting strong organic—inorganic hybrid bonding within the nanowire structure. The presence of hydrocarbon-related groups is further evident in the spectrum. The band at 1319 cm<sup>-1</sup> corresponds to C–H symmetric stretching, while the band at 1498 cm<sup>-1</sup> is attributed to asymmetric C–H stretching, confirming the incorporation of organic groups. The 1385 cm<sup>-1</sup> band, assigned to R–COO<sup>-</sup> bending, indicates the existence of carboxylate groups, a hallmark of surface functionalization that promotes stability and potential biomolecule attachment. The 1638 cm<sup>-1</sup> band is characteristic of O–H bending vibrations, providing further evidence of surface hydroxylation. In addition, the 2325 and 2346 cm<sup>-1</sup> peaks

correspond to O-C-O asymmetric stretching vibrations, confirming the presence of carbonate groups, which may form during synthesis or through CO<sub>2</sub> adsorption onto active surface sites.

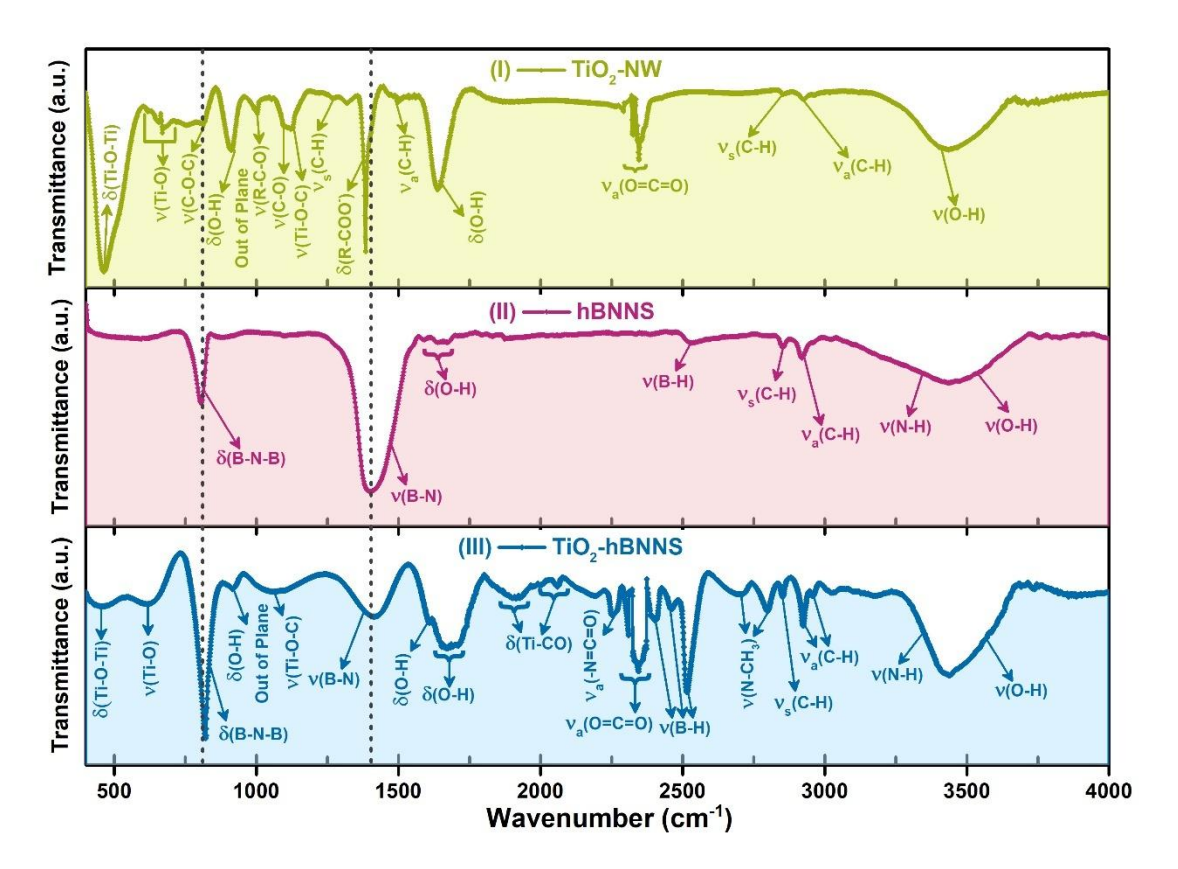


Figure 7.8: FTIR spectra of (I) TiO<sub>2</sub> nanowires (TiO<sub>2</sub>-NW), (II) hexagonal boron nitride nanosheets (hBNNS), and (III) TiO<sub>2</sub>-hBNNS composite were recorded in the 400–4000 cm<sup>-1</sup> wavenumber region to examine their functional group vibrations and bonding characteristics.

The aliphatic region of the spectrum reveals strong absorption peaks at 2853 cm<sup>-1</sup> and 2926 cm<sup>-1</sup>, assigned to symmetric and asymmetric C–H stretching vibrations, respectively, confirming the incorporation of hydrocarbon groups. Finally, the broad absorption at 3436 cm<sup>-1</sup> is attributed to O–H stretching, signifying abundant surface hydroxyl groups and adsorbed water molecules. These characteristic vibrational signatures confirm the successful synthesis of functionalized TiO<sub>2</sub> nanowires. The coexistence of Ti–O lattice vibrations, hydroxyl groups, carbon–oxygen linkages, and hydrocarbon bands demonstrates not only the formation of well-crystallized TiO<sub>2</sub> but also effective organic surface functionalization

Table 7.1: Wavenumber Assigned to FTIR peaks of (I) TiO<sub>2</sub>-NW, (II) hBNNS, and (III) TiO<sub>2</sub>-hBNNS respectively.

aa	Sample	Wavenumber			
S.NO.		(cm <sup>-1</sup> )	Assigned Bands		
		464	Ti-O-Ti Bend		
	TiO <sub>2</sub> -NW	670	Ti-O Stretch		
		809	C-O-C Stretch		
		912	Out of Plane Ti-OH Bend		
		1004	R-C-O Stretch		
		1100	C-O Stretch		
		1122	Ti-O-C Stretch		
1.		1319	C-H Symmetric Stretch		
		1385	R-COO <sup>-</sup> Bend		
		1498	C-H Asymmetric Stretch		
		1638	O-H Bend		
		2325, 2346	O-C-O Asymmetric Stretch		
		2853	C-H Symmetric Stretch		
		2926	C-H Asymmetric Stretch		
		3436	OH Stretch		
	hBNNS	806	B-N-B Bend		
		1398	B-N Stretch		
		1590	N-H Bend		
		1638, 1672	O-H Bend		
2.		2530	B-H Stretch		
		2852	C-H Symmetric Stretch		
		2920	C-H Asymmetric Stretch		
		3200-3500	N-H Stretch		
		>3500	OH Stretch		
	TiO2-hBNNS	453	Ti-O-Ti Bend		
		617	Ti-O Stretch		
		822	B-N-B Bend		
		917	Out of Plane O-H Bend		
		1056	Ti-O-C Stretch		
		1414	B-N Stretch		
		1608, 1668	O-H Bend		
		1712, 1913,	Ti-CO Bend		
		2060, 2192			
3.		2252	N-C-O (Asymmetric) Stretch		
		2309, 2345	O-C-O (Asymmetric) Stretch		
		2404, 2460, 2515	B-H Stretch		
		2704, 2798	N-CH <sub>3</sub> Stretch		
		2852	CH <sub>2</sub> (Symmetric) Stretch		
		2924, 2958	CH <sub>2</sub> (Asymmetric) Stretch		
		3400-3500	N-H Stretch		
		3521, 3827	OH Startak		
		(>3500)	OH Stretch		

The FT-IR spectrum of hexagonal boron nitride nanosheets (hBNNS) provides strong evidence of both the integrity of the BN lattice and the successful introduction of surface functional groups [32] **Fig. 7.8(II)**. The 806 cm<sup>-1</sup> band, attributed to B–N–B bending vibrations, is a fundamental fingerprint of the layered hexagonal BN structure.

Its presence indicates the preservation of the in-plane BN network, confirming the structural robustness of the nanosheets after synthesis and functionalization. The 1398 cm<sup>-1</sup> peak, assigned to B–N stretching, is another signature mode of hBN. It directly reflects the covalent bonding within the hexagonal lattice, signifying that the sp<sup>2</sup>-hybridized BN framework remains intact. This strong band is a hallmark of crystalline hBNNS and validates successful exfoliation or stabilization of the nanosheet morphology. Surface functionalization is evident from additional vibrational bands. The 1590 cm<sup>-1</sup> peak, corresponding to N–H bending, suggests incorporation of amine or related nitrogen-containing groups, enhancing chemical reactivity. Similarly, the 1638 and 1672 cm<sup>-1</sup> bands are linked to O–H bending vibrations, providing direct evidence of hydroxylated surfaces, which facilitate hydrogen bonding and promote interaction with polar molecules.

The 2530 cm<sup>-1</sup> band, attributed to B–H stretching, reflects hydrogen incorporation onto boron sites, an important marker of chemical functionalization. This suggests that hydrogenated boron centers have formed, which may act as anchoring points for further surface modification or hybridization with other nanomaterials. Hydrocarbon signatures further support functionalization. The 2852 cm<sup>-1</sup> and 2920 cm<sup>-1</sup> peaks, assigned to symmetric and asymmetric C–H stretching vibrations respectively, indicate the presence of alkyl or organic groups on the nanosheet surface. Such modifications enhance compatibility with organic solvents or polymer matrices, broadening application potential. The 3200–3500 cm<sup>-1</sup> region, attributed to N–H stretching, reflects surface-anchored amine functionalities, which not only stabilize the nanosheets but also provide sites for biomolecule immobilization and catalytic applications. Finally, the broad absorption beyond 3500 cm<sup>-1</sup>, corresponding to O–H stretching vibrations, indicates the presence of hydroxyl groups and adsorbed water molecules, confirming surface hydrophilicity and high reactivity.

The FT-IR spectrum of the TiO<sub>2</sub>-hBNNS nanocomposite provides clear evidence of lattice preservation, surface functionalization, and the synergistic coexistence of TiO<sub>2</sub> and hBNNS within a hybrid matrix Fig. 7.8(III). The low-frequency region displays characteristic lattice vibrations. The 453 cm<sup>-1</sup> band corresponds to Ti-O-Ti bending, while the 617 cm<sup>-1</sup> band reflects Ti-O stretching vibrations. These peaks confirm the presence of TiO<sub>2</sub> structural modes, which are essential markers of its crystalline integrity. Simultaneously, the 822 cm<sup>-1</sup> band, attributed to B-N-B bending, signifies the preservation of the in-plane hexagonal framework of hBNNS within the composite. In the mid-frequency region, several functionalization signatures are observed. The 917 cm<sup>-1</sup> peak, associated with out-of-plane O-H bending, indicates the presence of surface hydroxyl groups, which enhance hydrophilicity and facilitate further interactions. The 1056 cm<sup>-1</sup> vibration, assigned to Ti-O-C stretching, provides compelling evidence of strong interfacial bonding between TiO<sub>2</sub> and hBNNS, signifying chemical integration rather than simple physical mixing the 1414 cm<sup>-1</sup> band, corresponding to B-N stretching, further demonstrates that the core BN lattice remains intact. Adjacent 1608 and 1668 cm<sup>-1</sup> peaks, linked to O-H bending, confirm hydroxylation and suggest hydrogen-bonded interactions within the composite matrix.

Notably, a distinct set of bands appears at 1712, 1913, 2060, and 2192 cm<sup>-1</sup>, which are attributed to Ti–CO bending. These peaks highlight interactions of TiO<sub>2</sub> with carbonate or carboxylate species, which often arise during functionalization, reinforcing the

hybrid's surface chemistry. The 2252 cm<sup>-1</sup> band, corresponding to N–C–O asymmetric stretching, provides additional evidence of nitrogen-containing functional groups, expanding the chemical versatility of the composite. Further, the 2309 and 2345 cm<sup>-1</sup> bands assigned to O–C–O asymmetric stretching vibrations confirm the incorporation of carbonate-like groups, while the 2404, 2460, and 2515 cm<sup>-1</sup> bands, attributed to B–H stretching, directly point to hydrogen functionalization of boron centers, enhancing reactivity. In the higher-frequency region, 2704 and 2798 cm<sup>-1</sup> peaks represent N–CH<sub>3</sub> stretching vibrations, validating the incorporation of organic moieties. The 2852 cm<sup>-1</sup> (CH<sub>2</sub> symmetric stretch) and 2924, 2958 cm<sup>-1</sup> (CH<sub>2</sub> asymmetric stretches) confirm alkyl surface groups, which improve dispersibility in organic systems. The 3400–3500 cm<sup>-1</sup> region, attributed to N–H stretching vibrations, points to amine functionalities on the nanosheet surface, which serve as reactive anchors for biomolecule or catalyst binding. Finally, the 3521 and 3827 cm<sup>-1</sup> bands (>3500 cm<sup>-1</sup>) correspond to O–H stretching vibrations, confirming hydroxyl groups and adsorbed water molecules that impart hydrophilicity and enhance catalytic performance.

Optimizing the electrocatalytic efficiency of the TiO2-hBNNS nano-biosensor is inherently dependent on precise nano-biointerface engineering, with antibody immobilization time playing a decisive role. The FTIR spectra in Fig. 7.9 clearly demonstrate the progressive structural and chemical changes occurring at the electrode surface upon antibody binding. Comparison of the TiO2-hBNNS/ITO electrode before modification and after Anti-CEA immobilization for 12 h and 24 h highlights the mechanistic pathway of covalent attachment. Upon immobilization, the retention of B-N-B bending and B-N stretching vibrations, combined with the disappearance of TiO<sub>2</sub>and hBNNS-related functional group peaks, confirms the active participation of these groups in covalent amide bond formation through EDC-NHS activation chemistry. After 24 h, the FTIR profile reveals pronounced protein-specific vibrational signatures, including phosphorylation at 868 cm<sup>-1</sup>, symmetric phosphate stretching at 982 cm<sup>-1</sup>, polysaccharide stretching at 1092 cm<sup>-1</sup>, NH bending at 1268 cm<sup>-1</sup>, Amide II at 1568 cm<sup>-1</sup>, and Amide I at 1641 cm<sup>-1</sup>, all of which signify robust antibody anchoring. Intensification of aliphatic CH stretching (2736 cm<sup>-1</sup>), CH<sub>2</sub> stretching (2878 cm<sup>-1</sup>), Amide B stretching (2977 cm<sup>-1</sup>), Amide A stretching (3236 cm<sup>-1</sup>), and OH stretching (>3500 cm<sup>-1</sup>) further validates strong antibody adsorption. Additionally, a distinct absorption band at 2067 cm<sup>-1</sup> confirms successful EDC-NHS-mediated activation of carboxyl and amino groups. Unique peaks at 1442 and 1479 cm<sup>-1</sup> reflect glutamine complexation with hBNNS, while the band at 1716 cm<sup>-1</sup> highlights strong arginine-TiO<sub>2</sub> interactions. Further absorption at 2476 and 2516 cm<sup>-1</sup> signifies cysteine–TiO<sub>2</sub> complexation, confirming site-specific antibody interactions. Moreover, TiO2-lysine complexation is substantiated by NH<sub>2</sub> bending vibrations at 1630–1660 cm<sup>-1</sup>, the Amide II band near 1550 cm<sup>-1</sup>, broadened NH stretching between 3200–3400 cm<sup>-1</sup>, and possible Ti-O-N features within 500-700 cm<sup>-1</sup>. Collectively, these vibrational features confirm that 24 h of antibody incubation yields an optimal nano-biointerface with strong covalent anchoring, hydrogen bonding, and amino acid-nanostructure interactions, directly enhancing biosensor sensitivity, stability, and reliability.

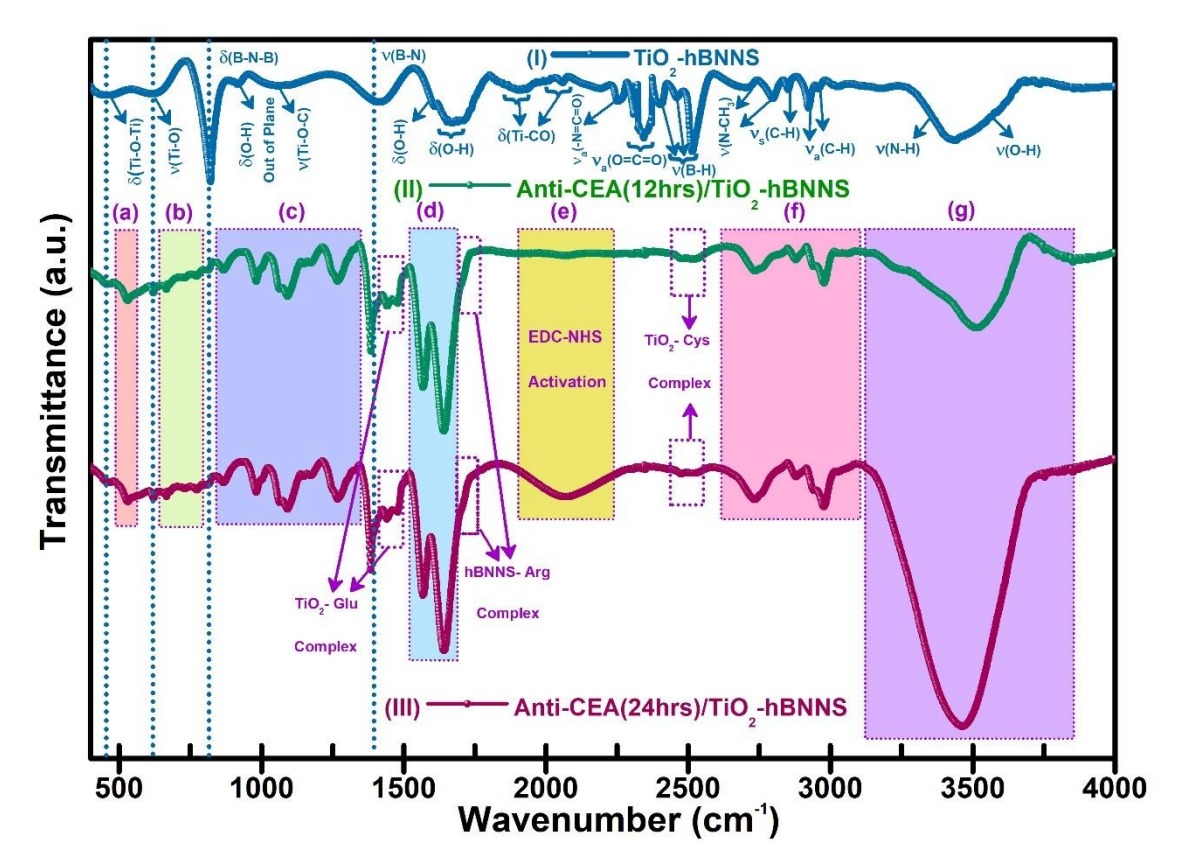


Figure 7.9: FTIR spectra analyzing Anti-CEA antibody immobilization on the TiO<sub>2</sub>-hBNNS/ITO electrode at 12 and 24 hours.

Sequential protein immobilization on the TiO<sub>2</sub>–hBNNS/ITO immunoelectrode was comprehensively validated by FTIR spectroscopy, as shown in **Fig. 7.10**. Following the optimized conjugation of EDC–NHS activated Anti-CEA antibodies onto the TiO<sub>2</sub>–hBNNS/ITO electrode [17] (**Fig. 7.10(II)**), a blocking step with 10 μL of BSA was introduced to ensure selective surface functionality. This step was indispensable, as BSA, being a globular protein, effectively masked unreacted functional groups and passivated unoccupied active sites, thereby preventing nonspecific protein adsorption and maintaining the fidelity of the bio-recognition interface. The FTIR spectra confirmed BSA immobilization through the emergence of characteristic vibrational features in region 'd' at 1566 cm<sup>-1</sup> (Amide II band) and 1637 cm<sup>-1</sup> (Amide I band), signifying that BSA retained its native-like secondary structure after immobilization (**Fig. 7.10(III)**). Moreover, the reduction in transmittance intensity across regions 'd–f' provided strong evidence of efficient suppression of background interferences, reinforcing the specificity and sensitivity of the electrode surface.

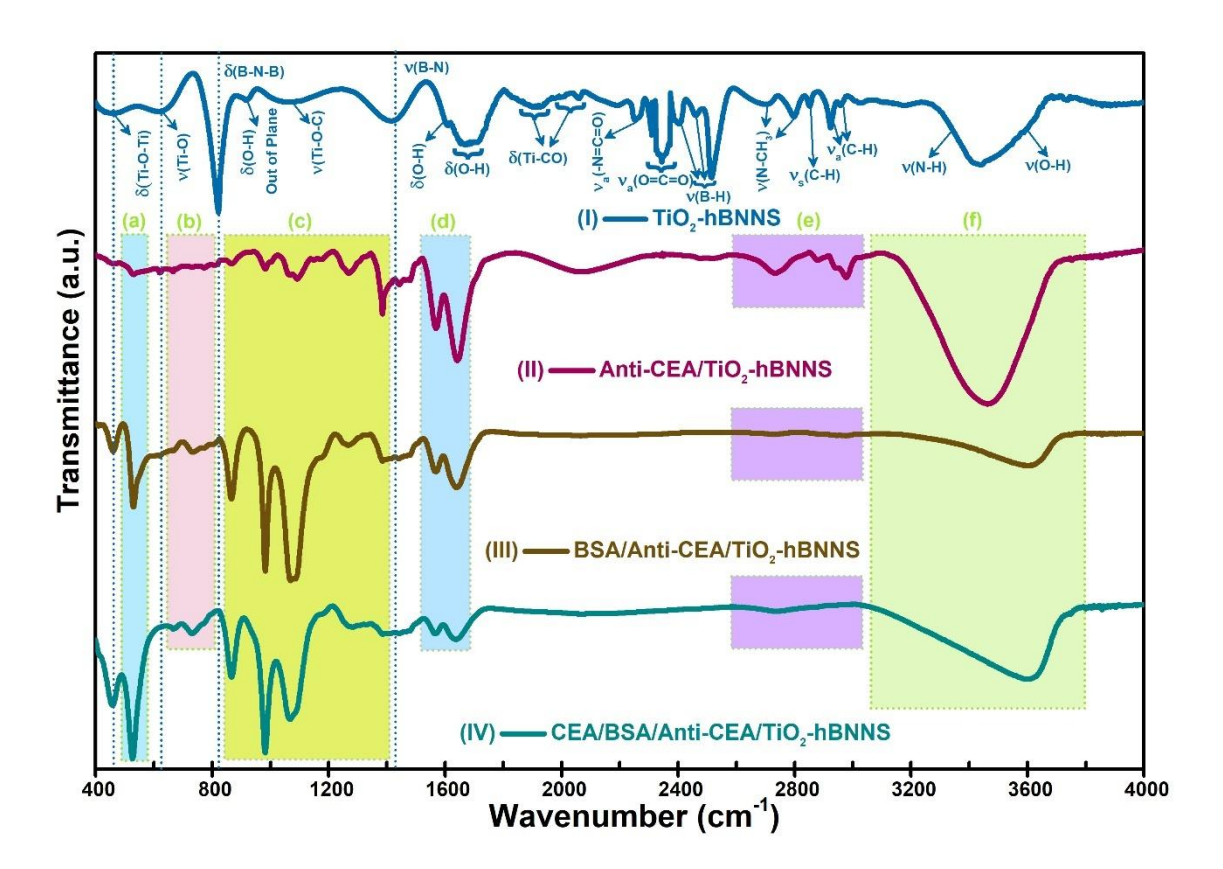


Figure 7.10: Immunoelectrode preparation on immobilization of Anti-CEA, BSA, and CEA onto TiO<sub>2</sub>-hBNNS/ITO electrode analyzed through FTIR spectroscopy

Subsequent immobilization of the target antigen, CEA, on the BSA/Anti-CEA/TiO<sub>2</sub>hBNNS/ITO electrode was evident from pronounced amplification of vibrational peaks in regions 'b, c, e, f' (Fig. 7.10(IV)). This spectral intensification is a hallmark of antibody-antigen complexation, where additional molecular vibrations arise due to secondary structural changes and increased hydrogen-bonding interactions. A progressive reduction in the B-N-B bending peak during the sequential addition of BSA and CEA provided further evidence of active site utilization on hBNNS nanostructures, reflecting effective crosslinking and surface engagement by biomolecular complexes. Most importantly, the broad absorption feature in region 'f', contributed collectively by aliphatic chains, hydroxyl groups, and overlapping amide stretching vibrations, validated the immobilization of CEA. This spectral broadening is a direct indicator of protein-rich layers anchoring to the functionalized nanocomposite, confirming the establishment of a stable, highly functional, and biologically active biorecognition interface. Altogether, the FTIR analysis provided a stepwise molecular fingerprint of BSA passivation and CEA capture, unequivocally proving the robustness and efficiency of the engineered immunoelectrode surface.

#### 7.3.2 Electrochemical Profiling and Analysis:

#### 7.3.2.1 Electrochemical Dynamics and Interfacial Kinetics Governing Sequential Protein Immobilization on TiO<sub>2</sub>-hBNNS Electrodes

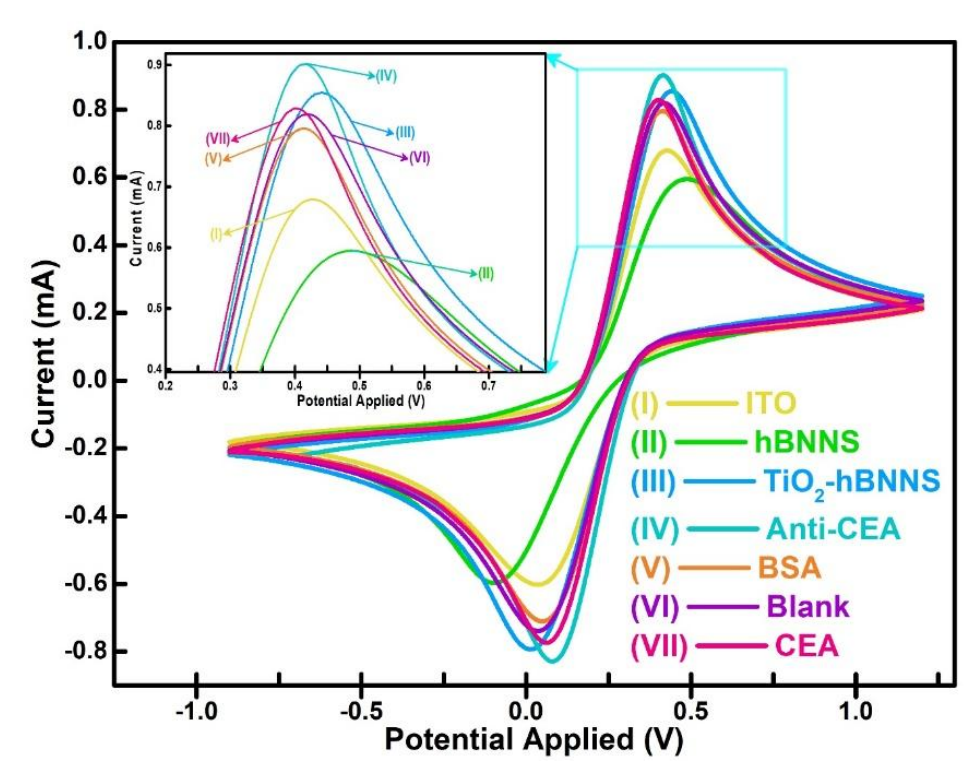


Figure 7.11: Cyclic voltammetry (CV) measurements performed within the potential window of -0.9 to 1.2 V demonstrate the sequential modification of the TiO2-hBNNS/ITO electrode with protein biomolecules, thereby confirming the progressive assembly of a stable and efficient bio-interface.

The sequential construction of the TiO<sub>2</sub>-hBNNS immunoelectrode was comprehensively validated through cyclic voltammetry (CV, **Fig. 7.11**) and differential pulse voltammetry (DPV, **Fig. 7.12**). Both techniques not only corroborated the FTIR findings but also revealed distinct and progressive alterations in anodic peak current (Ipa), DPV response, and diffusion coefficients during the immobilization of Anti-CEA, BSA, and CEA on the TiO<sub>2</sub>-hBNNS/ITO surface (Table S3). Importantly, the diffusion coefficients calculated using the Randle–Sevcik equation (**Eq. [7.10]**) at each stage provided direct quantitative evidence of dynamic interfacial charge-transfer processes, establishing a clear mechanistic relationship between biomolecular immobilization events and enhanced electrochemical performance of the biosensor.

$$I_p = (2.69 \times 10^5) n^{3/2} A C D^{1/2} \sqrt{\nu}$$
 [7.10]

Electrochemical characterization of the  $TiO_2$ –hBNNS/ITO electrode, interpreted through the Randles–Sevcik formalism, established a decisive enhancement in interfacial charge-transfer kinetics and biosensing performance. In the governing equation,  $I_p$  denotes the anodic or cathodic peak current, n the number of electrons exchanged (fixed at 1), A the electroactive surface area (0.64 cm²), C the concentration of the electroactive redox probe (5 × 10<sup>-3</sup> M), D the diffusion coefficient, and v the scan rate (50 mVs<sup>-1</sup>). Upon deposition of the  $TiO_2$ –hBNNS hybrid film onto the ITO

substrate, the electrode exhibited substantial improvements: a ~44% rise in CV peak current, a 1.8-fold increase in DPV current response, and nearly a two-fold elevation in the diffusion coefficient when compared to hBNNS/ITO baseline electrodes. This exceptional improvements in electrochemical behaviour were directly tied to the structural and electronic features of TiO<sub>2</sub> nanowires. Their high aspect ratio and surface reactivity introduced numerous accessible catalytic sites, while their crystalline lattice facilitated rapid electron transport. When hybridized with hBNNS nanosheets, the resulting composite architecture established a synergistic interface that optimized surface charge distribution, reinforced mechanical stability, and provided additional electron pathways. This synergistic assembly significantly enhanced catalytic efficiency and robustness under operational conditions.

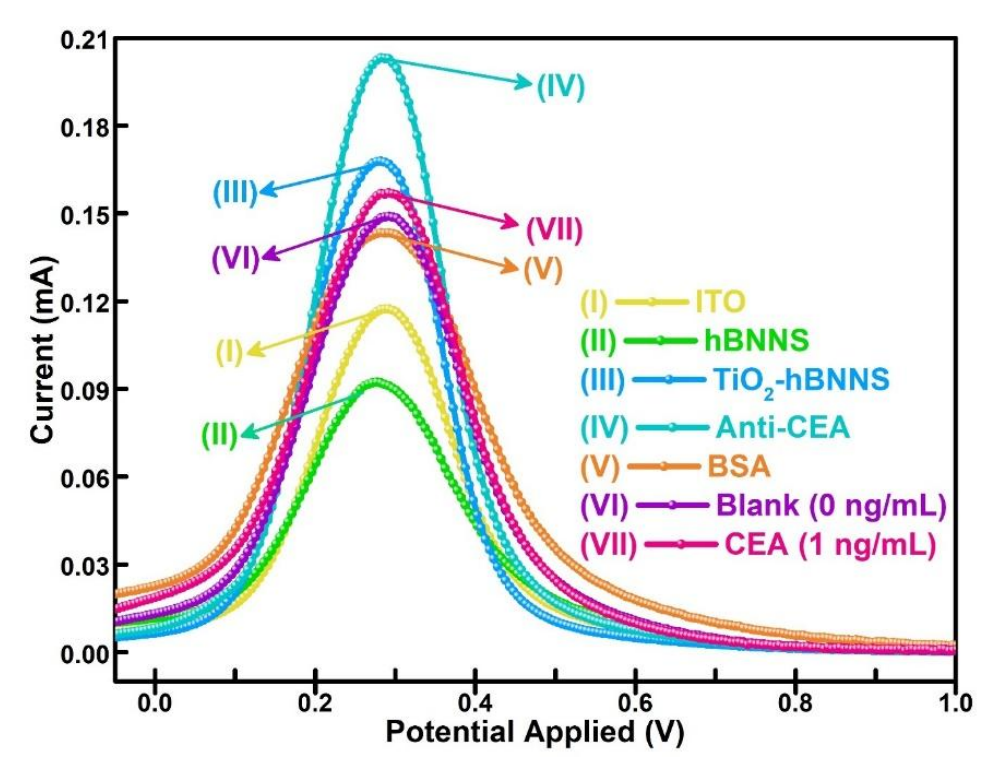


Figure 7.12: Stepwise biofunctionalization of TiO<sub>2</sub>-hBNNS/ITO electrodes is confirmed through DPV analysis conducted over the -0.2 to 1.2 V range, demonstrating precise control of protein immobilization and associated changes in electron transfer efficiency.

The pronounced difference between CV and DPV signals reflected the distinct current-generation mechanisms of the two methods—CV captures both faradaic and capacitive (non-faradaic) contributions, leading to higher currents, whereas DPV selectively suppresses capacitive effects, isolating faradaic currents to provide more precise, quantitative electrochemical outcomes. Following EDC–NHS mediated immobilization of Anti-CEA antibodies, CV and DPV responses enhanced by 5.5% and 21%, respectively, accompanied by a 12% increase in diffusion coefficient. These increments directly validate the efficiency of covalent antibody anchoring to the TiO<sub>2</sub>–hBNNS matrix, which not only preserved structural integrity of the nanohybrid but also maximized exposure of antigen-recognition sites. The porous TiO<sub>2</sub> framework facilitated efficient mass transport and fast electron relay, while hBNNS provided an

ideal interface for stable bio-conjugation. Altogether, this multi-scale integration of advanced nanomaterials and optimized biofunctionalization pathways establishes the TiO<sub>2</sub>–hBNNS/ITO electrode as a robust platform for highly sensitive, stable, and reproducible biosensing.

Following the immobilization of Anti-CEA, the subsequent incubation with BSA induced a pronounced reduction in current response, a direct manifestation of protein passivation. The bulky BSA molecules effectively occupied the available surface-active sites and obstructed the catalytic channels within the TiO2 nanowires, thereby suppressing non-specific adsorption and reinforcing biosensor selectivity. This controlled blocking step not only verified the stability of the functionalized interface but also enhanced the reliability of the biosensing platform by eliminating background interference. Intriguingly, the introduction of blank PBS resulted in a slight increase in current, emphasizing the contribution of ionic conduction to the modulation of electrode behaviour. Upon antigen immobilization, a sharp rise in current intensity was recorded, arising from the strong antibody-antigen recognition events and their coupled electron-transfer interactions with TiO<sub>2</sub> nanostructures. This distinct electrochemical response decisively confirmed the establishment of a robust, functionally active biorecognition interface and highlighted the immunoelectrode's capability for highly sensitive transduction of biomolecular binding events into amplified electrochemical signals.

#### 7.3.2.2 Scan Rate-Dependent Analysis of Interfacial Electron Dynamics in TiO<sub>2</sub>–hBNNS/ITO Nano-Biosensors

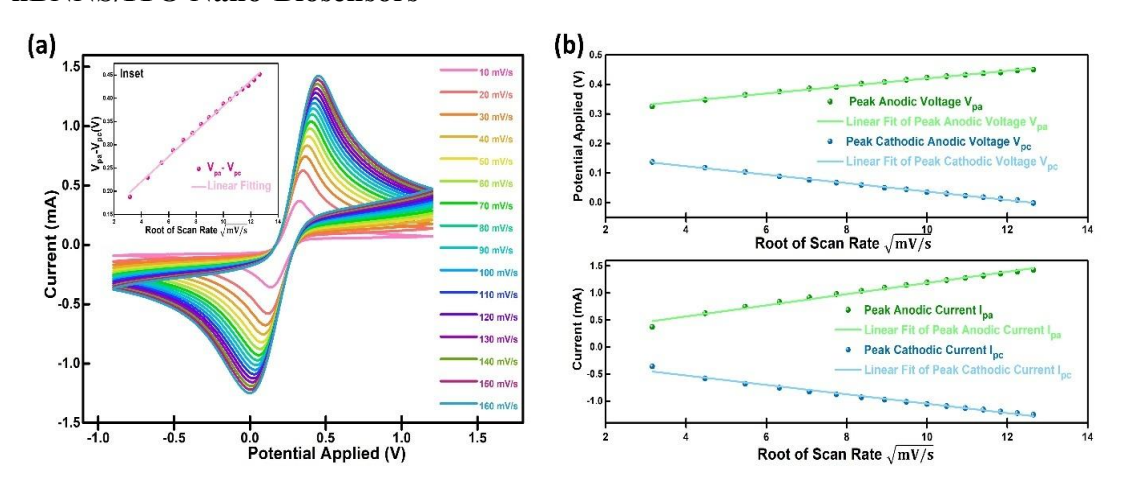


Figure 7.13: (a)Influence of scan rate on the cyclic voltammetric behaviour of the BSA/Anti-CEA/TiO<sub>2</sub>-hBNNS/ITO immunoelectrode recorded in  $[Fe(CN)_6]^{3-/4-}$  electrolyte, evaluated over a scan rate range of 10–160 mV/s., (b) Linear correlation between peak current response and the square root of scan rate for the BSA/Anti-CEA/TiO<sub>2</sub>-hBNNS/ITO immunoelectrode in  $[Fe(CN)_6]^{3-/4-}$  electrolyte, confirming diffusion-controlled electron transfer kinetics.

The interfacial kinetics of the BSA/Anti-CEA/TiO<sub>2</sub>-hBNNS/ITO nano-biosensor were systematically evaluated in PBS buffer (pH 7.0, 50 mM, 0.9% NaCl) through cyclic voltammetry (CV) at scan rates ranging from 10 to 160 mV/s (**Fig. 7.14**). The CV profiles displayed a consistent increase in both anodic and cathodic peak currents (Ipa

and Ipc) with rising scan rate, alongside measurable shifts in corresponding peak potentials (Vpa and Vpc). Linear fitting of Ipa and Ipc against the square root of scan rate (Fig. 7.13) established that the electron transfer at the nano-biointerface is predominantly diffusion-controlled. This behaviour underscores that charge transfer is largely dictated by the transport rate of redox-active species to the electrode surface. The progressive increase in current magnitude with scan rate reflects enhanced flux of electroactive species, while the proportional potential shifts confirm the reversibility of the underlying redox reactions. These results affirm that the biosensor operates under diffusion-governed electron transfer kinetics, a condition that ensures sensitive and reproducible electrochemical detection.

electroanalytical efficiency of BSA/Anti-CEA/TiO<sub>2</sub>–hBNNS/ITO immunoelectrode was quantitatively substantiated by monitoring the peak potential separation ( $\Delta Vp$ ) between anodic and cathodic processes. As presented in Fig. 7.13(inset),  $\Delta Vp$  maintained a linear dependence on the square root of the scan rate  $(\sqrt{v})$ , fully consistent with the theoretical prediction of Eq. [7.11]-[7.15]. This clear scaling behavior indicates that the biosensor operates under diffusion-controlled redox kinetics, free from major kinetic limitations, and demonstrates that the immobilized proteins are integrated into the electron transfer pathway rather than acting as insulative barriers. The minimal  $\Delta Vp$  values observed at slower scan rates serve as unambiguous indicators of fast interfacial electron exchange, reversible charge transport, and low resistive impedance, reflecting the synergistic integration of TiO<sub>2</sub> nanostructures with conductive hBNNS layers. At higher scan rates extending to 160 mV/s, however, a measurable but limited deviation in  $\Delta Vp$  was detected. This phenomenon is not indicative of compromised performance but arises naturally from the interplay of advanced electrochemical dynamics, including restricted relaxation of the Nernstian diffusion layer, diminished electron hopping rates across immobilized molecular bridges, increased solution resistance, capacitive accumulation at the double-layer interface, and instrumental constraints at elevated scan frequencies. Importantly, these deviations remained within tolerable limits and reinforced the biosensor's capacity to sustain stable and reproducible electron transfer even under demanding electrochemical interrogation. These findings firmly establish that the BSA/Anti-CEA/TiO<sub>2</sub>hBNNS/ITO immunoelectrode exhibits rapid, efficient, and reversible charge-transfer characteristics, ensuring its outstanding electrochemical responsiveness, operational stability, and long-term reliability for advanced biosensing applications.

$$\begin{split} &V_{pa} = [\ 2.925 \times 10^{-1}\ V +\ 1.281\ \times 10^{-2}\ V\sqrt{s/mV}\ \times \sqrt{Scan\ Rate[mV/s]}\ ]\ ; \\ &R^2 = 0.992 \quad [Eq.\ 7.11] \\ &V_{pc} = [\ 1.805 \times 10^{-1}\ V - 1.435 \times 10^{-2}\ V\sqrt{s/mV} \times \sqrt{Scan\ Rate[mV/s]}\ ]\ ; \\ &R^2 = 0.997 \quad [Eq.\ 7.12] \\ &I_{pa} = [\ 1.524 \times 10^{-1}A +\ 1.033 \times 10^{-1}\ A\sqrt{s/mV}\ \times \sqrt{Scan\ Rate[mV/s]}\ ]\ ; \\ &R^2 = 0.985 \quad [Eq.\ 7.13] \\ &I_{pc} = [\ -1.777 \times 10^{-1}A - 0.869 \times 10^{-1}\ A\sqrt{s/mV} \times \sqrt{Scan\ Rate[mV/s]}\ ]; \end{split}$$

$$\begin{split} R^2 &= 0.984 \quad \text{[Eq. 7.14]} \\ \Delta V_p &= [\ 1.\ 119 \times 10^{-1}\ V +\ 0.\ 271\ \times 10^{-1}\ V \sqrt{s/mV}\ \times \sqrt{Scan\ Rate[mV/s]}\ ]\ ; \\ R^2 &= 0.986 \quad \text{[Eq. 7.15]} \end{split}$$

## 7.3.2.3 Electrochemical Response Kinetics and Analysis of Sensing Performance of TiO<sub>2</sub>-hBNNS-Based Nano-Biosensing Interfaces

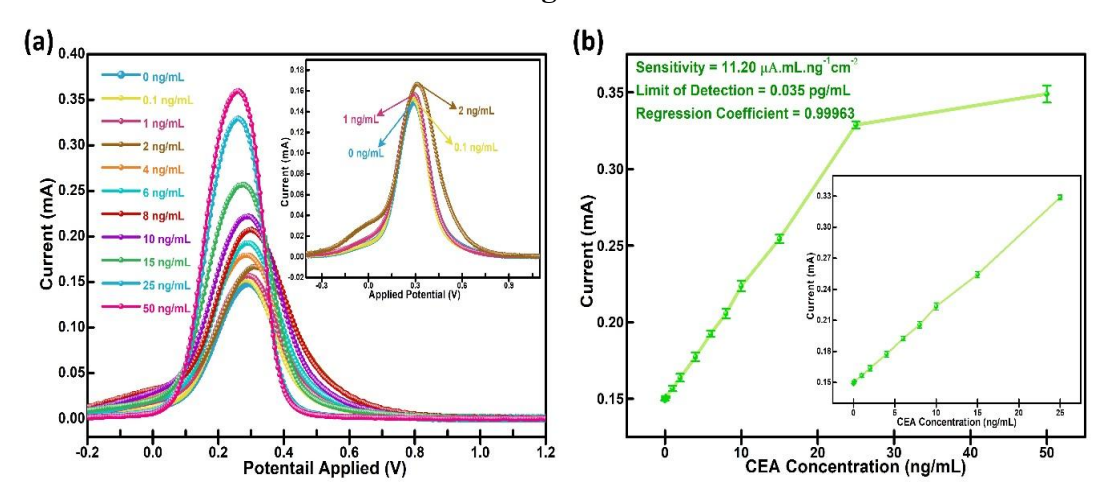


Figure 7. 14: (a) Differential pulse voltammetry (DPV) response illustrating the electrochemical interaction of CEA concentrations (0–50 ng/mL) with the BSA/Anti-CEA/TiO<sub>2</sub>-hBNNS/ITO immunoelectrode, and (b) calibration curve depicting the linear correlation between DPV signal on elevating CEA concentration.

Under optimized experimental conditions, the sensing performance of the BSA/Anti-CEA/TiO2-hBNNS/ITO nano-biosensor was systematically investigated for its capacity to achieve ultra-sensitive and quantitative detection of the carcinoembryonic antigen (CEA), a well-established biomarker closely associated with the early onset and progression of non-small cell lung cancer (NSCLC). In healthy individuals, CEA serum levels generally remain below 5 ng/mL, whereas significantly elevated concentrations are strongly correlated with malignant transformations, making CEA a critical diagnostic and prognostic indicator. To demonstrate the diagnostic potential of the TiO2-hBNNS-based immunoelectrode, differential pulse voltammetry (DPV) was employed to record the current response over an extended CEA concentration range (0– 50 ng/mL), as shown in Fig. 7.14(a). A consistent and progressive rise in DPV current intensity was observed up to 25 ng/mL, directly reflecting the accelerated interfacial electron transfer kinetics facilitated by the electrocatalytically active porous TiO<sub>2</sub> nanowires homogeneously integrated within the hBNNS framework. amplification in current response originates from the high density of active recognition sites and the efficient electron conduction pathways generated by the hybrid nanoarchitecture. However, beyond 25 ng/mL, the DPV signal exhibited saturation behavior, indicative of near-complete occupancy of the antibody binding domains on the immunosensor interface and the limited availability of additional recognition moieties for antigen binding.

Following these measurements, a precise calibration curve was generated (**Fig. 7.14(b)**) to establish the sensor's analytical performance parameters. Linear regression analysis of the DPV data revealed a remarkably well-defined correlation in the 0-25 ng/mL concentration window, expressed by the equation y = mx + c with an outstanding regression coefficient ( $R^2 = 0.99998$ ), as presented in **Eq. [7.16]**. Each data point was validated using triplicate experimental runs (n = 3), thereby confirming excellent reproducibility and eliminating statistical anomalies. The exceptional linearity, coupled with a strong signal-to-noise ratio and reproducible current outputs, underscores the nano-biosensor's superior sensitivity and diagnostic reliability. Collectively, these findings demonstrate that the  $TiO_2$ -hBNNS/ITO immunosensor translates molecular-level antibody-antigen interactions into quantifiable electrochemical signals with unprecedented precision, reinforcing its applicability for clinical diagnostics and real-time monitoring of NSCLC biomarkers.

$$I~(mA) = [~11.20~\mu A.~mL.~ng^{-1}.~cm^{-2}~\times (CEA~Concentration) + 0.~149~mA~] \label{eq:interpolation}$$
 [7.16]

The slope derived from the linear calibration curve was decisively utilized to quantify the sensitivity of the TiO<sub>2</sub>–hBNNS/ITO immunosensor, yielding a value of 11.20 μA·mL·ng<sup>-1</sup>·cm<sup>-2</sup>. This parameter was calculated through the established relation Slope/Surface Area, where the effective electroactive surface area of the electrode was accurately determined to be 0.64 cm<sup>2</sup>. The high slope value unambiguously reflects the superior electron transfer efficiency of the hybrid TiO<sub>2</sub>–hBNNS architecture and the strong, specific binding affinity between immobilized Anti-CEA antibodies and their target antigen. This synergistic interaction amplifies current signals, thereby elevating the biosensor's ability to detect subtle variations in analyte concentrations. Crucially, sensitivity in this context is not merely a performance indicator; it forms the cornerstone for evaluating the analytical precision of the biosensor in discriminating clinically relevant fluctuations in biomarker levels, which is indispensable for early-stage cancer detection.

furthermore, the lower limit of detection (LOD) was rigorously calculated by integrating the standard deviation ( $\sigma$ ) of the blank measurement with the sensor's sensitivity, in line with Eq. [7.17]. This statistical framework anchors the LOD in both the inherent electrochemical noise of the system and its amplification capability, yielding a robust and experimentally reliable threshold for the minimal concentration of CEA that can be consistently detected. The exceptionally low LOD obtained underscores the biosensor's ability to identify trace biomarker levels within the clinically significant range, reinforcing its diagnostic power. Collectively, the outcomes on sensitivity and LOD affirm that the  $\text{TiO}_2$ -hBNNS/ITO nano-biosensor exhibits a highly optimized and reliable sensing platform, capable of transforming minute biorecognition events into quantifiable electrochemical responses with clinical relevance.

Limit of Detection = 
$$(3 \times \sigma)/m$$
 [7.17]

The lower limit of detection (LOD) was rigorously quantified using the relation LOD =  $3\sigma/m$ , where  $\sigma$  represents the standard deviation of the blank response and m denotes the sensor sensitivity. The TiO<sub>2</sub>-hBNNS/ITO immunosensor achieved an exceptionally low LOD of 0.035 pg/mL, demonstrating its remarkable analytical strength. This

outstanding performance stems from the synergistic integration of hierarchical TiO<sub>2</sub> nanowires with the layered hBNNS framework, a hybrid configuration that maximizes electroactive sites, accelerates electron transfer dynamics, and stabilizes the electrode interface. The result is a highly sensitive and reproducible biosensing system with the capability to detect trace concentrations of CEA well below clinically critical thresholds. Notably, this LOD outperforms values reported for conventional metal- and semiconductor-based nanocomposites, thereby positioning TiO<sub>2</sub>–hBNNS as a next-generation platform for ultrasensitive immunosensing. The capacity to detect CEA at such ultra-trace levels marks a decisive advancement in early cancer diagnostics, directly underscoring the superiority of this nanostructured electrode design, as detailed in **Table 7.2**.

Table 7.2: Comparison of sensing characteristics of TiO<sub>2</sub>-hBNNS based nano-biosensor with existing metal-, metal oxidesand semiconductor-based immunosensors.

Sensing	Sensing Matrix	<b>Detection Technique</b>	Linear	Limit of	Sensitivity	Stability	Ref.
Platform			Range (ng/mL)	Detection			
Immunosensor	NiS@NiO/TiO2	Photoelectrochemical	0.001 - 45	0.167 pg/mL	-0.278 μΑ·(decade) <sup>-1</sup>	2 Weeks	[33]
Immunosensor	Au-TiO2	Photoelectrochemical	0.005 - 1000	5 pg/mL	4.3809 μA ·(decade) <sup>-1</sup>	3 Weeks	[34]
Immunosensor	TiO2-mp/(CS+Au-np)	Electrochemical	0.01 -1, 1- 20	0.01 ng/mL	2.146 μA·mL·ng <sup>-1</sup> , 0.120 μA·mL·ng <sup>-1</sup>	-	[35]
Immunosensor	Ncarbon dots/TiO2Pt modified paper	Electrochemical	0.002 - 200	1 pg/mL	42.76 μA:(decade) <sup>-</sup>	-	[36]
Immunosensor	TiO2-graphene	Electrochemical	0.1-10, 10 - 120	0.01 ng/mL	-	30 Days	[37]
Immunosensor	Au-TiO2 NPs	Electrochemical	0.02 - 120	12 pg/mL	6.09 μA·(decade) <sup>-</sup> <sup>1</sup> , 6.63 μA·(decade) <sup>-1</sup>	21 Days	[38]
Immunosensor	g-C3N4/TiO2	Photoelectrochemical	0.01 - 10	2.1 pg/mL	-	-	[39]
Immunosensor	Au-TiO2 particle	Electrochemical	0.2 -160	5.38 pg/mL	-32.50 μ <b>A</b> ·(decade) <sup>-1</sup>	30 Days	[40]
Immunosensor	Cu:TiO2/g-C3N4 nanocomposites	Photoelectrochemical	0.1 - 1000	1 pg/mL	1.327 μA·(decade) <sup>-</sup>	2 Weeks	[41]
Immunosensor	h-BNNS	Electrochemical	0 - 10	22.5 pg/mL	24.84 μA·mL·ng <sup>-1</sup> ·cm <sup>-2</sup>	5 weeks	[42]
Immunosensor	rGO-hBNNS	Electrochemical	0 - 15	5.47 pg/mL	9. 65 μA·mL·ng <sup>-1</sup> ·cm <sup>-2</sup>	8 weeks	[43]
Immunosensor	Cu/Cu <sub>x</sub> O-hBNNS	Electrochemical	0 - 25	3.22 pg/mL	8. 04 μA·mL·ng <sup>-1</sup> ·cm <sup>-2</sup>	60 days	[44]
Immunosensor	TiO <sub>2</sub> -hBNNS	Electrochemical	0 - 25	0.035 pg/mL	11.2 μA·mL·ng <sup>-1</sup> ·cm <sup>-2</sup>	60 days	Present Work

7.3.2.4 Systematic Assessment of Electroanalytical Efficiency and Functional Reliability in TiO<sub>2</sub>-hBNNS/ITO-Based Nano-Biosensors for Advanced Clinical Diagnostics

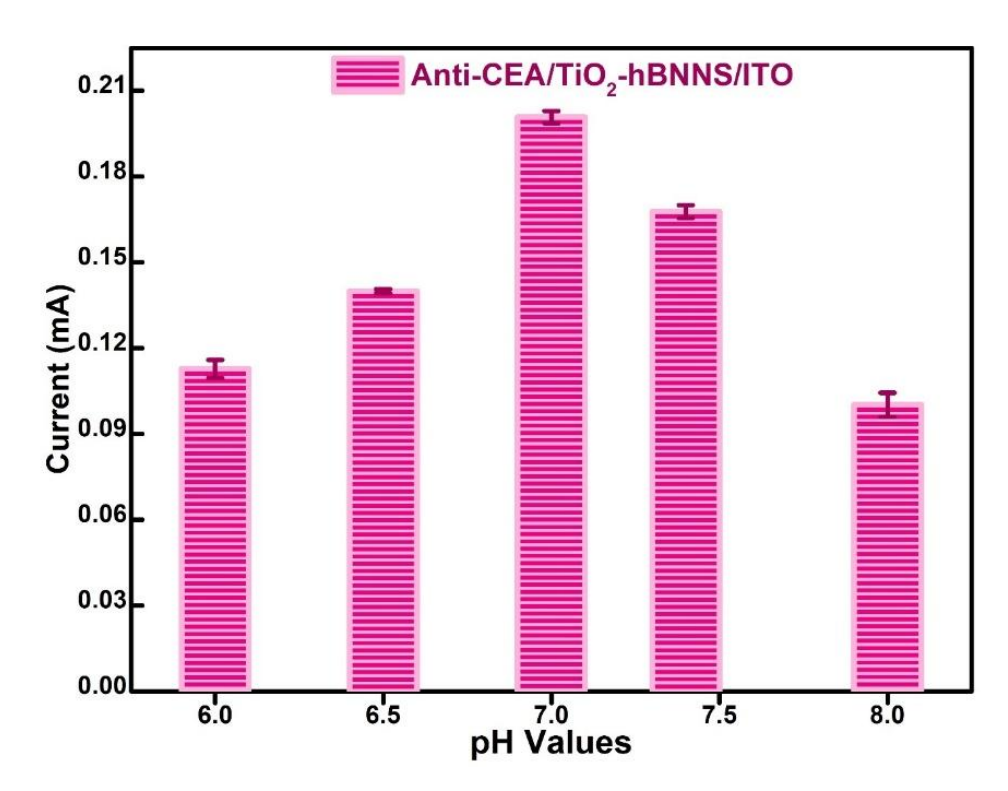


Figure 7.15: Bar plot representing the buffer pH dependence of peak DPV current for the Anti-CEA/TiO2-hBNNS/ITO immunosensor, establishing the optimal electrochemical environment for enhanced biosensor sensitivity and stability.

A systematic and detailed evaluation of pH effects was undertaken to establish the operational robustness and functional stability of the BSA/Anti-CEA/TiO2hBNNS/ITO immunoelectrode. Differential pulse voltammetry (DPV), conducted at a constant scan rate of 50 mV/s, was employed to capture precise electrochemical responses across a physiologically relevant pH spectrum (6.0-8.0) using PBS electrolyte enriched with the ferro/ferricyanide redox probe [5 mM, Fe(CN)<sub>6</sub><sup>3-/4-</sup>]. The resulting data, illustrated in Fig. 7.15, revealed a clear pH-dependent trend, where the DPV current reached its highest value at pH 7.0. This strongly demonstrates that neutral pH conditions are optimal for biosensor operation, as they preserve antibody structure, sustain antigen-binding capacity, and support efficient electron transport across the TiO<sub>2</sub>-hBNNS-modified interface. At acidic conditions (pH 6.0-6.5),immunoelectrode response was substantially reduced due to conformational changes in the antibody structure arising from protonation, which weakened molecular recognition and impaired redox coupling. Conversely, in alkaline conditions (pH 7.5-8.0), excessive deprotonation adversely influenced surface chemistry, disrupting molecular interactions and diminishing electron transfer efficiency due to increased resistive and capacitive interference. By pinpointing pH 7.0 as the optimal working environment, this investigation not only validated the electrode's electrochemical robustness but also provided mechanistic insights into the interplay between biomolecular stability and interfacial charge-transfer kinetics. Consequently, PBS at pH 7.0 was designated as the standard electrolyte for all subsequent electrochemical assays, thereby ensuring consistent reproducibility, high stability, and superior sensitivity of the biosensor under clinically relevant conditions.

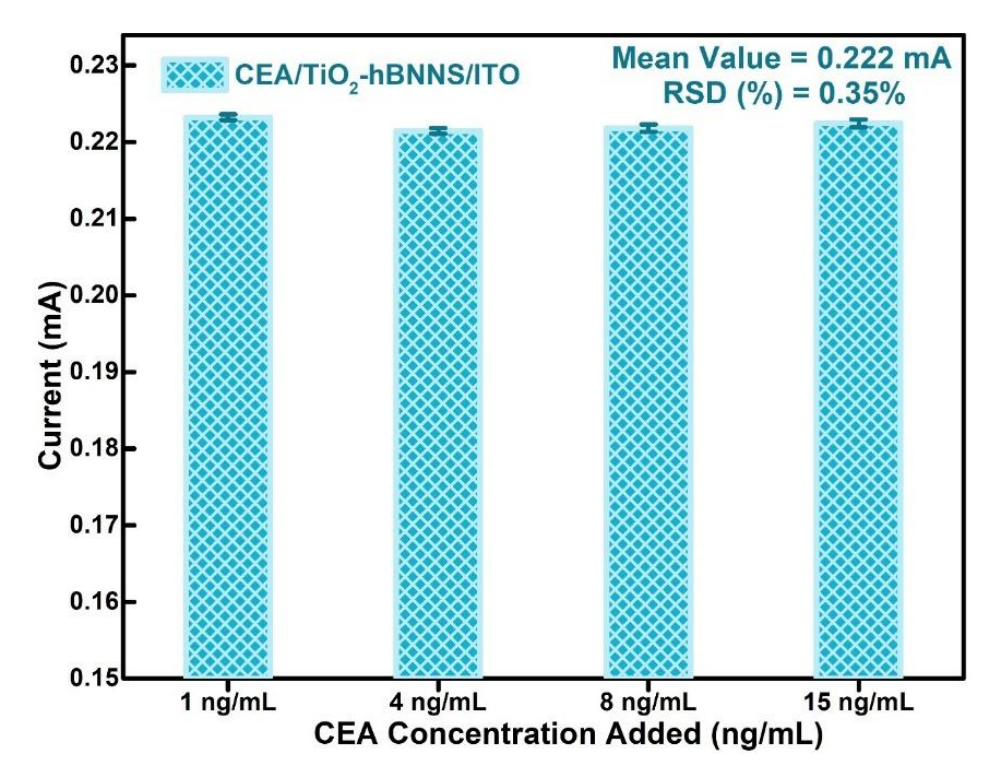


Figure 7.16: Quantitative bar plot illustrating the control experiment on TiO<sub>2</sub>-hBNNS/ITO electrodes, confirming the absence of significant electrochemical activity upon exposure to different CEA concentrations.

A negative control investigation was systematically carried out to verify that the electrochemical responses measured in the developed biosensing system arise from specific antigen-antibody interactions rather than from nonspecific adsorption phenomena. To achieve this, the bare TiO2-hBNNS/ITO electrode, devoid of immobilized Anti-CEA antibodies and blocking BSA layers, was deliberately exposed to increasing concentrations of the target antigen, CEA (1, 4, 8, and 15 ng/mL). Following antigen exposure, differential pulse voltammetry (DPV) was employed to monitor the current response under identical experimental conditions. As illustrated in Fig. 7.16, the bare TiO<sub>2</sub>-hBNNS/ITO electrode consistently displayed a steady DPV current of 0.222 mA with an exceptionally low relative standard deviation (RSD) of 0.35%, regardless of the antigen concentration. Crucially, no incremental rise in current was detected across the tested concentration range. This invariance was further substantiated, which collectively confirm that the TiO<sub>2</sub>-hBNNS/ITO matrix alone does not exhibit inherent affinity or binding capability toward the CEA biomarker. The absence of signal variation decisively eliminates the possibility of nonspecific adsorption, physisorption, or random molecular adherence of CEA to the electrode surface. Instead, these findings establish that a quantifiable electrochemical signal is only achieved when the electrode surface is precisely biofunctionalized with Anti-CEA antibodies and subsequently stabilized with BSA, thereby creating the BSA/AntiCEA/TiO<sub>2</sub>-hBNNS/ITO immunoelectrode. This control experiment underscores the importance of antibody—antigen specificity in dictating the biosensor's electroanalytical performance and reinforces its diagnostic reliability by removing the possibility of false positives. Furthermore, the data demonstrate that the porous, electrocatalytically active TiO<sub>2</sub> nanostructures anchored onto hBNNS serve exclusively as a conductive scaffold, enhancing electron transfer kinetics while remaining chemically inert to nonspecific biomolecular interactions. Such dual functionality—electrocatalytic enhancement coupled with chemical passivity—ensures that only authentic antigen recognition governs the biosensor's analytical output, thereby guaranteeing high specificity, reproducibility, and clinical reliability.

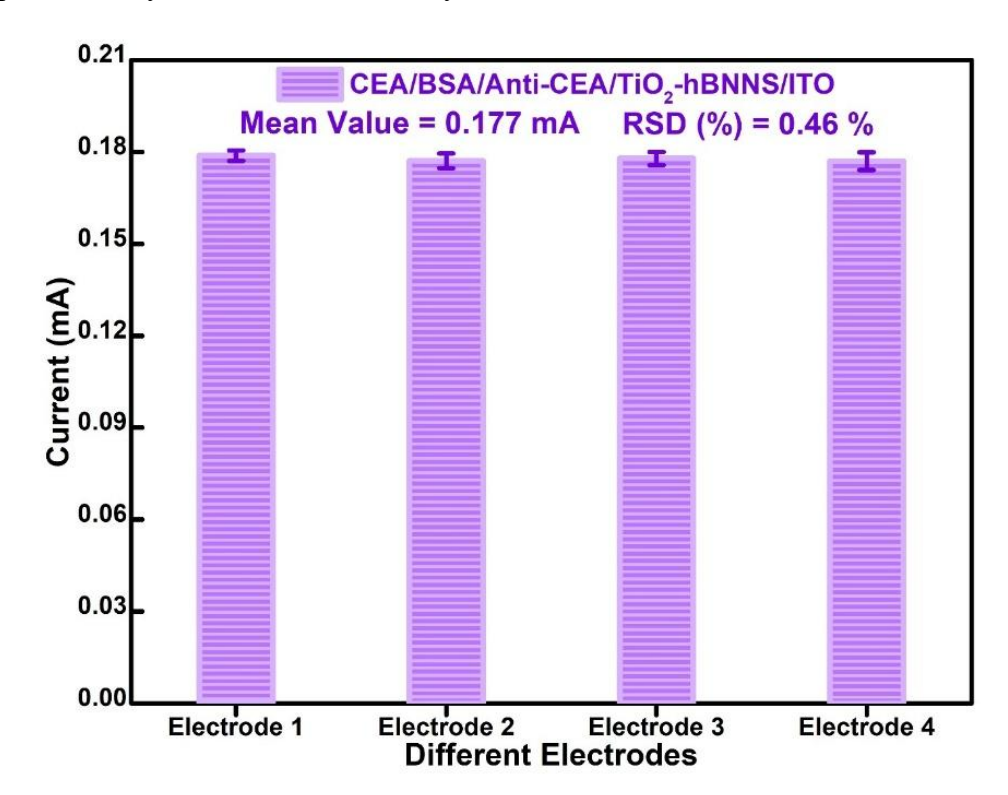


Figure 7.17: A reproducibility study was performed by preparing four individual BSA/anti-CEA/TiO<sub>2</sub>-hBNNS/ITO immunoelectrodes under consistent fabrication conditions and analyzing their electrochemical responses.

A detailed reproducibility study was performed to validate the robustness, consistency, and reliability of the TiO<sub>2</sub>-hBNNS-based immunosensor across multiple independently fabricated electrodes. Under strictly identical experimental conditions, four separate immunoelectrodes were fabricated, ensuring controlled nanostructure growth, consistent antibody loading, and proper stabilization through BSA blocking. These electrodes were then evaluated using Differential Pulse Voltammetry (DPV), with each device tested in triplicate (n = 3) to provide statistically significant results. As shown in **Fig.7.17**, the immunosensors exhibited a highly uniform electrochemical response, yielding an average peak current of 0.177 mA accompanied by a remarkably low relative standard deviation (RSD) of 0.46%. The narrow deviation in current response unambiguously establishes the high degree of reproducibility inherent to the fabrication and functionalization protocol employed.

Notably, the uniformity of the electrochemical outputs directly reflects precise control over nanostructure synthesis and biofunctionalization, both of which are essential for generating stable electrode–electrolyte interfacial properties. The reproducibility observed in this study further strengthens the reliability of the immunosensor, demonstrating that its performance is not a consequence of isolated or random fabrication success but rather a consistent outcome achievable across multiple electrodes. Importantly, the electrochemical characteristics obtained closely align with those documented during preliminary sensor characterization, affirming the stability and dependability of the device across multiple operational cycles.

The exceptionally low RSD value also highlights the scalability potential of this immunosensing platform, as reproducibility is a critical determinant when transitioning from laboratory-scale prototypes to clinically deployable diagnostic tools. By proving that the TiO<sub>2</sub>-hBNNS-based immunosensor can consistently deliver stable responses across independent samples, this study solidifies its practical applicability in biomedical diagnostics, where reliability, reproducibility, and standardization are indispensable for accurate patient outcomes.

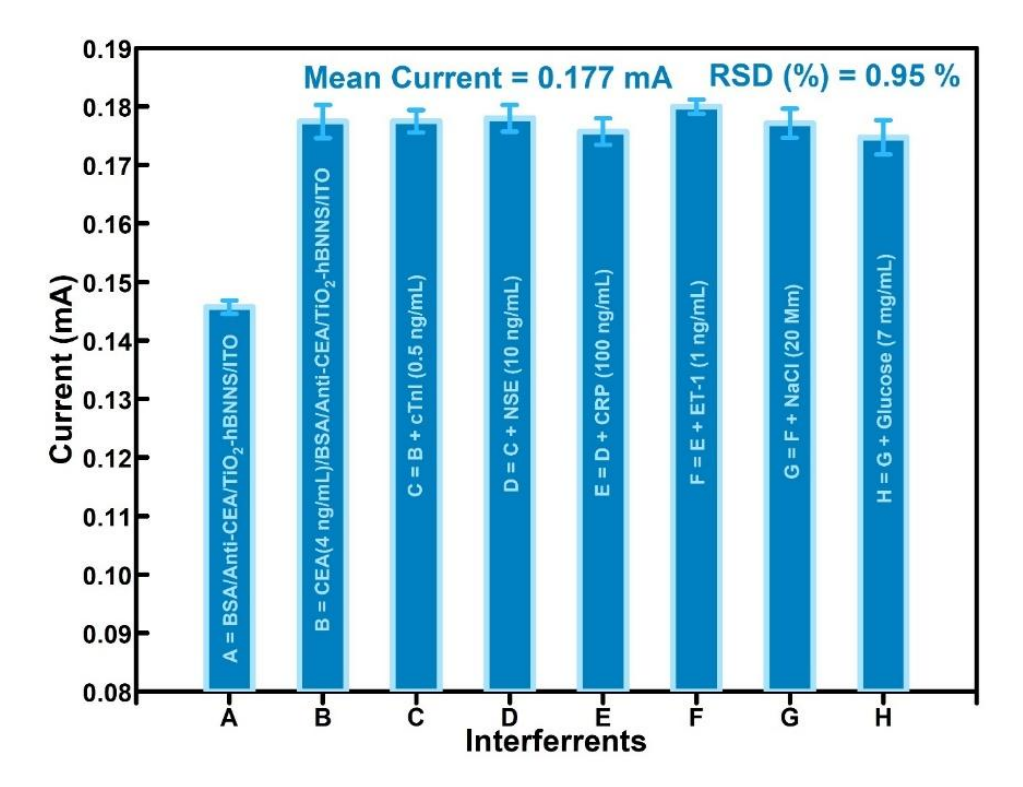


Figure 7.18: Quantitative bar chart depicting the sequential selectivity analysis of the BSA/Anti-CEA/TiO<sub>2</sub>-hBNNS/ITO immunoelectrode, examined through stepwise introduction of the target CEA (2 ng/mL) and potential interfering biomolecules: (A) BSA/Anti-CEA/TiO<sub>2</sub>-hBNNS/ITO, (B) + CEA, (C) + cTnI (0.5 ng/mL), (D) + NSE (10 ng/mL), (E) + CRP (100 ng/mL), (F) + ET-1 (1 ng/mL), (G) + NaCl (20 mM), and (H) + Glucose (7 ng/mL).

Ensuring the selectivity of the target analyte is a fundamental requirement for the accurate detection of carcinoembryonic antigen (CEA) in human serum, as the serum

environment is inherently complex and contains a variety of biomolecules that could potentially interfere with antigen–antibody interactions. To address this challenge, the TiO2–hBNNS-based immunosensor was subjected to an extensive selectivity study designed to assess its performance under conditions that closely mimic the biochemical complexity of real serum samples. Potential interfering species, including cardiac troponin I (cTnI), C-reactive protein (CRP), neuron-specific enolase (NSE), endothelin-1 (ET-1), glucose, and sodium chloride (NaCl), were carefully selected due to their frequent co-occurrence in human serum and their potential to disrupt electrochemical detection pathways (Fig. 7.18).

Successive concentrations of these interferents were individually introduced, and the resulting electrochemical signals were meticulously monitored using Differential Pulse Voltammetry (DPV). This experimental strategy allowed for the evaluation of both immediate and cumulative effects of interferents on the sensor's electrochemical response. The results, as illustrated in Fig. 7.18, demonstrated that the immunosensor exhibited negligible deviations in peak current values even in the presence of these potentially disruptive molecules. The calculated relative standard deviation (RSD) of 0.95% reflecting the exceptional reproducibility and specificity of the biosensing platform. The ability of the immunosensor to maintain an unaltered and stable response in the presence of competing analytes strongly validates the selective binding affinity of Anti-CEA antibodies immobilized onto the TiO2-hBNNS interface. This remarkable performance arises from the favorable electroactive architecture of the hybrid nanocomposite, which not only supports efficient electron transfer but also minimizes nonspecific adsorption by offering a structurally ordered and chemically inert background. By ensuring that only the intended antigen-antibody binding contributes to the electrochemical output, the immunosensor demonstrates its reliability for clinical use. The remarkable selectivity ensures that the device can be applied in real serum analysis, where high diagnostic precision is essential. By eliminating the risk of falsepositive responses and validating performance against multiple potential interferents, this study positions the TiO2-hBNNS-based nano-biosensor as a powerful diagnostic platform. Its capacity to deliver accurate, interference-free CEA detection emphasizes its practical utility for early cancer diagnostics, clinical monitoring, and routine biomedical screening.

The long-term operational stability of the TiO<sub>2</sub>–hBNNS-based immunosensor was rigorously evaluated to determine its durability and clinical reliability. As presented in **Fig. 7.19**, the stability study involved systematic Differential Pulse Voltammetry (DPV) measurements performed at regular 10-day intervals, with the sensor stored consistently at 4 °C to eliminate environmental variability. This methodology ensured that observed changes in electrochemical performance could be directly attributed to intrinsic time-dependent alterations in the biosensor, rather than external disturbances. The results revealed that the immunosensor retained nearly constant electrochemical activity for the first 60 days, underscoring its structural integrity, stable surface chemistry, and the strong preservation of antibody–antigen binding efficiency within the TiO<sub>2</sub>–hBNNS framework. The negligible decline during this period validates the robustness of the nanocomposite matrix in protecting biofunctional components against denaturation, leaching, or loss of conductivity. Beyond 60 days, however, progressive deterioration became evident. By day 70, the reduction in current response exceeded

5%, while by day 80, the sensor maintained approximately 90% of its initial peak current, indicating the onset of significant performance decline.

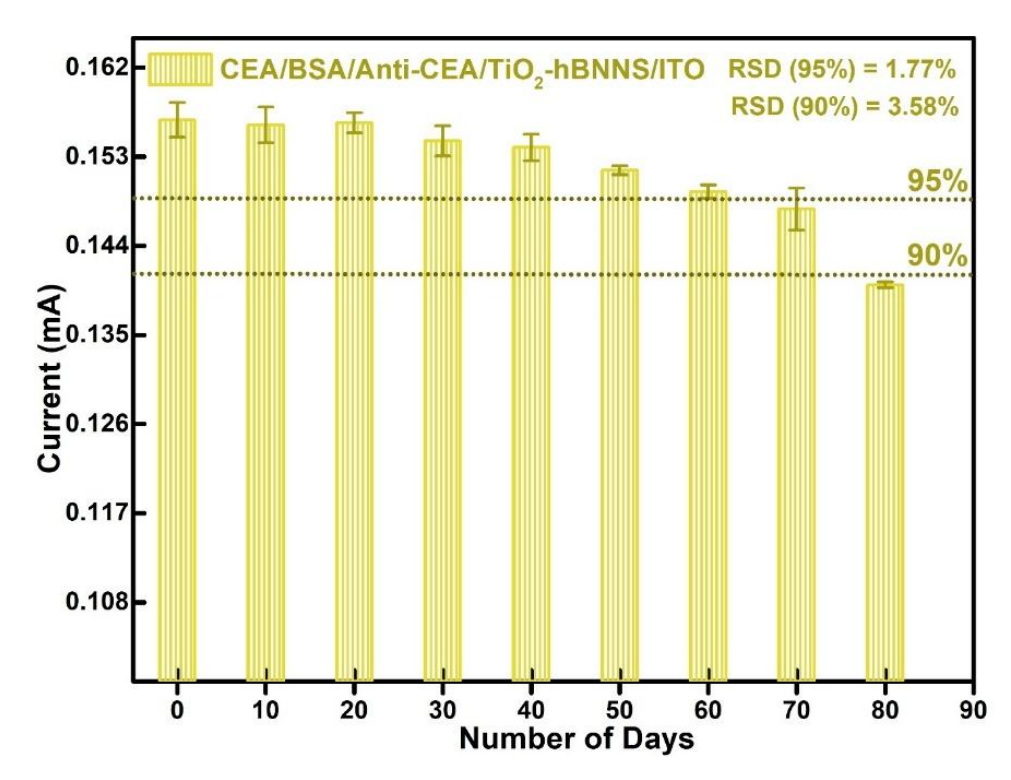


Figure 7.19: The shelf-life stability of the CEA/BSA/anti-CEA/TiO<sub>2</sub>-hBNNS/ITO immunoelectrode was assessed through differential pulse voltammetry (DPV), with electrochemical responses recorded at regular weekly intervals across a 10-day monitoring period.

The time-dependent trend suggests that, although the TiO<sub>2</sub>–hBNNS hybrid provides excellent immobilization and electron transport support, gradual antibody degradation or desorption over extended durations ultimately limits long-term activity. Importantly, this finding identifies the functional threshold of the device, establishing 60 days as the optimal operational window for consistent performance under refrigerated storage. These insights highlight the importance of both nanoscale architecture and biomolecule stability in defining the overall lifetime of electrochemical biosensors. Furthermore, the results emphasize the necessity of periodic calibration and systematic monitoring in clinical applications, ensuring reliability of diagnostics during extended storage and use. Collectively, this study confirms that the TiO<sub>2</sub>–hBNNS immunosensor demonstrates excellent long-term stability, a key parameter for real-world translation in point-of-care testing and biomedical diagnostics.

The analytical performance of the  $TiO_2$ –hBNNS/ITO-based nano-biosensor for detecting carcinoembryonic antigen (CEA) in real human serum was comprehensively validated using DPV measurements, as shown in **Fig. 7.21**. To simulate clinical conditions, serum samples were deliberately spiked with defined concentrations of CEA. Equal volumes of serum and antigen solution (10  $\mu$ L each) were thoroughly homogenized through repeated pipetting and subsequently incubated for 30 minutes to ensure uniform distribution of the antigen prior to immobilization on the BSA/Anti-

CEA/TiO<sub>2</sub>–hBNNS/ITO immunoelectrode. Recognizing that normal physiological CEA levels in healthy individuals remain below 5 ng/mL, the ability of the biosensor to detect higher concentrations with accuracy is of paramount importance for early-stage cancer diagnostics.

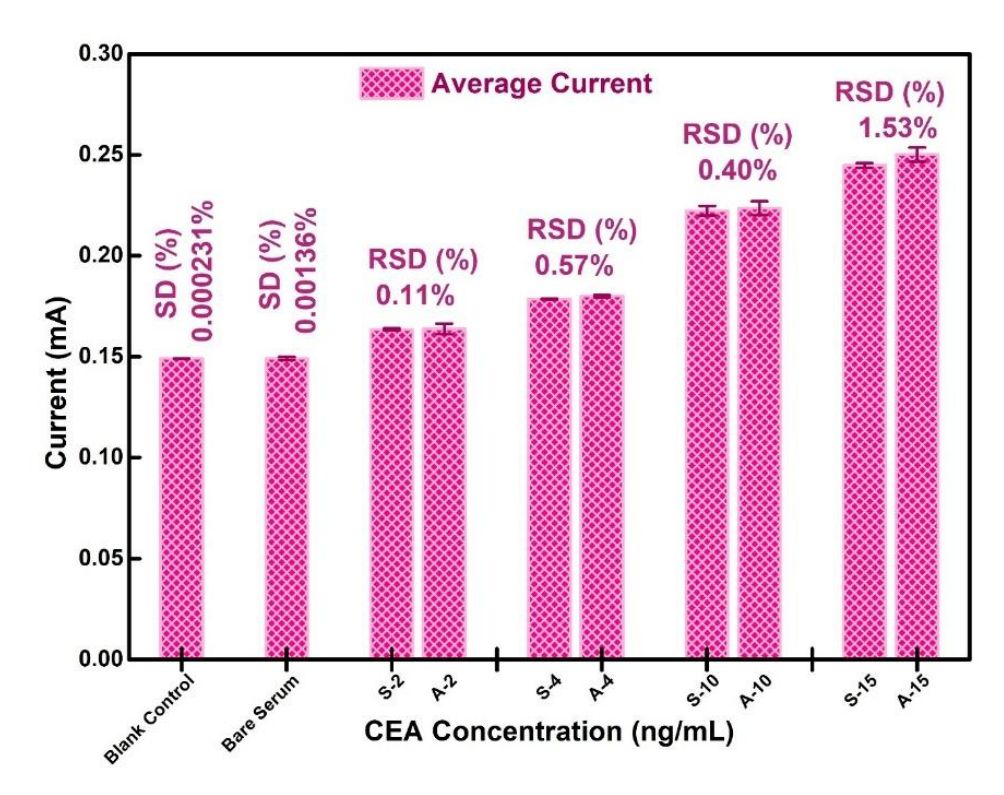


Figure 7.20: (a) Assessment of current reproducibility in the as-fabricated CEA/BSA/Anti-CEA/TiO<sub>2</sub>-hBNNS/ITO immunoelectrode. (b) Bar chart illustrating the selectivity study upon sequential addition of various interferents to CEA, defined as: A = BSA/Anti-CEA/rGO-hBNNS/ITO, B = A + CEA (2 ng/mL), C = B + CRP (100 ng/mL), D = C + cTnI (0.5 ng/mL), E = D + ET-1 (1 ng/mL), E = E + ET-1 (1 ng/mL), E = E + ET-1 (1 ng/mL), E = E + ET-1 (20 mM). (c) Stability evaluation of the CEA/BSA/Anti-CEA/TiO<sub>2</sub>-hBNNS/ITO immunoelectrode over 10-day intervals. (d) Bar graph presenting DPV response variations for spiked serum samples compared to actual CEA concentrations, validating sensor performance.

The DPV current responses obtained for pure CEA solutions (A) were directly compared with those for spiked serum samples (S), exhibiting remarkable concordance across all tested concentrations. This clearly establishes that the biosensor performs with high fidelity even in complex biological matrices. To further confirm analytical reliability, triplicate quantification was carried out using both the fabricated immunoelectrode and a conventional sandwich ELISA assay. In the ELISA procedure, Anti-CEA pre-coated wells were employed, and absorbance values were recorded at 450 nm. The ELISA results displayed strong consistency with electrochemical measurements, thereby validating the sensor's ability to produce clinically reliable outputs. The results presented in Fig. 7.20 clearly demonstrate the outstanding precision and reproducibility of the BSA/Anti-CEA/TiO<sub>2</sub>-hBNNS/ITO immunoelectrode. When evaluated at standard CEA concentrations of 2, 4, 10, and 15 ng/mL, the relative

standard deviations were remarkably low, calculated as 0.11%, 0.57%, 0.40%, and 1.53%, respectively. Such minimal variability highlights the strong stability of the electrode and the robustness of the DPV technique in delivering consistent responses. This high level of reproducibility across both standard solutions and spiked serum samples confirms the immunoelectrode's reliability and establishes its clinical relevance for accurate CEA detection. These results highlight the excellent sensitivity, precision, and reproducibility of the TiO<sub>2</sub>–hBNNS/ITO immunosensor. The robust correlation with ELISA not only confirms its accuracy but also underscores its readiness for real-world clinical biomarker monitoring, positioning the platform as a promising tool for early cancer diagnostics and point-of-care applications.

## **Conclusion**

The research conclusively establishes a high-performance nano-hybrid composite (NHC), engineered through the integration of self-assembled 1D TiO<sub>2</sub> nanowires onto hBNNS nanosheets, as a powerful immunoelectrode platform for carcinoembryonic antigen (CEA) detection. Each step of the fabrication process was strategically engineered and thoroughly validated by FT-IR spectroscopy and electrochemical characterization, ensuring precise control over structural and functional enhancements. The hierarchical design leveraged the high surface area of hBNNS to support TiO<sub>2</sub> nanowires, creating a synergistic architecture with extensive catalytic active sites, tunable chemical groups, and interconnected porosity that enabled efficient antibody immobilization and enhanced antigen binding affinity. The subsequent incorporation of TiO<sub>2</sub> nanowires further boosted electrochemical performance by facilitating rapid charge transfer, lowering redox activation barriers, and distributing reactive sites across multiple structural scales. This optimized configuration enabled the biosensor to achieve an ultralow limit of detection (0.035 pg/mL) and a broad linear response range (0-25 ng/mL), establishing its diagnostic superiority in early cancer biomarker monitoring. Furthermore, immunoelectrode demonstrated the reproducibility, stability over extended storage periods (maintaining performance for more than 60 days at 4 °C), and remarkable resistance to interference from biomolecules such as CRP, ET-1, and glucose, thereby ensuring robust signal fidelity in complex biological samples. Recovery analysis in spiked human serum further validated its translational capability, bridging the gap between laboratory innovation and clinical application. Taken together, this work positions the TiO2-hBNNS-based NHC as a transformative biosensing platform that not only advances precision cancer diagnostics but also lays the foundation for versatile, multifunctional biosensor systems adaptable to diverse biomedical applications.

#### References

- [1] Z. Ren, Y. Guo, C.-H. Liu, P.-X. Gao, Hierarchically nanostructured materials for sustainable environmental applications, Frontiers in Chemistry, Volume 1 2013 (2013).
- [2] B. Zhang, J. Sun, U. Salahuddin, P.-X. Gao, Hierarchical and scalable integration of nanostructures for energy and environmental applications: a review of processing, devices, and economic analyses, Nano Futures, 4 (2020) 012002.
- [3] C.A. Amarnath, S.S. Nanda, G.C. Papaefthymiou, D.K. Yi, U. Paik, Nanohybridization of Low-Dimensional Nanomaterials: Synthesis, Classification, and Application, Critical Reviews in Solid State and Materials Sciences, 38 (2013) 1-56.

- [4] S. Reghunath, D. Pinheiro, S.D. Kr, A review of hierarchical nanostructures of TiO2: Advances and applications, Applied Surface Science Advances, 3 (2021) 100063.
- [5] K. Hashimoto, H. Irie, A. Fujishima, TiO2 Photocatalysis: A Historical Overview and Future Prospects, Japanese Journal of Applied Physics, 44 (2005) 8269.
- [6] X. Chen, A. Selloni, Introduction: Titanium Dioxide (TiO2) Nanomaterials, Chemical Reviews, 114 (2014) 9281-9282.
- [7] T. Zhu, J. Li, Q. Wu, Construction of TiO2 Hierarchical Nanostructures from Nanocrystals and Their Photocatalytic Properties, ACS Applied Materials & Interfaces, 3 (2011) 3448-3453.
- [8] U. Diebold, Structure and properties of TiO2 surfaces: a brief review, Applied Physics A, 76 (2003) 681-687.
- [9] D. Dambournet, I. Belharouak, K. Amine, Tailored Preparation Methods of TiO2 Anatase, Rutile, Brookite: Mechanism of Formation and Electrochemical Properties, Chemistry of Materials, 22 (2010) 1173-1179.
- [10] K.M. Glassford, N. Troullier, J. Martins, J.R. Chelikowsky, Electronic and structural properties of TiO2 in the rutile structure, Solid State Communications, 76 (1990) 635-638.
- [11] R. Asahi, Y. Taga, W. Mannstadt, A.J. Freeman, Electronic and optical properties of anatase \${\mathrm{TiO}}} {2}\$, Physical Review B, 61 (2000) 7459-7465.
- [12] M.H. Samat, M.F.M. Taib, O.H. Hassan, M.Z.A. Yahya, A.M.M. Ali, Structural, electronic and optical properties of brookite phase titanium dioxide, Materials Research Express, 4 (2017) 044003.
- [13] W. Jin, W. Zhang, Y. Gao, G. Liang, A. Gu, L. Yuan, Surface functionalization of hexagonal boron nitride and its effect on the structure and performance of composites, Applied Surface Science, 270 (2013) 561-571.
- [14] L.H. Li, Y. Chen, Atomically thin boron nitride: unique properties and applications, Advanced Functional Materials, 26 (2016) 2594-2608.
- [15] M.J. Molaei, M. Younas, M. Rezakazemi, A Comprehensive Review on Recent Advances in Two-Dimensional (2D) Hexagonal Boron Nitride, ACS Applied Electronic Materials, 3 (2021) 5165-5187.
- [16] N. Kaur, M. Singh, A. Moumen, G. Duina, E. Comini, 1D Titanium Dioxide: Achievements in Chemical Sensing, Materials, 13 (2020) 2974.
- [17] S.K. Vashist, Comparison of 1-Ethyl-3-(3-Dimethylaminopropyl) Carbodiimide Based Strategies to Crosslink Antibodies on Amine-Functionalized Platforms for Immunodiagnostic Applications, Diagnostics, 2 (2012) 23-33.
- [18] V. Sai Phani Kumar, M. Verma, P.A. Deshpande, On interaction of arginine, cysteine and guanine with a nano-TiO2 cluster, Computational Biology and Chemistry, 86 (2020) 107236.
- [19] C.E. Giacomelli, M.J. Avena, C.P. De Pauli, Aspartic acid adsorption onto TiO2 particles surface. Experimental data and model calculations, Langmuir, 11 (1995) 3483-3490.
- [20] A.D. Roddick-Lanzilotta, P.A. Connor, A.J. McQuillan, An In Situ Infrared Spectroscopic Study of the Adsorption of Lysine to TiO2 from an Aqueous Solution, Langmuir, 14 (1998) 6479-6484.
- [21] L. Mao, Y. Wang, Y. Zhong, J. Ning, Y. Hu, Microwave-assisted deposition of metal sulfide/oxide nanocrystals onto a 3D hierarchical flower-like TiO2 nanostructure with improved photocatalytic activity, Journal of Materials Chemistry A, 1 (2013) 8101-8104.
- [22] H. Xu, G. Li, G. Zhu, K. Zhu, S. Jin, Enhanced photocatalytic degradation of rutile/anatase TiO2 heterojunction nanoflowers, Catalysis Communications, 62 (2015) 52-56.
- [23] R. Kaplan, B. Erjavec, G. Dražić, J. Grdadolnik, A. Pintar, Simple synthesis of anatase/rutile/brookite TiO2 nanocomposite with superior mineralization potential for photocatalytic degradation of water pollutants, Applied Catalysis B: Environmental, 181 (2016) 465-474.
- [24] K. Sharma, N.K. Puri, Enhanced electrochemical performance of hydrothermally exfoliated hexagonal boron nitride nanosheets for applications in electrochemistry, Journal of The Electrochemical Society, 168 (2021) 056512.

- [25] K. Ashok Kumar, J. Manonmani, J. Senthilselvan, Effect on interfacial charge transfer resistance by hybrid co-sensitization in DSSC applications, Journal of Materials Science: Materials in Electronics, 25 (2014) 5296-5301.
- [26] K. Yano, Y. Morimoto, Optical absorption properties of TiO2-doped silica glass in UV–VUV region, Journal of Non-Crystalline Solids, 349 (2004) 120-126.
- [27] N. Hosaka, T. Sekiya, C. Satoko, S. Kurita, Optical Properties of Single-Crystal Anatase TiO<SUB>2</SUB>, Journal of the Physical Society of Japan, 66 (1997) 877-880.
- [28] L. Hua Li, Y. Chen, B.-M. Cheng, M.-Y. Lin, S.-L. Chou, Y.-C. Peng, Photoluminescence of boron nitride nanosheets exfoliated by ball milling, Applied Physics Letters, 100 (2012) 261108.
- [29] C.A. Melendres, A. Narayanasamy, V.A. Maroni, R.W. Siegel, Raman spectroscopy of nanophase TiO2, Journal of Materials Research, 4 (1989) 1246-1250.
- [30] I. Stenger, L. Schué, M. Boukhicha, B. Berini, B. Plaçais, A. Loiseau, J. Barjon, Low frequency Raman spectroscopy of few-atomic-layer thick hBN crystals, 2D Materials, 4 (2017) 031003.
- [31] T. Lopez, E. Sanchez, P. Bosch, Y. Meas, R. Gomez, FTIR and UV-Vis (diffuse reflectance) spectroscopic characterization of TiO2 sol-gel, Materials Chemistry and Physics, 32 (1992) 141-152.
- [32] H. Harrison, J.T. Lamb, K.S. Nowlin, A.J. Guenthner, K.B. Ghiassi, A.D. Kelkar, J.R. Alston, Quantification of hexagonal boron nitride impurities in boron nitride nanotubes via FTIR spectroscopy, Nanoscale Advances, 1 (2019) 1693-1701.
- [33] D. Zheng, J. Yang, Z. Zheng, M. Peng, J. Chen, Y. Chen, W. Gao, A highly sensitive photoelectrochemical biosensor for CEA analysis based on hollow NiS@ NiO/TiO2 composite with typal pn heterostructure, Talanta, 246 (2022) 123523.
- [34] J. Li, Y. Zhang, X. Kuang, Z. Wang, Q. Wei, A network signal amplification strategy of ultrasensitive photoelectrochemical immunosensing carcinoembryonic antigen based on CdSe/melamine network as label, Biosensors and Bioelectronics, 85 (2016) 764-770.
- [35] S. Aslan, Ü. Anik, Development of TiO2 and Au nanocomposite electrode as CEA immunosensor transducer, Electroanalysis, 26 (2014) 1373-1381.
- [36] L. Li, T. Wang, Y. Zhang, C. Xu, L. Zhang, X. Cheng, H. Liu, X. Chen, J. Yu, Editable TiO2 nanomaterial-modified paper in situ for highly efficient detection of carcinoembryonic antigen by photoelectrochemical method, ACS applied materials & interfaces, 10 (2018) 14594-14601.
- [37] K.-J. Huang, Z.-W. Wu, Y.-Y. Wu, Y.-M. Liu, Electrochemical immunoassay of carcinoembryonic antigen based on TiO2–graphene/thionine/gold nanoparticles composite, Canadian Journal of Chemistry, 90 (2012) 608-615.
- [38] H. Yang, R. Yuan, Y. Chai, L. Mao, H. Su, W. Jiang, M. Liang, Electrochemical immunosensor for detecting carcinoembryonic antigen using hollow Pt nanospheres-labeled multiple enzyme-linked antibodies as labels for signal amplification, Biochemical engineering journal, 56 (2011) 116-124.
- [39] H. Wang, Y. Wang, Y. Zhang, Q. Wang, X. Ren, D. Wu, Q. Wei, Photoelectrochemical immunosensor for detection of carcinoembryonic antigen based on 2D TiO2 nanosheets and carboxylated graphitic carbon nitride, Scientific reports, 6 (2016) 27385.
- [40] Y. Zhang, R. Yuan, Y. Chai, Y. Xiang, X. Qian, H. Zhang, Sensitive label-free immunoassay of carcinoembryonic antigen based on Au–TiO2 hybrid nanocomposite film, Journal of colloid and interface science, 348 (2010) 108-113.
- [41] Y. Wang, G. Zhao, Y. Zhang, B. Du, Q. Wei, Ultrasensitive photoelectrochemical immunosensor based on Cu-doped TiO2 and carbon nitride for detection of carcinoembryonic antigen, Carbon, 146 (2019) 276-283.
- [42] K. Sharma, N.K. Puri, B. Singh, An efficient electrochemical nano-biosensor based on hydrothermally engineered ultrathin nanostructures of hexagonal boron nitride nanosheets for label-free detection of carcinoembryonic antigen, Applied Nanoscience, (2023) 1-14.

[43] K. Sharma, N.K. Puri, B. Singh, Fabrication of rGO-decorated hBNNS hybrid nanocomposite via organic–inorganic interfacial chemistry for enhanced electrocatalytic detection of carcinoembryonic antigen, Analytical and Bioanalytical Chemistry, (2024) 1-17. [44] K. Sharma, N.K. Puri, B. Singh, Self-assembled nano-hybrid composite based on Cu/CuXO nanoflower decorated onto hBNNS for high-performance and ultra-sensitive electrochemical detection of CEA biomarker, Bioelectrochemistry, 165 (2025) 108993.

# Chapter 8

# **Summary and Future Scope**

This thesis comprehensively investigated the synthesis, characterization, electrochemical applications of hexagonal boron nitride nanosheets (hBNNS) and their nano-hybrid composites for the development of ultrasensitive carcinoembryonic antigen (CEA) biosensors. Pristine hBNNS, despite their exceptional physicochemical stability, dielectric nature, and atomically smooth layered structure, suffer from intrinsic chemical inertness and poor charge-transfer capability, which hinder their direct utility in electrochemical biosensing. To address these limitations, this work systematically engineered hybrid interfaces of hBNNS with layered, non-layered, and one-dimensional materials, thereby enhancing their electrochemical performance through synergistic interactions. Specifically, reduced graphene oxide (rGO, 2D) was employed to improve conductivity and electron mobility, copper/copper oxide (Cu/CuXO, 3D) introduced abundant catalytic sites and redox activity, while titanium dioxide (TiO<sub>2</sub>, 1D) contributed high surface area and chemical stability. The integration of these materials with hBNNS created unique nano-interfaces that facilitated efficient charge transport, defect-mediated active site generation, and improved biomolecule immobilization. These hybrid architectures collectively overcame the inherent challenges of pristine hBN, enabling enhanced sensitivity, selectivity, and stability of CEA biosensors. Electrochemical studies confirmed significant improvement in charge-transfer kinetics, reduced interfacial resistance, and amplified detection response in hBNNS-based nano-hybrids compared to pristine hBN. The resulting biosensor platforms exhibited strong potential for reliable cancer biomarker detection with superior performance metrics. In conclusion, this thesis establishes hBNNS nanohybrid composites as a promising class of multifunctional materials for advanced biosensing applications. The insights gained not only highlight the versatility of hybrid material engineering but also provide a framework for future nano-biosensor development across diverse biomedical domains.

# **Summary**

## Chapter 1

This chapter address the critical global health challenge posed by cancer, with particular emphasis on the prevalence and mortality associated with lung cancer. The urgent necessity for innovative diagnostic tools for early detection is underscored, highlighting the transformative role of biosensors in clinical diagnostics. The chapter elaborates on the fundamental components of nano-biosensors, including bio-recognition elements, nano-interface matrices for protein immobilization, transducers classifications, and signal display mechanisms. It emphasizes the revolutionary impact of nanoscience and nanotechnology in developing detection platforms with enhanced sensitivity, specificity, and stability. A comprehensive literature review categorizes nanomaterials according to their dimensionality, with special focus on two-dimensional (2D) nanomaterials due to their unique physicochemical properties. Hexagonal boron nitride nanosheets (hBNNS) are identified as a promising nano-interface material, offering structural robustness, chemical inertness, and biocompatibility. However, challenges in achieving stable, scalable, and cost-effective fabrication of nano-interface matrices for biosensors remain a bottleneck in clinical translation. This chapter establishes the rationale for advancing nano-hybrid composites as a strategic pathway to overcome the inherent limitations of pristine hBNNS. By integrating layered and non-layered materials with hBNNS, it becomes possible to significantly augment electroanalytical performance, thereby paving the way for the development of clinically viable biosensing devices. The motivation of this chapter lies in defining a clear and compelling framework for exploring the synthesis, structural optimization, and application of hBNNS-based nano-hybrids, ultimately addressing unmet clinical needs in early cancer detection through robust biosensor technologies.

#### Chapter 2

This chapter provides a critical review of synthesis methodologies for fabricating inorganic layered nanomaterials with two-dimensional morphologies, classifying them broadly into bottom-up and top-down techniques. In the context of developing scalable, facile, cost-effective, and high-quality hexagonal boron nitride nanosheets (hBNNS) at relatively low temperatures, the hydrothermal method is presented as a particularly effective technique. Its capacity for precise morphological control and suitability for composite formation is emphasized. Additional synthesis strategies, including the polyol method, chemical exfoliation, and sol-gel synthesis, are also discussed, with an emphasis on their ability to tailor nanostructures for specific applications. This chapter further elaborates on electrode preparation methodologies, with detailed emphasis on the stepwise fabrication of nano-interface matrices onto indium tin oxide (ITO) using electrophoretic deposition (EPD). The optimization immunoelectrodes for clinical use is also systematically presented. A comprehensive overview of material characterization techniques is included, spanning spectroscopic methods (XRD, UV-Vis, Raman, FTIR), imaging methods (SEM, TEM, AFM, EDAX), thermal analysis (TGA), and cytotoxicity evaluation. The significance of these techniques in elucidating the crystal structure, morphology, electronic properties, chemical composition, and biocompatibility of 2D nanomaterials and their composites is emphasized. Additionally, the chapter provides detailed insights into electrochemical characterization techniques such as cyclic voltammetry (CV), differential pulse voltammetry (DPV), and electrochemical impedance spectroscopy (EIS). These methods are critically analyzed for their role in monitoring and validating the functional performance of fabricated nano-biosensors, thereby ensuring their applicability and reliability in clinical diagnostics.

#### Chapter 3

This chapter focuses on hexagonal boron nitride (hBN), a Group III–V layered material often termed "white graphene." Despite its promising features, hBN faces intrinsic challenges, including scalable synthesis, interlayer exfoliation, limited surface functionality, and restricted bandgap tunability. Addressing these limitations, this study systematically optimizes the two-dimensional morphology of hBN nanosheets (hBNNS) to enhance both intrinsic and extrinsic properties, establishing a solid foundation for their application in biosensing. Structural and surface integrity were comprehensively investigated using advanced characterization techniques: X-ray diffraction (XRD) for crystallinity, Raman and UV-Visible spectroscopy for vibrational and optical transitions, and microscopy methods (SEM, TEM, AFM) for morphological and nanoscale analysis. Chemical bonding interactions were further examined using Fourier-transform infrared spectroscopy (FTIR). To translate these structural improvements into electrochemical functionality, hBNNS/ITO electrodes were fabricated using electrophoretic deposition (EPD). Electrochemical analyses revealed that optimized hBNNS exhibited a 69.96% enhancement in redox peak current and a 71.04% increase in electroactive surface area compared to bulk hBN. Additionally, the nanosheets demonstrated reduced charge transfer resistance and improved Warburg admittance, highlighting their enhanced electroanalytical capabilities. These findings confirm that engineered hBNNS with optimized morphology can effectively overcome the limitations of bulk hBN, making them highly promising for advanced electroanalytical and biosensing applications. This chapter thus establishes hBNNS as a viable platform for integration into next-generation biosensors, providing both structural robustness and electrochemical efficiency critical for clinical utility.

#### Chapter 4

This chapter highlights the successful engineering of ultrathin hexagonal boron nitride nanosheets (hBNNS), demonstrating their potential as highly effective nano-interfaces for biosensing applications. With their exceptional specific surface area, efficient mass transport channels, and inherent biocompatibility, hBNNS are positioned as a nextgeneration material for biosensor development. The chapter presents a detailed investigation into the electroanalytical performance of hBNNS for the label-free detection of carcinoembryonic antigen (CEA), a clinically significant cancer biomarker. Biocompatibility was confirmed through cytotoxicity studies using MTT assays on HEK 293 human cell lines, validating their safe application in biomedical environments. Structural, morphological, and optical properties of hBNNS were thoroughly characterized using XRD, SEM, TEM, Raman spectroscopy, and UV-Vis analysis. The fabrication of hBNNS/ITO micro-electrodes was carried out via electrophoretic deposition (EPD), providing uniform and stable platforms for subsequent antibody immobilization. A robust strategy for anchoring monoclonal anti-CEA antibodies was employed, utilizing EDC-NHS chemistry and BSA blocking to ensure specificity and stability. The fabricated hBNNS/ITO biosensor exhibited a highly sensitive response, with a sensitivity of 24.84 µA mL/ng/cm<sup>2</sup>, a remarkably low

limit of detection (22.5 pg/mL), and a wide linear detection range (0–50 ng/mL), validated by a correlation coefficient of 0.99988. Furthermore, the sensor demonstrated negligible cross-reactivity, long shelf life, and excellent recovery in human serum samples. These results highlight the strong clinical applicability of hBNNS-based biosensors, establishing them as promising candidates for reliable and precise early cancer detection.

#### Chapter 5

This chapter focuses on addressing the inherent limitations of pristine hexagonal boron nitride nanosheets (hBNNS) through the strategic development of nano-hybrid composites. While hBNNS offer remarkable chemical stability, biocompatibility, and structural robustness, their low electrical conductivity and chemical inertness restrict their direct electrochemical applications. To overcome these challenges, synergistic hybridization with layered, one-dimensional, and three-dimensional nanostructures is introduced as an effective pathway to enhance their functional capabilities. Reduced graphene oxide (rGO), titanium dioxide (TiO<sub>2</sub>), and copper/copper oxide (Cu/CuO) were selected as complementary materials to engineer layered, 1D, and 3D nanohybrids, respectively. Each hybridization strategy was designed to exploit host-guest chemistry, defect induction, and interfacial coupling effects, thereby augmenting charge transfer kinetics, enhancing electroactive surface area, and improving biomolecule immobilization efficiency. The synthesis of these hybrid nanostructures was systematically optimized through hydrothermal and solvothermal methods, ensuring morphological integrity, scalable fabrication, and reproducibility. Comprehensive characterization using XRD, TEM, Raman, and FTIR confirmed the structural compatibility and successful integration of hBNNS with the chosen nanomaterials. Electrochemical analyses, including cyclic voltammetry and electrochemical impedance spectroscopy, revealed substantial improvements in redox activity, conductivity, and charge transfer dynamics compared to pristine hBNNS. The hybrid systems thus developed not only overcome the insulating limitations of hBNNS but also provide a multifunctional platform for biosensing applications. This chapter establishes nano-hybrid engineering as a transformative strategy to advance hBNNS from a structurally robust but electrochemically inert material to a highly active and versatile interface suitable for clinical biosensing technologies.

#### Chapter 6

This chapter presents a detailed evaluation of the electrochemical biosensing performance of hBNNS-based nano-hybrid composites for carcinoembryonic antigen (CEA) detection. The fabricated hybrids—hBNNS/rGO (2D–2D), hBNNS/TiO<sub>2</sub> (2D–1D), and hBNNS/Cu–CuO (2D–3D)—were systematically investigated to determine their role in improving electrochemical response, stability, and selectivity. Each hybrid composite demonstrated unique contributions to enhancing biosensor performance. The hBNNS/rGO composite exploited high electrical conductivity and large surface area, resulting in efficient electron transport and antibody anchoring. The hBNNS/TiO<sub>2</sub> hybrid benefitted from excellent charge mobility and photocatalytic activity, enabling faster redox reactions and stable immobilization of biomolecules. Meanwhile, the hBNNS/Cu–CuO hybrid offered a combination of metallic conductivity and catalytic activity, further amplifying signal response. Fabricated electrodes were characterized by cyclic voltammetry (CV), differential pulse voltammetry (DPV), and

electrochemical impedance spectroscopy (EIS), with results confirming significant improvements in electroactive surface area, reduced charge transfer resistance, and enhanced sensitivity compared to pristine hBNNS. Functionalized electrodes demonstrated remarkable detection performance for CEA, achieving ultralow limits of detection, broad linear response ranges, and high correlation coefficients. Furthermore, the biosensors exhibited excellent reproducibility, minimal cross-reactivity, and robust stability over extended storage, affirming their suitability for clinical applications. This chapter underscores the effectiveness of nano-hybrid engineering in overcoming the electrochemical limitations of hBNNS, establishing these composites as high-performance transducer platforms for early cancer biomarker detection. The integration of complementary nanomaterials not only enhances the intrinsic properties of hBNNS but also drives translational potential in biomedical diagnostics.

## Chapter 7

This chapter consolidates the findings of the research, providing a comprehensive conclusion and highlighting the broader implications of the study. The synthesis and systematic optimization of hexagonal boron nitride nanosheets (hBNNS) have demonstrated their structural robustness, biocompatibility, and potential as biosensing interfaces. However, the intrinsic insulating nature of pristine hBNNS was shown to restrict their direct electrochemical applicability. To address this, the integration of hBNNS with complementary nanostructures, including reduced graphene oxide, titanium dioxide, and copper/copper oxide, was strategically engineered to create layered, one-dimensional, and three-dimensional nano-hybrid composites. These hybrids successfully enhanced the electroanalytical properties of hBNNS by improving charge transfer kinetics, increasing electroactive surface area, and facilitating efficient biomolecule immobilization. The hBNNS-based nano-hybrid biosensors fabricated in work exhibited highly sensitive, selective, and stable detection carcinoembryonic antigen (CEA), achieving low limits of detection, broad linear ranges, and high reproducibility, thereby meeting essential clinical diagnostic requirements. The findings underscore the transformative role of nano-hybrid engineering in advancing hBNNS from a chemically inert material to a highly functional biosensing platform. The study not only establishes a foundation for future research on inorganic layered materials but also paves the way for the development of next-generation electrochemical biosensors for early cancer detection. This work contributes significantly to the growing field of nano-biosensing by offering new insights into material hybridization strategies, practical biosensor fabrication, and translational potential in clinical diagnostics.

### **Comparison Table for Sensing Performance**

Sensing Platform	Sensing Matrix	Detection Technique	Linear Range (ng/mL)	Limit of Detection	Sensitivity	Stability
Only 2D Nanosheets	h-BNNS	Electrochemical	0 – 10	22.5 pg/mL	24.84 μA·mL·ng <sup>-</sup>	5 weeks
2D-2D Nanosheets	rGO- hBNNS	Electrochemical	0 - 15	5.47 pg/mL	9. 65 μA·mL·ng <sup>-</sup> <sup>1</sup> ·cm <sup>-2</sup>	8 weeks
3D Nanoflowers- 2D Nanosheets	Cu/CuXO- hBNNS	Electrochemical	0 - 25	3.22 pg/mL	8. 04 μA·mL·ng <sup>-</sup> 1·cm <sup>-2</sup>	60 days
1D Nanowires- 2D Nanosheets	TiO2- hBNNS	Electrochemical	0 - 25	0.035 pg/mL	11.2 µA·mL·ng <sup>-</sup> <sup>1</sup> ·cm <sup>-2</sup>	60 days

#### Conclusion

The hexagonal boron nitride nanosheets (hBNNS) and their nano-hybrid composites-based nano-biosensors were synthesized using a hydrothermal method, which offers an efficient, facile, scalable, and cost-effective route for material fabrication. The hydrothermal process ensures controlled growth of nanostructures under moderate temperature, pressure and precise precursor concentration, facilitating homogeneous dispersion of dopants or hybrid nanostructures, precise tuning of morphology, uniform particle size distribution and reproducible synthesis outcomes without requiring complex instrumentation. Also, the use of inexpensive precursors, and analytical-grade reagents further reduces the overall synthesis cost, making the process suitable for large-scale production. This method minimizes process variability and enhances material uniformity, which is critical for achieving reproducible sensor performance. Additionally, the synthesis carried out in aqueous-based reaction media minimizes the use of hazardous solvents, making the fabrication process environmentally benign and economically viable for large-scale production.

The microelectrodes were fabricated through electrophoretic deposition (EPD) technique, a versatile, reliable and reproducible technique that enables uniform coating of nanomaterials on conductive substrates with precise control over thickness and morphology. EPD is particularly advantageous due to its low equipment requirements, ease of operation, and compatibility with various substrate geometries. In addition, EPD-based fabrication is economically viable, time-efficient, and suitable for large-scale microelectrode production. The integration of hBNNS and their nano-hybrid composites onto conductive surfaces of microelectrodes with excellent control over film thickness and homogeneity through EPD provided excellent adhesion, uniformity, and enhanced electron transfer characteristics, ensuring excellent reproducibility across multiple electrodes, long-term stability, and durability of the fabricated sensors. This method is particularly advantageous because it does not require complex instrumentation in lithography technique or high-vacuum environments, which further strengthens the cost-effectiveness. Moreover, EPD allows easy tuning of deposition

parameters such as applied voltage, deposition time, and suspension concentration to optimize the film's electrochemical properties and ensure sensor consistency.

In terms of reliability and repeatability of measurements, the fabricated hBNNS-based nano-biosensors demonstrated stable and reproducible electrochemical responses, confirming the robustness of intrinsic properties of hBN together with key role of the hydrothermal synthesis and EPD-based microelectrode fabrication processes. The sensors showed minimal variation in signal intensity across repeated measurements, highlighting the stability of the electrode surface and the uniformity of material deposition. Moreover, the hydrothermal synthesis coupled with EPD-based electrode fabrication demonstrates a reproducible workflow that maintains structural integrity and electrochemical performance over multiple testing cycles. Overall, the adopted methods collectively ensure a cost-efficient, reliable, and scalable fabrication strategy, making these hBNNS-based nano-hybrid sensors promising candidates for practical biosensing applications.

The pristine hBNNS exhibited excellent electrochemical performance, characterized by stable electron mobility and remarkable charge transfer kinetics, owing to its atomically thin structure and wide bandgap. This superior electron mobility arises from its atomically thin layered structure and wide bandgap, which together promote stable and rapid redox reactions at the electrode–electrolyte interface. Their atomically thin structure and planar  $\pi$ -conjugated domains facilitate rapid electron transport across the surface and between the electrode and the analyte. This leads to amplified signal response for changes in analyte concentration. Hence, the slope of the calibration curve (signal vs. concentration) is steep, indicating high sensitivity. Such behaviour is advantageous for maintaining signal stability and minimizing background noise during electrochemical measurements, demonstrating its intrinsic potential as a robust sensing material.

However, despite its outstanding charge transfer capabilities, pristine hBNNS demonstrated limited biomolecule immobilization capacity, which ultimately resulted in a relatively higher limit of detection (LOD) compared to its hybrid counterparts. This limitation is primarily attributed to the chemically inert nature of the hBN surface, which offers few active sites for covalent or non-covalent anchoring of biomolecules such as antibodies or enzymes. The lack of functional surface groups restricts the density and orientation of biomolecule attachment, thereby reducing the overall sensitivity and efficiency of biorecognition events. LOD depends not only on sensitivity but also on baseline noise, signal reproducibility, and target capture efficiency. In this study, we observed hBNNS demonstrated high sensitivity as each binding event produces a strong signal, yet have a relatively high LOD due to poor surface functionalization or low affinity toward the analyte.

The pristine hexagonal boron nitride nanosheets (hBNNS) were further modified to form nanohybrid composites by integrating them with both layered (2D-rGO) and non-layered materials (1D-TiO<sub>2</sub> nanowires and 3D-Cu/Cu<sub>X</sub>O nanoflowers), with the primary objective of enhancing biomolecule immobilization efficiency by overcome their inherent limitations of surface functionalization in hBNNS. Despite atomically smooth surface, biocompatibility and excellent chemical stability in hBNNS, their intrinsic chemical inertness and limited surface functionalization sites restrict the

effective anchoring of biomolecules essential for biosensing applications. This limited functionalization capacity restricts the direct antibodies immobilization, which is essential for achieving selective and efficient biosensing. This challenge was address by introducing layered (such as reduced graphene oxide) and non-layered (TiO<sub>2</sub> nanowires or Cu/Cu<sub>X</sub>O nanostructures) materials, the surface of hBNNS was engineered to include additional functional moieties—hydroxyl, carboxyl, and oxygenvacancy sites was employed to form heterostructured composites with tailored surface chemistry and enhanced physicochemical characteristics that provide a greater number of active binding sites for biomolecule conjugation.

# **Future Prospects**

The rapid advancements in two-dimensional (2D) nanomaterials-based composites have created transformative opportunities in the field of cancer diagnostics, offering both immediate clinical relevance and expansive future research directions. Among these materials, hexagonal boron nitride nanosheets (hBNNS) have emerged as a highly promising inorganic layered system due to their exceptional chemical stability, large surface area, dielectric properties, and biocompatibility. While their potential in biosensing has been effectively demonstrated, their scope extends far beyond cancer detection, positioning them as versatile materials capable of driving innovations across multiple technological domains.

In the domain of energy storage and harvesting, hBNNS-based composites present remarkable opportunities for integration into advanced devices such as supercapacitors, rechargeable batteries, and hybrid energy storage systems. Their outstanding dielectric properties, combined with efficient ionic transport mechanisms, enable rapid charge—discharge cycles and enhanced storage capacities. Furthermore, their ability to withstand harsh thermal and chemical environments makes them particularly suitable for high-performance and long-lasting energy storage solutions, addressing critical challenges in sustainable energy technologies. This adaptability positions hBNNS as a key component for the next generation of portable electronics, electric vehicles, and renewable energy systems.

Beyond energy applications, hBNNS serve as highly effective sensing matrices capable of advancing the design of next-generation nanostructured platforms. Their compatibility with covalent organic frameworks (COFs), metal—organic frameworks (MOFs), and functional polymers enables the creation of hybrid architectures with superior chemical reactivity, porosity, and functional tunability. For instance, hBNNS-COF and hBNNS-MOF composites can offer highly selective molecular recognition and controlled electron transport pathways, features that are essential for the fabrication of ultrasensitive, label-free electrochemical and piezoelectric biosensors. These developments have the potential to revolutionize biomedical diagnostics by achieving early detection of cancer biomarkers with unprecedented precision and reliability.

Furthermore, the integration of hBNNS with nano-engineered hybrid systems is expected to redefine the landscape of point-of-care diagnostics and flexible electronics. Their tuneable surface chemistry allows for the immobilization of biomolecules with high specificity, while their structural robustness supports stable performance under flexible and miniaturized device configurations. This adaptability creates opportunities

for wearable biosensors, implantable medical devices, and portable diagnostic systems that combine rapid detection with user-friendly interfaces. Such innovations hold immense promise in decentralizing healthcare by enabling real-time, on-site monitoring of cancer and other chronic diseases.

In the realm of next-generation energy technologies, hBNNS composites are poised to revolutionize energy storage and harvesting devices. Their capacity to endure extreme operating environments makes them ideal for high-performance supercapacitors, solid-state batteries, and hybrid devices that integrate energy storage with energy conversion. These features are particularly vital for renewable energy applications, electric vehicles, and space exploration, where reliability and durability are paramount.

hBNNS-based systems also hold immense promise for environmental monitoring and remediation. Functionalized hBNNS hybrids can act as highly selective platforms for detecting environmental toxins, heavy metals, and hazardous gases with high sensitivity. Their chemical inertness and adaptability further allow them to serve as catalytic supports for pollutant degradation or water purification, contributing to sustainable environmental management.

Another critical prospect lies in wearable and implantable bioelectronics. With the rise of flexible and miniaturized devices, hBNNS composites can be seamlessly incorporated into smart textiles, skin-interfaced electronics, and implantable diagnostic devices. Their mechanical resilience, coupled with excellent biocompatibility, ensures stable performance in continuous monitoring of vital parameters, offering transformative possibilities in preventive healthcare and human—machine interfacing.

In addition, the field of neuromorphic and quantum technologies represents an exciting opportunity. Due to their unique dielectric and insulating properties, hBNNS can act as reliable substrates and insulating barriers in neuromorphic computing devices and quantum sensors. Their integration with other 2D materials, such as graphene and transition metal dichalcogenides, could accelerate the development of high-performance quantum devices, thereby advancing information processing and communication technologies.

Finally, the synergistic use of hBNNS in multifunctional hybrid architectures, such as covalent organic frameworks (COFs), metal—organic frameworks (MOFs), and polymer-based piezoelectric platforms, will drive innovations in cross-disciplinary applications. These hybrid composites will not only enhance biosensing sensitivity and selectivity but also contribute to multifunctional devices that can simultaneously sense, store, and convert energy.

Looking ahead, the future scope of hBNNS-based composites is defined by their capacity to serve as multifunctional materials bridging healthcare, energy, and environmental applications. Their role in developing multifunctional biosensing platforms can be further extended by integrating them with artificial intelligence and machine learning-driven data analytics, leading to smart diagnostic systems capable of predictive and personalized healthcare. Simultaneously, their utility in energy systems aligns with the global pursuit of sustainable technologies, allowing cross-disciplinary solutions that address both medical and environmental challenges.

In conclusion, the future prospects of hBNNS-based composites extend far beyond cancer diagnostics, encompassing healthcare, energy, environment, wearable technologies, and advanced computing. Their integration into next-generation platforms signifies a paradigm shift where materials science, nanotechnology, and biomedical engineering converge to address global challenges. With continuous advancements in nano-engineering and hybrid composite design, hBNNS stands positioned to define the future of sustainable, intelligent, and multifunctional technologies.